

CERN-ACC-Note-2020-0002  
Version v1.0  
Geneva, February 21, 2020



# The Large Hadron-Electron Collider at the HL-LHC

LHeC Study Group



To be submitted to J.Phys. G

## LHeC Study Group

P. Agostini<sup>1</sup>, H. Aksakal<sup>2</sup>, H. Alan<sup>3</sup>, S. Alekhin<sup>4,5</sup>, P. P. Allport<sup>6</sup>, N. Andari<sup>7</sup>, K. D. J. Andre<sup>8,9</sup>, D. Angal-Kalinin<sup>10,11</sup>, S. Antusch<sup>12</sup>, L. Aperio Bella<sup>13</sup>, L. Apolinario<sup>14</sup>, R. Apsimon<sup>15,11</sup>, A. Apyan<sup>16</sup>, G. Arduini<sup>9</sup>, V. Ari<sup>17</sup>, A. Armbruster<sup>9</sup>, N. Armesto<sup>1</sup>, B. Auchmann<sup>9</sup>, K. Aulenbacher<sup>18,19</sup>, G. Azuelos<sup>20</sup>, S. Backovic<sup>21</sup>, I. Bailey<sup>15,11</sup>, S. Bailey<sup>22</sup>, F. Balli<sup>7</sup>, S. Behera<sup>23</sup>, O. Behnke<sup>24</sup>, I. Ben-Zvi<sup>25</sup>, J. Bernauer<sup>26</sup>, S. Bertolucci<sup>9,27</sup>, S. S. Biswal<sup>28</sup>, J. Blümlein<sup>24</sup>, A. Bogacz<sup>29</sup>, M. Bonvini<sup>30</sup>, M. Boonekamp<sup>31</sup>, F. Bordry<sup>9</sup>, G. R. Boroun<sup>32</sup>, L. Bottura<sup>9</sup>, S. Bousson<sup>7</sup>, A. O. Bouzas<sup>33</sup>, C. Bracco<sup>9</sup>, J. Bracinik<sup>6</sup>, D. Britzger<sup>34</sup>, S. J. Brodsky<sup>35</sup>, C. Bruni<sup>7</sup>, O. Brüning<sup>9</sup>, H. Burkhardt<sup>9</sup>, I. T. Cakir<sup>36</sup>, O. Cakir<sup>17</sup>, R. Calaga<sup>9</sup>, A. Caldwell<sup>34</sup>, A. Caliskan<sup>37</sup>, S. Camarda<sup>9</sup>, N. C. Catalan-Lasheras<sup>9</sup>, K. Cassou<sup>38</sup>, J. Cepila<sup>39</sup>, V. Cetinkaya<sup>17</sup>, V. Chetvertkova<sup>9</sup>, B. Cole<sup>40</sup>, B. Coleppa<sup>41</sup>, J. G. Contreras<sup>39</sup>, A. Cooper-Sarkar<sup>22</sup>, E. Cormier<sup>42</sup>, A. S. Cornell<sup>43</sup>, R. Corsini<sup>9</sup>, E. Cruz-Alaniz<sup>8</sup>, D. Curtin<sup>44</sup>, M. D'Onofrio<sup>8</sup>, E. Daly<sup>29</sup>, A. Das<sup>45</sup>, S. P. Das<sup>46</sup>, L. Dassa<sup>9</sup>, J. De Blas<sup>47</sup>, L. Delle Rose<sup>48</sup>, H. Denizli<sup>49</sup>, K. S. Deshpande<sup>50</sup>, D. Douglas<sup>29</sup>, L. Duarte<sup>51</sup>, K. Dupraz<sup>38,52</sup>, S. Dutta<sup>53</sup>, A. V. Efremov<sup>54</sup>, R. Eichhorn<sup>55</sup>, K. J. Eskola<sup>3</sup>, E. G. Ferreira<sup>1</sup>, O. Fischer<sup>56</sup>, O. Flores-Sánchez<sup>57</sup>, S. Forte<sup>58,59</sup>, A. Gaddi<sup>9</sup>, J. Gao<sup>60</sup>, T. Gehrman<sup>61</sup>, F. Gerigk<sup>9</sup>, A. Gilbert<sup>62</sup>, F. Giuli<sup>22</sup>, A. Glazov<sup>24</sup>, R. M. Godbole<sup>63</sup>, B. Goddard<sup>9</sup>, V. Gonçalves<sup>64</sup>, G. A. Gonzalez-Sprinberg<sup>51</sup>, A. Goyal<sup>65</sup>, J. Grames<sup>29</sup>, E. Granados<sup>9</sup>, A. Grassellino<sup>66</sup>, Y. O. Gunaydin<sup>67</sup>, Y. Guo<sup>68</sup>, V. Guzey<sup>69</sup>, C. Gwenlan<sup>22</sup>, A. Hammad<sup>12</sup>, C. C. Han<sup>70,71</sup>, L. Harland-Lang<sup>22</sup>, F. Haug<sup>9</sup>, F. Hautmann<sup>22</sup>, D. Hayden<sup>72</sup>, J. Heßler<sup>34</sup>, I. Helenius<sup>3</sup>, J. Henry<sup>29</sup>, J. Hernandez-Sanchez<sup>57</sup>, H. Hesari<sup>73</sup>, T. J. Hobbs<sup>74</sup>, N. Hod<sup>75</sup>, G. H. Hoffstaetter<sup>55</sup>, B. Holzer<sup>9</sup>, C. G. Honorato<sup>57</sup>, B. Hounsell<sup>8,11,38</sup>, N. Hu<sup>38</sup>, F. Hug<sup>18,19</sup>, A. Huss<sup>9</sup>, A. Hutton<sup>29</sup>, R. Islam<sup>23</sup>, S. Iwamoto<sup>76</sup>, S. Jana<sup>56</sup>, M. Jansova<sup>77</sup>, E. Jensen<sup>9</sup>, T. Jones<sup>8</sup>, J. Jowett<sup>9</sup>, W. Kaabi<sup>38</sup>, M. Kado<sup>30</sup>, D. A. Kalinin<sup>10,11</sup>, H. Karadeniz<sup>78</sup>, U. Kaya<sup>79</sup>, R. A. Khalek<sup>80</sup>, H. Khanpour<sup>73</sup>, M. Klein<sup>8</sup>, S. Klein<sup>81</sup>, U. Klein<sup>8</sup>, M. Köksal<sup>82</sup>, M. Korostelev<sup>22</sup>, P. Kostka<sup>8</sup>, M. Krelina<sup>83</sup>, J. Kretschmar<sup>8</sup>, S. Kuday<sup>17</sup>, G. Kulipanov<sup>84</sup>, M. Kumar<sup>85</sup>, M. Kuze<sup>86</sup>, T. Lappi<sup>3</sup>, F. Larios<sup>33</sup>, A. Latina<sup>9</sup>, P. Laycock<sup>25</sup>, G. Lei<sup>87</sup>, E. Levitchev<sup>84</sup>, A. Levy<sup>88</sup>, R. Li<sup>89</sup>, X. Li<sup>60</sup>, H. Liang<sup>60</sup>, M. Lindner<sup>56</sup>, V. Litvinenko<sup>25,90</sup>, M. Liu<sup>68</sup>, T. Liu<sup>91</sup>, W. Liu<sup>92</sup>, Y. Liu<sup>93</sup>, S. Liuti<sup>94</sup>, E. Lobodzinska<sup>24</sup>, D. Longuevergne<sup>38</sup>, X. Luo<sup>95</sup>, W. Ma<sup>60</sup>, M. Machado<sup>96</sup>, S. Mandal<sup>97</sup>, F. Marhauser<sup>29</sup>, C. Marquet<sup>98</sup>, A. Martens<sup>38</sup>, R. Martin<sup>9</sup>, S. Marzani<sup>99,100</sup>, J. McFayden<sup>9</sup>, P. Mcintosh<sup>10</sup>, B. Mellado<sup>85</sup>, F. Meot<sup>55</sup>, A. Milanese<sup>9</sup>, J. G. Milhano<sup>14</sup>, B. Militsin<sup>10,11</sup>, M. Mitra<sup>101</sup>, S. Moch<sup>24</sup>, S. Mondal<sup>102</sup>, S. Moretti<sup>103</sup>, A. Morreale<sup>90</sup>, P. Nadolsky<sup>74</sup>, M. M. Najafabadi<sup>73</sup>, F. Navarra<sup>104</sup>, Z. Nergiz<sup>9</sup>, P. Newman<sup>6</sup>, J. Niehues<sup>105</sup>, E. W. Nissen<sup>9</sup>, M. Nowakowski<sup>106</sup>, N. Okada<sup>107</sup>, G. Olivier<sup>38</sup>, F. Olness<sup>74</sup>, G. Olry<sup>38</sup>, J. A. Osborne<sup>9</sup>, A. Ozansoy<sup>17</sup>, R. Pan<sup>108</sup>, B. Parker<sup>25</sup>, M. Patra<sup>109</sup>, H. Paukkunen<sup>3</sup>, Y. Peinaud<sup>38</sup>, D. Pellegrini<sup>9</sup>, G. Perez-Segurana<sup>15,11</sup>, D. Perini<sup>9</sup>, L. Perrot<sup>38</sup>, N. Pietralla<sup>110</sup>, B. Pire<sup>98</sup>, R. Placakyte<sup>111</sup>, M. Poelker<sup>29</sup>, R. Polifka<sup>112</sup>, A. Pollini<sup>27,113</sup>, P. Poulou<sup>23</sup>, G. Pownall<sup>22</sup>, Y. A. Pupkov<sup>84</sup>, F. S. Queiroz<sup>114</sup>, K. Rabbertz<sup>115</sup>, V. Radescu<sup>116</sup>, R. Rahaman<sup>117</sup>, N. Raicevic<sup>118</sup>, P. Ratoff<sup>15,11</sup>, D. Raut<sup>119</sup>, S. Raychaudhuri<sup>109</sup>, J. Repond<sup>120</sup>, R. Rimmer<sup>29</sup>, L. Rinolfi<sup>9</sup>, W. Rodejohann<sup>56</sup>, J. Rojo<sup>80</sup>, A. Rosado<sup>57</sup>, X. Ruan<sup>85</sup>, S. Russenschuck<sup>9</sup>, M. Sahin<sup>121</sup>, C. A. Salgado<sup>1</sup>, O. A. Sampayo<sup>122</sup>, K. R. Santosh<sup>101</sup>, K. Satendra<sup>23</sup>, N. Satyanarayan<sup>123</sup>, B. Schenke<sup>25</sup>, K. Schirm<sup>9</sup>, H. Schopper<sup>9</sup>, M. Schott<sup>19</sup>, D. Schulte<sup>9</sup>, C. Schwanenberger<sup>24</sup>, A. Senol<sup>49</sup>, A. Seryi<sup>29</sup>, S. Setiniyaz<sup>15,11</sup>, L. Shang<sup>124</sup>, X. Shen<sup>89</sup>, N. Shipman<sup>9</sup>, N. Sinha<sup>125</sup>, W. Slominski<sup>126</sup>, S. Smith<sup>10,11</sup>, C. Solans<sup>9</sup>, M. Song<sup>127</sup>, H. Spiesberger<sup>19</sup>, J. Stanyard<sup>9</sup>, A. Starostenko<sup>84</sup>, A. Stasto<sup>128</sup>, A. Stocchi<sup>38</sup>, M. Strikman<sup>128</sup>, M. J. Stuart<sup>9</sup>, S. Sultansoy<sup>79</sup>, H. Sun<sup>95</sup>, M. Sutton<sup>129</sup>, L. Szymanowski<sup>130</sup>, D. Tapia-Takaki<sup>131</sup>, M. Tanaka<sup>86</sup>, Y. Tang<sup>132</sup>, A. T. Tasci<sup>133</sup>, A. T. Ten-Kate<sup>9</sup>, P. Thonet<sup>9</sup>, R. Tomas-Garcia<sup>9</sup>, D. Tommasini<sup>9</sup>, D. Trbojevic<sup>25,55</sup>, M. Trott<sup>134</sup>, I. Tsurin<sup>8</sup>, A. Tudora<sup>9</sup>, K. Tywoniuk<sup>135</sup>, C. Vallerand<sup>38</sup>, A. Valloni<sup>9</sup>, D. Verney<sup>38</sup>, E. Vilella<sup>8</sup>, D. Walker<sup>47</sup>, S. Wallon<sup>38</sup>, B. Wang<sup>89</sup>, K. Wang<sup>136</sup>, K. Wang<sup>137</sup>, X. Wang<sup>95</sup>, Z. S. Wang<sup>138</sup>, H. Wei<sup>139</sup>, C. Welsch<sup>8,11</sup>, G. Willering<sup>9</sup>, P. Williams<sup>10,11</sup>, D. Wollmann<sup>9</sup>, C. Xiaohao<sup>13</sup>, T. Xu<sup>140</sup>, C. E. Yaguna<sup>141</sup>, Y. Yamazaki<sup>142</sup>, H. Yang<sup>81</sup>, A. Yilmaz<sup>78</sup>, P. Yock<sup>143</sup>, C. Yue<sup>68</sup>, S. G. Zadeh<sup>144</sup>, O. Zenaiev<sup>9</sup>, C. Zhang<sup>145</sup>, J. Zhang<sup>146</sup>, R. Zhang<sup>60</sup>, Z. Zhang<sup>38</sup>, G. Zhu<sup>89</sup>, S. Zhu<sup>124</sup>, F. Zimmermann<sup>9</sup>,

F. Zomer<sup>38</sup>, J. Zurita<sup>147,148</sup>, P. Zurita<sup>149</sup>

<sup>1</sup> IGFAE, Universidade de Santiago de Compostela (USC), Santiago de Compostela, Spain

<sup>2</sup> Nigde Universitesi, Nigde, Turkey

<sup>3</sup> University of Jyvaskyla, Jyvaskyla, Finland

<sup>4</sup> Universität Hamburg, Hamburg, Germany

<sup>5</sup> Institute of High Energy Physics (IHEP), Protvino, Russia

<sup>6</sup> University of Birmingham, Birmingham, United Kingdom

<sup>7</sup> Université Paris-Saclay, Saint-Aubin, France

<sup>8</sup> University of Liverpool, Liverpool, United Kingdom

<sup>9</sup> European Organization for Nuclear Research (CERN), Genève, Switzerland

<sup>10</sup> Science & Technology Facilities Council (STFC) - Daresbury Laboratory, Daresbury, United Kingdom

<sup>11</sup> Cockcroft Institute of Accelerator Science and Technology, Daresbury, United Kingdom

<sup>12</sup> Universität Basel, Basel, Switzerland

<sup>13</sup> Chinese Academy of Sciences - Institute of High Energy Physics (IHEP), Beijing, China

<sup>14</sup> Laboratório de Instrumentação e Física Experimental de Partículas (LIP), Lisbon, Portugal

<sup>15</sup> University of Lancaster, Lancaster, United Kingdom

<sup>16</sup> A. Alikhanian National Laboratory (AANL), Yerevan, Armenia

<sup>17</sup> Ankara University, Ankara, Turkey

<sup>18</sup> Johannes Gutenberg University Mainz (JGU) - PRISMA Cluster of Excellence, Mainz, Germany

<sup>19</sup> Johannes Gutenberg-Universität Mainz (JGU), Mainz, Germany

<sup>20</sup> Université de Montréal, Montreal, Canada

<sup>21</sup> University of Montenegro, Podgorica, Montenegro

<sup>22</sup> University of Oxford, Oxford, United Kingdom

<sup>23</sup> Indian Institute of Technology, North, Guwahati, Guwahati

<sup>24</sup> Deutsches Elektronen-Synchrotron (DESY), Hamburg, Germany

<sup>25</sup> Brookhaven National Laboratory (BNL), Upton, USA

<sup>26</sup> Massachusetts Institute of Technology (MIT), Cambridge, USA

<sup>27</sup> Università di Bologna, Bologna, Italy

<sup>28</sup> Ravenshaw University, Cuttack, India

<sup>29</sup> Thomas Jefferson National Accelerator Facility (Jefferson Lab), Newport News, USA

<sup>30</sup> Istituto Nazionale di Fisica Nucleare (INFN) - Sezione di Roma, Rome, Italy

<sup>31</sup> Commissariat à l'Énergie Atomique (CEA) - Institut de Recherche sur les Lois Fondamentales de l'Univers (IRFU), Gif-sur-Yvette, France

<sup>32</sup> Razi University, Kermanshah, Iran

<sup>33</sup> Centro de Investigación y Estudios Avanzados (CINVESTAV), San Pedro, Mexico

<sup>34</sup> Max-Planck-Institut für Physik - Werner-Heisenberg-Institut, Munich, Germany

<sup>35</sup> SLAC National Accelerator Laboratory, Menlo Park, USA

<sup>36</sup> Ankara Nuclear Research and Training Center, Ankara, Turkey

<sup>37</sup> Gumushane University, Gumushane, Turkey

<sup>38</sup> Université Paris-Saclay, CNRS/IN2P3, IJCLab, Orsay, France

<sup>39</sup> Inst. of Technological Investigations, Prague, Czech Republic

<sup>40</sup> Columbia University, New York, USA

<sup>41</sup> Indian Institute of Technology (IIT), Gandhinagar, India

<sup>42</sup> Centre Lasers Intenses et Applications (CELIA), Bordeaux, France

<sup>43</sup> University of Johannesburg (UJ), Johannesburg, South Africa

<sup>44</sup> University of Toronto, Toronto, Canada

<sup>45</sup> Osaka University, Osaka, Japan

- 46 Universidad de los Andes, Santiago, Columbia  
47 Durham University - Institute for Particle Physics Phenomenology, Durham, United Kingdom  
48 Istituto Nazionale di Fisica Nucleare (INFN) - Sezione di Firenze, Firenze, Italy  
49 Abant Izzet Baysal University, Golkoy Kampusu, Turkey  
50 University of Maryland, College Park, USA  
51 Universidad de la Republica - Instituto de Fisica Facultad de Ciencias (IFFC), Montevideo, Uruguay  
52 Université Paris-Sud, Orsay, France  
53 Sri Guru Tegh Badadur Khalsa College, Delhi, India  
54 Joint Institute for Nuclear Research (JINR), Dubna, Russia  
55 Cornell University, Ithaca, USA  
56 Max-Planck-Institut für Kernphysik, Heidelberg, Germany  
57 Benemerita Universidad Autonoma de Puebla (BUAP), Puebla, Mexico  
58 Università degli Studi di Milano, Milano, Italy  
59 Istituto Nazionale di Fisica Nucleare (INFN) - Sezione di Milano, Milano, Italy  
60 University of Science and Technology of China (USTC), Hefei, China  
61 Universität Zürich, Zurich, Switzerland  
62 Northwestern University, Evanston, USA  
63 Indian Institute of Science (IISc), Bangalore, India  
64 Universidade Federal de Pelotas (UFPel), Pelotas, Brazil  
65 University of Delhi, Delhi, India  
66 Fermi National Accelerator Laboratory (FNAL), Batavia, USA  
67 University of Iowa, Iowa City, USA  
68 Liaoning Normal University (LNNU), Dalian, China  
69 Petersburg Nuclear Physics Institute (PNPI), Petersburg, Russia  
70 University of Tokyo, Tokyo, Japan  
71 Kavli Institute for the Physics and Mathematics of the Universe (KIPMU), Kashiwa, Japan  
72 Michigan State University, East Lansing, USA  
73 Institute for Research in Fundamental Sciences (IPM), Tehran, Iran  
74 Southern Methodist University, Dallas, USA  
75 Weizmann Institute of Science, Rehovot, Israel  
76 Università degli Studi di Padova, Padua, Italy  
77 Université de Strasbourg, Strasbourg, France  
78 Giresun University, Giresun, Turkey  
79 TOBB University of Economic and Technology (TOBB ETU), Ankara, Turkey  
80 Vrije University, Amsterdam, Netherlands  
81 Lawrence Berkeley National Laboratory (LBNL), Berkeley, USA  
82 Cumhuriyet Univ., Alsancak, Turkey  
83 Universidad Tecnica Federico Santa Maria, Valparaiso, Chile  
84 Siberian Branch of Russian Academy of Science - Budker Institute of Nuclear Physics (BINP), Novosibirsk, Russia  
85 University of the Witwatersrand, Johannesburg, South Africa  
86 Tokyo Institute of Technology, Tokyo, Japan  
87 Tsinghua University, Beijing, China  
88 Tel-Aviv University, Tel Aviv, Israel  
89 Hangzhou University (HZU), Hangzhou, China  
90 Los Alamos National Laboratory, Los Alamos, USA  
91 Xiamen University (XMU), Xiamen, China  
92 University College London, London, United Kingdom

- 93 Henan Institute of Science and Technology (HIST), Xinxiang, China
- 94 University of Virginia, Charlottesville, USA
- 95 Dalian University of Technology (DLUT), Dalian, China
- 96 Universidade Federal do Rio Grande do Sul (UFRGS), Porto Alegre, Brazil
- 97 Institute of Physics, Bhubaneswar, India
- 98 Laboratoire Leprince-Ringuet (LLR), Palaiseau, France
- 99 Università degli Studi di Genova, Genova, Italy
- 100 Istituto Nazionale di Fisica Nucleare (INFN) - Sezione di Genova, Genova, Italy
- 101 Harish-Chandra Research Institute (HRI), Allahabad, India
- 102 University of Helsinki, Helsinki, Finland
- 103 University of Southampton, Southampton, United Kingdom
- 104 Universidade de Sao Paulo (USP), Sao, Paolo
- 105 Universität Aachen, Aachen, Germany
- 106 Universidad de los Andes, Carrera, Colombia
- 107 The University of Alabama, Tuscaloosa, USA
- 108 Zhejiang Institute of Modern Physics (ZIMP), Hangzhou, China
- 109 Tata Institute of Fundamental Research (TIFR), Mumbai, India
- 110 Technische Universität Darmstadt, Darmstadt, Germany
- 111 Homeday GmbH Berlin, Berlin, Germany
- 112 Charles University, Prague, Czech Republic
- 113 Istituto Nazionale di Fisica Nucleare (INFN) - Sezione di Bologna, Bologna, Italy
- 114 Univ. Federal do Rio Grande do Norte, Natal, Brazil
- 115 Karlsruher Institut für Technologie (KIT), Karlsruhe, Germany
- 116 IBM Deutschland R&D, GmbH, Urbar, Germany
- 117 Indian Institute of Science Education and Research (IISER), Kolkata, India
- 118 Univ. of Montenegro, Podgorica, YUOGSLAVIA
- 119 University of Delaware, Newark, USA
- 120 Argonne National Laboratory, Argonne, USA
- 121 Usak University, Usak, Turkey
- 122 National University of Mar del Plata, ???, Argentina
- 123 Oklahoma State University (OSU), Stillwater, USA
- 124 Peking University (PKU), Beijing, China
- 125 Institute of Mathematical Sciences (IMSc), Chennai, India
- 126 Jagiellonian University, Cracow, Poland
- 127 Anhui University (AHU), Hefei, China
- 128 Pennsylvania State University (PSU), University Park, USA
- 129 University of Sussex, Sussex, United Kingdom
- 130 Narodowe Centrum Badań Jądrowych (NCBJ), Warsaw, Poland
- 131 Kansas State University, Manhattan, USA
- 132 Korea Institute for Advanced Study (KIAS), Cheongryangri-dong, Korea
- 133 Kastamonu University, Kastamonu, Turkey
- 134 Københavns, Universitet - Niels Bohr Institutet (NBI), Copenhagen
- 135 University of Bergen, Bergen, Norway
- 136 Zhejiang University (ZJU), Hangzhou, China
- 137 Wuhan University (WHU), Wuhan, China
- 138 Asia Pacific Center for Theoretical Physics (APCTP), Pohang, Korea
- 139 University of California (UC), Riverside, USA
- 140 Hebrew University of Jerusalem - Racah Inst. of Physics, Jerusalem, Israel
- 141 Universidad Pedagógica y Tecnológica de Colombia, Tunja, Colombia

<sup>142</sup> Kobe University, Kobe, Japan

<sup>143</sup> Auckland, New Zealand

<sup>144</sup> Universität Rostock, Rostock, Germany

<sup>145</sup> National Center for Theoretical Sciences (NCTS), Hsinchu, Taiwan

<sup>146</sup> Nankai University (NKU), Tianjin, China

<sup>147</sup> Karlsruher Institut für Technologie (KIT) - Institut für Theoretische Teilchenphysik (TTP), Karlsruhe, Germany

<sup>148</sup> Karlsruher Institut für Technologie (KIT) - Institut für Kernphysik (IKP), Karlsruhe, Germany

<sup>149</sup> Universität Regensburg, Regensburg, Germany

## Abstract

The Large Hadron electron Collider, LHeC, is the means to move deep inelastic physics following the Hadron-Elektron-Ringanlage, HERA, to the energy frontier of particle physics as it is being exploited by the High Luminosity-Large Hadron Collider, HL-LHC. The paper presents a thorough update of the initial LHeC Conceptual Design Report (CDR) published in 2012. It comprises new results on the far reaching physics programme on parton structure, QCD dynamics, electroweak and top physics. It is shown how LHeC will open a new chapter of nuclear particle physics by extending the kinematic range in lepton-nucleus scattering by several orders of magnitude. Owing to an enhanced luminosity goal, the high centre of mass energy and the cleanliness of the neutral and charged current final states, the LHeC has a very remarkable Higgs programme and a promising potential to discover new physics beyond the Standard Model. The design is for concurrent LHeC and HL-LHC operation which paves the way for transforming the LHC in its final phase of operation to a high precision Higgs and electroweak physics facility with also a much increased range to explore new physics up to 100 TeV mass, as is demonstrated in a separate chapter. Building on the CDR, the paper presents a detailed updated design of the energy recovery electron linac (ERL) including new lattice, magnet, superconducting radio frequency (SRF) technology and interaction region designs. A lower energy, high current ERL facility, PERLE at Orsay, is described which uses the basic LHeC configuration parameters, a 3-turn racetrack, the source, and cryo-module designs, enabling it to serve as a development facility assisting the design and anticipated operation of the LHeC. The electron accelerator frequency is now chosen to be 801.58 MHz and the first 5-cell Niobium cavity is presented which has reached a  $Q_0$  of  $3 \cdot 10^{10}$  exceeding the design goal. An updated detector design, including a forward hadron tagger, is presented as a base for the acceptance, resolution and calibration goals which arise from the Higgs and parton density function (PDF) physics programme. The detector is shown to require an installation time of two years which is commensurate with typical LHC shutdown durations. The paper comprises a brief report of the LHeC international advisory committee with recommendations on the next steps to be made in preparing the possible endorsement of the LHeC as part of the LHC project. While the paper is dedicated to the LHeC, it also presents novel results on the Future Circular Collider in electron-hadron mode, FCC-eh, which is designed to utilise the same ERL technology, or a relocated LHeC depending on future developments of the energy frontier collider landscape.

# Preface

This paper represents the updated design study of the Large Hadron-electron Collider, the LHeC, a TeV energy scale electron-hadron ( $eh$ ) collider which may come into operation during the third decade of the lifetime of the Large Hadron Collider (LHC) at CERN. It is an account, accompanied by numerous papers in the literature, for many years of study and development, guided by an International Advisory Committee (IAC) which was charged by the CERN Directorate to advise on the directions of energy frontier electron-hadron physics at CERN. End of 2019 the IAC summarised its observations and recommendations in a brief report to the Director General of CERN, which is here reproduced as an Appendix.

The paper outlines a unique, far reaching physics programme, a design concept for a new generation collider detector, together with a novel configuration of the intense, high energy electron beam. This study builds on the previous, detailed LHeC Conceptual Design Report (CDR), which was published eight years ago [1]. It surpasses the initial study in essential characteristics: i) the depth of the physics programme, owing to the insight obtained mainly with the LHC, and ii) the luminosity prospect, for enabling a novel Higgs facility to be built and the prospects to search for and discover new physics to be strengthened. It builds on recent and forthcoming progress of modern technology, due to major advances especially of the superconducting RF technology and as well new detector techniques.

Unlike in 2012, there has now a decision been taken to configure the LHeC as an electron linac-proton or nucleus ring configuration, which leaves the ring-ring option [1] as a backup. In  $ep$ , the high instantaneous luminosity of about  $10^{34} \text{ cm}^{-2}\text{s}^{-1}$  may be achieved with the electron accelerator built as an energy recovery linac (ERL) and because the brightness of the LHC exceeds early expectations by far, not least through the upgrade of the LHC to its high luminosity version, the HL-LHC [2, 3]. For  $e\text{Pb}$  collisions, the corresponding per nucleon instantaneous luminosity would be about  $10^{33} \text{ cm}^{-2}\text{s}^{-1}$ . The LHeC is designed to operate concurrently with the LHC. It thus represents a unique opportunity to advance particle physics by building on the singular investments which CERN and its global partners have made into the LHC facility.

Extending much beyond the CDR, a configuration has newly been designed for a low energy ERL facility, termed PERLE [4], which is moving ahead to be built at Orsay by an international collaboration. The major parameters of PERLE have been taken from the LHeC, such as the 3-turn configuration, source, the 802 MHz frequency and cavity-cryomodule technology, in order to make PERLE a suitable facility for the development of LHeC ERL technology and the accumulation of operating experience prior to and later in parallel with the LHeC. In addition, the PERLE facility has a striking low energy physics programme, industrial applications and will be an enabler for ERL technology as the first facility to operate in the 10 MW power regime.

While the 2012 CDR focussed the physics discussion on the genuine physics of deep inelastic

37 scattering (DIS) leading much beyond HERA, the focus here is shifted to the challenges posed  
38 by the LHC. It is demonstrated that DIS at the LHeC can play a crucial role in sustaining  
39 and enriching the LHC programme, a consequence of the results obtained at the LHC, i.e.  
40 the discovery of the Higgs boson, the non-observation of supersymmetry (SUSY) or other non  
41 Standard Model (SM) exotic particles and, not least, the unexpected realisation of the huge  
42 potential of the LHC for discovery through precision measurements in the strong and electroweak  
43 sectors. Thus, it was felt time to summarise the recent seven years of LHeC development, also  
44 in support of the current discussions on the future of particle physics, especially at the energy  
45 frontier. Both for the LHeC [5–7] and PERLE [8], documents were submitted for consideration  
46 to the European Strategy for Particle Physics Update.

47 The LHeC has something of a one in our lifetime opportunity for substantial progress in particle  
48 physics. It comprises, with a linac shorter than the pioneering two-mile linac at SLAC, a most  
49 ambitious and exciting physics programme, the introduction of novel accelerator technology  
50 and the complete exploitation of the unique values of and spendings into the LHC. It requires  
51 probably less courage than that of Pief Panowsky and colleagues half a century ago. Finally,  
52 not least, one may realise that the power LHeC needed without the energy recovery technique  
53 is beyond 1 GW. It so appears to be a significant step towards green accelerator technology,  
54 a major general desire and requirement of our times. This paper aims at substantiating these  
55 statements in the various chapters following.

# Contents

<b>Preface</b>	<b>1</b>
<b>1 Introduction</b>	<b>8</b>
1.1 The Context	8
1.1.1 Particle Physics - an unfinished Area of Fundamental Science	8
1.1.2 Deep Inelastic Scattering and HERA	9
1.2 The Paper	11
1.2.1 The LHeC Physics Programme	11
1.2.2 The Accelerator	12
1.2.3 PERLE	13
1.2.4 The Detector	14
<b>2 LHeC Configuration and Parameters</b>	<b>16</b>
2.1 Introduction	16
2.2 Cost Estimate, Default Configuration and Staging	17
2.3 Configuration Parameters	18
2.4 Luminosity	19
2.4.1 Electron-Proton Collisions	20
2.4.2 Electron-Ion Collisions	21
2.5 Linac Parameters	22
2.6 Operation Schedule	22
<b>3 Precision Standard Model Physics with LHeC</b>	<b>25</b>
3.1 Resolving the Parton Substructure of the Proton	25
3.1.1 Open Questions on the QCD of PDFs <i>needed?</i>	26
3.1.2 Parton Distributions and DIS	27
3.1.3 HERA PDFs and the methodology of PDF fits	27
3.1.4 Simulated LHeC Data Sets	28
3.1.5 Expectations on PDFs with LHeC inclusive DIS data	32
3.1.6 Heavy Quark PDFs	39
3.1.7 PDFs and the HL-LHC	47
3.1.8 Summary on PDFs (in progress!)	50
3.2 Pushing the limits of QCD with high precision measurements	51
3.2.1 Determination of the strong coupling constant	52
3.2.2 New QCD Dynamics at Small $x$	60
3.2.3 Low $x$ and the Longitudinal Structure Function $F_L$	66
3.2.4 Disentangling non-linear QCD dynamics at the LHeC	72
3.2.5 The 3D Structure of the Proton	77
3.2.6 Inclusive diffraction	83

3.2.7	Light-Front Holography and Superconformal Algebra . . . . .	91
3.3	Electroweak Physics . . . . .	95
3.3.1	Electroweak effects in inclusive NC and CC DIS cross sections . . . . .	95
3.3.2	Methodology of a combined EW and QCD fit . . . . .	96
3.3.3	Weak boson masses $M_W$ and $M_Z$ . . . . .	97
3.3.4	Further mass determinations . . . . .	98
3.3.5	Weak Neutral Current Couplings . . . . .	99
3.3.6	The neutral current $\rho_{\text{NC}}$ and $\kappa_{\text{NC}}$ parameters . . . . .	100
3.3.7	The effective weak mixing angle $\sin^2 \theta_{\text{W}}^{\text{eff},\ell}$ . . . . .	102
3.3.8	Electroweak effects in charged-current scattering . . . . .	104
3.3.9	Direct $W$ and $Z$ production and Anomalous Triple Gauge Couplings . . .	104
3.3.10	Radiation Amplitude Zero . . . . .	108
3.3.11	Conclusion . . . . .	108
3.4	Top Quark Physics . . . . .	109
3.4.1	$Wtq$ Couplings . . . . .	109
3.4.2	FCNC Top Quark Couplings . . . . .	110
3.4.3	Other Top Quark Property Measurements and Searches for New Physics .	112
3.4.4	Summary Top Quark Physics . . . . .	112
<b>4</b>	<b>Nuclear Particle Physics with Electron-Ion Scattering at the LHeC</b>	<b>114</b>
4.1	Introduction . . . . .	114
4.2	Nuclear Parton Densities . . . . .	116
4.2.1	Pseudodata . . . . .	117
4.2.2	Nuclear gluon PDFs in a global-fit context . . . . .	119
4.2.3	nPDFs from DIS on a single nucleus . . . . .	121
4.3	Nuclear diffraction . . . . .	126
4.3.1	Exclusive vector meson diffraction . . . . .	126
4.3.2	Inclusive diffraction on nuclei . . . . .	131
4.4	New Dynamics at Small $x$ with Nuclear Targets . . . . .	133
4.5	Collective effects in dense environments – the ‘ridge’ . . . . .	134
4.6	Novel QCD Nuclear Phenomena at the LHeC . . . . .	134
<b>5</b>	<b>Higgs Physics with LHeC</b>	<b>138</b>
5.1	Signal Strength and Couplings . . . . .	138
5.1.1	Introduction . . . . .	138
5.1.2	Higgs Production in Deep Inelastic Scattering . . . . .	139
5.1.3	Kinematics of Higgs Production . . . . .	139
5.1.4	Cross Sections and Rates . . . . .	141
5.1.5	Higgs Signal Strength Measurements . . . . .	142
5.1.6	Higgs Decay into Bottom and Charm Quarks . . . . .	144
5.1.7	Higgs Decay into $WW$ . . . . .	149
5.1.8	Accessing Further Decay Channels . . . . .	152
5.1.9	Systematic and Theoretical Errors . . . . .	153
5.1.10	Higgs Coupling Analyses . . . . .	155
5.1.11	Parton Distributions . . . . .	157
5.2	Measuring the Top-quark–Higgs Yukawa Coupling . . . . .	158
5.3	Higgs Decay into Invisible Particles . . . . .	163
<b>6</b>	<b>Searches for Physics Beyond the Standard Model</b>	<b>166</b>
6.1	Introduction . . . . .	166

6.2	Extensions of the SM Higgs Sector . . . . .	166
6.2.1	Modifications of the Top-Higgs interaction . . . . .	167
6.2.2	Charged scalars . . . . .	167
6.2.3	Neutral scalars . . . . .	168
6.2.4	Modifications of Higgs self-couplings . . . . .	170
6.2.5	Exotic Higgs boson decays . . . . .	170
6.3	Searches for supersymmetry . . . . .	171
6.3.1	Search for the SUSY Electroweak Sector: prompt signatures . . . . .	171
6.3.2	Search for the SUSY Electroweak Sector: long-lived particles . . . . .	172
6.3.3	R-parity violating signatures . . . . .	174
6.4	Feebly Interacting Particles . . . . .	174
6.4.1	Searches for heavy neutrinos . . . . .	174
6.4.2	Fermion triplets in type III seesaw . . . . .	176
6.4.3	Dark photons . . . . .	176
6.4.4	Axion-like particles . . . . .	177
6.5	Anomalous Gauge Couplings . . . . .	178
6.6	Theories with heavy resonances and contact interaction . . . . .	179
6.6.1	Leptoquarks . . . . .	180
6.6.2	Vector-like quarks . . . . .	181
6.6.3	Excited fermions ( $\nu^*, e^*, u^*$ ) . . . . .	181
6.6.4	Colour octet leptons . . . . .	182
6.6.5	Quark substructure and Contact interactions . . . . .	182
6.7	Summary and conclusion . . . . .	183
<b>7</b>	<b>Influence of the LHeC on Physics at the HL-LHC</b> . . . . .	<b>185</b>
7.1	Precision Electroweak Measurements at the HL-LHC . . . . .	185
7.1.1	The effective weak mixing angle . . . . .	185
7.1.2	The $W$ -boson mass . . . . .	187
7.1.3	Impact on electroweak precision tests . . . . .	189
7.2	Higgs Physics . . . . .	192
7.2.1	Impact of LHeC data on Higgs cross section predictions at the LHC . . .	192
7.2.2	Higgs Couplings from a simultaneous analysis of $pp$ and $ep$ collision data	193
7.3	Further precision Standard Model measurements at the HL-LHC . . . . .	196
7.4	High Mass Searches at the LHC . . . . .	200
7.4.1	Strongly-produced supersymmetric particles . . . . .	200
7.4.2	Contact interactions . . . . .	200
7.5	Heavy Ion Physics with $eA$ Input . . . . .	201
<b>8</b>	<b>The Electron Energy Recovery Linac</b> . . . . .	<b>206</b>
8.1	Introduction – Design Goals . . . . .	206
8.2	The ERL Configuration of the LHeC . . . . .	207
8.2.1	Baseline Design – Lattice Architecture . . . . .	208
8.2.2	30 GeV ERL Options . . . . .	216
8.2.3	Component Summary . . . . .	217
8.3	Electron-Ion Collisions . . . . .	217
8.4	Beam-Beam Interactions . . . . .	218
8.4.1	Effect on the electron beam . . . . .	219
8.4.2	Effect on the proton beam . . . . .	221
8.5	Arc Magnets . . . . .	221
8.5.1	Dipole magnets . . . . .	221

8.5.2	Quadrupole magnets . . . . .	223
8.6	LINAC and SRF . . . . .	224
8.6.1	Choice of Frequency . . . . .	225
8.6.2	Cavity Prototype . . . . .	226
8.6.3	Cavity-Cryomodule . . . . .	228
8.6.4	Electron sources and injectors . . . . .	232
8.6.5	Compensation of Synchrotron Radiation Losses . . . . .	236
8.6.6	LINAC Configuration and Infrastructure . . . . .	238
8.7	Interaction Region . . . . .	238
8.7.1	Layout . . . . .	238
8.7.2	Proton Optics . . . . .	241
8.7.3	Electron Optics . . . . .	247
8.7.4	Interaction Region Magnet Design . . . . .	256
8.8	Civil Engineering . . . . .	259
8.8.1	Placement and Geology . . . . .	260
8.8.2	Underground infrastructure . . . . .	261
8.8.3	Construction Methods . . . . .	263
8.8.4	Civil Engineering for FCC-eh . . . . .	263
8.8.5	Cost estimates . . . . .	266
8.8.6	Spoil management . . . . .	266
<b>9</b>	<b>Technology of ERL and PERLE</b>	<b>267</b>
9.1	Energy Recovery Linac Technology - Status and Prospects . . . . .	267
9.1.1	ERL Applications . . . . .	267
9.1.2	Challenges . . . . .	267
9.1.3	ERL Landscape . . . . .	270
9.2	The ERL Facility PERLE . . . . .	271
9.2.1	Configuration . . . . .	272
9.2.2	Importance of PERLE towards the LHeC . . . . .	272
9.2.3	PERLE Layout and Beam Parameters . . . . .	273
9.2.4	PERLE Lattice . . . . .	274
9.2.5	The Site . . . . .	276
9.2.6	Staging Strategy and Time Schedule . . . . .	276
9.2.7	Concluding Remark . . . . .	278
<b>10</b>	<b>Experimentation at the LHeC</b>	<b>279</b>
10.1	Introduction . . . . .	279
10.2	Overview of Main Detector Elements . . . . .	281
10.3	Inner Tracking . . . . .	282
10.4	Calorimetry . . . . .	285
10.5	Muon Detector . . . . .	286
10.6	Forward and Backward Detectors . . . . .	289
10.6.1	Zero-Degree (Neutron) Calorimeter . . . . .	290
10.7	Detector Installation and Infrastructure . . . . .	293
10.8	Detector Design for a Low Energy FCC-eh . . . . .	296
<b>11</b>	<b>Conclusion</b>	<b>299</b>
<b>A</b>	<b>Statement of the International Advisory Committee</b>	<b>302</b>



# Chapter 1

## Introduction

### 1.1 The Context

#### 1.1.1 Particle Physics - an unfinished Area of Fundamental Science

Despite the striking success of the Standard Model, it has been recognised to have major deficiencies. These may be summarised in various ways. Some major questions concern the:

- **Higgs boson** Is the electroweak scale stabilised by new particles, interactions, symmetries? Is the Higgs boson discovered in 2012 the SM Higgs boson, what is its potential? Do more Higgs bosons exist as are predicted for example in SUSY?
- **Elementary Particles** The SM has 61 discovered particles (12 leptons, 36 quarks, 12 mediators, 1 H boson). Are these too many or too few? Do right handed neutrinos exist? Why are there 3 families? What makes leptons and quarks different? Do leptoquarks exist, is there further substructure?
- **Strong Interactions** What is the true parton dynamics and structure of proton and nuclei at different levels of resolution? How is confinement explained and how do partons hadronise? How can the many body dynamics of the Quark Gluon Plasma (QGP) state be described in terms of the elementary fields of Quantum Chromodynamics? What is the meaning of the AdS/CFT relation and of SUSY in strong interactions? Do axions, odderons, instantons exist?
- **GUT** Is there a genuine, grand unification of the interactions at high scales, would this include gravitation? What is the real value of the strong coupling constant, is lattice correct in this respect?
- **Neutrinos** Do Majorana neutrinos exist, is there CP violation in the neutrino sector, is the proton stable?

These (and others) are known and persistent questions in Particle Physics. They are intimately related and any future strategic programme should not be confined to only one or a few of these. The field is far from being understood, despite the phenomenological success of the  $SU_L(2) \times U(1) \times SU_c(3)$  gauge field theory termed the Standard Model. Attempts to declare its end [9], despite their perhaps stimulating irritation, may possibly be compared with Kelvin's prediction about the future which comprised precision only as all principal questions had already been solved, back in around 1900. The question is not why to end particle physics but how to

87 proceed. The answer is not hidden in philosophy but requires new, better, affordable experi-  
88 ments. Indeed the situation is special as expressed by Guido Altarelli a few years ago: *It is now*  
89 *less unconceivable that no new physics will show up at the LHC. . . We expected complexity and*  
90 *instead we have found a maximum of simplicity. The possibility that the Standard model holds*  
91 *well beyond the electroweak scale must now be seriously considered [10].* This is reminiscent of  
92 the time before 1969, prior to anything like a Standard Model, when gauge theory was just for  
93 theorists, while a series of new accelerators, such as the 2 mile electron linac at Stanford or the  
94 SPS at CERN were planned which caused a complete change of the paradigm of particle physics.

95 Major challenges for particle physics also comprise basic puzzles on the Universe, especially  
96 on the nature of Dark Matter. Ingenuitive theoretical hypotheses, such as on the existence of  
97 extra dimensions, on SUSY, of un-particles or the embedding in higher gauge groups, like E8,  
98 are a strong motivation to develop high energy physics rigorously further. In this endeavour  
99 a substantial increase of precision, the conservation of diversity and a broadening of kinematic  
100 coverage is a necessity, which may turn out to be of fundamental importance. The strategic  
101 question in this context, therefore, is not just which new collider should be built next, as one  
102 often hears, but how we may challenge the current and incomplete knowledge best. A realistic  
103 step to progress requires to build a new  $e^+e^-$  collider, preferentially in Asia, and to complement  
104 the LHC in the thirties with an electron ERL to synchronously operate  $pp$  with  $ep$  at the LHC,  
105 the topic of this paper.

106 One may call these machines first technology generation colliders as their technology has been  
107 proven to principally work [11]. Beyond these times there is a long-term future reaching to the  
108 year 2050 and much beyond, of a second, further generation of hadron, lepton and electron-  
109 hadron colliders, which is not considered in the present paper <sup>1</sup>. For CERN a joint design study  
110 has recently been published of a future circular collider (FCC) accelerator complex [12–14], which  
111 would provide a corresponding base. A similar prospect is being discussed in China [15, 16].

112 A new collider for CERN at the level of  $\mathcal{O}(10)$  GSF cost should have the potential to change  
113 the paradigm of particle physics with direct, high energy discoveries in the 10 TeV mass range.  
114 This may only be achieved with the FCC-hh including an  $eh$  experiment. The FCC-hh accesses  
115 physics to several hundred TeV, assisted by a qualitatively new level of QCD/DIS input. It  
116 is the only collider to measure the Higgs potential as its major goal and thus may not fail.  
117 It reaches rare H decays, high scales and, when combined with  $ep$ , it measures the SM Higgs  
118 couplings to below percent precision. There is a huge, fundamental program on electroweak  
119 and strong interactions, flavour and heavy ions. It is CERN's unique opportunity to build on  
120 the ongoing LHC program, for many decades ahead. The FCC-hh requires high field dipoles.  
121 A strongly supported magnet R+D program shall find an affordable, high field solution, to be  
122 selected in the early thirties, and not this time. The size of the FCC-hh, in any case, requires  
123 this to be established as a global enterprise. The LHeC can be understood as a very important  
124 step towards this major new facility, both in terms of physics and technology.

### 125 1.1.2 Deep Inelastic Scattering and HERA

126 The field of deep inelastic lepton-hadron scattering (DIS) [17] was born with the discovery [18, 19]  
127 of partons [20, 21] about 50 years ago. It readily contributed fundamental insight, for example  
128 on the development of QCD with the confirmation of fractional quark charges and of asymptotic

---

<sup>1</sup>There are a few exceptions when studies are presented not only for the LHeC but also the  $ep$  version of the Future Circular Collider, the FCC-eh, which uses, seen from today, the same ERL technology and possibly hardware as is currently under development for the LHeC.

129 freedom or with the spectacular finding that the right handed weak isospin charge of the electron  
 130 was zero [22] which established the Glashow-Weinberg-Salam *model of leptons* [23] as the base of  
 131 the united electroweak theory. The quest to reach higher energies in accelerator based particle  
 132 physics led to generations of colliders, with HERA [24] as the so far only electron-proton collider.

133 HERA collided electrons (and positrons) of about 27.6 GeV energy,  $E_e$ , off protons of 920 GeV  
 134 energy,  $E_p$ , achieving a centre of mass energy  $\sqrt{s} = 2\sqrt{E_e E_p}$  of about 320 GeV. It therefore  
 135 extended the kinematic range covered by fixed target experiments by two orders of magnitude  
 136 in Bjorken  $x$  and in four-momentum transfer squared,  $Q^2$ , with its limit  $Q_{max}^2 = s$ . HERA  
 137 had a unique collider physics programme and success [25]. It was built in less than a decade  
 138 and it operated for 16 years. Together with the Tevatron and LEP, HERA was pivotal to the  
 139 development of the Standard Model. It established QCD as the correct description of proton  
 140 substructure and parton dynamics down to  $10^{-19}$  m. It demonstrated electroweak theory to  
 141 hold in the newly accessed range, especially with the measurement of neutral and charged  
 142 current  $ep$  scattering cross sections beyond  $Q^2 \sim M_{W,Z}^2$  and with the proof of electroweak  
 143 interference at high scales through the measurement of the interference structure functions  $F_2^{\gamma Z}$   
 144 and  $x F_3^{\gamma Z}$ . The HERA collider has been the basis of the physics of parton distributions, not only  
 145 in providing the genuine base to measure longitudinal gluon, valence, light and heavy sea quark  
 146 momentum distributions, but as well in supporting the foundation of the theory of unintegrated,  
 147 diffractive, photon, neutron PDFs through a series of corresponding measurements. It discovered  
 148 the rise of the parton distributions towards small momentum fractions  $x$  supporting early QCD  
 149 expectations on the asymptotic behaviour of the structure functions [26]. Like the  $p\bar{p}$  and  $e^+e^-$   
 150 colliders exploring the Fermi scale of a few hundred GeV energy, determined by the vacuum  
 151 expectation value of the Higgs field,  $v = 1/\sqrt{\sqrt{2}G_F} = 2M_W/g \simeq 246$  GeV, HERA showed that  
 152 there was no SUSY or other exotic particle with reasonable couplings existing at Fermi energies.

153 HERA established electron-proton scattering as an integral part of modern high energy particle  
 154 physics. It demonstrated the richness of DIS physics, and the feasibility of constructing and  
 155 operating energy frontier  $ep$  colliders. What did we learn to take into a next higher energy  $ep$   
 156 collider design? Perhaps there were three lessons about

- 157 • *the need for higher energy*, for three reasons: i) to make charged currents a real, precision  
 158 part of  $ep$  physics, for instance for the complete unfolding of the flavour composition of  
 159 the sea and valence quarks, ii) to produce heavier mass particles (Higgs, top, exotics) with  
 160 favourable cross sections and iii) to discover or disprove the existence of gluon saturation  
 161 for which one needs to measure at lower  $x \propto Q^2/s$  than HERA could;
- 162 • *the need for much higher luminosity*: the first almost ten years of HERA provided just a  
 163 hundred  $\text{pb}^{-1}$ . As a consequence, HERA could not accurately access the high  $x$  region,  
 164 and it was inefficient and short of statistics in resolving puzzling event fluctuations;
- 165 • *the complexity of the interaction region* when a bent electron beam caused synchrotron  
 166 radiation while the opposite proton beam generated quite some halo background through  
 167 beam-gas and beam-wall proton-ion interactions.

168 Based on these and further lessons, the LHeC design has been pursued recognising that the  
 169 LHC is the only base to realise a TeV energy scale electron-hadron collider in the accessible  
 170 future. It offers highly energetic, intense hadron beams, a long time perspective and a unique  
 171 infrastructure and expertise, i.e. everything required for an energy frontier DIS physics and  
 172 innovative accelerator programme.

173 **1.2 The Paper**

174 **1.2.1 The LHeC Physics Programme**

175 This paper presents a design concept of the LHeC, using a 50 GeV energy electron beam to  
 176 be scattered off the LHC hadron beams (proton and ion) in concurrent operation. Its main  
 177 characteristics are presented in **Chapter 2**. The instantaneous luminosity is designed to exceed  
 178 that of HERA, which achieved a few times  $10^{31} \text{ cm}^{-2}\text{s}^{-1}$ , by a factor of several hundreds. The  
 179 kinematic range nominally is extended by a factor of about 15, but in fact by a larger amount  
 180 because of the hugely increased luminosity which is required to explore the maximum  $Q^2$  and  
 181 large  $x \leq 1$  regions, which was a major deficiency of HERA. The coverage of the  $Q^2, x$  plane  
 by previous and future DIS experiments is illustrated in Fig. 1.1.

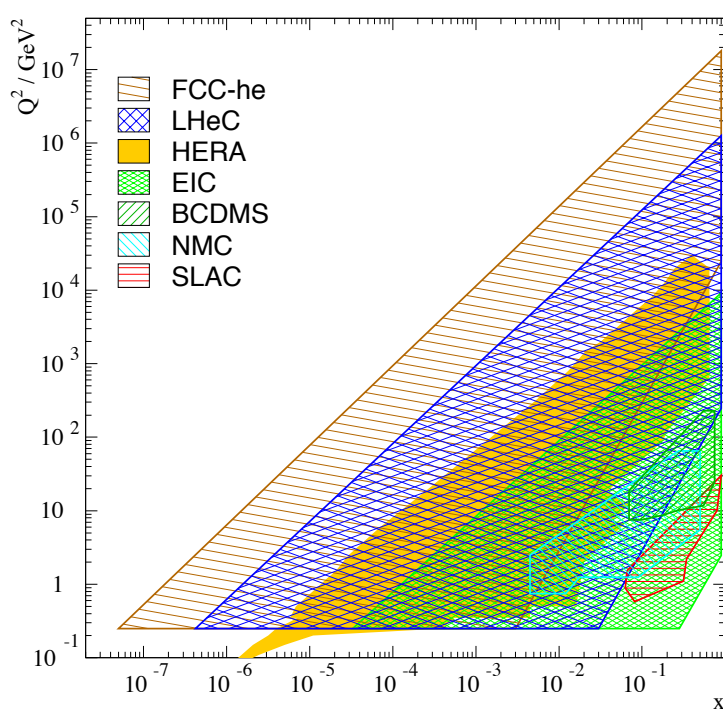


**Figure 1.1:** Coverage of the kinematic plane in DIS by some initial fixed target experiments with electrons (SLAC) and muons (NMS,BCDMS), by the future electron ion collider (EIC,green), HERA (yellow), the LHeC (blue) and the FCC-eh (brown). The low  $Q^2$  region for the colliders is here limited to about  $0.2 \text{ GeV}^2$ , which is covered by the central detectors, roughly and perhaps using low electron beam data. Electron taggers may extend this to even lower  $Q^2$ . The high  $Q^2$  limit is given by the line of inelasticity  $y = 1$ . Approximate limitations of acceptance at medium  $x$ , low  $Q^2$  are drawn using polar angle limits of  $\eta = -\ln \tan \theta/2$  of 4, 5, 6 for the EIC, LHeC, and FCC-eh, respectively. Since these lines are given by  $x = \exp \eta \cdot \sqrt{Q^2}/2E_p$ , it is clear that largest  $x$  values at low  $Q^2$  are covered by the EIC (green area bottom, right).

182

183 The LHeC would provide a major extension of the kinematics as is adequate for a physics  
 184 programme of the next DIS generation. For the LHC, the  $ep/A$  detector would be the new  
 185 major experiment. Centred around different kinematic regions, a number of major themes  
 186 would be developed as are discussed in quite some detail in this paper:

- 187 • Based on the unique hadron beams of the LHC and employing a point-like probe, the  
188 LHeC would represent the world’s cleanest, high resolution microscope for exploring the  
189 substructure of and dynamics inside matter, which may be termed the Hubble telescope for  
190 the smallest dimensions. It would clarify the dynamics of parton interactions at small  $x$  as  
191 is necessary for any future hadron collider, including the HL- LHC. The LHeC would chal-  
192 lenge the SM to utmost precision in electroweak interactions, diffractive and top physics  
193 (c.f. Chapter 3):
- 194 • The LHeC extends the kinematic range in lepton-nucleus scattering by nearly four orders  
195 of magnitude. It so will transform nuclear particle physics completely, by resolving the  
196 hitherto hidden parton dynamics and substructure of nuclei and establishing the QCD  
197 base for the collective dynamics observed in QGP phenomena (c.f. Chapter 4);
- 198 • The clean DIS final state in neutral and charged current scattering enables a high precision  
199 Higgs physics programme with the LHeC. This delivers unique insight especially into the  
200  $H - WW$  and  $H - bb/cc$  couplings (c.f. Chapter 5);
- 201 • As a new, unique, luminous TeV scale collider, the LHeC has an outstanding opportunity  
202 to discover new physics, such as in the exotic Higgs, dark matter, heavy neutrino and QCD  
203 areas, which is presented in Chapter 6;
- 204 • With concurrent  $ep$  and  $pp$  operation, the LHeC would transform the LHC into a 3-  
205 beam, twin-collider of greatly improved potential (c.f. Chapter 7). Through ultra-precise  
206 strong and electroweak interaction measurements, the  $ep$  results would make the HL-  
207 LHC complex a much more powerful search and measurement laboratory than current  
208 expectations based on  $pp$  only could possibly entail. The joint  $pp/ep$  LHC facility can  
209 become a Higgs factory of unprecedented impact as it challenges and complements what  
210  $e^+e^-$  promises.

211 The development of particle physics including and leading beyond DIS, the future of CERN, the  
212 exploitation of the unprecedented LHC investments, the culture of accelerator art, all make the  
213 LHeC a project of singular interest with the advantage of being realistic in terms of technology,  
214 time and budget constraints.

## 215 1.2.2 The Accelerator

216 The LHeC should provide an intense, high energy electron beam to collide with the LHC.  
217 The intensity is gauged through the integrated luminosity goal of  $\mathcal{O}(1)\text{ab}^{-1}$ . The electron  
218 beam energy is chosen to achieve a TeV energy collision and enable competitive searches and  
219 Higgs boson measurements. A cost-physics-energy evaluation is presented here which points  
220 to choosing  $E_e \geq 50\text{ GeV}$  as the default value. The wall plug power of the default design [1]  
221 had been constrained to 100 MW. In that configuration two super-conducting linacs, opposite  
222 to each other, accelerate the passing electrons by 8.3 GeV to 10 GeV each. This leads to a final  
223 electron beam energy of about 50 GeV in a 3-turn racetrack configuration. For measuring at  
224 very low  $Q^2$  and/or determining  $F_L$ , see below, the electron beam energy may be reduced to  
225 a minimum of perhaps 20 GeV. For maximising the acceptance at large Bjorken  $x$ , the proton  
226 beam energy,  $E_p$ , may be reduced to 1 TeV about. If the ERL may be combined in the further  
227 future with the double energy HE-LHC [27],  $E_p$  could reach 14 TeV. One therefore considers a  
228 DIS scattering complex with an energy range between  $\sqrt{s} \simeq 300$  to 1800 GeV. It thus covers  
229 an energy range from HERA to the TeV region, at hugely increased luminosity and much more  
230 sophisticated experimental techniques.

231 The ERL beam configuration is located inside the LHC ring but outside its tunnel, which  
232 minimises any interference with the main hadron beam infrastructure. The electron accelerator  
233 may thus be built independently, to a considerable extent, of the status of operation of the  
234 proton machine.

235 The chosen energy of 50 GeV leads to a circumference  $U$  of the electron racetrack of 5.4 km,  
236 smaller than the SPS. This length is a fraction  $1/n$  of the LHC circumference, for  $n = 5$ , as  
237 is required for the  $e$  and  $p$  matching of bunch patterns. It is chosen also in order to limit the  
238 energy loss in the last return arc and as a result of a cost optimisation between the fractions of  
239 the circumference covered by SRF and by return arcs. That configuration is adopted also as the  
240 default for the FCC-he.

241 For the LHC, the ERL would be tangential to IP2 which, according to the current plans, is  
242 taken by the ALICE detector until the first long shutdown following the three year pause of  
243 the LHC operation for upgrading the luminosity performance and detectors. This shutdown  
244 is termed LS4 and is scheduled to start in 2031. For FCC-he the preferred position is IP L  
245 for geological reasons mainly, and the time of operation fully depending on the progress with  
246 FCC-hh, beginning at the earliest in 2050.

247 The LHeC operation is transparent to the LHC collider experiments owing to the low lepton  
248 bunch charge and resulting small beam-beam tune shift experienced by the protons. The LHeC  
249 is thus designed to run simultaneously with  $pp$  (or  $pA$  or  $AA$ ) collisions with a dedicated final  
250 operation of a few years.

251 The paper presents in considerable detail the design of the LHeC (c.f. Chapter 8), i.e. the optics  
252 and lattice, components, magnets, as well as designs of the linac and interaction region besides  
253 special topics such as the prospects for electron-ion scattering, positron-proton operation and  
254 a novel analysis of beam-beam interaction effects. With the more ambitious luminosity goal, a  
255 new lattice for the new default energy of 50 GeV, with progress on the IR design, a novel analysis  
256 of the civil engineering work and especially the production and successful test [28] of the first SC  
257 cavity, at the newly chosen default frequency of 801.58 MHz, this report considerably extends  
258 beyond the initial CDR. Large progress has been made in the development of superconducting,  
259 high gradient cavities with quality factors beyond  $10^{10}$ . This will enable the exploitation of ERLs  
260 in high-energy physics colliders, with the LHeC as the prime example, while considerations are  
261 also brought forward for future  $e^+e^-$  colliders [29].

### 262 1.2.3 PERLE

263 The status and challenges of ERLs are summarised in Chapter 9. This also presents the design,  
264 status and prospects for the ERL development facility PERLE. The major parameters of PERLE  
265 have been taken from the LHeC, such as the 3-turn configuration, source, frequency and cavity-  
266 cryomodule technology, in order to make PERLE a suitable facility for the development of LHeC  
267 ERL technology and the accumulation of operating experience prior to and later in parallel with  
268 the LHeC. An international collaboration has been invited to build PERLE at Orsay. With  
269 the design goals of 500 MeV electron energy obtained in three passes through two cryo-modules  
270 and of 20 mA, corresponding to 500 nC charge at 40 MHz bunch frequency, PERLE is set to  
271 become the first ERL facility to operate at 10 MW power. Following its CDR [4] and a paper  
272 submitted to the European strategy [8], work is directed to build a first dressed cavity and to  
273 release a TDR by 2021. Besides its interest in accelerator and ERL technology, PERLE is also  
274 of importance for pursuing a low energy physics programme, see [4], and for several possible  
275 industrial applications. It also serves as a local hub for the education of accelerator physicists

276 at a place, previously called Linear Accelerator Laboratory (LAL), which has long been at the  
277 forefront of accelerator design and operation.

278 The realisation of the ERL for the LHeC at CERN represents a unique opportunity not only for  
279 physics and technology but as well for a next and the current generation of accelerator physi-  
280 cists, engineers and technicians to realise an ambitious collider project while the plans for very  
281 expensive next machines may take shape. Similarly, this holds for a new generation of detector  
282 experts, as the design of the upgrade of the general purpose detectors (GPDs) at the LHC is  
283 reaching completion, with the question increasingly posed about opportunities for new collider  
284 detector construction to not lose the expertise nor the infrastructure for building trackers,  
285 calorimeters and alike. The LHeC offers the opportunity for a novel  $4\pi$  particle physics detector  
286 design, construction and operation. As a linac-ring accelerator, it may serve one detector of a  
287 size smaller than CMS and larger than H1.

#### 288 1.2.4 The Detector

289 Chapter 10 on the detector relies to a large extent on the very detailed write-up on the kinematics,  
290 design considerations, and realisation of a detector for the LHeC as was presented in the CDR [1].  
291 In the previous report one finds detailed studies not only on the central detector and its magnets,  
292 a central solenoid for momentum measurements and an extended dipole for ensuring head-on  $ep$   
293 collisions, but as well on the forward ( $p$  and  $n$ ) and backward ( $e$  and  $\gamma$ ) tagging devices. The  
294 work on the detector as presented here was focussed on an optimisation of the performance and  
295 on the scaling of the design towards higher proton beam energies. It presents a new, consistent  
296 design and summaries of the essential characteristics in support of many physics analyses this  
297 paper entails.

298 The most demanding performance requirements arise from the  $ep$  Higgs measurement pro-  
299 gramme, especially the large acceptance and high precision desirable for heavy flavour tagging  
300 and the wish to resolve the hadronic final states completely. This has been influenced by the  
301 acceptance ambitions and the technology progress of the HL-LHC detector upgrades, a key ex-  
302 ample being the high granularity and low material prospects of HV-CMOS Silicon technology,  
303 which is here sketched also.

304 Therefore we have now completed two studies of design: previously, of a rather conventional de-  
305 tector with limited cost and, here, of a more ambitious device. Both of these, perhaps, extremes  
306 appear realisable. This regards also the installation. The paper presents a brief description of  
307 the installation of the LHeC detector at IP2 with the result that it may proceed within two  
308 years, including the dismantling of the then residing detector. This calls for modularity and  
309 pre-mounting of detector elements on the surface, as was done for CMS too. It will be for the  
310 LHeC detector Collaboration, to be established with and for the approval of the project, to  
311 design the detector according to its understanding and technical capabilities.

312 Subsequently follow the chapters as mentioned above: Chapter 2 summarises the LHeC charac-  
313 teristics. Chapter 3 presents key topics on how the SM will be developed and tested through  
314 high precision measurements in the PDF, strong, electroweak and top physics sector, with a  
315 section on novel QCD phenomena to be found. Ample space is given to the question of parton  
316 saturation at small  $x$ . Chapter 4 presents the unique potential of the LHeC to advance nuclear  
317 particle physics with its far reaching, luminous electron-ion scattering programme. Chapter 5  
318 presents a detailed analysis of the opportunity for precision SM Higgs boson physics with CC

319 and NC  $ep$  scattering. Chapter 6 is a description of the striking variety of opportunities to  
320 discover physics beyond the Standard Model with the LHeC, including non-SM Higgs physics,  
321 right-handed neutrinos, physics of the dark sector or heavy resonances. Chapter 7 describes the  
322 interplay of  $ep$  and  $pp$  physics, i.e. the necessity to have the LHeC in order to fully exploit the  
323 search and measurement potential of the LHC facility. Chapter 8 presents the update of the  
324 CDR on the ERL configuration with many novel results as on the lattice and interaction region  
325 design, besides new specifications of components. It also presents the very encouraging results  
326 of the first LHeC 802 MHz cavity. Chapter 9 is devoted, first, to the status and challenges of  
327 energy recovery based accelerators and, second, to the description of the PERLE facility, be-  
328 tween its CDR and a forthcoming TDR. Chapter 10 describes the update of the detector study  
329 towards an optimum configuration in terms of acceptance and performance. Chapter 11 presents  
330 a summary of the paper including a time line for realising the LHeC to operate with the LHC.

## Chapter 2

# LHeC Configuration and Parameters

### 2.1 Introduction

The Conceptual Design Report (CDR) of the LHeC was published in 2012 [1]. The CDR default configuration uses a 60 GeV energy electron beam derived from a racetrack, three-turn, intense energy recovery linac (ERL) achieving a cms energy of  $\sqrt{s} = 1.3 \text{ TeV}$ , where  $s = 4E_p E_e$  is determined by the electron and proton beam energies,  $E_e$  and  $E_p$ . In 2012, the Higgs boson,  $H$ , was discovered which has become a central topic of current and future high energy physics. The Higgs production cross section in charged current (CC) deep inelastic scattering (DIS) at the LHeC is roughly 100 fb. The Large Hadron Collider has so far not led to the discovery of any exotic phenomenon. This forces searches to be pursued, in  $pp$  but as well in  $ep$ , with the highest achievable precision in order to access a maximum range of phase space and possibly rare channels. The DIS cross section at large  $x$  roughly behaves like  $(1-x)^3/Q^4$ , demanding very high luminosities for exploiting the unknown regions of Bjorken  $x$  near 1 and very high  $Q^2$ , the negative four-momentum transfer squared between the electron and the proton. For the current update of the design of the LHeC this has set a luminosity goal about an order of magnitude higher than the  $10^{33} \text{ cm}^{-2}\text{s}^{-1}$  which had been adopted for the CDR. There arises the potential, as described subsequently in this paper, to transform the LHC into a high precision electroweak, Higgs and top quark physics facility.

The  $ep$  Higgs production cross section rises approximately with  $E_e$ . New physics may be related to the heaviest known elementary particle, the top quark, the  $ep$  production cross section of which rises more strongly than linearly with  $E_e$  in the LHeC kinematic range as that is not very far from the  $t\bar{t}$  threshold. Searches for heavy neutrinos, SUSY particles, etc. are the more promising the higher the energy is. The region of deep inelastic scattering and pQCD requires that  $Q^2$  be larger than  $M_p^2 \simeq 1 \text{ GeV}^2$ . Access with DIS to very low Bjorken  $x$  requires high energies because of  $x = Q^2/s$ , for inelasticity  $y = 1$ . In DIS, one needs  $Q^2 > M_p^2 \simeq 1 \text{ GeV}^2$ . Physics therefore requires a maximally large energy. However, cost and effort set realistic limits such that twice the HERA electron beam energy, of about 27 GeV, appeared as a reasonable and affordable target value.

In the CDR [1] the default electron energy was chosen to be 60 GeV. This can be achieved with an ERL circumference of 1/3 of that of the LHC. Recently, the cost was estimated in quite some detail [30], comparing also with other accelerator projects. Aiming at a cost optimisation and providing an option for a staged installation, the cost estimate lead to defining a new default configuration of  $E_e = 50 \text{ GeV}$  with the option of starting in an initial phase with a beam energy

365 of  $E_e = 30$  GeV and a circumference of 5.4 km which is 1/5 of the LHC length. Lowering  
 366  $E_e$  is also advantageous for mastering the synchrotron radiation challenges in the interaction  
 367 region. Naturally, the decision on  $E_e$  is not taken now. This paper comprises studies with  
 368 different energy configurations, mainly  $E_e = 50$  and 60 GeV, which are close in their centre of  
 369 mass energy values of 1.2 and 1.3 TeV, respectively.

370 Up to beam energies of about 60 GeV, the ERL cost is dominated by the cost for the supercon-  
 371 ducting RF of the linacs. Up to this energy the ERL cost scales approximately linearly with the  
 372 beam energy. Above this energy the return arcs represent the main contribution to the cost and  
 373 to the ERL cost scaling is no longer linear. Given the non-linear dependence of the cost on  $E_e$ ,  
 374 for energies larger than about 60 GeV, significantly larger electron beam energy values may only  
 375 be justified by overriding arguments, such as, for example, the existence of leptoquarks <sup>1</sup>. Higher  
 376 values of  $\sqrt{s}$  are also provided with enlarged proton beam energies by the High Energy LHC  
 377 ( $E_p = 13.5$  TeV) [27] and the FCC-hh [14] with  $E_p$  between 20 and possibly 75 TeV, depending  
 378 on the dipole magnet technology.

## 379 2.2 Cost Estimate, Default Configuration and Staging

380 In 2018 a detailed cost estimate was carried out [30] following the guidance and practice of  
 381 CERN accelerator studies. The assumptions were also compared with the DESY XFEL cost.  
 382 The result was that for the 60 GeV configuration about half of the total cost was due to the two  
 383 SC linacs. The cost of the arcs decreases more strongly than linearly with decreasing energy,  
 384 about  $\propto E^4$  for synchrotron radiation losses and  $\propto E^3$  when emittance dilution is required to be  
 385 avoided [31]. It was therefore considered to set a new default of 50 GeV with a circumference of  
 386 1/5 of that of the LHC, see Sect. 2.3, compared to 1/3 for 60 GeV. Furthermore, an initial phase  
 387 at 30 GeV was considered, within the 1/5 configuration but with only partially equipped linacs.  
 388 The HERA electron beam energy was 27 GeV. The main results, taken from [30] are reproduced  
 389 in Tab. 2.1.

390 The choice of a default of 50 GeV at 1/5 of the LHC circumference results, as displayed, in  
 391 a total cost of 1,075 MCHF for the initial 30 GeV configuration and an additional, upgrade  
 392 cost to 50 GeV of 296 MCHF. If one restricted the LHeC to a non-upgradeable 30 GeV only  
 393 configuration one would, still in a triple racetrack configuration, come to roughly a 1 km long  
 394 structure with two linacs of about 500 m length, probably in a single linac tunnel configuration.  
 395 The cost of this version of the LHeC is roughly 800 MSF, i.e. about half the 60 GeV estimated  
 396 cost. However, this would essentially reduce the LHeC to a QCD and electroweak machine, still  
 397 very powerful but accepting substantial losses in its Higgs, top and BSM programme.

398 A detailed study was made on the cost of the civil engineering, which is also discussed subse-  
 399 quently. This concerned a comparison of the 1/3 vs the 1/5 LHC circumference versions, and  
 400 the FCC-eh. The result is illustrated in Fig. 2.1. It shows that the CE cost for the 1/5 version is  
 401 about a quarter of the total cost. The reduction from 1/3 to 1/5 economises about 100 MCHF.

402 Choices of the final energy will be made later. They depend not only on a budget but also on the  
 403 future development of particle physics at large. For example, it may turn out that, for some years

---

<sup>1</sup>If these existed with a mass of say  $M = 1.5$  TeV this would require, at the LHC with  $E_p = 7$  TeV, to  
 choose  $E_e$  to be larger than 90 GeV, and to pay for it. Leptoquarks would be produced by  $ep$  fusion and appear as  
 resonances, much like the  $Z$  boson in  $e^+e^-$  and would therefore fix  $E_e$  (given certain  $E_p$  which at the FCC exceeds  
 7 TeV). The genuine DIS kinematics, however, is spacelike, the exchanged four-momentum squared  $q^2 = -Q^2$   
 being negative, which implies that the choice of the energies is less constrained than in an  $e^+e^-$  collider aiming  
 at the study of the  $Z$  or  $H$  bosons.

Component	CDR 2012 (60 GeV)	Stage 1 (30 GeV)	Default (50 GeV)
SRF System	805	402	670
SRF R+D and Prototyping	31	31	31
Injector	40	40	40
Arc Magnets and Vacuum	215	103	103
SC IR Magnets	105	105	105
Source and Dump System	5	5	5
Cryogenic Infrastructure	100	41	69
General Infrastructure and Installation	69	58	58
Civil Engineering	386	289	289
Total Cost	1756	1075	1371

**Table 2.1:** Summary of cost estimates, in MCHF, from [30]. The 60 GeV configuration is built with a 9 km triple racetrack configuration as was considered in the CDR [1]. It is taken as the default configuration for FCC-eh, with an additional CE cost of 40 MCHF due to the larger depth on point L (FCC) as compared to IP2 (LHC). Both the 30 and the 50 GeV assume a 5.4 km configuration, i.e. the 30 GeV is assumed to be a first stage of LHeC upgradeable to 50 GeV ERL. Whenever a choice was to be made on estimates, in [30] the conservative number was chosen.

404 into the future, the community may not find the  $\mathcal{O}(10)$  GCHF required to build any of the  $e^+e^-$   
405 colliders currently considered. Then the only way to improve on the Higgs measurements beyond  
406 HL-LHC substantially is the high energy (50 – 60 GeV), high luminosity ( $\int L = 1 \text{ ab}^{-1}$ ) LHeC.  
407 Obviously, physics and cost are intimately related. Based on such considerations, but also taking  
408 into account technical constraints as resulting from the amount of synchrotron radiation losses  
409 in the interaction region and the arcs, we have chosen 50 GeV in a 1/5 of U(LHC) configuration  
410 as the new default. This economises about 400 MCHF as compared to the CDR configuration.

411 If the LHeC ERL were built, it may later be transferred, with some reconfiguration and upgrades,  
412 to the FCC to serve as the FCC-eh. The FCC-eh has its own location, L, for the ERL which  
413 requires a new accelerator tunnel. It has been decided to keep the 60 GeV configuration for the  
414 FCC, as described in the recently published CDR of the FCC [14]. The LHeC ERL configuration  
415 may also be used as a top-up injector for the  $Z$  and possibly  $WW$  phase of the FCC-e should  
416 the FCC-ee indeed precede the FCC-hh/eh phase.

## 417 2.3 Configuration Parameters

418 A possible transition from the 60 GeV to the 50 GeV configuration of the LHeC was already  
419 envisaged in 2018, as considered in the paper submitted to the European Strategy [6]. The  
420 machine layout shown in that paper is reproduced in Fig. 2.2. It is a rough sketch illustrating  
421 the reduction from a 60 GeV to a 50 GeV configuration, which results not only in a reduction of  
422 capital costs, as discussed above, but also of effort.

423 The ERL configuration has been recently revisited [31] considering its dependence on the electron  
424 beam energy. Applying a dimension scaling which preserves the emittance dilution, the results  
425 have been obtained as are summarised in Tab. 2.2. The 1/5 configuration is chosen as the new  
426 LHeC default while the CDR on the LHeC from 2012 and the recent CDR on FCC-eh have used  
427 the 1/3 configuration. The energy and configuration may be decided as physics, cost and effort  
428 dictate, once a decision is taken.

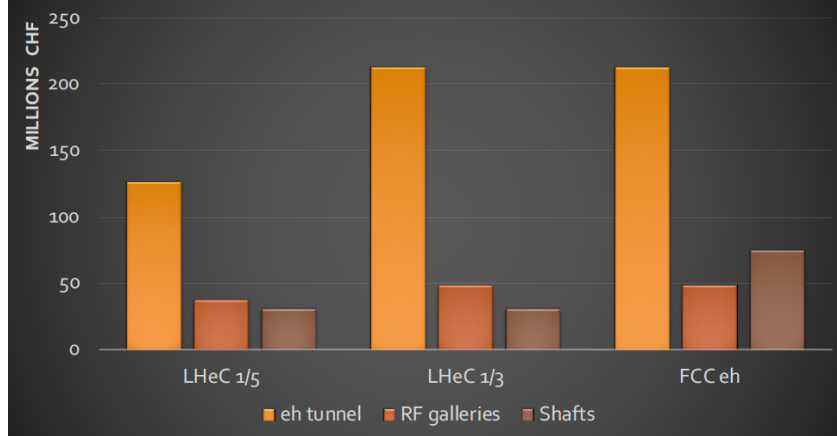


**Figure 2.1:** Cost estimate for the civil engineering work for the tunnel, rf galleries and shafts for the LHeC at 1/5 of the LHC circumference (left), at 1/3 (middle) and the FCC-eh (right). The unit costs and percentages are consistent with FCC and CLIC unit prices. The estimate is considered reliable to 30%. The cost estimates include: Site investigations: 2%, Preliminary design, tender documents and project changes: 12% and the Contractors profit: 3%. Surface site work is not included, which for LHeC exists with IP2.

Parameter	Unit	LHeC option			
		1/3 LHC	1/4 LHC	1/5 LHC	1/6 LHC
Circumference	m	9000	6750	5332	4500
Arc radius	$m \cdot 2\pi$	1058	737	536	427
Linac length	$m \cdot 2$	1025	909	829	758
Spreader and recombiner length	$m \cdot 4$	76	76	76	76
Electron energy	GeV	61.1	54.2	49.1	45.2

**Table 2.2:** Scaling of the electron beam energy, linac and further accelerator element dimensions with the choice of the total circumference in units  $1/n$  of the LHC circumference. For comparison, the CERN SPS has a circumference of 6.9 km, only somewhat larger than 1/4 of that of the LHC.

## 429 2.4 Luminosity

430 The luminosity  $L$  for the LHeC in its linac-ring configuration is determined as

$$L = \frac{N_e N_p n_p f_{rev} \gamma_p}{4\pi \epsilon_p \beta^*} \cdot \prod_{i=1}^3 H_i, \quad (2.1)$$

431 where  $N_{e(p)}$  is the number of electrons (protons) per bunch,  $n_p$  the number of proton bunches  
432 in the LHC,  $f_{rev}$  the revolution frequency in the LHC [the bunch spacing in a batch is given  
433 by  $\Delta$ , equal to 25 ns for protons in the LHC] and  $\gamma_p$  the relativistic factor  $E_p/M_p$  of the proton  
434 beam. Further,  $\epsilon_p$  denotes the normalised proton transverse beam emittance and  $\beta^*$  the proton  
435 beta function at the IP, assumed to be equal in  $x$  and  $y$ . The luminosity is moderated by the  
436 hourglass factor,  $H_1 = H_{geo} \simeq 0.9$ , the pinch or beam-beam correction factor,  $H_2 = H_{b-b} \simeq 1.3$ ,  
437 and the filling factor  $H_3 = H_{coll} \simeq 0.8$ , should an ion clearing gap in the electron beam be  
438 required. This justifies taking the product of these factors. As the product is close to unity, the  
439 factors are not listed for simplicity in the subsequent tables.

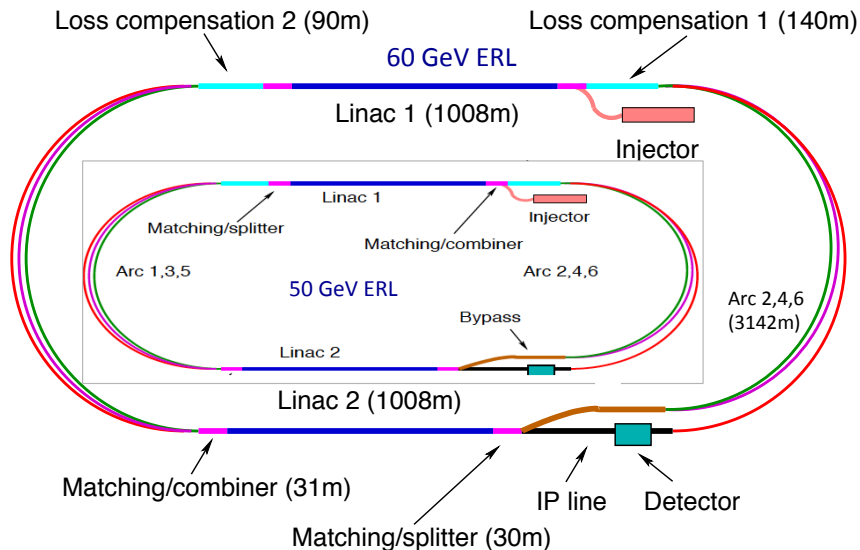


**Figure 2.2:** Schematic view of the three-turn LHeC configuration with two oppositely positioned electron linacs and three arcs housed in the same tunnel. Two configurations are shown: Outer: Default  $E_e = 60$  GeV with linacs of about 1 km length and 1 km arc radius leading to an ERL circumference of about 9 km, or 1/3 of the LHC length. Inner: Sketch for  $E_e = 50$  GeV with linacs of about 0.8 km length and 0.55 km arc radius leading to an ERL circumference of 5.4 km, or 1/5 of the LHC length, which is smaller than the size of the SPS. The 1/5 circumference configuration is flexible: it entails the possibility to stage the project as funds of physics dictate by using only partially equipped linacs, and it also permits upgrading to somewhat higher energies if one admits increased synchrotron power losses and operates at higher gradients.

440 The electron beam current is given as

$$I_e = eN_e f, \quad (2.2)$$

441 where  $f$  is the bunch frequency  $1/\Delta$ . The current for the LHeC is limited by the charge delivery  
 442 of the source. In the new default design we have  $I_e = 20$  mA which results from a charge of  
 443 500 pC for the bunch frequency of 40 MHz. It is one of the tasks of the PERLE facility to  
 444 investigate the stability of the 3-turn ERL configuration in view of the challenge for each cavity  
 445 to hold the sixfold current due to the simultaneous acceleration and deceleration of bunches at  
 446 three different beam energies each.

### 447 2.4.1 Electron-Proton Collisions

448 The design parameters of the luminosity were recently provided in a note describing the FCC-eh  
 449 configuration [32], including the LHeC. Tab. 2.3 represents an update comprising in addition  
 450 the initial 30 GeV configuration and the lower energy version of the FCC-hh based on the LHC  
 451 magnets<sup>2</sup>. For the LHeC, as noted above, we assume  $E_e = 50$  GeV while for FCC-eh we retain  
 452 60 GeV. Since the source limits the electron current, the peak luminosity may be taken not to

<sup>2</sup> The low energy FCC-pp collider, as of today, uses a 6 T LHC magnet in a 100 km tunnel. If, sometime in the coming decades, high field magnets become available based on HTS technology, then a 20 TeV proton beam energy may even be achievable in the LHC tunnel. To this extent the low energy FCC considered here and an HTS based HE-LHC would be comparable options in terms of their energy reach.

453 depend on  $E_e$ . Studies of the interaction region design, presented in this paper, show that one  
 454 may be confident of reaching a  $\beta^*$  of 10 cm but it will be a challenge to reach even smaller values.  
 455 Similarly, it will be quite a challenge to operate with a current much beyond 20 mA. That has  
 456 nevertheless been considered [33] for a possible dedicated LHeC operation mode for a few years  
 following the  $pp$  operation program.

Parameter	Unit	LHeC				FCC-eh	
		CDR	Run 5	Run 6	Dedicated	$E_p=20$ TeV	$E_p=50$ TeV
$E_e$	GeV	60	30	50	50	60	60
$N_p$	$10^{11}$	1.7	2.2	2.2	2.2	1	1
$\epsilon_p$	$\mu\text{m}$	3.7	2.5	2.5	2.5	2.2	2.2
$I_e$	mA	6.4	15	20	50	20	20
$N_e$	$10^9$	1	2.3	3.1	7.8	3.1	3.1
$\beta^*$	cm	10	10	7	7	12	15
Luminosity	$10^{33} \text{ cm}^{-2}\text{s}^{-1}$	1	5	9	23	8	15

**Table 2.3:** Summary of luminosity parameter values for the LHeC and FCC-eh. Left: CDR from 2012; Middle: LHeC in three stages, an initial run, possibly during Run 5 of the LHC, the 50 GeV operation during Run 6, both concurrently with the LHC, and a final, dedicated, stand-alone  $ep$  phase; Right: FCC-eh with a 20 and a 50 TeV proton beam, in synchronous operation.

457

458 The peak luminosity values exceed those at HERA by 2–3 orders of magnitude. The operation  
 459 of HERA in its first, extended running period, 1992-2000, provided an integrated luminosity  
 460 of about  $0.1 \text{ fb}^{-1}$  for the collider experiments H1 and ZEUS. This may now be expected to be  
 461 taken in a day of initial LHeC operation.

## 462 2.4.2 Electron-Ion Collisions

463 The design parameters and luminosity were also provided recently [32] for collisions of electrons  
 464 and lead nuclei (fully stripped  $^{208}\text{Pb}^{82+}$  ions). Tab. 2.4 is an update of the numbers presented  
 465 there for consistency with the Run 6 LHeC configuration in Tab. 2.3 and with the addition  
 466 of parameters corresponding to the  $E_p = 20$  TeV FCC-hh configuration. Further discussion of  
 467 this operating mode and motivations for the parameter choices in this table are provided in  
 468 Section 8.3.

469 One can expect the average luminosity during fills to be about 50% of the peak in Tab. 2.4  
 470 and we assume an overall operational efficiency of 50%. Then, a year of  $eA$  operation, possibly  
 471 composed by combining shorter periods of operation, would have the potential to provide an  
 472 integrated data set of about 5 (25)  $\text{fb}^{-1}$  for the LHeC (FCC-eh), respectively. This exceeds  
 473 the HERA electron-proton luminosity value by about tenfold for the LHeC and much more at  
 474 FCC-eh while the fixed target nuclear DIS experiment kinematics is extended by 3 – 4 orders of  
 475 magnitude. These energy frontier electron-ion configurations therefore have the unique potential  
 476 to radically modify our present view of nuclear structure and parton dynamics. This is discussed  
 477 in Chapter 4.

Parameter	Unit	LHeC	FCC-eh ( $E_p=20$ TeV)	FCC-eh ( $E_p=50$ TeV)
Ion energy $E_{Pb}$	PeV	0.574	1.64	4.1
Ion energy/nucleon $E_{Pb}/A$	TeV	2.76	7.88	19.7
Electron beam energy $E_e$	GeV	50	60	60
Electron-nucleon CMS $\sqrt{s_{eN}}$	TeV	0.74	1.4	2.2
Bunch spacing	ns	50	100	100
Number of bunches		1200	2072	2072
Ions per bunch	$10^8$	1.8	1.8	1.8
Normalised emittance $\epsilon_n$	$\mu\text{m}$	1.5	1.5	1.5
Electrons per bunch	$10^9$	6.2	6.2	6.2
Electron current	mA	20	20	20
IP beta function $\beta_A^*$	cm	10	10	15
e-N Luminosity	$10^{32}\text{cm}^{-2}\text{s}^{-1}$	7	14	35

**Table 2.4:** Baseline parameters of future electron-ion collider configurations based on the electron ERL, in concurrent  $eA$  and  $AA$  operation mode with the LHC and the two versions of a future hadron collider at CERN. Following established convention in this field, the luminosity quoted, at the start of a fill, is the *electron-nucleon* luminosity which is a factor  $A$  larger than the usual (i.e. electron-nucleus) luminosity.

## 478 2.5 Linac Parameters

479 The brief summary of the main LHeC characteristics here concludes with a table of the main  
480 ERL parameters for the new default electron energy of 50 GeV, Tab. 2.5, which are discussed in detail in Chapter 8.

Parameter	Unit	Value
Frequency	MHz	801.58
Bunch charge	pC	499
Bunch spacing	ns	24.95
Electron current	mA	20
Injector energy	MeV	500
Gradient	MV/m	19.73
Cavity length, active	m	0.918
Cavity length, flange-to-flange	m	1.5
Cavities per cryomodule		4
Length of cryomodule	m	7
Acceleration per cryomodule	MeV	72.45
Total number of cryomodules		112
Acceleration energy per pass	GeV	8.1

**Table 2.5:** Basic LHeC ERL characteristics for the default configuration using two such linacs located opposite to each other in a racetrack of 5.4 km length. Each linac is passed three times for acceleration and three times for deceleration.

481

## 482 2.6 Operation Schedule

483 The LHeC parameters are determined to be compatible with a parasitic operation with the  
484 nominal HL-LHC proton-proton operation. This implies limiting the electron bunch current to

485 sufficiently small values so that the proton beam-beam parameter remains small enough to be  
486 negligible for the proton beam dynamics.

487 Assuming a ten year construction period for the LHeC after approval of the project and a  
488 required installation window of two years for the LHeC detector, the earliest realistic operation  
489 period for the LHeC coincides with the LHC Run 5 period in 2032 and with a detector installation  
490 during LS4 which is currently scheduled during 2030 and would need to be extended by one year  
491 to 2031. The baseline HL-LHC operation mode assumes 160 days of proton operation, 20 days  
492 of ion operation and 20 days of machine development time for the Run4 period, amounting to  
493 a total of 200 operation days per year. After the Run4 period the HL-LHC does at the moment  
494 not consider ion operation and assumes 190 days for proton operation. The HL-LHC project  
495 assumes an overall machine efficiency of 54 % (e.g. fraction of scheduled operation time spent in  
496 physics production) and we assume that the ERL does not contribute to significant additional  
497 downtime for the operation. Assuming an initial 15 mA of electron beam current, a  $\beta^*$  of 10 cm  
498 and HL-LHC proton beam parameters, the LHeC reaches a peak luminosity of  $0.5 \cdot 10^{34} \text{cm}^{-2} \text{s}^{-1}$ .  
499 Assuming further a proton beam lifetime of 16.7 hours, a proton fill length of 11.7 hours and an  
500 average proton beam turnaround time of 4 hours, the LHeC can reach in this configuration an  
501 annual integrated luminosity of  $20 \text{fb}^{-1}$ .

502 For the evaluation of the physics potential it is important to note that the Run5 initial  $ep$   
503 operation period may accumulate about  $50 \text{fb}^{-1}$  of integrated luminosity. This is the hundredfold  
504 value which H1 (or ZEUS) took over a HERA lifetime of 15 years. As one may expect, for details  
505 see Chapter 3, such a huge DIS luminosity is ample for pursuing basically the complete QCD  
506 programme. In particular, the LHeC would deliver on time for the HL-LHC precision analyses  
507 the external, precise PDFs and with just a fraction of the  $50 \text{fb}^{-1}$  the secrets of low  $x$  parton  
508 dynamics would unfold. Higher  $ep$  luminosity is necessary for ultimate precision and for the top,  
509 BSM and the Higgs programme of the LHeC to be of competitive value.

510 For the Run6 period of the HL-LHC, the last of the HL-LHC operation periods, we assume  
511 that the number of machine development sessions for the LHC can be suppressed, providing  
512 an increase in the operation time for physics production from 190 days to 200 days per year.  
513 Furthermore, we assume that the electron beam parameters can be slightly further pushed.  
514 Assuming a  $\beta^*$  reduced to 7 cm, an electron beam current of up to 25 mA and still nominal  
515 HL-LHC proton beam parameters, the LHeC reaches a peak performance of  $1.2 \cdot 10^{34} \text{cm}^{-2} \text{s}^{-1}$   
516 and an annual integrated luminosity of  $50 \text{fb}^{-1}$ . This would add up to an integrated luminosity  
517 of a few hundred  $\text{fb}^{-1}$ , a strong base for top, BSM and Higgs physics at the LHeC.

518 Beyond the HL-LHC exploitation period, the electron beam parameters could be further pushed  
519 in dedicated  $ep$  operation, when the requirement of a parasitic operation to the HL-LHC proton-  
520 proton operation may no longer be imposed. The proton beam lifetime without proton-proton  
521 collisions would be significantly larger than in the HL-LHC configuration. In the following we  
522 assume a proton beam lifetime of 100 hours and a proton beam efficiency of 60 % without proton-  
523 proton beam collisions. The electron beam current in this configuration would only be limited  
524 by the electron beam dynamics and the SRF beam current limit. Assuming that electron beam  
525 currents of up to 50 mA, the LHeC would reach a peak luminosity of  $2.4 \cdot 10^{34} \text{cm}^{-2} \text{s}^{-1}$  and an  
526 annual integrated luminosity of up to  $180 \text{fb}^{-1}$ . Table 2.6 summarises the LHeC configurations  
527 over these three periods of operation.

528 Depending on the years available for a dedicated final operation (or through an extension of  
529 the  $pp$  LHC run, currently not planned but interesting for collecting 4 instead of  $3 \text{ab}^{-1}$  to, for  
530 example, observe di-Higgs production at the LHC), a total luminosity of  $1 \text{ab}^{-1}$  could be available  
531 for the LHeC. This would double the precision of Higgs couplings measured in  $ep$  as compared to

Parameter	Unit	Run 5 Period	Run 6 Period	Dedicated
Brightness $N_p/(\gamma\epsilon_p)$	$10^{17}\text{m}^{-1}$	2.2/2.5	2.2/2.5	2.2/2.5
Electron beam current	mA	15	25	50?
Proton $\beta^*$	m	0.1	0.7	0.7
Peak luminosity	$10^{34}\text{cm}^{-2}\text{s}^{-1}$	0.5	1.2	2.4
Proton beam lifetime	h	16.7	16.7	100
Fill duration	h	11.7	11.7	21
Turnaround time	h	4	4	3
Overall efficiency	%	54	54	60
Physics time / year	days	160	180	185
Annual integrated lumi.	$\text{fb}^{-1}$	20	50	180

**Table 2.6:** The LHeC performance levels during different operation modes.

532 the default HL-LHC run period with  $ep$  added as described. It would also significantly enlarge  
 533 the potential to observe or/and quantify rare and new physics phenomena. Obviously such  
 534 considerations are subject to the grand developments at CERN. A period with most interesting  
 535 physics and on-site operation activity could be particularly welcome for narrowing a possible  
 536 large time gap between the LHC and its grand successor, the FCC-hh. One may, however, be  
 537 interested in ending LHC on time. It thus is important for the LHeC project to recognise its  
 538 particular value as an asset of the HL-LHC, and on its own, with even less than the ultimate  
 539 luminosity, albeit values which had been dreamt of at HERA.

## Chapter 3

# Precision Standard Model Physics with LHeC

The LHeC provides the opportunity to push our Standard Model (SM) measurements to unprecedented precision. In this Chapter we describe the opportunities that the LHeC offers for precision studies of many aspects of the Standard Model. First, in Secs. 3.1 and 3.2 the focus lies on QCD: on conventional parton structure through parton densities in the former; and on less conventional aspects where the limit of our current understanding of QCD can be pushed, in the latter. Then, Sec. 3.3 is devoted to precision electron-weak physics, while top quark physics is the subject of Sec. 3.4. Some focus is put on the fact, that precision SM measurements at the LHeC will further allow stringent searches for deviations from the SM predictions which may signal the presence of undiscovered channels involving physics beyond the SM (BSM).

add what is discussed in this chapter. PDFs,  $\alpha_s$ , QCD phenomena, low- $x$ ,  $F_L$ , 3D structure of proton, diffraction, EW physics, Top-quark physics

While direct production of BSM physics may be limited by the centre-of-mass (CoM) energy ( $\sqrt{s}$ ) of the machine, indirect precision measurements can probe scales many times larger than the CoM energy; this is an area where the LHeC excels. While the LHeC can directly probe the TeV scale, it offers the most promising avenue to search for BSM physics signals at multi-TeV scales, gathering clues as how to design the next-generation of accelerator experiments such as the FCC program.

### 3.1 Resolving the Parton Substructure of the Proton

An essential step in advancing our knowledge about the Standard Model is improving our knowledge of the Parton Distribution Functions (PDFs). For many precision measurements and *standard-candle* observables at the HL-LHC, a dominant systematic limitation on our sensitivity to the highest energy scales is the PDF uncertainty, as well as uncertainties on a number of related hadron structure observables (??). PDF uncertainty reductions therefore have the potential to greatly extend the programme of precision Standard Model measurements at hadron colliders. Furthermore, the sensitivity of collider-based BSM physics searches, both in terms of the interaction strengths and effective masses of hypothetical degrees-of-freedom, are greatly enhanced with precisely known PDFs and the LHeC can be expected to have a sizeable impact

570 on BSM searches by helping to relieve PDF limitations of BSM searches at the HL-LHC and  
571 other facilities.

### 572 3.1.1 Open Questions on the QCD of PDFs **needed?**

573 **do we need this section or title?? All reads fairly repetitive to other paragraphs.**

574 The explorations of PDFs at the LHeC will be instrumental in disentangling many fundamental  
575 issues in QCD and the structure of hadrons and nuclei, for which many open questions remain.  
576 For example, the detailed flavour structure of the nucleon remains imperfectly determined, with  
577 very large uncertainties in the magnitude and shape of the proton's strangeness content as well  
578 as the exact nature of flavour-symmetry breaking in the light-quark sea (e.g. the behaviour  
579 of the PDF ratio  $\bar{d}/\bar{u}$ ) being representative examples. The precision and kinematic reach of  
580 the LHeC will allow it to significantly clarify these issues, as well as related ones that must be  
581 addressed in the push for high-precision nucleon PDFs, such as the nature and size of quark-level  
582 charge-symmetry violation [34].

583 The increased energy and luminosity of the LHeC will enable explorations of extreme regions  
584 in the kinematic  $(x, Q^2)$  plane to study new QCD phenomena. These include the rise of the  
585 proton's inclusive DIS structure function  $F_2^p$  at low  $x$ , which may suggest the onset of parton  
586 saturation and point to new contributions which are not included in the DGLAP framework  
587 of leading-twist linear evolution equations. Here, the LHeC can offer us a glimpse of the high-  
588 density regime of QCD where we can study collective effects and test/refine our theoretical  
589 resummation tools.

590 The measurement of heavy-quark production at the LHeC will be especially important to im-  
591 prove our knowledge of the gluon, strange, charm and bottom PDFs. The challenge is that the  
592 computation of heavy-quark production in the framework of perturbative QCD is complicated  
593 due to the presence of several large scales like the heavy-quark masses,  $m_Q$ , the transverse mo-  
594 mentum,  $p_T$ , of the produced quarks, and the momentum transfer,  $Q^2$ . In this case, the large  
595 kinematic reach of the LHeC will be extremely advantageous as the span from the low-energy  
596 *decoupling* region into the high-energy *asymptotic* region will allow improved understanding of  
597 the treatment of mass in perturbative QCD calculations.

598 **drop? We point out that analogous questions to these (and others) apply to nuclear PDFs, for**  
599 **which experimental constraints are far more limited at the present time. While the question of**  
600 **LHeC impacts on the nuclear PDFs will be addressed in Chapter 4, we stress that improved**  
601 **knowledge of nuclear-medium effects and nuclear PDFs that LHeC might furnish could substan-**  
602 **tially improve free-nucleon PDFs, for which contemporary attempts to separate the PDF flavour**  
603 **dependence often involve measurements on nuclear targets. Also, when measuring more com-**  
604 **plicated hadronic final states, the LHeC might also provide information sensitive to the PDFs**  
605 **of other hadrons, including the lighter mesons, which would shed light on aspects of QCD.**

606 *PDFs* have two meanings in that i) they represent a probability view on the substructure of  
607 the proton, or similarly of other hadrons, at a given distance  $1/\sqrt{Q^2}$ , and ii) they describe,  
608 supposedly universally through cross section factorisation theorems [35], the hard scattering  
609 processes involving partons. In his referee report on the LHeC CDR, in 2012, Guido Altarelli  
610 noted on the factorisation theorem in QCD for hadron colliders that: *many people still advance*  
611 *doubts. Actually this question could be studied experimentally, in that the LHeC, with its im-*  
612 *proved precision, could put bounds on the allowed amount of possible factorisation violations*  
613 *(e.g. by measuring in DIS the gluon at large  $x$  and then comparing with jet production at large*

614  $p_T$  in hadron colliders). This question was addressed also in a previous LHeC paper [36]. It  
 615 receives extra emphasis because in the relevant kinematic region at the LHC both new physics  
 616 and violations of factorisation may be superimposed. This requires very high luminosity in  $ep$  in  
 617 order to distinguish valence from sea quarks, up from down flavours and the gluon from quarks  
 618 at high  $x$ .

### 619 3.1.2 Parton Distributions and DIS

620 The momentum distributions of partons inside the proton must be determined from experiment  
 621 and the most reliable base so far have been the HERA data [37,38]. These data provide a first  
 622 set of PDFs. From the LHC and Tevatron, Drell-Yan, jet cross section and other data can be  
 623 employed to obtain additional constraints on PDFs, while all of these still have to use HERA  
 624 data also (see Sect. 3.1.7). It is one of the important principal goals and opportunities of the  
 625 LHeC to provide a complete data set which has the potential to replace all previous data.

626 The most suited process to obtain an unbiased determination of the quark and gluon distribu-  
 627 tions is inclusive deep inelastic neutral current (NC) and charged current (CC) scattering. It  
 628 is theoretically cleanest, it is free of colour interactions in the initial or final state, it enables  
 629 a prescribed selection of  $Q^2$ , and it allows the determination of the kinematics externally to  
 630 the intrinsic scattering process. It also clearly distinguishes the NC from CC probes of proton  
 631 structure.

632 The way to do PDF determinations with  $ep$  collider data has been paved over decades with  
 633 HERA. The methodology and results from HERA PDF analyses are therefore briefly outlined  
 634 in the following, and subsequently the prospects for PDFs at LHeC are discussed.

### 635 3.1.3 HERA PDFs and the methodology of PDF fits

636 Full sets of PDFs are determined by QCD fits to inclusive DIS data from exclusively HERA  
 637 experiments, H1 and ZEUS [37]. These PDFs are denoted *HERAPDF*, and the fits use infor-  
 638 mation from both  $e^\pm p$  neutral current (NC) and charged current (CC) scattering up to high  
 639  $Q^2 = 30,000 \text{ GeV}^2$ . The lower- $Q^2$  NC data constrain the low- $x$  sea-quark distributions and,  
 640 through their precisely measured  $Q^2$  variations, also the gluon distribution. The difference  
 641 between the NC  $e^+p$  and  $e^-p$  cross sections at high  $Q^2$ , together with the high- $Q^2$  CC data,  
 642 constrain the valence distributions. Data from different centre-of-mass energies of  $\sqrt{s} = 920, 820,$   
 643  $575$  and  $460 \text{ GeV}$  give information on the longitudinal structure function  $F_L$  and hence further  
 644 constrain the gluon distribution (see also the discussion on  $F_L$  at the LHeC in Sect. 3.2.3). The  
 645 precision of the HERA combined data is below 1.5% over the  $Q^2$  range of  $3 < Q^2 < 500 \text{ GeV}^2$   
 646 and remains below 3% up to  $Q^2 = 3000 \text{ GeV}^2$ .

647 The evolution equations of QCD yield the PDFs at any value of  $Q^2$  given that they are param-  
 648 eterised as functions of  $x$  at an initial scale  $Q_0^2$ . The evolved PDFs are then convoluted with  
 649 QCD-calculable coefficient functions to predict the DIS structure functions and thus to give  
 650 predictions for the DIS cross sections at the measured values of  $Q^2$ . These are then confronted  
 651 with the data through a  $\chi^2$  fit, which determines the PDF parameters. The QCD analysis is  
 652 performed at LO, NLO and NNLO and the latest version is the HERAPDF2.0 family [37]

653 The QCD analysis uses the *xFitter* framework [38–40]. The DGLAP evolution of the PDFs, as  
 654 well as the light-quark coefficient functions, are calculated using QCDNUM [41,42]. The contri-  
 655 butions of heavy quarks are calculated in the general-mass variable-flavour-number (GMVFN)

656 scheme of Refs. [43, 44]. The renormalisation and factorisation scales for the DIS processes  
 657 are taken as  $\mu_r = \mu_f = \sqrt{Q^2}$ . The program MINUIT [45] is used for the  $\chi^2$  minimisation.  
 658 Experimental uncertainties are determined using the Hessian method.

659 In the HERAPDF analysis, the starting scale is chosen to be  $Q_0^2 = 1.9 \text{ GeV}^2$  such that it is  
 660 below the threshold at the charm mass  $m_c^2$ . The heavy quark masses are  $m_c = 1.43 \text{ GeV}$  and  
 661  $m_b = 4.5 \text{ GeV}$ , following the results of an analysis of the HERA combined charm and beauty data.  
 662 The strong coupling constant is set to  $\alpha_S(M_Z) = 0.118$ . A minimum  $Q^2$  cut  $Q_{min}^2 \geq 3.5 \text{ GeV}^2$   
 663 is imposed on the HERA data. All these assumptions are varied in the evaluation of model  
 664 uncertainties on the final fit.

665 The quark distributions at the initial scale are represented by the generic form

$$xq_i(x) = A_i x^{B_i} (1-x)^{C_i} P_i(x), \quad (3.1)$$

666 where  $i$  specifies the flavour of the quark distribution and  $P_i(x) = (1 + D_i x + E_i x^2)$ . The param-  
 667 eterised quark distributions,  $xq_i$ , are chosen to be the valence quark distributions ( $xu_v$ ,  $xd_v$ )  
 668 and the light anti-quark distributions ( $x\bar{u}$ ,  $x\bar{d}$ ). The gluon distribution is parameterised with  
 669 the more flexible form  $xg(x) = A_g x^{B_g} (1-x)^{C_g} P_g(x) - A'_g x^{B'_g} (1-x)^{C'_g}$ . The parameters  $A_{u_v}$   
 670 and  $A_{d_v}$  are fixed using the quark counting rule and  $A_g$  using the momentum sum rule. The  
 671 normalisation and slope parameters,  $A$  and  $B$ , of  $\bar{u}$  and  $\bar{d}$  are set equal such that  $x\bar{u} = x\bar{d}$   
 672 at  $x \rightarrow 0$ . The strange quark PDF  $x\bar{s}$  is set as a fixed fraction  $r_s = 0.67$  of the  $x\bar{d}$  PDF.  
 673 This fraction is varied in the determination of model uncertainties. By default it is assumed  
 674 that  $xs = x\bar{s}$ . The  $D, E$  and  $F$  terms in the polynomial  $P_i(x)$  are used only if required by  
 675 the data, following the procedure described in Ref. [38]. This leads to two additional terms,  
 676  $P_{u_v}(x) = 1 + E_{u_v} x^2$  and  $P_{\bar{u}} = 1 + D_{\bar{u}} x$ . Alternative parameterisations are used in the evaluation  
 677 of a parameterisation uncertainty. These variations include: introducing extra parameters  $D$ ,  
 678  $E$  for each quark distribution; the removal of primed gluon parameters; and the relaxation of  
 679 assumptions about the low- $x$  sea. These fits provide alternative extracted PDFs with similar  
 680 fit  $\chi^2$ . The maximum deviation from the central PDF at each value of  $x$  is taken as an enve-  
 681 lope and added in quadrature with the experimental and model uncertainties to give the total  
 682 uncertainty. Full details on the fit methodology are given in [37].

683 The results of the HERAPDF analysis are shown for the HERAPDF2.0NNLO PDF set, display-  
 684 ing experimental, model and parameterisation uncertainties separately, in Fig. 3.1 and compared  
 685 to other PDFs (using total uncertainties) in Fig. 3.2. Note that the HERAPDF differs from  
 686 other PDF sets in that; i) it represents a fit to a consistent data set with small correlated sys-  
 687 tematic uncertainties; ii) it uses data on a proton target such that no heavy target corrections  
 688 are needed and the assumption of strong isospin invariance,  $d_{\text{proton}} = u_{\text{neutron}}$ , is not required;  
 689 iii) the kinematic region is chosen such that no regions where higher twist effects are important  
 690 are included in the analysis.

691 **Todo.Add: What have we learned from HERAPDF in view of LHeC.**

692 **A sentence about  $\alpha_s$ , and that it cannot be determined from inclusive DIS data.**

### 693 3.1.4 Simulated LHeC Data Sets

694 In order to estimate the uncertainties of PDFs from LHeC, several sets of LHeC inclusive NC/CC  
 695 DIS data with a full set of uncertainties is simulated and described in the following. The system-  
 696 atic uncertainties of the DIS cross sections have a number of sources, which can be classified as  
 697 uncorrelated and correlated across bin boundaries. For the NC case, the uncorrelated sources,

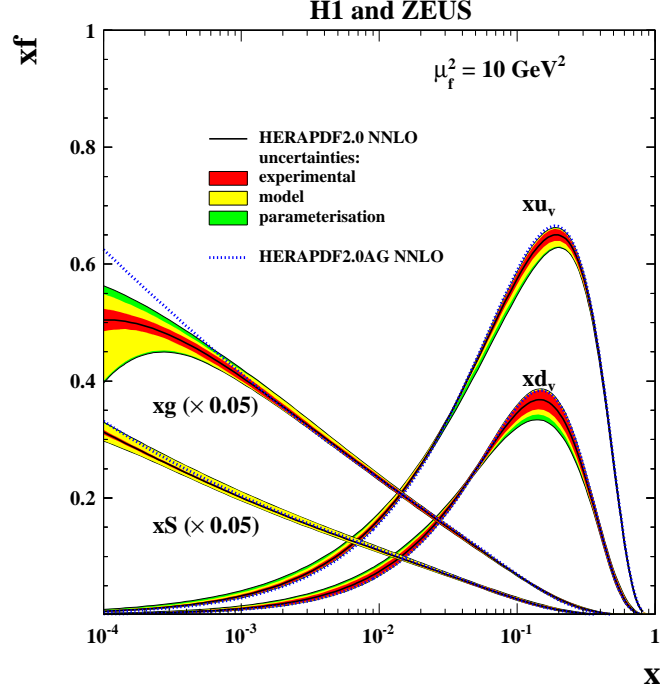


**Figure 3.1:** The PDF set HERAPDF2.0NNLO for valence, gluon and total sea quark distributions at factorisation scale  $\mu_f^2 = 10 \text{ GeV}^2$ . The color coding represents the experimental, model and parameterisation uncertainties separately. An alternative (AG) PDF with no negative term added to the gluon parameterisation is also shown.

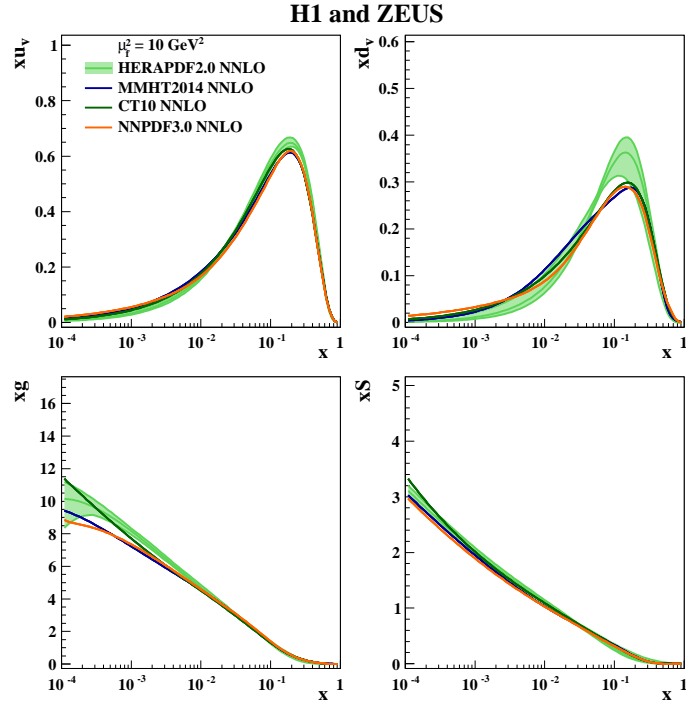


**Figure 3.2:** The PDF set HERAPDF2.0NNLO for valence, gluon and total sea quark distributions compared to other PDF sets MMHT14, CT10, NNPDF3.0, at a factorisation scale  $\mu_f^2 = 10 \text{ GeV}^2$ .

698 apart from event statistics, are a global efficiency uncertainty, due for example to tracking  
699 or electron identification errors, as well as uncertainties due to photo-production background,  
700 calorimeter noise and radiative corrections. The correlated uncertainties result from imperfect  
701 electromagnetic and hadronic energy scale and angle calibrations. In the classic  $ep$  kinematic  
702 reconstruction methods used here, the scattered electron energy  $E'_e$  and polar angle  $\theta_e$ , comple-  
703 mented by the energy of the hadronic final state  $E_h$  can be employed to determine  $Q^2$  and  $x$  in  
704 a redundant way.

705 Briefly,  $Q^2$  is best determined with the electron kinematics and  $x$  is calculated from  $y = Q^2/sx$ .  
706 At large  $y$  the inelasticity is essentially measured with the electron energy  $y_e \simeq 1 - E'_e/E_e$ .  
707 At low  $y$  the relation  $y_h = E_h \sin^2(\theta_h/2)/E_e$  is used to provide a measurement of the inelas-  
708 ticity with the hadronic final state energy  $E_h$  and angle  $\theta_h$ , resulting in  $\delta y_h/y_h \simeq \delta E_h/E_h$  to  
709 good approximation. There have been various refined methods proposed to determine the DIS  
710 kinematics, such as the double angle method, which is commonly used to calibrate the electro-  
711 magnetic energy scale, or the so-called Sigma method [46], which exhibits reduced sensitivity  
712 to QED radiative corrections, see a discussion in Ref. ???. For the estimate of the cross section  
713 uncertainty the electron method ( $Q_e^2, y_e$ ) is used at large  $y$ , and at low  $y$  we use  $Q_e^2, y_h$ , which is  
714 transparent and accurate to better than a factor of two. In much of the phase space, moreover,  
715 it is rather the uncorrelated efficiency or further specific errors than the kinematic correlations,  
716 which dominate the cross section measurement precision.

717 The assumptions used in the simulation of pseudodata are summarised in Tab. 3.1. The proce-  
718 dure was gauged with full H1 Monte Carlo simulations and the assumptions are corresponding  
719 to H1's achievements with an improvement by at most a factor of two. Using a numerical proce-  
720 dure [47] the scale uncertainties were transformed to kinematics-dependent correlated cross  
section uncertainties caused by imperfect measurements of  $E'_e$ ,  $\theta_e$  and  $E_h$ . These data uncer-

Source of uncertainty	Uncertainty
Scattered electron energy scale $\Delta E'_e/E'_e$	0.1 %
Scattered electron polar angle	0.1 mrad
Hadronic energy scale $\Delta E_h/E_h$	0.5 %
Radiative corrections	0.3 %
Photoproduction background (only $y > 0.5$ )	1 %
Global efficiency error	0.5 %

**Table 3.1:** Assumptions used in the simulation of the NC cross sections on the size of uncertainties from various sources. The top three are uncertainties on the calibrations which are transported to provide correlated systematic cross section errors. The lower three values are uncertainties of the cross section caused by various sources.

721 tainties were imposed for all data sets, NC and CC, as are subsequently listed and described.  
722

723 The design of the LHeC assumes that it operates with the LHC in the high luminosity phase,  
724 following LS4 at the earliest. As detailed in Chapter 2, it is assumed there will be an initial  
725 phase, during which LHeC may collect  $50 \text{ fb}^{-1}$  of data. This may begin with a sample of  $5 \text{ fb}^{-1}$ .  
726 Such values are very high when compared with HERA, corresponding to the hundred(ten)-fold  
727 of luminosity which H1 collected in its about 15 years lifetime. The total luminosity may reach  
728 about  $1 \text{ ab}^{-1}$ . The bulk of the data is likely to be taken with electrons, possibly at large negative  
729 helicity  $P_e$ , because this configuration maximises the number of Higgs bosons one can produce  
730 at the LHeC:  $e^-$  couples to  $W^-$  which interacts primarily with an up-quark and the CC cross  
731 section is proportional to  $(1 - P_e)$ . However, for electroweak physics there is a strong interest  
732 to vary the polarisation and charge. With a linac source, the generation of an intense positron

733 beam is very challenging and will not be able to compete with the electron intensity. Finally, a  
 734 dataset has also been produced with reduced proton beam energy which enlarges the acceptance  
 towards large  $x$  at smaller  $Q^2$ . The full list of sets is provided in Tab. 3.2.

Parameter	Unit	Data set								
		D1	D2	D3	D4	D5	D6	D7	D8	D9
Proton beam energy	TeV	7	7	7	7	1	7	7	7	7
Lepton charge		-1	-1	-1	-1	-1	+1	+1	-1	-1
Longitudinal lepton polarisation		-0.8	-0.8	0	-0.8	0	0	0	+0.8	+0.8
Integrated luminosity	fb <sup>-1</sup>	5	50	50	1000	1	1	10	10	50

**Table 3.2:** Summary of characteristic parameters of data sets used to simulate neutral and charged current  $e^\pm$  cross section data, for a lepton beam energy of  $E_e = 50$  GeV.

735

736 The highest energies obviously give access to the smallest  $x$  at a given  $Q^2$ , and to the maximum  
 737  $Q^2$  at fixed  $x$ . This is illustrated with the kinematic plane and iso-energy and iso-angle lines, see Fig. 3.3.

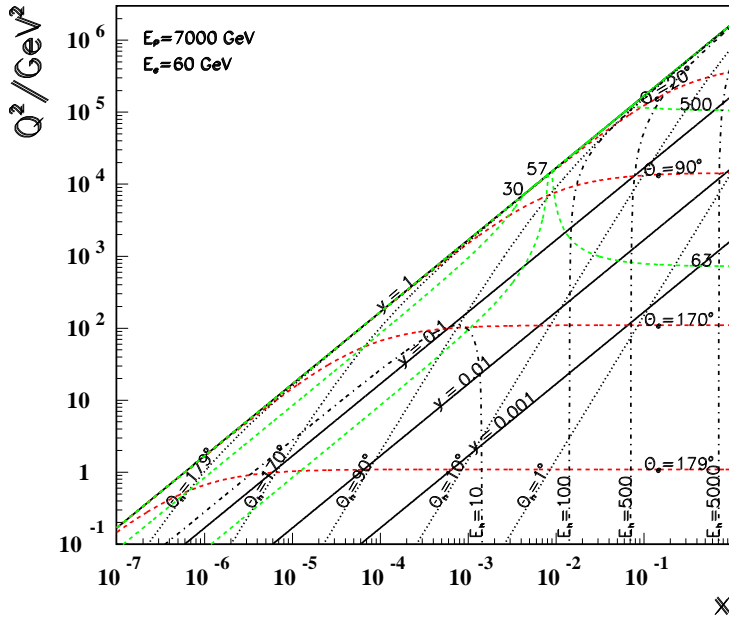


**Figure 3.3:** Kinematic plane covered with the maximum beam energies at LHeC. Red dashed: Lines of constant scattered electron polar angle. Note that low  $Q^2$  is measured with electrons scattered into the backward region, highest  $Q^2$  is reached with Rutherford backscattering; Black dotted: lines of constant angle of the hadronic final state; Black solid: Lines of constant inelasticity  $y = Q^2/sx$ ; Green dashed: Lines of constant scattered electron energy  $E'_e$ . Most of the central region is covered by what is termed the kinematic peak, where  $E'_e \simeq E_e$ . The small  $x$  region is accessed with small energies  $E'_e$  below  $E_e$  while the very forward, high  $Q^2$  electrons carry TeV energies; Black dashed-dotted: lines of constant hadronic final state energy  $E_h$ . Note that the very forward, large  $x$  region sees very high hadronic energy deposits too.

738

739 It is instructive to see how the variation of the proton beam energy changes the kinematics  
 740 considerably and enables additional coverage of various regions. This is clear from Fig. 3.4  
 741 which shows the kinematic plane choosing the about minimum energies the LHeC could operate

with. There are striking changes one may note which are related to kinematics (c.f. Ref. [47]).

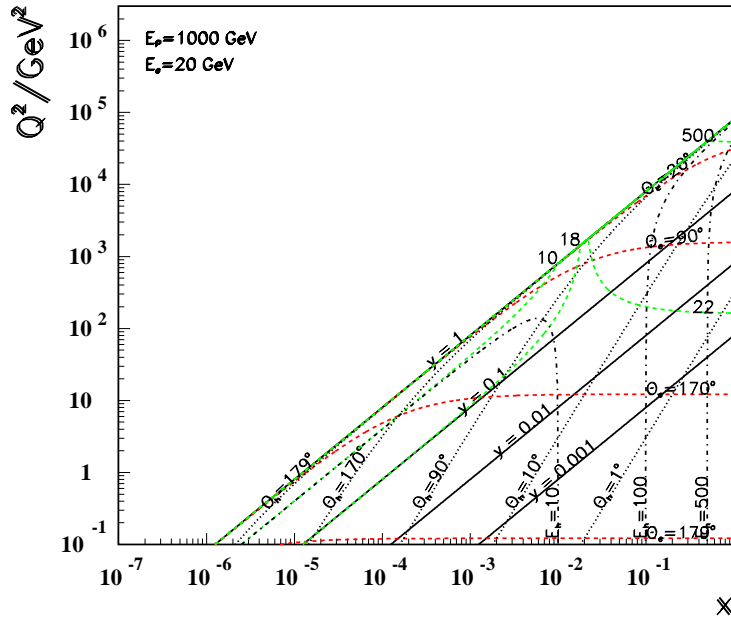


**Figure 3.4:** Kinematic plane covered with the minimum beam energies at LHeC. The meaning of the curves is the same as in the previous figure. This coverage is very similar to that by HERA as the energies are about the same.

742

743 One can see that the line of  $\theta_e = 179^\circ$  now corresponds to  $Q^2 \simeq 1 \text{ GeV}^2$  which is due to lowering  
 744  $E_e$  as compared to the maximum energy case, Fig. 3.3. Similarly, comparing the two figures one  
 745 finds that the lower  $Q^2$ , larger  $x$  region becomes much easier accessible with lower energies, in  
 746 this case solely owing to the reduction of  $E_p$  from 7 to 1 TeV. It is worthwhile to note that the  
 747 LHeC, when operating at these low energies, would permit a complete repetition of the HERA  
 748 programme, within not many days of data taking.

749 The coverage of the kinematic plane is illustrated in the plot of the  $x, Q^2$  bin centers of data  
 750 points used in simulations, see Fig. 3.5 [48]. The full coverage at highest Bjorken- $x$ , i.e. very  
 751 close to  $x = 1$ , is enabled by the high luminosity of the LHeC. This was impossible to achieve for  
 752 HERA as the NC/CC DIS cross sections decrease proportional to some power of  $(1 - x)$  when  
 753  $x$  approaches 1, as has long been established with Regge counting [49–51].

754 It has been a prime goal, leading much beyond previous PDF studies, to understand the im-  
 755 portance of these varying conditions for measuring PDFs with the LHeC. This holds especially  
 756 for the question about what can be expected from the initial LHeC operation period, which is  
 757 of highest interest for the LHC analyses during the HL-LHC period. Some special data sets of  
 758 lowered electron energy have also been produced in order to evaluate the potential to measure  
 759  $F_L$ , see Sect. 3.2.3. These data sets have not been included in the analyses which are presented  
 760 in the following.

### 761 3.1.5 Expectations on PDFs with LHeC inclusive DIS data

762 In this section, PDF constraints from the full simulation of LHeC inclusive NC and CC cross  
 763 section measurements are investigated. The expectations for the “LHeC final inclusive” dataset,

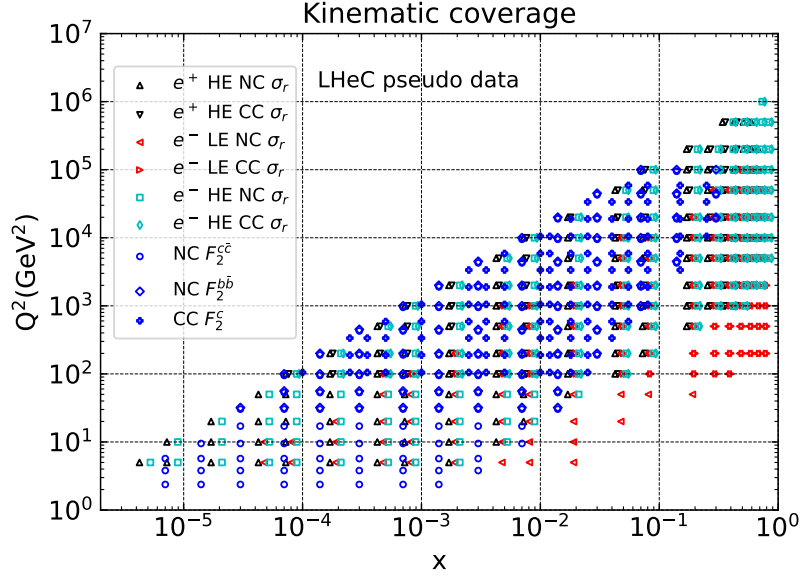


**Figure 3.5:** Illustration of the  $x, Q^2$  values of simulated cross section and heavy quark density data used in LHeC studies. The red points illustrate the gain in acceptance towards large  $x$  at fixed  $Q^2$  when  $E_p$  is lowered, see text.

764 corresponding to the combination of datasets D4+D5+D7+D8, are presented. While this full  
 765 combination is recorded concurrently to the HL-LHC operation, it will be available only after  
 766 the end of HL-LHC, and will become valuable for re-analysis or re-interpretation of (HL-)LHC  
 767 data, and for further-future hadron colliders.

768 Given the expected timeline for the HL-LHC, it is of high relevance that the LHeC can deliver  
 769 PDFs of transformative precision already on a short timescale, in order to be useful already  
 770 within the lifetime of the HL-LHC. Therefore, in the present study particular attention is paid  
 771 on PDF constraints that are possible from the first  $50 \text{ fb}^{-1}$  of electron-proton data, which cor-  
 772 responds to the first three years of LHeC operation. This dataset is labelled D2 (**This was D3**  
 773 **previously. Max, please check and make it consistent further below!**) in Tab. 3.2 and is referred  
 774 to as “LHeC 1st run” in the following. Infact, it is expected that the data recorded during a few  
 775 days of data taking are valuable and will impose additional PDF constraints, and these analyses  
 776 will provide the starting point for the LHeC PDF programme.

777 Additional dedicated studies of the impact of  $s, c, b$  data on the PDFs are then also presented,  
 778 based on a small amount ( $10 \text{ fb}^{-1}$ ) of  $e^-p$  simulated data. Note, the precision measurements  
 779 of  $s, c, b$  final states are not exploited in “LHeC 1st run” study, which considers only inclusive  
 780 NC/CC DIS data.

781 Additional PDF constraints that would be provided by a measurement of  $F_L$  (c.f. Sect. 3.2.3)  
 782 and  $ep$  jet measurements (c.f. Sect. 3.2.1) are not considered in the present study.

783 To assess the importance of different operating conditions, the impact of datasets with: differ-  
 784 ing amounts of integrated luminosity (D1 vs. D4); positrons (D6 vs. D7); and with different  
 785 polarisation states for the leptons (D3 vs. D8) are also considered.

786 For the QCD analyses presented in this section, the xFitter [52] framework has been used, with  
 787 settings based on the HERAPDF QCD fit analysis [37], described above, but with some differing

788 or relaxed assumptions as detailed below.

## 789 **Fit Procedure**

790 In order to study the effects of the simulated LHeC data on the knowledge of PDFs, PDF fits  
791 to the simulated input datasets, including their full systematic uncertainties as detailed above,  
792 are performed in NLO QCD. Fits in NNLO have been performed as a cross check. The present  
793 analysis follows closely the HERA QCD fit procedure as outlined above, with a minimum  $Q^2$  of  
794  $3.5 \text{ GeV}^2$  and an evolution starting scale  $Q_0^2 = 1.9 \text{ GeV}^2$  where the parametric functions as in  
795 eq. (3.1) is used. The parameterised PDFs are the valence distributions  $xu_v$  and  $xd_v$ , the gluon  
796 distribution  $xg$ , and the  $x\bar{U}$  and  $x\bar{D}$  distributions, where  $x\bar{U} = x\bar{u}$ ,  $x\bar{D} = x\bar{d} + x\bar{s}$ . The chosen  
797 fit parameters are similar, albeit to some extent more flexible, than for HERAPDF2.0 and in  
798 total 14 parameters are free for the nominal fits<sup>1</sup>.

799 This ansatz is natural to the extent that the NC and CC inclusive cross sections determine  
800 the sums of up and down quark distributions, and their anti-quark distributions, as the four  
801 independent sets of PDFs, which may be transformed to the ones chosen if one assumes  $u_v =$   
802  $U - \bar{U}$  and  $d_v = D - \bar{D}$ , i.e. the equality of anti- and sea-quark distributions of given flavour.  
803 For the majority of the QCD fits presented, the strange quark distribution at  $Q_0^2$  is assumed to  
804 be a constant fraction of  $\bar{D}$ ,  $x\bar{s} = f_s x\bar{D}$  with  $f_s = 0.4$  as for HERAPDF, while this assumption  
805 is relaxed for the fits including simulated  $s, c, b$  data.

806 Note, that the prospects presented here are illustrations for a different era of PDF physics, which  
807 will be richer and deeper than one may be able to simulate now. For instance, without real data  
808 one cannot study the actual parameterisation needed for the PDFs. In particular the low  $x$   
809 kinematic region was so far unexplored and the simulated data relies on a simple extrapolation  
810 of nowadays PDFs, and no data or model is available that provides constraints on this region<sup>2</sup>.  
811 The LHeC data explores new corners of phase space with high precision, and therefore it will  
812 have a great potential to determine the parameterisation, much larger than HERA had. As  
813 another example, with LHeC data one can directly derive relations for how the valence quarks  
814 are determined with a set of NC and CC cross section data in a redundant way, since the gluon  
815 distribution at small  $x$  can be determined from the  $Q^2$  derivative of  $F_2$  and from a measurement  
816 of  $F_L$ . The question of the optimal gluon parameterisation may then be settled by analysing  
817 these constraints and not by some specific behaviour of a given fit. Furthermore, the precise  
818 direct determinations of  $s, c$  and  $b$  densities with measurements of the impact parameter of their  
819 decays, will put the treatment of heavy flavours in PDF analyses on a new level. The need for  
820 the phenomenological introduction of the  $f_s$  factor will disappear and the debate on the value  
821 of fixed and variable heavy flavour schemes will be settled.

---

<sup>1</sup> Specifically, the following parameters are set free:  $B_g, C_g, D_g, B_{uv}, C_{uv}, E_{uv}, B_{dv}, C_{dv}, A_{\bar{U}}, B_{\bar{U}}, C_{\bar{U}}, A_{\bar{D}}, B_{\bar{D}}, C_{\bar{D}}$ . Note, the  $B$  parameters for  $u_v$  and  $d_v$ , and the  $A$  and  $B$  parameters for  $\bar{U}$  and  $\bar{D}$  are fitted independently, such that the up and down valence and sea quark distributions are uncorrelated in the analysis, whereas for HERAPDF2.0  $x\bar{u} \rightarrow x\bar{d}$  as  $x \rightarrow 0$  is imposed. The other main difference is that no negative gluon term has been included, i.e.  $A'_g = 0$ .

<sup>2</sup> It is expected that real LHeC data, and also the inclusion of further information such as  $F_L$ , will certainly lead to a quite different optimal parameterisation ansatz as was used in the present analysis. Though, it has been checked that with a more relaxed set of parameters, very similar results on the PDF uncertainties are obtained, which justifies the size of the prospected PDF uncertainties.

823 The improvement that can be expected for the valence quark distributions from LHeC is illus-  
 824 trated in Fig. 3.6, and compared to a variety of modern PDF sets [Refs missing](#). Today, the  
 825 knowledge of the valence quark distributions, particularly at large or small  $x$ , is fairly limited, as  
 826 it can be derived from the Figure. At high  $x$ , this is due to the limited luminosity, challenging  
 827 systematics that rise with  $\propto 1/(1-x)$ , and due to nuclear correction uncertainties, while at  
 828 low  $x$ , this is because the valence quark distributions are small compared to the sea quarks and  
 cannot be separated from those from first principles.

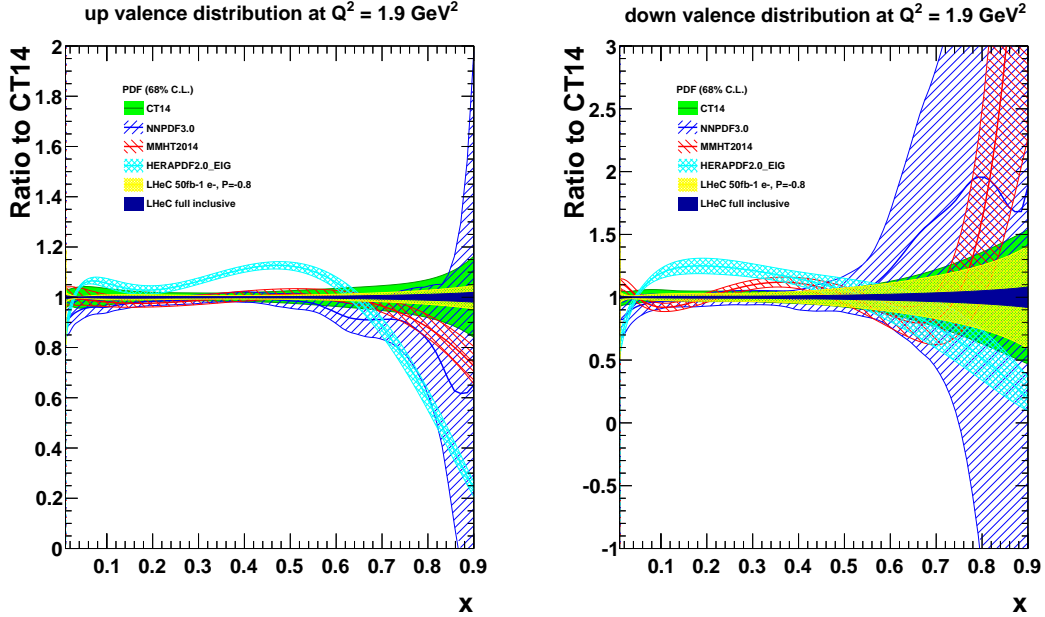


**Figure 3.6:** Valence quark distributions at  $Q^2 = 1.9 \text{ GeV}^2$  as a function of  $x$ , presented as the ratio to the CT14 [53] central values. The yellow band corresponds to the “LHeC 1st run” PDFs (D2), while the dark blue shows the “LHeC final inclusive” PDFs based on the data sets (D4+D5+D7+D8), as described in the text. For the purposes of illustrating the improvement to the uncertainties more clearly, the central value of the LHeC PDF has been scaled to the CT14 PDF, which itself is displayed by the green band.

829

830 The  $u$  valence quark distribution is better known than the  $d$  valence, since it enters with a  
 831 four-fold weight in  $F_2$  due to the electric quark charge ratio squared. Nevertheless, a substantial  
 832 improvement in  $d_v$  is also visible, because the relative weight of  $d_v$  to  $u_v$  is changing favourably  
 833 towards the down quark due to the influence of weak NC and CC interactions at high  $Q^2$  where  
 834 the LHeC is providing very accurate data. The most important constraints to the highest  $x$   
 835 valence distributions are due to the very high integrated luminosity and corresponding extension  
 836 in kinematic reach of the data in  $x$  (and  $Q^2$ ) in comparison to HERA. At the LHC, in contrast,  
 837 the highest  $x$  are only accessible as convolutions with partons at lower  $x$ , and those can therefore  
 838 not be constraint.

839 Note that “LHeC 1st run” PDF, displayed by the yellow band in Fig. 3.6, includes only electron,  
 840 i.e. no positron, data. Infact, from the  $e^\pm p$  cross section differences access to valence quarks at  
 841 low  $x$  can be obtained. As has already been illustrated in the CDR from 2012 [1] the sum of  
 842  $2u_v + d_v$  may be measured directly with the NC  $\gamma Z$  interference structure function  $x F_3^{\gamma Z}$  down  
 843 to  $x \simeq 10^{-4}$  with very good precision. This tests the assumption of the equality of sea- and  
 844 anti-quark densities.

845 The precise determinations of the valence quark distributions at large  $x$  have strong implications  
 for physics at the HL-LHC, in particular for BSM searches, as further discussed Sect. 3.1.7. In

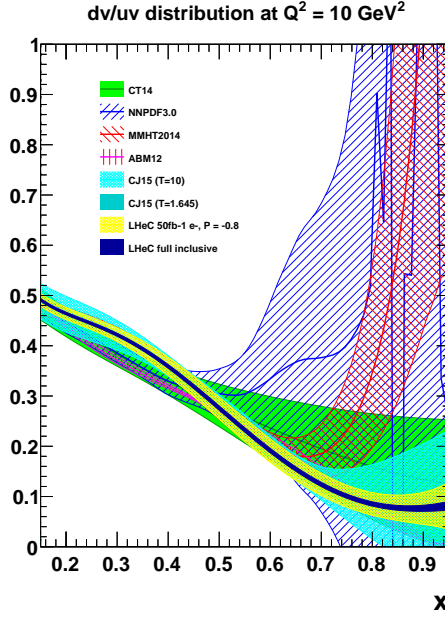


**Figure 3.7:** The  $d_v/u_v$  distribution at  $Q^2 = 10 \text{ GeV}^2$  as a function of  $x$ . The yellow band corresponds to the “LHeC 1st run” PDFs (D2), while the dark blue shows the “LHeC final inclusive” PDFs (D4+D5+D7+D8), as described in the text. Both LHeC PDFs shown are scaled to the central value of CT14.

846  
 847 addition, precise determinations of the valence quarks will likely resolve the mystery of the  $d/u$   
 848 ratio at large  $x$ . As exemplarily shown in Fig. 3.7, there are currently conflicting theoretical  
 849 pictures for the central value of the  $d/u$  ratio, albeit the large uncertainty bands of the different  
 850 PDF mainly overlap. As of today, the constraints from data are inconclusive statistically and  
 851 also suffer from large nuclear uncertainties, and therefore cause those large uncertainties.

## 852 Sea Quark PDFs

853 The distributions of  $\bar{U}$  and  $\bar{D}$  for the PDFs from the 1st run and the final LHeC data are shown  
 854 in Fig. 3.8 and compared to present PDF analyses. Our today's knowledge about the anti-quark  
 855 distributions is fairly poor and uncertainties are very large at smaller values of  $x$ , and also at  
 856 highest  $x$ . In particular at low  $x$  the size of the anti-quark PDFs are large and they contribute  
 857 significantly to precision SM measurements at the HL-LHC.

858 Our knowledge about the anti-quark PDFs will be changed completely with LHeC data. Pre-  
 859 cise constraints are obtained with inclusive NC/CC DIS data despite the relaxation of any  
 860 assumptions in the fit ansatz that would force  $\bar{u} \rightarrow \bar{d}$  as  $x \rightarrow 0$ , as it is present in other PDF  
 861 determinations. At smaller  $Q^2$  in DIS one measures essentially  $F_2 \propto 4\bar{U} + \bar{D}$ . At HERA, thus  
 862 one could not resolve the two parts, neither will that be possible at any other lower energy  $ep$   
 863 collider. At the LHeC, in contrast, the CC DIS cross sections are measured very well down to  
 864  $x$  values even below  $10^{-4}$ , and in addition there are the weak current contributions to the NC  
 865 cross section. This enables this distinction of  $\bar{U}$  and  $\bar{D}$ .

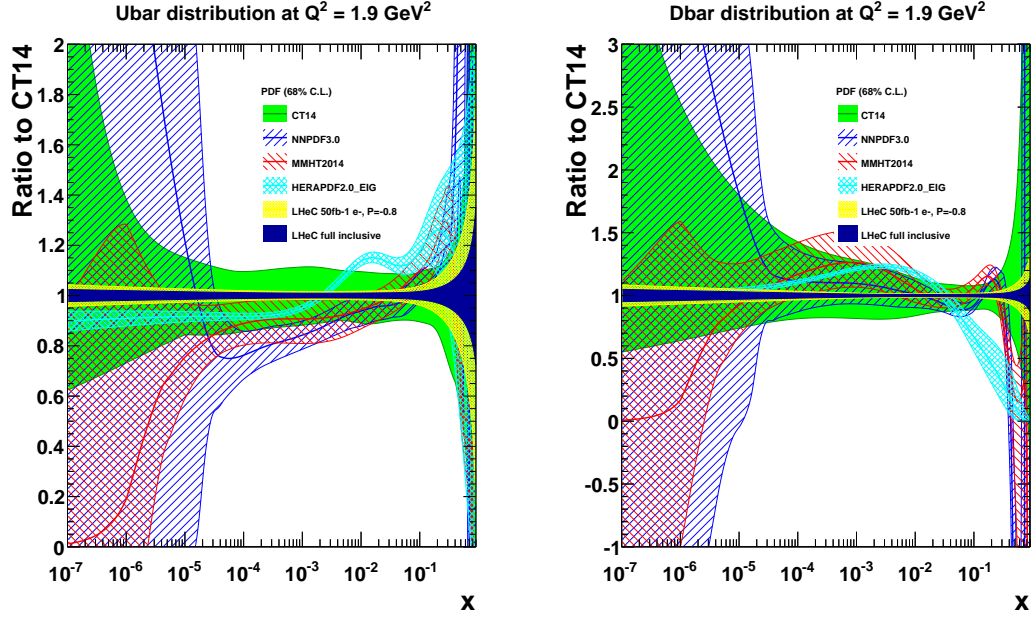


**Figure 3.8:** Sea quark distributions at  $Q^2 = 1.9 \text{ GeV}^2$  as a function of  $x$ , presented as the ratio to the CT14 central values. The yellow band corresponds to the “LHeC 1st run” PDFs (D2), while the dark blue shows the “LHeC final inclusive” PDFs (D4+D5+D7+D8), as described in the text. Both LHeC PDFs shown are scaled to the central value of CT14.

## 866 The Gluon PDF

867 **DB: section needs revision.** The LHeC, with hugely increased precision and kinematic range of  
 868 the most appropriate process (DIS) to explore  $xg(x, Q^2)$ , can pin down the gluon distribution  
 869 much more accurately than the situation today. This primarily comes from the extension of  
 870 range and precision in the measurement of  $\partial F_2 / \partial \log Q^2$ , which at small  $x$  is a measure of  
 871  $xg$ . The precision determination of the quark distributions, discussed previously, also strongly  
 872 constrains  $xg$ . Further sensitivity arises with the high- $y$  part of the NC cross section which is  
 873 controlled by the longitudinal structure function as is discussed below.

874 The result for the gluon distribution from the LHeC inclusive NC and CC data is presented in  
 875 Fig. 3.9, compared to several other modern PDF sets. On the left, the distribution is presented  
 876 as a ratio to CT14, and is displayed on a log- $x$  scale to highlight the small  $x$  region. On the  
 877 right, the  $xg$  distribution is shown on a linear- $x$  scale, accentuating the region of large  $x$ . The  
 878 determination of  $xg$  is predicted to be radically improved with the LHeC NC and CC precision  
 879 data, which extend down to lowest  $x$  values close to  $10^{-6}$  and large  $x \leq 0.8$ .

880 Below  $x \simeq 10^{-3}$ , the HERA data have almost vanishing constraining power due to kinematic  
 881 range limitations, as one needs a lever arm to determine the  $Q^2$  derivative, and so the gluon  
 882 is simply not determined at low  $x$ . With the LHeC, a precision of a few per cent at small  $x$   
 883 becomes possible. This has direct implications for the LHC: with the extension of the rapidity  
 884 range to about 4 at the HL-LHC by ATLAS and CMS, Higgs physics will become small  $x$  physics  
 885 for which  $xg$  must be known as  $gg \rightarrow H$  is the dominant production mechanism.

886 While the analysis performed here has used standard DGLAP evolution, the precise measure-  
 887 ment of  $F_L$  at the LHeC (not yet included in the analysis presented here), in addition to  $F_2$ ,  
 888 can discover whether  $xg$  saturates, and whether the DGLAP equations need to be replaced by

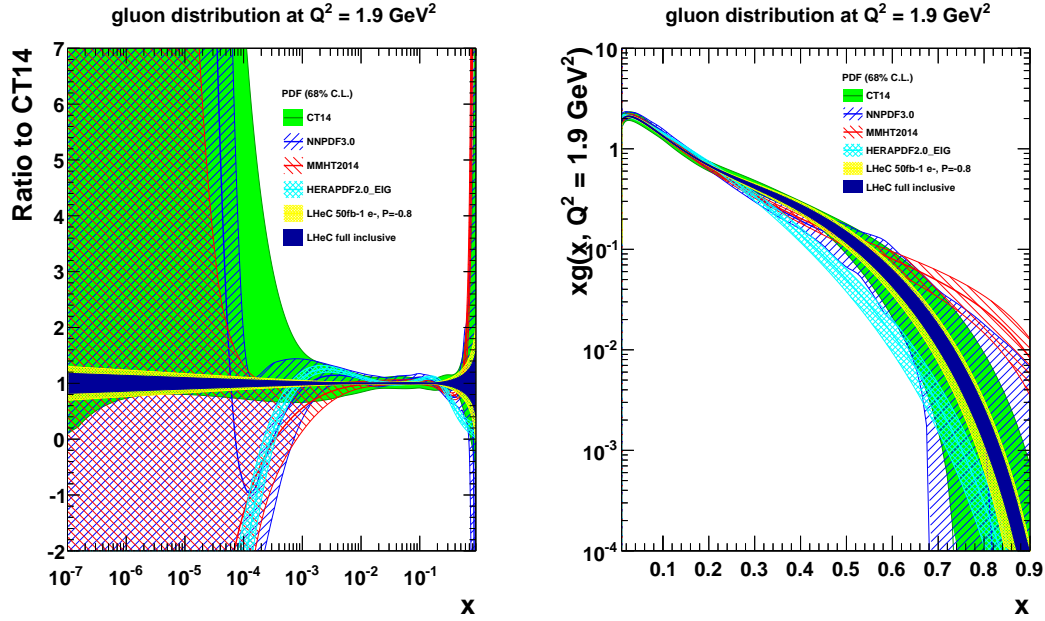


**Figure 3.9:** Gluon distribution at  $Q^2 = 1.9 \text{ GeV}^2$  as a function of  $x$ , highlighting (left) the low  $x$  and (right) the high  $x$  regions. The yellow band corresponds to the “LHeC 1st run” PDFs (D2), while the dark blue shows the “LHeC final inclusive” PDFs (D4+D5+D7+D8), as described in the text. Both LHeC PDFs shown are scaled to the central value of CT14.

889 non-linear parton evolution equations, as is also discussed in several Sections below.

890 At large  $x \geq 0.3$  the gluon distribution becomes very small and large variations appear in its  
 891 determination from different PDF groups, differing by orders of magnitude, which is related  
 892 to uncertainties on jet measurements, theoretical uncertainties, and the fact that HERA did  
 893 not have sufficient luminosity to cover the high  $x$  region where, moreover, the sensitivity to  $xg$   
 894 diminishes, since the valence quark evolution is insensitive to it. For the LHeC, the sensitivity  
 895 at large  $x$  comes as part of the overall package: large luminosity allowing access to  $x$  values close  
 896 to 1, fully constrained quark distributions and strong constraints at small  $x$  which feed through  
 897 to large  $x$  via the momentum sum rule. The high precision illustrated will be crucial for BSM  
 898 searches at high scales. It is also important for testing QCD factorisation and scale choices, as  
 899 well as electroweak effects.

900 It is worth noting that the uncertainties considered here are restricted to those related to the  
 901 genuine cross section measurement uncertainties. There are further uncertainties, for instance,  
 902 related to the difficulty of parameterising the PDFs and choosing the optimum solution in such  
 903 a fit analysis. These would also be considerably reduced with the LHeC extended data base as  
 904 was mentioned above. Moreover, the analysis presented here has not made use of the additional  
 905 information that can be provided at the LHeC in measurements of  $F_2^{c,b}$  (see Sec 3.1.6) or  $F_L$ . The  
 906 large  $x$  situation can be expected to further improve by using LHeC jet data, providing further,  
 907 direct constraints at large  $x$  which, however, have not yet been studied in any comparable detail.

908 The LHeC is the ideal laboratory to resolve all unknowns of the gluon density, which is the cause  
 909 for essentially all visible matter, and one of the particular secrets of particle physics for it cannot  
 910 directly be observed but is confined inside hadrons. It is obvious that resolving this puzzle is an  
 911 energy frontier DIS task and goal, including electron-ion scattering since the gluon inside heavy  
 912 matter is known even much less. Therefore, the special importance of this part of high energy

913 PDF physics is not primarily related to the smallness of uncertainties: it is about a consistent  
914 understanding and resolution of QCD at all regions of spatial and momentum dimensions which  
915 the LHeC will explore, and later the FCC-eh too.

### 916 PDF determinations with different datasets

917 It is informative to study the transition of the PDF uncertainties from the “LHeC 1st run”  
918 PDFs, which exploits only a single electron-proton dataset, D2, through to the “LHeC final  
919 inclusive” PDFs, which makes use of the full datasets D4+D5+D7+D8. Various intermediate  
920 PDF fits are performed using subsets of the datasets summarised in Tab.3.2. The results are  
921 illustrated in Figs.3.10 and 3.11, which show the distributions of the: (a)  $u_v$ , (b)  $d_v$ , (c)–(d)  
922 gluon, and (e)–(f) sea quarks.

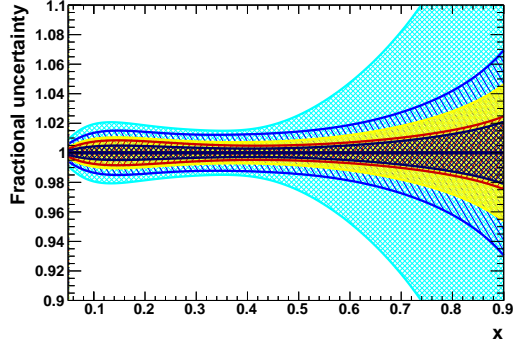
923 The impact of the increasing amount of integrated luminosity of  $e^-p$  data is illustrated in  
924 Fig. 3.10 by the transition from the blue  $\rightarrow$  yellow  $\rightarrow$  red bands. It is observed, that the  
925 small and medium- $x$  regions are *quickly* constrained, even with only  $5 \text{ fb}^{-1}$ . This corresponds  
926 to approximately the 1st year of LHeC operation. In contrast, the high  $x$  region considerably  
927 benefits from increased luminosity. In comparison to the analogous HERA fit, it becomes clear,  
928 that the vast majority of the gain comes already from the first  $50 \text{ fb}^{-1}$ .

929 The impact on the PDF uncertainties when adding additionally positron data to the fits is  
930 illustrated in Fig.3.11. In both cases the positron data is added to the baseline “LHeC 1st run”  
931 dataset. It is observed, that the addition of even a small amount of positrons does bring benefits.  
932 This is most prominent for the  $d$ -valence PDF, and primarily due to the sensitivity gained via  
933 the CC cross section of the positron data.

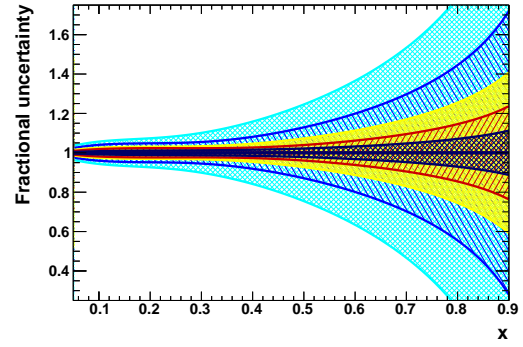
934 PDF fits including LHeC simulated data with different electron-polarisations were also studied,  
935 and found to have only a small impact on the PDF determination. Potential benefits are primar-  
936 ily from the overall increase (decrease) in inclusive CC cross section for negatively (positively)  
937 polarised electrons, as this scales linearly with the electron beam polarisation. However, while  
938 the impact for PDFs may be small, the datasets with both negatively and positively polarised  
939 leptons are important for the electroweak programme of the LHeC, as described in Sect. 3.3.

### 940 3.1.6 Heavy Quark PDFs

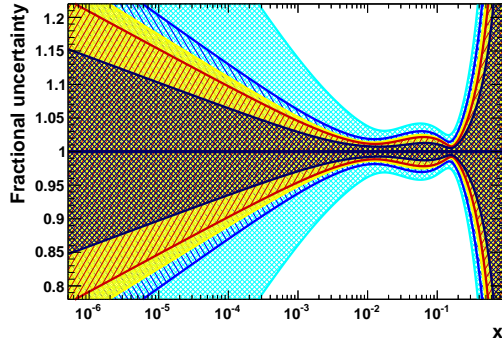
941 One of the unsolved mysteries of the Standard Model is the existence of three generations of  
942 quarks and leptons. The strongly interacting fermion sector contains altogether six quarks with  
943 masses differing by up to five orders of magnitude. This hierarchy of masses is on one hand  
944 a challenge to explain, on the other hand it offers a unique opportunity to explore dynamics  
945 at variety of different scales and thus learn different facets of strong interactions. While the  
946 light quarks at low scales are non-perturbative and couple strongly, the heavier quarks charm,  
947 bottom and top are separated from the soft sea by their masses and thus can serve as a good  
948 probe of the soft part of QCD. There are number of deep and unsolved questions that can be  
949 posed in the context of the proton structure: what is the individual contribution of the different  
950 quark flavors to the structure functions, are heavy quarks like charm and bottom radiatively  
951 generated or is there also an intrinsic heavy quark component in the proton, to what extent the  
952 universality and factorization theorems work in the presence of heavy quarks. It is therefore  
953 imperative to be able to perform precise measurements of each individual quark flavour and their  
954 contribution to the proton structure. The addition of more exclusive measurements to the PDF  
955 fits, for example measurements of the strange density and of  $F_2^{c,b}$  will allow individual quark



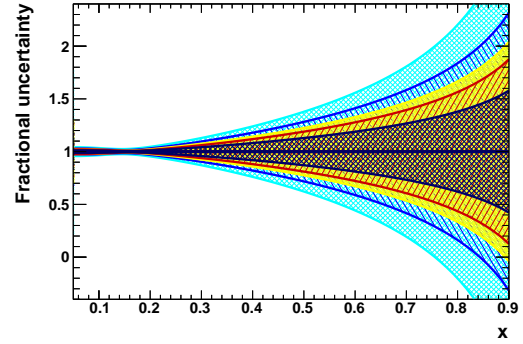
(a)  $u$ -valence distribution.



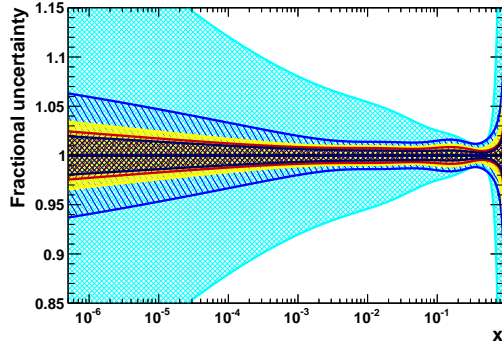
(b)  $d$ -valence distribution.



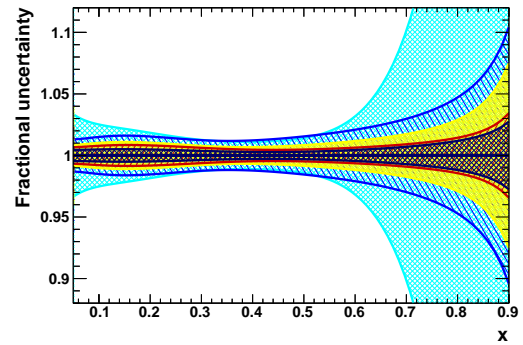
(c) Gluon distribution ( $\log_{10} x$  scale).



(d) Gluon distribution (linear  $x$  scale).

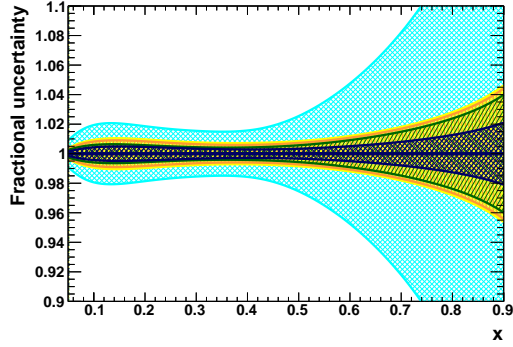


(e) Sea quark distribution ( $\log_{10} x$  scale).

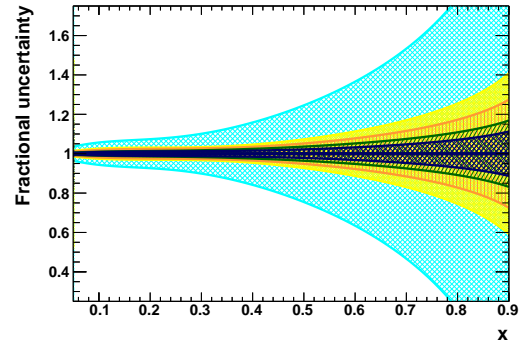


(f) Sea quark distribution (linear  $x$  scale).

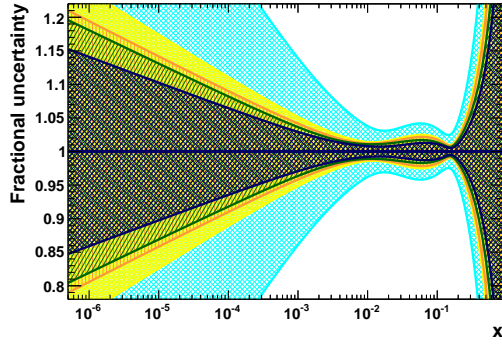
**Figure 3.10:** PDF distributions at  $Q^2 = 1.9 \text{ GeV}^2$  as a function of  $x$ , illustrating the impact of different amounts of integrated luminosity. **Please add legend to the figure(s).** The blue, yellow and red bands correspond to LHeC PDFs using electron-only NC and CC inclusive measurements with 5, 50 and  $1000 \text{ fb}^{-1}$  (datasets D1, D2 and D4), respectively. The yellow band is therefore equivalent to the “LHeC 1st run” PDF. For reference, the dark blue band shows the results of the “LHeC final inclusive” PDF. For comparison, the cyan band represents an identical PDF fit using HERA combined inclusive NC and CC data [37], rather than LHeC simulated data.



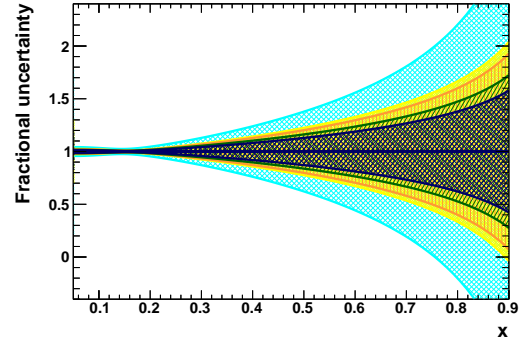
(a)  $u$ -valence distribution.



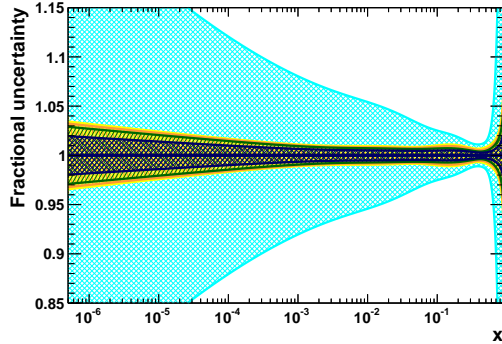
(b)  $d$ -valence distribution.



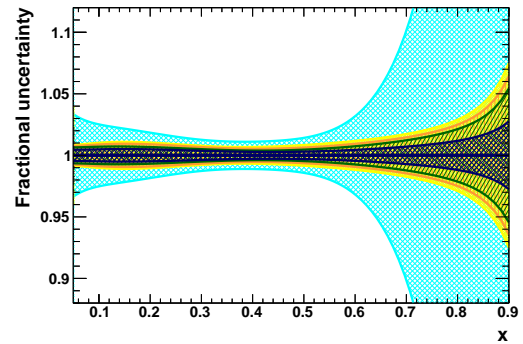
(c) Gluon distribution ( $\log_{10} x$  scale).



(d) Gluon distribution (linear  $x$  scale).



(e) Sea quark distribution ( $\log_{10} x$  scale).



(f) Sea quark distribution (linear  $x$  scale).

**Figure 3.11:** PDF distributions at  $Q^2 = 1.9 \text{ GeV}^2$  as a function of  $x$ , illustrating the impact of including positron data. The yellow (“LHeC 1st run”) and dark blue (“LHeC final inclusive”) and cyan bands (HERA data) are as in Fig. 3.10. The orange band corresponds to a fit with  $1 \text{ fb}^{-1}$  of inclusive NC and CC positron-proton data, in addition to  $50 \text{ fb}^{-1}$  of electron-proton data (D2+D6), while the green band is similar, but with  $10 \text{ fb}^{-1}$  of positron-proton data (D2+D7).

956 flavours to be determined. In this section, some brief studies are presented which highlight these  
957 constraints.

## 958 **The strange quark PDF**

959 The determination of the strange PDF has generated significant controversy in the literature for  
960 more than a decade. Fixed-target neutrino DIS measurements [54–58] typically prefer a strange  
961 PDF that is roughly half of the up and down sea distribution;  $\kappa = (s + \bar{s})/(\bar{u} + \bar{d}) \sim 0.5$ . The  
962 recent measurements from the LHC [59–62] and related studies [63,64] suggest a larger strange  
963 quark distribution, that may potentially even be larger than the up and down sea quarks. The  
964 precise knowledge of the strange quark PDF is of high relevance, since it provides a significant  
965 contribution to *standard candle* measurements at the HL-LHC, such as  $W/Z$  production, and it  
966 imposes a significant uncertainty on the  $W$  mass measurements at the LHC. The LHeC provides  
967 the opportunity to resolve many of these open questions on the strange quark PDF and further  
968 greatly improved the precision of  $s(x)$ .

969 The constraints of the inclusive NC/CC DIS data on the strange PDF is discussed briefly in  
970 Sect. 3.1.7. More direct constraints on the strange quark PDFs are obtained from exclusive  
971 NC cross section measurement, or from charm production cross sections in CC DIS. Those are  
972 discussed in the following.

## 973 **The strange quark PDF from heavy flavor measurements in NC DIS**

974 A short study is presented which highlights the constraints on the strange quark PDFs, when  
975 in addition to the inclusive NC/CC DIS data an LHeC measurement of the strange density is  
976 included in the PDF fit. In the studies presented previously, the parameterised PDFs are the  
977 four quark distributions  $xu_v, xd_v, x\bar{U}, x\bar{D}$  and  $g$  (a 4+1 parameterisation), as the inclusive NC  
978 and CC data determine only the sums of the up and down quark and anti-quark distribution,  
979 as discussed previously. The strange quark PDF was then assumed to be a constant fraction of  
980  $x\bar{D} = x\bar{d} + x\bar{s}$ .

981 In order to assess the impact of dedicated strange density measurements at the LHeC, the  
982 assumptions imposed in the PDF fit are relaxed. For all fits presented in the following, the  $\bar{d}$  and  
983  $\bar{s}$  are treated now separately, and therefore a total of five quark distributions are parameterised  
984 ( $xu_v, xd_v, x\bar{U}, x\bar{d}, x\bar{s}$ ) as well as  $g$  (i.e. a 5+1 parameterisation). The total number of free  
985 parameters of the PDF fit then becomes 17.

986 Results of the 5+1 PDF fits are shown in Fig. 3.12, where fits to inclusive NC/CC DIS data are  
987 displayed as reference (both for the 4+1 and 5+1 ansatz) and the fits where in addition strange  
988 density measurements and even further measurements of  $F_2^{c,b}$  are considered. As expected, the  
989 uncertainties of the 5+1 fit to the inclusive DIS data, especially on the  $\bar{d}$  and  $\bar{s}$  distributions (c.f.  
990 Fig. 3.12 bottom), become substantially larger in comparison to the respective 4+1 fit, since the  
991  $\bar{d}$  and  $\bar{s}$  distributions are treated now separately. This demonstrates that the inclusive DIS data  
992 alone does not have the flavour separating power to determine the individual distributions very  
993 precisely.

994 When including an LHeC measurement of the  $\bar{s}$  quark density based on  $10 \text{ fb}^{-1}$  of  $e^-p$  data in  
995 addition to the 5+1 fit, the uncertainties on the  $\bar{d}$  and  $\bar{s}$  PDFs become significantly smaller.  
996 By chance, those uncertainties are then comparable to the ad-hoc constrained 4+1 fit. For  
997 this study the assumption  $s = \bar{s}$  has been imposed. However, if a measurement of the  $s$ -quark

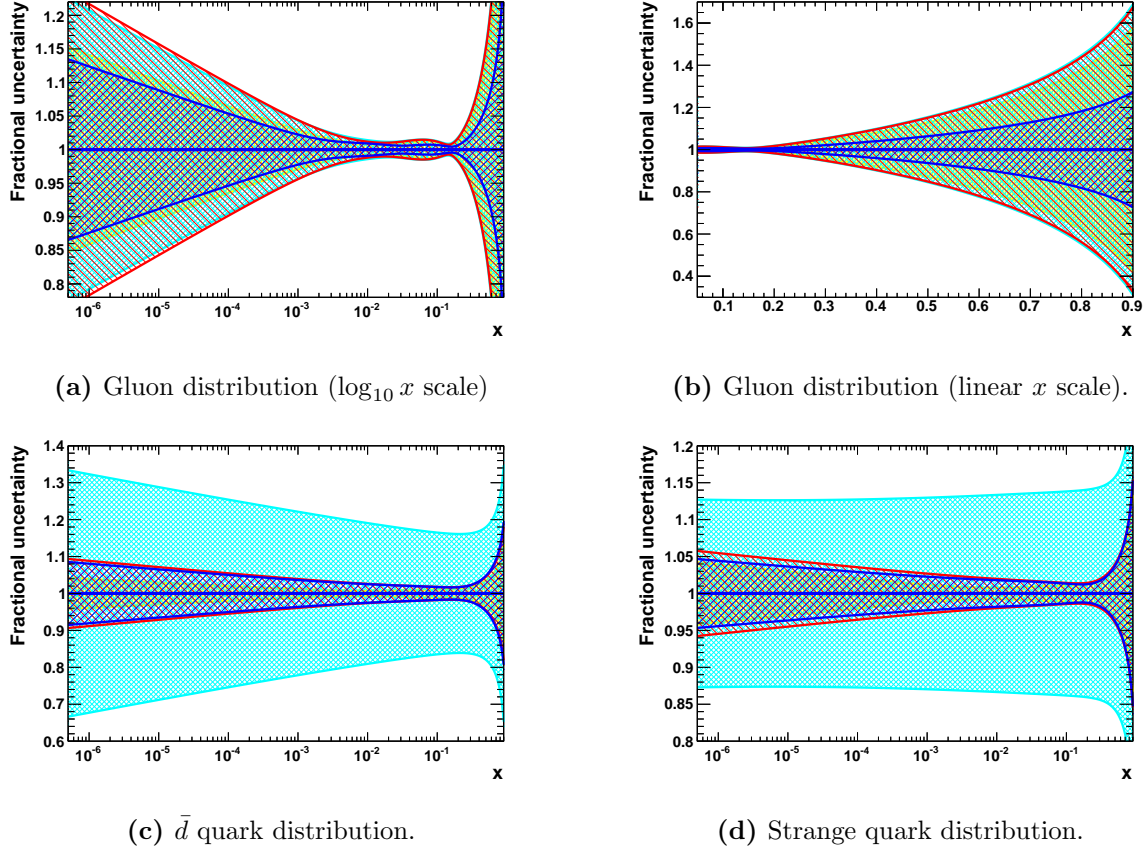


**Figure 3.12:** PDF uncertainties at  $Q^2 = 1.9 \text{ GeV}^2$  as a function of  $x$  to illustrate the constraints from additional heavy quark sensitive measurements at LHeC. Displayed are the gluon distribution on a logarithmic and linear scale (top) and the  $\bar{d}$  and  $\bar{s}$  distributions (bottom). The yellow band displays the uncertainties of the nominal “LHeC final inclusive” PDF, which was obtained in a 4+1 PDF fit. From the same dataset, results of the more flexible 5+1 fit (see text) are displayed as a cyan band. The red band displays the results, when in addition an LHeC measurement of the  $\bar{s}$  quark density is included. When even further including LHeC measurements of  $F_2^c$  and  $F_2^b$ , the PDF fits yields uncertainties as displayed by the blue band. The heavy quark data assumes an integrated luminosity of  $10 \text{ fb}^{-1}$ , as it can be collected during the first three years of data taking with electron-proton collisions.

998 density from  $e^+p$  data are further available, then even the  $s$  and  $\bar{s}$  distributions can be separately  
 999 determined with high precision.

### 1000 The strange quark PDF from CC DIS charm quark production

1001 The constraints from a measurement of charm quark production cross sections in charged current  
 1002 (CC) DIS is studied in Ref. [65]. At leading-order QCD, the subprocess under consideration is  
 1003  $Ws \rightarrow c$ , where the  $s$  represents an intrinsic strange quark. The study is performed using LHeC  
 1004 pseudodata for CC charm production, and its constraints on the PDFs are explored using a  
 1005 PDF profiling tool, where NNPDF3.1 served as a baseline PDF.

1006 Fig. 3.13 displays the improved constraints on the strange PDF of the LHeC pseudodata for the  
 1007 CC charm production channel [65]. It is found that the LHeC can provide strong constraints on  
 1008 the strange-quark PDF, especially in the previously poorly constraint small  $x$  region,  $x < 10^{-2}$ .  
 1009 In a variation of the study, a large reduction of uncertainties is already observed when restricting

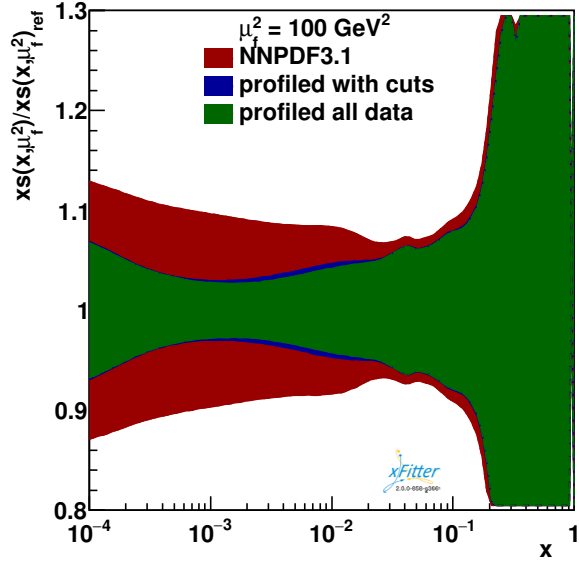


**Figure 3.13:** Constraints on the strange quark PDF  $x_s$  using simulate data for charged-current production of charm quarks at the LHeC [65]. The red band displays the nominal NNPDF3.1 PDF uncertainties, and the green and blue bands the improved uncertainties due to the LHeC data.

1010 the input data to the kinematic range where the differences between the different heavy flavour  
 1011 schemes (VFNS and FFNS) are not larger than the present PDF uncertainties. This further  
 1012 indicates that the PDF constraints are stable and independent of the particular heavy-flavour  
 1013 scheme.

1014 In summary, we find that CC DIS charm production at the LHeC provides strong constraints  
 1015 on the strange PDF, while this process represents a complementary channel to other data sets  
 1016 at the LHeC.

## 1017 Heavy Quarks Production in DIS

1018 **Needs to be revised. Some parts are repetitive and may go to intro of this HQ section 3.1.6,**  
 1019 **some to the next subsection.** The production of heavy quarks at HERA (charm and bottom)  
 1020 was an especially interesting process as the quark mass introduced a new scale ( $m = m_{c,b}$ ) which  
 1021 was neither heavy or light (see e.g. reviews [66,67]). Actually, the treatment of heavy quark  
 1022 mass effects is essential in PDF fits which include data from fixed target to collider energies  
 1023 and thus require the computation of physical cross sections over a large range of perturbative  
 1024 scales  $\mu^2$ . With these scales passing through (or close to) the thresholds for charm, bottom and,  
 1025 eventually, top, precise computations demand the incorporation of heavy quark mass effects close  
 1026 to threshold,  $\mu^2 \sim m^2$ , and the resummation of collinear logarithms  $\ln(\mu^2/m^2)$  at scales far above  
 1027 the threshold,  $\mu^2 \gg m^2$ . The first problem can be dealt with through the use of massive matrix  
 1028 elements for the generation of heavy quark-antiquark pairs but keeping a fixed number of parton  
 1029 densities (fixed flavour number schemes, FFNS). On the other hand, the proper consideration  
 1030 of resummation is achieved through the use of variable flavour number schemes (VFNS) which  
 1031 consider an increasing number of massless parton species, evolved through standard DGLAP,  
 1032 when the scale is increased above heavy quark mass thresholds. At present, calculations involving  
 1033 heavy quarks in DIS in different schemes (generalised mass VFNS) with different numbers of  
 1034 active flavours participating to DGLAP evolution are combined to derive an expression for

1035 the coefficient functions which is valid both close to threshold, and far above it. Such multi-  
 1036 scale problems are particularly difficulty, and numerous techniques were developed to cope with  
 1037 this challenging problem [68–77]. Additional complications, see e.g. Ref. [78], arise when the  
 1038 possibility of a non-perturbative origin of heavy quark distributions is allowed above the heavy  
 1039 quark mass threshold - intrinsic heavy flavour.

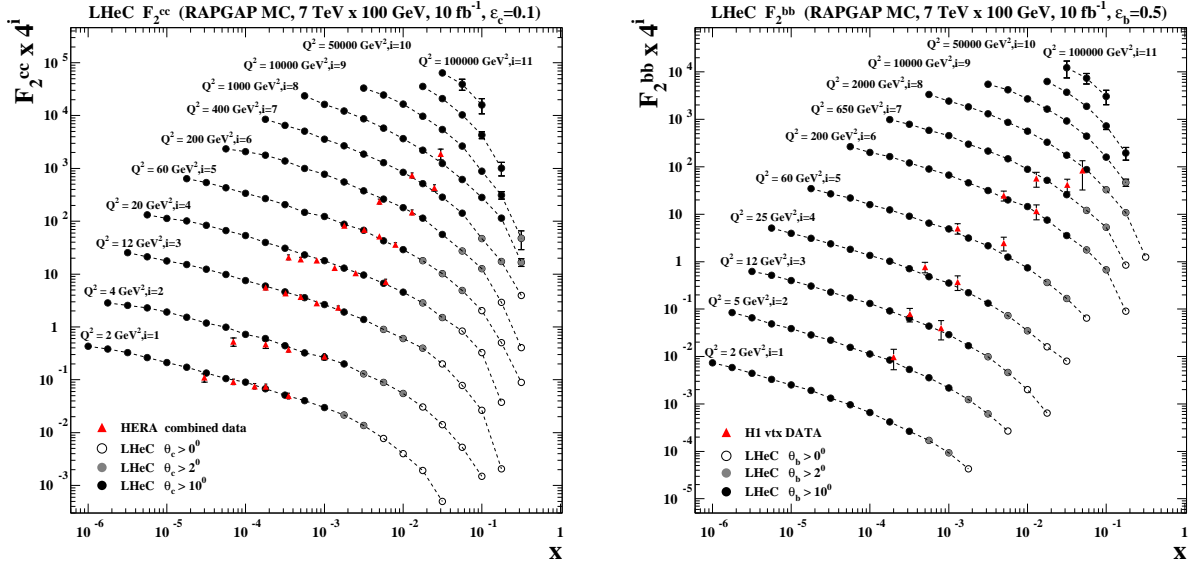


**Figure 3.14:** Heavy quark structure functions  $F_2^{c\bar{c}}$  and  $F_2^{b\bar{b}}$  showing the comparison of the HERA data to LHeC pseudodata.

1040 At the LHeC, the increased centre-of-mass energy allows us to extend to very large  $Q^2$  values.  
 1041 Thus, the LHeC can comprehensively explore the *asymptotic* high energy limit where  $m_{c,b}^2/Q^2 \rightarrow$   
 1042 0, as well as low energy *decoupling* region  $m_{c,b}^2/Q^2 \sim 1$ . In Fig. 3.14 we display the kinematic  
 1043 reach of  $F_2^{c\bar{c}}$  and  $F_2^{b\bar{b}}$ , and contrast this with the HERA combined data. The extended reach in  
 1044 comparison to HERA is dramatic. These channels can also help improve the determination of the  
 1045 charm and bottom quark masses and bring these uncertainties into the range of  $\Delta m_{c,b} \lesssim 10$  MeV.  
 1046 These are also essential for the determination of the  $W$ -boson mass in  $pp$ , see Sec. 7.1.2, and  
 1047 the extraction of the  $H \rightarrow c\bar{c}$  coupling in  $ep$ , see Chapter 5. Such extraction with an accuracy  
 1048  $\delta(m_c) \sim 3$  MeV demands the availability of calculations with higher orders in pQCD, and those  
 1049 computations are already ongoing [79–81]. Note that in PDF fits the heavy quark mass is an  
 1050 effective parameter that has to be related with the pole mass, see e.g. Ref. [82] and refs. therein.

### 1051 The impact of charm and bottom measurements on PDFs

1052 In Sect. 3.1.6, the constraints of an additional strange density measurement on the PDFs has  
 1053 been discussed. Even further constraints on the PDFs are then obtained when additionally  
 1054 including the LHeC measurements of  $F_2^c$  and  $F_2^b$ . For this purpose, simulated  $e^-p$  data with  
 1055 an integrated luminosity of  $10 \text{ fb}^{-1}$  are included into LHeC PDF fit and the resulting PDFs are  
 1056 displayed also in Fig. 3.12 of Sect. 3.1.6.

1057 An important impact of the  $F_2^{c,b}$  data is observed in the gluon PDFs and those uncertainties are  
 1058 substantially reduced.

1059 **The Top quark PDF**

1060 Somebody has to write at least a very few sentences here !! Christian, Nestor, Max, Daniel,  
1061 Anna ???

1062 **Summary on heavy flavor production and PDFs**

1063 **todo!** In summary, the complete provision of inclusive NC/CC DIS and tagged  $s$ ,  $c$  and  $b$  data  
1064 resolves the partonic substructure of the proton completely. This holds similarly for the nuclear  
1065 parton distributions presented below.

1066 **New theoretical concepts on intrinsic heavy quark phenomena**

1067 One of the most interesting nonperturbative quantum field theoretic aspects of hadron light front  
1068 wavefunctions in QCD are the intrinsic heavy-quark Fock states [83–85]. Consider a heavy-quark  
1069 loop insertion to the proton’s self-energy. The heavy-quark loop can be attached by gluons to  
1070 just one valence quark. The cut of such diagrams yields the standard DGLAP gluon splitting  
1071 contribution to the proton’s heavy quark structure function. In this case, the heavy quarks are  
1072 produced at very small  $x$ . However, the heavy quark loop can also be attached to two or more  
1073 valence quarks in the proton self-energy. In the case of QED this is corresponds to the light-  
1074 by-light lepton loop insertion in an atomic wavefunction. In the case of QCD, the heavy quark  
1075 loop can be attached by three gluons to two or three valence quarks in the proton self-energy.  
1076 This is a non-Abelian insertion to the hadron’s self-energy. The cut of such diagrams gives the  
1077 *intrinsic* heavy-quark contribution to the proton’s light-front wavefunction. In the case of QCD,  
1078 the probability for an intrinsic heavy  $Q\bar{Q}$  pair scales as  $\frac{1}{M_Q^2}$ ; this is in contrast to heavy  $\ell\bar{\ell}$  lepton  
1079 pairs in QED where the probability for heavy lepton pairs in an atomic wavefunction scales as  
1080  $\frac{1}{M_\ell^4}$ . This difference in heavy-particle scaling in mass distinguishes Abelian from non-Abelian  
1081 theories.

1082 A basic property of hadronic light-front wavefunctions is that they have strong fall-off with the  
1083 invariant mass of the Fock state. For example, the Light-Front Wave Functions (LFWFs) of  
1084 the colour-confining AdS/QCD models [86]  $\mathcal{M}^2 = [\sum_i k_i^\mu]^2$  of the Fock state constituents. This  
1085 means that the probability is maximised when the constituents have equal true rapidity, i.e.  
1086  $x_i \propto (k_{\perp i}^2 + m_i^2)^{1/2}$ . Thus the heavy quarks carry most of the momentum in an intrinsic heavy  
1087 quark Fock state. For example, the charm quark in the intrinsic charm Fock state  $|uudc\bar{c}\rangle$  of a  
1088 proton carries about 40% of the proton’s momentum:  $x_c \sim 0.4$ . After a high-energy collision,  
1089 the co-moving constituents can then recombine to form the final state hadrons. along the proton.  
1090 Thus, in a  $ep$  collision the comoving  $udc$  quarks from the  $|uudc\bar{c}\rangle$  intrinsic 5-quark Fock state can  
1091 recombine to a  $\Lambda_c$ , where  $x_{\Lambda_c} = x_c + x_u + x_d \sim 0.5$ . Similarly, the comoving  $dcc$  in the  $|uudc\bar{c}\bar{c}\rangle$   
1092 intrinsic 7-quark Fock state can recombine to a  $\Xi(ccd)^+$ , with  $x_{\Xi(ccd)} = x_c + x_c + x_d \sim 0.9$ .

1093 Therefore, in the intrinsic heavy quark model the wavefunction of a hadron in QCD can be rep-  
1094 resented as a superposition of Fock state fluctuations, e.g.  $|n_V\rangle$ ,  $|n_V g\rangle$ ,  $|n_V Q\bar{Q}\rangle$ ,  $\dots$  components  
1095 where  $n_V \equiv dds$  for  $\Sigma^-$ ,  $uud$  for proton,  $\bar{u}d$  for  $\pi^-$  and  $u\bar{d}$  for  $\pi^+$ . Charm hadrons can be  
1096 produced by coalescence in the wavefunctions of the moving hadron. Doubly-charmed hadrons  
1097 require fluctuations such as  $|n_V c\bar{c}\bar{c}\bar{c}\rangle$ . The probability for these Fock state fluctuations to come  
1098 on mass shell is inversely proportional to the square of the quark mass,  $\mathcal{O}(m_Q^{-2n})$  where  $n$  is the  
1099 number of  $Q\bar{Q}$  pairs in the hadron. Thus the natural domain for heavy hadrons produced from

1100 heavy quark Fock states is  $\bar{k}_{\perp Q}^2 \sim m_Q^2$  and high light-front momentum fraction  $x_Q$  [83,84,84,85].  
 1101 For example, the rapidity regime for double-charm hadron production  $y_{ccd} \sim 3$  at low energies is  
 1102 well within the kinematic experiment domain of a fixed target experiment such as SELEX at the  
 1103 Tevatron [87]. Note that the intrinsic heavy-quark mechanism can account for many previous  
 1104 observations of forward heavy hadron production single and double  $J/\psi$  production by pions ob-  
 1105 served at high  $x_F > 0.4$  in the low energy fixed target NA3 experiment, the high  $x_F$  production  
 1106 of  $pp \rightarrow \Lambda_c + X$  and  $pp \rightarrow \Lambda_b + X$  observed at the ISR; single and double  $\Upsilon(b\bar{b})$  production, as  
 1107 well as *quadra-bottom* tetraquark  $[bb\bar{b}\bar{b}]$  production observed recently by the AnDY experiment  
 1108 at RHIC [88]. In addition the EMC collaboration observed that the charm quark distribution  
 1109 in the proton at  $x = 0.42$  and  $Q^2 = 75 \text{ GeV}^2$  is 30 times larger than expected from DGLAP  
 1110 evolution. All of these experimental observations are naturally explained by the intrinsic heavy  
 1111 quark mechanism. The SELEX observation [87] of double charm baryons at high  $x_F$  reflects  
 1112 production from double intrinsic heavy quark Fock states of the baryon projectile. Similarly,  
 1113 the high  $x_F$  domain – which would be accessible at forward high  $x_F$  – is the natural production  
 1114 domain for heavy hadron production at the LHeC.

1115 The production of heavy hadrons based on intrinsic heavy quark Fock states is thus remarkable  
 1116 efficient and greatly extends the kinematic domain of the LHeC, e.g. for processes such as  
 1117  $\gamma^* b \rightarrow Z^0 b$ . This is in contrast with the standard production cross sections based on gluon  
 1118 splitting, where only a small fraction of the incident momentum is effective in creating heavy  
 1119 hadrons.

### 1120 3.1.7 PDFs and the HL-LHC

1121 The particle physics community is busy preparing for the extensive precision and discovery  
 1122 physics programme that will come from Run III of the LHC and, most significantly, for the  
 1123 major upgrade beginning in the mid-2020s, the High-Luminosity LHC (HL-LHC). Here, protons  
 1124 will be collided with an instantaneous luminosity a factor of five greater than at the LHC and  
 1125 will accumulate up to ten times more data, resulting in an integrated luminosity of around  
 1126  $\mathcal{L} = 3 \text{ ab}^{-1}$  for both the ATLAS and CMS detectors, and  $300 \text{ fb}^{-1}$  for LHCb. In this context,  
 1127 a precise determination of PDFs is an essential ingredient for the success of the HL-LHC and  
 1128 conversely, the HL-LHC itself offers a significant opportunity to improve our understanding of  
 1129 proton structure.

### 1130 PDF Prospects with the HL-LHC

1131 In Ref. [89] the HL-LHC potential to constrain PDFs was analysed in detail, focussing on SM  
 1132 processes that are expected to have the most impact at higher  $x$ . In particular, projections for  
 1133 the production of top quark pairs, inclusive jets, forward  $W$  + charm quark and direct photons,  
 1134 as well as forward and high-mass Drell-Yan and the  $Z$  boson  $p_{\perp}$  distribution were included. It  
 1135 was found that PDF uncertainties on LHC processes can be reduced by a factor between two  
 1136 and five, depending on the specific flavour combination and on the optimistic assumptions about  
 1137 the reduction of the (experimental) systematic uncertainties.

1138 It is of interest to compare these constraints with those expected to come from the LHeC itself, as  
 1139 well as potential improvements from a combined PDF fit to the HL-LHC and LHeC datasets; this  
 1140 was studied in [48]. The basic procedure consists in generating HL-LHC and LHeC pseudodata  
 1141 with the PDF4LHC15 set [90] and then applying Hessian PDF profiling [91,92], in other words  
 1142 a simplified version of a full refit, to this baseline to assess the expected impact of the data.

1143 While the HL-LHC datasets are described above, the LHeC pseudodata correspond to the most  
 1144 recent publicly available official LHeC projections, see Section 3.1.4, for electron and positron  
 1145 neutral-current (NC) and charged-current (CC) scattering. As well as inclusive data at different  
 1146 beam energies ( $E_p = 1, 7$  TeV), charm and bottom heavy quark NC and charm production in  
 1147  $e^-p$  CC scattering are included.

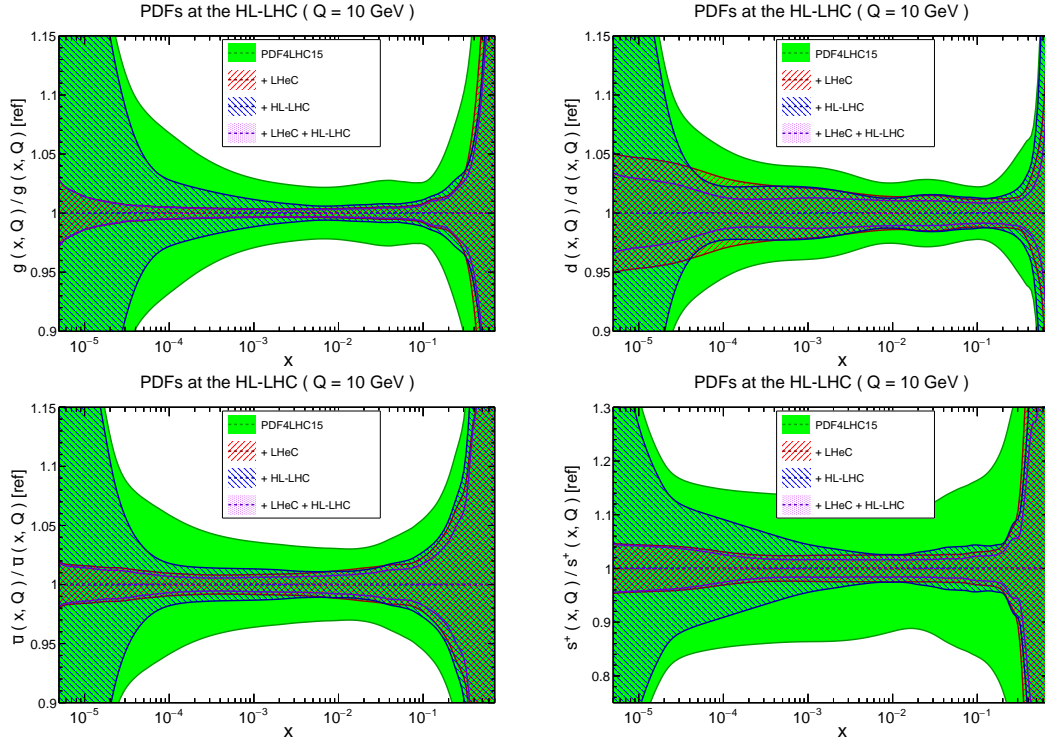


**Figure 3.15:** Impact of LHeC on the  $1\text{-}\sigma$  relative PDF uncertainties of the gluon, down quark, anti-up quark and strangeness distributions, with respect to the PDF4LHC15 baseline set (green band). Results for the LHeC (red), the HL-LHC (blue) and their combination (violet) are shown.

1148 The expected impact of the HL-LHC, LHeC and their combination on the PDF uncertainties of  
 1149 the gluon, down quark, anti-up quark and strangeness distributions are shown in Fig. 3.15. One  
 1150 observes that at low  $x$  the LHeC data place in general by far the strongest constraint, in partic-  
 1151 ular for the gluon, as expected from its greatly extended coverage at small  $x$ . At intermediate  
 1152  $x$  the impact of the HL-LHC and LHeC are more comparable in size, but nonetheless the LHeC  
 1153 is generally expected to have a larger impact. At higher  $x$  the constraints are again comparable  
 1154 in size, with the HL-LHC resulting in a somewhat larger reduction in the gluon and strangeness  
 1155 uncertainty, while the LHeC has a somewhat larger impact for the down and anti-up quark  
 1156 distributions. Thus, the combination of both HL-LHC and LHeC pseudodata nicely illustrate  
 1157 a clear and significant reduction in PDF uncertainties over a very wide range of  $x$ , improving  
 1158 upon the constraints from the individual datasets in a non-negligible way.

### 1159 Parton luminosities at the HL-LHC

1160 In Fig. 3.16 we show the impact on the gluon-gluon, quark-gluon, quark-antiquark and quark-  
 1161 quark partonic luminosities for a center-of-mass energy  $\sqrt{s} = 14$  TeV. Some clear trends are  
 1162 evident from this comparison, consistent with the results from the individual PDFs. We can  
 1163 in particular observe that at low mass the LHeC places the dominant constraint, while at

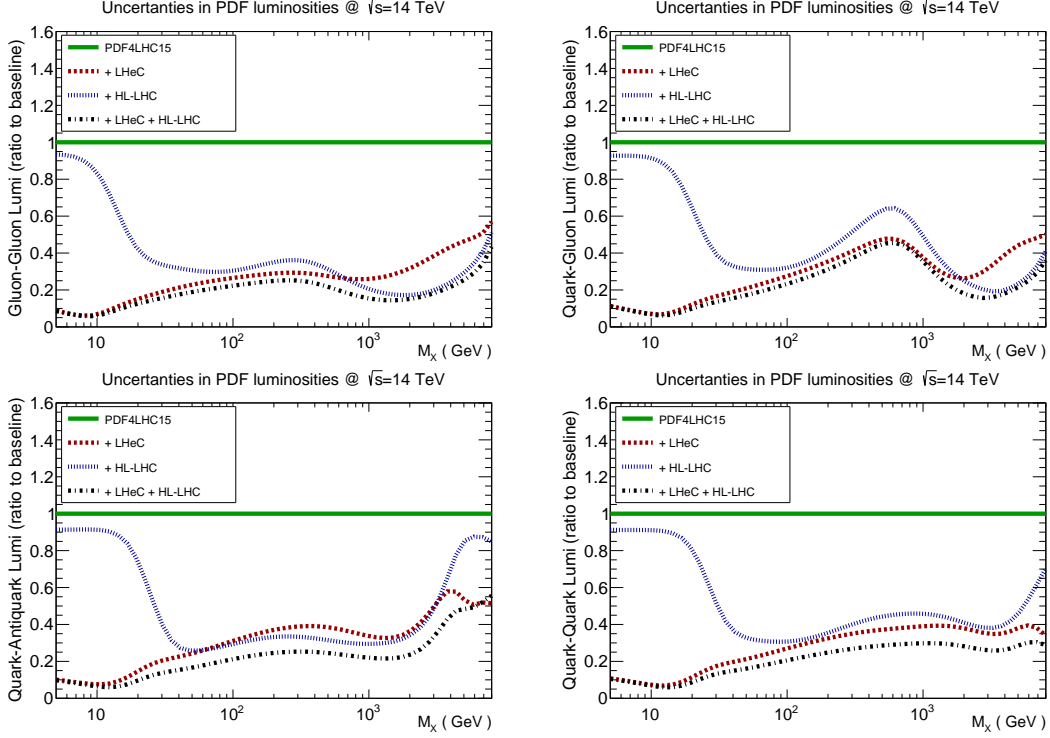


**Figure 3.16:** Impact of LHeC, HL-LHC and combined LHeC + HL-LHC pseudodata on the uncertainties of the gluon-gluon, quark-gluon, quark-antiquark and quark-quark luminosities, with respect to the PDF4LHC15 baseline set. In this comparison we display the relative reduction of the PDF uncertainty in the luminosities compared to the baseline.

1164 intermediate masses the LHeC and HL-LHC constraints are comparable in size, and at high  
 1165 mass the stronger constraint on the gluon-gluon and quark-gluon luminosities comes from the  
 1166 HL-LHC, with the LHeC dominating for the quark-quark and quark-antiquark luminosities. As  
 1167 in the case of the PDFs, for the partonic luminosities the combination of the HL-LHC and LHeC  
 1168 constraints leads to a clear reduction in the PDF uncertainties in comparison to the individual  
 1169 cases, by up to an order of magnitude over a wide range of invariant masses,  $M_X$ , of the produced  
 1170 final state.

1171 In summary, these results demonstrate that while the HL-LHC alone is expected to have a size-  
 1172 able impact on PDF constraints, the LHeC can improve our current precision on PDFs signifi-  
 1173 cantly in comparison to this, in particular at low to intermediate  $x$ . Moreover, the combination  
 1174 of both the LHeC and HL-LHC pseudodata leads to a significantly superior PDF error reduction  
 1175 in comparison to the two facilities individually. Further details, including LHeC-only studies as  
 1176 well as an investigation of the impact of the PDF baseline on the uncertainty projections, can  
 1177 be found in Ref. [48].

### 1178 PDF Sensitivity: Comparing HL-LHC and LHeC

1179 While the experimental reach of each facility in the  $\{x, Q^2\}$  kinematic plane provides a useful  
 1180 comparison, there are more factors to consider – especially when we are striving for ultra-high  
 1181 precision measurements. One measure that provides a dimension beyond the  $\{x, Q^2\}$  plane is  
 1182 the *sensitivity*; this is a combination of the correlation coefficient times a scaled residual [93,94].  
 1183 This provides an extra dimension of information in comparison to a simple  $\{x, Q^2\}$  map and

1184 represents a measure of the impact of the data.

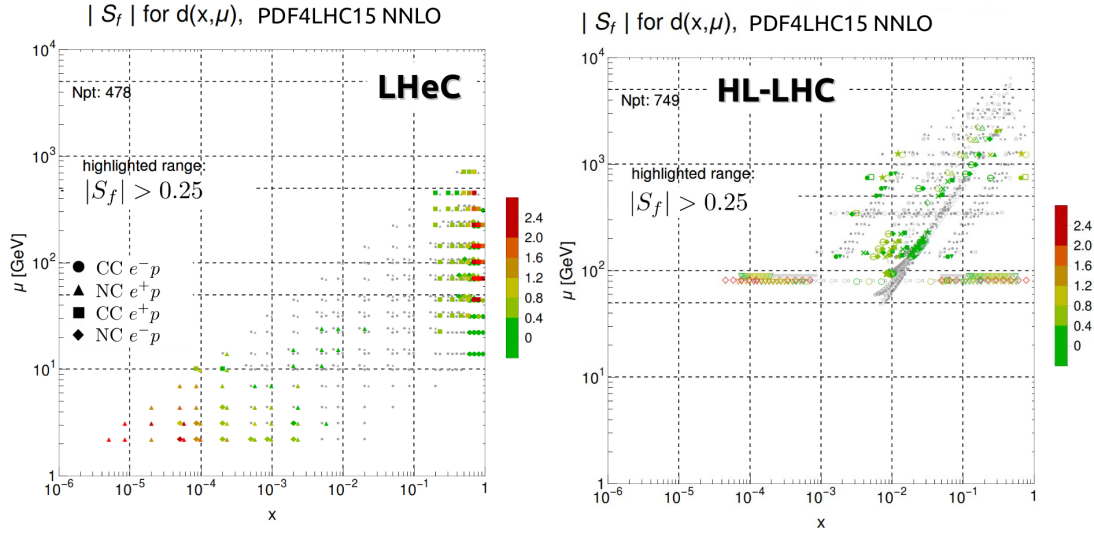


**Figure 3.17:** Sensitivity for a sample flavour  $\{d(x, Q)\}$  in the  $\{x, Q^2\}$  kinematic plane for the LHeC (left) and the HL-LHC (right) calculated with pseudodata [94]. We observe the LHeC is particularly sensitive in both the high and low  $x$  regions, and the HL-LHC covers the intermediate  $x$  region out to large  $Q$  scales.

1185 In Fig. 3.17 this PDF sensitivity for a sample PDF flavour is displayed for the LHeC and the  
 1186 HL-LHC pseudo-data. In particular, one observe that the LHeC provides strong sensitivity in  
 1187 the high- $x$  region, which is of great importance for BSM searches, and also in the low- $x$  region,  
 1188 which is relevant for QCD phenomena such as saturation. The HL-LHC provides constraints  
 1189 coming from  $W/Z$  production ( $Q \sim M_{W/Z}$ ) as well as from jets at high scales. The combination  
 1190 of these measurements will provide strongest constraints on the various PDF flavours across the  
 1191 broad  $\{x, Q^2\}$  kinematic plane.

### 1192 3.1.8 Summary on PDFs (in progress!)

1193 The LHeC will cover a hitherto not accessible kinematic region (c.f. Fig. 1.1 in the Introduction).  
 1194 This spans almost six orders of magnitude in  $x$  as well as in  $Q^2$ . It makes full use of the weak  
 1195 interactions in NC and CC, thus enabling a complete separation of flavour contributions, which  
 1196 would otherwise not be possible with data only from fixed target experiments on  $F_2$ . Other  
 1197 lepton-nucleon DIS experiments, such as the EIC, miss the low  $x$  as well as the high  $Q^2$  region  
 1198 by one to two orders of magnitude as even compared to HERA and those can therefore not solve  
 1199 the problem of non-DGLAP evolution and cannot separate different flavours reliably.

1200 The PDF programme of the LHeC is of unprecedented depth for the following reasons:

- 1201 • it will resolve the partonic structure of the proton (and nuclei, Chapter 4) for the first time  
 1202 completely, i.e. determine  $P = u_v, d_v, u, d, s, c, b$  and the top and gluon momentum  
 1203 distributions through NC and CC cross section and direct heavy quark measurements in  
 1204 a huge kinematic range, from below  $x = 10^{-6}$  to  $x = 0.9$  and in  $Q^2$  from below the DIS  
 1205 region to nearly  $Q^2 = 4E_e E_p = 1.4 \cdot 10^6 \text{ GeV}^2$ ;
- 1206 • a thousand-fold increase of the HERA luminosity, unprecedented precision from new de-  
 1207 tector technology and the redundant evaluation of the event kinematics from the lepton  
 1208 and hadron final state components will lead to extremely large precision. Also, technically

1209 important, to the fixation of the various PDF analysis parameters from the LHeC data  
1210 themselves;

- 1211 • because at high energy the CC cross section becomes as large as the NC one, no other  
1212 data will be required, besides dedicated measurements of the strange, charm and bottom  
1213 quark densities with impact parameter tags. This means that there is no influence from  
1214 higher twists, hadronisation nor nuclear uncertainties, and no other experiment needed,  
1215 i.e. the LHeC will indeed provide a unique and complete base for PDFs, for predictions,  
1216 discovery and novel tests of theory.

1217 Given the impressive theoretical progress on pQCD, one will have these PDFs available to at  
1218 least [79] N<sup>3</sup>LO. This is important to reduce scale uncertainties but as well for a coherent  
1219 analysis, for example of Higgs production at the LHC which has already been calculated to  
1220 N<sup>3</sup>LO. For QCD, this will resolve many open issues (and probably create new ones) such as on  
1221 the correct value of  $\alpha_s$ , discussed below, the question on the persistence (or not) of linear parton  
1222 evolution at small  $x$  and, as mentioned, it will also decisively test whether factorisation holds or  
1223 not between DIS and Drell-Yan scattering.

1224 The LHeC will offer novel tests of QCD, of data consistency, of improved searches for new  
1225 particles at high mass - possibly non-resonant, etc. It will open a thoroughly new phase of  
1226 parton distribution physics. This is detailed subsequently.

1227 **unrelated text fragments:**

1228 Indeed, the LHeC is the cleanest microscope for resolving the dynamics and structure of matter  
1229 which may be built during the coming decade.

1230 The fits are extended to the lowest  $x$  for illustration, even though at such low- $x$  values non-linear  
1231 effects are expected to appear, eventually altering the evolution laws, see Sec. 3.2.4.

1232 **move to ? Note also that such a determination is free from higher twist corrections, which plague**  
1233 **all fixed target data, and from nuclear uncertainties as the  $u - d$  distinction at LHeC is achieved**  
1234 **in high luminosity, high  $Q^2$   $ep$  scattering only.**

## 1235 **3.2 Pushing the limits of QCD with high precision measure-** 1236 **ments**

1237 The straightforward and strikingly simple formalism of Quantum Chromodynamics (QCD) pro-  
1238 vides a very successful description of strong interactions. Despite its undoubted success, the  
1239 strong force remains one of the least known fundamental sectors of (particle) physics and many  
1240 of its phenomena are known only with moderate or even poor precision, and several aspects still  
1241 need to be explored, see the introductory Chapter 1.

1242 For an improved understanding of strong interactions and to answer a variety of those open  
1243 questions additional measurements with highest precision have to be performed. At the LHeC,  
1244 deep-inelastic electron-proton and lepton-nucleus reactions will extend tests of QCD phenomena  
1245 to a new and yet unexplored domain up to the TeV scale and to  $x$  values as low as  $10^{-6}$ , and  
1246 QCD measurements can be performed with very high experimental precision. This is because  
1247 the proton is a *strongly* bound system and in deep-inelastic scattering (DIS) the exchanged  
1248 *colourless* photon (or  $Z$ ) between the electron and the parton inside the proton acts as a neutral  
1249 observer with respect to the phenomena of the strong force. In addition, the over-constrained  
1250 kinematic system in DIS allows for precise (*in-situ*) calibrations of the detector to measure the

1251 kinematics of the scattered lepton, and, more importantly here, also the hadronic final state. In  
1252 DIS, in many cases, the virtuality of the exchanged  $\gamma/Z$  boson often provides a reasonable scale  
1253 to stabilise theoretical predictions.

1254 In this Section, selected topics of QCD studies at the LHeC are discussed. [Maybe list the topics](#)  
1255 [here?](#)

### 1256 3.2.1 Determination of the strong coupling constant

1257 Quantum Chromodynamics (QCD) [95, 96] has been established as the theory of strong inter-  
1258 actions within the Standard Model of particle physics. While there are manifold aspects both  
1259 from the theoretical and from the experimental point-of-view, by far the most important pa-  
1260 rameter of QCD is the coupling strength which is most commonly expressed at the mass of the  
1261  $Z$  boson,  $M_Z$ , as  $\alpha_s(M_Z)$ . Its (renormalisation) scale dependence is given by the QCD gauge  
1262 group  $SU(3)$  [97, 98]. Predictions for numerous processes in  $e^+e^-$ ,  $pp$  or  $ep$  collisions are then  
1263 commonly performed in the framework of perturbative QCD, and (the lack of) higher-order  
1264 QCD corrections often represent limiting aspects for precision physics. Therefore, the deter-  
1265 mination of the strong coupling constant  $\alpha_s(M_Z)$  constitutes one of the most crucial tasks for  
1266 future precision physics, while at the same time the study of the scale dependence of  $\alpha_s$  provides  
1267 an inevitable test of the validity of QCD as the theory of strong interactions and the portal for  
1268 GUT theories.

1269 Different processes and methodologies can be considered for a determination of  $\alpha_s(M_Z)$  (see e.g.  
1270 reviews [99–101]). Since QCD is an asymptotically free theory, with free behaviour at high scales  
1271 but confinement at low scales, a high sensitivity to the value of  $\alpha_s(M_Z)$  is naturally obtained  
1272 from low-scale measurements. However, the high-scale behaviour must then be calculated by  
1273 solving the renormalisation group equation, which implies the strict validity of the theory and  
1274 an excellent understanding of all subleading effects, such as the behaviour around quark-mass  
1275 thresholds.

1276 Precision measurements at the LHeC offer the unique opportunity to exploit many of these  
1277 aspects. Measurements of jet production cross sections or inclusive NC and CC DIS cross  
1278 sections provide a high sensitivity to the value of  $\alpha_s(M_Z)$ , since these measurements can be  
1279 performed at comparably low scales and with high experimental precision. At the same time,  
1280 the LHeC provides the opportunity to test the running of the strong coupling constant over a  
1281 large kinematic range. In this Section, the prospects for a determination of the strong coupling  
1282 constant with inclusive jet cross sections and with inclusive NC/CC DIS cross sections are  
1283 studied.

#### 1284 Strong coupling from inclusive jet cross sections

1285 The measurement of inclusive jet or di-jet production cross sections in NC DIS provides a high  
1286 sensitivity to the strong coupling constant and to the gluon PDF of the proton. This is because  
1287 jet cross sections in NC DIS are measured in the Breit reference frame [102], where the virtual  
1288 boson  $\gamma^*$  or  $Z$  collides head-on with the struck parton from the proton and the outgoing jets are  
1289 required to have a non-zero transverse momentum in that reference frame. The leading order  
1290 QCD diagrams are QCD Compton and boson-gluon fusion and are both  $\mathcal{O}(\alpha_s)$ , see Fig. 3.18.

1291 At HERA, jets are most commonly defined by the longitudinally invariant  $k_t$  jet algorithm [104]  
1292 with a distance parameter  $R = 1.0$  [103, 105–121]. This provides an infrared safe jet definition

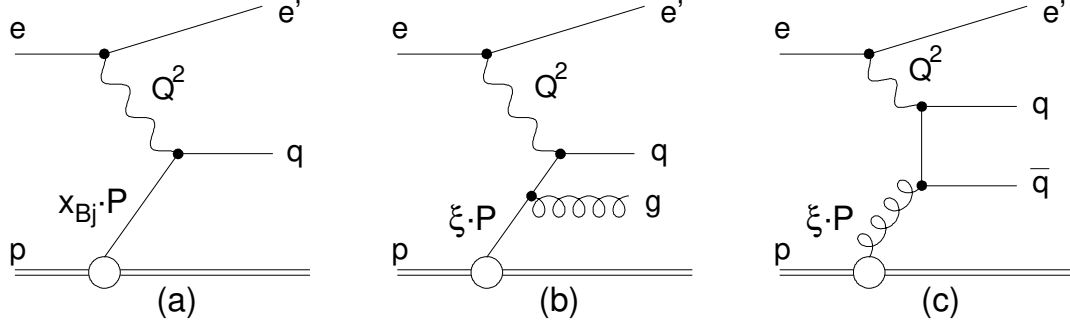


**Figure 3.18:** Leading order diagrams for inclusive DIS (a) and jet production (b,c) in the Breit frame (taken from Ref. [103]).

1293 and the chosen distance parameter guarantees a small dependence on non-perturbative effects,  
 1294 such as hadronisation. Differently than in  $pp$  at the LHC [122–125], jet algorithms at the LHeC  
 1295 do not require any pile-up subtraction and any reduction of the dependence on minimum bias  
 1296 or underlying event, due to the absence of such effects. Therefore, for this study we adopt the  
 1297 choices made at HERA.

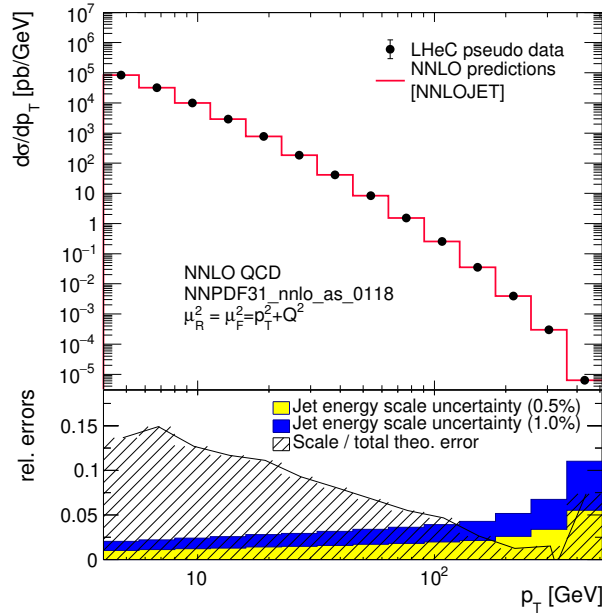


**Figure 3.19:** Inclusive jet cross sections calculated in NNLO QCD as a function of the jet transverse momentum in the Breit frame,  $p_T$ . The shaded area indicates NNLO scale uncertainties and the yellow band shows the estimated experimental jet energy scale uncertainty (JES) of 0.5%. The blue band shows a very conservative assumption on the JES of 1%.

1298 In Fig. 3.19 the next-to-next-to-leading order QCD (NNLO) predictions [126, 127] for cross  
 1299 sections for inclusive jet production in NC DIS as a function of the transverse momentum of the  
 1300 jets in the Breit frame are displayed. The calculations are performed for an electron beam energy  
 1301 of  $E_e = 60$  GeV and include  $\gamma/Z$  and  $Z$  exchange terms and account for the electron polarisation  
 1302  $P_e = -0.8$ . The NC DIS kinematic range is set to  $Q^2 > 4$  GeV<sup>2</sup>. The calculations are performed  
 1303 using the NNLOJET program [128] interfaced to the fastNLO (applfast) library [129–131].

1304 The kinematically accessible range in jet- $P_T$  ranges over two orders of magnitude,  $4 < P_T \lesssim$

1305 400 GeV. The size of the cross section extends over many orders in magnitude, thus imposing  
 1306 challenging demands on LHeC experimental conditions, triggers and DAQ bandwidth, calibra-  
 1307 tion, and data processing capabilities. The scale uncertainty of the NNLO predictions is about  
 1308 10 % at low values of  $P_T$  and significantly decreases with increasing values of  $P_T$ . Future im-  
 1309 proved predictions will further reduce these theoretical uncertainties.

1310 For the purpose of estimating the uncertainty of  $\alpha_s(M_Z)$  in a determination from inclusive jet  
 1311 cross sections at the LHeC, double-differential cross sections as a function of  $Q^2$  and  $P_T$  with  
 1312 a full set of experimental uncertainties are generated. Altogether 509 cross section values are  
 1313 calculated in the kinematic range  $8 < Q^2 < 500\,000 \text{ GeV}^2$  and  $4 < P_T < 512 \text{ GeV}$ , and the bin  
 1314 grid is similar to the ones used by CMS, H1 or ZEUS [37,122,131,132]. The various error sources  
 1315 considered are summarised in Tab. 3.3. The uncertainties related to the reconstruction of the NC  
 1316 DIS kinematic variables,  $Q^2$ ,  $y$  and  $x_{bj}$ , are similar to the estimates for the inclusive NC DIS cross  
 1317 sections (see section 3.1.4). For the reconstruction of hadronic final state particles which are the  
 1318 input to the jet algorithm, jet energy scale uncertainty (JES), calorimetric noise and the polar  
 1319 angle uncertainty are considered. The size of the uncertainties is gauged with achieved values by  
 1320 H1, ZEUS, ATLAS and CMS [112,120,133–135]. The size of the dominant JES one is assumed  
 1321 to be 0.5 % for reconstructed particles in the laboratory rest frame, yielding an uncertainty of  
 1322 0.2–4.4 % on the cross section after the boost to the Breit frame. A JES uncertainty of 0.5 %  
 1323 is well justified by improved calorimeters, since already H1 and ZEUS reported uncertainties  
 1324 of 1 % [112,120,133], and ATLAS and CMS achieved 1 % over a wide range in  $P_T$  [134,135],  
 1325 albeit the presence of pile-up and the considerably more complicated definition of a reference  
 1326 object for the in-situ calibration. The size of the JES uncertainty is also displayed in Fig. 3.19.  
 1327 The calorimetric noise of  $\pm 20 \text{ MeV}$  on every calorimeter cluster, as reported by H1, yields an  
 1328 uncertainty of up to 0.7 % on the jet cross sections. A minimum size of the statistical uncertainty  
 1329 of 0.15 % is imposed for each cross section bin. An overall normalisation uncertainty of 1.0 %  
 1330 is assumed, which will be mainly dominated by the luminosity uncertainty. In addition, an  
 1331 uncorrelated uncertainty component of 0.6 % collects various smaller error sources, such as for  
 1332 instance radiative corrections, unfolding or model uncertainties. Studies on the size and the  
 1333 correlation model of these uncertainties are performed below.

Exp. uncertainty	Shift	Size on $\sigma$ [%]
Statistics with $1 \text{ ab}^{-1}$	min. 0.15 %	0.15–5
Electron energy	0.1 %	0.02–0.62
Polar angle	2 mrad	0.02–0.48
Calorimeter noise	$\pm 20 \text{ MeV}$	0.01–0.74
Jet energy scale (JES)	0.5 %	0.2–4.4
Uncorrelated uncert.	0.6 %	0.6
Normalisation uncert.	1.0 %	1.0

**Table 3.3:** Anticipated uncertainties of inclusive jet cross section measurements at the LHeC.

1333

1334 The value and uncertainty of  $\alpha_s(M_Z)$  is obtained in a  $\chi^2$ -fit of NNLO predictions [126,127] to  
 1335 the simulated data with  $\alpha_s(M_Z)$  being a free fit parameter. The methodology follows closely  
 1336 analyses of HERA jet data [131,132] and the  $\chi^2$  quantity is calculated from relative uncertainties,  
 1337 i.e. those of the right column of Tab. 3.3. The predictions for the cross section  $\sigma$  account for  
 1338 both  $\alpha_s$ -dependent terms in the NNLO calculations, i.e. in the DGLAP operator and the hard  
 1339 matrix elements, by using

$$\sigma = f_{\mu_0} \otimes P_{\mu_0 \rightarrow \mu_F}(\alpha_s(M_z)) \otimes \hat{\sigma}(\alpha_s(M_z), \mu), \quad (3.2)$$

1340 where  $f_{\mu_0}$  are the PDFs at a scale of  $\mu_0 = 30 \text{ GeV}$ , and  $P_{\mu_0 \rightarrow \mu_F}$  denotes the DGLAP operator,  
 1341 which is dependent on the value of  $\alpha_s(M_Z)$ . The  $\alpha_s$  uncertainty is obtained by linear error  
 1342 propagation and is validated with a separate study of the  $\Delta\chi^2 = 1$  criterion.

1343 In the fit of NNLO QCD predictions to the simulated double-differential LHeC inclusive jet cross  
 1344 sections an uncertainty of

$$\Delta\alpha_s(M_Z)(\text{jets}) = \pm 0.00013_{(\text{exp})} \pm 0.00010_{(\text{PDF})} \quad (3.3)$$

1345 is found. The PDF uncertainty is estimated from a PDF set obtained from LHeC inclusive DIS  
 1346 data (see Sec. 3.1.5). These uncertainties promise a determination of  $\alpha_s(M_Z)$  with the highest  
 1347 precision and would represent a considerable reduction of the current world average value with  
 1348 a present uncertainty of  $\pm 0.00110$  [100].

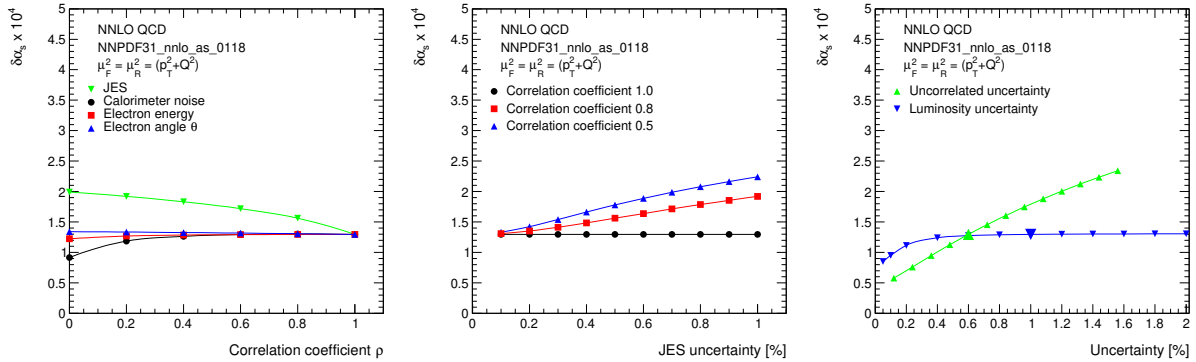


**Figure 3.20:** Studies of the size and correlations of experimental uncertainties impacting the uncertainty of  $\alpha_s(M_Z)$ . Left: Study of the value of the correlation coefficient  $\rho$  for different systematic uncertainties. Common systematic uncertainties are considered as fully correlated,  $\rho = 1$ . Middle: Size of the JES uncertainty for three different values of  $\rho_{\text{JES}}$ . Right: Impact of the uncorrelated and normalisation uncertainties on  $\Delta\alpha_s(M_Z)$ .

1349 The uncertainty of  $\alpha_s$  is studied for different values of the experimental uncertainties for the  
 1350 inclusive jet cross section measurement and for different assumption on bin-to-bin correlations,  
 1351 expressed by the correlation coefficient  $\rho$ , of individual uncertainty sources, as shown in Fig. 3.20.  
 1352 It is observed that, even for quite conservative scenarios,  $\alpha_s(M_Z)$  will be determined with an  
 1353 uncertainty smaller than 2‰. For this, it is important to keep the size of the uncorrelated  
 1354 uncertainty or the uncorrelated components of other systematic uncertainties under good control.

1355 In the present formalism theoretical uncertainties from scale variations of the NNLO predictions  
 1356 amount to about  $\Delta\alpha_s(M_Z) = 0.0035$  (NNLO). These can be reduced with suitable cuts in  $P_T$   
 1357 or  $Q^2$  to about  $\Delta\alpha_s(M_Z) \approx 0.0010$ . However, it is expected that improved predictions, e.g. with  
 1358 resummed contributions or N<sup>3</sup>LO predictions will significantly reduce these uncertainties in the  
 1359 future. Uncertainties on non-perturbative hadronisation effects will have to be considered as  
 1360 well, but these will be under good control due to the measurements of charged particle spectra  
 1361 at the LHeC and improved phenomenological models.

### 1362 The running of the strong coupling

1363 The dependence of the coupling strength as a function of the renormalisation scale  $\mu_R$  is predicted  
 1364 by QCD, which is often called the *running* of the strong coupling. Its study with experimental  
 1365 data represents an important consistency and validity test of QCD. Using inclusive jet cross

1366 sections the running of the strong coupling can be tested by determining the value of  $\alpha_s$  at  
 1367 different values of  $\mu_R$  by grouping data points with similar values of  $\mu_R$  and determining the  
 1368 value of  $\alpha_s(\mu_R)$  from these subsets of data points. The assumptions on the running of  $\alpha_s(\mu_R)$   
 1369 are then imposed only for the limited range of the chosen interval, and not to the full measured  
 1370 interval as in the previous study. Here we set  $\mu_R^2 = Q^2 + P_T^2$ <sup>3</sup>. The experimental uncertainties  
 from the fits to subsets of the inclusive jet pseudodata are displayed in Fig. 3.21. These results

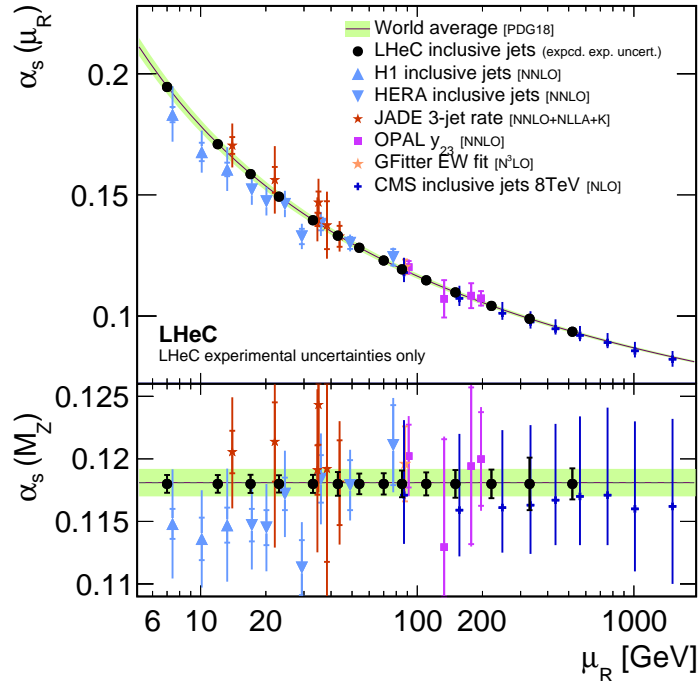


**Figure 3.21:** Uncertainties of  $\alpha_s(M_Z)$  and corresponding  $\alpha_s(\mu_R)$  in a determination of  $\alpha_s$  using LHeC inclusive jet cross sections at different values of  $\mu_R^2 = Q^2 + p_T^2$ . Only experimental uncertainties are shown for LHeC and are compared with a number of presently available measurements and the world average value.

1371 demonstrate a high sensitivity to  $\alpha_s$  over two orders of magnitude in renormalisation scale up  
 1372 to values of about  $\mu_R \approx 500$  GeV. In the range  $6 < \mu_R \lesssim 200$  GeV the experimental uncertainty  
 1373 is found to be smaller than the expectation from the world average value [143]. This region is of  
 1374 particular interest since it connects the precision determinations from lattice calculations [144]  
 1375 or  $\tau$  decay measurements [145], which are at low scales  $\mathcal{O}(\text{GeV})$ , to the measurements at the  
 1376  $Z$  pole [146] and to the applications to scales which are relevant for the LHC, e.g. for Higgs  
 1377 or top-quark physics or high-mass searches. This kinematic region of scales  $\mathcal{O}(10 \text{ GeV})$  cannot  
 1378 be accessed by (HL-)LHC experiments because of limitations due to pile-up and underlying  
 1379 event [147].  
 1380

<sup>3</sup> The choice of the scales follows a *conventional* scale setting procedure and uncertainties for the scale choice and for unknown higher order terms are estimated by varying the scales. Such variations are sensitive only to the terms which govern the behaviour of the running coupling, and may become unreliable due to renormalons [136]. An alternative way to fix the scales is provided by the Principle of Maximum Conformality (PMC) [137–141]. The PMC method was recently applied to predictions of event shape observables in  $e^+e^- \rightarrow \text{hadrons}$  [142]. When applying the PMC method to observables in DIS, the alternative scale setting provides a profound alternative to verify the running of  $\alpha_s(\mu_R)$ . Such a procedure could be particularly relevant for DIS event shape observables, where the leading-order terms are insensitive to  $\alpha_s$  and conventional scale choices may not be adequately related to the  $\alpha_s$ -sensitive higher order QCD corrections.

1381 **Strong coupling from inclusive DIS cross sections**

1382 Inclusive DIS cross sections are sensitive to  $\alpha_s(M_Z)$  through higher-order QCD corrections,  
 1383 contributions from the  $F_L$  structure function and the scale dependence of the cross section at  
 1384 high  $x$  (*scaling violations*). The value of  $\alpha_s(M_Z)$  can then be determined in a combined fit  
 1385 of the PDFs and  $\alpha_s(M_Z)$  [132]. While a simultaneous determination of  $\alpha_s(M_Z)$  and PDFs is  
 1386 not possible with HERA inclusive DIS data alone due to its limited precision and kinematic  
 1387 coverage [37, 132], the large kinematic coverage, high precision and the integrated luminosity of  
 1388 the LHeC data will allow for the first time such an  $\alpha_s$  analysis.

1389 For the purpose of the determination of  $\alpha_s(M_Z)$  from inclusive NC/CC DIS data, a combined  
 1390 PDF+ $\alpha_s$  fit to the simulated data is performed, similar to the studies in Sec. 3.1. Other technical  
 1391 details are outlined in Ref. [132]. In this fit, however, the numbers of free parameters of the  
 1392 gluon parameterisation is increased, since the gluon PDF and  $\alpha_s(M_Z)$  are highly correlated and  
 1393 LHeC data are sensitive to values down to  $x < 10^{-5}$ , which requires additional freedom for the  
 1394 gluon parameterisation. The inclusive data are restricted to  $Q^2 > 3.5 \text{ GeV}^2$  in order to avoid a  
 1395 region where effects beyond fixed-order perturbation theory may become sizeable [37, 148].

1396 Exploiting the full LHeC inclusive NC/CC DIS data with  $E_e = 50 \text{ GeV}$ , the value of  $\alpha_s(M_Z)$  can  
 1397 be determined with an uncertainty  $\Delta\alpha_s(M_Z) = \pm 0.00038$ . With a more optimistic assumption  
 1398 on the dominant uncorrelated uncertainty of  $\delta\sigma_{\text{(uncor.)}} = 0.25 \%$ , an uncertainty as small as

$$\Delta\alpha_s(M_Z)(\text{incl. DIS}) = \pm 0.00022_{(\text{exp+PDF})} \quad (3.4)$$

1399 is achieved. This would represent a considerable improvement over the present world average  
 1400 value. Given these small uncertainties, theoretical uncertainties from missing higher orders or  
 heavy quark effects have to be considered in addition. In a dedicated study, the fit is repeated

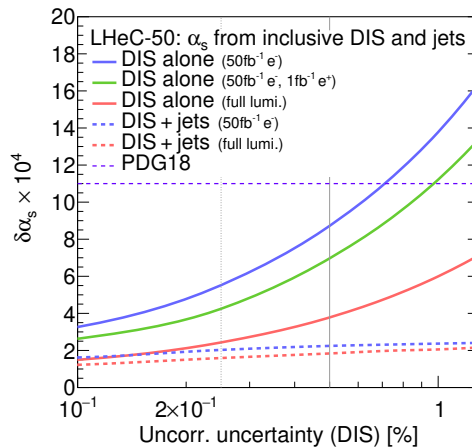


**Figure 3.22:** Uncertainties of  $\alpha_s(M_Z)$  from simultaneous fits of  $\alpha_s(M_Z)$  and PDFs to inclusive NC/CC DIS data as a function of the size of the uncorrelated uncertainty of the NC/CC DIS data. The full lines indicate the uncertainties obtained with different assumptions on the data taking scenario and integrated luminosity. The dashed lines indicate results where, additionally to the inclusive NC/CC DIS data, inclusive jet cross section data are considered.

1401 with a reduced data set which can be accumulated already during a single year of operation <sup>4</sup>,  
 1402 corresponding to about  $\mathcal{L} \sim 50 \text{ fb}^{-1}$ . Already these data will be able to improve the world  
 1403 average value. These studies are displayed in Fig. 3.22.  
 1404

<sup>4</sup>Two different assumptions are made. One fit is performed with only electron data corresponding to  $\mathcal{L} \sim 50 \text{ fb}^{-1}$ , and an alternative scenario considers further positron data corresponding to  $\mathcal{L} \sim 1 \text{ fb}^{-1}$ .

## 1405 Inclusive DIS and inclusive jet data

1406 The highest sensitivity to  $\alpha_s(M_Z)$  and an optimal treatment of the PDFs is obtained by using  
1407 inclusive jet data together with inclusive NC/CC DIS data in a combined determination of  
1408  $\alpha_s(M_Z)$  and the PDFs. Jet data will provide an enhanced sensitivity to  $\alpha_s(M_Z)$ , while inclusive  
1409 DIS data has the highest sensitivity to the determination of the PDFs. Furthermore, a consistent  
1410 theoretical QCD framework can be employed.

1411 For this study, the double-differential inclusive jet data as described above, and additionally  
1412 the inclusive NC/CC DIS data with  $E_e = 50$  GeV as introduced in Sec. 3.1.4, are employed.  
1413 Besides the normalisation uncertainty, all sources of systematic uncertainties are considered as  
1414 uncorrelated between the two processes. A fit of NNLO QCD predictions to these data sets is  
1415 then performed, and  $\alpha_s(M_Z)$  and the parameters of the PDFs are determined. The methodology  
1416 follows closely the methodology sketched in the previous study. Using inclusive jet and inclusive  
1417 DIS data in a single analysis, the value of  $\alpha_s(M_Z)$  is determined with an uncertainty of

$$\Delta\alpha_s(M_Z)(\text{incl. DIS \& jets}) = \pm 0.00018_{(\text{exp+PDF})}. \quad (3.5)$$

1418 This result will improve the world average value considerably. However, theoretical uncertainties  
1419 are not included and new mathematical tools and an improved understanding of QCD will  
1420 be needed in order to achieve small values similar to the experimental ones. The dominant  
1421 sensitivity in this study arises from the jet data. This can be seen from Fig. 3.22, where  
1422  $\Delta\alpha_s(M_Z)$  changes only moderately with different assumptions imposed on the inclusive NC/CC  
1423 DIS data. Assumptions made for the uncertainties of the inclusive jet data have been studied  
1424 above, and these results can be translated easily to this PDF+ $\alpha_s$  fit.

## 1425 Discussion of $\alpha_s(M_Z)$ determinations at LHeC

1426 The expected values for  $\alpha_s(M_Z)$  obtained from inclusive jets or from inclusive NC/CC DIS data  
1427 are compared in Fig. 3.23 with present determinations from global fits based on DIS data (called  
1428 *PDF fits*) and the world average value [100]. It is observed that LHeC will have the potential  
1429 to improve considerably the world average value. Already after one year of data taking, the  
1430 experimental uncertainties of the NC/CC DIS data are competitive with the world average  
1431 value. The measurement of jet cross sections will further improve that value (not shown).

1432 Furthermore, LHeC will be able to address a long standing puzzle. All  $\alpha_s$  determinations from  
1433 global fits based on NC/CC DIS data find a lower value of  $\alpha_s(M_Z)$  than determinations in the  
1434 lattice QCD framework, from  $\tau$  decays or in a global electroweak fit. With the expected precision  
1435 from LHeC this discrepancy will be resolved.

## 1436 Strong coupling from other processes

1437 A detailed study for the determination of  $\alpha_s(M_Z)$  from NC/CC DIS and from inclusive jet data  
1438 was presented in the previous paragraphs. However, a large number of additional processes  
1439 and observables that are measured at the LHeC can also be considered for a determination of  
1440  $\alpha_s(M_Z)$ . Suitable observables or processes are di-jet and multi-jet production, heavy flavour  
1441 production, jets in photoproduction or event shape observables. These processes all exploit  
1442 the  $\alpha_s$  dependence of the hard interaction. Using suitable predictions, also *softer* processes  
1443 can be exploited for an  $\alpha_s$  determination. Examples could be jet shapes or other substructure  
1444 observables, or charged particle multiplicities.

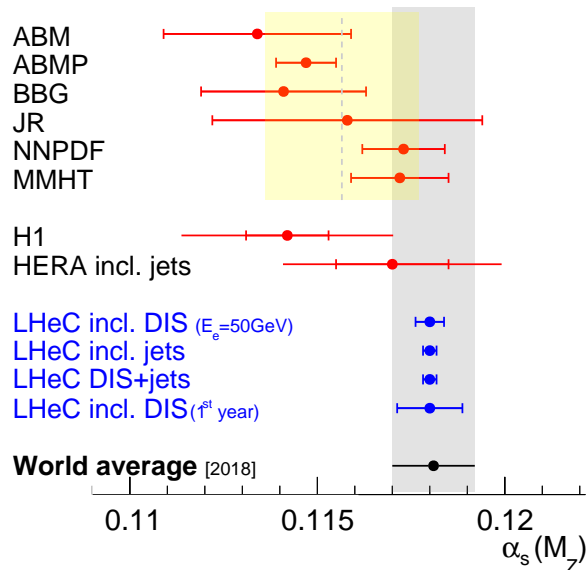


**Figure 3.23:** Summary of  $\alpha_s(M_Z)$  values in comparison with present values.

1445 Since  $\alpha_s(M_Z)$  is a parameter of a phenomenological model, the total uncertainty of  $\alpha_s(M_Z)$  is  
 1446 always a sum of experimental and theoretical uncertainties which are related to the definition of  
 1447 the observable and to the applied model, e.g. hadronisation uncertainties, diagram removal/sub-  
 1448 traction uncertainties or uncertainties from missing higher orders. Therefore, credible prospects  
 1449 for the total uncertainty of  $\alpha_s(M_Z)$  from other observables or processes are altogether difficult  
 1450 to predict, even more since LHeC will explore a new kinematic regime that was previously  
 1451 unmeasured.

1452 In a first approximation, for any process the sensitivity to  $\alpha_s(M_Z)$  scales with the order  $n$  of  $\alpha_s$   
 1453 in the leading-order diagram,  $\alpha_s^n$ . The higher the power  $n$  the higher the sensitivity to  $\alpha_s(M_Z)$ .  
 1454 Consequently, the experimental uncertainty of an  $\alpha_s$  fit may reduce with increasing power  $n$ .  
 1455 Already at HERA three-jet cross section were proven to have a high sensitivity to  $\alpha_s(M_Z)$  albeit  
 1456 their sizeable statistical uncertainties [103, 113]. At the LHeC, due to the higher  $\sqrt{s}$  and huge  
 1457 integrated luminosity, as well as the larger acceptance of the detector, three-, four- or five-jet  
 1458 cross sections represent highly sensitive observables for a precise determination of  $\alpha_s(M_Z)$ , and  
 1459 high experimental precision can be achieved. In these cases, fixed order pQCD predictions may  
 1460 become limiting factors, since they are more complicated for large  $n$ .

1461 Di-jet observables are expected to yield a fairly similar experimental uncertainty than inclusive  
 1462 jet cross sections, as studied in the previous paragraphs, since both have  $n = 1$  at LO. How-  
 1463 ever, their theoretical uncertainties may be smaller, since di-jet observables are less sensitive to  
 1464 additional higher-order radiation, in particular at lower scales where  $\alpha_s(\mu_R)$  is larger.

1465 Event shape observables in DIS exploit additional radiation in DIS events (see e.g. review [149]  
 1466 or HERA measurements [150, 151]). Consequently, once measured at the LHeC the experi-  
 1467 mental uncertainties of  $\alpha_s(M_Z)$  from these observables are expected to become very similar  
 1468 to that in Eq. (3.5), since both the event sample and the process is similar to the inclusive  
 1469 jet cross sections <sup>5</sup>. However, different reconstruction techniques of the observables may yield

<sup>5</sup>It shall be noted, that event shape observables in NC DIS can be defined in the laboratory rest frame or the Breit frame.

1470 reduced experimental uncertainties, and the calculation of event shape observables allow for  
 1471 the resummation of large logarithms, and steady theoretical advances promise small theoretical  
 1472 uncertainties [152–158].

1473 Jet production cross sections in photoproduction represents a unique opportunity for another  
 1474 precision determination of  $\alpha_s(M_Z)$ . Such measurements have been performed at HERA [159–  
 1475 162]. The sizeable photoproduction cross section provides a huge event sample, which is statis-  
 1476 tically independent from NC DIS events, and already the leading-order predictions are sensitive  
 1477 to  $\alpha_s(M_Z)$  [163]. Also its running can be largely measured since the scale of the process is well  
 1478 estimated by the transverse momentum of the jets  $\mu_R \sim P_T^{\text{jet}}$ . Limiting theoretical aspects are  
 1479 due to the presence of a quasi-real photon and the poorly known photon PDF [164, 165].

1480 A different class of observables represent heavy flavour (HF) cross sections, which are discussed in  
 1481 Sec. 3.1.6. Due to flavour conservation, these are commonly proportional to  $\mathcal{O}(\alpha_s^1)$  at leading-  
 1482 order. However, when considering inclusive HF cross sections above the heavy quark mass  
 1483 threshold heavy quarks can be factorised into the PDFs, and the leading structure functions  
 1484  $F_2^{c,b}$  are sensitive to  $\alpha_s$  only beyond the LO approximation (see reviews [66, 67], recent HERA  
 1485 measurements [166, 167] and references therein). The presence of the heavy quark mass as an  
 1486 additional scale stabilises perturbative calculations, and reduced theoretical uncertainties are  
 1487 expected.

1488 At the LHeC the structure of jets and the formation of hadrons can be studied with unprece-  
 1489 dented precision. This is so because of the presence of a single hadron in the initial state.  
 1490 Therefore, limiting effects like the underlying event or pile-up are absent or greatly diminished.  
 1491 Precise measurements of jet shape observables, or the study of jet substructure observables [168],  
 1492 are highly sensitive to the value of  $\alpha_s(M_Z)$ , because parton shower and hadronisation take place  
 1493 at lower scales where the strong coupling becomes large and an increased sensitivity to  $\alpha_s(M_Z)$   
 1494 is attained [169, 170].

1495 Finally, also the determination of  $\alpha_s(M_Z)$  from inclusive NC DIS cross sections can be improved.  
 1496 For NC DIS the dominant sensitivity to  $\alpha_s$  arises from the  $F_L$  structure function and from scaling  
 1497 violations of  $F_2$  at lower values of  $Q^2$  but at very high values of  $x$ . Dedicated measurements of  
 1498 these kinematic regions will further improve the experimental uncertainties from the estimated  
 1499 values in Eq. (3.4).

### 1500 3.2.2 New QCD Dynamics at Small $x$

1501 The LHeC machine will offer access to a completely novel kinematic regime of DIS characterised  
 1502 by very small values of  $x$ . From the kinematical plane in  $(x, Q^2)$  depicted in Fig. 1.1, it is clear  
 1503 that the LHeC will be able to probe Bjorken- $x$  values as low as  $10^{-6}$  for perturbative values of  
 1504  $Q^2$ . At low values of  $x$  various phenomena may occur which go beyond the standard collinear  
 1505 perturbative description based on DGLAP evolution. Since the seminal works of Balitsky, Fadin,  
 1506 Kuraev and Lipatov [171–173] it has been known that, at large values of centre-of-mass energy  
 1507  $\sqrt{s}$  or, to be more precise, in the Regge limit, there are large logarithms of energy which need  
 1508 to be resummed. Thus, even at low values of the strong coupling  $\alpha_s$ , logarithms of energy  $\ln s$   
 1509 may be sufficiently large, such that terms like  $(\alpha_s \ln s)^n$  will start to dominate the cross section.

1510 The calculation of scattering amplitudes in the high-energy limit and the resummation of  
 1511  $(\alpha_s \ln s)^n$  series in the leading logarithmic order was performed in [171–173] and it resulted  
 1512 in the famous BFKL evolution equation. This small  $x$  evolution equation, written for the so-  
 1513 called gluon Green’s function or the unintegrated gluon density, is a differential equation in

1514  $\ln 1/x$ . An important property of this equation is that it keeps the transverse momenta un-  
 1515 ordered along the gluon cascade. This has to be contrasted with DGLAP evolution which is  
 1516 differential in the hard scale  $Q^2$  and relies on the strong ordering in the transverse momenta of  
 1517 the exchanged partons in the parton cascade. The solution to the BFKL equation is a gluon  
 1518 density which grows sharply with decreasing  $x$ , as a power i.e.  $\sim x^{-\omega_{IP}}$ , where  $\omega_{IP}$  is the hard  
 1519 Pomeron intercept, and in the leading logarithmic approximation equals  $\frac{N_c \alpha_s}{\pi} 4 \ln 2$ , which gives  
 1520 a value of about 0.5 for typical values of the strong coupling. The leading logarithmic (LLx)  
 1521 result yielded a growth of the gluon density which was too steep for the experimental data at  
 1522 HERA. The next-to-leading logarithmic (NLLx) calculation performed in the late 90s [174, 175]  
 1523 resulted in large negative corrections to the LLx value of the hard Pomeron intercept and yielded  
 1524 some instabilities in the cross section [176–180].

1525 The appearance of the large negative corrections at NLLx motivated the search for the appro-  
 1526 priate resummation which would stabilize the result. It was understood very early that the  
 1527 large corrections which appear in BFKL at NLLx are mostly due to the kinematics [181–183]  
 1528 as well as DGLAP terms and the running of the strong coupling. First attempts at combining  
 1529 the BFKL and DGLAP dynamics together with the proper kinematics [184] yielded encouraging  
 1530 results, and allowed a description of HERA data on structure functions with good accuracy. The  
 1531 complete resummation program was developed in a series of works [185–198]. In these works  
 1532 the resummation for the gluon Green’s function and the splitting functions was developed.

1533 The low- $x$  resummation was recently applied to the description of structure function data at  
 1534 HERA using the methodology of NNPDF [199]. It was demonstrated that the resummed fits  
 1535 provide a better description of the structure function data than the pure DGLAP based fits at  
 1536 fixed NN order. In particular, it was shown that the  $\chi^2$  of the fits does not vary appreciably  
 1537 when more small  $x$  data are included in the case of the fits which include the effects of the small- $x$   
 1538 resummation. On the other hand, the fits based on NNLO DGLAP evolution exhibit a worsening  
 1539 of their quality in the region of low  $x$  and low to moderate values of  $Q^2$ . This indicates that  
 1540 there is some tension in the fixed order fits based on DGLAP, and that resummation alleviates  
 1541 it. In addition, it was shown that the description of the longitudinal structure function  $F_L$   
 1542 from HERA data is improved in the fits with the small  $x$  resummation. This analysis suggests  
 1543 that the small  $x$  resummation effects are indeed visible in the HERA kinematic region. Such  
 1544 effects will be strongly magnified at the LHeC, which probes values of  $x$  more than one order  
 1545 of magnitude lower than HERA. The NNPDF group also performed simulation of the structure  
 1546 functions  $F_2$  and  $F_L$  with and without resummation in the LHeC range as well as for the next  
 1547 generation electron-hadron collider FCC-eh [199]. The predictions for the structure functions as  
 1548 a function of  $x$  for fixed values of  $Q^2$  are shown in Figs. 3.24.

1549 The simulations were done using APFEL [200] together with the HELL package [201] which  
 1550 implements the small  $x$  resummation. From Fig. 3.24 it is clear that LHeC will have much  
 1551 higher sensitivity to discriminate between fixed order and resummed scenarios than the HERA  
 1552 collider, with even better discrimination at the FCC-eh. The differences between the central  
 1553 values for the two predictions are of the order of 15% for the case of  $F_2$  and this is much larger  
 1554 than the projected error bar on the reduced cross section or structure function  $F_2$  which could be  
 1555 measured at LHeC. For comparison, the simulated pseudodata for  $F_2$  are shown together with  
 1556 the expected experimental uncertainties. The total uncertainties of the simulated pseudodata  
 1557 are at the few percent level at most, and are therefore much smaller than the uncertainties  
 1558 coming from the PDFs in most of the kinematic range.

1559 It is evident that fits to the LHeC data will have power to discriminate between the different  
 1560 frameworks. In the right plot in Fig. 3.24, the predictions for the longitudinal structure function

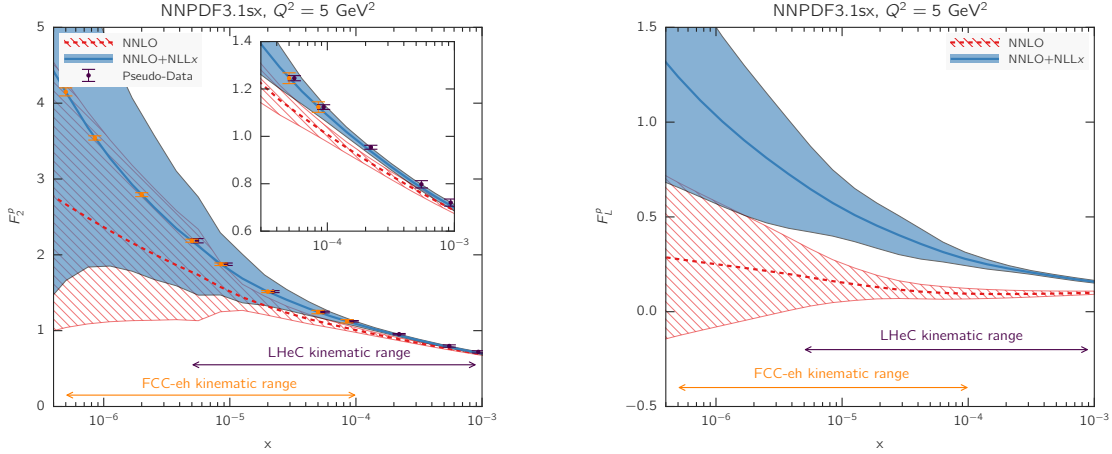


**Figure 3.24:** Predictions for the  $F_2$  and  $F_L$  structure functions using the NNPDF3.1sx NNLO and NNLO+NLLx fits at  $Q^2 = 5 \text{ GeV}^2$  for the kinematics of the LHeC and FCC-eh. In the case of  $F_2$ , we also show the expected total experimental uncertainties based on the simulated pseudodata, assuming the NNLO+NLLx values as the central prediction. A small offset has been applied to the LHeC pseudodata as some of the values of  $x$  overlap with the FCC-eh pseudodata points. The inset in the left plot shows a magnified view in the kinematic region  $x > 3 \times 10^{-5}$ , corresponding to the reach of HERA data. Figure taken from Ref. [199].

1561 are shown. We see that in the case of the  $F_L$  structure function, the differences between the  
 1562 fixed order and resummed predictions are even larger, consistently over the entire range of  $x$ .  
 1563 This indicates the importance of the measurement of the longitudinal structure function  $F_L$   
 1564 which can provide further vital constraints on the QCD dynamics in the low  $x$  region due to its  
 1565 sensitivity to the gluon density in the proton.

1566 To further illustrate the power of a high energy DIS collider like the LHeC in exploring the  
 1567 dynamics at low  $x$ , fits which include the simulated data were performed. The NNLO+NLLx  
 1568 resummed calculation was used to obtain the simulated pseudodata, both for the LHeC, in a  
 1569 scenario of a 60 GeV electron beam on a 7 TeV proton beam as well as in the case of the FCC-eh  
 1570 scenario with a 50 TeV proton beam. All the experimental uncertainties for the pseudodata have  
 1571 been added in quadrature. Next, fits were performed to the DIS HERA as well as LHeC and  
 1572 FCC-eh pseudodata using the theory with and without the resummation at low  $x$ . Hadronic  
 1573 data like jet, Drell-Yan or top, were not included for this analysis but, as demonstrated in [199],  
 1574 these data do not have much of the constraining power at low  $x$ , and therefore the results of  
 1575 the analysis at low  $x$  are independent of the additional non-DIS data sets. The quality of the  
 1576 fits characterised by the  $\chi^2$  was markedly worse when the NNLO DGLAP framework was used  
 1577 to fit the HERA data and the pseudodata from LHeC and/or FCC-eh than was the case with  
 1578 resummation. To be precise, the  $\chi^2$  per degree of freedom for the HERA data set was equal to  
 1579 1.22 for the NNLO fit, and 1.07 for the resummed fit. For the case of the LHeC/FCC-eh the  $\chi^2$   
 1580 per degree of freedom was equal to 1.71/2.72 and 1.22/1.34 for NNLO and NNLO+resummation  
 1581 fits, respectively. These results demonstrate the huge discriminatory power of the new DIS  
 1582 machines between the DGLAP and resummed frameworks, and the large sensitivity to the low  
 1583  $x$  region while simultaneously probing low to moderate  $Q^2$  values.

1584 In Fig. 3.25 the comparison of the gluon and quark distributions from the NNLO + NLLx  
 1585 fits is shown at  $Q = 100 \text{ GeV}$  as a function of  $x$ , with and without including the simulated  
 1586 pseudodata from LHeC as well as FCC-eh. The large differences at large  $x$  are due to the

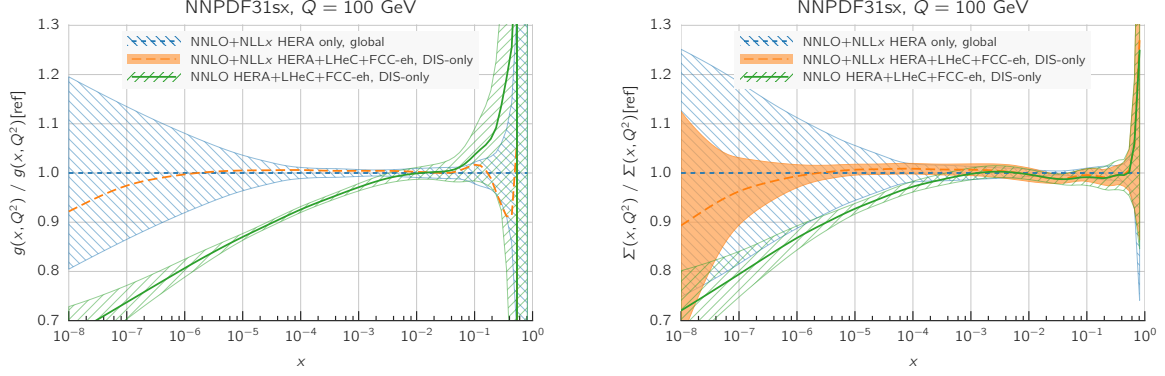


**Figure 3.25:** Comparison between the gluon (left plot) and the quark singlet (right plot) PDFs in the NNPDF3.1sx NNLO+NNLx fits without (blue hatched band) and with the LHeC+FCC-eh pseudodata (orange band) on inclusive structure functions. For completeness, we also show the results of the corresponding NNPDF3.1sx NNLO fit with LHeC+FCC-eh pseudodata (green hatched band). Figure taken from Ref. [199].

1587 fact that only DIS data were included in the fits, and not the hadronic data. The central  
 1588 values of the extracted PDFs using only HERA or using HERA and the simulated pseudodata  
 1589 coincide with each other, but a large reduction in uncertainty is visible when the new data are  
 1590 included. The uncertainties from the fits based on the HERA data only increase sharply already  
 1591 at  $x \sim 10^{-4}$ . On the other hand, including the pseudodata from LHeC and/or FCC-eh can  
 1592 extend this regime by order(s) of magnitude down in  $x$ . Furthermore, fits without resummation,  
 1593 based only on NNLO DGLAP, were performed to the HERA data and the pseudodata. We see  
 1594 that in this case the extracted gluon and singlet quark densities differ significantly from the fits  
 1595 using the NNLO+NNLx. Already at  $x = 10^{-4}$  the central values of the gluon differ by 10% and  
 1596 at  $x = 10^{-5}$ , which is the LHeC regime, the central values for the gluon differ by 15%. This  
 1597 difference is much larger than the precision with which the gluon can be extracted from the DIS  
 1598 data, which is of the order of  $\sim 1\%$ .

1599 The presented analysis demonstrates that the fixed order prediction based on the DGLAP  
 1600 evolution would likely fail to describe accurately the structure function data in the new DIS  
 1601 machines and that in that regime new dynamics including resummation are mandatory for  
 1602 quantitative predictions. Therefore, the LHeC machine has an unprecedented potential to pin  
 1603 down the details of the QCD dynamics at low values of Bjorken  $x$ .

## 1604 Synergies with ultrahigh energy neutrino and astroparticle physics

1605 The small- $x$  region probed by the LHeC is also very important in the context of ultra-high energy  
 1606 neutrino physics and astroparticle physics. Highly energetic neutrinos provide a unique window  
 1607 into the Universe, due to their weak interaction with matter, for a review see for example [202].  
 1608 They can travel long distances from distant sources, undeflected by the magnetic fields inside  
 1609 and in between galaxies, and thus provide complementary information to cosmic rays, gamma  
 1610 rays and gravitational wave signals. The IceCube observatory on Antarctica [203] is sensitive  
 1611 to neutrinos with energies from 100 GeV up (above 10 GeV with the use of their Deep Core  
 1612 detector). Knowledge about low- $x$  physics becomes indispensable in two contexts: neutrino  
 1613 interactions and neutrino production. At energies beyond the TeV scale the dominant part of the  
 1614 cross section is due to the neutrino DIS CC and NC interaction with the hadronic targets [202].

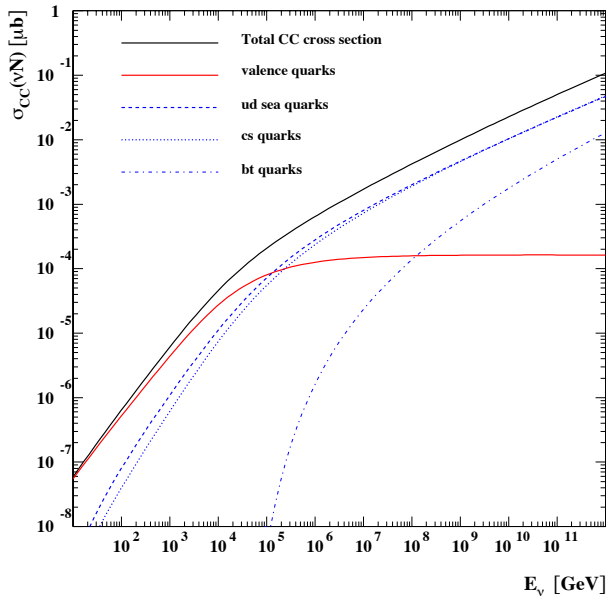


**Figure 3.26:** Charged current cross section for the neutrino - nucleon interaction on a isoscalar target as a function of neutrino energy. The total CC cross section is broken down into several contributions due to valence, up-down, strange-charm and bottom-top quarks. The calculation was based on Ref. [204].

1615 In Fig. 3.26 we show the charged current neutrino cross section as a function of the neutrino  
 1616 energy for an isoscalar target (in the laboratory frame where the target is at rest), using a  
 1617 calculation [204] based on the resummed model in [184]. We see that at energies below  $\sim 50$  TeV  
 1618 the cross section grows roughly linearly with energy, and in this region it is dominated by  
 1619 contributions from the large- $x$  valence region. Beyond that energy the neutrino cross section  
 1620 grows slower, roughly as a power  $\sim E_\nu^\lambda$  with  $\lambda \simeq 0.3$ . This high energy behaviour is totally  
 1621 controlled by the small- $x$  behaviour of the parton distributions. The dominance of the sea  
 1622 contributions to the cross section is clearly seen in Fig. 3.26. To illustrate more precisely the  
 1623 contributing values of  $x$  and  $Q^2$ , in Fig. 3.27 we show the differential cross section for the CC  
 1624 interaction  $xQ^2 d\sigma^{CC}/dx dQ^2$  for a neutrino energy  $E_\nu = 10^{11}$  GeV (in the frame where the  
 1625 hadronic target is at rest). We see a clear peak of the cross section at roughly a value of  
 1626  $Q^2 = M_W^2$  and an  $x$  value

$$x \simeq \frac{M_W^2}{2ME_\nu}, \quad (3.6)$$

1627 which in this case is about  $3 \times 10^{-8}$ . We note that IceCube extracted the DIS cross section from  
 1628 neutrino observations [205] in the region of neutrino energies 10 – 1000 TeV. The extraction  
 1629 is consistent, within the large error bands, with the predictions based on the QCD, like those  
 1630 illustrated in Fig. 3.26. It is important to note that the IceCube extraction is limited to these  
 1631 energies by the statistics due to the steeply falling flux of neutrinos at high energy. We thus  
 1632 see that the neutrino interaction cross section at high energies is sensitive to a region which is  
 1633 currently completely unconstrained by existing precision DIS data.

1634 Another instance where dynamics at low  $x$  are crucial for neutrino physics is in understand-  
 1635 ing the mechanisms of ultra-high energy neutrino production. The neutrinos are produced in  
 1636 interactions which involve hadrons, either in  $\gamma p$  or in  $pp$  interactions. They emerge as decay  
 1637 products of pions, kaons and charmed mesons, and possibly beauty mesons if the energy is high

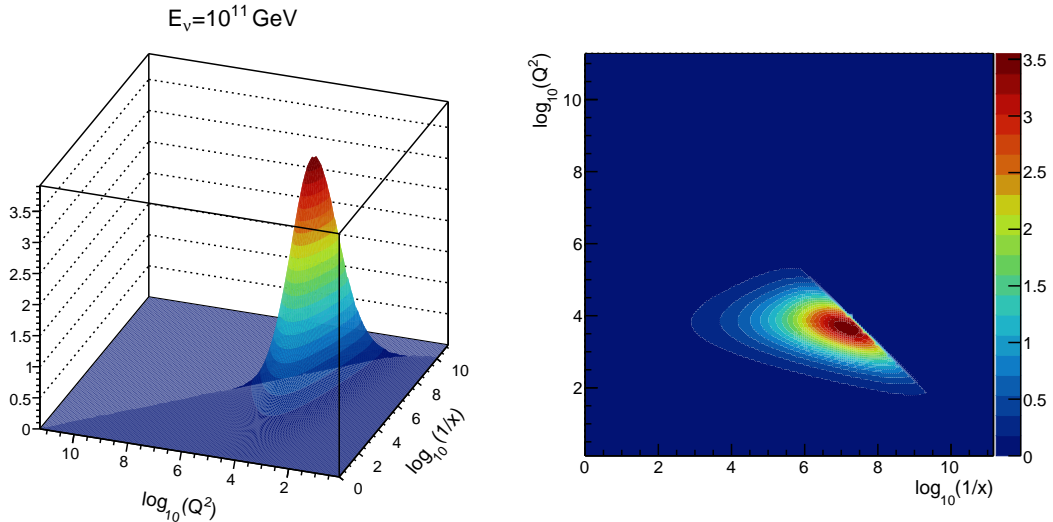


**Figure 3.27:** Differential charged current neutrino cross section  $10^5 \cdot xQ^2 d\sigma^{CC}/dx dQ^2$  [nb] as a function of  $Q^2$  and  $x$  for fixed neutrino energy  $E_\nu = 10^{11}$  GeV. Left: surface plot; right: contour plot.

1638 enough [206]. For example, in the atmosphere neutrinos are produced in the interactions of the  
 1639 highly energetic cosmic rays with nitrogen and oxygen nuclei. The lower energy part of the  
 1640 atmospheric neutrino spectrum, up to about 100 TeV or so, is dominated by the decay of pions  
 1641 and kaons. This is called the conventional atmospheric neutrino flux. Above that energy the  
 1642 neutrino flux is dominated by the decay of the shorter-lived charmed mesons. Thus, this part of  
 1643 the neutrino flux is called the prompt-neutrino flux. The reason why the prompt-neutrino flux  
 1644 dominates at high energies is precisely related to the life-time of the intermediate mesons (and  
 1645 also baryons like  $\Lambda_c$ ). The longer lived pions and kaons have a high probability of interacting  
 1646 before they decay, thus degrading their energy and leading to a steeply falling neutrino flux.  
 1647 The cross section for the production of charmed mesons is smaller than that for pions and kaons,  
 1648 but the charmed mesons  $D^\pm, D^0, D_s$  and baryon  $\Lambda_c$  live shorter than pions and kaons, and thus  
 1649 decay prior to any interaction. Thus, at energies about 100 TeV the prompt neutrino flux will  
 1650 dominate over the conventional atmospheric neutrino flux. Therefore, the knowledge of this part  
 1651 of the spectrum is essential as it provides a background for the sought-after astrophysical neu-  
 1652 trinos [207]. Charmed mesons in high energy hadron-hadron interactions are produced through  
 1653 gluon-gluon fusion into  $c\bar{c}$  pairs, where one gluon carries rather large  $x$  and the other one carries  
 1654 very small  $x$ . Since the scales are small, of the order of the charm masses, the values of the  
 1655 longitudinal momentum fractions involved are also very small and thus the knowledge of the  
 1656 parton distributions in this region is essential [208]. The predictions for the prompt neutrino  
 1657 flux become extremely sensitive to the behaviour of the gluon distribution at low  $x$  (and low  
 1658  $Q^2$ ), where novel QCD phenomena like resummation as well as gluon saturation are likely to  
 1659 occur [209].

1660 Finally, the low- $x$  dynamics will become even more important at the HL-LHC and FCC hadron  
 1661 colliders. With increasing centre-of-mass energy, hadron colliders will probe values of  $x$  pre-  
 1662 viously unconstrained by HERA data. It is evident that all the predictions in  $pp$  interactions  
 1663 at high energy will heavily rely on the PDF extrapolations to the small  $x$  region which carry  
 1664 large uncertainties. As discussed in detail in this Section, resummation will play an increasingly  
 1665 important role in the low  $x$  region of PDFs. A precision DIS machine is thus an indispensable  
 1666 tool for constraining the QCD dynamics at low  $x$  with great precision as well as for providing  
 1667 complementary information and independent measurements to hadronic colliders.

1668 **3.2.3 Low  $x$  and the Longitudinal Structure Function  $F_L$**

1669 **DIS Cross Section and the Challenge to Access  $F_L$**

1670 The inclusive, deep inelastic electron-proton scattering cross section at low  $Q^2 \ll M_Z^2$ ,

$$\frac{Q^4 x}{2\pi\alpha^2 Y_+} \cdot \frac{d^2\sigma}{dx dQ^2} = \sigma_r \simeq F_2(x, Q^2) - f(y) \cdot F_L(x, Q^2) = F_2 \cdot \left(1 - f(y) \frac{R}{1+R}\right) \quad (3.7)$$

1671 is defined by two proton structure functions,  $F_2$  and  $F_L$ , with  $y = Q^2/sx$ ,  $Y_+ = 1 + (1-y)^2$   
 1672 and  $f(y) = y^2/Y_+$ . The cross section may also be expressed [210] as a sum of two contributions,  
 1673  $\sigma_r \propto (\sigma_T + \epsilon\sigma_L)$ , referring to the transverse and longitudinal polarisation state of the exchanged  
 1674 boson, with  $\epsilon$  characterising the ratio of the longitudinal to the transverse polarisation. The  
 1675 ratio of the longitudinal to transverse cross sections is termed

$$R(x, Q^2) = \frac{\sigma_L}{\sigma_T} = \frac{F_L}{F_2 - F_L}, \quad (3.8)$$

1676 which is related to  $F_2$  and  $F_L$  as given above. Due to the positivity of the cross sections  $\sigma_{L,T}$   
 1677 one observes that  $F_L \leq F_2$ . The reduced cross section  $\sigma_r$ , Eq. (3.7), is therefore a direct measure  
 1678 of  $F_2$ , apart from a limited region of high  $y$  where a contribution of  $F_L$  may be sizeable. To  
 1679 leading order, for spin 1/2 particles, one expected  $R = 0$ . The initial measurements of  $R$  at  
 1680 SLAC [211, 212] showed that  $R$  was indeed small,  $R \simeq 0.18$ , which was taken as evidence for  
 1681 quarks to carry spin 1/2.

1682 The task to measure  $F_L$  thus requires to precisely measure the inclusive DIS cross section near  
 1683 to  $y = 1$  and to then disentangle the two structure functions by exploiting the  $f(y) = y^2/Y_+$   
 1684 variation which depends on  $x$ ,  $Q^2$  and  $s$ . By varying the centre-of-mass (cms) beam energy,  $s$ , one  
 1685 can disentangle  $F_2$  and  $F_L$  obtaining independent measurements at each common, fixed point of  
 1686  $x$ ,  $Q^2$ . This is particularly challenging not only because the  $F_L$  part is small, calling for utmost  
 1687 precision, but also because it requires to measure at high  $y$ . The inelasticity  $y = 1 - E'/E_e$ ,  
 1688 however, is large only for scattered electron energies  $E'_e$  much smaller than the electron beam  
 1689 energy  $E_e$ , for example  $E'_e = 2.7$  GeV for  $y = 0.9$  at HERA <sup>6</sup>. In the region where  $E'$  is a few GeV  
 1690 only, the electron identification becomes a major problem and the electromagnetic ( $\pi^0 \rightarrow \gamma\gamma$ )  
 1691 and hadronic backgrounds, mainly from unrecognised photoproduction, rise strongly.

1692 The history and achievements on  $F_L$ , the role of HERA and the prospects as sketched in the  
 1693 CDR of the LHeC, were summarised in detail in [213]. The measurement of  $F_L$  at HERA [214]  
 1694 was given very limited time and it collected about 5.9 and 12.2 pb<sup>-1</sup> of data at reduced beam  
 1695 energies which were analysed together with about 100 pb<sup>-1</sup> at nominal HERA energies. The  
 1696 result may well be illustrated with the data obtained on the ratio  $R(x, Q^2)$  shown in Fig. 3.28.  
 1697 To good approximation,  $R(x, Q^2)$  is a constant which was determined as  $R = 0.23 \pm 0.04$ ,  
 1698 in good agreement with the SLAC values of  $R \simeq 0.18$  despite the hugely extended kinematic  
 1699 range. The rather small variation of  $R$  towards small  $x$ , at fixed  $y = Q^2/sx$ , may appear to be  
 1700 astonishing as one observed  $F_2$  to strongly rise towards low  $x$ . A constant  $R$  of e.g. 0.25 means  
 1701 that  $F_2 = (1+R)F_L/R$  is five times larger than  $F_L$ , and that they rise together, as they have  
 1702 a common origin, the rise of the gluon density. This can be understood in approximations to  
 1703 the DGLAP expression of the  $Q^2$  derivative of  $F_2$  and the so-called Altarelli-Martinelli relation

---

<sup>6</sup>The nominal electron beam energy  $E_e$  at the LHeC is doubled as compared to HERA. Ideally one would like to vary the proton beam energy in an  $F_L$  measurement at the LHeC, which yet would affect the hadron collider operation. In the present study it was therefore considered to lower  $E_e$  which may be done independently of the HL-LHC.

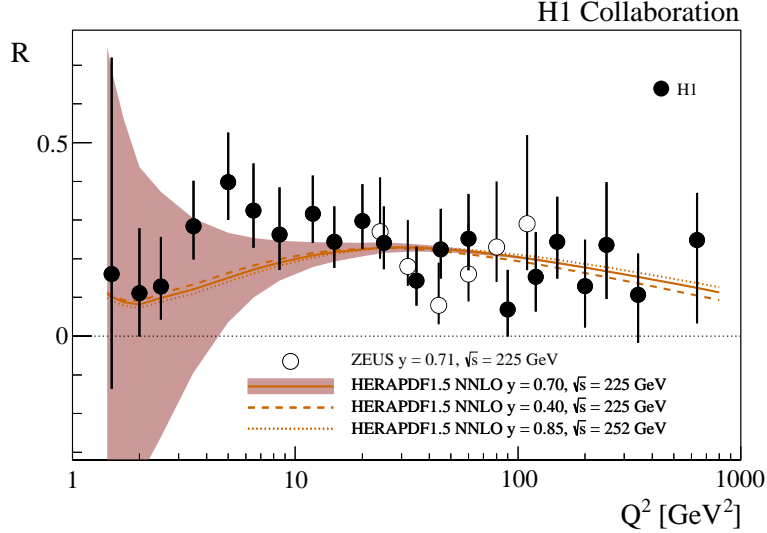


**Figure 3.28:** Measurement of the structure function ratio  $R = F_L/(F_2 - F_L)$  by H1 (solid points) and ZEUS (open circles), from a variation of proton beam energy in the final half year of HERA operation. The curve represents an NNLO QCD fit analysis of the other HERA data. This becomes uncertain for  $Q^2$  below  $10 \text{ GeV}^2$  where the  $Q^2$  dependence of  $F_2$  at HERA does not permit an accurate determination of the gluon density which dominates the prediction on  $F_L$ .

1704 of  $F_L$  to the parton densities [215,216], see the discussion in Ref. [213]. The resulting H1 value  
 1705 also obeyed the condition  $R \leq 0.37$ , which had been obtained in a rigorous attempt to derive  
 1706 the dipole model for inelastic DIS [217].

### 1707 Parton Evolution at Low $x$

1708 Parton distributions are to be extracted from experiment as their  $x$  dependence and flavour  
 1709 sharing are not predicted in QCD. They acquire a particular meaning through the theoretical  
 1710 prescription of their kinematic evolution. PDFs, as they are frequently used for LHC analyses,  
 1711 are predominantly defined through the now classic DGLAP formalism, in which the  $Q^2$  depen-  
 1712 dence of parton distributions is regulated by splitting functions while the DIS cross section,  
 1713 determined by the structure functions, is calculable by folding the PDFs with coefficient func-  
 1714 tions. Deep inelastic scattering is known to be the most suited process to extract PDFs from  
 1715 the experiment, for which the HERA collider has so far delivered the most useful data. Through  
 1716 factorisation theorems the PDFs are considered to be universal such that PDFs extracted in  $ep$   
 1717 DIS shall be suited to describe for example Drell-Yan scattering cross sections in  $pp$  at the LHC.  
 1718 This view has been formulated to third order pQCD already and been quite successful in the  
 1719 interpretation of LHC measurements, which by themselves also constrain PDFs in parton-parton  
 1720 scattering sub-processes.

1721 As commented in Sec. 3.2.2, the question has long been posed about the universal validity of  
 1722 the DGLAP formalism, especially for the region of small Bjorken  $x$  where logarithms  $\propto \ln(1/x)$   
 1723 become very sizeable. This feature of the perturbation expansion is expected to significantly  
 1724 modify the splitting functions. This in turn changes the theory underlying the physics of parton  
 1725 distributions, and predictions for the LHC and its successor will correspondingly have to be  
 1726 altered. This mechanism, for an equivalent  $Q^2$  of a few  $\text{GeV}^2$ , is illustrated in Fig. 3.29, taken  
 1727 from Ref. [218]. It shows the  $x$  dependence of the gluon-gluon and the quark-gluon splitting  
 1728 functions,  $P_{gg}$  and  $P_{qg}$ , calculated in DGLAP QCD. It is observed that at NNLO  $P_{gg}$  strongly

1729 decreases towards small  $x$ , becoming smaller than  $P_{gg}$  for  $x$  below  $10^{-4}$ . Resummation of  
 1730 the large  $\ln(1/x)$  terms, see Ref. [218], here performed to next-to-leading log  $x$ , restores the  
 1731 dominance of the  $gg$  splitting over the  $qg$  one. Consequently, the gluon distribution in the  
 resummed theory exceeds the one derived in pure DGLAP. While this observation has been

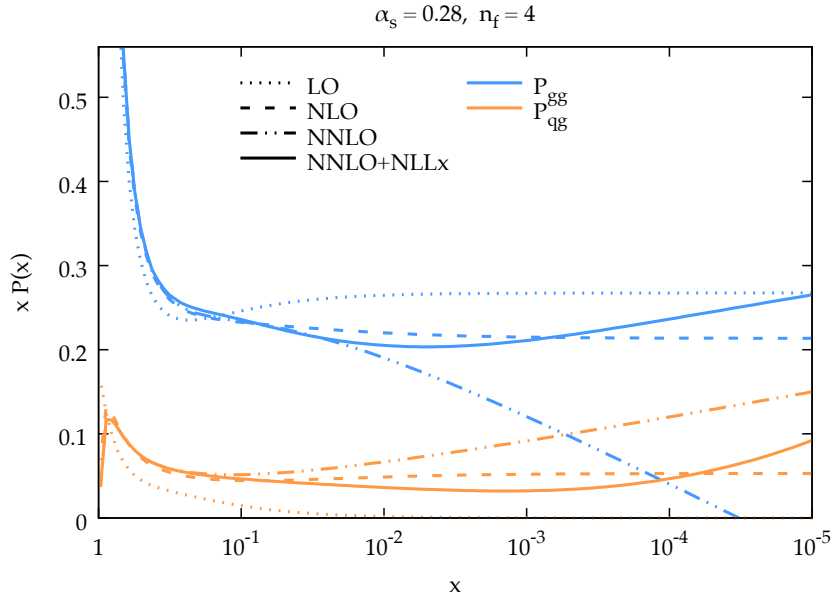


**Figure 3.29:** Calculation of splitting functions  $P_{gg}$  (top, blue) and  $P_{qg}$  (bottom, brown) in resummed NNLO (solid) as compared to non-resummed calculations at LO (dotted), NLO (dashed) and NNLO (dashed-dotted) as functions of  $x$  for  $n_f = 4$  at a large value of  $\alpha_s$  corresponding to a  $Q^2$  of a few  $\text{GeV}^2$ , from Ref. [218]. The resummed calculation is seen to restore the dominance of  $P_{gg}$  over  $P_{qg}$  as  $x$  becomes small (towards the right side), which is violated at NNLO.

1732 supported by the HERA data, it yet relies on limited kinematic coverage and precision. The  
 1733 LHeC will examine this in detail, at a hugely extended range and is thus expected to resolve the  
 1734 long known question about the validity of the BFKL evolution and the transition from DGLAP  
 1735 to BFKL as  $x$  decreases while  $Q^2$  remains large enough for pQCD to apply.  
 1736

### 1737 Kinematics of Higgs Production at the HL-LHC

1738 The clarification of the evolution and the accurate and complete determination of the parton  
 1739 distributions is of direct importance for the LHC. This can be illustrated with the kinematics of  
 1740 Higgs production at HL-LHC which is dominated by gluon-gluon fusion. With the luminosity  
 1741 upgrade, the detector acceptance is being extended into the forward region to pseudorapidity  
 1742 values of  $|\eta| = 4$ , where  $\eta = \ln \tan \theta/2$  is a very good approximation of the rapidity. In Drell-Yan  
 1743 scattering of two partons with Bjorken  $x$  values of  $x_{1,2}$  these are related to the rapidity via the  
 1744 relation  $x_{1,2} = \exp(\pm\eta) \cdot M/\sqrt{s}$  where  $\sqrt{s} = 2E_p$  is the cms energy and  $M$  the mass of the  
 1745 produced particle. It is interesting to see that  $\eta = \pm 4$  corresponds to  $x_1 = 0.5$  and  $x = 0.00016$   
 1746 for the SM Higgs boson of mass  $M = 125 \text{ GeV}$ . Consequently, Higgs physics at the HL-LHC  
 1747 will depend on understanding PDFs at high  $x$ , a challenge resolved by the LHeC too, and on  
 1748 clarifying the evolution at small  $x$ . At the FCC-hh, in its 100 TeV energy version, the small  $x$   
 1749 value for  $\eta = 4$  will be as low as  $2 \cdot 10^{-5}$ . Both the laws of QCD and the resulting phenomenology  
 1750 of particle production at the HL-LHC and its successor demand to clarify the evolution of the  
 1751 parton contents at small  $x$  as a function of the resolution scale  $Q^2$ . This concerns in particular

1752 the unambiguous, accurate determination of the gluon distribution, which dominates the small- $x$   
 1753 parton densities and as well the production of the Higgs boson in  $pp$  scattering.

### 1754 Indications for Resummation in H1 $F_L$ Data

1755 The simultaneous measurement of the two structure functions  $F_2$  and  $F_L$  is the cleanest way  
 1756 to establish new parton dynamics at low  $x$ . This holds because their independent constraints  
 1757 on the dominating gluon density at low  $x$  ought to lead to consistent results. In other words,  
 1758 one may constrain all partons with a complete PDF analysis of the inclusive cross section in  
 1759 the kinematic region where its  $F_L$  part is negligible and confront the  $F_L$  measurement with  
 1760 this result. A significant deviation from  $F_L$  data signals the necessity to introduce new, non-  
 1761 DGLAP physics in the theory of parton evolution, especially at small  $x$ . The salient value of the  
 1762  $F_L$  structure function results from its inclusive character enabling a clean theoretical treatment  
 1763 as has early on been recognised [215, 216]. This procedure has recently been illustrated [218]  
 using the H1 data on  $F_L$  [219] which are the only accurate data from HERA at smallest  $x$ . The

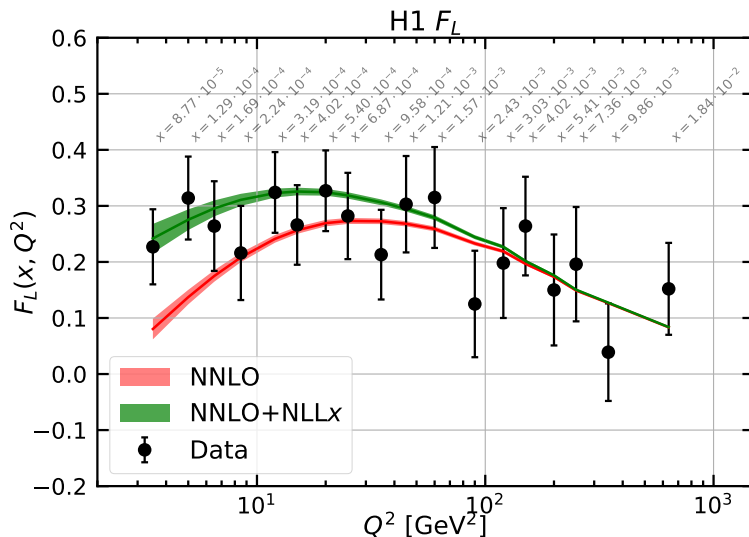


**Figure 3.30:** Measurement of the longitudinal structure function  $F_L$ , obtained as an average results over a number of  $x$  dependent points at fixed  $Q^2$ , plotted vs  $Q^2$  with the corresponding  $x$  values indicated in grey. Red curve: NNLO fit to the H1 cross section data; green curve: NNLO fit including NLLx resummation, from Ref. [218].

1764 result is shown in Fig. 3.30. One observes the trend described above: the resummed prediction  
 1765 is higher than the pure NNLO curve, and the description at smallest  $x$ , below  $5 \cdot 10^{-4}$ , appears  
 1766 to be improved. The difference between the two curves increases as  $x$  decreases. However, due  
 1767 to the peculiarity of the DIS kinematics, which relates  $x$  to  $Q^2/sy$ , one faces the difficulty of  
 1768  $Q^2$  decreasing with  $x$  at fixed  $s$  for large  $y \geq 0.6$ , which is the region of sensitivity to  $F_L$ . Thus  
 1769 one not only wishes to improve substantially the precision of the  $F_L$  data but also to increase  
 1770 substantially  $s$  in order to avoid the region of non-perturbative behaviour while testing theory  
 1771 at small  $x$ . This is the double and principal advantage which the LHeC offers - a much increased  
 1772 precision and more than a decade of extension of kinematic range.  
 1773

1775 Following the method described above, inclusive cross section data have been simulated for  
 1776  $E_p = 7$  TeV and three electron beam energies  $E_e$  of 60,  $\sim 30$  and 20 GeV. The assumed integrated  
 1777 luminosity values are 10,  $\sim 1$  and  $1 \text{ fb}^{-1}$ , respectively. These are about a factor of a hundred  
 1778 larger than the corresponding H1 luminosities. At large  $y$ , the kinematics is best reconstructed  
 1779 using the scattered electron energy,  $E'_e$ , and polar angle,  $\theta_e$ . The experimental methods to  
 1780 calibrate the angular and energy measurements are described in [214]. For the present study  
 1781 similar results are assumed: for  $E'_e$  a scale uncertainty of 0.5% at small  $y$  (compared to 0.2%  
 1782 with H1) rising linearly to 1.2%, in the range of  $y = 0.4$  to 0.9. For the polar angle, given  
 1783 the superior quality of the anticipated LHeC Silicon tracker as compared to the H1 tracker,  
 1784 it is assumed that  $\theta_e$  may be calibrated to 0.2 mrad, as compared to 0.5 mrad at H1. The  
 1785 residual photo-production background contamination is assumed to be 0.5% at largest  $y$ , twice  
 1786 better than with H1. There is further an assumption made on the radiative corrections which  
 1787 are assumed to be uncertain to 1% and treated as a correlated error. The main challenge is to  
 1788 reduce the uncorrelated uncertainty, which here was varied between 0.2 and 0.5%. This is about  
 1789 ten to three times more accurate than the H1 result which may be a reasonable assumption: the  
 1790 hundred fold increase in statistics sets a totally different scale to the treatment of uncorrelated  
 1791 uncertainties, as from imperfect simulations, trigger efficiency or Monte Carlo statistics. It  
 1792 is very difficult to transport previous results to the modern and future conditions. It could,  
 1793 however, be an important fix point if one knows that the most precise measurement of  $Z$  boson  
 1794 production by ATLAS at the LHC had a total systematic error of just 0.5% [220].

1795 The method here used is that of a simple straight-line fit of  $\sigma_r = F_2 - f(y)F_L$  (Eq. (3.7)), in  
 1796 which  $F_L$  is obtained as the slope of the  $f(y)$  dependence <sup>7</sup>. The predictions for  $F_2$  and  $F_L$  were  
 1797 obtained using LO formulae for the PDF set of MSTW 2008. In this method any common factor  
 1798 does not alter the absolute uncertainty of  $F_L$ . This also implies that the estimated absolute error  
 1799 on  $F_L$  is independent of whether  $F_L$  is larger or smaller than here assumed. For illustration,  
 1800  $F_L$  was scaled by a factor of two. Since  $f(y) \propto y^2$ , the accuracy is optimised with a non-linear  
 1801 choice of lowered beam energies. The fit takes into account cross section uncertainties and their  
 1802 correlations, calculated numerically following [47], by considering each source separately and  
 1803 adding the results of the various correlated sources to one correlated systematic error which is  
 1804 added quadratically to the statistical and uncorrelated uncertainties to obtain one total error.

1805 The result is illustrated in Fig. 3.31 presenting the  $x$ -dependent results, for some selected  $Q^2$   
 1806 values, of both H1, with their average over  $x$ , and the prospect LHeC results. It reflects the  
 1807 huge extension of kinematic range, towards low  $x$  and high  $Q^2$  by the LHeC as compared to  
 1808 HERA. It also illustrates the striking improvement in precision which the LHeC promises to  
 1809 provide. The  $F_L$  measurement will cover an  $x$  range from  $2 \cdot 10^{-6}$  to above  $x = 0.01$ . Surely,  
 1810 when comparing with Fig. 3.30, one can safely expect that any non-DGLAP parton evolution  
 1811 would be discovered with such data, in their combination with a very precise  $F_2$  measurement.

1812 A few comments are in order on the variation of the different error components with the kine-  
 1813 matics, essentially  $Q^2$  since the whole  $F_L$  sensitivity is restricted to high  $y$  which in turn for each  
 1814  $Q^2$  defines a not wide interval of  $x$  values covered. One observes in Fig. 3.31 that the precision  
 1815 is spoiled towards large  $x \propto 1/y$ , see e.g. the result for  $Q^2 = 8.5 \text{ GeV}^2$ . The assumptions on  
 1816 the integrated luminosity basically define a  $Q^2$  range for the measurement. For example, the  
 1817 statistical uncertainty for  $Q^2 = 4.5 \text{ GeV}^2$  and  $x = 10^{-5}$ , a medium  $x$  value at this  $Q^2$  interval,  
 1818 is only 0.6% (or 0.001 in absolute for  $F_L = 0.22$ ). At  $Q^2 = 2000 \text{ GeV}^2$  it rises to 21% (or 0.012

<sup>7</sup>Better results were achieved by H1 using a  $\chi^2$  minimisation technique, see Ref. [221], which for the rough estimate on the projected  $F_L$  uncertainty at the LHeC has not been considered.

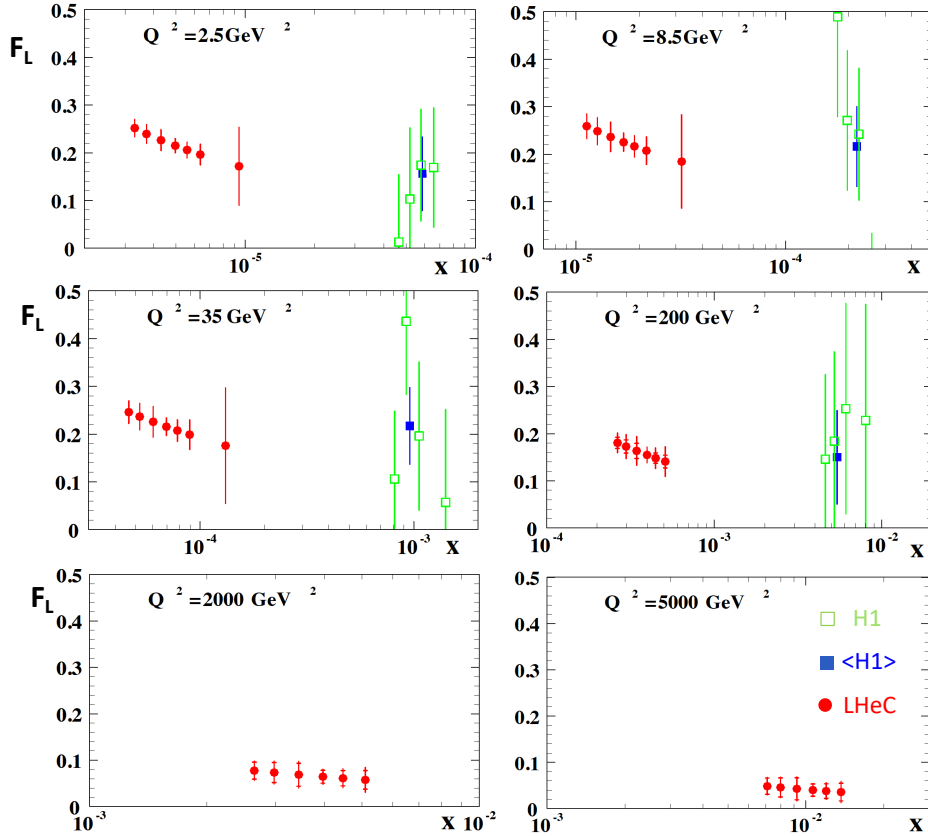


**Figure 3.31:** H1 measurement and LHeC simulation of data on the longitudinal structure function  $F_L(x, Q^2)$ . Green: Data by H1, for selected  $Q^2$  intervals from Ref. [219]; Blue: Weighted average of the (green) data points at fixed  $Q^2$ ; Red: Simulated data from an  $F_L$  measurement at the LHeC with varying beam energy, see text. The H1 error bars denote the total measurement uncertainty. The LHeC inner error bars represent the data statistics, visible only for  $Q^2 \geq 200 \text{ GeV}^2$ , while the outer error bars are the total uncertainty. Since the  $F_L$  measurement is sensitive only at high values of inelasticity,  $y = Q^2/sx$ , each  $Q^2$  value is sensitive only to a certain limited interval of  $x$  values which increase with  $Q^2$ . Thus each panel has a different  $x$  axis. The covered  $x$  range similarly varies with  $s$ , i.e. H1  $x$  values are roughly twenty times larger at a given  $Q^2$ . There are no H1 data for high  $Q^2$ , beyond  $1000 \text{ GeV}^2$ , see Ref. [219].

1819 for  $F_L = 0.064$ ). One thus can perform the  $F_L$  measurement at the LHeC, with a focus on only  
1820 small  $x$ , with much less luminosity than the  $1 \text{ fb}^{-1}$  here used. The relative size of the various  
1821 systematic error sources also varies considerably, which is due to the kinematic relations between  
1822 angles and energies and their dependence on  $x$  and  $Q^2$ . This is detailed in [47]. It implies, for ex-  
1823 ample, that the  $0.2 \text{ mrad}$  polar angle scale uncertainty becomes the dominant error at small  $Q^2$ ,  
1824 which is the backward region where the electron is scattered near the beam axis in the direction  
1825 of the electron beam. For large  $Q^2$ , however, the electron is more centrally scattered and the  
1826  $\theta_e$  calibration requirement may be more relaxed. The  $E'_e$  scale uncertainty has a twice smaller  
1827 effect than that due to the  $\theta_e$  calibration at lowest  $Q^2$  but becomes the dominant correlated  
1828 systematic error source at high  $Q^2$ . The here used overall assumptions on scale uncertainties  
1829 are therefore only rough first approximations and would be replaced by kinematics and detector  
1830 dependent requirements when this measurement may be pursued. These could also exploit the  
1831 cross calibration opportunities which result from the redundant determination of the inclusive  
1832 DIS scattering kinematics through both the electron and the hadronic final state. This had been  
1833 noted very early at HERA times, see Ref. [222–224] and was worked out in considerable detail

1834 by both H1 and ZEUS using independent and different methods. A feature used by H1 in their  
1835  $F_L$  measurement includes a number of decays such as  $\pi^0 \rightarrow \gamma\gamma$  and  $J/\psi \rightarrow e^+e^-$  for calibrating  
1836 the low energy measurement or  $K_s^0 \rightarrow \pi^+\pi^-$  and  $\Lambda \rightarrow p\pi$  for the determination of tracker scales,  
1837 see Ref. [214].

1838 It is obvious that the prospect to measure  $F_L$  as presented here is striking. For nearly a decade,  
1839 Guido Altarelli was a chief theory advisor to the development of the LHeC. In 2011, he publishes  
1840 an article [221], in honour of Mario Greco, about *The Early Days of QCD (as seen from Rome)*  
1841 in which he describes one of his main achievements [215], and persistent irritation, regarding  
1842 the longitudinal structure function,  $F_L$ , and its measurement: ... *The present data, recently*  
1843 *obtained by the H1 experiment at DESY, are in agreement with our [!this] LO QCD prediction*  
1844 *but the accuracy of the test is still far from being satisfactory for such a basic quantity.* The  
1845 LHeC developments had not been rapid enough to let Guido see results of much higher quality  
1846 on  $F_L$  with which the existence of departures from the DGLAP evolution, to high orders pQCD,  
1847 may be expected to most safely be discovered.

### 1848 3.2.4 Disentangling non-linear QCD dynamics at the LHeC

1849 The LHeC will extend the kinematic reach of HERA at small- $x$  by one order of magnitude in  
1850 the perturbative regime  $Q \gtrsim 1 \text{ GeV}$  [1]. This extension will allow unprecedented tests of the  
1851 strong interaction in this extreme region, where deviations from the linear DGLAP evolution are  
1852 expected to appear. In particular, it has been argued that the strong growth of the gluon PDF  
1853 at small- $x$  should eventually lead to gluon recombination [225] to avoid violating the unitary  
1854 bounds. The onset of such non-linear dynamics, also known as saturation, has been extensively  
1855 searched but so far there is no conclusive evidence of its presence, at least within the HERA  
1856 inclusive structure function measurements. In this context, the extended kinematic range of the  
1857 LHeC provides unique avenues to explore the possible onset of non-linear QCD dynamics at  
1858 small- $x$ . The discovery of saturation, a radically new regime of QCD, would then represent an  
1859 important milestone in our understanding of the strong interactions.

1860 The main challenge in disentangling saturation lies in the fact that non-linear corrections are  
1861 expected to be moderate even at the LHeC, since they are small (if present at all) in the region  
1862 covered by HERA. Therefore, great care needs to be employed in order to separate such effects  
1863 from those of standard DGLAP linear evolution. Indeed, it is well known that HERA data at  
1864 small- $x$  in the perturbative region can be equally well described, at least at the qualitative level,  
1865 both by PDF fits based on the DGLAP framework as well as by saturation-inspired models.  
1866 However, rapid progress both in theory calculations and methodological developments have  
1867 pushed QCD fits to a new level of sophistication, and recently it has been shown that subtle but  
1868 clear evidence of BFKL resummation at small- $x$  is present in HERA data, both for inclusive and  
1869 for heavy quark structure functions [218, 226]. Such studies highlight how it should be possible  
1870 to tell apart non-linear from linear dynamics using state-of-the-art fitting methods even if these  
1871 are moderate, provided that they are within the LHeC reach.

1872 Here we want to assess the sensitivity of the LHeC to detect the possible onset of non-linear  
1873 saturation dynamics. This study will be carried out by generalising a recent analysis [48] that  
1874 quantified the impact of LHeC inclusive and semi-inclusive measurements on the PDF4LHC15  
1875 PDFs [90, 227] by means of Hessian profiling [91]. There, the LHeC pseudodata was generated  
1876 assuming that linear DGLAP evolution was valid in the entire LHeC kinematic range using  
1877 the PDF4LHC15 set as input. To ascertain the possibility of pinning down saturation at the  
1878 LHeC, here we have revisited this study but now generating the LHeC pseudodata by means of

1879 a saturation-inspired calculation. By monitoring the statistical significance of the tension that  
 1880 will be introduced (by construction) between the saturation pseudodata and the DGLAP theory  
 1881 assumed in the PDF fit, we aim to determine the likelihood of disentangling non-linear from  
 1882 linear evolution effects at the LHeC. See also [228] for previous related studies along the same  
 1883 direction.

### 1884 Analysis settings

1885 In this study we adopt the settings of [48,89], to which we refer the interested reader for further  
 1886 details. In Ref. [48] the impact on the proton PDFs of inclusive and semi-inclusive neutral-  
 1887 current (NC) and charged current (CC) DIS structure functions from the LHeC was quantified.  
 1888 These results were then compared with the corresponding projections for the PDF sensitivity of  
 1889 the High-Luminosity upgrade of the LHC (HL-LHC). In the left panel of Fig. 3.32 we display  
 1890 the kinematic range in the  $(x, Q^2)$  plane of the LHeC pseudodata employed in that analysis,  
 1891 which illustrated how the LHeC can provide unique constraints on the behaviour of the quark  
 1892 and gluon PDFs in the very small- $x$  region.

1893 Since non-linear dynamics are known to become sizeable only at small- $x$ , for the present analysis  
 1894 it is sufficient to consider the NC  $e^-p$  inclusive scattering cross sections from proton beam en-  
 1895 ergies of  $E_p = 7$  TeV and  $E_p = 1$  TeV. In the right panel in Fig. 3.32 we show the bins in  $(x, Q^2)$   
 1896 for which LHeC pseudodata for inclusive structure functions has been generated according to  
 1897 a saturation-based calculation. Specifically, we have adopted here the DGLAP-improved satu-  
 1898 ration model of Ref. [229], in which the scattering matrix is modelled through eikonal iteration  
 1899 of two gluon exchanges. This model was further extended to include heavy flavour in [230].  
 1900 The specific parameters that we use were taken from Fit 2 in [231], where parameterisations  
 1901 are provided that can be used for  $x < 0.01$  and  $Q^2 < 700$  GeV<sup>2</sup>. These parameters were ex-  
 1902 tracted from a fit to the HERA legacy inclusive structure function measurements [37] restricted  
 1903 to  $x < 0.01$  and  $0.045 < Q^2 < 650$  GeV<sup>2</sup>. In contrast to other saturation models, the one we  
 1904 assume here [231] provides a reasonable description for large  $Q^2$  in the small  $x$  region, where it  
 1905 ensure a smooth transition to standard fixed-order perturbative results.

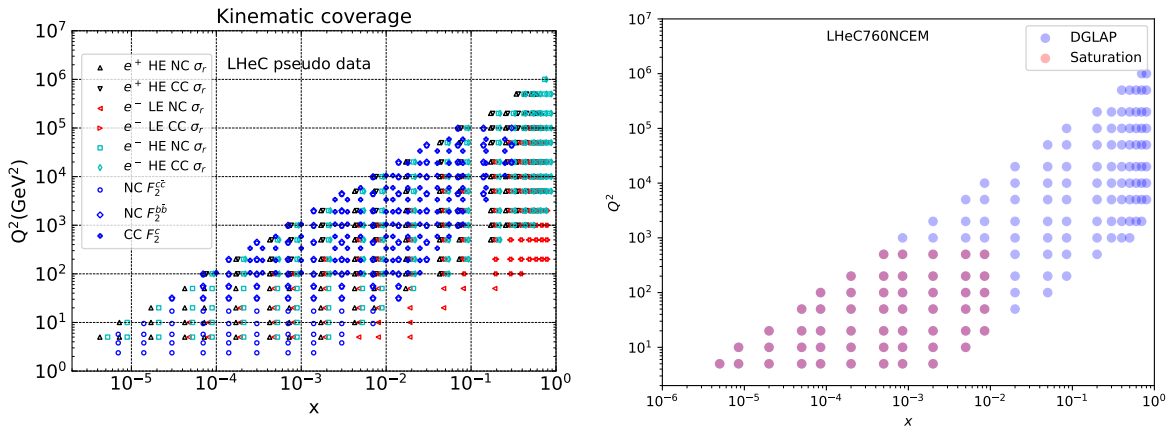


**Figure 3.32:** Left: the kinematic range in the  $(x, Q^2)$  plane of the LHeC pseudodata on inclusive and semi-inclusive DIS structure functions used in the PDF projections of [48]. Right: the kinematic coverage of the NC  $e^-p$  scattering pseudodata at the LHeC, where the blue (red) points indicate those bins for which DGLAP (saturation) predictions are available.

1906 Note that the above discussion refers only to the generated LHeC pseudodata: all other aspects of

1907 the QCD analysis of [48] are left unchanged. In particular, the PDF profiling will be carried out  
 1908 using theory calculations obtained by means of DGLAP evolution with the NNLO PDF4LHC15  
 1909 set (see also [232]), with heavy quark structure functions evaluated by means of the FONLL-  
 1910 B general-mass variable flavour number scheme [75]. In order to ensure consistency with the  
 1911 PDF4LHC15 prior, here we will replace the DGLAP pseudodata by the saturation calculation  
 1912 only in the kinematic region for  $x \lesssim 10^{-4}$ , rather than for all the bins indicated in red in  
 1913 Fig. 3.32. The reason for this choice is that PDF4LHC15 already includes HERA data down to  
 1914  $x \simeq 10^{-4}$  which is successfully described via the DGLAP framework, and therefore if we assume  
 1915 departures from DGLAP in the LHeC pseudodata this should only be done for smaller values  
 1916 of  $x$ .

## 1917 Results and discussion

1918 Using the analysis settings described above, we have carried out the profiling of PDF4LHC15  
 1919 with the LHeC inclusive structure function pseudodata, which for  $x \leq 10^{-4}$  ( $x > 10^{-4}$ ) has  
 1920 been generated using the GBW saturation (DGLAP) calculations, and compare them with the  
 1921 results of the profiling where the pseudodata follows the DGLAP prediction. We have generated  
 1922  $N_{\text{exp}} = 500$  independent sets LHeC pseudodata, each one characterised by different random  
 1923 fluctuations (determined by the experimental uncertainties) around the underlying central value.

1924 To begin with, it is instructive to compare the data versus theory agreement,  $\chi^2/n_{\text{dat}}$ , between  
 1925 the pre-fit and post-fit calculations, in order to assess the differences between the DGLAP and  
 1926 saturation cases. In the upper plots of Fig. 3.33 we show the distributions of pre-fit and post-fit  
 1927 values of  $\chi^2/n_{\text{dat}}$  for the  $N_{\text{exp}} = 500$  sets of generated LHeC pseudodata. We compare the results  
 1928 of the profiling of the LHeC pseudodata based on DGLAP calculations in the entire range of  
 1929  $x$  with those where the pseudodata is based on the saturation model in the region  $x < 10^{-4}$ .  
 1930 Then in the bottom plot we compare of the post-fit  $\chi^2$  distributions between the two scenarios.  
 1931 Note that in these three plots the ranges in the  $x$  axes are different.

1932 From this comparison we can observe that for the case where the pseudodata is generated using  
 1933 a consistent DGLAP framework (PDF4LHC15) as the one adopted for the theory calculations  
 1934 used in the fit, as expected the agreement is already good at the pre-fit level, and it is further  
 1935 improved at the post-fit level. However the situation is rather different in the case where a  
 1936 subset of the LHeC pseudodata is generated using a saturation model: at the pre-fit level the  
 1937 agreement between theory and pseudodata is poor, with  $\chi^2/n_{\text{dat}} \simeq 7$ . The situation markedly  
 1938 improves at the post-fit level, where now the  $\chi^2/n_{\text{dat}}$  distributions peaks around 1.3. This result  
 1939 implies that the DGLAP fit manages to absorb most of the differences in theory present in  
 1940 the saturation pseudodata. This said, the DGLAP fit cannot entirely *fit away* the non-linear  
 1941 corrections: as shown in the lower plot of Fig. 3.33, even at the post-fit level one can still tell  
 1942 apart the  $\chi^2/n_{\text{dat}}$  distributions between the two cases, with the DGLAP (saturation) pseudodata  
 1943 peaking at around 0.9 (1.3). This comparison highlights that it is not possible for the DGLAP  
 1944 fit to completely absorb the saturation effects into a PDF redefinition.

1945 In order to identify the origin of the worse agreement between theory predictions and LHeC  
 1946 pseudodata in the saturation case, it is illustrative to take a closer look at the pulls defined as

$$P(x, Q^2) = \frac{\mathcal{F}_{\text{fit}}(x, Q^2) - \mathcal{F}_{\text{dat}}(x, Q^2)}{\delta_{\text{exp}}\mathcal{F}(x, Q^2)}, \quad (3.9)$$

1947 where  $\mathcal{F}_{\text{fit}}$  is the central value of the profiled results for the observable  $\mathcal{F}$  (in this case the reduced  
 1948 neutral current DIS cross section),  $\mathcal{F}_{\text{dat}}$  is the corresponding central value of the pseudodata,

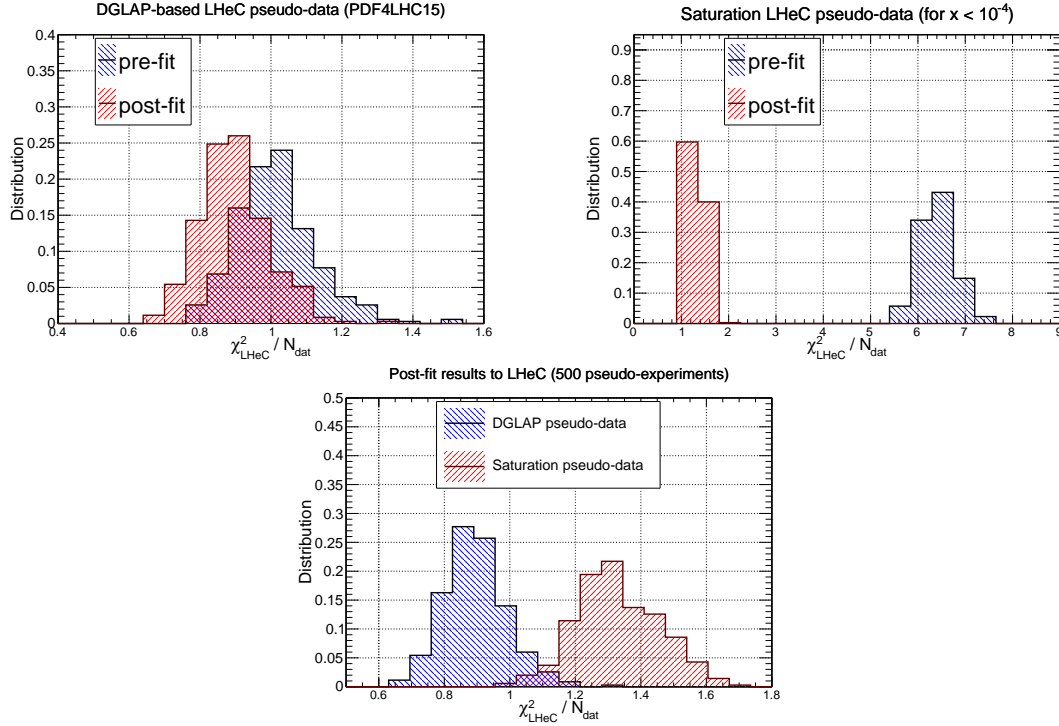


**Figure 3.33:** Upper plots: the distribution of pre-fit and post-fit values of  $\chi^2/n_{\text{dat}}$  for the  $N_{\text{exp}} = 500$  sets of generated LHeC pseudodata. We compare the results of the profiling of the LHeC pseudodata based on DGLAP calculations in the entire range of  $x$  (left) with those where the pseudodata is based on the saturation model in the region  $x < 10^{-4}$  (right plot). Bottom plot: comparison of the post-fit  $\chi^2/n_{\text{dat}}$  distributions between these two scenarios for the pseudodata generation.

1949 and  $\delta_{\text{exp}}\mathcal{F}$  represents the associated total experimental uncertainty. In Fig. 3.34 we display the  
 1950 pulls between the post-fit prediction and the central value of the LHeC pseudodata for different  
 1951 bins in  $Q^2$ . We compare the cases where the pseudodata has been generated using a consistent  
 1952 theory calculation (DGLAP) with that based on the GBW saturation model.

1953 The comparisons in Fig. 3.34 show first of all that in the DGLAP case the pulls are  $\mathcal{O}(1)$  in  
 1954 the entire kinematical range. This is of course expected, given that the LHeC pseudodata is  
 1955 generated using the same theory as the one subsequently used for the fit. In the case where  
 1956 the pseudodata has been partially generated with the saturation calculation, on the other hand,  
 1957 one finds a systematic tension between the theory used for the fit (DGLAP) and the one used  
 1958 to generate the pseudodata (saturation). Indeed, we find that at the smallest values of  $x$  the  
 1959 theory prediction undershoots the data by a significant amount, while at higher  $x$  the opposite  
 1960 behaviour takes place. One can also see that in the region  $10^{-4} \lesssim x \lesssim 10^{-3}$  the fit overshoots  
 1961 the pseudodata by a large amount.

1962 These comparisons highlight how a QCD fit to the saturation pseudodata is obtained as a  
 1963 compromise between opposite trends: the theory wants to overshoot the data at very small  $x$   
 1964 and overshoot it at larger values of  $x$ . These tensions result in a distorted fit, explaining the  
 1965 larger  $\chi^2/n_{\text{dat}}$  values as compared to the DGLAP case. Such a behaviour can be partially traced  
 1966 back by the different scaling in  $Q^2$  between DGLAP and GBW: while a different  $x$  dependence  
 1967 could eventually be absorbed into a change of the PDFs at the parameterisation scale  $Q_0$ , this  
 1968 is not possible with a  $Q^2$  dependence.

1969 The pull analysis of Fig. 3.34 highlights how in order to tell apart linear from non-linear QCD

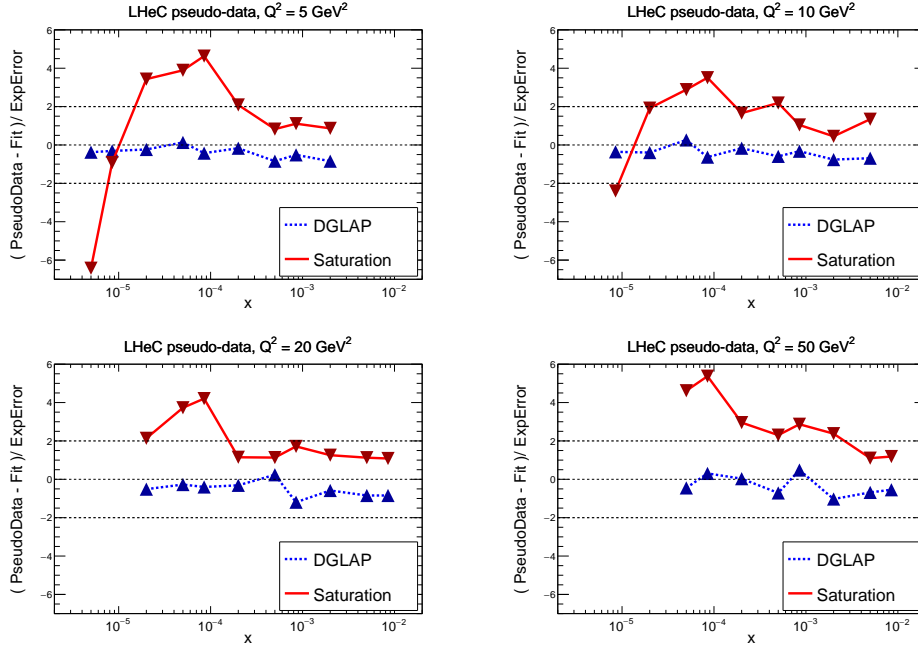


**Figure 3.34:** The pulls between the post-fit prediction and the central value of the LHeC pseudodata, Eq. (3.9), for four different bins in  $Q^2$ . We compare the results of the profiling where the LHeC pseudodata has been generated using a consistent DGLAP theory with that partially based on the saturation calculations.

1970 evolution effects at small- $x$  it would be crucial to ensure a lever arm in  $Q^2$  as large as possible  
 1971 in the perturbative region. This way it becomes possible to disentangle the different scaling  
 1972 in  $Q^2$  for the two cases. The lack of a sufficiently large lever arm in  $Q^2$  at HERA at small  $x$   
 1973 could explain in part why both frameworks are able to describe the same structure function  
 1974 measurements at the qualitative level. Furthermore, we find that amplifying the significance  
 1975 of these subtle effects can be achieved by monitoring the  $\chi^2$  behaviour in the  $Q^2$  bins more  
 1976 affected by the saturation corrections. The reason is that the total  $\chi^2$ , such as that reported  
 1977 in Fig. 3.33, is somewhat less informative since the deviations at small- $Q$  are washed out by  
 1978 the good agreement between theory and pseudodata in the rest of the kinematical range of the  
 1979 LHeC summarised in Fig. 3.32.

1980 To conclude this analysis, in Fig. 3.35 we display the comparison between the PDF4LHC15  
 1981 baseline with the results of the PDF profiling of the LHeC pseudodata for the gluon (left) and  
 1982 quark singlet (right) for  $Q = 10 \text{ GeV}$ . We show the cases where the pseudodata is generated  
 1983 using DGLAP calculations and where it is partially based on the GBW saturation model (for  
 1984  $x \lesssim 10^{-4}$ ). We find that the distortion induced by the mismatch between theory and pseudodata  
 1985 in the saturation case is typically larger than the PDF uncertainties expected once the LHeC  
 1986 constraints are taken into account. While of course in a realistic situation such a comparison  
 1987 would not be possible, the results of Fig. 3.35 show that saturation-induced effects are expected  
 1988 to be larger than the typical PDF errors in the LHeC era, and thus that it should be possible to  
 1989 tell them apart using for example tools such as the pull analysis of Fig. 3.34 or other statistical  
 1990 methods.

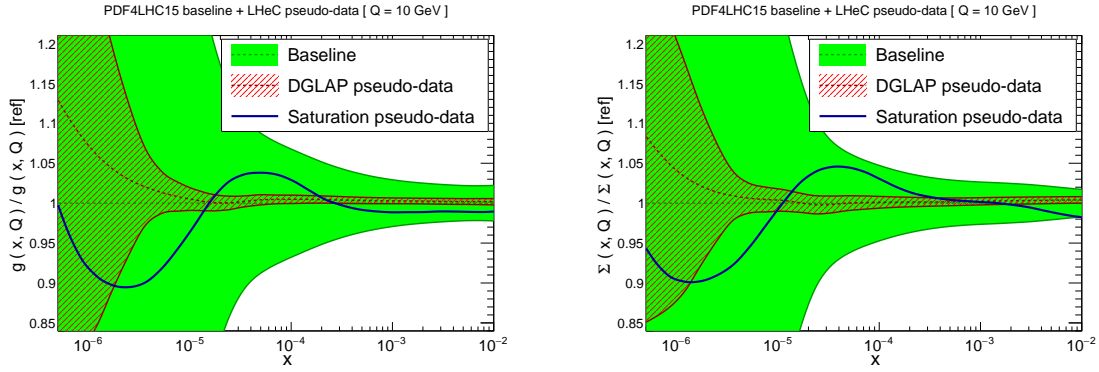


**Figure 3.35:** Comparison between the PDF4LHC15 baseline (green band) with the results of the profiling of the LHeC pseudodata for the gluon (left) and quark singlet (right) for  $Q = 10$  GeV. We show the cases where the pseudodata is generated using DGLAP calculations (red hatched band) and where it is partially based on the GBW saturation model (blue curve).

## 1991 Summary

1992 Here we have assessed the feasibility of disentangling DGLAP evolution from non-linear effects at  
 1993 the LHeC. By means of a QCD analysis where LHeC pseudodata is generated using a saturation  
 1994 model, we have demonstrated that the LHeC should be possible to identify non-linear effects  
 1995 with large statistical significance, provided their size is the one predicted by current calculations  
 1996 such as the that of [231] that have been tuned to HERA data. A more refined analysis would  
 1997 require to study whether or not small- $x$  BFKL resummation effects can partially mask the  
 1998 impact of non-linear dynamics, though this is unlikely since the main difference arises in their  
 1999  $Q^2$  scaling. The discovery of non-linear dynamics would represent an important milestone for  
 2000 the physics program of the LHeC, demonstrating the onset of a new gluon-dominated regime of  
 2001 the strong interactions and paving the way for detailed studies of the properties of this new state  
 2002 of matter. Such discovery would have also implications outside nuclear and particle physics, for  
 2003 instance it would affect the theory predictions for the scattering of ultra-high energy neutrinos  
 2004 with matter [233].

## 2005 3.2.5 The 3D Structure of the Proton

2006 As is evident from the discussion in the previous Sections, the LHeC machine will be able to  
 2007 measure the collinear parton distribution functions with unprecedented accuracy in its extended  
 2008 range of  $x$  and  $Q^2$ . Thus, it will provide a new insight into the details of the one-dimensional  
 2009 structure of the proton and nuclei, including novel phenomena at low  $x$ . In addition to collinear  
 2010 dynamics, the LHeC opens a new window into proton and nuclear structure by allowing a precise  
 2011 investigation of the partonic structure in more than just the one dimension of the longitudinal  
 2012 momentum. Precision DIS thus gives access to multidimensional aspects of hadron structure.  
 2013 This can be achieved by accurately measuring processes with more exclusive final states like pro-  
 2014 duction of jets, semi-inclusive production of hadrons and exclusive processes, in particular the  
 2015 elastic diffractive production of vector mesons and deeply virtual Compton (DVCS) scattering.  
 2016 These processes have the potential to provide information not only on the longitudinal distribu-  
 2017 tion of partons in the proton or nucleus, but also on the dependence of the parton distribution  
 2018 on transverse momenta and momentum transfer. Therefore, future, high precision DIS machines  
 2019 like the LHeC or the Electron Ion Collider (EIC) in the US [234], open a unique window into  
 2020 the details of the 3D structure of hadrons.

2021 The most general quantity that can be defined in QCD that would contain very detailed infor-  
 2022 mation about the partonic content of the hadron, is the Wigner distribution [235]. This function  
 2023  $W(x, \mathbf{k}, \mathbf{b})$  is a 1+4 dimensional function. One can think of it as the mother or master parton  
 2024 distribution, from which lower-dimensional distributions can be obtained. In the definition of  
 2025 the Wigner function,  $\mathbf{k}$  is the transverse momentum of the parton and  $\mathbf{b}$  is the 2-dimensional  
 2026 impact parameter, which can be defined as a Fourier conjugate to the momentum transfer of  
 2027 the process. The other, lower dimensional parton distributions can be obtained by integrating  
 2028 out different variables. Thus, transverse momentum dependent (TMD) parton distributions  
 2029 (or unintegrated parton distribution functions)  $f_{\text{TMD}}(x, \mathbf{k})$  can be obtained by integrating out  
 2030 the impact parameter  $\mathbf{b}$  in the Wigner function, while the generalised parton densities (GPD),  
 2031  $f_{\text{GPD}}(x, \mathbf{b})$ , can be obtained from the Wigner function through the integration over the trans-  
 2032 verse momentum  $\mathbf{k}$ . In the regime of small  $x$ , or high energy, a suitable formalism is that of  
 2033 the dipole picture [236–241], where the fundamental quantity which contains the details of the  
 2034 partonic distribution is the dipole amplitude  $N(x, \mathbf{r}, \mathbf{b})$ . This object contains the dependence  
 2035 on the impact parameter  $\mathbf{b}$  as well as another transverse size  $\mathbf{r}$ , the dipole size, which can be  
 2036 related to the transverse momentum of the parton  $\mathbf{k}$  through a Fourier transform. The impor-  
 2037 tant feature of the dipole amplitude is that it should obey the unitarity limit  $N \leq 1$ . The dipole  
 2038 amplitude  $N$  within this formalism can be roughly interpreted as a Wigner function in the high  
 2039 energy limit, as it contains information about the spatial distribution of the partons in addition  
 2040 to the dependence on the longitudinal momentum fraction  $x$ .

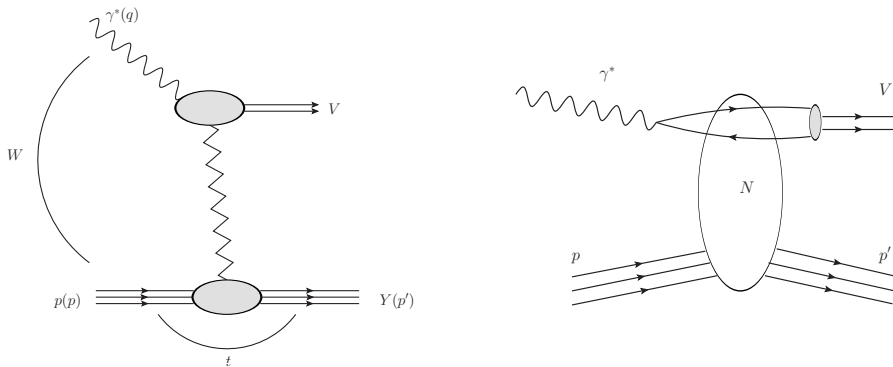


**Figure 3.36:** Left: diagram for the quasi-elastic production of the vector meson. Right: schematic illustration of the same process, quasi-elastic vector meson production, within the framework of the dipole picture. The initial virtual photon, fluctuates into a quark-antiquark pair which then scatters off the hadronic target and forms the vector meson. The details of the hadronic interaction of the dipole with the target are encoded in the dipole amplitude  $N$ .

2041 Detailed simulations of elastic  $J/\psi$  vector meson production were performed for the LHeC  
 2042 kinematic region and beyond [1], using the formalism of the dipole picture. This particular  
 2043 process is shown in Fig. 3.36, left plot. The proton is scattered elastically with momentum  
 2044 transfer  $t$ , and the vector meson is produced, which is separated from the final state proton  
 2045 by a rapidity gap. Of particular importance is the measurement of the  $t$  slope of this process,  
 2046 since it can be related directly to the impact parameter distribution and is thus sensitive to the  
 2047 transverse variation of the partonic density in the target. The first type of analysis like this,  
 2048 in the context of elastic scattering, was performed by Amaldi and Schubert [242], where it was  
 2049 demonstrated that the Fourier transform of the elastic cross section yields access to the impact  
 2050 parameter profile of the scattering amplitude. This method can be used in the context of vector  
 2051 meson scattering in DIS, where the transverse distribution of partons, in the perturbative regime,  
 2052 can be extracted through the appropriate Fourier transform [243]. The additional advantage of

2053 studying diffractive vector meson production is the fact that the partonic distributions can be  
 2054 studied as a function of the hard scale in this process given by the mass of the vector meson  $M_V^2$   
 2055 in the photoproduction case or  $Q^2$  (or more precisely a combination of  $Q^2$  and  $M_V^2$ ) in the case  
 2056 of the diffractive DIS production of vector mesons, as well as the energy  $W$  of the photon-proton  
 2057 system available in the process which is closely related to  $x$ .

2058 The differential cross section for elastic vector meson production can be expressed in the following  
 2059 form:

$$\frac{d\sigma^{\gamma^* p \rightarrow J/\psi p}}{dt} = \frac{1}{16\pi} |\mathcal{A}(x, Q, \Delta)|^2, \quad (3.10)$$

2060 where the amplitude for the process of elastic diffractive vector meson production in the high  
 2061 energy limit, in the dipole picture, is given by

$$\mathcal{A}(x, Q, \Delta) = \sum_{h\bar{h}} \int d^2\mathbf{r} \int dz \Psi_{h\bar{h}}^*(z, \mathbf{r}, Q) \mathcal{N}(x, \mathbf{r}, \Delta) \Psi_{h\bar{h}}^V(z, \mathbf{r}). \quad (3.11)$$

2062 In the above formula,  $\Psi_{h\bar{h}}^*(z, \mathbf{r}, Q)$  is the photon wave function which describes the splitting  
 2063 of the virtual photon  $\gamma^*$  into a  $q\bar{q}$  pair. This wave function can be calculated in perturbative  
 2064 QCD. The function  $\Psi_{h\bar{h}}^V(z, \mathbf{r})$  is the wave function of the vector meson. Finally,  $\mathcal{N}(x, \mathbf{r}, \Delta)$  is the  
 2065 dipole amplitude which contains all the information about the interaction of the quark-antiquark  
 2066 dipole with the target. The formula (3.11) can be interpreted as the process of fluctuation of the  
 2067 virtual photon into a  $q\bar{q}$  pair, which subsequently interacts with the target through the dipole  
 2068 amplitude  $\mathcal{N}$  and then forms the vector meson, given by the amplitude  $\Psi^V$ , see Fig. 3.36, right  
 2069 plot. The two integrals in the definition Eq. (3.11) are performed over the dipole size which is  
 2070 denoted by  $\mathbf{r}$ , and  $z$  which is the longitudinal momentum fraction of the photon carried by the  
 2071 quark. The scattering amplitude depends on the value of the momentum transfer  $\Delta$ , which is  
 2072 related to the Mandelstam variable  $t = -\Delta^2$ . The sum is performed over the helicity states of  
 2073 the quark and antiquark.

2074 The dipole amplitude  $\mathcal{N}(x, \mathbf{r}, \Delta)$  can be related to the dipole amplitude in coordinate space  
 2075 through the appropriate Fourier transform

$$N(x, \mathbf{r}, \mathbf{b}) = \int d^2\Delta e^{i\Delta \cdot \mathbf{b}} \mathcal{N}(x, \mathbf{r}, \Delta). \quad (3.12)$$

2076 We stress that  $\mathbf{r}$  and  $\mathbf{b}$  are two different transverse sizes here. The dipole size  $\mathbf{r}$  is conjugate  
 2077 to the transverse momentum of the partons  $\mathbf{k}$ , whereas the impact parameter is roughly the  
 2078 distance between the centre of the scattering target to the centre-of-mass of the quark-antiquark  
 2079 dipole and is related to the Fourier conjugate variable, the momentum transfer  $\Delta$ .

2080 The dipole amplitude  $N(x, \mathbf{r}, \mathbf{b})$  contains rich information about the dynamics of the hadronic  
 2081 interaction. It is a 5-dimensional function and it depends on the longitudinal momentum frac-  
 2082 tion, and two two-dimensional coordinates. The dependence on the longitudinal momentum  
 2083 fraction is obviously related to the evolution with the centre-of-mass energy of the process,  
 2084 while the dependence on  $\mathbf{b}$  provides information about the spatial distribution of the partons in  
 2085 the target. The dipole amplitude is related to the distribution of gluons in impact parameter  
 2086 space. The dipole amplitude has a nice property that its value should be bounded from above  
 2087 by the unitarity requirement  $N \leq 1$ . The complicated dependence on energy, dipole size and  
 2088 impact parameter of this amplitude can provide a unique insight into the dynamics of QCD,  
 2089 and on the approach to the dense partonic regime. Besides, from Eqs. (3.10), (3.11) and (3.12) it  
 2090 is evident that the information about the spatial distribution in impact parameter  $\mathbf{b}$  is related  
 2091 through the Fourier transform to the dependence of the cross section on the momentum transfer  
 2092  $t = -\Delta^2$ .

2093 To see how the details of the distribution, and in particular the approach to unitarity, can  
 2094 be studied through the VM elastic production, calculations based on the dipole model were  
 2095 performed [244], and extended to energies which can be reached at the LHeC as well as the  
 2096 FCC-eh. The parameterisations used in the calculation were the so-called IP-Sat [245, 246]  
 2097 and b-CGC [247] models. In both cases the impact parameter dependence has to be modelled  
 2098 phenomenologically. In the IP-Sat model the dipole amplitude has the following form

$$N(x, \mathbf{r}, \mathbf{b}) = 1 - \exp \left[ -\frac{\pi^2 r^2}{2N_c} \alpha_s(\mu^2) x g(x, \mu^2) T_G(b) \right], \quad (3.13)$$

2099 where  $xg(x, \mu^2)$  is the collinear gluon density, evolved using LO DGLAP (without quarks), from  
 2100 an initial scale  $\mu_0^2$  up to the scale  $\mu^2$  set by the dipole size  $\mu^2 = \frac{4}{r^2} + \mu_0^2$ .  $\alpha_s(\mu^2)$  is the strong  
 2101 coupling. The parameterisation of the gluon density at the initial scale  $\mu_0^2$  is given by

$$xg(x, \mu_0^2) = A_g x^{-\lambda_g} (1-x)^{5.6}, \quad (3.14)$$

2102 and the impact parameter profile for the gluon by

$$T_G(b) = \frac{1}{2\pi B_G} \exp(-b^2/2B_G). \quad (3.15)$$

An alternative parameterisation is given by the b-CGC model [247] which has the form

$$N(x, \mathbf{r}, \mathbf{b}) = \begin{cases} N_0 \left( \frac{rQ_s}{2} \right)^{2\gamma_{\text{eff}}} & \text{for } rQ_s \leq 2, \\ 1 - \exp(-\mathcal{A} \ln^2(\mathcal{B}rQ_s)) & \text{for } rQ_s > 2. \end{cases} \quad (3.16)$$

2103 Here the effective anomalous dimension  $\gamma_{\text{eff}}$  and the saturation scale  $Q_s$  of the proton explicitly  
 2104 depend on the impact parameter and are defined as

$$\begin{aligned} \gamma_{\text{eff}} &= \gamma_s + \frac{1}{\kappa \lambda \ln 1/x} \ln \left( \frac{2}{rQ_s} \right), \\ Q_s(x, b) &= \left( \frac{x_0}{x} \right)^{\lambda/2} \exp \left[ -\frac{b^2}{4\gamma_s B_{\text{CGC}}} \right] \text{ GeV}, \end{aligned} \quad (3.17)$$

2105 where  $\kappa = \chi''(\gamma_s)/\chi'(\gamma_s)$ , with  $\chi(\gamma)$  being the leading-logarithmic BFKL kernel eigenvalue  
 2106 function [173]. The parameters  $\mathcal{A}$  and  $\mathcal{B}$  in Eq.(3.16) are determined uniquely from the matching  
 2107 of the dipole amplitude and its logarithmic derivatives at the limiting value of  $rQ_s = 2$ . The  
 2108 b-CGC model is constructed by smoothly interpolating between two analytically known limiting  
 2109 cases [247], namely the solution of the BFKL equation in the vicinity of the saturation line for  
 2110 small dipole sizes  $r < 2/Q_s$ , and the solution of the BK equation deep inside the saturation  
 2111 region for large dipole sizes  $r > 2/Q_s$ .

2112 The parameters  $\mu_0, A_g, \lambda_g$  of the IP-Sat model and  $N_0, \gamma_s, x_0 \lambda$  of the b-CGC model were fitted  
 2113 to obtain the best description of the inclusive data for the structure function  $F_2$  at HERA. The  
 2114 slope parameters  $B_g$  and  $B_{\text{CGC}}$ , which control the  $b$ -dependence in both models, were fitted to  
 2115 obtain the best description of elastic diffractive  $J/\psi$  production, in particular its  $t$ -dependence,  
 2116 at small values of  $t$ .

2117 In Figs. 3.37 and 3.38 we show the simulated differential cross section  $d\sigma/dt$  as a function of  $|t|$   
 2118 and study its variation with energy and virtuality, and its model dependence. First, in Fig. 3.37  
 2119 we show the differential cross section as a function of  $t$  for fixed energy  $W = 1$  TeV, in the case of  
 2120 the photoproduction of  $J/\psi$  (left plot) and for the case of DIS with  $Q^2 = 10$  GeV<sup>2</sup> (right plot).

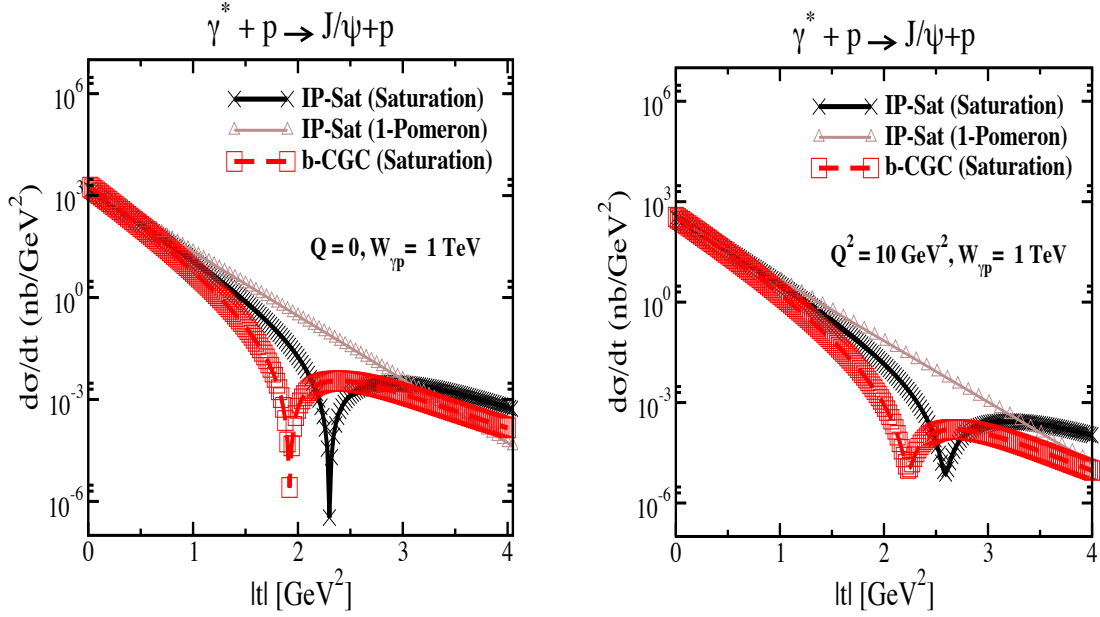


**Figure 3.37:** Differential cross section for the elastic  $J/\psi$  production as a function of  $|t|$  within the IP-Sat (saturation), b-CGC and 1-Pomeron models at a fixed  $W_{\gamma p} = 1$  TeV, which corresponds to the LHeC kinematics, and for two different values of photon virtuality  $Q = 0$  and  $Q^2 = 10$  GeV $^2$ . The thickness of points includes the uncertainties associated with the freedom to choose different values for the charm quark mass within the range  $m_c = 1.2 - 1.4$  GeV.

2121 The energy  $W$  corresponds to the LHeC kinematics. There are three different calculations in  
2122 each plot, using the IP-sat model, the b-CGC model and the 1-Pomeron approximation. The  
2123 last one is obtained by keeping just the first non-trivial term in the expansion of the eikonalised  
2124 formula of the IP-Sat amplitude (3.13). First, let us observe that all three models coincide  
2125 for very low values of  $t$ , where the dependence on  $t$  is exponential. This is because for low  
2126  $|t|$ , relatively large values of impact parameter are probed in Eq. (3.11) where the amplitude  
2127 is small, and therefore the tail in impact parameter is Gaussian in all three cases. Since the  
2128 Fourier transform of the Gaussian in  $b$  is an exponential in  $t$ , the result at low  $t$  follows. On  
2129 the other hand, the three scenarios differ significantly for large values of  $|t|$ . In the case of the  
2130 1-Pomeron approximation the dependence is still exponential, without any dips, which is easily  
2131 understood since the impact parameter profile is perfectly Gaussian in this case. For the two  
2132 other scenarios, dips in  $d\sigma/dt$  as a function in  $t$  emerge. They signal the departure from the  
2133 Gaussian profile in  $b$  for small values of  $b$  where the system is dense. A similar pattern can be  
2134 observed when performing the Fourier transform of the Wood-Saxon distribution, which is the  
2135 typical distribution used for the description of the matter density in nuclei. When  $Q^2$  is increased  
2136 the pattern of dips also changes. This is illustrated in Fig. 3.37. It is seen that the dips move to  
2137 higher values of  $|t|$  for DIS than for photoproduction. This can be understood from the dipole  
2138 formula Eq. (3.11) which contains the integral over the dipole size. Larger values of  $Q^2$  select  
2139 smaller values of dipole size  $r$ , where the amplitude is smaller and thus in the dilute regime,  
2140 where the profile in  $b$  is again Gaussian. On the other hand, small scales select large dipole sizes  
2141 for which the dipole amplitude is larger and thus the saturation effects more prominent, leading  
2142 to the distortion of the impact parameter profile and therefore to the emergence of dips in the  
2143 differential cross section  $d\sigma/dt$  when studied as a function of  $t$ .

2144 In the next Fig. 3.38 we show the same calculation but for higher energy  $W = 2.5$  TeV, which  
2145 could be explored in the FCC-eh. In this case we see that the dips move to lower values of

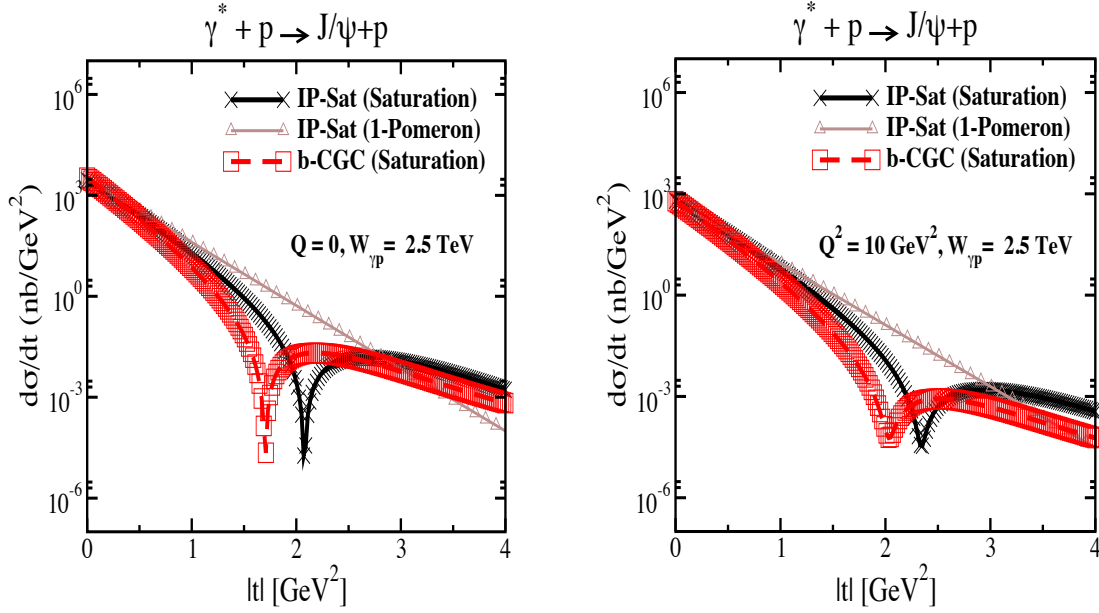


**Figure 3.38:** Differential cross section for elastic  $J/\psi$  production as a function of  $|t|$  within the IP-Sat (saturation), b-CGC and 1-Pomeron models at a fixed  $W_{\gamma p} = 2.5$  TeV, which corresponds to the region that can be explored by FCC-eh, and for two different values of photon virtuality  $Q = 0$  (left plot) and  $Q^2 = 10$  GeV $^2$  (right plot). The thickness of points includes the uncertainties associated with the freedom to choose different values for the charm quark mass within the range  $m_c = 1.2 - 1.4$  GeV .

2146  $|t|$ . This can be easily understood, as with increasing energy the dipole scattering amplitude  
 2147 increases, and thus the dilute-dense boundary shifts to larger values of  $b$ , meaning that the  
 2148 deviation from the exponential fall off occurs for smaller values of  $|t|$ . Similar studies [244]  
 2149 show also the change of the position of the dips with the mass of the vector meson: for lighter  
 2150 vector mesons like  $\rho, \omega, \phi$  the dips occur at smaller  $t$  than for the heavier vector mesons  $J/\psi$   
 2151 or  $\Upsilon$ . We note that, of course, the positions of the dips depend crucially on the details of the  
 2152 models, which are currently not constrained by the existing HERA data. We also note the  
 2153 sizeable uncertainties due to the charm quark mass (the fits to inclusive HERA data from which  
 2154 parameters of the models have been extracted are performed at each fixed value of the charm  
 2155 mass that is then used to compute exclusive  $J/\psi$  production).

2156 We thus see that the precise measurement of the  $t$ -slope in the elastic production of vector mesons  
 2157 at the LHeC, and its variation with  $x$  and scales, provide a unique opportunity to explore the  
 2158 transition between the dilute and dense partonic regimes. As mentioned earlier, elastic diffractive  
 2159 production is one among several different measurements which can be performed to explore the  
 2160 3D structure of the hadron. Another one is Deeply Virtual Compton Scattering which is a  
 2161 process sensitive to the spatial distribution of quarks inside the hadron. Previous preliminary  
 2162 analyses [1] indicate a huge potential of LHeC for the measurement of DVCS. Another example  
 2163 of a process that could be studied at the LHeC, is diffractive exclusive dijet production. It  
 2164 has been suggested [248] that this process is sensitive to the Wigner function, and that the  
 2165 transverse momentum and spatial distribution of partons can be extracted by measuring this  
 2166 process. The transverse momentum of jets would be sensitive to the transverse momentum of  
 2167 the participating partons, whereas the momentum transfer of the elastically scattered proton  
 2168 would give a handle on the impact parameter distribution of the partons in the target [249–251],  
 2169 thus giving a possibility to extract information about the Wigner distribution.

2170 So far we have referred to coherent diffraction, i.e. to a scenario in which the proton remains

2171 intact after the collision. There also exists incoherent diffraction, where the proton gets excited  
 2172 into some state with the quantum numbers of the proton and separated from the rest of the  
 2173 event by a large rapidity gap. In order to apply the dipole formalism to the incoherent case,  
 2174 see Sec. 4.3.1 where the formulae applicable for both protons and nuclei are shown. Here one  
 2175 must consider a more involved structure of the proton (e.g. as composed by a fixed [252–255]  
 2176 or a growing number with  $1/x$  of hot spots [256–258]). As discussed in Sec. 4.3.1, coherent  
 2177 diffraction is sensitive to the gluon distribution in transverse space, while incoherent diffraction  
 2178 is particularly sensitive to fluctuations of the gluon distribution. A prediction of the model with  
 2179 a growing number of hot spots, both in models where this increasing number is implemented  
 2180 by hand [256–258] and in those where it is dynamically generated [255] from a fixed number  
 2181 at larger  $x$ , is that the ratio of incoherent to coherent diffraction will decrease with  $W$ , and  
 2182 that this decrease is sensitive to the details of the distribution of hot spots. Thus, to the  
 2183 fluctuations of the gluon distribution in transverse space. In order to check these ideas, both  
 2184 the experimental capability to separate coherent from incoherent diffraction and a large lever  
 2185 arm in  $W$ , as available at the LHeC, are required.

### 2186 3.2.6 Inclusive diffraction

2187 An important discovery of HERA was the observation of a large ( $\sim 10\%$ ) fraction of diffractive  
 2188 events in DIS [259, 260]. In these events the proton stays intact or dissociates into a state with  
 2189 the proton quantum numbers, despite undergoing a violent, highly energetic collision, and is  
 2190 separated from the rest of the produced particles by a large rapidity gap. In a series of ground-  
 2191 breaking papers (see Ref. [261] for a review), the HERA experiments determined the deep  
 2192 inelastic structure of the  $t$ -channel exchange in these events in the form of diffractive parton  
 2193 densities.

2194 The precise measurement of diffraction in DIS is of great importance for our understanding of the  
 2195 strong interaction. First, the mechanism through which a composite strongly interacting object  
 2196 interacts perturbatively while keeping colour neutrality offers information about the confinement  
 2197 mechanism. Second, diffraction is known to be highly sensitive to the low- $x$  partonic content  
 2198 of the proton and its evolution with energy and it therefore has considerable promise to reveal  
 2199 deviations from standard linear evolution through higher twist effects or, eventually, non-linear  
 2200 dynamics. Third, it allows checks of basic theory predictions such as the relation between  
 2201 diffraction in  $ep$  scattering and nuclear shadowing [262]. Finally, the accurate extraction of  
 2202 diffractive parton distribution functions facilitates tests of the range of validity of perturbative  
 2203 factorisation [263–265]. The potential studies of inclusive diffraction that would be possible at  
 2204 the LHeC are presented here (see Ref. [266] for further details). They substantially extend the  
 2205 kinematic coverage of the HERA analyses, leading to much more detailed tests of theoretical  
 2206 ideas than have been possible hitherto. Although we work here at NLO of QCD, it is worth  
 2207 noting that similar analyses in the HERA context have recently extended to NNLO [267].

2208 In Fig. 3.39 we show a diagram depicting a neutral current diffractive deep inelastic event.  
 2209 Charged currents could also be considered and were measured at HERA [268] but with large  
 2210 statistical uncertainties and in a very restricted region of phase space. Although they could be  
 2211 measured at both the LHeC and the FCC-eh with larger statistics and more extended kinematics,  
 2212 in this first study we limit ourselves to neutral currents. The incoming electron or positron, with  
 2213 four momentum  $k$ , scatters off the proton, with incoming four momentum  $p$ , and the interaction  
 2214 proceeds through the exchange of a virtual photon with four-momentum  $q$ . The kinematic

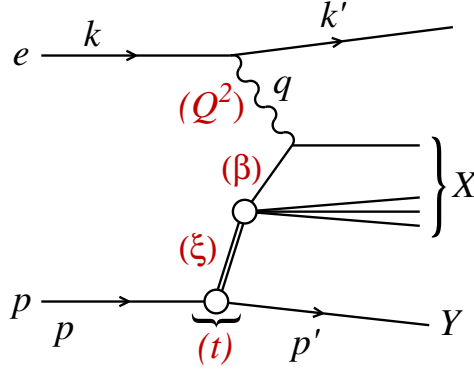


**Figure 3.39:** A diagram of a diffractive NC event in DIS together with the corresponding variables, in the one-photon exchange approximation. The large rapidity gap is between the system  $X$  and the scattered proton (or its low mass excitation)  $Y$ .

2215 variables for such an event include the standard deep inelastic variables

$$Q^2 = -q^2, \quad x = \frac{-q^2}{2p \cdot q}, \quad y = \frac{p \cdot q}{p \cdot k}, \quad (3.18)$$

2216 where  $Q^2$  describes the photon virtuality,  $x$  is the Bjorken variable and  $y$  the inelasticity of the  
2217 process. In addition, the variables

$$s = (k + p)^2, \quad W^2 = (q + p)^2, \quad (3.19)$$

2218 are the electron-proton centre-of-mass energy squared and the photon-proton centre-of-mass  
2219 energy squared, respectively. A distinguishing feature of the diffractive event  $ep \rightarrow eXY$  is the  
2220 presence of the large rapidity gap between the diffractive system, characterised by the invariant  
2221 mass  $M_X$  and the final proton (or its low-mass excitation)  $Y$  with four momentum  $p'$ . In  
2222 addition to the standard DIS variables listed above, diffractive events are also characterised by  
2223 an additional set of variables defined as

$$t = (p - p')^2, \quad \xi = \frac{Q^2 + M_X^2 - t}{Q^2 + W^2}, \quad \beta = \frac{Q^2}{Q^2 + M_X^2 - t}. \quad (3.20)$$

2224 In the above  $t$  is the squared four-momentum transfer at the proton vertex,  $\xi$  (alternatively  
2225 denoted by  $x_{IP}$ ) can be interpreted as the momentum fraction of the *diffractive exchange* with  
2226 respect to the hadron, and  $\beta$  is the momentum fraction of the parton with respect to the  
2227 diffractive exchange. The two momentum fractions combine to give Bjorken- $x$ ,  $x = \beta\xi$ .

2228 The kinematic range in  $(\beta, Q^2, \xi)$  that we consider at the LHeC is restricted by the following  
2229 cuts:

- 2230 •  $Q^2 \geq 1.8 \text{ GeV}^2$ : due to the fact that the initial distribution for the DGLAP evolution is  
2231 parameterised at  $\mu_0^2 = 1.8 \text{ GeV}^2$ . The renormalization and factorisation scales are taken  
2232 to be equal to  $Q^2$ .
- 2233 •  $\xi < 0.4$ : constrained by physical and experimental limitations. This rather high  $\xi$  value is  
2234 an experimental challenge and physically enters the phase-space region where the Pomeron  
2235 contribution should become negligible compared with sub-leading exchanges. Within the  
2236 two-component model, see Eq. (3.25) below, at high  $\xi$  the cross section is dominated by  
2237 the secondary Reggeon contribution, which is poorly fixed by the HERA data. We present  
2238 this high  $\xi$  ( $> 0.1$ ) region for illustrative purpose and for the sake of discussion of the fit  
2239 results below.

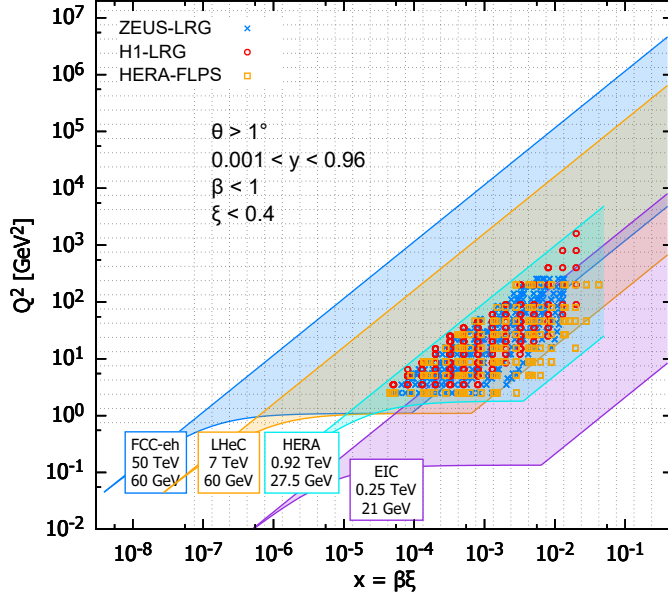


**Figure 3.40:** Kinematic phase space for inclusive diffraction in  $(x, Q^2)$  for the EIC (magenta region), the LHeC (orange region) and the FCC-eh (dark blue region) as compared with the HERA data (light blue region, ZEUS-LRG [269], H1-LRG [270], HERA-FLPS [271]). The acceptance limit for the electron in the detector design has been assumed to be  $1^\circ$ , and we take  $\xi < 0.4$ .

2240 In Fig. 3.40 the accessible kinematic range in  $(x, Q^2)$  is shown for three machines: HERA, LHeC  
 2241 and FCC-eh. For the LHeC design the range in  $x$  is increased by a factor  $\sim 20$  over HERA  
 2242 and the maximum available  $Q^2$  by a factor  $\sim 100$ . The FCC-eh machine would further increase  
 2243 this range with respect to LHeC by roughly one order of magnitude in both  $x$  and  $Q^2$ . We  
 2244 also show the EIC kinematic region for comparison. The three different machines are clearly  
 2245 complementary in their kinematic coverage, with LHeC and EIC adding sensitivity at lower and  
 2246 higher  $x$  than HERA, respectively.

2247 In Fig. 3.41 the phase space in  $(\beta, Q^2)$  is shown for fixed  $\xi$  for the LHeC. The LHeC machine  
 2248 probes very small values of  $\xi$ , reaching  $10^{-4}$  with a wide range of  $\beta$ . Of course, the ranges in  
 2249  $\beta$  and  $\xi$  are correlated since  $x = \beta\xi$ . Therefore, for small values of  $\xi$  only large values of  $\beta$   
 2250 are accessible while for large  $\xi$  the range in  $\beta$  extends to very small values.

2251 Diffractive cross sections in the neutral current case can be presented in the form of the reduced  
 2252 cross sections integrated over  $t$  [268]:

$$\frac{d^3\sigma^D}{d\xi d\beta dQ^2} = \frac{2\pi\alpha_{\text{em}}^2}{\beta Q^4} Y_+ \sigma_{\text{red}}^{\text{D}(3)}, \quad (3.21)$$

2253 where  $Y_+ = 1 + (1-y)^2$  and the reduced cross sections can be expressed in terms of two diffractive  
 2254 structure functions  $F_2^{\text{D}}$  and  $F_L^{\text{D}}$ . In the one-photon approximation, the relations are

$$\sigma_{\text{red}}^{\text{D}(3)} = F_2^{\text{D}(3)}(\beta, \xi, Q^2) - \frac{y^2}{Y_+} F_L^{\text{D}(3)}(\beta, \xi, Q^2). \quad (3.22)$$

2255 In this analysis we neglect  $Z^0$  exchange, though it should be included in future studies.

2256 Both  $\sigma_{\text{red}}^{\text{D}(3)}$  and  $\sigma_{\text{red}}^{\text{D}(4)}$  have been measured at the HERA collider [259, 260, 268–270, 272–275] and  
 2257 used to obtain QCD-inspired parameterisations.

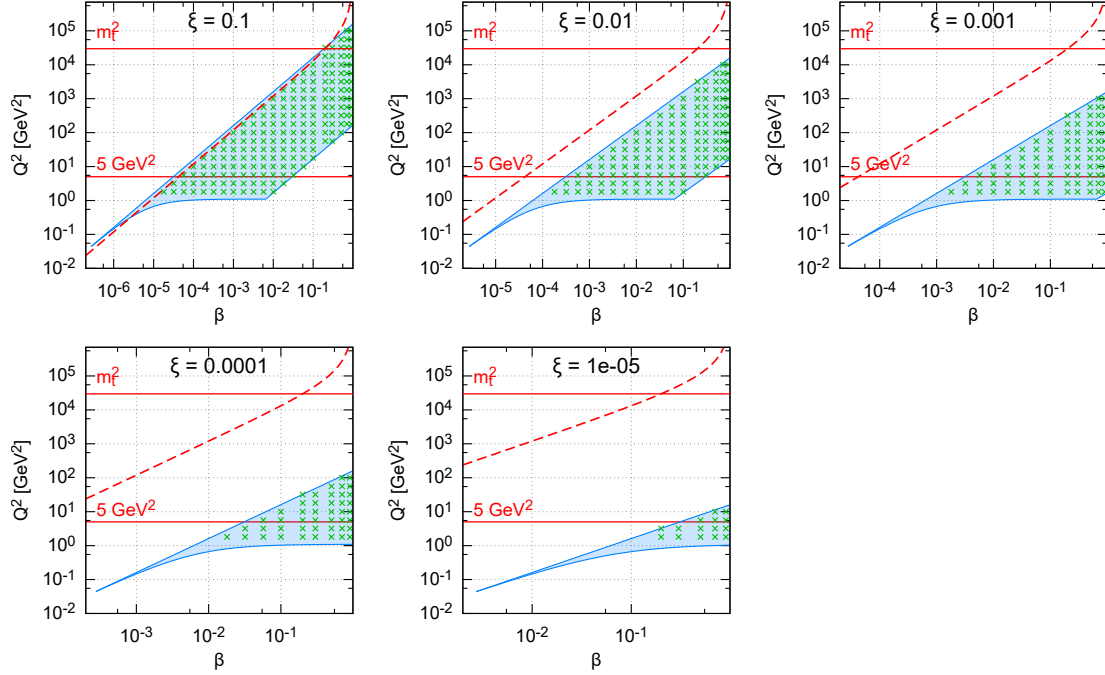


**Figure 3.41:** Kinematic phase space for inclusive diffraction in  $(\beta, Q^2)$  for fixed values of  $\xi$  for the LHeC design. The horizontal lines indicate correspondingly,  $Q^2 = 5 \text{ GeV}^2$ , the lowest data value for the DGLAP fit performed in this study and  $m_t^2$  the 6-flavour threshold. The dashed line marks the kinematic limit for  $t\bar{t}$  production.

2258 The standard perturbative QCD approach to diffractive cross sections is based on collinear  
 2259 factorisation [263–265]. It was demonstrated that, similarly to the inclusive DIS cross section,  
 2260 the diffractive cross section can be written, up to terms of order  $\mathcal{O}(\Lambda^2/Q^2)$ , where  $\Lambda$  is the  
 2261 hadronic scale, in a factorised form

$$d\sigma^{ep \rightarrow eXY}(\beta, \xi, Q^2, t) = \sum_i \int_{\beta}^1 dz d\hat{\sigma}^{ei} \left( \frac{\beta}{z}, Q^2 \right) f_i^D(z, \xi, Q^2, t), \quad (3.23)$$

2262 where the sum is performed over all parton flavours (gluon,  $d$ -quark,  $u$ -quark, etc.). The hard  
 2263 scattering partonic cross section  $d\hat{\sigma}^{ei}$  can be computed perturbatively in QCD and is the same  
 2264 as in the inclusive deep inelastic scattering case. The long distance part  $f_i^D$  corresponds to the  
 2265 diffractive parton distribution functions, which can be interpreted as conditional probabilities  
 2266 for partons in the proton, provided the proton is scattered into the final state system  $Y$  with  
 2267 specified 4-momentum  $p^l$ . They are evolved using the DGLAP evolution equations [276–279]  
 2268 similarly to the inclusive case. The analogous formula for the  $t$ -integrated structure functions  
 2269 reads

$$F_{2/L}^{D(3)}(\beta, \xi, Q^2) = \sum_i \int_{\beta}^1 \frac{dz}{z} C_{2/L,i} \left( \frac{\beta}{z} \right) f_i^{D(3)}(z, \xi, Q^2), \quad (3.24)$$

2270 where the coefficient functions  $C_{2/L,i}$  are the same as in inclusive DIS.

2271 Fits to the diffractive structure functions usually [268, 274] parameterise the diffractive PDFs in  
 2272 a two component model, which is a sum of two diffractive exchange contributions,  $\mathbb{P}$  and  $\mathbb{R}$ :

$$f_i^{D(4)}(z, \xi, Q^2, t) = f_{\mathbb{P}}^p(\xi, t) f_i^{\mathbb{P}}(z, Q^2) + f_{\mathbb{R}}^p(\xi, t) f_i^{\mathbb{R}}(z, Q^2). \quad (3.25)$$

2273 For both of these terms proton vertex factorisation is separately assumed, meaning that the  
 2274 diffractive exchange can be interpreted as colourless objects called a *Pomeron* or a *Reggeon*

2275 with parton distributions  $f_i^{P,R}(\beta, Q^2)$ . The flux factors  $f_{P,R}^p(\xi, t)$  represent the probability  
 2276 that a Pomeron/Reggeon with given values  $\xi, t$  couples to the proton. They are parameterised  
 2277 using the form motivated by Regge theory,

$$f_{P,R}^p(\xi, t) = A_{P,R} \frac{e^{B_{P,R}t}}{\xi^{2\alpha_{P,R}(t)-1}}, \quad (3.26)$$

2278 with a linear trajectory  $\alpha_{P,R}(t) = \alpha_{P,R}(0) + \alpha'_{P,R}t$ . The diffractive PDFs relevant to the  
 2279  $t$ -integrated cross sections read

$$f_i^{D(3)}(z, \xi, Q^2) = \phi_{P,R}^p(\xi) f_i^P(z, Q^2) + \phi_{R,R}^p(\xi) f_i^R(z, Q^2), \quad (3.27)$$

2280 with

$$\phi_{P,R}^p(\xi) = \int dt f_{P,R}^p(\xi, t). \quad (3.28)$$

2281 Note that, the notions of *Pomeron* and *Reggeon* used here to model hard diffraction in DIS are,  
 2282 in principle, different from those describing the soft hadron-hadron interactions; in particular,  
 2283 the parameters of the fluxes may be different.

2284 The diffractive parton distributions of the Pomeron at the initial scale  $\mu_0^2 = 1.8 \text{ GeV}^2$  are  
 2285 parameterised as

$$z f_i^P(z, \mu_0^2) = A_i z^{B_i} (1-z)^{C_i}, \quad (3.29)$$

2286 where  $i$  is a gluon or a light quark and the momentum fraction  $z = \beta$  in the case of quarks. In the  
 2287 diffractive parameterisations the contributions of all the light quarks (anti-quarks) are assumed  
 2288 to be equal. For the treatment of heavy flavours, a variable flavour number scheme (VFNS)  
 2289 is adopted, where the charm and bottom quark DPDFs are generated radiatively via DGLAP  
 2290 evolution, and no intrinsic heavy quark distributions are assumed. The structure functions are  
 2291 calculated in a General-Mass Variable Flavour Number scheme (GM-VFNS) [280, 281] which  
 2292 ensures a smooth transition of  $F_{2,L}$  across the flavour thresholds by including  $\mathcal{O}(m_h^2/Q^2)$  correc-  
 2293 tions. The parton distributions for the Reggeon component are taken from a parameterisation  
 2294 which was obtained from fits to the pion structure function [282, 283].

2295 In Eq. (3.25) the normalisation factors of fluxes,  $A_{P,R}$  and of DPDFs,  $A_i$  enter in the product.  
 2296 To resolve the ambiguity we fix<sup>8</sup>  $A_P$  and use  $f_i^R(z, Q^2)$  normalised to the pion structure function,  
 2297 which results in  $A_i$  and  $A_R$  being well defined free fit parameters. For full details, see Ref. [266].

## 2298 Pseudodata for diffractive structure functions

2299 The reduced cross sections are extrapolated using the ZEUS-SJ DPDFs. Following the scenario  
 2300 of the ZEUS fit [274] we work within the VFNS scheme at NLO accuracy. The transition scales  
 2301 for DGLAP evolution are fixed by the heavy quark masses,  $\mu^2 = m_h^2$  and the structure functions  
 2302 are calculated in the Thorne–Roberts GM-VFNS [284]. The Reggeon PDFs are taken from the  
 2303 GRV pion set [283], the numerical parameters are taken from Tables 1 and 3 of Ref. [274], the  
 2304 heavy quark masses are  $m_c = 1.35 \text{ GeV}$ ,  $m_b = 4.3 \text{ GeV}$ , and  $\alpha_s(M_Z^2) = 0.118$ .

2305 The pseudodata were generated using the extrapolation of the fit to HERA data, which pro-  
 2306 vides the central values, amended with a random Gaussian smearing with standard deviation  
 2307 corresponding to the relative error  $\delta$ . An uncorrelated 5% systematic error was assumed giving  
 2308 a total uncertainty

$$\delta = \sqrt{\delta_{\text{sys}}^2 + \delta_{\text{stat}}^2}. \quad (3.30)$$

---

<sup>8</sup>Here, as in the HERA fits,  $A_P$  is fixed by normalizing  $\phi_P^p(0.003) = 1$ .

2309 The statistical error was computed assuming a very modest integrated luminosity of  $2 \text{ fb}^{-1}$ , see  
 2310 Ref. [32, 33]. For the binning adopted in this study, the statistical uncertainties have a very  
 2311 small effect on the uncertainties in the extracted DPDFs. Obviously, a much larger luminosity  
 2312 would allow a denser binning that would result in smaller DPDF uncertainties.

2313 In Fig. 3.42 we show a subset of the simulated data for the diffractive reduced cross section  $\xi\sigma_{\text{red}}$   
 2314 as a function of  $\beta$  in selected bins of  $\xi$  and  $Q^2$  for the LHeC. For the most part the errors are  
 2315 very small, and are dominated by the systematics. The breaking of Regge factorisation evident  
 2316 at large  $\xi$  comes from the large Reggeon contribution in that region, whose validity could be  
 2317 further investigated at the LHeC.

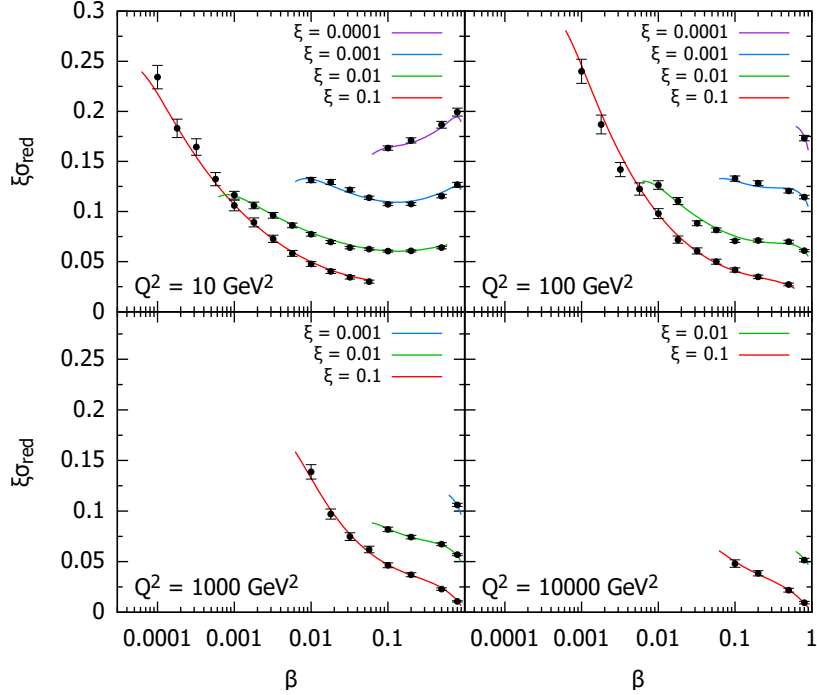


**Figure 3.42:** Selected subset of the simulated data for the diffractive reduced cross section as a function of  $\beta$  in bins of  $\xi$  and  $Q^2$  for  $ep$  collisions at the LHeC. The curves for  $\xi = 0.01, 0.001, 0.0001$  are shifted up by 0.04, 0.08, 0.12, respectively.

### 2318 Potential for constraining diffractive PDFs at the LHeC and FCC-eh

2319 With the aim of establishing the experimental precision with which DPDFs could be extracted  
 2320 when LHeC data become available, we generate the central values of the pseudodata using the  
 2321 central set of the ZEUS-SJ fit that are distributed according to a Gaussian with experimental  
 2322 width given by Eq. (3.30), that also provides the uncertainty in the pseudodata. We then include  
 2323 the pseudodata in a fit alongside the existing HERA data using the same functional form and,  
 2324 as expected, obtain a  $\chi^2/\text{ndf} \sim 1$ , which demonstrates the consistency of the approach.

2325 To evaluate the experimental precision with which the DPDFs can be determined, several pseudo-  
 2326 data sets, corresponding to independent random error samples, were generated. Each pseudo-  
 2327 data set was fitted separately. The minimal value of  $Q^2$  for the data considered in the fits was set  
 2328 to  $Q_{\text{min}}^2 = 5 \text{ GeV}^2$ . The reason for this cut-off is to show the feasibility of the fits including just  
 2329 the range in which standard twist-2 DGLAP evolution is expected to be trustable. At HERA,  
 2330 the  $Q_{\text{min}}^2$  values giving acceptable DGLAP (twist-2) fits were  $8 \text{ GeV}^2$  [268] and  $5 \text{ GeV}^2$  [269] for

2331 H1 and ZEUS, respectively. The maximum value of  $\xi$  was set by default to  $\xi_{\max} = 0.1$ , above  
 2332 which the cross section starts to be dominated by the Reggeon exchange. The binning adopted  
 2333 in this study corresponds roughly to 4 bins per order of magnitude in each of  $\xi, \beta, Q^2$ . For  
 2334  $Q_{\min}^2 = 5 \text{ GeV}^2$ ,  $\xi_{\max} = 0.1$  and below the top threshold this results in 1229 and 1735 pseudo-  
 2335 data points for the LHeC and FCC-eh, respectively. The top-quark region adds 17 points for the  
 2336 LHeC and 255 for FCC-eh. Lowering  $Q_{\min}^2$  down to  $1.8 \text{ GeV}^2$  we get 1589 and 2171 pseudodata  
 2337 points, while increasing  $\xi$  up to 0.32 adds around 180 points for both proposed machines.

2338 The potential for determination of the gluon DPDF was investigated by fitting the inclusive  
 2339 diffractive DIS pseudodata with two models with different numbers of parameters, named S and  
 2340 C (see Ref. [266]) with  $\alpha_{IP,IR}(0)$  fixed, in order to focus on the shape of the Pomeron's PDFs. At  
 2341 HERA, both S and C fits provide equally good descriptions of the data with  $\chi^2/\text{ndf} = 1.19$  and  
 2342 1.18, respectively, despite different gluon DPDF shapes. The LHeC pseudodata are much more  
 2343 sensitive to gluons, resulting in  $\chi^2/\text{ndf}$  values of 1.05 and 1.4 for the S and C fits, respectively.  
 2344 This motivates the use of the larger number of parameters in the fit-S model, which we employ  
 2345 in the following studies. It also shows clearly the potential of the LHeC and the FCC-eh to  
 2346 better constrain the low- $x$  gluon and, therefore, unravel eventual departures from standard  
 2347 linear evolution.

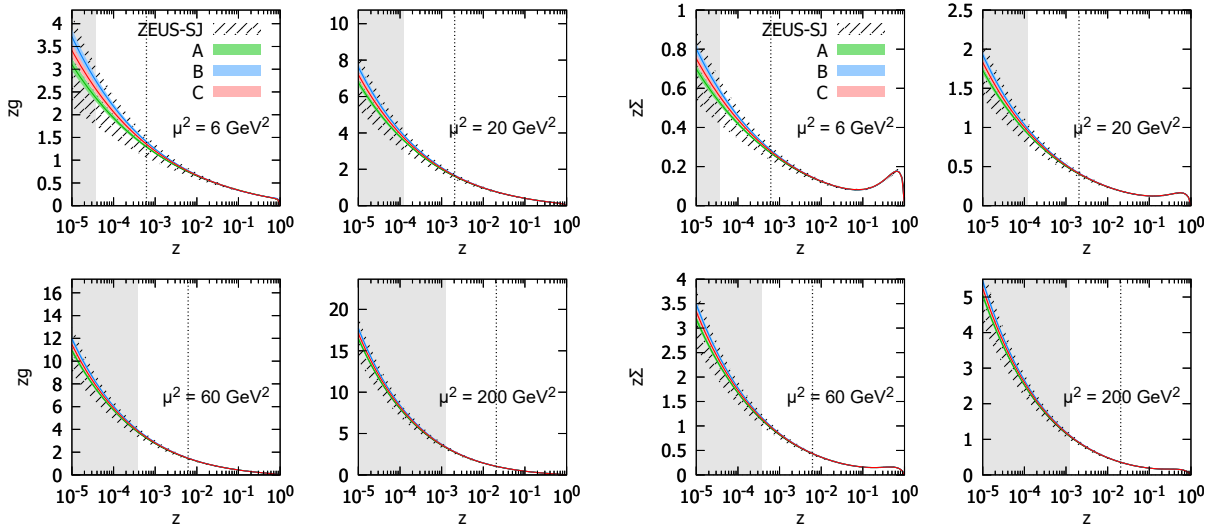


**Figure 3.43:** Diffractive PDFs for gluon and quark in the LHeC kinematics as a function of momentum fraction  $z$  for fixed values of scale  $\mu^2$ . Results of fits to three (A,B,C) pseudodata replicas are shown together with the experimental error bands. For comparison, the extrapolated ZEUS-SJ fit is also shown (black) with error bands marked with the hatched pattern. The vertical dotted lines indicate the HERA kinematic limit. The bands indicate only the experimental uncertainties.

2348 In Fig. 3.43 the diffractive gluon and quark distributions are shown for the LHeC and FCC-eh,  
 2349 respectively, as a function of momentum fraction  $z$  for fixed scales  $\mu^2 = 6, 20, 60, 200 \text{ GeV}^2$ .  
 2350 The bands labelled A, B, C denote fits to three statistically independent pseudodata replicas,  
 2351 obtained from the same central values and statistical and systematic uncertainties. Hereafter the  
 2352 uncertainty bands shown correspond to  $\Delta\chi^2 = 2.7$  (90% CL). Also the extrapolated ZEUS-SJ  
 2353 DPDFs are shown with error bands marked by the '/' hatched area. Note that the depicted  
 2354 uncertainty bands come solely from experimental errors, neglecting theoretical sources, such as  
 2355 fixed input parameters and parameterisation biases. The extrapolation beyond the reach of  
 2356 LHeC/FCC-eh is marked in grey and the HERA kinematic limit is marked with the vertical  
 2357 dotted line. The stability of the results with respect to the independent pseudodata replicas

2358 used for the analysis is evident, so in the following only one will be employed. The low  $x$  DPDF  
 2359 determination accuracy improves with respect to HERA by a factor of 5–7 for the LHeC and  
 2360 10–15 for the FCC-eh and completely new kinematic regimes are accessed.

2361 For a better illustration of the precision, in Fig. 3.44 the relative uncertainties are shown for  
 2362 parton distributions at different scales. The different bands show the variation with the upper  
 2363 cut on the available  $\xi$  range, from 0.01 to 0.32. In the best constrained region of  $z \simeq 0.1$ ,  
 2364 the precision reaches the 1% level. We observe only a modest improvement in the achievable  
 2365 accuracy of the extracted DPDFs with the change of  $\xi$  by an order of magnitude from 0.01  
 2366 to 0.1. An almost negligible effect is observed when further extending the  $\xi$  range up to 0.32.  
 2367 This is encouraging, since the measurement for the very large values of  $\xi$  is challenging. It  
 2368 reflects the dominance of the secondary Reggeon in this region. We stress again that only  
 2369 experimental errors are included in our uncertainty bands. Neither theoretical uncertainties nor  
 2370 the parameterisation biases are considered. For a detailed discussion of this and other aspects  
 2371 of the fits, see Ref. [266].

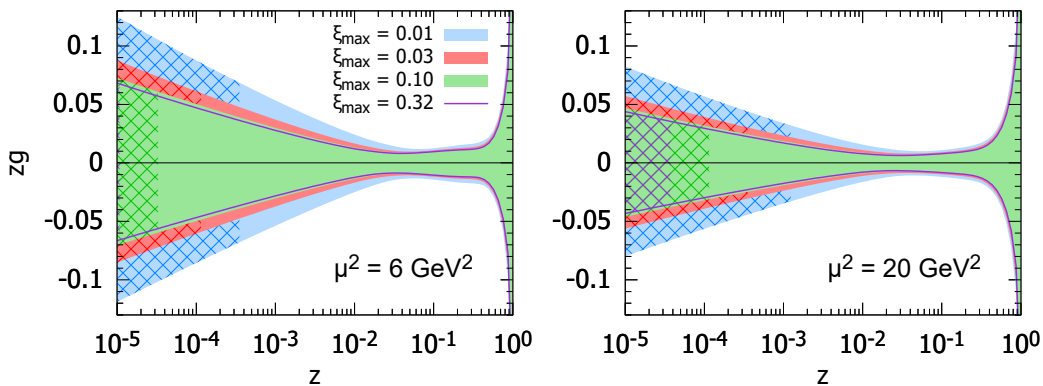


**Figure 3.44:** Relative uncertainties on the diffractive gluon PDFs for the LHeC kinematics. Two different choices of scales are considered  $\mu^2 = 6$  and  $\mu^2 = 20 \text{ GeV}^2$ . The blue, red, green bands and magenta line correspond to different maximal values of  $\xi = 0.01, 0.03, 0.1, 0.32$ , respectively. The cross-hatched areas show kinematically excluded regions. The bands indicate only the experimental uncertainties, see the text.

### 2372 Factorisation tests using Hadronic Final States in Diffractive DIS

2373 The factorisation properties of diffractive DIS were a major topic of study at HERA [261] and  
 2374 are highly relevant to the interpretation of diffractive processes at the LHC [285]. A general theoretical framework is provided by the proof [263] of a hard scattering collinear QCD factorisation theorem for semi-inclusive DIS scattering processes such as  $ep \rightarrow epX$ . This implies that the DPDFs extracted in fits to inclusive diffractive DIS may be used to predict perturbative cross sections for hadronic final state observables such as heavy flavour or jet production. Testing this factorisation pushes at the boundaries of applicability of perturbative QCD and will be a major topic of study at the LHeC.

2381 Tests of diffractive factorisation at HERA are strongly limited by the kinematics. The mass of the dissociation system  $X$  is limited to approximately  $M_X < 30 \text{ GeV}$ , which implies for example that jet transverse momenta cannot be larger than about 15 GeV and more generally leaves very little phase space for any studies at perturbative scales. As well as restricting the kinematic range of studies, this restriction also implied large hadronisation and scale uncertainties in theoretical predictions, which in turn limit the precision with which tests can be made.

2387 The higher centre-of-mass energy of the LHeC opens up a completely new regime for diffractive  
 2388 hadronic final state observables in which masses and transverse momenta are larger and theo-  
 2389 retical uncertainties are correspondingly reduced. For example,  $M_X$  values in excess of 250 GeV  
 2390 are accessible, whilst remaining in the region  $\xi < 0.05$  where the leading diffractive (pomeron)  
 2391 exchange dominates. The precision of tests is also improved by the development of techniques  
 2392 for NNLO calculations for diffractive jets [286].

2393 Fig. 3.45 shows a simulation of the expected diffractive jet cross section at the LHeC, assuming  
 2394 DPDFs extrapolated from H1 at HERA [268], using the NLOJET++ framework [287]. An  
 2395 integrated luminosity of  $100 \text{ fb}^{-1}$  is assumed and the kinematic range considered is  $Q^2 > 2 \text{ GeV}^2$ ,  
 2396  $0.1 < y < 0.7$  and scattered electron angles larger than  $1^\circ$ . Jets are reconstructed using the  $k_T$   
 2397 algorithm with  $R = 1$ . The statistical precision remains excellent up to jet transverse momenta  
 2398 of almost 50 GeV and the theoretical scale uncertainties (shaded bands) are substantially reduced  
 2399 compared with HERA measurements. Comparing a measurement of this sort of quality with  
 2400 predictions refined using DPDFs from inclusive LHeC data would clearly provide an exacting  
 2401 test of diffractive factorisation.

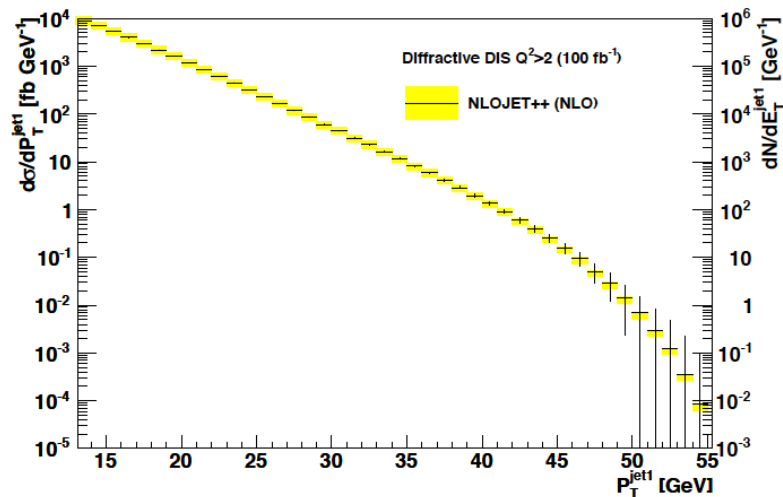


**Figure 3.45:** Simulated diffractive dijet cross section as a function of leading jet transverse momentum in the kinematic range  $Q^2 > 2 \text{ GeV}^2$  and  $0.1 < y < 0.7$ , with scattered electron angles in excess of  $1^\circ$ . The error bars indicate predicted statistical uncertainties for a luminosity of  $100 \text{ fb}^{-1}$ . The coloured bands correspond to theoretical uncertainties when varying the renormalisation and factorisation scales by factors of 2.

2402 Further interesting hadronic final state observables that were studied at HERA and could be  
 2403 extended at the LHeC include open charm production, thrust and other event shapes, charged  
 2404 particle multiplicities and energy flows. In addition, the LHeC opens up completely new chan-  
 2405 nels, notably diffractive beauty,  $W$  and  $Z$  production, the latter giving complementary sensitivity  
 2406 to the quark densities to that offered by inclusive diffraction.

### 2407 3.2.7 Light-Front Holography and Superconformal Algebra

2408 The LHeC has the potential of probing the high mass spectrum of QCD, such as the spectroscopy  
 2409 and structure of hadrons consisting of heavy quarks. Insights into this new domain of hadron  
 2410 physics can now be derived by new non-perturbative colour-confining methods based on light-  
 2411 front (LF) holography. A remarkable feature is universal Regge trajectories with universal  
 2412 slopes in both the principal quantum number  $n$  and internal orbital angular momentum  $L$ . A

2413 key feature is di-quark clustering and supersymmetric relations between the masses of meson,  
 2414 baryons, and tetraquarks. In addition the running coupling is determined at all scales, including  
 2415 the soft domain relevant to rescattering corrections to LHeC processes. The combination of  
 2416 lightfront holography with superconformal algebra leads to the novel prediction that hadron  
 2417 physics has supersymmetric properties in both spectroscopy and dynamics.

## 2418 **Light-front holography and recent theoretical advances**

2419 Five-dimensional AdS<sub>5</sub> space provides a geometrical representation of the conformal group.  
 2420 Remarkably, AdS<sub>5</sub> is holographically dual to 3 + 1 spacetime at fixed LF time  $\tau$  [288]. A  
 2421 colour-confining LF equation for mesons of arbitrary spin  $J$  can be derived from the holographic  
 2422 mapping of the *soft-wall model* modification of AdS<sub>5</sub> space for the specific dilaton profile  $e^{+\kappa^2 z^2}$ ,  
 2423 where  $z$  is the fifth dimension variable of the five-dimensional AdS<sub>5</sub> space. A holographic  
 2424 dictionary maps the fifth dimension  $z$  to the LF radial variable  $\zeta$ , with  $\zeta^2 = b_{\perp}^2(1 - x)$ . The  
 2425 same physics transformation maps the AdS<sub>5</sub> and (3 + 1) LF expressions for electromagnetic and  
 2426 gravitational form factors to each other [289].

2427 A key tool is the remarkable dAFF principle [290] which shows how a mass scale can appear in a  
 2428 Hamiltonian and its equations of motion while retaining the conformal symmetry of the action.  
 2429 When applying it to LF holography, a mass scale  $\kappa$  appears which determines universal Regge  
 2430 slopes, and the hadron masses. The resulting *LF Schrödinger Equation* incorporates colour  
 2431 confinement and other essential spectroscopic and dynamical features of hadron physics, includ-  
 2432 ing Regge theory, the Veneziano formula [291], a massless pion for zero quark mass and linear  
 2433 Regge trajectories with the universal slope in the radial quantum number  $n$  and the internal  
 2434 orbital angular momentum  $L$ . The combination of LF dynamics, its holographic mapping to  
 2435 AdS<sub>5</sub> space, and the dAFF procedure provides new insight into the physics underlying colour  
 2436 confinement, the non-perturbative QCD coupling, and the QCD mass scale. The  $q\bar{q}$  mesons and  
 2437 their valence LFWFs are the eigensolutions of the frame-independent a relativistic bound-state  
 2438 LF Schrödinger equation.

2439 The mesonic  $q\bar{q}$  bound-state eigenvalues for massless quarks are  $M^2(n, L, S) = 4\kappa^2(n + L + S/2)$ .  
 2440 This equation predicts that the pion eigenstate  $n = L = S = 0$  is massless for zero quark mass.  
 2441 When quark masses are included in the LF kinetic energy  $\sum_i \frac{k_{\perp i}^2 + m^2}{x_i}$ , the spectroscopy of mesons  
 2442 are predicted correctly, with equal slope in the principal quantum number  $n$  and the internal  
 2443 orbital angular momentum  $L$ . A comprehensive review is given in Ref. [288].

## 2444 **The QCD Running Coupling at all Scales from Light-Front Holography**

2445 The QCD running coupling  $\alpha_s(Q^2)$  sets the strength of the interactions of quarks and gluons  
 2446 as a function of the momentum transfer  $Q$  (see Sec. 3.2.1). The dependence of the coupling  
 2447  $Q^2$  is needed to describe hadronic interactions at both long and short distances [292]. It can  
 2448 be defined [293] at all momentum scales from a perturbatively calculable observable, such as  
 2449 the coupling  $\alpha_s^{g_1}(Q^2)$ , which is defined using the Bjorken sum rule [294], and determined from  
 2450 the sum rule prediction at high  $Q^2$  and, below, from its measurements [295–297]. At high  $Q^2$ ,  
 2451 such *effective charges* satisfy asymptotic freedom, obey the usual pQCD renormalisation group  
 2452 equations, and can be related to each other without scale ambiguity by commensurate scale  
 2453 relations [298].

2454 The high  $Q^2$  dependence of  $\alpha_s^{g_1}(Q^2)$  is predicted by pQCD. In the small  $Q^2$  domain its functional

2455 behaviour can be predicted by the dilaton  $e^{+\kappa^2 z^2}$  soft-wall modification of the AdS<sub>5</sub> metric,  
 2456 together with LF holography [299], as  $\alpha_s^{g_1}(Q^2) = \pi e^{-Q^2/4\kappa^2}$ . The parameter  $\kappa$  determines the  
 2457 mass scale of hadrons and Regge slopes in the zero quark mass limit, and it was shown that it can  
 2458 be connected to the mass scale  $\Lambda_s$ , which controls the evolution of the pQCD coupling [299–301].  
 2459 Measurements of  $\alpha_s^{g_1}(Q^2)$  [302,303] are remarkably consistent with this predicted Gaussian form,  
 2460 and a fit gives  $\kappa = 0.513 \pm 0.007$  GeV, see Fig. 3.46.

2461 The matching of the high and low  $Q^2$  regimes of  $\alpha_s^{g_1}(Q^2)$  determines a scale  $Q_0$ , which sets the  
 2462 interface between perturbative and non-perturbative hadron dynamics. This connection can be  
 2463 done for any choice of renormalisation scheme and one obtains an effective QCD coupling at all  
 2464 momenta. In the  $\overline{\text{MS}}$  scheme one gets  $Q_0 = 0.87 \pm 0.08$  GeV [304]. The corresponding value of  
 2465  $\Lambda_{\overline{\text{MS}}}$  agrees well with the measured world average value and its value allows to compute hadron  
 2466 masses using the AdS/QCD superconformal predictions for hadron spectroscopy. The value of  
 2467  $Q_0$  can further be used to set the factorization scale for DGLAP evolution [277–279] or the ERBL  
 2468 evolution of distribution amplitudes [305,306]. The use of the scale  $Q_0$  to resolve the factorization  
 2469 scale uncertainty in structure functions and fragmentation functions, in combination with the  
 2470 scheme-independent *principle of maximum conformality* (PMC) [140] for setting renormalization  
 2471 scales, can greatly improve the precision of pQCD predictions for collider phenomenology at  
 2472 LHeC and HL-LHC.

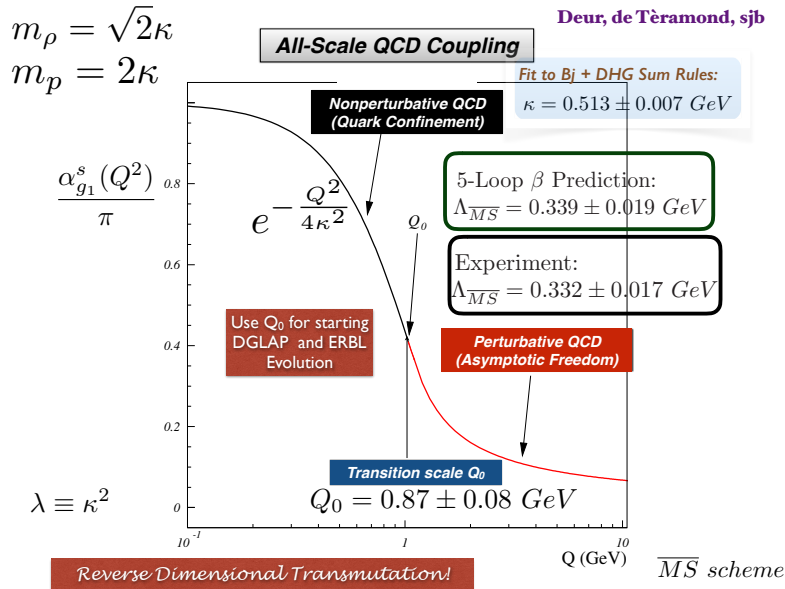


**Figure 3.46:** Prediction for the running coupling  $\alpha_s^{g_1}(Q^2)$  at all scales. At lower  $Q^2$  predictions are obtained from LF Holography and at higher  $Q^2$  from perturbative QCD. The magnitude and derivative of the perturbative and non-perturbative coupling are matched at the scale  $Q_0$ . This matching connects the perturbative scale  $\Lambda_{\overline{\text{MS}}}$  to the non-perturbative scale  $\kappa$  which underlies the hadron mass scale.

### 2473 Superconformal Algebra and Hadron Physics with LHeC data

2474 If one generalises LF holography using *superconformal algebra* the resulting LF eigensolutions  
 2475 yield a unified Regge spectroscopy of mesons, baryons and tetraquarks, including remark-  
 2476 able supersymmetric relations between the masses of mesons and baryons of the same par-

2477 ity <sup>9</sup> [307, 308]. This generalisation further predicts hadron dynamics, including vector meson  
 2478 electroproduction, hadronic LFWFs, distribution amplitudes, form factors, and valence structure  
 2479 functions [309, 310]. Applications to the deuteron elastic form factors and structure functions  
 2480 are given in Refs. [311, 312]

2481 The eigensolutions of superconformal algebra predict the Regge spectroscopy of mesons, baryons,  
 2482 and tetraquarks of the same parity and twist as equal-mass members of the same 4-plet repre-  
 2483 sentation with a universal Regge slope [313–315]. A comparison with experiment is shown in  
 2484 Fig. 3.47. The  $q\bar{q}$  mesons with orbital angular momentum  $L_M = L_B + 1$  have the same mass as  
 their baryonic partners with orbital angular momentum  $L_B$  [313, 316].

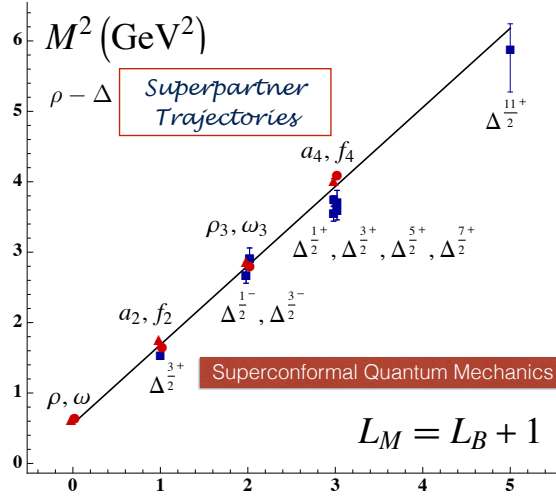


**Figure 3.47:** Comparison of the  $\rho/\omega$  meson Regge trajectory with the  $J = 3/2$   $\Delta$  baryon trajectory. Superconformal algebra predicts the mass degeneracy of the meson and baryon trajectories if one identifies a meson with internal orbital angular momentum  $L_M$  with its superpartner baryon with  $L_M = L_B + 1$ . See Refs. [313, 316].

2485

2486 The predictions from LF holography and superconformal algebra can also be extended to mesons,  
 2487 baryons, and tetraquarks with strange, charm and bottom quarks. Although conformal symme-  
 2488 try is strongly broken by the heavy quark masses, the basic underlying supersymmetric mech-  
 2489 anism, which transforms mesons to baryons (and baryons to tetraquarks), still holds and gives  
 2490 remarkable mass degeneracy across the entire spectrum of light, heavy-light and double-heavy  
 2491 hadrons.

2492 The 4-plet symmetry of quark-antiquark mesons, quark-diquark baryons, and diquark-antidiquark  
 2493 tetraquarks are important predictions by superconformal algebra [304, 307]. Recently the AnDY  
 2494 experiment at RHIC has reported the observation of a state at 18 GeV which can be identified  
 2495 with the  $[bb][\bar{b}\bar{b}]$  tetraquark [88]. The states with heavy quarks such as the  $[bb][\bar{b}\bar{b}]$  tetraquark  
 2496 can be produced at the LHeC, especially at high  $x_F$  along the proton beam direction. New  
 2497 measurements at the LHeC are therefore inevitable to manifest the superconformal nature of  
 2498 hadronic bound states.

<sup>9</sup> QCD is not supersymmetrical in the usual sense, since the QCD Lagrangian is based on quark and gluonic fields, not squarks or gluinos. However, its hadronic eigensolutions conform to a representation of superconformal algebra, reflecting the underlying conformal symmetry of chiral QCD and its Pauli matrix representation.

2499 **3.3 Electroweak Physics**

2500 With the discovery of the Standard Model (SM) Higgs boson at the CERN LHC experiments  
 2501 and subsequent measurements of its properties, all fundamental parameters of the SM have now  
 2502 been measured directly and with remarkable precision. To further establish the validity of the  
 2503 theory of electroweak interactions [23,317–320], validate the mechanism of electroweak symmetry  
 2504 breaking and the nature of the Higgs sector [321–323], new electroweak measurements have to  
 2505 be performed at highest precision. Such high-precision measurements can be considered as a  
 2506 portal to new physics, since non-SM contributions, as for instance loop-insertions, may cause  
 2507 significant deviations for some precisely measurable and calculable observables. At the LHeC,  
 2508 the greatly enlarged kinematic reach to higher mass scales in comparison to HERA [324–326]  
 2509 and the large targeted luminosity will enable electroweak measurements in  $ep$  scattering with  
 2510 higher precision than ever before.

2511 **3.3.1 Electroweak effects in inclusive NC and CC DIS cross sections**

2512 Electroweak NC interactions in inclusive  $e^\pm p$  DIS are mediated by exchange of a virtual photon  
 2513 ( $\gamma$ ) or a  $Z$  boson in the  $t$ -channel, while CC DIS is mediated exclusively by  $W$ -boson exchange  
 2514 as a purely *weak* process. Inclusive NC DIS cross sections are expressed in terms of generalised  
 2515 structure functions  $\tilde{F}_2^\pm$ ,  $x\tilde{F}_3^\pm$  and  $\tilde{F}_L^\pm$  at EW leading order (LO) as

$$\frac{d^2\sigma^{\text{NC}}(e^\pm p)}{dx dQ^2} = \frac{2\pi\alpha^2}{xQ^4} \left[ Y_+ \tilde{F}_2^\pm(x, Q^2) \mp Y_- x\tilde{F}_3^\pm(x, Q^2) - y^2 \tilde{F}_L^\pm(x, Q^2) \right], \quad (3.31)$$

where  $\alpha$  denotes the fine structure constant. The terms  $Y_\pm = 1 \pm (1 - y)^2$ , with  $y = Q^2/sx$ , describe the helicity dependence of the process. The generalised structure functions are separated into contributions from pure  $\gamma$ - and  $Z$ -exchange and their interference [100,327]:

$$\tilde{F}_2^\pm = F_2 - (g_V^e \pm P_e g_A^e) \varkappa_Z F_2^{\gamma Z} + [(g_V^e g_V^e + g_A^e g_A^e) \pm 2P_e g_V^e g_A^e] \varkappa_Z^2 F_2^Z, \quad (3.32)$$

$$\tilde{F}_3^\pm = -(g_A^e \pm P_e g_V^e) \varkappa_Z F_3^{\gamma Z} + [2g_V^e g_A^e \pm P_e (g_V^e g_V^e + g_A^e g_A^e)] \varkappa_Z^2 F_3^Z. \quad (3.33)$$

Similar expressions hold for  $\tilde{F}_L$ . In the naive quark-parton model, which corresponds to the LO QCD approximation, the structure functions are calculated as

$$\left[ F_2, F_2^{\gamma Z}, F_2^Z \right] = x \sum_q \left[ Q_q^2, 2Q_q g_V^q, g_V^q g_V^q + g_A^q g_A^q \right] \{q + \bar{q}\}, \quad (3.34)$$

$$x \left[ F_3^{\gamma Z}, F_3^Z \right] = x \sum_q \left[ 2Q_q g_A^q, 2g_V^q g_A^q \right] \{q - \bar{q}\}, \quad (3.35)$$

representing two independent combinations of the quark and anti-quark momentum distributions,  $xq$  and  $x\bar{q}$ . In Eq. (3.33), the quantities  $g_V^f$  and  $g_A^f$  stand for the vector and axial-vector couplings of a fermion ( $f = e$  or  $f = q$  for electron or quark) to the  $Z$  boson, and the coefficient  $\varkappa_Z$  accounts for the  $Z$ -boson propagator including the normalisation of the weak couplings. Both parameters are fully calculable from the electroweak theory. The (effective) coupling parameters depend on the electric charge,  $Q_f$  and the third component of the weak-isospin,  $I_{L,f}^3$ . Using  $\sin^2\theta_W = 1 - \frac{M_W^2}{M_Z^2}$ , one can write

$$g_V^f = \sqrt{\rho_{\text{NC},f}} (I_{L,f}^3 - 2Q_f \kappa_{\text{NC},f} \sin^2\theta_W), \quad \text{and} \quad (3.36)$$

$$g_A^f = \sqrt{\rho_{\text{NC},f}} I_{L,f}^3 \quad \text{with } f = (e, u, d). \quad (3.37)$$

2516 The parameters  $\rho_{NC,f}$  and  $\kappa_{NC,f}$  are calculated as real parts of complex form factors which  
 2517 include the higher-order loop corrections [328–330]. They contain non-leading flavour-specific  
 2518 components.

2519 Predictions for CC DIS are written in terms of the CC structure functions  $W_2$ ,  $xW_3$  and  $W_L$  and  
 2520 higher-order electroweak effects are collected in two form factors  $\rho_{CC,eq}$  and  $\rho_{CC,e\bar{q}}$  [331, 332].

2521 In this study, the on-shell scheme is adopted for the calculation of higher-order corrections.  
 2522 This means that the independent parameters are chosen as the fine structure constant  $\alpha$  and  
 2523 the masses of the weak bosons, the Higgs boson and the fermions. The weak mixing angle is  
 2524 then fixed and  $G_F$  is a prediction, whose higher-order corrections are included in the well-known  
 2525 correction factor  $\Delta r$  [333–335] (see discussion of further contributions in Ref. [100]).

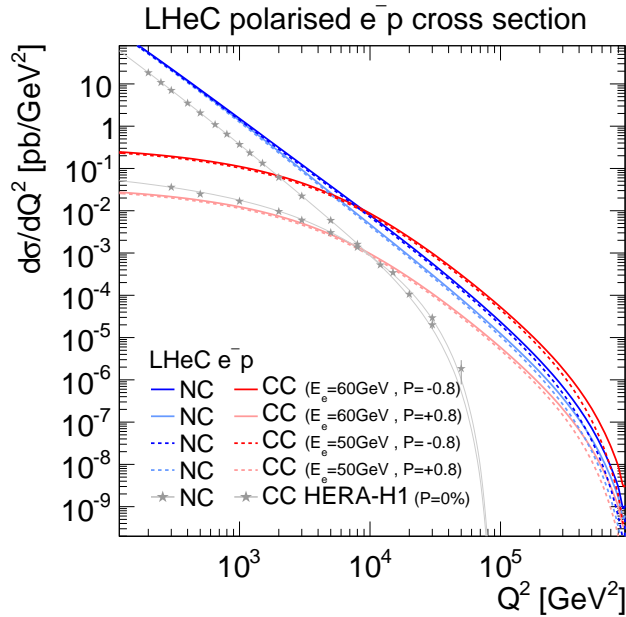


**Figure 3.48:** Single differential cross sections for polarised  $e^-p$  NC and CC DIS at LHeC for two different electron beam energies ( $E_e$ ). Cross sections for longitudinal electron beam polarisations of  $P_e = -0.8$  and  $+0.8$  are displayed. For comparison also measurements at centre-of-mass energies of  $\sqrt{s} = 920$  GeV by H1 at HERA for unpolarised ( $P_e = 0\%$ ) electron beams are displayed [336].

2526 The predicted single-differential inclusive NC and CC DIS cross sections for polarised  $e^-p$  scat-  
 2527 tering as a function of  $Q^2$  are displayed in Fig. 3.48. For NC DIS and at higher  $Q^2$ , electroweak  
 2528 effects are important through  $\gamma Z$  interference and pure  $Z$ -exchange terms and the polarisation  
 2529 of the LHeC electron beam of  $P_e = \pm 0.8$  will considerably alter the cross sections. For CC DIS,  
 2530 the cross section scales linearly with  $P_e$ . Two different electron beam energies are displayed in  
 2531 Fig. 3.48, and albeit the impact of a reduction from  $E_e = 60$  to  $50$  GeV appears to be small,  
 2532 a larger electron beam energy would yield higher precision for the measurement of electroweak  
 2533 parameters, since these are predominantly sensitive to the cross sections at highest scales, as  
 2534 will be shown in the following.

### 2535 3.3.2 Methodology of a combined EW and QCD fit

2536 A complete electroweak analysis of DIS data has to consider PDFs together with electroweak  
 2537 parameters [337]. In this study, the uncertainties of electroweak parameters are obtained in

2538 a combined fit of electroweak parameters and the PDFs, and the inclusive NC and CC DIS  
 2539 pseudodata (see Sec. 3.2.6) are explored as input data. The PDFs are parameterised with 13  
 2540 parameters at a starting scale  $Q_0^2$  and NNLO DGLAP evolution is applied [41, 42]. In this  
 2541 way, uncertainties from the PDFs are taken into account, which is very reasonable, since the  
 2542 PDFs will predominantly be determined from those LHeC data in the future. The details of  
 2543 the PDF fit are altogether fairly similar to the PDF fits outlined in Sec. 3.1. Noteworthy  
 2544 differences are that additionally EW effects are included into the calculation by considering the  
 2545 full set of 1-loop electroweak corrections [338], and the  $\chi^2$  quantity [112], which is input to the  
 2546 minimisation and error propagation, is based on normal-distributed relative uncertainties. In  
 2547 this way, a dependence on the actual size of the simulated cross sections is avoided. The size of  
 2548 the pseudodata are therefore set equivalent to the predictions [339].

### 2549 3.3.3 Weak boson masses $M_W$ and $M_Z$

The expected uncertainties for a determination of the weak boson masses,  $M_W$  and  $M_Z$ , are determined in the PDF+EW-fit, where one of the masses is determined together with the PDFs, while the other mass parameter is taken as external input. The expected uncertainties for  $M_W$  are

$$\begin{aligned} \Delta M_W(\text{LHeC-60}) &= \pm 5_{(\text{exp})} \pm 8_{(\text{PDF})} \text{ MeV} = 10_{(\text{tot})} \text{ MeV} \quad \text{and} \quad (3.38) \\ \Delta M_W(\text{LHeC-50}) &= \pm 8_{(\text{exp})} \pm 9_{(\text{PDF})} \text{ MeV} = 12_{(\text{tot})} \text{ MeV} \end{aligned}$$

for LHeC with  $E_e = 60 \text{ GeV}$  or  $50 \text{ GeV}$ , respectively. The breakdown into experimental and PDF uncertainties is obtained by repeating the fit with PDF parameters fixed. These uncertainties

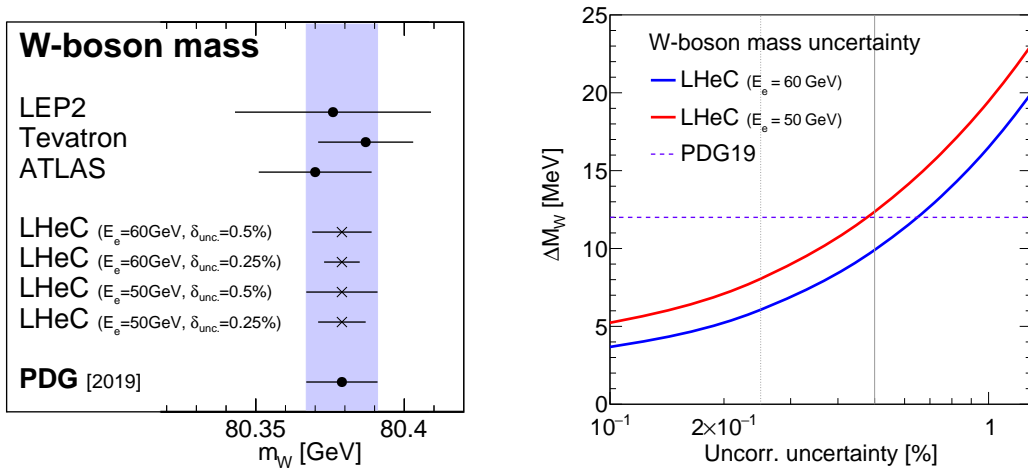


**Figure 3.49:** Left: Measurements of the  $W$ -boson mass assuming fixed values for the top-quark and  $Z$ -boson masses at the LHeC for different scenarios in comparison with today's measurements [340–342] and the world average value (PDG19) [143]. For LHeC, prospects for  $E_e = 60 \text{ GeV}$  and  $50 \text{ GeV}$  are displayed, as well as results for the two scenarios with 0.5% or 0.25% uncorrelated uncertainty (see text). Right: Comparison of the precision for  $M_W$  for different assumptions of the uncorrelated uncertainty of the pseudodata. The uncertainty of the world average value is displayed as horizontal line. The nominal (and alternative) size of the uncorrelated uncertainty of the inclusive NC/CC DIS pseudodata is indicated by the vertical line (see text).

are displayed in Fig. 3.49 and compared to the values obtained by LEP2 [341], Tevatron [340], ATLAS [342] and the PDG value [143]. The LHeC measurement will become the most precise

measurement from one single experiment and will greatly improve over the best measurement achieved by H1, which was  $M_W(\text{H1}) = 80.520 \pm 0.115 \text{ GeV}$  [326]. If the dominating uncorrelated uncertainties can be reduced from the prospected 0.5% to 0.25%<sup>10</sup>, a precision for  $M_W$  of up to

$$\begin{aligned} \Delta M_W(\text{LHeC-60}) &= \pm 3_{(\text{exp})} \pm 5_{(\text{PDF})} \text{ MeV} = 6_{(\text{tot})} \text{ MeV} \quad \text{and} \\ \Delta M_W(\text{LHeC-50}) &= \pm 6_{(\text{exp})} \pm 6_{(\text{PDF})} \text{ MeV} = 8_{(\text{tot})} \text{ MeV} \end{aligned} \quad (3.39)$$

for LHeC-60 and LHeC-50 may be achieved, respectively. A complete dependence of the expected total experimental uncertainty  $\Delta M_W$  on the size of the uncorrelated uncertainty component is displayed in Fig. 3.49, and with a more optimistic scenario an uncertainty of up to  $\Delta M_W \approx 5 \text{ MeV}$  can be achieved. In view of such a high accuracy, it will be important to study carefully theoretical uncertainties. For instance the parameteric uncertainty due to the dependence on the top-quark mass of 0.5 GeV will yield an additional error of  $\Delta M_W = 2.5 \text{ MeV}$ . Also higher-order corrections, at least the dominating 2-loop corrections will have to be studied and kept under control. Then, the prospected determination of the  $W$ -boson mass from LHeC data will be among the most precise determinations and significantly improve the world average value of  $M_W$ . It will also become competitive with its prediction from global EW fits with present uncertainties of about  $\Delta M_W = 7 \text{ MeV}$  [143, 343, 344].

While the determination of  $M_W$  from LHeC data is competitive with other measurements, the experimental uncertainties of a determination of  $M_Z$  are estimated to be about 11 MeV and 13 MeV for LHeC-60 and LHeC-50, respectively. Therefore, the precision of the determination of  $M_Z$  at LHeC cannot compete with the precise measurements at the  $Z$ -pole by LEP+SLD and future  $e^+e^-$  colliders may even improve on that.

A simultaneous determination of  $M_W$  and  $M_Z$  is displayed in Fig. 3.50 (left). Although the precision of these two mass parameters is only moderate, a meaningful test of the high-energy behaviour of electroweak theory is obtained by using  $G_F$  as additional input: The high precision of the  $G_F$  measurement [345] yields a very shallow error ellipse and a precise test of the SM can be performed with only NC and CC DIS cross sections alone. Such a fit determines and simultaneously tests the high-energy behaviour of electroweak theory, while using only low-energy parameters  $\alpha$  and  $G_F$  as input (plus values for masses like  $M_t$  and  $M_H$  needed for loop corrections).

### 3.3.4 Further mass determinations

Inclusive DIS data are sensitive to the top-quark mass  $M_t$  indirectly through radiative corrections.  $M_t$ -dependent terms are dominantly due to corrections from the gauge boson self-energy corrections. They are contained in the  $\rho$  and  $\kappa$  parameters and in the correction factor  $\Delta r$ . The leading contributions are proportional to  $M_t^2$ . This allows for an indirect determination of the top-quark mass using LHeC inclusive DIS data, and a determination of  $M_t$  will yield an uncertainty of  $\Delta M_t = 1.8 \text{ GeV}$  to  $2.2 \text{ GeV}$ . Assuming an uncorrelated uncertainty of the DIS data of 0.25% the uncertainty of  $M_t$  becomes as small as

$$\Delta M_t = 1.1 \text{ to } 1.4 \text{ GeV} \quad (3.40)$$

<sup>10</sup>Due to performance reasons, the pseudodata are generated for a rather coarse grid. With a binning which is closely related to the resolution of the LHeC detector, much finer grids in  $x$  and  $Q^2$  are feasible. Already such a change would alter the uncertainties of the fit parameters. However, such an effect can be reflected by a changed uncorrelated uncertainty, and a value of 0.25% appears like an optimistic, but achievable, alternative scenario.

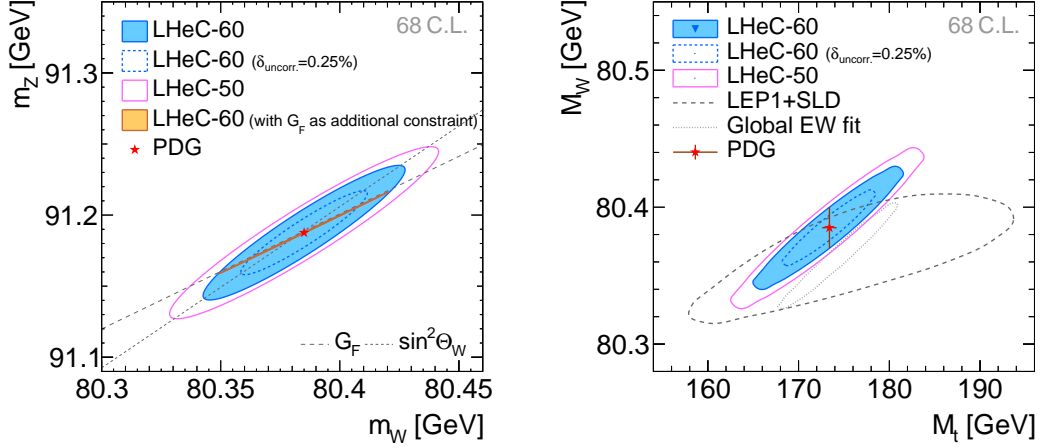


**Figure 3.50:** Simultaneous determination of the top-quark mass  $M_t$  and  $W$ -boson mass  $M_W$  from LHeC-60 or LHeC-50 data (left). Simultaneous determination of the  $W$ -boson and  $Z$ -boson masses from LHeC-60 or LHeC-50 data (right).

2582 for 60 and 50 GeV electron beams, respectively. This would represent a very precise indirect  
 2583 determination of the top-quark mass from purely electroweak corrections and thus being fully  
 2584 complementary to measurements based on real  $t$ -quark production, which often suffer from  
 2585 sizeable QCD corrections. The precision achievable in this way will be competitive with indirect  
 2586 determinations from global EW fits after the HL-LHC [346].

2587 More generally, and to some extent depending on the choice of the renormalisation scheme, the  
 2588 leading self-energy corrections are proportional to  $\frac{M_t^2}{M_W^2}$  and thus a simultaneous determination  
 2589 of  $M_t$  and  $M_W$  is desirable. The prospects for a simultaneous determination of  $M_t$  and  $M_W$   
 2590 is displayed in Fig. 3.50 (right). It is remarkable that the precision of the LHeC is superior  
 2591 to that of the LEP+SLD combination [347]. In an optimistic scenario an uncertainty similar  
 2592 to the global electroweak fit [344] can be achieved. In a fit without PDF parameters similar  
 2593 uncertainties are found (not shown), which illustrates that the determination of EW parameters  
 2594 is to a large extent independent of the QCD phenomenology and the PDFs.

2595 The subleading contributions to self-energy corrections have a Higgs-boson mass dependence  
 2596 and are proportional to  $\log \frac{M_H^2}{M_W^2}$ . When fixing all other EW parameters the Higgs boson mass  
 2597 could be constrained indirectly through these loop corrections with an experimental uncertainty  
 2598 of  $\Delta m_H = {}^{+29}_{-23}$  to  ${}^{+24}_{-20}$  GeV for different LHeC scenarios, which is again similar to the indirect  
 2599 constraints from a global electroweak fit [344], but not competitive with direct measurements.

### 2600 3.3.5 Weak Neutral Current Couplings

2601 The vector and axial-vector couplings of up-type and down-type quarks to the  $Z$ ,  $g_V^q$  and  $g_A^q$ ,  
 2602 see Eq. (3.37), are determined in a fit of the four coupling parameters together with the PDFs.

2603 The resulting uncertainties are collected in Tab. 3.4. The two-dimensional uncertainty contours  
 2604 at 68 % confidence level obtained from LHeC data with  $E_e = 50$  GeV are displayed in Fig. 3.51  
 2605 for the two quark families and compared with available measurements. While all the current  
 2606 determinations from  $e^+e^-$ ,  $ep$  or  $p\bar{p}$  data have a similar precision, the future LHeC data will  
 2607 greatly improve the precision of the weak neutral-current couplings and expected uncertainties

Coupling parameter	PDG value	Expected uncertainties		
		LHeC-60	LHeC-60 ( $\delta_{\text{uncor.}}=0.25\%$ )	LHeC-50
$g_A^u$	$0.50^{+0.04}_{-0.05}$	0.0022	0.0015	0.0035
$g_A^d$	$-0.514^{+0.050}_{-0.029}$	0.0055	0.0034	0.0083
$g_V^u$	$0.18 \pm 0.05$	0.0015	0.0010	0.0028
$g_V^d$	$-0.35^{+0.05}_{-0.06}$	0.0046	0.0027	0.0067

**Table 3.4:** Light-quark weak NC couplings ( $g_A^u, g_A^d, g_V^u, g_V^d$ ) and their currently most precise values from the PDG [143] compared with the prospected uncertainties for different LHeC scenarios. The LHeC prospects are obtained in a simultaneous fit of the PDF parameters and all four coupling parameters determined at a time.

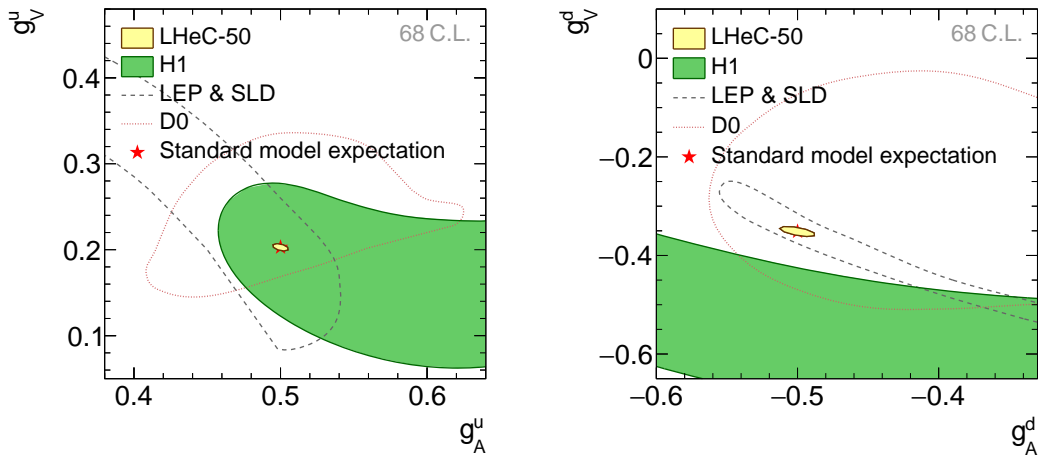


**Figure 3.51:** Weak NC vector and axial-vector couplings of  $u$ -type (left) and  $d$ -type quarks (right) at 68% confidence level (C.L.) for simulated LHeC data with  $E_e = 50$  GeV. The LHeC expectation is compared with results from the combined LEP+SLD experiments [347], a single measurement from D0 [348] and one from H1 [326]. The standard model expectations are displayed by a red star, partially hidden by the LHeC prospects.

2608 are an order of magnitude smaller than the currently most precise ones [143]. An increased  
2609 electron beam energy of  $E_e = 60$  GeV or improved experimental uncertainties would further  
2610 improve this measurement.

2611 The determination of the couplings of the electron to the  $Z$  boson,  $g_V^e$  and  $g_A^e$ , can be determined  
2612 at the LHeC with uncertainties of up to  $\Delta g_V^e = 0.0013$  and  $\Delta g_A^e = \pm 0.0009$ , which is similar  
2613 to the results of a single LEP experiment and about a factor three larger than the LEP+SLD  
2614 combination [347].

### 2615 3.3.6 The neutral-current $\rho_{\text{NC}}$ and $\kappa_{\text{NC}}$ parameters

2616 Beyond Born approximation, the weak couplings are subject to higher-order loop corrections.  
2617 These corrections are commonly parameterised by quantities called  $\rho_{\text{NC}}$ ,  $\kappa_{\text{NC}}$  and  $\rho_{\text{CC}}$ . They are  
2618 sensitive to contributions beyond the SM and the structure of the Higgs sector. It is important  
2619 to keep in mind that these effective coupling parameters depend on the momentum transfer  
2620 and are, indeed, form factors rather than constants. It is particularly interesting to investigate  
2621 the so-called effective weak mixing angle defined as  $\sin^2 \theta_{\text{W}}^{\text{eff}} = \kappa_{\text{NC}} \sin^2 \theta_{\text{W}}$ . At the  $Z$ -pole it

is well accessible through asymmetry measurements in  $e^+e^-$  collisions. In DIS at the LHeC, the scale dependence of the effective weak mixing angle is not negligible. It can be determined only together with the  $\rho$  parameter due to the  $Q^2$  dependence and the presence of the photon exchange terms. Therefore, we introduce (multiplicative) anomalous contributions to these factors, denoted as  $\rho'_{\text{NC},\text{CC}}$  and  $\kappa'_{\text{NC}}$ , and test their agreement with unity (for more details see Ref. [326]), and uncertainties of these parameters are obtained in a fit together with the PDFs. The two-dimensional uncertainty contours of the anomalous form factors  $\rho'_{\text{NC},f}$  and  $\kappa'_{\text{NC},f}$  are

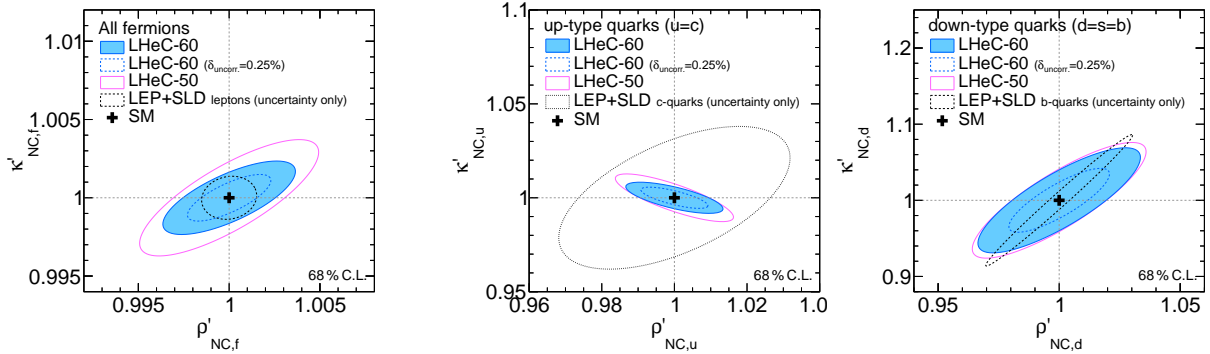


**Figure 3.52:** Expectations at 68 % confidence level for the determination of the  $\rho'_{\text{NC}}$  and  $\kappa'_{\text{NC}}$  parameters assuming a single anomalous factor equal for all fermions (left). The results for three different LHeC scenarios are compared with the achieved uncertainties from the LEP+SLD combination [347] for the determination the respective leptonic quantities. Right: uncertainties for the simultaneous determination of the anomalous form factors for  $u$  and  $d$ -type quarks, assuming known values for the electron parameters. The values are compared with uncertainties reported by LEP+SLD for the determination of the values  $\rho_{\text{NC},(c,b)}$  and  $\sin\theta_{\text{W}}^{\text{eff},(c,b)}$  for charm or bottom quarks, respectively.

displayed for three different LHeC scenarios in Fig. 3.52 (left), and compared with uncertainties from the LEP+SLD combination<sup>11</sup> [347]. It is found that these parameters can be determined with very high experimental precision.

Assuming the couplings of the electron are given by the SM, the anomalous form factors for the two quark families can be determined and results are displayed in Fig. 3.52 (right). Since these measurements represent unique determinations of parameters sensitive to the light-quark couplings, we can compare only with nowadays measurements of the parameters for heavy-quarks of the same charge and it is found that the LHeC will provide high-precision determinations of the  $\rho'_{\text{NC}}$  and  $\kappa'_{\text{NC}}$  parameters.

A meaningful test of the SM can be performed by determining the effective coupling parameters as a function of the momentum transfer. In case of  $\kappa'_{\text{NC}}$ , this is equivalent to measuring the running of the effective weak mixing angle,  $\sin\theta_{\text{W}}^{\text{eff}}(\mu)$  (see also Sec. 3.3.7). However, DIS is quite complementary to other measurements since the process is mediated by space-like momentum transfer, i.e.  $q^2 = -Q^2 < 0$  with  $q$  being the boson four-momentum. Prospects for a determination of  $\rho'_{\text{NC}}$  or  $\kappa'_{\text{NC}}$  at different  $Q^2$  values are displayed in Fig. 3.53 and compared to results obtained by H1. The value of  $\kappa'_{\text{NC}}(\mu)$  can be easily translated to a measurement of  $\sin\theta_{\text{W}}^{\text{eff}}(\mu)$ . From Fig. 3.53 one can conclude that this quantity can be determined with a precision of up to 0.1 % and better than 1 % over a wide kinematic range of about  $25 < \sqrt{Q^2} < 700$  GeV.

<sup>11</sup>Since in the LEP+SLD analysis the values of  $\rho_{\text{NC}}$  and  $\kappa_{\text{NC}}\sin^2\theta_{\text{W}}$  are determined, we compare only the size of the uncertainties in these figures. Furthermore it shall be noted, that LEP is mainly sensitive to the parameters of leptons or heavy quarks, while LHeC data is more sensitive to light quarks ( $u,d,s$ ), and thus the LHeC measurements are highly complementary.

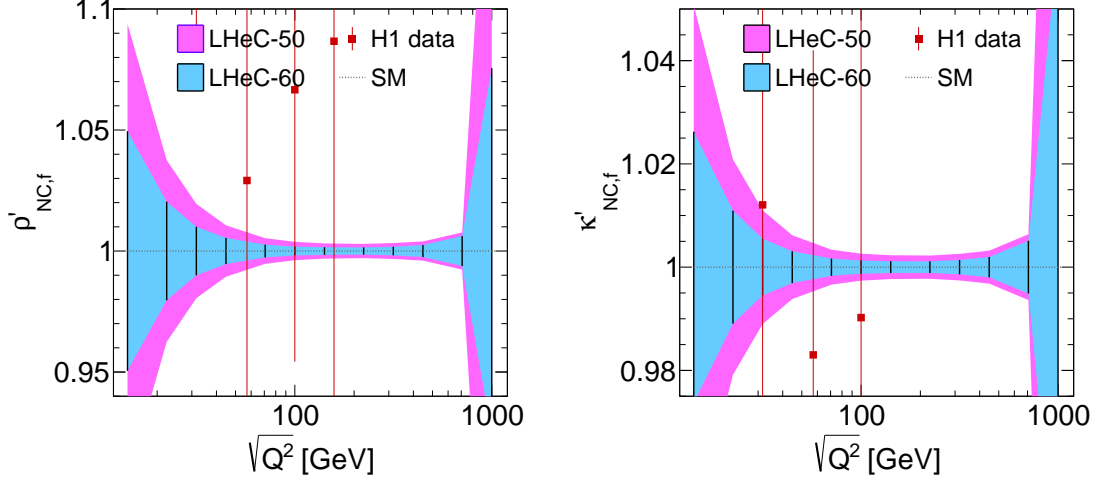


**Figure 3.53:** Test of the scale dependence of the anomalous  $\rho$  and  $\kappa$  parameters for two different LHeC scenarios. For the case of LHeC-60, i.e.  $E_e = 60$  GeV, we assume an uncorrelated uncertainty of 0.25%. The uncertainties of the parameter  $\kappa'_{NC,f}$  can be interpreted as sensitivity to the scale-dependence of the weak mixing angle,  $\sin^2 \theta_W^{\text{eff}}(\mu)$ .

### 2647 3.3.7 The effective weak mixing angle $\sin^2 \theta_W^{\text{eff},\ell}$

2648 The leptonic effective weak mixing angle is defined as  $\sin^2 \theta_W^{\text{eff},\ell}(\mu^2) = \kappa_{NC,\ell}(\mu^2) \sin^2 \theta_W$ . Due to  
 2649 its high sensitivity to loop corrections it represents an ideal quantity for precision tests of the  
 2650 Standard Model. Its value is scheme dependent and it exhibits a scale dependence. Near the  
 2651  $Z$  pole,  $\mu^2 = M_Z^2$ , its value was precisely measured at LEP and at SLD. Those analyses were  
 2652 based on the measurement of asymmetries and their interpretation in terms of the leptonic weak  
 2653 mixing angle was simplified by the fact that many non-leptonic corrections and contributions  
 2654 from box graphs cancel or can be taken into account by subtracting their SM predictions. The  
 2655 highest sensitivity to  $\sin^2 \theta_W^{\text{eff},\ell}(M_Z)$  to date arises from a measurement of  $A_{\text{fb}}^{0,b}$  [347], where  
 2656 the non-universal flavour-specific corrections to the quark couplings are taken from the SM  
 2657 and consequently these measurements are interpreted to be sensitive only to the universal, i.e.  
 2658 flavour-independent<sup>12</sup>, non-SM contributions to  $\kappa_{NC}$ . Applying this assumption also to the DIS  
 2659 cross sections, the determination of  $\kappa'_{NC,f}$  can directly be interpreted as a sensitivity study of  
 2660 the leptonic effective weak mixing angle  $\sin^2 \theta_W^{\text{eff},\ell}$ .

2661 The prospects for a determination of  $\sin^2 \theta_W^{\text{eff},\ell}$  are listed in Tab. 3.5. Two fits have been studied:  
 2662 one with a fixed parameter  $\rho'_{NC}$  and one where  $\sin^2 \theta_W^{\text{eff},\ell}$  is determined together with  $\rho'_{NC}$  (see  
 2663 Fig. 3.52 (left)). At the LHeC, it will be possible to determine the value of  $\sin^2 \theta_W^{\text{eff},\ell}(M_Z^2)$  with  
 2664 an experimental uncertainty of up to

$$\Delta \sin^2 \theta_W^{\text{eff},\ell} = \pm 0.00015, \quad (3.41)$$

2665 where PDF uncertainties are already included. If the PDF parameters are artificially kept  
 2666 fixed, the uncertainties are of very similar size, which demonstrates that these measurements  
 2667 are fairly insensitive to the QCD effects and the PDFs. The uncertainties are compared<sup>13</sup> to  
 2668 recent average values in Fig. 3.54. One can see that the LHeC measurement has the potential to

<sup>12</sup>Flavour-specific tests have been discussed to some extent in the previous Section.

<sup>13</sup>It shall be noted, that in order to compare the LHeC measurements with the  $Z$ -pole measurements at  $\mu^2 = M_Z^2$  in a conclusive way, one has to assume the validity of the SM framework. In particular the scale-dependence of

Fit parameters	Parameter of interest	SM value	Expected uncertainties			
			LHeC-50 ( $\delta_{\text{uncor.}} = 0.50\%$ )	LHeC-60	LHeC-50 ( $\delta_{\text{uncor.}} = 0.25\%$ )	LHeC-60
$\kappa'_{\text{NC},f}$ , PDFs	$\sin^2 \theta_{\text{W}}^{\text{eff},\ell}(M_Z^2)$	0.23154	0.00033	0.00025	0.00022	0.00015
$\kappa'_{\text{NC},f}, \rho'_{\text{NC},f}$ , PDFs	$\sin^2 \theta_{\text{W}}^{\text{eff},\ell}(M_Z^2)$	0.23154	0.00071	0.00036	0.00056	0.00023
$\kappa'_{\text{NC},e}$ , PDFs	$\sin^2 \theta_{\text{W}}^{\text{eff},e}(M_Z^2)$	0.23154	0.00059	0.00047	0.00038	0.00028
$\kappa'_{\text{NC},e}, \kappa'_{\text{NC},u}, \kappa'_{\text{NC},d}$ , PDFs	$\sin^2 \theta_{\text{W}}^{\text{eff},e}(M_Z^2)$	0.23154	0.00111	0.00095	0.00069	0.00056
$\kappa'_{\text{NC},f}$	$\sin^2 \theta_{\text{W}}^{\text{eff},\ell}(M_Z^2)$	0.23154	0.00028	0.00023	0.00017	0.00014

**Table 3.5:** Determination of  $\sin^2 \theta_{\text{W}}^{\text{eff},\ell}(M_Z^2)$  with inclusive DIS data at the LHeC for different scenarios. Since the value of the effective weak mixing angle at the  $Z$  pole cannot be determined directly in DIS, a fit of the  $\kappa'_{\text{NC},f}$  parameter is performed instead and its uncertainty is translated to  $\sin^2 \theta_{\text{W}}^{\text{eff},\ell}(M_Z^2)$ . Different assumptions on the fit parameters are studied, and results include uncertainties from the PDFs. Only the last line shows results where the PDF parameters are kept fixed. See text for more details.

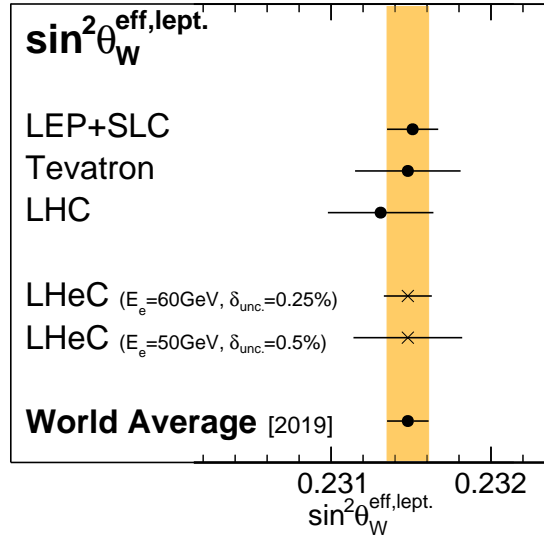


**Figure 3.54:** Comparison of the determination of  $\sin^2 \theta_{\text{W}}^{\text{eff},\ell}(M_Z^2)$  from LHeC inclusive DIS data with recent averaged values. Results from LEP+SLC [347], Tevatron [349], LHC [350–353] and the world average value [353] are all obtained from a combination of various separate measurements (not shown individually) (see also Ref. [354] for additional discussions). For LHeC, the experimental and PDF uncertainties are displayed.

2669 become the most precise single measurement in the future with a significant impact to the world  
2670 average value. It is obvious that a conclusive interpretation of experimental results with such a  
2671 high precision will require correspondingly precise theoretical predictions, and the investigation  
2672 of two-loop corrections for DIS will become important.

2673 This LHeC measurement will become competitive with measurements at the HL-LHC [147].  
2674 Since in  $pp$  collisions one of the dominant uncertainty is from the PDFs, future improvements  
2675 can (only) be achieved with a common analysis of LHeC and HL-LHC data. Such a study will

$\kappa_{\text{NC},\ell}$  must be known in addition to the flavour-specific corrections. On the other hand, the scale dependence can be tested itself with the LHeC data which cover a large range of space-like  $Q^2$ . In this aspect, DIS provides a unique opportunity for precision measurements in the space-like regime ( $\mu^2 < 0$ ) as has been discussed in the previous Section, see Fig. 3.53 (right).

2676 yield highest experimental precision and the challenging theoretical and experimental aspects for  
 2677 a complete understanding of such an analysis will deepen our understanding of the electroweak  
 2678 sector.

2679 It may be further of interest, to determine the value of the effective weak mixing angle of the  
 2680 electron separately in order to compare with measurements in  $pp$  and test furthermore lepton-  
 2681 specific contributions to  $\kappa_{\text{NC,lept.}}$ . Such fits are summarised in Table 3.5 and a reasonable  
 2682 precision is achieved with LHeC.

### 2683 3.3.8 Electroweak effects in charged-current scattering

2684 The charged-current sector of the SM can be uniquely measured at high scales over many orders  
 2685 of magnitude in  $Q^2$  at the LHeC, due to the excellent tracking detectors, calorimetry, and high-  
 2686 bandwidth triggers. Similarly as in the NC case, the form factors of the effective couplings of  
 2687 the fermions to the  $W$  boson can be measured. In the SM formalism, only two of these form  
 2688 factors are present,  $\rho_{CC,eq}$  and  $\rho_{CC,e\bar{q}}$ . We thus introduce two anomalous modifications to them,  
 2689  $\rho_{CC,(eq/e\bar{q})} \rightarrow \rho'_{CC,(eq/e\bar{q})}\rho_{CC,(eq/e\bar{q})}$  (see Ref. [326]). The prospects for the determination of these  
 2690 parameters are displayed in Fig. 3.55, and it is found, that with the LHeC these parameters  
 2691 can be determined with a precision up to 0.2–0.3%. Also their  $Q^2$  dependence can be uniquely  
 studied with high precision up to  $\sqrt{Q^2}$  values of about 400 GeV.

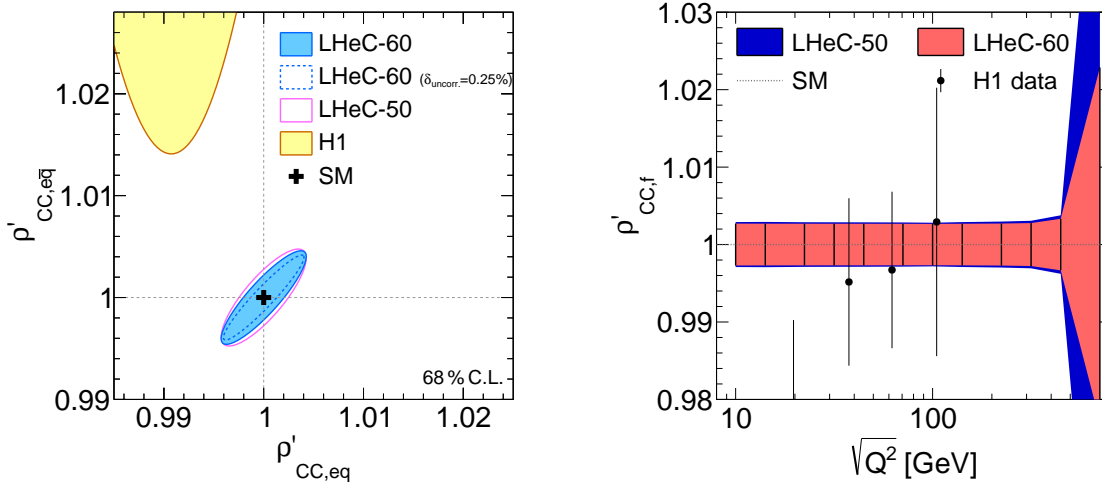


**Figure 3.55:** Left: anomalous modifications of the charged current form factors  $\rho'_{CC,eq}$  and  $\rho'_{CC,e\bar{q}}$  for different LHeC scenarios in comparison with the H1 measurement [326]. Right: scale dependent measurement of the anomalous modification of the charged current form factor  $\rho'_{CC}(Q^2)$ , assuming  $\rho'_{CC,eq} = \rho'_{CC,e\bar{q}} = \rho'_{CC}$ .

2692

### 2693 3.3.9 Direct $W$ and $Z$ production and Anomalous Triple Gauge Couplings

2694 The direct production of single  $W$  and  $Z$  bosons as a crucial signal represents an important  
 2695 channel for EW precision measurements. The production of  $W$  bosons has been measured at  
 2696  $\sqrt{s} \simeq 320$  GeV at HERA [355–357]. With the full  $e^\pm p$  data set collected by the H1 and ZEUS  
 2697 experiments together, corresponding to an integrated luminosity of about  $\mathcal{L} \sim 1 \text{ fb}^{-1}$ , a few  
 2698 dozens of  $W$  boson event candidates have been identified in the  $e$ ,  $\mu$  or  $\tau$  decay channel.

2699 Detailed studies of direct  $W/Z$  production in  $ep$  collisions at higher centre-of-mass energies have  
 2700 been presented in the past, see Refs. [358–360]. These theoretical studies were performed for  
 2701 a proton beam energy of  $E_p = 8$  TeV and electron beam energies of  $E_e = 55$  GeV or 100 GeV,  
 2702 which correspond to a very similar centre-of-mass energy as the LHeC. Measurements at the  
 2703 LHeC will benefit considerably from the large integrated luminosity, in comparison to earlier  
 2704 projections.

2705 The  $W$  or  $Z$  direct production in  $e^-p$  collisions can be classified into five processes

$$\begin{aligned} e^-p &\rightarrow e^-W^+j, & e^-p &\rightarrow e^-W^-j, \\ e^-p &\rightarrow \nu_e^-W^-j, & e^-p &\rightarrow \nu_e^-Zj \end{aligned} \quad (3.42)$$

2706 and

$$e^-p \rightarrow e^-Zj, \quad (3.43)$$

2707 where  $j$  denotes the hadronic the final state (i.e. the *forward jet*). According to the above  
 2708 classification, the four processes in Eq.(3.42) can be used to study Tripe Gauge Couplings  
 2709 (TGCs), e.g.  $WW\gamma$  and  $WWZ$  couplings, since some contributing diagrams represent Vector  
 2710 Boson Fusion (VBF) processes. The process shown in Eq.(3.43) does not contain any TGC  
 2711 vertex. The processes for positron-proton collisions can be easily derived from Eqs. (3.42)  
 2712 and (3.43), but are not discussed further here due to the small integrated luminosity of the  
 2713 LHeC  $e^+p$  data.

2714 The MadGraph5\_v2.4.2 program [361] is employed for matrix element calculation and event gen-  
 2715 eration and the PDF NNPDF23\_nlo\_as\_0119\_qed [362] is used. Technical cuts on the transverse  
 2716 momentum of the outgoing scattered lepton,  $p_T^\ell$ , of 10 GeV or alternatively 5 GeV, are imposed  
 2717 and other basic cuts are  $p_T^j > 20$  GeV,  $|\eta_{e,j}| < 5$  and  $\Delta R_{ej} < 0.4$ . The resulting Standard Model  
 total cross sections of the above processes are listed in Tab. 3.6.

Process	$E_e = 50$ GeV, $E_p = 7$ TeV $p_T^e > 10$ GeV	$E_e = 60$ GeV, $E_p = 7$ TeV $p_T^e > 10$ GeV	$E_e = 60$ GeV, $E_p = 7$ TeV $p_T^e > 5$ GeV
$e^-W^+j$	1.00 pb	1.18 pb	1.60 pb
$e^-W^-j$	0.930 pb	1.11 pb	1.41 pb
$\nu_e^-W^-j$	0.796 pb	0.956 pb	0.956 pb
$\nu_e^-Zj$	0.412 pb	0.502 pb	0.502 pb
$e^-Zj$	0.177 pb	0.204 pb	0.242 pb

**Table 3.6:** The SM predictions of direct  $W$  and  $Z$  production cross sections in  $e^-p$  collisions for different collider beam energy options,  $E_e$ , and final state forward electron transverse momentum cut,  $p_T^e$ . Two different electron beam energy options are considered,  $E_e = 50$  GeV and 60 GeV.

2718

2719 The process with the largest production cross section in  $e^-p$  scattering is the single  $W^+$  boson  
 2720 production. This will be the optimal channel of both the SM measurement and new physics  
 2721 probes in the EW sector. Also, this channel is experimentally preferred since the  $W^+$  is produced  
 2722 in NC scattering, so the beam electron is measured in the detector, and the  $W$ -boson has opposite  
 2723 charge to the beam lepton and thus in a leptonic decay an opposite charge lepton and missing  
 2724 transverse momentum is observed. Altogether, it is expected that a few million of direct  $W$ -  
 2725 boson events are measured at LHeC.

2726 Several  $10^5$  direct  $Z$  events are measured, which corresponds approximately to the size of the  
 2727 event sample of the SLD experiment [347], but at the LHeC these  $Z$  bosons are predominantly  
 2728 produced in VBF events.

2729 All these total cross sections increase significantly with smaller transverse momentum of the  
 2730 outgoing scattered lepton. Therefore it will become important to decrease that threshold with  
 2731 dedicated electron taggers, see Chapter 10.

2732 The measurement of gauge boson production processes provides a precise measurement of the  
 2733 triple gauge boson vertex. The measurement is sensitive to new physics contributions in *anoma-*  
 2734 *lous* Tripe Gauge Couplings (aTGC). The LHeC has advantages of a higher centre-of-mass  
 2735 energy and easier kinematic analysis in the measurement of aTGCs.

2736 In the effective field theory language, aTGCs in the Lagrangian are generally parameterised as

$$\begin{aligned}
 \mathcal{L}_{TGC}/g_{WWV} &= ig_{1,V}(W_{\mu\nu}^+W_{\mu}^-V_{\nu} - W_{\mu\nu}^-W_{\mu}^+V_{\nu}) + i\kappa_V W_{\mu}^+W_{\nu}^-V_{\mu\nu} + \frac{i\lambda_V}{M_W^2}W_{\mu\nu}^+W_{\nu\rho}^-V_{\rho\mu} \\
 &+ g_5^V \epsilon_{\mu\nu\rho\sigma}(W_{\mu}^+ \overleftrightarrow{\partial}_{\rho} W_{\nu}^-)V_{\sigma} - g_4^V W_{\mu}^+W_{\nu}^-(\partial_{\mu}V_{\nu} + \partial_{\nu}V_{\mu}) \\
 &+ i\tilde{\kappa}_V W_{\mu}^+W_{\nu}^- \tilde{V}_{\mu\nu} + \frac{i\tilde{\lambda}_V}{M_W^2}W_{\lambda\mu}^+W_{\mu\nu}^- \tilde{V}_{\nu\lambda},
 \end{aligned} \tag{3.44}$$

2737 where  $V = \gamma, Z$ . The gauge couplings  $g_{WW\gamma} = -e$ ,  $g_{WWZ} = -e \cot \theta_W$  and the weak mixing  
 2738 angle  $\theta_W$  are from the SM.  $\tilde{V}_{\mu\nu}$  and  $A \overleftrightarrow{\partial}_{\mu} B$  are defined as  $\tilde{V}_{\mu\nu} = \frac{1}{2}\epsilon_{\mu\nu\rho\sigma}V_{\rho\sigma}$ ,  $A \overleftrightarrow{\partial}_{\mu} B = A(\partial_{\mu}B) -$   
 2739  $(\partial_{\mu}A)B$ , respectively. There are five aTGCs ( $g_{1,Z}$ ,  $\kappa_V$ , and  $\lambda_V$ ) conserving the  $C$  and  $CP$   
 2740 condition with electromagnetic gauge symmetry requires  $g_{1,\gamma} = 1$ . Only three of them are  
 2741 independent because  $\lambda_Z = \lambda_{\gamma}$  and  $\Delta\kappa_Z = \Delta g_{1,Z} - \tan^2 \theta_W \Delta\kappa_{\gamma}$  [363–365]. The LHeC can set  
 2742 future constraints on  $\Delta\kappa_{\gamma}$  and  $\lambda_{\gamma}$ .

2743 In the direct  $Z/\gamma$  production process, the anomalous  $WWZ$  and  $WW\gamma$  couplings can be sep-  
 2744 arately measured without being influenced by their interference [366, 367]. In the direct  $W$   
 2745 production process, both the deviation in signal cross section and the kinematic distributions  
 2746 can effectively constrain the  $WW\gamma$  aTGC, while anomalous  $WWZ$  contribution in this channel  
 2747 is insensitive as a result of the suppression from  $Z$  boson mass [368–370].

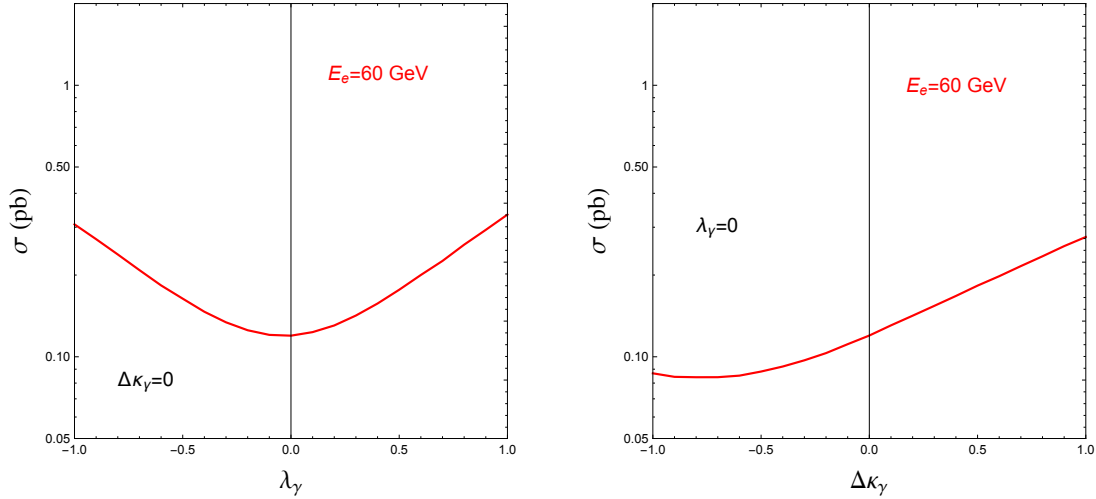


**Figure 3.56:** Total cross sections of the  $e^-p \rightarrow e^-\mu^+\nu_\mu j$  process with varying  $\lambda_\gamma$  (left plot) and  $\Delta\kappa_\gamma$  (right plot).

2748 The  $W$  decay into muon channel is the expected optimal measurement for the anomalous  $WW\gamma$   
 2749 coupling because of the discrimination of final states and mistagging efficiencies [368]. Fig. 3.56  
 2750 shows the cross section of single  $W^+$  production process followed by  $W^+ \rightarrow \mu^+\nu_\mu$  decay, with  
 2751 different  $\lambda_\gamma$  and  $\Delta\kappa_\gamma$  values. Large anomalous coupling leads to measurable deviation to the

2752 SM prediction. The cross section increases monotonically with  $\Delta\kappa_\gamma$  and the absolute value of  
 2753  $\lambda_\gamma$  within the region of  $-1.0 \leq \lambda_\gamma/\Delta\kappa_\gamma \leq 1.0$ .

2754 Kinematic analysis is necessary for the precise aTGC measurement. At LHeC, the  $e^-p \rightarrow$   
 2755  $e^-W^\pm j$  process with leptonic  $W$  boson decay can be fully reconstructed because the unde-  
 2756 tected neutrino information is reconstructed either with energy-momentum conservation or the  
 2757 recoil mass method. This allows to use angular correlation observables, which are sensitive to  
 2758 the  $W$  boson polarization. Helicity amplitude calculation indicates that a non-SM value of  $\lambda_\gamma$   
 2759 leads to a significant enhancement in the transverse polarization fraction of the  $W$  boson in the  
 2760  $e^-p \rightarrow e^-W^+j$  process, while a non-SM value of  $\Delta\kappa_\gamma$  leads to enhancement in the longitudinal  
 2761 component fraction [358]. The angle  $\theta_{\ell W}$  is defined as the angle between the decay product  
 2762 lepton  $\ell$  in the  $W$  rest frame and  $W$  moving direction in the collision rest frame. Making use  
 2763 of the energetic final states in the forward direction, a second useful angle  $\Delta\phi_{ej}$  is defined as  
 2764 the separation of final state jet and electron on the azimuthal plane. In an optimised analysis,  
 2765 assuming an integrated luminosity of  $1 \text{ ab}^{-1}$ , the observable  $\Delta\phi_{ej}$  can impose stringent con-  
 2766 straints on both  $\lambda_\gamma$  and  $\Delta\kappa_\gamma$ , and uncertainties within  $[-0.007, 0.0056]$  and  $[-0.0043, 0.0054]$   
 2767 are achieved, respectively. The  $\cos\theta_{\mu W}$  observable is also sensitive to  $\Delta\kappa_\gamma$  at the same order,  
 2768 but fails to constrain  $\lambda_\gamma$ . The analysis is described in detail in Ref. [368].

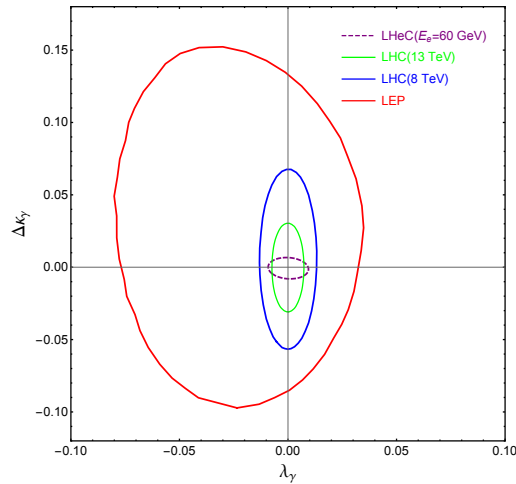


**Figure 3.57:** The 95% C.L. exclusion limit on the  $\Delta\kappa_\gamma$ - $\lambda_\gamma$  plane. The purple dashed contour is the projected LHeC exclusion limit with  $1 \text{ ab}^{-1}$  integrated luminosity [368]. The blue, green and red contours are current bounds from LHC [371, 372] and LEP [373].

2769 Fig. 3.57 shows the two-parameter aTGC constraint on the  $\lambda_\gamma$ - $\Delta\kappa_\gamma$  plane based on a  $\chi^2$  analysis  
 2770 of  $\Delta\phi_{ej}$  at parton-level and assuming an electron beam energy of  $E_e = 60 \text{ GeV}$ . When comparing  
 2771 with the current LHC (blue and green) and LEP (red) bounds, the LHeC has the potential  
 2772 to significantly improve the constraints, in particular on the  $\Delta\kappa_\gamma$  parameter. The polarised  
 2773 electron beam is found to improve the aTGC measurement [367, 370]. In consideration of the  
 2774 *realistic* analysis at detector level, one expects  $2\text{-}3 \text{ ab}^{-1}$  integrated luminosity to achieve same  
 2775 results [368].

2776 One uncertainty in the aTGC measurement at the (HL-)LHC comes from the PDF uncertainty.  
 2777 Future LHeC PDF measurement will improve the precision of aTGC measurement in the  $x \simeq$   
 2778  $\mathcal{O}(10^{-2})$  region.

2779 **3.3.10 Radiation Amplitude Zero**

2780 The LHeC is ideal for testing a novel feature of the Standard Model: the *radiation amplitude*  
 2781 *zero* [374–377] of the amplitude  $\gamma W^- \rightarrow c\bar{b}$  and related amplitudes, see Fig. 3.58. The Born  
 2782 amplitude is predicted to vanish and change sign at  $\cos\theta_{CM} = \frac{e_{\bar{b}}}{e_{\gamma W}} = -1/3$ . This LHeC mea-  
 2783 surement tests  $W$  compositeness and its zero anomalous magnetic moment at leading order:  
 2784  $g_W = 2, \kappa_W = 1$ , as well as  $g_q = 2$  for quarks.. One can also test the radiation amplitude zero  
 for the top quark from  $\gamma b \rightarrow W^- t$ .

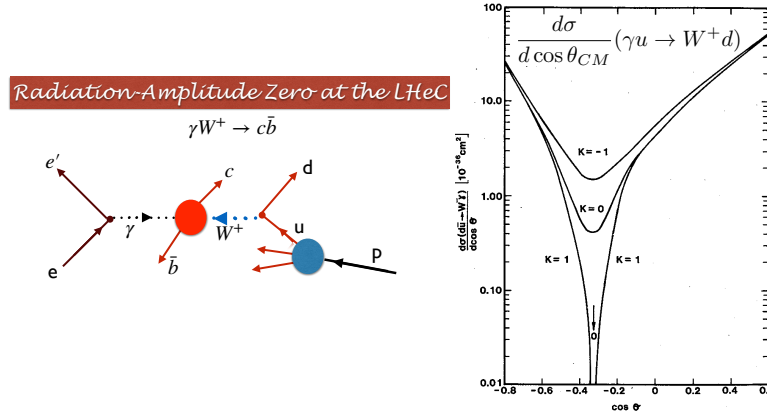


**Figure 3.58:** The radiation amplitude zero of the Standard Model in  $\gamma W^+ \rightarrow c\bar{b}$  and  $\gamma u \rightarrow W^+ d$ . The prediction for the angular distribution  $\frac{d\sigma}{d\cos(\theta_{CM})}(\gamma u \rightarrow W^+ d)$  is from Ref. [377].

2785

2786 **3.3.11 Conclusion**

2787 With LHeC inclusive NC and CC DIS data, unique measurements of electroweak parameters can  
 2788 be performed with highest precision. Since inclusive DIS is mediated through space-like momen-  
 2789 tum transfer ( $t$ -channel exchange) the results are often complementary to other experiments,  
 2790 such as  $pp$  or  $e^+e^-$  collider experiments, where measurements are performed in the time-like  
 2791 regime and most often at the  $Z$  peak. Among many other quantities, measurements of the weak  
 2792 couplings of the light quarks,  $u$  and  $d$ , or their anomalous form factors  $\rho'_{NC,u/d}$  and  $\kappa'_{NC,u/d}$ ,  
 2793 can be performed uniquely due to the important contributions of valence quarks in the initial  
 2794 state. Also scale dependent measurements of weak interactions can be performed over a large  
 2795 range in  $\sqrt{Q^2}$ , which provides an interesting portal to BSM physics. The  $W$  boson mass can be  
 2796 determined with very small experimental uncertainties, such that theoretical uncertainties are  
 2797 expected to become more important than experimental uncertainties. While the parameters of  
 2798 the PDFs are determined together with the EW parameters in the present study, it is found  
 2799 that the PDFs do not induce a limitation of the uncertainties. Considering the dominating  
 2800 top-quark mass dependence of higher-order electroweak effects, one can realise that the LHeC  
 2801 will be competitive with the global electroweak fit after the HL-LHC era [147, 346].

2802 Besides proving its own remarkable prospect on high-precision electroweak physics, the LHeC  
 2803 will further significantly improve the electroweak measurements in  $pp$  collisions at the LHC by  
 2804 reducing the presently sizeable influence of PDF and  $\alpha_s$  uncertainties. This is discussed in Sec. 7.

### 2805 3.4 Top Quark Physics

2806 SM top quark production at a future ep collider is dominated by single top quark production,  
 2807 mainly via CC DIS production. An example graph is shown in Fig. 3.59 (left). The total cross  
 2808 section is 1.89 pb at the LHeC [378] and with an electron beam energy of 60 GeV, and an LHC  
 2809 proton beam of 7 TeV, leading to a centre-of-mass energy of 1.3 TeV, respectively. The other  
 2810 important top quark production mode is  $t\bar{t}$  photoproduction with a total cross section of 0.05 pb  
 2811 at the LHeC [379]. An example graph is shown in Fig. 3.59 (right). This makes a future LHeC a  
 2812 top quark factory and an ideal tool to study top quarks with a high precision, and to analyse in  
 2813 particular their electroweak interaction. Selected highlights in top quark physics are summarised  
 2814 here.

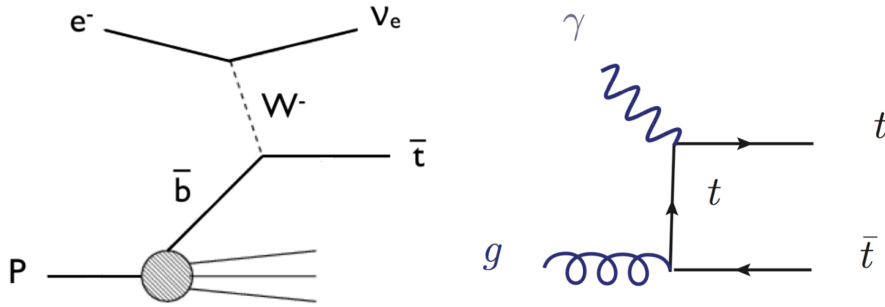


**Figure 3.59:** Example graphs for CC DIS top quark production (left) and top quark photoproduction (right).

#### 2815 3.4.1 $Wtq$ Couplings

2816 One flagship measurement is the direct measurement of the CKM matrix element  $|V_{tb}|$ , i.e.  
 2817 without making any model assumptions such as on the unitarity of the CKM matrix or the  
 2818 number of quark generations. An elaborate analysis of the single top quark CC DIS process  
 2819 at the LHeC including a detailed detector simulation using the DELPHES package [380] shows  
 2820 that already at  $100 \text{ fb}^{-1}$  of integrated luminosity an uncertainty of 1% can be expected. This  
 2821 compares to a total uncertainty of 4.1% of the currently most accurate result at the LHC Run-I  
 2822 performed by the CMS experiment [381].

2823 The same analysis [378] can also be used to search for anomalous left- and right-handed  $Wtb$   
 2824 vector ( $f_1^L, f_1^R$ ) and tensor ( $f_2^L, f_2^R$ ) couplings analyzing the following effective Lagrangian:

$$L = -\frac{g}{\sqrt{2}} \bar{b} \gamma^\mu V_{tb} (f_1^L P_L - f_1^R P_R) t W_\mu^- - \frac{g}{\sqrt{2}} \bar{b} \frac{i\sigma^{\mu\nu} q_\nu}{M_W} (f_2^L P_L - f_2^R P_R) t W_\mu^- + h.c. \quad (3.45)$$

2825 In the SM  $f_1^L = 1$  and  $f_1^R = f_2^L = f_2^R = 0$ . The effect of anomalous  $Wtb$  couplings is consistently  
 2826 evaluated in the production and the decay of the antitop quark, cf. Fig. 3.59 (left). Using  
 2827 hadronic top quark decays only, the expected accuracies in a measurement of these couplings  
 2828 as a function of the integrated luminosity are presented in Fig. 3.60 (upper left), derived from  
 2829 expected 95% C.L. limits on the cross section yields. The couplings can be measured with  
 2830 accuracies of 1% for the SM  $f_1^L$  coupling determining  $|V_{tb}|$  (as discussed above) and of 4% for  
 2831  $f_2^L$ , 9% for  $f_2^R$ , and 14% for  $f_1^R$  at  $1 \text{ ab}^{-1}$ .

2832 Similarly, the CKM matrix elements  $|V_{tx}|$  ( $x = d, s$ ) can be extracted using a parameterisation of  
 2833 deviations from their SM values with very high precision through  $W$  boson and bottom (light)

2834 quark associated production channels, where the  $W$  boson and  $b$ -jet (light jet  $j = d, s$ ) final  
 2835 states can be produced via s-channel single top quark decay or t-channel top quark exchange as  
 2836 outlined in [382]. As an example, analysing the processes

2837 Signal 1:  $pe^- \rightarrow \nu_e \bar{t} \rightarrow \nu_e W^- \bar{b} \rightarrow \nu_e \ell^- \nu_\ell \bar{b}$

2838 Signal 2:  $pe^- \rightarrow \nu_e W^- b \rightarrow \nu_e \ell^- \nu_\ell b$

2839 Signal 3:  $pe^- \rightarrow \nu_e \bar{t} \rightarrow \nu_e W^- j \rightarrow \nu_e \ell^- \nu_\ell j$

2840 in an elaborate analysis including a detailed detector simulation using the DELPHES pack-  
 2841 age [380], the expected accuracies on  $|V_{td}|$  and  $|V_{ts}|$  at the  $2\sigma$  confidence level (C.L.) are shown  
 2842 as a function of the integrated luminosity in Fig. 3.60 (upper right, middle left). At  $1 \text{ ab}^{-1}$  of  
 2843 integrated luminosity and an electron polarization of 80%, the  $2\sigma$  limits improve on existing  
 2844 limits from the LHC [383] (interpreted by [384]) by a factor of  $\approx 3.5$ . Analyzing Signal 3 alone,  
 2845 and even more when combining Signals 1, 2 and 3, will allow for the first time to achieve an ac-  
 2846 curacy of the order of the actual SM value of  $|V_{ts}^{\text{SM}}| = 0.04108_{-0.0057}^{+0.0030}$  as derived from an indirect  
 2847 global CKM matrix fit [385], and will therefore represent a direct high precision measurement  
 2848 of this important top quark property. In these studies, upper limits at the  $2\sigma$  level down to  
 2849  $|V_{ts}| < 0.06$ , and  $|V_{td}| < 0.06$  can be achieved.

### 2850 3.4.2 FCNC Top Quark Couplings

2851 Single top quark NC DIS production can be used to search for flavour Changing Neutral Current  
 2852 (FCNC)  $tu\gamma$ ,  $tc\gamma$ ,  $tuZ$ , and  $tcZ$  couplings [386, 387] as represented by the Lagrangian

$$L = \sum_{q=u,c} \left( \frac{g_e}{2m_t} \bar{t} \sigma^{\mu\nu} (\lambda_q^L P_L + \lambda_q^R P_R) q A_{\mu\nu} + \frac{g_W}{4c_W m_Z} \bar{t} \sigma^{\mu\nu} (\kappa_q^L P_L + \kappa_q^R P_R) q Z_{\mu\nu} \right) + h.c. , \quad (3.46)$$

2853 where  $g_e$  ( $g_W$ ) is the electromagnetic (weak) coupling constant,  $c_W$  is the cosine of the weak  
 2854 mixing angle,  $\lambda_q^{L,R}$  and  $\kappa_q^{L,R}$  are the strengths of the anomalous top FCNC couplings (the values  
 2855 of these couplings vanish at the lowest order in the SM). In an elaborate analysis including  
 2856 at least one electron and three jets (hadronic top quark decay) with high transverse momentum  
 2857 and within the pseudorapidity acceptance range of the detector are selected. The distributions  
 2858 of the invariant mass of two jets (reconstructed  $W$  boson mass) and an additional jet tagged as  
 2859  $b$ -jet (reconstructed top quark mass) are used to further enhance signal over background events,  
 2860 mainly given by  $W + \text{jets}$  production. Signal and background interference effects are included.  
 2861 A detector simulation with DELPHES [380] is applied.

2862 The expected limits on the branching ratios  $\text{BR}(t \rightarrow q\gamma)$  and  $\text{BR}(t \rightarrow qZ)$  as a function of the  
 2863 integrated luminosity at the  $2\sigma$  C.L. are presented in Fig. 3.60 (middle right). Assuming an  
 2864 integrated luminosity of  $1 \text{ ab}^{-1}$ , limits of  $\text{BR}(t \rightarrow q\gamma) < 1 \cdot 10^{-5}$  and  $\text{BR}(t \rightarrow qZ) < 4 \cdot 10^{-5}$  are  
 2865 expected. This level of precision is close to actual predictions of concrete new phenomena models,  
 2866 such as SUSY, little Higgs, and technicolour, that have the potential to produce FCNC top quark  
 2867 couplings. This will improve on existing limits from the LHC by one order of magnitude [12].  
 2868 Fig. 3.60 (lower left) shows how this sensitivity on  $\text{BR}(t \rightarrow q\gamma)$  and  $\text{BR}(t \rightarrow qZ)$  changes as a  
 2869 function of centre-of-mass energy. At a future FCC-ep [12] with, for example, an electron beam  
 2870 energy of 60 GeV, and a proton beam energy of 50 TeV, leading to a centre-of-mass energy of  
 2871 3.5 TeV, the sensitivity on FCNC  $tq\gamma$  couplings even exceed expected sensitivities from the High  
 2872 Luminosity-LHC (HL-LHC) with  $300 \text{ fb}^{-1}$  at  $\sqrt{s} = 14 \text{ TeV}$ , and from the International Linear  
 2873 Collider (ILC) with  $500 \text{ fb}^{-1}$  at  $\sqrt{s} = 250 \text{ GeV}$  [389, 390].

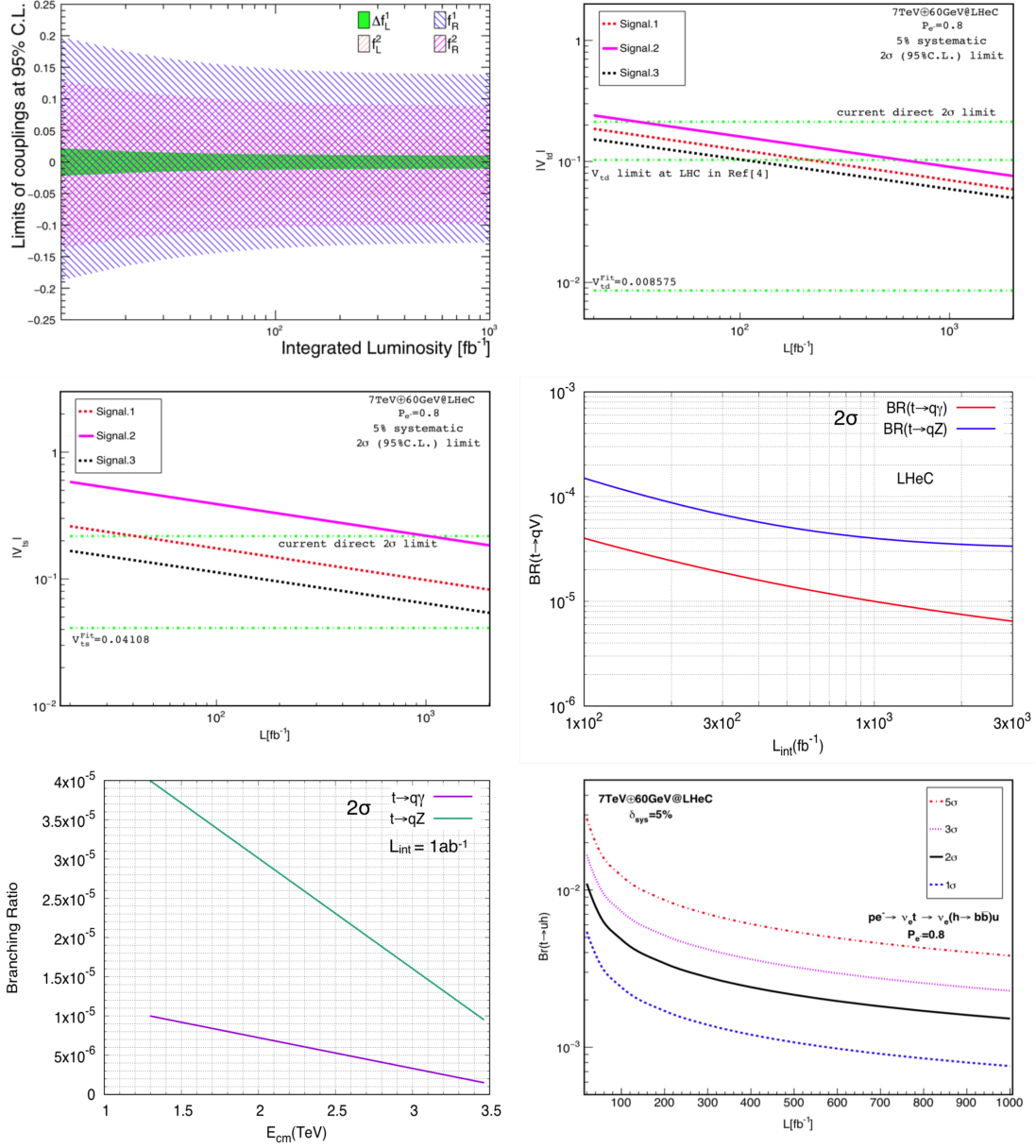


**Figure 3.60:** Expected sensitivities as a function of the integrated luminosity on the SM and anomalous  $Wtb$  couplings [378] (upper left), on  $|V_{td}|$  (upper right) and  $|V_{ts}|$  (middle left) [382], on FCNC  $t \rightarrow qV$  branching ratios (middle right) [386, 387], and on FCNC  $t \rightarrow uH$  branching ratios [388] (lower left). The expected upper limits on FCNC  $t \rightarrow qV$  branching ratios are also shown as a function of the centre-of-mass-energy (lower right).

2874 Another example for a sensitive search for anomalous top quark couplings is the one for FCNC  
 2875  $tHq$  couplings as defined in

$$L = \kappa_{tuH} \bar{t}uH + \kappa_{tcH} \bar{t}cH + h.c. \quad (3.47)$$

2876 This can be studied in CC DIS production, where singly produced top anti-quarks could decay  
 2877 via such couplings into a light anti-quark and a Higgs boson decaying into a bottom quark-  
 2878 antiquark pair,  $e^-p \rightarrow \nu_e \bar{t} \rightarrow \nu_e H \bar{q} \rightarrow \nu_e b \bar{b} \bar{q}$  [388]. Another signal involves the FCNC  $tHq$   
 2879 coupling in the production vertex, i.e. a light quark from the proton interacts via t-channel top  
 2880 quark exchange with a  $W$  boson radiated from the initial electron producing a  $b$  quark and a  
 2881 Higgs boson decaying into a bottom quark-antiquark pair,  $e^-p \rightarrow \nu_e H b \rightarrow \nu_e b \bar{b} b$  [388]. This  
 2882 channel is superior in sensitivity to the previous one due to the clean experimental environment  
 2883 when requiring three identified  $b$ -jets. Largest backgrounds are given by  $Z \rightarrow b \bar{b}$ , SM  $H \rightarrow b \bar{b}$ ,  
 2884 and single top quark production with hadronic top quark decays. A 5% systematic uncertainty  
 2885 for the background yields is added. Furthermore, the analysis assumes parameterised resolutions  
 2886 for electrons, photons, muons, jets and unclustered energy using typical parameters taken from  
 2887 the ATLAS experiment. Furthermore, a  $b$ -tag rate of 60%, a  $c$ -jet fake rate of 10%, and a light-  
 2888 jet fake rate of 1% is assumed. The selection is optimised for the different signal contributions  
 2889 separately. Fig. 3.60 (lower right), shows the expected upper limit on the branching ratio  
 2890  $\text{Br}(t \rightarrow Hu)$  with  $1\sigma$ ,  $2\sigma$ ,  $3\sigma$ , and  $5\sigma$  C.L. as a function of the integrated luminosity for the  
 2891  $e^-p \rightarrow \nu_e H b \rightarrow \nu_e b \bar{b} b$  signal process. For an integrated luminosity of  $1 \text{ ab}^{-1}$ , upper limits of  
 2892  $\text{Br}(t \rightarrow Hu) < 0.15 \cdot 10^{-3}$  are expected at the  $2\sigma$  C.L.

2893 In Fig. 3.61 the different expected limits on various flavour-changing neutral current (FCNC)  
 2894 top quark couplings from the LHeC are summarised, and compared to results from the LHC  
 2895 and the HL-LHC. This clearly shows the competitiveness of the LHeC results, and documents  
 2896 the complementarity of the results gained at different colliders.

### 2897 3.4.3 Other Top Quark Property Measurements and Searches for New Physics

2898 Other exciting results not presented here involve, for example, the study of the CP-nature  
 2899 in  $t\bar{t}H$  production [391] (see Section 5.2), searches for anomalous  $t\bar{t}\gamma$  and  $t\bar{t}Z$  chromoelectric  
 2900 and chromomagnetic dipole moments in  $t\bar{t}$  production [379], the study of top quark spin and  
 2901 polarisation [392], and the investigation of the top quark structure function inside the proton [1,  
 2902 393].

### 2903 3.4.4 Summary Top Quark Physics

2904 Top quark physics at the LHeC represents a very rich and diverse field of research involving high  
 2905 precision measurements of top quark properties, and sensitive searches for new physics. Only a  
 2906 few highlights involving  $Wtq$  and FCNC top quark couplings are presented here. One particular  
 2907 highlight is the expected direct measurement of the CKM matrix element  $|V_{tb}|$  with a precision  
 2908 of less than 1%. Furthermore, FCNC top quark couplings can be studied with a precision high  
 2909 enough to explore those couplings in a regime that might be affected by actual new phenomena  
 2910 models, such as SUSY, little Higgs, and technicolour.

2911 It has been shown [12], that results from future  $e^+e^-$ -colliders,  $eh$ -colliders, and  $hh$ -colliders  
 2912 deliver complimentary information and will therefore give us a more complete understanding of  
 2913 the properties of the heaviest elementary particle known to date, and of the top quark sector in  
 2914 general.

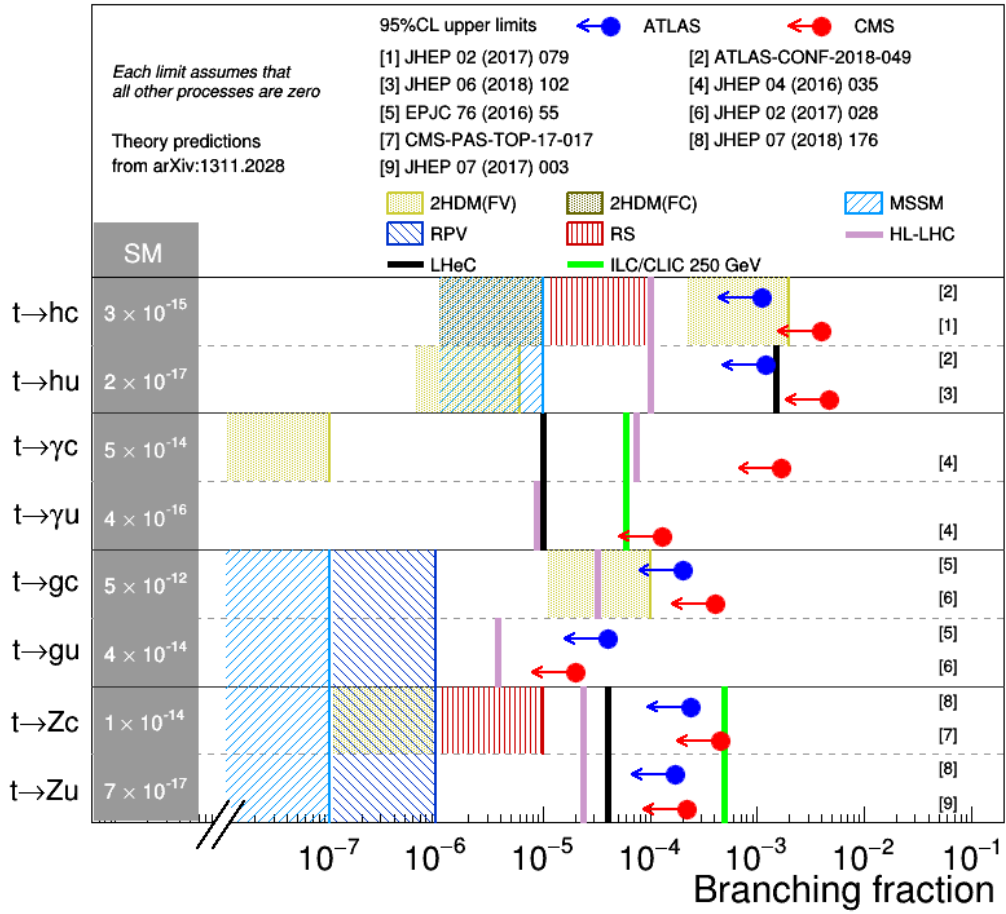


**Figure 3.61:** Comparison of top quark FCNC branching ratio limits at the LHC, HL-LHC, LHeC, and ILC/CLIC colliders.

## Chapter 4

# Nuclear Particle Physics with Electron-Ion Scattering at the LHeC

### 4.1 Introduction

The LHeC accelerator, in addition to being a powerful machine for exploring proton structure, will allow for the first time studies of DIS off nuclei in a collider mode at the energy frontier. The nuclear structure has been previously studied in fixed target experiments with charged lepton and neutrino beams, see [55–57, 394–403] and references therein. Due to the energy limitations of the machines operating in this mode, the kinematic range covered by these experiments is rather narrow, mostly limited to relatively large values of  $x \geq 0.01$  and low to moderate  $Q^2$ , in the range  $Q^2 < 100 \text{ GeV}^2$ . The precise kinematic range covered by experiments is shown in Fig. 4.1, where the DIS experiments overlap to a large degree with the data from hadronic collisions using the Drell-Yan (DY) process. These fixed target DIS and DY data dominate the data sets used in the fits for the nuclear parton distribution functions. In addition, in some analyses of nuclear PDFs, data on inclusive single hadron production in  $d\text{Au}$  collisions at RHIC and on EW bosons and dijets in  $p\text{Pb}$  collisions at the LHC are included.

As is clear from Fig. 4.1, the LHeC will be able to cover a very large range in  $(x, Q^2)$  in  $eA$ , previously unexplored in experiments. It will extend the range in  $x$  down to  $\sim 10^{-6}$  and have a huge lever arm in  $Q^2$  from very low values up to  $\sim 10^6 \text{ GeV}^2$ . It will also be complementary to the EIC [234] machine, extending the range in  $x$  and  $Q^2$  by about two orders of magnitude with respect to it. The extension of these ranges will be even larger at the FCC-eh.

Due to large statistics and modern, specialised detectors, it will be possible to study nuclear structure at the LHeC with unprecedented precision in a kinematical range far wider than previously possible and with the controlled systematics of one single experiment. There are a large number of important physics topics that can be addressed in  $eA$  collisions at the LHeC:

- A precise determination of nuclear parton densities for a single nucleus (lead, and eventually lighter ions) will be possible. In particular, the current huge uncertainties in nuclear gluon and sea quark densities at low  $x$  will be dramatically improved using the data from the LHeC. In analogy to the proton PDF extraction described in previous sections, full flavour decomposition in the nuclear case could be achieved using both NC and CC data with heavy flavour identification.
- Precision measurement of semi-inclusive and exclusive processes will enable an exploration

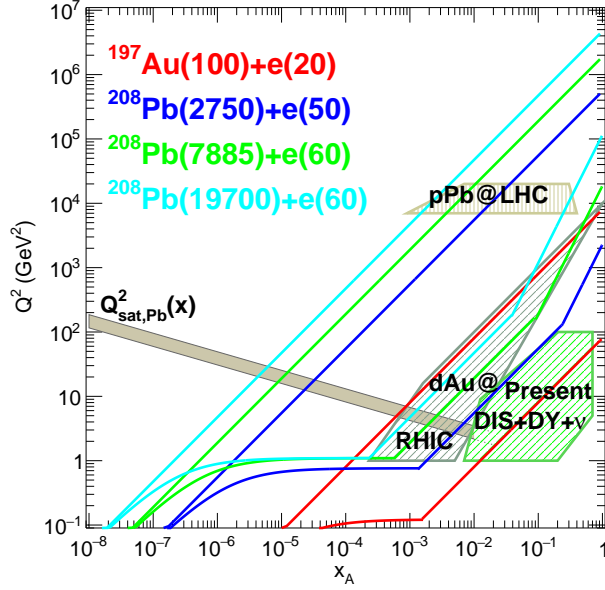


**Figure 4.1:** Kinematic regions in the  $x - Q^2$  plane explored by different data sets (charged lepton and neutrino DIS, DY,  $dAu$  at RHIC and  $pPb$  at the LHC) used in present nPDF analyses [404], compared to the ones achievable at the EIC (red), the LHeC (ERL against the HL-LHC beams, dark blue) and two FCC-eh versions (with Pb beams corresponding to proton energies  $E_p = 20$  TeV - green and  $E_p = 50$  TeV - light blue). Acceptance of the detector for the electrons is taken to be  $1^\circ < \theta < 179^\circ$ , and  $0.01(0.001) < y < 1$  for the EIC (all other colliders). The saturation scale  $Q_{sat}$  shown here for indicative purposes only, see also [405], has been drawn for a Pb nucleus considering an uncertainty  $\sim 2$  and a behaviour with energy following the model in [406]. Note that it only indicates a region where saturation effects are expected to be important but there is no sharp transition between the linear and non-linear regimes.

2947  
2948  
2949  
2950  
2951  
2952  
2953  
2954  
2955  
2956  
2957  
2958  
2959  
2960  
2961  
2962  
2963  
2964  
2965  
2966

of new details of the nuclear structure. Similarly to the proton case, DVCS and exclusive vector-meson production will provide unique insight into 3D nuclear structure.

- The LHeC will offer unprecedented opportunities to extract diffractive parton densities in nuclei for the first time. A first detailed analysis [266] indicates that the achievable precision on diffractive PDFs in nuclei will be comparable to that possible in the proton case. The measurements of diffraction on protons and nuclei as well as the inclusive structure functions in the nuclear case will allow us to explore the very important relation between nuclear shadowing and diffraction [407].
- The LHeC will be able to test and establish or exclude the phenomenon of parton saturation at low  $x$  in protons and nuclei. According to the Color Glass Condensate framework [408, 409], parton saturation is a density effect that can be achieved in two ways, either by decreasing the value of  $x$  or by increasing the size of the target by increasing  $A$ . The LHeC will be a unique machine to address both of their variations, such that the ideas of saturation could be precisely tested. It will be possible to search for parton saturation in a variety of ways which include, among others, the search for tensions in DGLAP fits, the study of the diffraction, in particular the ratios of diffractive to inclusive cross sections, and the study of particle azimuthal de-correlations.
- Finally, the LHeC machine in  $eA$  mode will have a huge impact onto physics explored in  $pA$  and  $AA$  collisions, see Sec. 7.5, where it will provide vital input and constraints on the ‘baseline’ initial state in nuclear collisions, measurements of the impact of a cold nuclear

2967 medium on hard probes and effects of hadronisation. It will also explore the initial state  
 2968 correlations on the final state observables relevant for understanding collectivity in small  
 2969 systems explored in  $pp$  or  $pA$  collisions.

2970 As commented below, these aims will require an experimental apparatus with large rapidity  
 2971 coverage and associated forward and backward electron, photons, hadron and nuclear detectors.  
 2972 In addition the detector design should allow to precisely measure diffractive events in  $eA$  and  
 2973 allow the clean separation of radiative events, most important for the case of DVCS and exclusive  
 2974 diffraction.

2975 In this Chapter we do not address issues on the nuclear modification on jet yields and fragmen-  
 2976 tation that are expected to show dramatic effects and to be of great importance for heavy-ion  
 2977 collisions. All these aspects were previously discussed in Ref. [1].

## 2978 4.2 Nuclear Parton Densities

2979 PDFs are essential ingredients in our understanding of the dynamics of the strong interaction.  
 2980 First, they encode important information about the structure of hadrons [410,411]. Second, they  
 2981 are indispensable for the description of hadronic collisions within standard collinear factorisa-  
 2982 tion [35]. Concerning nuclei, it has been known for more than 40 years that structure functions  
 2983 are strongly affected by the nuclear environment [402,403] so that they cannot be interpreted as  
 2984 a simple superposition of structure functions of free nucleons. In the standard approach, within  
 2985 collinear factorization, the nuclear modification is included in the parametrisation of the parton  
 2986 densities. This means that the parton densities in a bound nucleon are different from those in  
 2987 a free nucleon, and the difference is encoded in the non-perturbative initial conditions of the  
 2988 parton densities at some low, initial scale  $Q_0^2$ . The present status of nuclear parton densities  
 2989 (nPDFs), see for example [412,413], can be summarised as follows:

- 2990 • Modern analyses [404,414–416] are performed at next-to-leading order (NLO) and next-to-  
 2991 next-to-leading order (NNLO) [417,418]. Differences between the different groups mainly  
 2992 arise from the different sets of data included in the analyses <sup>1</sup> and from the different  
 2993 functional forms employed for the initial conditions.
- 2994 • Many sets of data are presented as ratios of cross section for a given nucleus over that in  
 2995 deuterium, which is loosely bound and isoscalar. Therefore, it has become customary to  
 2996 work in terms of ratios of nPDFs:

$$R_i(x, Q^2) = \frac{f_i^A(x, Q^2)}{A f_i^p(x, Q^2)}, \quad i = u, d, s, c, b, g, \dots, \quad (4.1)$$

2997 with  $f_i^{p(A)}(x, Q^2)$  the corresponding parton density in a free proton  $p$  or in nucleus  $A$ .  
 2998 These nuclear modification factors are parametrised at initial scale  $Q_0^2$  (assuming isospin  
 2999 symmetry to hold). The nPDFs are then obtained multiplying the nuclear modification  
 3000 factors by some given set of free proton PDFs.

- 3001 • The available data come from a large variety of nuclei and the number of data points for  
 3002 any of them individually is very small compared to the proton analyses. In particular,  
 3003 for the Pb nucleus there are less than 50 points coming from the fixed target DIS and

---

<sup>1</sup>The main difference lies in the use or not of neutrino-Pb cross sections (whose usage has been controver-  
 sial [419–421], particularly the NuTeV data [56] from the Fe nucleus) from CHORUS and  $\pi^{0,\pm}$  transverse mo-  
 mentum spectra from  $dAu$  collisions at the Relativistic Heavy Ion Collider (RHIC).

3004 DY experiments and from particle production data in  $p$ Pb collisions at the LHC. The fit  
 3005 for a single nucleus is therefore impossible and the modelling of the  $A$ -dependence of the  
 3006 parameters in the initial conditions becomes mandatory [404, 416]. The most up to date  
 3007 analyses include between 1000 and 2000 data points for 14 nuclei.

- 3008 • The kinematic coverage in  $Q^2$  and  $x$  with existing data is very small compared to that  
 3009 of present hadronic colliders. The ultimate precision and large coverage of the kinematic  
 3010 plane for nPDFs can only be provided by a high energy electron-ion collider. Meanwhile,  
 3011 the only experimental collision system where nPDFs can be currently constrained are  
 3012 hadronic and ultraperipheral collisions (UPCs). It is important to stress that extracting  
 3013 PDFs from these collisions presents many theoretical challenges. These are related to the  
 3014 question of applicability of collinear factorization for nuclear collisions, higher twist effects,  
 3015 scale choices and other theoretical uncertainties.

3016 All parton species are very weakly constrained at small  $x < 10^{-2}$  [422], gluons are poorly  
 3017 known at large  $x > 0.2$ , and the flavour decomposition is largely unknown - a natural fact  
 3018 for  $u$  and  $d$  due to the approximate isospin symmetry in nuclei <sup>2</sup>. The impact of presently  
 3019 available LHC data, studied using reweighting [91, 423] in [424, 425] and included in the fit  
 3020 in [404], is quite modest with some constrains on the gluon and the strange quark in the region  
 3021  $0.01 < x < 0.3$ . On the other hand, theoretical predictions for nuclear shadowing of quark and  
 3022 gluon PDFs based on  $s$ -channel unitarity and diffractive nucleon PDFs are available down to  
 3023  $x \sim 10^{-4} - 10^{-5}$  [407, 426, 427]. Predictions on the flavour dependence of nuclear effects in the  
 3024 antishadowing region [428] cannot be confirmed with present data.

3025 Future runs at the LHC will offer some further possibilities for improving our knowledge on  
 3026 nPDFs [429]. However, the ideal place to determine parton densities is DIS, either at the Electron  
 3027 Ion Collider (EIC) [234] in the USA or, in a much larger kinematic domain (see Fig. 4.1), at the  
 3028 LHeC. DIS measurements in such configurations offer unprecedented possibilities to enlarge our  
 3029 knowledge of parton densities through a complete unfolding of all flavours.

3030 In the following, we show the possibilities for constraining the PDFs for a Pb nucleus at the  
 3031 LHeC. In the next subsection, Subsec. 4.2.1, we discuss the corresponding pseudodata for the  
 3032 inclusive cross section in electron-nucleus scattering. Next, in Subsec. 4.2.2 we discuss how the  
 3033 pseudodata will be introduced in a global nPDF fit. Finally, in Subsec. 4.2.3 it is demonstrated  
 3034 how the PDFs of Pb can be extracted with a very good precision from the LHeC data only,  
 3035 without requiring any other set of data.

### 3036 4.2.1 Pseudodata

3037 The LHeC provides measurements of  $eA$  scattering cross sections in the deep inelastic scattering  
 3038 region  $Q^2 > 1 \text{ GeV}^2$  reaching values of  $Q^2$  up to about  $5 \cdot 10^5 \text{ GeV}^2$  and corresponding  $x$  values  
 3039 between a few times  $10^{-6}$  and near to  $x = 1$ . This enables the determination of a complete  
 3040 set of nPDFs in  $e$ Pb scattering at the LHeC from the inclusive neutral and charged current  
 3041 cross sections with a clean separation of up and down valence and sea quark distributions. The  
 3042 very high  $Q^2$  region which reaches much beyond the  $W$  mass squared makes the CC measure-  
 3043 ments extremely valuable for the separation of different flavours when taken together with the  
 3044 NC, from photon and  $Z$  boson exchange. Charm tagging in CC determines the anti-strange  
 3045 quark distribution in a wide kinematic range to typically 10 – 20 % precision, while charm and  
 3046 beauty tagging in NC provide high precision determinations of  $xc$  and  $xb$  from nuclei. Using

---

<sup>2</sup>The  $u$ - $d$  difference is suppressed by a factor  $2Z/A - 1$ .

3047 coherent data from just this one experiment the uncertainties of these nPDFs will follow from  
 3048 a straightforward  $\Delta\chi^2 = 1$  criterion.

3049 The QCD analyses of pseudo LHeC cross section data illustrated subsequently employ sets of  
 3050 simulated NC and CC measurements under assumptions on precision which are summarised in  
 3051 Table 4.1, see Ref. [430]. The cross section simulation was done numerically employing deriva-  
 3052 tive formulae from [47] and found to compare well to a detailed Monte Carlo simulation when  
 3053 tested for the conditions of the H1 experiment. The assumptions made are all reasonable when  
 3054 comparing with the H1 achievements, allowing for further improvements owing to new detector  
 3055 techniques and higher statistics. The control of radiative corrections in  $eA$  scattering is a spe-  
 3056 cial challenge as these grow  $\propto Z^2$ . The LHeC detector thus needs to be equipped with reliable  
 3057 photon detectors and the exploitation of the energy-momentum conservation, via the  $E - p_z$   
 3058 cut, should further reduce the effect of photon radiation to a few per cent level. It is also to be  
 3059 noted that the semi-inclusive measurements of the  $s$ ,  $c$  and  $b$  quark distributions carry additional  
 uncertainties for tagging, acceptance and background influences.

Source of uncertainty	Error on the source or cross section
Scattered electron energy scale	0.1 %
Scattered electron polar angle	0.1 mrad
Hadronic energy scale	0.5 %
Calorimeter noise ( $y < 0.01$ )	1–3 %
Radiative corrections	1–2 %
Photoproduction background	1 %
Global efficiency error	0.7 %

**Table 4.1:** Summary of assumed systematic uncertainties for future inclusive cross section measurements at the LHeC.

3060

3061 Fig. 4.2 illustrates the kinematic reach of the NC+CC pseudodata at the LHeC and the FCC-eh,  
 3062 in  $ep$  and  $ePb$  collisions (for per nucleon integrated luminosities  $\leq 1$  and  $10 \text{ fb}^{-1}$  respectively). In  
 3063 addition to inclusive data, semi-inclusive measurements with flavour sensitivity are also included.  
 3064 They will allow us to determine the strange, charm and beauty (also the top) PDFs. The  
 3065 principal technique is charm tagging (in CC for  $xs$ , in NC for  $xc$ ) and beauty tagging (in NC  
 3066 for  $xb$ ). The beam spot of the LHeC has a transverse extension of about  $(7 \mu\text{m})^2$ . Modern Si  
 3067 detectors have a resolution of a few microns to be compared with typical decay lengths of charm  
 3068 and beauty particles of hundreds of  $\mu\text{m}$ . The experimental challenges then are the beam pipe  
 3069 radius, coping at the LHeC with strong synchrotron radiation effects, and the forward tagging  
 3070 acceptance, similar to the HL-LHC challenges.

3071 A study was made of the possible measurements of the anti-strange density in nuclei (see Fig. 4.3)  
 3072 using impact parameter tagging in  $eA$  CC scattering, and of the charm and beauty structure  
 3073 functions in NC (see Fig. 4.4). Following experience on heavy flavour tagging at HERA and  
 3074 ATLAS, assumptions were made on the charm and beauty tagging efficiencies to be 10% and  
 3075 60%, respectively. The light quark background in the charm analysis is assumed to be control-  
 3076 lable to per cent level, while the charm background in the beauty tagging sample is assumed  
 3077 to be 10%. The tagging efficiencies and background contaminations affect the statistical error.  
 3078 Moreover, an additional systematic error is assumed in the simulated NC (CC) measurements  
 3079 of 3 (5)%. These result in very promising measurements of the heavier quark distributions: to  
 3080 about 10 – 20% total uncertainty on the strange and 3 – 5% on the charm and beauty mea-  
 3081 surements, for typically  $x$  between  $10^{-4}$  and 0.1 and  $Q^2$  extending from below threshold  $m_Q^2$  up  
 3082 to a few times  $10^4 \text{ GeV}^2$ . The knowledge of the heavy quark densities is of prime relevance for

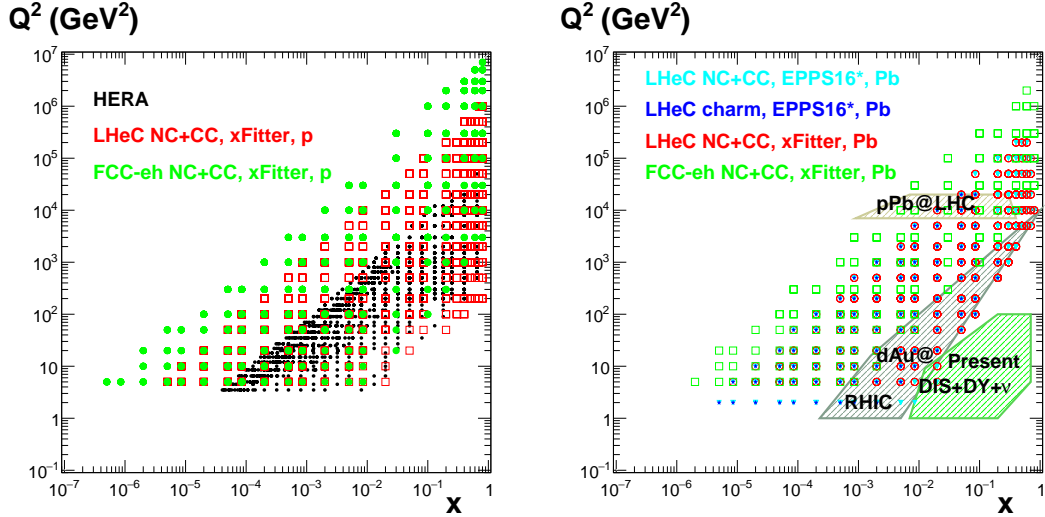


**Figure 4.2:** Left: kinematic  $x - Q^2$  plot of the NC+CC pseudodata on a proton at the LHeC (red symbols) and the FCC-eh (green symbols) used in the xFitter analysis in Section 4.2.3; data used in analysis at HERA (black symbols) are shown for comparison. Right: kinematic  $x - Q^2$  plot of the pseudodata on Pb used in the EPPS16 analysis at the LHeC (NC+CC, light blue symbols, and charm, dark blue symbols) in Section 4.2.2, and in the xFitter analysis in Subsec. 4.2.3 (at the LHeC, red symbols, and the FCC-eh, green symbols); the regions explored by currently available data sets (charged lepton and neutrino DIS, DY,  $dAu$  at RHIC and  $pPb$  at the LHC) used in present nPDF analyses [404] are shown for comparison.

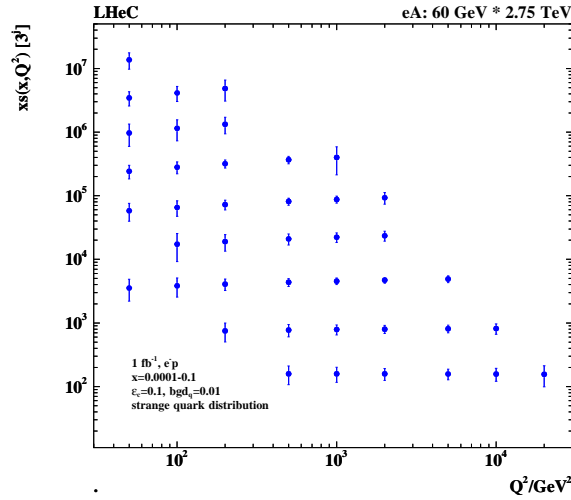


**Figure 4.3:** Simulation of the measurement of the (anti)-strange quark distribution  $x\bar{s}(x, Q^2)$  in charged current  $eA$  scattering through the  $t$ -channel reaction  $W^- \bar{s} \rightarrow c$ . The data are plotted with full systematic and statistical errors added in quadrature.

3083 understanding nuclear structure and the development of QCD as has often been emphasised.

## 3084 4.2.2 Nuclear gluon PDFs in a global-fit context

3085 To illustrate the impact of the LHeC  $ePb$  pseudodata in the global context, they have been  
 3086 added [431] into the EPPS16 global analysis of nuclear PDFs [404]. The EPPS16 strategy is

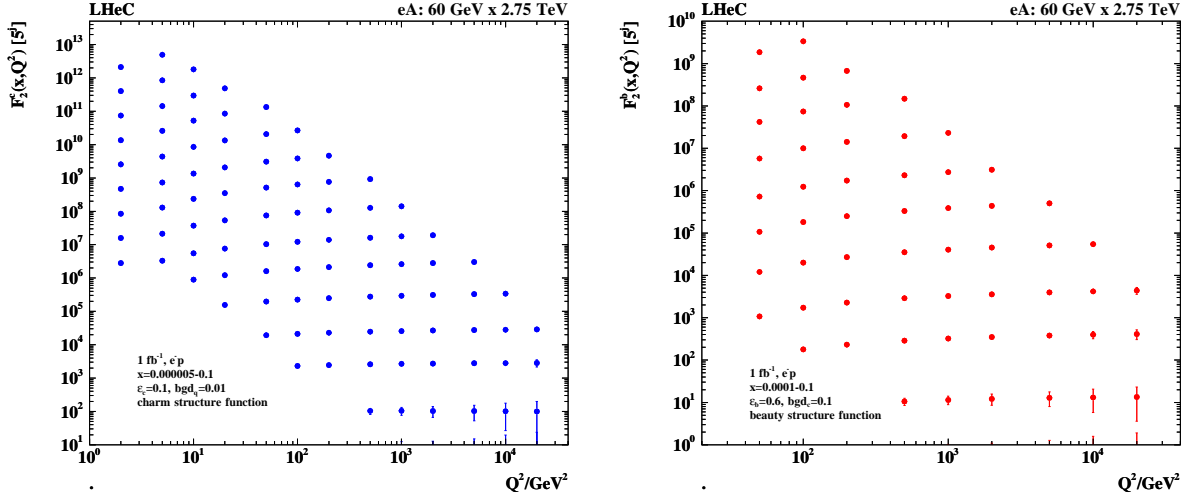


**Figure 4.4:** Left: Simulation of the measurement of the charm quark distribution expressed as  $F_2^c = e_c^2 x(c + \bar{c})$  in neutral current  $eA$  scattering; Right: Simulation of the measurement of the bottom quark distribution expressed as  $F_2^b = e_b^2 x(b + \bar{b})$  in neutral current  $eA$  scattering. The data are plotted with full systematic and statistical errors added in quadrature.

3087 to parametrise the nuclear modification ratios  $R_i(x, Q^2)$  between the bound-proton PDFs  $f_i^{p/Pb}$   
 3088 and proton PDFs  $f_i^p$ ,

$$R_i(x, Q^2) \equiv \frac{f_i^{p/Pb}(x, Q^2)}{f_i^p(x, Q^2)}, \quad (4.2)$$

3089 at the charm mass threshold  $Q^2 = m_{charm}^2 = (1.3 \text{ GeV})^2$ . At higher  $Q^2$  the nuclear PDFs are  
 3090 obtained by solving the standard DGLAP evolution equations at next-to-leading order in QCD.  
 3091 As the LHeC pseudodata reach to significantly lower  $x$  than the data that were used in the  
 3092 EPPS16 analysis, an extended small- $x$  parametrisation was used for gluons, see Figure 4.5. The  
 3093 framework is almost identical to that in Ref. [432]. The introduced functional form allows for  
 3094 rather wild – arguably unphysical – behaviour at small- $x$  where e.g. significant enhancement is  
 3095 allowed. This is contrary to the theoretical expectations from the saturation conjecture and looks  
 3096 also to be an improbable scenario given the recent LHCb D and B meson measurements [433,434]  
 3097 which impressively indicate [435] gluon shadowing down to  $x \sim 10^{-5}$  at interaction scales as low  
 3098 as  $Q^2 \sim m_{charm}^2$ . On the other hand, given that there are no prior DIS measurements in this  
 3099 kinematic range for nuclei other than the proton, and that the D and B meson production in  
 3100  $pPb$  collisions could be affected by strong final-state effects (which could eventually be resolved  
 3101 by e.g. measurements of forward prompt photons [436] in  $pPb$ ), we hypothesise that any kind  
 3102 of behaviour is possible at this stage. Anyway, with the extended parametrisation – called  
 3103 here EPPS16\* – the uncertainties in the small- $x$  regime get significantly larger than in the  
 3104 standard EPPS16 set. This is reflected as significantly larger PDF error bands in comparison  
 3105 to the projected LHeC pseudodata. It is shown in Figure 4.6 where EPPS16\* predictions are  
 3106 compared with the LHeC pseudodata for inclusive NC and CC reactions, as well as charm  
 3107 production in neutral-current scattering. The uncertainties are estimated using the Hessian  
 3108 method [437] and the same overall tolerance  $\Delta\chi^2 = 52$  as in the EPPS16 analysis has been used  
 3109 when defining the error bands. Because there are no small- $x$  data constraints for gluons, the  
 3110 gluon uncertainty is enormous and the Hessian method used for estimating the uncertainties is  
 3111 not particularly accurate, i.e. the true  $\Delta\chi^2 = 52$  error bands are likely to be even larger. At  
 3112 some point the downward uncertainty will be limited by positivity constraints e.g. for  $F_L$ , but

3113 will depend strongly on which  $Q^2$  is used to set the positivity constraints (e.g. in the EPPS16  
 3114 analysis  $F_L$  is required to remain positive at  $Q^2 = m_{charm}^2$ ).

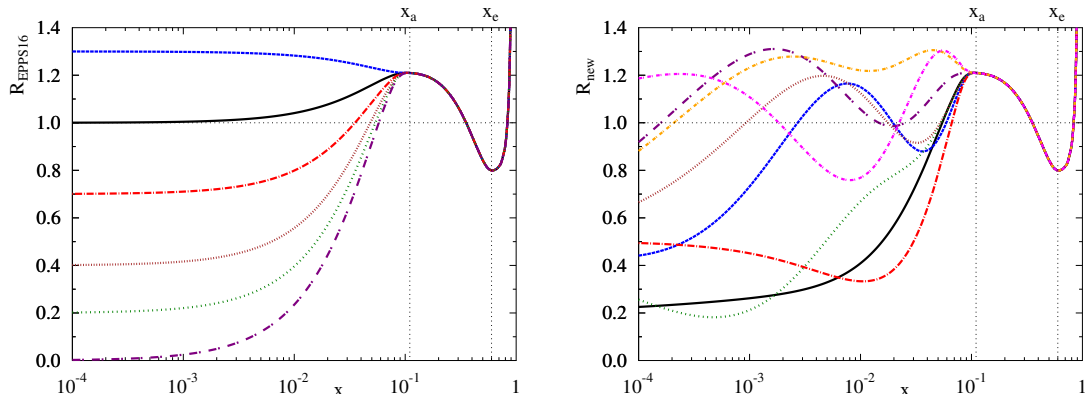


**Figure 4.5:** Left: Illustration of the functional behaviours allowed at small  $x$  in the EPPS16 analysis. Right: Illustration of the possible functional variations at small  $x$  in the extended parametrisation that we employ here.

3115 Upon including the LHeC  $e$ Pb pseudodata in the fit, the new nPDFs adapt to reproduce the  
 3116 pseudodata and their uncertainties are greatly reduced, as shown in Figure 4.7. The overall  
 3117 tolerance has been kept fixed to the default value  $\Delta\chi^2 = 52$ . The impact on the nuclear  
 3118 modification of the gluon PDF is illustrated in Figure 4.8 at two values of  $Q^2$ :  $Q^2 = 1.69 \text{ GeV}^2$   
 3119 (the parametrisation scale) and  $Q^2 = 10 \text{ GeV}^2$ . Already the inclusive pseudodata are able to  
 3120 reduce the small- $x$  gluon uncertainty quite significantly, and the addition of the charm data  
 3121 promises an even more dramatic reduction in the errors. The analysis indicates that the LHeC  
 3122 will nail the nuclear gluon PDF to a high precision down to  $x$  of at least  $10^{-5}$ .

### 3123 4.2.3 nPDFs from DIS on a single nucleus

3124 Another approach that becomes possible with the large kinematic coverage and volume of data  
 3125 for a single nucleus, Pb, at the LHeC and FCC-eh, is to perform a fit to only Pb data in order  
 3126 to extract the Pb PDFs, removing the need to interpolate between different nuclei. Then the  
 3127 corresponding ratios or nuclear modification factors for each parton species can be obtained  
 3128 using either a proton PDF set from a global fit or, as we do here (see [12, 438, 439]), from a  
 3129 fit to proton LHeC and FCC-eh pseudodata. In this way, there will be no need to introduce a  
 3130 nuclear size dependence in the parameters for the initial condition for DGLAP evolution. Such  
 3131 nPDFs can then be used for comparing to those obtained from global fits and for precision tests  
 3132 of collinear factorisation in nuclear collisions.

3133 The fits are performed using xFitter [52], where 484 (150) NC+CC Pb data points at the LHeC  
 3134 (FCC-eh) have been used in the fitted region  $Q^2 > 3.5 \text{ GeV}^2$ , see Fig. 4.2. A HERAPDF2.0-  
 3135 type parametrisation [37] has been employed to provide both the central values for the reduced  
 3136 cross sections (therefore, the extracted nuclear modification factors are centered at 1) and the  
 3137 fit functional form; in this way, neither theory uncertainties (treatment of heavy flavours, value  
 3138 of  $\alpha_s$ , order in the perturbative expansion) nor the uncertainty related to the functional form  
 3139 of the initial condition – parametrisation bias – are considered in our study, in agreement  
 3140 with our goal of estimating the *ultimate achievable experimental* precision in the extraction of  
 3141 nPDFs. We have worked at NNLO using the Roberts-Thorne improved heavy quark scheme,

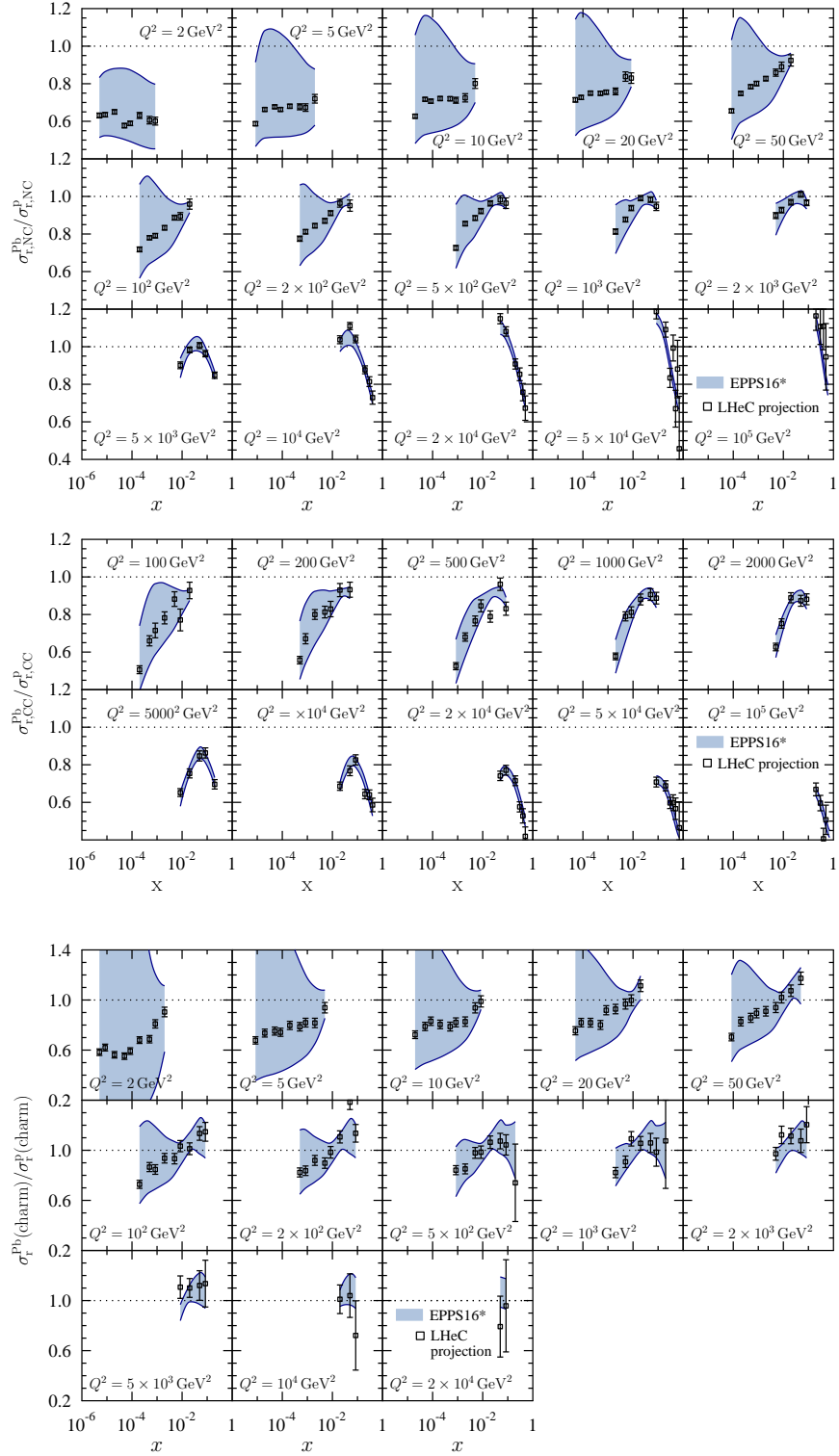


**Figure 4.6:** Top: Simulated ratios of neutral-current reduced cross sections between  $e\text{Pb}$  and  $ep$  collisions compared with the predictions from a EPPS16-type global fit of nuclear PDFs using an extended parametrisation for gluons. Middle: Charged-current cross section ratios. Bottom: Neutral-current charm-production cross section ratios.

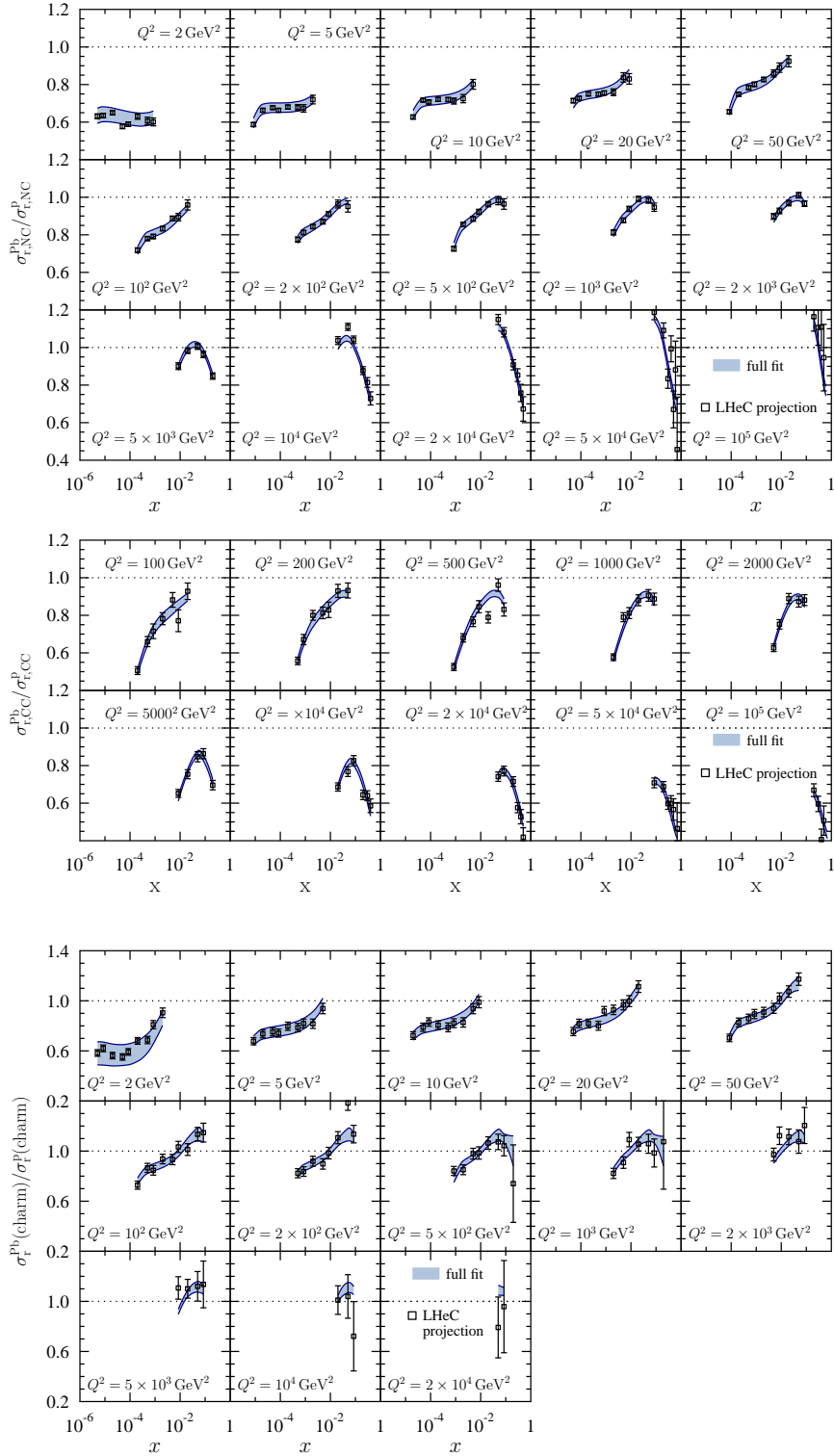


**Figure 4.7:** As Figure 4.6 but with fit results after including the LHeC pseudodata in the global analysis.

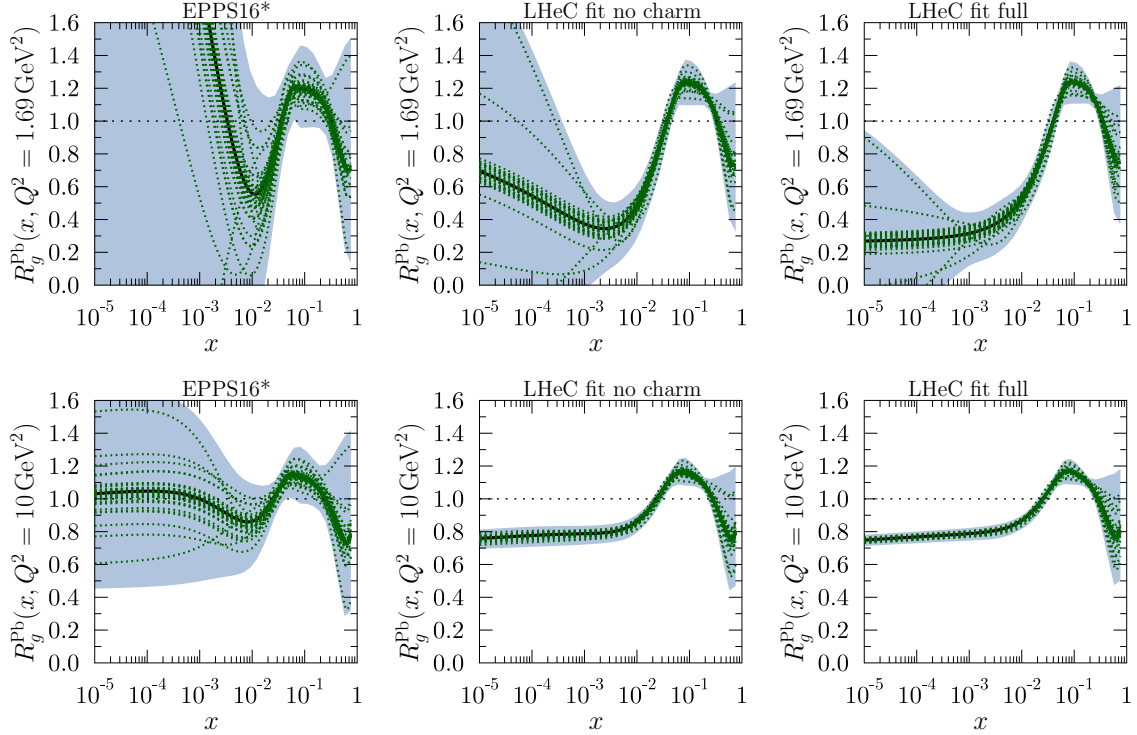


**Figure 4.8:** Upper panels: The gluon nuclear modification for the Pb nucleus at  $Q^2 = 1.69 \text{ GeV}^2$  in EPPS16\* (left), LHeC analysis without charm pseudodata (middle), and full LHeC analysis (right). The blue bands mark the total uncertainty and the green dotted curves correspond to individual Hessian error sets. Lower panels: As the upper panels but at  $Q^2 = 10 \text{ GeV}^2$ .

3142 and  $\alpha_s(m_Z^2) = 0.118$ . The treatment of systematics and the tolerance  $\Delta\chi^2 = 1$  are identical to  
 3143 the approach in the HERAPDF2.0 fits, as achievable in a single experiment.

3144 The results for the relative uncertainties in the nuclear modification factors are shown in Figs. 4.9,  
 3145 4.10 and 4.11 for valence, sea and gluon, respectively. The uncertainties in these plots reflect the  
 3146 assumed uncertainties in the pseudodata, both statistics (mainly at large  $x$ ) and systematics from  
 3147 detector efficiencies, radiative corrections, etc., see Sec. 4.2.1. As expected, the uncertainty in the  
 3148 extraction of the valence at small  $x$  is sizeably larger than that for the sea and gluon. While a very  
 3149 high precision looks achievable at the LHeC and the FCC-eh, for the comparison with EPPS16  
 3150 (or any other global fit) shown in the plots and with previous works in that setup [431, 432] some  
 3151 caution is required. First, the effective EPPS16 tolerance criterion  $\Delta\chi^2 \simeq 52$  implies that naively  
 3152 the uncertainty bands should be compared after rescaling by a factor  $\sqrt{52}$ . Second, the treatment  
 3153 of systematics is rather different, considering correlations in the xFitter exercise and taking them  
 3154 as fully uncorrelated (and added quadratically to the statistical ones) in the EPPS16 approach.  
 3155 Finally, EPPS16 uses parametrisations for the nuclear modification factors for different parton  
 3156 species while in xFitter just the (n)PDF combinations that enter the reduced cross sections are  
 3157 parametrised and employed for the fit. In this respect let us note that, in analogy to proton  
 3158 PDFs, a full flavour decomposition can be achieved using both NC and CC with heavy flavour  
 3159 identification that will verify the existing ideas on flavour dependence of nuclear effects on parton  
 3160 densities [428].

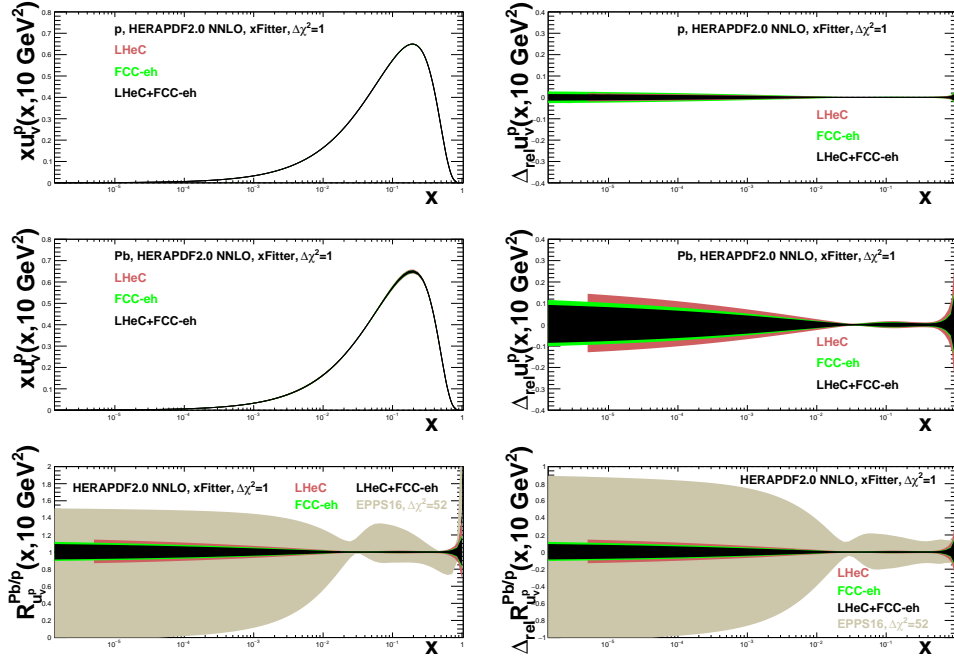


**Figure 4.9:** Distributions (left) and their relative uncertainties (right) of the valence  $u$ -quark density in the proton (top), Pb (middle) and the corresponding nuclear modification factor (bottom) in an analysis of  $ep$  and  $e\text{Pb}$  LHeC and FCC-eh NC plus CC pseudodata using xFitter (both a single set of data and all combined), compared to the results of EPPS16 [404], see the text for details.

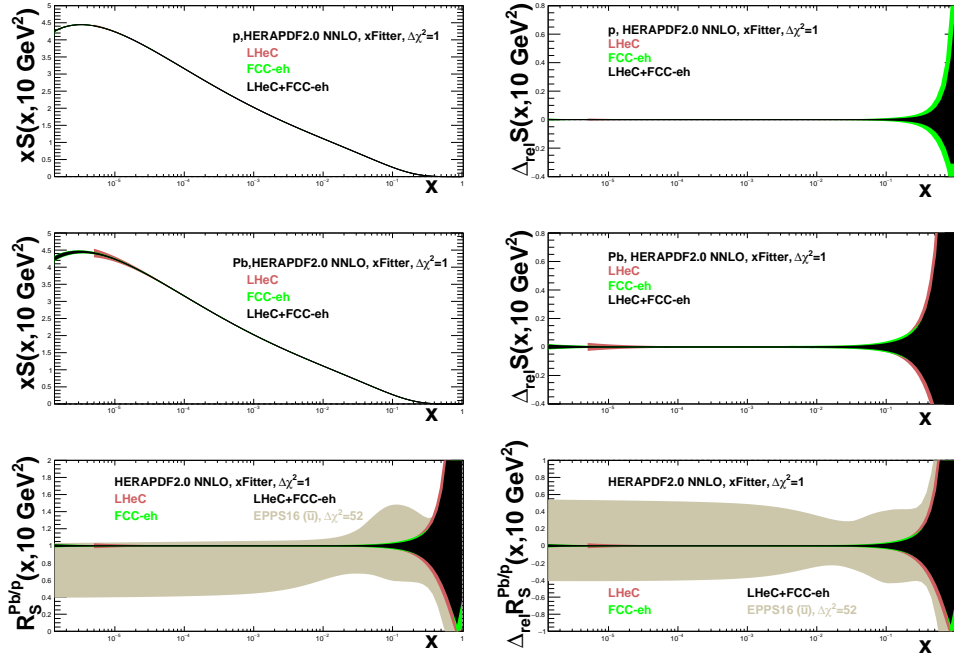


**Figure 4.10:** Distributions (left) and their relative uncertainties (right) of the sea quark density in the proton (top), Pb (middle) and the corresponding nuclear modifications factor (bottom) in an analysis of  $ep$  and  $e\text{Pb}$  LHeC and FCC-eh NC plus CC pseudodata using xFitter (both a single set of data and all combined), compared to the results of EPPS16 [404] for  $\bar{u}$ , see the text for details.

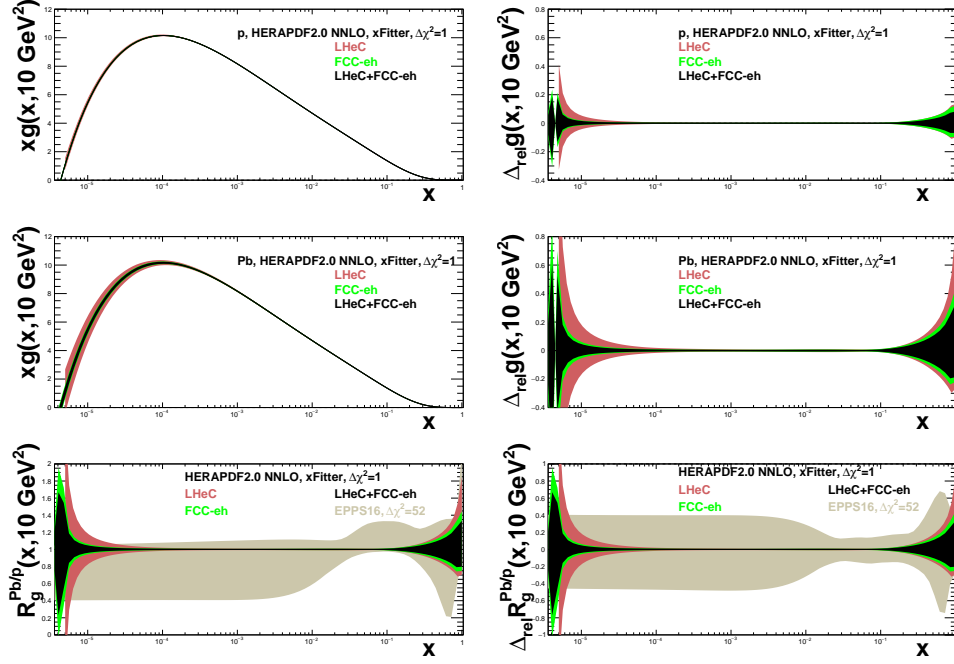


**Figure 4.11:** Distributions (left) and their relative uncertainties (right) of the gluon density in the proton (top), Pb (middle) and the corresponding nuclear modifications factor (bottom) in an analysis of  $ep$  and  $ePb$  LHeC and FCC-eh NC plus CC pseudodata using xFitter (both a single set of data and all combined), compared to the results of EPPS16 [404], see the text for details.

### 3161 4.3 Nuclear diffraction

3162 In Sec. 3.2.5 we have discussed specific processes which will probe the details of the 3D structure  
 3163 of the proton. The same processes can be studied in the context of electron-ion scattering  
 3164 and used to learn about the partonic structure of nuclei. Inclusive diffraction on nuclei can  
 3165 provide important information about the nuclear diffractive parton distribution similarly to the  
 3166 diffraction on the proton, see Sec. 3.2.6. Diffractive vector meson production can be studied in  
 3167 the nuclear case as well, e.g. within the framework of the dipole model suitable for high energy  
 3168 and including non-linear effects in density. In the nuclear case though, one needs to make a  
 3169 distinction between coherent and incoherent diffraction. In the coherent process, the nucleus  
 3170 scatters elastically and stays intact after the collision. In incoherent diffraction, the nucleus  
 3171 breaks up, and individual nucleons can be set free. Still, there will be a large rapidity gap between  
 3172 the produced diffractive system and the dissociated nucleus. It is expected that this process will  
 3173 dominate the diffractive cross section for medium and large values of momentum transfer. It is  
 3174 only in the region of small values of momentum transfer where elastic diffraction is the dominant  
 3175 contribution. Dedicated instrumentation in the forward region must be constructed in order to  
 3176 clearly distinguish between the two scenarios, see Chapter 10.

#### 3177 4.3.1 Exclusive vector meson diffraction

3178 Calculations for the case of Pb for the coherent diffractive  $J/\psi$  production were performed using  
 3179 the dipole model [254], see Sec. 3.2.5. In order to apply the dipole model calculation to the  
 3180 nuclear case, one takes the independent scattering approximation that is Glauber theory [440].

3181 The dipole amplitude can then be represented in the form

$$N_A(x, \mathbf{r}, \mathbf{b}) = 1 - \prod_{i=1}^A [1 - N(x, \mathbf{r}, \mathbf{b} - \mathbf{b}_i)] . \quad (4.3)$$

3182 Here  $N(x, \mathbf{r}, \mathbf{b} - \mathbf{b}_i)$  is the dipole amplitude for the nucleon (see Sec. 3.2.5) and  $\mathbf{b}_i$  denotes the  
 3183 transverse positions of the nucleons in the nucleus. The interpretation of Eq. (4.3) is that  $1 - N$   
 3184 is the probability not to scatter off an individual nucleon, and thus  $\prod_{i=1}^A [1 - N(\mathbf{r}, \mathbf{b} - \mathbf{b}_i, x)]$  is  
 3185 the probability not to scatter off the entire nucleus.

3186 In addition, the following simulation includes the fluctuations of the density profile in the proton,  
 3187 following the prescription given in [252–254]. To include these proton structure fluctuations one  
 3188 assumes that the gluonic density of the proton in the transverse plane is distributed around  
 3189 three constituent quarks (hot spots). These hot spots are assumed to be Gaussian. In practical  
 3190 terms one replaces the proton profile  $T_p(\mathbf{b})$

$$T_p(\mathbf{b}) = \frac{1}{2\pi B_p} e^{-b^2/(2B_p)} , \quad (4.4)$$

3191 that appears in each individual nucleon scattering probability  $N(x, \mathbf{r}, \mathbf{b} - \mathbf{b}_i)$  by the function

$$T_p(\mathbf{b}) = \sum_{i=1}^3 T_q(\mathbf{b} - \mathbf{b}_{q,i}) , \quad (4.5)$$

3192 where the ‘quark’ density profile is given by

$$T_q(\mathbf{b}) = \frac{1}{2\pi B_q} e^{-b^2/(2B_q)} . \quad (4.6)$$

3193 Here  $\mathbf{b}_{q,i}$  are the location of the hotspots that are sampled from a two dimensional Gaussian  
 3194 distribution whose width is given by parameter  $B_{qc}$ . The free parameters  $B_q$  and  $B_{qc}$  were  
 3195 obtained in [253] by comparing with HERA data on coherent and incoherent  $J/\psi$  production at  
 3196 a photon-proton centre-of-mass energy  $W = 75$  GeV, corresponding to fractional hadronic target  
 3197 energy loss  $x_{IP} = 10^{-3}$ . The proton fluctuation parameters obtained are  $B_{qc} = 3.3$  GeV $^{-2}$  and  
 3198  $B_q = 0.7$  GeV $^{-2}$ .

3199 The results for the differential cross section at  $t = 0$  for coherent production of  $J/\psi$  as a  
 3200 function of (virtual) photon-proton energy  $W$  for fixed values of  $Q^2$  are shown in Figs. 4.12  
 3201 and Figs. 4.13. The calculations for Pb are compared to those on the proton target. We see  
 3202 that the cross sections for the nuclear case increase with energy slower than for the proton case  
 3203 and are always smaller. Note that, we have already rescaled the diffractive cross section by  
 3204 a factor  $A^2$ , as appropriate for comparison of the diffractive cross section on the proton and  
 3205 nucleus. In the absence of nuclear corrections their ratio should be equal to 1. The differences  
 3206 between the scattering off a nucleus and a proton are also a function of  $Q^2$ . They are larger  
 3207 for smaller values of  $Q^2$  and for photoproduction. This is understood from the dipole formulae,  
 3208 see Eqs. (3.10), (3.11), (3.12). As explained previously, larger values of scale  $Q^2$  select smaller  
 3209 size dipoles, for which the density effects are smaller. Similarly, the differences between the lead  
 3210 and proton cases are larger for higher energies. This is because the dipole amplitude grows with  
 3211 decreasing values of  $x$  which are probed when the energy is increased, and thus the non-linear  
 3212 density effects are more prominent at low values of  $x$  and  $Q^2$ .

3213 These findings can be summarised by inspecting the ratio of the cross sections, presented as a  
 3214 function of  $x$  defined as

$$x = \frac{Q^2 + m_{J/\psi}^2}{Q^2 + W^2 + m_{J/\psi}^2 - m_N^2} \quad (4.7)$$

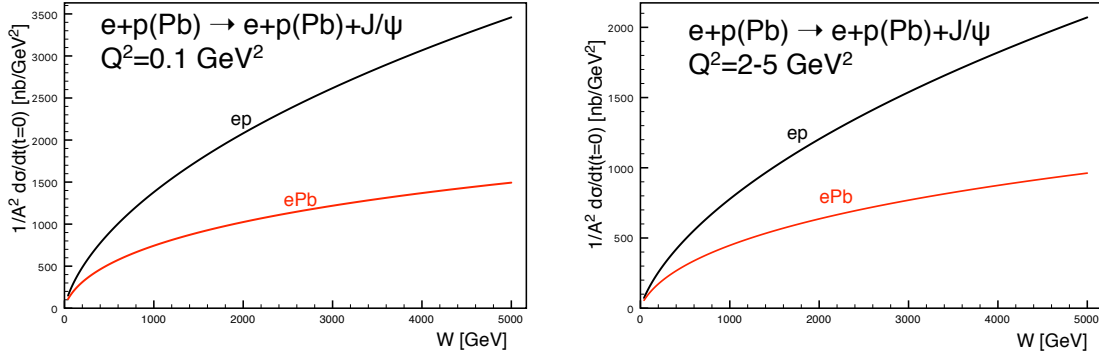


**Figure 4.12:** Cross section for the coherent diffractive production of the vector meson  $J/\psi$  in  $ePb$  (red solid curves) and  $ep$  (black solid curves) collisions, as a function of the energy  $W$ . Left: photoproduction case  $Q^2 \simeq 0$ , right:  $Q^2 = 2 - 5 \text{ GeV}^2$

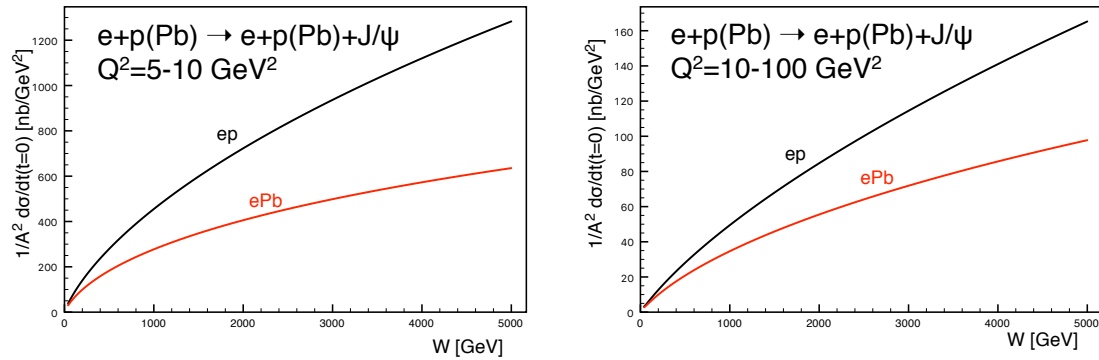


**Figure 4.13:** Cross section for the coherent diffractive production of the vector meson  $J/\psi$  in  $ePb$  (red solid curves) and  $ep$  (black solid curves) collisions, as a function of the energy  $W$ . Left:  $Q^2 = 5 - 10 \text{ GeV}^2$ , right:  $Q^2 = 10 - 100 \text{ GeV}^2$ .

3215 which is shown in Fig. 4.14. We observe that the ratio is smaller for smaller values of  $Q^2$ , and it  
3216 decreases for decreasing values of  $x$ . The results from the dipole model calculations are compared  
3217 with the ratio of the gluon density squared obtained from the nuclear PDFs using the EPPS16  
3218 set [404]. The reason why one can compare the diffractive cross section ratios with the ratios  
3219 for the gluon density squared can be understood from Eqs. (3.10) and (3.11). The diffractive  
3220 amplitude is proportional to the gluon density  $xg(x, Q^2)$ . On the other hand the diffractive cross  
3221 section is proportional to the amplitude squared, thus having enhanced sensitivity to the gluon  
3222 density. The nuclear PDFs have large uncertainties, which is indicated by the region between  
3223 the two sets of dotted lines. The EPPS16 parametrisation is practically unconstrained in the  
3224 region below  $x = 0.01$ . Nevertheless, the estimate based on the dipole model calculation and  
3225 the central value of the EPPS16 parametrisation are consistent with each other. This strongly  
3226 suggests that it will be hard to disentangle nuclear effects from saturation effects and that only  
3227 through a detailed combined analysis of data on the proton and the nucleus firm conclusions  
3228 can be established on the existence of a new non-linear regime of QCD.

3229 The differential cross section  $d\sigma/dt$  as a function of the negative four momentum transfer squared  
3230  $-t$  for the case of coherent and incoherent production is shown in Fig. 4.15. Coherent and inco-  
3231 herent diffraction cross sections are computed from the dipole model in the following way. The  
3232 coherent diffractive cross section is obtained by averaging the diffractive scattering amplitude

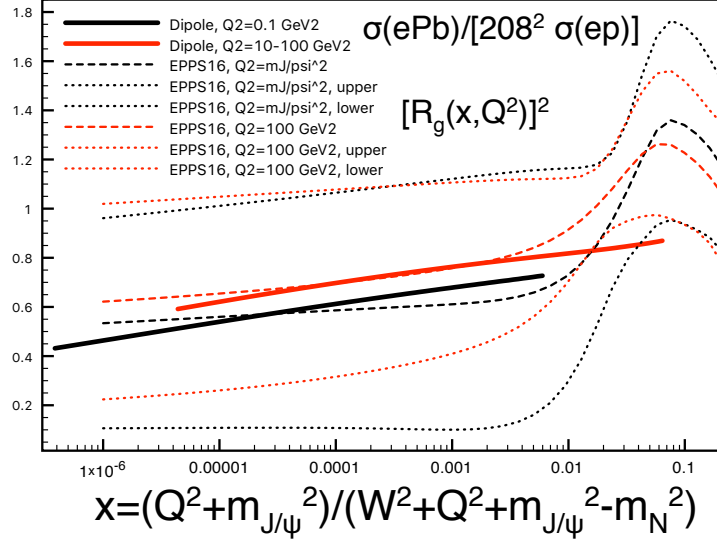


**Figure 4.14:** Ratio of coherent  $J/\psi$  production diffractive cross sections for Pb and proton as a function of the variable  $x$  defined in Eq. (4.7). Solid lines: dipole model calculation, for  $Q^2 = 0.1 \text{ GeV}^2$  (black) and  $Q^2 = 10 - 100 \text{ GeV}^2$  (red). Dotted and dashed lines correspond to the nuclear ratio for the gluon density squared using the EPPS16 parametrisation [404] of the nuclear parton distribution functions. Black and red dashed lines are the central sets for  $Q^2 = M_{J/\psi}^2$  and  $Q^2 = 100 \text{ GeV}^2$ . The dotted lines correspond to the low and high edges of the Hessian uncertainty in the EPPS16 parametrisation. The difference between the two dotted lines is thus indicative of the parametrisation uncertainty for the nuclear ratio. These ratios, that can also be measured in ultraperipheral collisions [441], are larger than the values  $0.2 - 0.4$  at  $x \simeq 10^{-5}$  predicted by the relation between diffraction and nuclear shadowing [407].

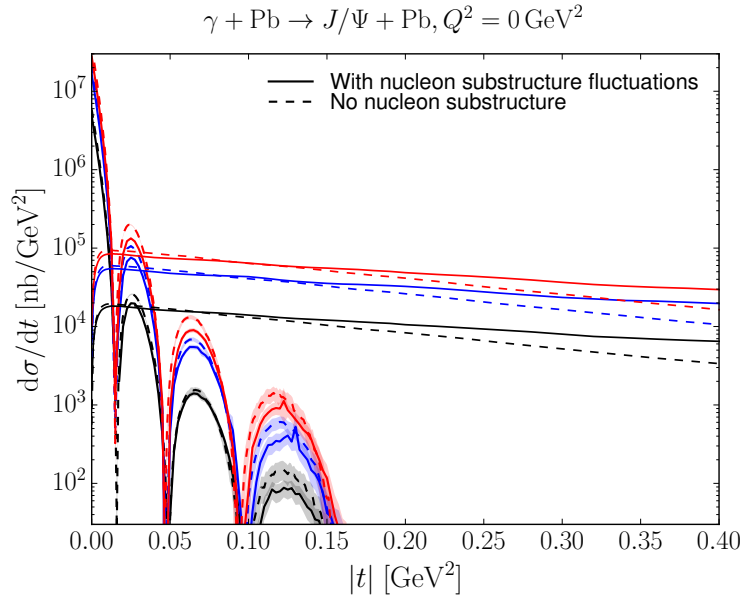


**Figure 4.15:** The differential cross sections for coherent and incoherent production of  $J/\psi$  in  $e\text{Pb}$  as a function of the negative four momentum transfer squared  $-t$ , for photoproduction,  $Q^2 = 0$ . The lines showing dips are for coherent production, and those extending to large  $|t|$  are for incoherent. The solid (dashed) lines are the results with (without) nucleon substructure fluctuations. Black, blue, red are for  $W = 0.1, 0.813, 2.5 \text{ TeV}$ , respectively.

3233 over the target configurations and taking the square

$$\frac{d\sigma}{dt} = \frac{1}{16\pi} |\langle \mathcal{A}(x, Q, \Delta) \rangle|^2. \quad (4.8)$$

3234 Here the brackets  $\langle \dots \rangle$  refer to averages over different configurations of the target. The incoher-  
 3235 ent cross section is obtained by subtracting the coherent cross section from the total diffractive  
 3236 cross section. It is standardly assumed that it takes the form of a variance of the diffractive  
 3237 scattering amplitude

$$\frac{d\sigma}{dt} = \frac{1}{16\pi} \left( \langle |\mathcal{A}(x, Q, \Delta)|^2 \rangle - |\langle \mathcal{A}(x, Q, \Delta) \rangle|^2 \right), \quad (4.9)$$

3238 which should be valid for small  $|t|$ . The  $t$  dependence, and the relation between the impact  
 3239 parameter and  $t$  through the Fourier transform, makes diffractive scattering a sensitive probe  
 3240 of the internal geometric structure of hadrons and nuclei. In particular, because the incoherent  
 3241 cross section has the form of a variance of the amplitude, it is sensitive to the amount of  
 3242 fluctuations in impact parameter space.

3243 The results in Fig. 4.15 (results for higher  $Q^2$  are very similar) indicate that the incoherent  
 3244 production is dominant for most values of  $-t$ , except for the very small momentum transfers,  
 3245 about  $|t| < 0.02 \text{ GeV}^2$ . Thus, dedicated instrumentation which will allow us to distinguish  
 3246 between the two cases is essential if one wants to measure the coherent process in a reasonably  
 3247 wide range of  $|t|$ . As in the proton case, the coherent  $t$  distribution exhibits characteristic dips.  
 3248 However, in the case of the nuclear targets the dips occur for much smaller values of  $t$ . This is  
 3249 related to the much larger value of the dipole amplitude for a wide range of impact parameters  
 3250 in the case of nuclear targets compared to the proton case.

3251 Another interesting aspect, see Sec. 3.2.5, is the effect of the transverse structure of the target in  
 3252 nuclear coherent and incoherent diffraction. For example, in the formulation shown above [254]  
 3253 a fixed number of hot spots was considered, while in [258] (see also [255] for a realisation  
 3254 using small- $x$  evolution) a growing number with  $1/x$  is implemented. In both cases, the ratio  
 3255 of incoherent to coherent diffraction decreases with  $W$ , being smaller for larger nuclei. This  
 3256 decrease is sensitive to the details of the distribution of hot spots - thus, to the fluctuations  
 3257 of the gluon distribution in transverse space. It also shows interesting dependencies on the  
 3258 mass of the produced vector meson and on  $Q^2$ , resulting in the ratio being smaller for lighter  
 3259 vector mesons and for lower  $Q^2$ . Besides, the hot spot treatment also has some effects on the  
 3260 distributions in momentum transfer, see Fig. 4.15. In order to check these ideas, both the  
 3261 experimental capability to separate coherent from incoherent diffraction, and a large lever arm  
 3262 in  $W$  and  $Q^2$  as available at the LHeC, are required.

3263 We thus conclude that by investigating coherent and incoherent diffractive scattering on nuclei,  
 3264 one gets unique insight into the spatial structure of matter in nuclei. On the one hand, the  
 3265 coherent cross section, which is obtained by averaging the amplitude before squaring it, is  
 3266 sensitive to the average spatial density distribution of gluons in transverse space. On the other  
 3267 hand, the incoherent cross section, which is governed by the variance of the amplitude with  
 3268 respect to the initial nucleon configurations of the nucleus, measures fluctuations of the gluon  
 3269 density inside the nucleus. In the case of a nucleus, the diffractive production rate is controlled by  
 3270 two different scales related to the proton and nucleus size. At momentum scales corresponding  
 3271 to the nucleon size  $|t| \sim 1/R_p^2$  the diffractive cross section is almost purely incoherent. The  
 3272  $t$ -distribution in coherent diffractive production off the nucleus gives rise to a dip-type structure  
 3273 for both saturation and non-saturation models, while in the case of incoherent production at  
 3274 small  $|t|$ , both saturation and non-saturation models do not lead to dips [254]. This is in drastic

3275 contrast to the diffractive production off the proton where only saturation models lead to a  
 3276 dip-type structure in the  $t$ -distribution at values of  $|t|$  that can be experimentally accessible.  
 3277 Therefore, diffractive production offers a unique opportunity to measure the spatial distribution  
 3278 of partons in the protons and nuclei. It is also an excellent tool to investigate the approach to  
 3279 unitarity in the high energy limit of QCD.

3280 While we have focused here on  $J/\psi$  production, lighter vector mesons like  $\rho, \omega, \phi$  could also be  
 3281 studied. They should show a different  $Q^2$  dependence and their larger sizes would make them  
 3282 lie closer to the black disk regime. Also the dominance of two-jet events in photoproduction  
 3283 would provide sensitivity to the approach to the unitarity limit [407].

### 3284 4.3.2 Inclusive diffraction on nuclei

3285 In Sec. 3.2.6, a study of the prospects for extracting diffractive parton densities in the proton was  
 3286 presented following [266]. Similar considerations apply to diffraction in  $eA$  as to  $ep$  collisions.  
 3287 The main difference is the larger contribution from incoherent diffraction <sup>3</sup>  $e + A \rightarrow e + X + A^*$   
 3288 than from coherent diffraction  $e + A \rightarrow e + X + A$ , the former dominating for  $|t|$  larger than  
 3289 a few hundredths of a  $\text{GeV}^2$ . In the following we focus on coherent diffraction, which could be  
 3290 distinguished from the incoherent case using forward detectors [1].

3291 Assuming the same framework (collinear factorization for hard diffraction, such that Eq. (3.23),  
 3292 and Regge factorization, Eq. (3.25) as introduced for  $ep$  in Sec. 3.2.6 also hold for  $eA$ ), nuclear  
 3293 diffractive PDFs (nDPDFs) can be extracted from the diffractive reduced cross sections. It  
 3294 should be noted that such nDPDFs have never been measured. With the same electron energy  
 3295  $E_e = 60 \text{ GeV}$  and nuclear beams with  $E_N = 2.76 \text{ TeV/nucleon}$  for the LHeC, the kinematic  
 3296 coverage is very similar to that shown in Fig. 3.40. For details, see Ref. [266].

3297 The nuclear modification factors for  $F_2^{D(3)}$  and  $F_L^{D(3)}$  from the FGS models [407] are shown in  
 3298 Fig. 4.16 where, in analogy to Eq. (4.1), the diffractive nuclear modification factor reads

$$R_k^A(\beta, \xi, Q^2) = \frac{f_{k/A}^{D(3)}(\beta, \xi, Q^2)}{A f_{k/p}^{D(3)}(\beta, \xi, Q^2)}. \quad (4.10)$$

3299 The model in [407] employs Gribov inelastic shadowing [262] which relates diffraction in  $ep$   
 3300 to nuclear shadowing for total and diffractive  $eA$  cross sections. It assumes that the nuclear  
 3301 wave function squared can be approximated by the product of one-nucleon densities, neglects  
 3302 the  $t$ -dependence of the diffractive  $\gamma^*$ -nucleon amplitude compared to the nuclear form factor,  
 3303 introduces a real part in the amplitudes [442], and considers the colour fluctuation formalism  
 3304 for the inelastic intermediate nucleon states [443]. There are two variants of the model, named  
 3305 H and L, corresponding to different strengths of the colour fluctuations, giving rise to larger and  
 3306 smaller probabilities for diffraction in nuclei with respect to that in proton, respectively. Results  
 3307 from both model versions are shown in Figs. 4.16 and 4.17.

3308 The pseudodata for the reduced cross sections are generated assuming 5% systematic error  
 3309 and statistic errors calculated for the integrated luminosity of  $2 \text{ fb}^{-1}$ . A selected subset of  
 3310 the simulated data is shown in Fig. 4.17. The large kinematic coverage and small uncertainty  
 3311 (dominated by the assumed systematics) illustrated in this figure compared to Fig. 3.42 make it  
 3312 clear that an accurate extraction of nDPDFs in  $^{208}\text{Pb}$  in an extended kinematic region, similar  
 3313 to that shown in Figs. 3.43 and 3.44, will be possible.

<sup>3</sup> $A^*$  denotes a final state in which the nucleus has dissociated to a system of at least two hadrons, but the rapidity gap signature that defines the diffractive event is still present.

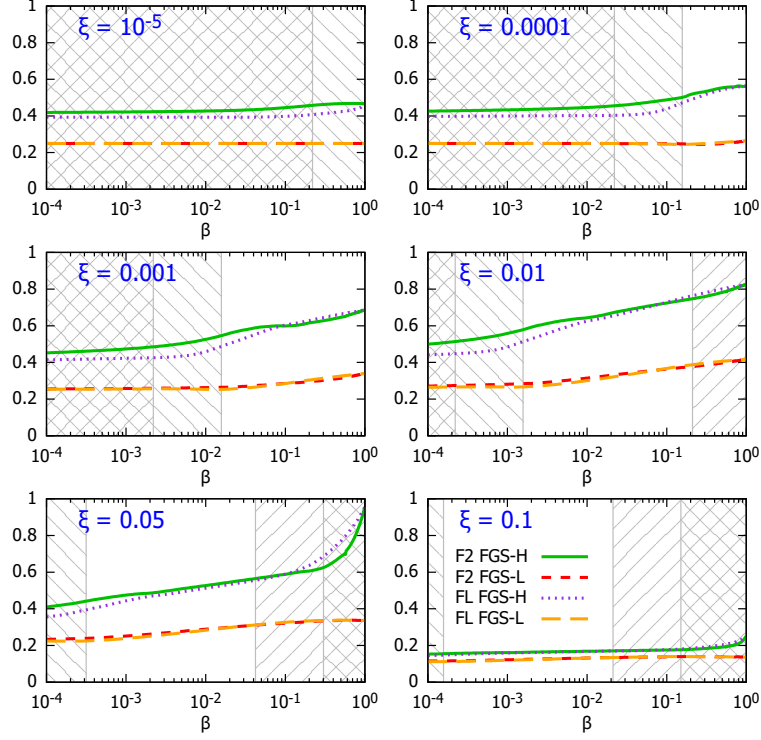


**Figure 4.16:** Nuclear modification factor, Eq. (4.10), for  $F_2^{D(3)}$  and  $F_L^{D(3)}$  in  $^{208}\text{Pb}$  versus  $\beta$ , at  $Q^2 = 10 \text{ GeV}^2$  and for different  $\xi$ , for the models H and L in [407]. The ‘\’ and ‘/’ hatched areas show kinematically excluded regions for  $E = 2.76$  and  $19.7 \text{ TeV/nucleon}$ , respectively.

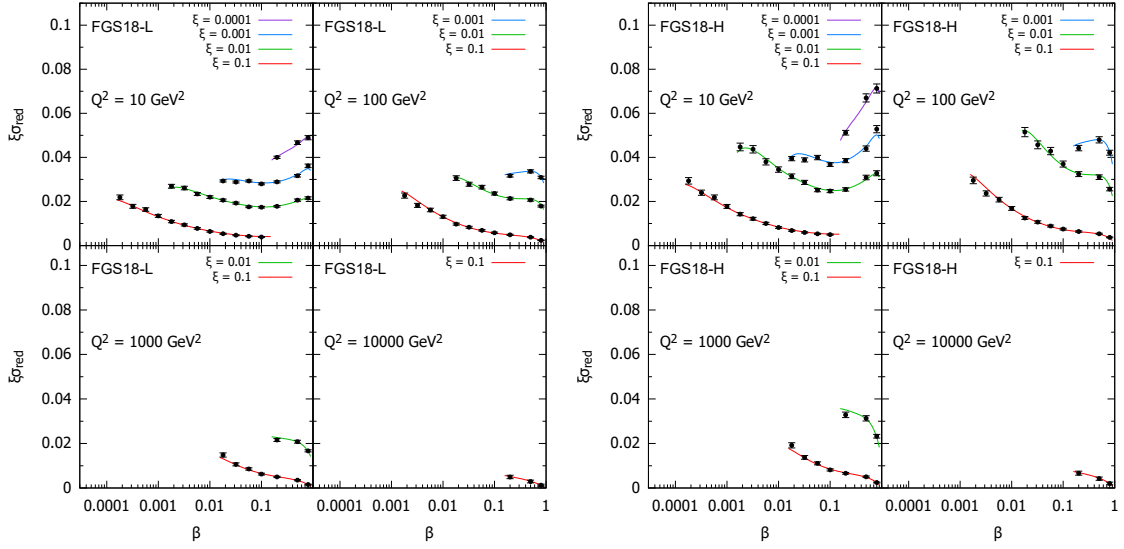


**Figure 4.17:** An indicative subset of simulated data for the diffractive reduced cross section as a function of  $\beta$  in bins of  $\xi$  and  $Q^2$  for  $e^{208}\text{Pb}$  collisions at the LHeC, in the models in [407]. The curves for  $\xi = 0.01, 0.001, 0.0001$  are shifted up by  $0.01, 0.02, 0.03$ , respectively.

## 4.4 New Dynamics at Small $x$ with Nuclear Targets

As discussed in Sec. 3.2.2, theoretical expectations [409] indicate that fixed-order perturbation theory leading to the DGLAP evolution equations should eventually fail. When  $x$  decreases,  $\alpha_s \ln 1/x$  becomes large and these large logarithms must be resummed, leading to the BFKL equation. Furthermore, when the parton density becomes large, the linear approximation that underlies both DGLAP and BFKL breaks, and non-linear processes must be taken into account to compute parton evolution. The CGC [408] offers a non-perturbative but weak coupling effective theory to treat dense parton systems in a systematic and controlled way. One of the important predictions of the CGC is that in a dense parton system saturation occurs leading to the emergence of a new dynamical scale – the saturation scale  $Q_{sat}$ , which increases with the energy.

The parton density in a hadron becomes high both through evolution – when energy or  $1/x$  becomes large, and/or when partons are accumulated by overlapping nucleons – when mass number  $A$  becomes large in a nucleus. In the nucleus rest frame, the virtual photon fluctuations at small  $x < (2m_N R_A)^{-1}$ , with  $m_N$  the nucleon mass and  $R_A$  the nuclear radius, acquire a lifetime larger than the time taken to traverse the nucleus and, thus, all partons within a transverse area  $\sim 1/Q^2$  are simultaneously probed. Actually, the parameter determining the transition between linear and non-linear dynamics is the parton density and, therefore, the onset of this new regime of QCD and its explanation must be tested, as commented in [1], exploring both decreasing values of  $x$  and increasing values of  $A$  in a kinematic  $x - Q^2$  region where, in order to be sensitive to differences in evolution, enough lever arm in  $Q^2 \gg \Lambda_{\text{QCD}}^2$  at small  $x$  is available. The saturation scale  $Q_{sat}$  that characterises the typical gluon momentum in a saturated hadron wave function increases with nuclear size,  $Q_{sat}^2 \propto A^{1/3}$ . Therefore, in  $eA$  collisions the perturbatively saturated regime is achieved at parametrically larger  $x$  than in a proton – a prediction not only of the CGC but of all multiple scattering models that anticipate an approach to the black disk, unitarity limit.

The opportunities to establish the existence of saturation in lepton-nucleus collisions are numerous. They include inclusive observables, both total and diffractive cross sections, and less inclusive ones like correlations:

- Tension in DGLAP fits for inclusive observables: As discussed in [1, 228] and in Sec. 3.2.4, deviations from fixed-order perturbation theory can be tested by the tension that would appear in the description within a DGLAP fit of observables with different sensitivities to the sea and the glue, for example  $F_2$  and  $F_L$  (or reduced cross sections at different energies) or  $F_2^{\text{inclusive}}$  and  $F_2^{\text{heavy quarks}}$ . In [444], such an exercise was performed considering  $F_2$  and  $F_L$  pseudodata for  $eAu$  collisions at the EIC [234] using reweighting techniques. While the results for EIC energies are shown not to be conclusive due to the reduced lever arm in  $Q^2 > Q_{sat}^2 \gg \Lambda_{\text{QCD}}^2$ , the much larger centre-of-mass energies at the LHeC (and FCC-eh) should make possible a search for tensions between different observables.
- Saturation effects in diffraction: A longstanding prediction of saturation [239, 445, 446] is a modification of the diffractive cross section in nuclei with respect to protons, with a suppression (enhancement) at small (large)  $\beta$  due to the approach of the nucleus to the black disk limit, where elastic and diffractive scattering become maximal, and the behaviour of the different Fock components of the virtual photon wave function. Such effects can also be discussed in terms of a competition of nuclear shadowing with the probability that the event remains diffractive in the multiple scattering process [407]. This leads to the generic expectation of an enhancement of the ratio of the coherent diffractive

3360 cross section in nucleus over that in protons, in non-linear approaches with respect to  
3361 linear ones [234].

3362 • Correlations: Correlations have been considered for a long time as sensitive probes of the  
3363 underlying production dynamics. For example, the cross section for the production of  
3364 two jets with the same hardness and widely separated in rapidity, called Mueller-Navelet  
3365 jets [447], was proposed as a test of BFKL versus DGLAP dynamics, but the effect of  
3366 saturation has not been widely studied although it has the large potentiality of differ-  
3367 entiating linear resummation from non-linear saturation where non-trivial nuclear effects  
3368 could appear. Correlations between jets were analysed in [1] for the LHeC kinematics,  
3369 both in inclusive and diffractive events, see the formalism in [448]. On the other hand, the  
3370 azimuthal decorrelation of particles and jets when saturation effects are at work – at small  
3371  $x$ , studied by the difference between collisions involving proton and nuclei, was proposed  
3372 long ago in  $dAu$  collisions at the Relativistic Hadron Collider [449, 450]. It was studied  
3373 in [1] for the LHeC kinematics, see recent developments in [451] and the extension to  
3374 forward dijet production in [452]. It could also be analysed in ultraperipheral collisions at  
3375 the LHC, see Sec. 7.5.

## 3376 4.5 Collective effects in dense environments – the ‘ridge’

3377 One of the most striking discoveries [453] at the LHC is, that in all collision systems, from  
3378 small ( $pp$  and  $pA$ ) to large ( $AA$ ), many of the features that are considered as indicative of the  
3379 production of a dense hot partonic medium are observed (see e.g. reviews [454–456] and references  
3380 therein). The most celebrated of such features is the long rapidity range particle correlations  
3381 collimated in azimuth, named the ‘ridge’, shown in Fig. 4.18. The dynamics underlying this  
3382 phenomena, either the formation of QGP and the existence of strong final state interactions, or  
3383 some initial state dynamics that leaves imprint on the final observables, is under discussion [457].  
3384 While observed in photoproduction on Pb in UPCs at the LHC [458], its existence in smaller  
3385 systems like  $e^+e^-$  [459] at LEP and  $ep$  at HERA [460] has been scrutinised, but the results are  
3386 not conclusive.

3387 In this respect, measurements in  $ep$  and  $eA$  collisions at the LHeC at considerable center-of-  
3388 mass energies will offer crucial additional information. For example, the collision of the virtual  
3389 photon with the proton at the LHeC can be considered as a high energy collision of two jets or  
3390 ‘flux tubes’, as discussed in Refs. [463, 464] and illustrated in Fig. 4.18. This can lead to the  
3391 production of ‘ridges’ and other novel configurations of gluons and quarks and will be measured  
3392 uniquely at the LHeC.

## 3393 4.6 Novel QCD Nuclear Phenomena at the LHeC

3394 Beyond the topics discussed above there are many novel phenomena which can be explored in  $eA$   
3395 collisions at LHeC or FCC-eh, in a high energy regime and using dedicated instrumentation. We  
3396 shall briefly review some of these phenomena, which can be understood utilizing the light-front  
3397 framework of QCD, for a review see [465].

3398 One of the most important theoretical tools in high energy physics is Dirac’s light-front (LF)  
3399 time:  $\tau = x^+ = t + z/c$ , the time along the light-front [466], a concept which allows all of the  
3400 tools and insights of Schrödinger’s quantum mechanics and the Hamiltonian formalism to be

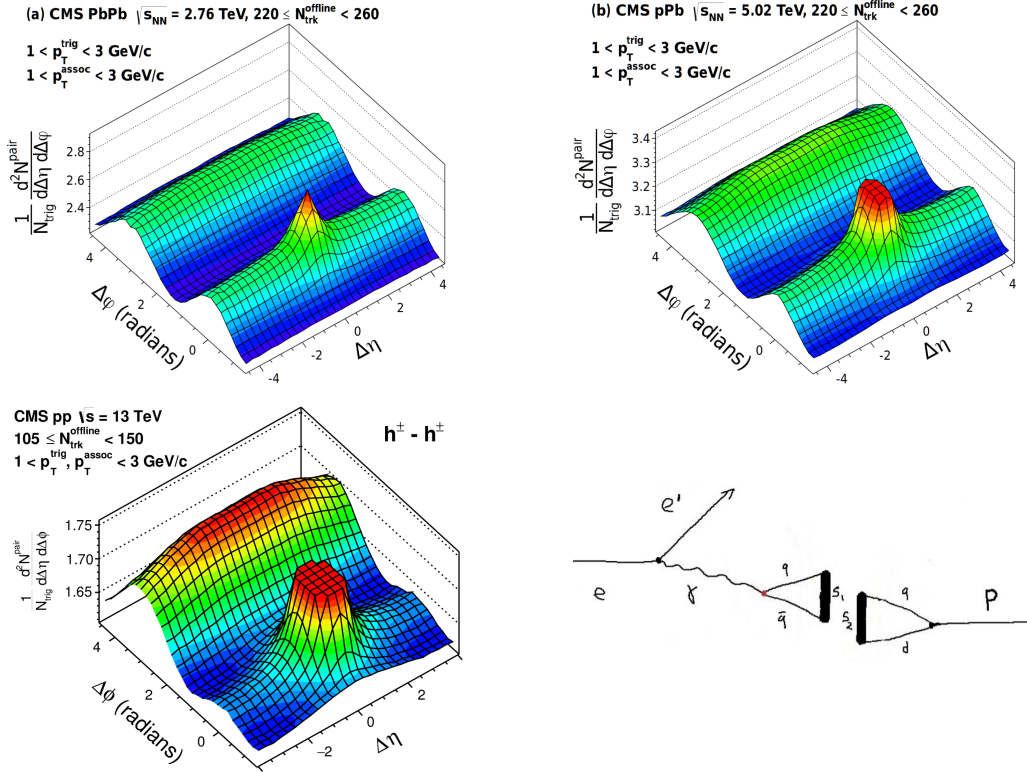


**Figure 4.18:** Left and top right: Collective effects seen in high-multiplicity two-particle azimuthal correlation, as observed by CMS in PbPb, pPb [461], and pp [462] collisions. Bottom right: Schematic illustration for the production of *ridge*-like effects in ep or eA scattering at the LHeC [463].

3401 applied to relativistic physics [465]. When one takes a photograph, the object is observed at a  
 3402 fixed LF time. Similarly, Compton  $\gamma p \rightarrow \gamma' p''$  and deep-inelastic lepton-proton scattering are  
 3403 measurements of proton structure at fixed LF time. Unlike ordinary *instant time*  $t$ , physics at  
 3404 fixed  $\tau$  is Poincaré invariant; i.e. independent of the observer's Lorentz frame. Observations  
 3405 at fixed  $\tau$  are made within the causal horizon. LF time  $\tau$  reduces to ordinary time  $t$  in the  
 3406 nonrelativistic limit  $c \rightarrow \infty$ .

3407 The LF wavefunctions (LFWF) of hadrons are superpositions of  $\Psi_n^H(x_i, \vec{k}_{\perp i}, \lambda_i) = \langle \Psi_H | n \rangle$ ,  
 3408 the Fock state projections of the eigensolution of the QCD LF Hamiltonian  $H_{QCD} | \Psi_H \rangle =$   
 3409  $M_H^2 | \Psi_H \rangle$ . They encode the underlying structure of bound states in quantum field theory and  
 3410 underlie virtually every observable in hadron physics. Hadronic LFWFs can also be measured  
 3411 directly by the Ashery method [467], the coherent diffractive dissociation of high energy hadrons  
 3412 into jets [468, 469]. In the diffractive dissociation of a high energy hadron into quark and gluon  
 3413 jets by two-gluon exchange, the cross-section measures the square of the second transverse  
 3414 derivative of the projectile LFWF. Similarly, the dissociation of a high energy atom such as  
 3415 positronium or *true muonium* ( $[\mu^+ \mu^-]$ ) can be used to measure the transverse derivative of its  
 3416 LFWFs.

3417 Hadronic LFWFs are defined at fixed  $\tau = -x^+ = t + z/c$ ; they are thus off-shell in the total  
 3418  $P^- = P^0 - P^z$ , not energy  $P^0$  [465]. Thus LFWFs are also off-shell in  $\mathcal{M}^2 = P^+ P^- - P_{\perp}^2 =$   
 3419  $[\sum_i k_i^\mu]^2 = \sum_i \frac{k_{\perp i}^2 + m^2}{x_i}$ , the invariant mass squared of the constituents in the  $n$ -particle Fock  
 3420 state. LFWFs are thus functions of the invariant mass squared of the constituents in the  
 3421 Fock state. For a two-particle Fock state,  $\mathcal{M}^2 = \frac{k_{\perp}^2 + m^2}{x(1-x)}$ . Thus, the constituent transverse

3422 momenta  $k_{\perp i}^2$  do appear alone as a separate factor in the LFWF; the transverse momenta are  
 3423 always coupled to the longitudinal LF momentum fractions  $x_i$ . This is the light-front version  
 3424 of rotational invariance. Only positive  $k_i^+ = k_i^0 + k_i^z \geq 0$  and  $0 \leq x_i = \frac{k_i^+}{P^+} \leq 1$  appear,  
 3425 where  $\sum_i x_i = 1$ . In addition,  $J^z = \sum_i L_i^z + S_i^z$ , as well as  $P^+ = \sum_i k_i^+$  and  $\vec{P}_{\perp} = \sum_i \vec{k}_{\perp i}$  are  
 3426 conserved at every vertex – essential covariant kinematical constraints. A remarkable property:  
 3427 the anomalous gravitomagnetic moment of every LF Fock state vanishes at  $Q^2 = 0$ . The  
 3428 LFWFs of bound states are off-shell in  $P^- = \sum_i k_i^-$ , but they tend to be maximal at minimal  
 3429 off-shellness; i.e. minimal invariant mass. In fact, in the holographic LFWFs where colour is  
 3430 confined, the LFWFs of hadrons have fast Gaussian fall-off in invariant mass. This feature also  
 3431 underlie intrinsic heavy quark Fock states: the LFWFs have maximal support when all of the  
 3432 constituents have the same rapidity  $y_i$ ; i.e.  $x_i \propto \sqrt{m_i^2 + k_{\perp i}^2}$ . Thus the heavy quarks have the  
 3433 highest momentum fractions  $x_i$ .

3434 Conversely, light-front wavefunctions provide the boost-invariant transition amplitude which  
 3435 convert the free quark and gluons into the hadronic eigenstates of QCD. Thus, knowing the  
 3436 LFWFs allows one to compute *hadronization at the amplitude level* – how the coloured quarks  
 3437 and gluons produced in a deep inelastic scattering event  $ep \rightarrow e'X$  at the LHeC are confined  
 3438 and emerge as final-state hadrons.

3439 The LF formalism leads to many novel nuclear phenomena, such as *hidden colour* [470] *colour*  
 3440 *transparency* [471], *nuclear-bound quarkonium* [472], *nuclear shadowing and antishadowing* of  
 3441 nuclear structure functions, etc. For example, there are five distinct colour-singlet QCD Fock  
 3442 state representations of the six colour-triplet quarks of the deuteron. These hidden-colour Fock  
 3443 states become manifest when the deuteron fluctuates to a small transverse size, as in mea-  
 3444 surements of the deuteron form factor at large momentum transfer. One can also probe the  
 3445 hidden-colour Fock states of the deuteron by studying the final state of the dissociation of the  
 3446 deuteron in deep inelastic lepton scattering at the LHeC  $eD \rightarrow e'X$ , where  $X$  can be  $\Delta^{++} + \Delta^-$ ,  
 3447 six quark jets, or other novel colour-singlet final states.

3448 The LF wave functions provide the input for scattering experiments at the amplitude level,  
 3449 encoding the structure of a projectile at a single light-front time  $\tau$  [465]. For example, consider  
 3450 photon-ion collisions. The incoming photon probes the finite size structure of the incoming  
 3451 nucleus at fixed LF time, like a photograph – not at a fixed instant time, which is acausal.  
 3452 Since the nuclear state is an eigenstate of the LF Hamiltonian, its structure is independent of  
 3453 its momentum, as required by Poincaré invariance. One gets the same answer in the ion rest  
 3454 frame, the CM frame, or even if the incident particles move in the same direction, but collide  
 3455 transversely. There are no colliding *pancakes* using the LF formalism.

3456 The resulting photon-ion cross-section is not point-like; it is shadowed:  $\sigma(\gamma A \rightarrow X) = A^{\alpha} \sigma(\gamma N \rightarrow$   
 3457  $X)$ , where  $A$  is the mass number of the ion,  $N$  stands for a nucleon, and the power  $\alpha \approx 0.8$   
 3458 reflects Glauber shadowing [473]. The shadowing stems from the destructive interference of  
 3459 two-step and one-step amplitudes, where the two-step processes involve diffractive reactions on  
 3460 a front-surface nucleon which shadows the interior nucleons. Thus the photon interacts primar-  
 3461 ily on the front surface. Similarly, a high energy ion-ion collision  $A_1 + A_2 \rightarrow X$  involves the  
 3462 overlap of the incident frame-independent LFWFs. The initial interaction on the front surface  
 3463 of the colliding ions can resemble a shock wave.

3464 In the case of a deep inelastic lepton-nucleus collision  $\gamma^* A \rightarrow X$ , the two-step amplitude involves  
 3465 a leading-twist diffractive deep inelastic scattering (DDIS)  $\gamma^* N_1 \rightarrow V^* N_1$  on a front surface  
 3466 nucleon  $N_1$  and then the on-shell propagation of the vector system  $V^*$  to a downstream nucleon  
 3467  $N_2$  where it interacts inelastically:  $V^* N_2 \rightarrow X$ . If the DDIS involves Pomeron exchange, the two-

3468 step amplitude interferers destructively with the one-step amplitude  $\gamma^* N_1 \rightarrow X$  thus producing  
3469 shadowing of the nuclear parton distribution function at low  $x < 0.1$ . On the other hand, if  
3470 the DDIS process involves  $I = 1$  Reggeon exchange, the interference is constructive, producing  
3471 *flavour-dependent* leading-twist antishadowing [473] in the domain  $0.1 < x < 0.2$ .

3472 One can also show that the Gribov-Glauber processes, which arise from leading-twist diffractive  
3473 deep inelastic scattering on nucleons and underly the shadowing and antishadowing of nuclear  
3474 structure functions [473], prevent the application of the operator product expansion to the  
3475 virtual Compton scattering amplitude  $\gamma^* A \rightarrow \gamma^* A$  on nuclei and thus negate the validity of the  
3476 momentum sum rule for deep inelastic nuclear structure functions [474].

## Chapter 5

# Higgs Physics with LHeC

### 5.1 Signal Strength and Couplings

#### 5.1.1 Introduction

The Higgs boson was discovered in 2012 by ATLAS [475] and CMS [476] at the Large Hadron Collider (LHC). It is the most recently discovered and least explored part of the Standard Model. The Higgs boson ( $H$ ) is of fundamental importance as it is related to the spontaneous breaking of a locally symmetric gauge theory, to a mechanism predicted by [322, 323, 477] and independently by [478], in which the intermediate vector bosons are explained to be massive<sup>1</sup> while the photon remains massless. Fermions obtain a mass via the Yukawa couplings with the Higgs field. Following the discovery of the Higgs boson, its physics and thorough exploration has become a central theme of the physics programme at the LHC. Any high-energy future collider project, beginning with the high luminosity upgrade of the Large Hadron Collider, the HL-LHC, underway to collect data in a decade hence, has put the potential to precisely study the properties of the Higgs boson into its center of attention, for understanding its characteristics and hoping to open a new window into physics extending beyond the Standard Model, see for example [479, 480]. In this section we present the potential to explore the SM Higgs physics at the LHeC and to certain extent at FCC-eh also.

A first challenge on the physics of the Higgs boson is to establish whether it indeed satisfies the properties inherent to the Standard Model (SM) regarding its production and decay mechanisms. The SM neutral  $H$  boson decays into pairs of fermions,  $f\bar{f}$ . The dominant decay is  $H \rightarrow b\bar{b}$  with a branching fraction of about 58%. The branching scales with the square of the fermion mass,  $m_f^2$ . The next prominent fermionic decay therefore is  $H \rightarrow \tau^+\tau^-$  with 6.3% followed by the charm decay with a predicted branching fraction of 2.9%. The Higgs boson also decays into pairs of  $W$  and  $Z$  bosons at a rate of 21.5% and 2.6%, respectively. Loop diagrams enable the decay into gluon and photon pairs with a branching of 8.2 and 0.2%, respectively. The seven most frequent decay channels, ordered according to descending branching fractions, thus are into  $b\bar{b}$ ,  $W^+W^-$ ,  $gg$ ,  $\tau^+\tau^-$ ,  $c\bar{c}$ ,  $ZZ$  and  $\gamma\gamma$ . Together these are predicted to represent a total SM branching fraction of 99.9%. At the LHC these and rarer decays can be reconstructed,

---

<sup>1</sup> The mass of the  $W$  boson,  $M_W$ , is generated through the vacuum expectation value,  $\eta$ , of the Higgs field ( $\Phi$ ) and given by the simple relation  $M_W = g\eta/\sqrt{2}$  where  $g$  is the weak interaction coupling. Here  $\eta = \sqrt{-\mu^2/2\lambda}$  with the two parameters of the Higgs potential that is predicted to be  $V = -\mu^2\Phi^+\Phi - \lambda(\Phi^+\Phi)^2$ . The Higgs mass is given as  $M_H = 2\eta\sqrt{\lambda}$  while the mass of the  $Z$  boson is related to  $M_W$  with the electroweak mixing angle,  $M_Z = M_W/\cos\Theta_W$ .

3506 with the exception of the charm decay for reasons of prohibitive combinatorial background. The  
 3507 main purpose of this paper is to evaluate the prospects for precisely measuring these channels  
 3508 in electron-proton scattering.

### 3509 5.1.2 Higgs Production in Deep Inelastic Scattering

3510 In deep inelastic electron-proton scattering, the Higgs boson is predominantly produced through  
 3511  $WW$  fusion in charged current DIS (CC) scattering, Fig. 1. The next large Higgs production  
 3512 mode in  $ep$  is  $ZZ \rightarrow H$  fusion in neutral current DIS (NC) scattering, Fig. 1, which has a smaller  
 but still sizable cross section. These  $ep$  Higgs production processes are very clean for a number

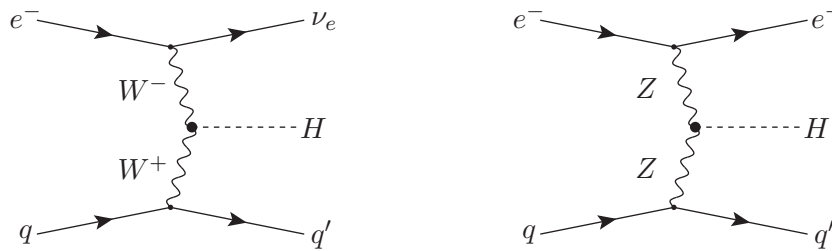


**Figure 5.1:** Higgs boson production in charged (left) and neutral (right) current deep inelastic electron-proton scattering to leading order.

3513  
 3514 of reasons:

- 3515 • even at the high luminosity of  $10^{34} \text{ cm}^{-2} \text{ s}^{-1}$  the inclusive pileup is only 0.1 (1) for the  
 3516 LHeC (FCC-eh) and the final state signature therefore free from event overlap, in contrast  
 3517 to the HL-LHC where it will typically be 150;
- 3518 • in  $ep$ , contrary to  $pp$ , there is no initial nor final state colour (re)connection;
- 3519 • the higher-order corrections are small. For the total CC process they were estimated [481]  
 3520 to be of the order of only 1% for the QCD part, subject to cut dependencies yielding  
 3521 shape changes up to 20%, and  $-5\%$  for the QED part (with a weak dependence on  
 3522 the PDF choice). The smallness of the QCD corrections was attributed mainly to the  
 3523 absorption of gluon and quark radiation effects in the evolution of the parton distributions  
 3524 (PDFs) [481]. The PDFs will be measured with very high precision at any of the  $ep$   
 3525 colliders here considered, see Chapter 3, thus allowing a unique self-consistency of Higgs  
 3526 cross section measurements.

3527 The NC reaction is even cleaner than the CC process as the scattered electron fixes the kinematics  
 3528 more accurately than the missing energy. While in  $pp$  both  $WW$  and  $ZZ$  processes are hardly  
 3529 distinguishable, in  $ep$  they uniquely are, which provides an important, precise constraint on the  
 3530  $WWH$  and  $ZZH$  couplings.

### 3531 5.1.3 Kinematics of Higgs Production

3532 At HERA the kinematics was conveniently reconstructed through event-wise measurements of  
 3533  $Q^2$  and  $y$ . The reconstruction of the kinematics in charged currents uses the inclusive hadronic  
 3534 final state measurements. Based on the energies  $E'_e$  and  $E_h$  and the polar angles  $\Theta_e$  and  $\Theta_h$

3535 of the scattered electron and the hadronic final state, respectively, one obtains a redundant  
 3536 determination of the kinematics in neutral current scattering. This permits a cross calibration  
 3537 of calorimetric measurements, of the electromagnetic and hadronic parts and of different regions  
 3538 of the detector, which is a major means to achieve superb, sub-percent precision in  $ep$  collider  
 3539 measurements. Methods have been developed to optimise the kinematics reconstruction and  
 3540 maximise the acceptance by exploiting the redundant determination of the scattering kinematics,  
 3541 see for example [46]. The basic kinematic distributions of  $Q^2$ ,  $x$  and  $y$  are shown in Fig. 5.2.  
 The average  $(Q^2, x)$  values for Higgs production at the LHeC [FCC-eh] are  $(2000 \text{ GeV}^2, 0.02)$

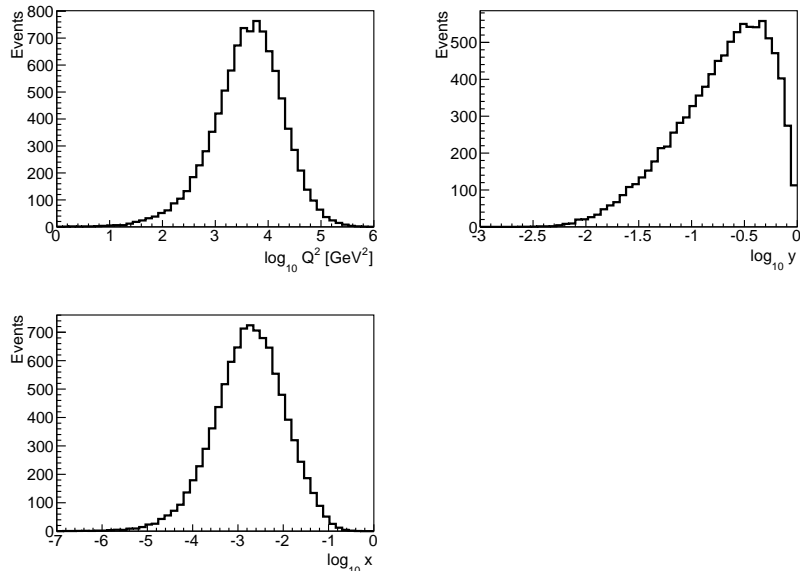


**Figure 5.2:** Distributions for  $ep \rightarrow \nu H X$  events of the parton-level negative 4-momentum transfer squared,  $Q^2$  (top left), Bjorken  $x$  (bottom left) and the inelasticity  $y = Q^2/sx$  (top right) for the FCC-eh ( $\sqrt{s} = 3.5 \text{ TeV}$ ). Events generated with MadGraph, see Tab. 5.1.

3542 [(6500  $\text{GeV}^2, 0.0016$ )]. This is placed very well in the kinematic plane, shown above.  
 3543

3544 As is described in this paper elsewhere, constraints for a large pseudorapidity or polar angle,  
 3545  $\eta = \ln \tan \theta/2$ , acceptance of the apparatus arise i) for the backward region (the polar angle  
 3546 is defined w.r.t. the proton beam direction) from the need to reconstruct electrons at low  $Q^2$   
 3547 enabling low  $x$  physics and ii) for the forward region to cover a maximum region towards large  
 3548  $x$  at medium  $Q^2$  with the reconstruction of the hadronic final state. The acceptance therefore  
 3549 extends, for the LHeC, to pseudorapidities of  $\eta = \pm 5$ , which for the FCC-eh case is extended to  
 3550  $\eta = \pm 6$ . The large acceptance is in particular suitable for the reconstruction of Vector-Boson-  
 3551 Fusion Higgs boson event signatures, see Fig. 5.3 for the typical pseudorapidity distributions of  
 3552 Higgs boson event signature in DIS at the most asymmetric FCC-eh collider configuration.

3553 Geometric acceptances due to kinematic constraints in the pseudorapidity on the Higgs decay  
 3554 products for both LHeC and FCC-eh are further illustrated in Fig. 5.4. The acceptances are  
 3555 calculated for a basic selection of all final states with  $p_T > 15 \text{ GeV}$  and a coverage of the forward  
 3556 jet up to  $\eta = 5$  and  $\eta = 6$ , respectively, for both colliders. As seen from Fig. 5.4, the acceptances  
 3557 are higher for the less asymmetric LHeC beam configuration and about the same for hadronic  
 3558 calorimetry up to  $\eta = 5$  and  $\eta = 6$ . Hence, the LHeC calorimeter is designed for  $\eta = 5$ . The  
 3559 optimal hadronic calorimetry coverage for FCC-eh is clearly  $\eta = 6$  yielding significantly higher  
 3560 acceptances in comparison to an  $\eta = 5$  calorimetry. From Fig. 5.4, it is apparent that for both  
 3561 collider configurations the Higgs decay products would require tagging capabilities up  $\eta = 3.5$ ,

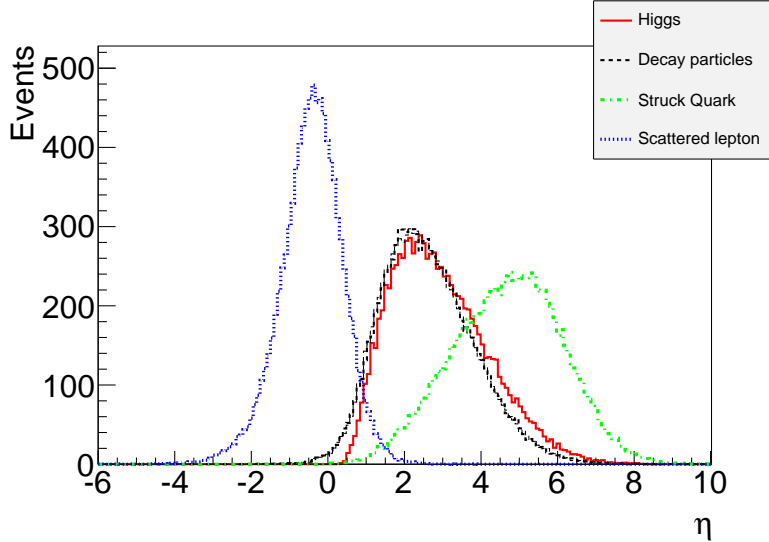


**Figure 5.3:** Pseudorapidity ( $\eta$ ) distributions, at parton-level, characterising the Vector-Boson-Fusion production and decay of the Higgs boson to  $WW$  in DIS scattering at FCC-eh. The scattered lepton (blue) in the NC case (or missing energy for CC) has an average  $\eta$  of about  $-0.5$ , i.e. it is scattered somewhat backwards (in electron beam direction). The pseudorapidity distributions of the generated Higgs boson (red) and its decay particles (black) are very similar and peak at  $\eta \simeq 2$ . The struck quark, especially at the FCC-eh as compared to LHeC, generates a very forward jet requiring forward calorimetry up to  $\eta \simeq 6$  as is foreseen in the FCC-eh detector design. Events are generated with MadGraph, see setup in Tab. 5.1.

3562 e.g. for heavy flavour and tau decays. Suitably designed muon detectors covering  $\eta = 4$  appear  
 3563 feasible for both collider configurations, those would result in high  $H \rightarrow \mu\mu$  acceptances of about  
 3564 72% (63%) for LHeC (FCC-eh) for selecting all final states with  $p_T > 15$  GeV and a coverage  
 3565 of the forward jet up to  $\eta = 5$  ( $\eta = 6$ ). A further extension to a  $1^\circ$  muon acceptance, would  
 3566 change the acceptances marginally to 72.9% (67.5%) for LHeC (FCC-eh).

#### 3567 5.1.4 Cross Sections and Rates

3568 The cross sections for Higgs production in CC and NC DIS  $e^-p$  scattering at three different  
 3569 proton energies, for LHeC, HE-LHeC and FCC-eh, are summarised in Tab. 5.1. The cross  
 3570 sections are calculated to leading order with MadGraph (MG5 v2.5.1) using the CTEQ6L1  
 3571 proton PDF and  $M_H = 125$  GeV. The CC  $e^-p$  cross section is directly proportional to the  
 3572 beam polarisation,  $P$ , as  $\sigma_{CC} \propto (1 - P)$  while the NC cross section only weakly depends on  
 3573 the polarisation [327]. It is observed that the CC Higgs production cross section at LHeC is  
 3574 comparable to that of a 250 GeV  $e^+e^-$  collider. One thus expects, roughly, results of comparable  
 3575 sensitivity, the difference being that  $e^+e^-$  favours the  $H$  to  $ZZ$  couplings while  $ep$  is dominantly  
 3576 sensitive to  $WW \rightarrow H$  production. This provides a very basic complementarity. The CC  $e^-p$   
 3577 cross section is enlarged with the (negative) electron beam polarisation,  $P_e$ , while the NC cross  
 3578 section is less sensitive to  $P_e$ . The cross section at FCC-eh reaches values of pb. Combined with  
 3579 long operation time one reaches sub-permille precision of the Higgs couplings. Similarly, the  
 3580  $HH$  cross section approaches one fb values only with the highest energy. It is correspondingly  
 3581 a major challenge, investigated in Ref. [484], to access the Higgs self-coupling even at FCC-eh,  
 3582 and this is not further discussed here.

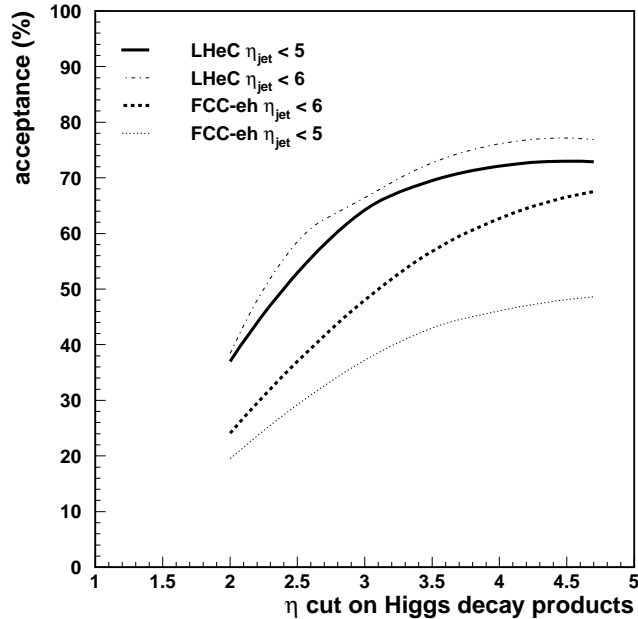


**Figure 5.4:** Acceptance of DIS Higgs candidates ( $y$  axis) in dependence on the pseudorapidity ( $\eta$ ) cut requirement on the Higgs decay products ( $x$  axis) for two scenarios of the coverage of the hadronic final states. All final states are selected with  $p_T > 15$  GeV. The forward jet is accepted up to  $\eta = 5$  and  $\eta = 6$  for LHeC (full and dashed-dotted lines), and FCC-eh (dotted and dashed lines), respectively. Calculations are at parton-level using MadGraph.

3583 The polarised  $e^+p$  cross section is calculated to be significantly smaller than the  $e^-p$  value, by a  
3584 factor of  $197/58 \simeq 6$  at the LHeC, mainly because the  $W^-u \rightarrow \bar{d}$  reaction is more frequent than  
3585  $W^+d \rightarrow u$ . Furthermore, positron sources are currently considered to be much less intense (by  
3586 a factor of about ten or even a hundred) than electron sources. It is desirable to take  $e^+p$  data  
3587 at future  $ep$  colliders for electroweak physics but in the linac-ring version their amount will be  
3588 limited and unlikely suitable for precision Higgs physics.

3589 Tab. 5.2 provides an illustration, for FCC-eh, of the statistics which is expected to be available  
3590 in charged and neutral current scattering for nine decay channels ordered by their branching  
3591 ratios. The first seven most frequent channels are used in the subsequent signal strength and  
3592 coupling analysis. Accessing rarer SM Higgs decay channels is the particular strength of  $pp$   
3593 scattering rather than that of  $ep$  or  $e^+e^-$ . The statistics at LHeC would be about ten times  
3594 lower than that at FCC-eh since the cross section is diminished by  $\simeq 1/5$  and due to a shorter  
3595 expected running time, the luminosity is assumed to be half of that at FCC-eh. The analyses  
3596 subsequently presented deal with the seven most frequent decays representing 99.9% of the SM  
3597 decays. In addition, there is a significant potential for a measurement of the  $H \rightarrow \mu\mu$  decay at  
3598 the FCC-eh, which, as is seen in Tab. 5.2, may provide about 500 (45) events, from CC and NC  
3599 DIS at FCC-eh (LHeC). Thus one may be able to measure this process to about 6% precision  
3600 at the FCC-eh and 18% at LHeC.

### 3601 5.1.5 Higgs Signal Strength Measurements

3602 Standard Model Higgs production in deep inelastic  $ep$  scattering proceeds via Vector-Boson-  
3603 Fusion in either charged or neutral current scattering as is illustrated in Fig. 1. The scattering

Parameter	Unit	LHeC	HE-LHeC	FCC-eh	FCC-eh
$E_p$	TeV	7	13.5	20	50
$\sqrt{s}$	TeV	1.30	1.77	2.2	3.46
$\sigma_{CC} (P = -0.8)$	fb	197	372	516	1038
$\sigma_{NC} (P = -0.8)$	fb	24	48	70	149
$\sigma_{CC} (P = 0)$	fb	110	206	289	577
$\sigma_{NC} (P = 0)$	fb	20	41	64	127
HH in CC	fb	0.02	0.07	0.13	0.46

**Table 5.1:** Total cross sections, in fb, for inclusive Higgs production,  $M_H = 125$  GeV, in charged and neutral current deep inelastic  $e^-p$  scattering for an  $E_e = 60$  GeV electron beam and four different proton beam energies,  $E_p$ , for LHeC, HE-LHeC and two values for FCC-eh. The c.m.s. energy squared in  $ep$  is  $s = 4E_e E_p$ . The last row shows the double-Higgs CC production cross sections in fb. The calculations are at LO QCD using the CTEQ6L1 PDF [482] and the default scale of MadGraph [483] with dependencies due to scale choices of 5-10 %.

Channel	Fraction	No. of events at FCC-eh	
		Charged Current	Neutral Current
$b\bar{b}$	0.581	1 208 000	175 000
$W^+W^-$	0.215	447 000	64 000
$gg$	0.082	171 000	25 000
$\tau^+\tau^-$	0.063	131 000	20 000
$c\bar{c}$	0.029	60 000	9 000
$ZZ$	0.026	54 000	7 900
$\gamma\gamma$	0.0023	5 000	700
$Z\gamma$	0.0015	3 000	450
$\mu^+\mu^-$	0.0002	400	70
$\sigma$ [pb]		1.04	0.15

**Table 5.2:** Total event rates for SM Higgs decays in the charged ( $ep \rightarrow \nu HX$ ) and neutral ( $ep \rightarrow eHX$ ) current production of the Higgs boson in polarised ( $P = -0.8$ ) electron-proton deep inelastic scattering at the FCC-eh, for an integrated luminosity of  $2 \text{ ab}^{-1}$ . The branching fractions are taken from [485]. The estimates are at LO QCD using the CTEQ6L1 PDF and the default scale of MadGraph, see setup in Tab. 5.1.

3604 cross sections, including the decay of the Higgs boson into a pair of particles  $A_i$  can be written  
3605 as

$$\sigma_{CC}^i = \sigma_{CC} \cdot \frac{\Gamma^i}{\Gamma_H} \quad \text{and} \quad \sigma_{NC}^i = \sigma_{NC} \cdot \frac{\Gamma^i}{\Gamma_H}. \quad (5.1)$$

3606 Here the ratio of the partial to the total Higgs decay width defines the branching ratio,  $br_i$ ,  
3607 for each decay into  $A_i \bar{A}_i$ . The  $ep$  Higgs production cross section and the  $\text{O}(1) \text{ ab}^{-1}$  luminosity  
3608 prospects enable to consider the seven most frequent SM Higgs decays, i.e. those into fermions  
3609 ( $b\bar{b}$ ,  $c\bar{c}$ ,  $\tau^+\tau^-$ ) and into gauge particles ( $WW$ ,  $ZZ$ ,  $gg$ ,  $\gamma\gamma$ ) with high precision at the LHeC  
3610 and its higher energy versions.

3611 In  $ep$  one obtains constraints on the Higgs production characteristics from CC and NC scattering,  
3612 which probe uniquely either the HWW and the HZZ production, respectively. Event by event  
3613 via the selection of the final state lepton which is either an electron (NC DIS) or missing energy  
3614 (CC DIS) those production vertices can be uniquely distinguished, in contrast to  $pp$ . In  $e^+e^-$ ,  
3615 at the ILC, one has considered operation at 250 GeV and separately at 500 GeV to optimise  
3616 the HZZ versus the HWW sensitive production cross section measurements [486]. For CLIC

3617 the c.m.s. energy may be set to 350 GeV as a compromise working point for joint NC and CC  
 3618 measurements, including access to top production [487]. The salient advantage of the  $e^+e^-$   
 3619 reaction, similarly considered for the more recent circular collider proposals, CEPC [16] and  
 3620 FCC-ee [488], stems from the kinematic constraint of the  $Z$ -strahlung,  $e^+e^- \rightarrow Z^* \rightarrow ZH$ ,  
 3621 which determines the total Higgs production cross section independently of its decay.

3622 The sum of the branching ratios for the seven Higgs decay channels here under study for  $ep$  adds  
 3623 up to 99.87% of the total SM width [489]. As is discussed in Sect. 5.3, significant constraints  
 3624 of the  $H \rightarrow invisible$  decay can be set with  $ep$  also albeit not being able to exclude exotic,  
 3625 unnoticed Higgs decays. The accurate reconstruction of all decays considered here will present  
 3626 a severe constraint on the total cross section and with that of the total decay width of the  
 3627 Higgs boson in the SM. For the evaluation of the measurement accuracy, the cross section  
 3628 measurement prospects for a decay channel  $i$  are presented here as relative signal strengths  
 3629  $\mu^i(NC, CC)$ , obtained from division by the SM cross section.

3630 Initially, detailed simulations and Higgs extraction studies for LHeC were made for the dominant  
 3631  $H \rightarrow b\bar{b}$  [490–494] and the challenging  $H \rightarrow c\bar{c}$  [494, 495] channels. The focus on the  $H \rightarrow b\bar{b}$   
 3632 decay has been driven not only by its dominance but as well by the difficulty of its accurate  
 3633 reconstruction at the LHC. It has been natural to extend this to the  $H \rightarrow c\bar{c}$  which currently is  
 3634 considered to not be observable at the HL-LHC, for permutation and large background reasons.  
 3635 The results of the updated  $b$  and  $c$  decay studies, using cuts and boosted decision tree (BDT)  
 3636 techniques, are presented below.

3637 A next detailed analysis has been performed for the  $H \rightarrow W^+W^-$  decay. The total of the  $WW$   
 3638 decays represents 21.5% of the Higgs branching into SM particles. There is a special interest  
 3639 in its reconstruction in the DIS charged current reaction as this channel uniquely determines  
 3640 the  $HWW$  coupling to its fourth power. A complete signal and background simulation and  
 3641 eventual BDT analysis of the  $H \rightarrow W^+W^-$  decay in charged currents has been performed  
 3642 which is subsequently described. Unlike at LHC, this uses the purely hadronic decays which in  
 3643  $pp$  are very difficult to exploit.

3644 Finally, as summarised below, an analysis using acceptance, efficiency and signal-to-background  
 3645 scale factors has been established for the residual four of the seven dominant decay channels,  
 3646 Tab. 5.2. This estimate could be successfully benchmarked with the detailed simulations for  
 3647 heavy quark and  $W$  decays. The present study therefore covers more than 99% of the SM Higgs  
 3648 decays, which in  $ep$  are redundantly measured, in both neutral and charged current reactions.  
 3649 This opens interesting prospects for precision Higgs physics in  $ep$ , but as well in combination  
 3650 with  $pp$ , i.e. of LHeC with HL-LHC, and later of FCC-eh with FCC-hh.

### 3651 5.1.6 Higgs Decay into Bottom and Charm Quarks

3652 The Higgs boson decays dominantly into  $b\bar{b}$  with a 58% branching ratio in the SM. Its reconstruc-  
 3653 tion at the LHC has been complicated by large combinatorial background. Recently this decay  
 3654 was established with signal strengths, relatively to the SM, of  $\mu_{bb} = 1.01 \pm 0.12(stat) \pm_{0.15}^{0.16}(exp)$   
 3655 by ATLAS [496] with a luminosity of  $79.8 \text{ fb}^{-1}$  and of  $\mu_{bb} = 1.01 \pm 0.22$  by CMS [497] with  
 3656 a luminosity of  $41.3 \text{ fb}^{-1}$ . This is a remarkable experimental LHC achievement since for long  
 3657 one expected to not be able to measure this decay to better than about 10% at the future  
 3658 HL-LHC. Meanwhile this expectation has become more optimistic with the updated HL-LHC  
 3659 prospects [498], as is briefly discussed in Sect. 5.1.11, however, the most hopeful assumption for  
 3660 the  $H \rightarrow c\bar{c}$  decay is a limit to two times the SM expectation.

3661 Because of the special importance of determining the frequent  $b\bar{b}$  decay most accurately, and  
3662 with it the full set of SM branchings, the prime attention of the LHeC Higgs prospect studies  
3663 has been given to those two channels. The first PGS detector-level study was published with the  
3664 CDR [1] assuming  $M_H = 120$  GeV, shortly before the announcement of the discovery of the Higgs  
3665 boson. This and subsequent analyses use samples generated by MadGraph5 [483], for both signal  
3666 and background events with fragmentation and hadronization via PYTHIA 6.4 [499] in an  $ep$   
3667 customised programme version<sup>2</sup>. Subsequent analyses have been updated to  $M_H = 125$  GeV and  
3668 to state-of-the art fast detector simulation with DELPHES 3 [501] as testbed for  $ep$  detector  
3669 configurations. Both cut-based and boosted decision tree (BDT) analyses were performed in  
3670 independent evaluations.

3671 As shown in the CDR, the  $H \rightarrow b\bar{b}$  decay could be measured via applying classical kinematic  
3672 selection requirements as follows:

- 3673 • CC DIS kinematic cuts of  $Q_h^2 > 500$  GeV<sup>2</sup>,  $y_h < 0.9$ , missing energy  $E_T^{\text{miss}} > 30$  GeV, and  
3674 no electrons in the final state to reject NC DIS;
- 3675 • at least three anti-kt  $R = 0.7$  jets with  $p_T > 20$  GeV which are subject to further b-tagging  
3676 requirements;
- 3677 • a Higgs candidate from two b-tagged jets with b-tagging efficiencies of 60 to 75 %, charm  
3678 (light quark) misidentification efficiencies of 10 to 5 % (1 %) ;
- 3679 • rejection of single-top events via requiring a dijet W candidate mass of greater than  
3680 130 GeV and a three-jet top candidate mass of larger than 250 GeV using a combina-  
3681 tion with one of the b-jets of the Higgs mass candidate;
- 3682 • a forward scattered jet with  $\eta > 2$ , and a large  $\Delta\phi_{b, MET} > 0.2$  between the b-tagged jet  
3683 and the missing energy.

3684 The dominant backgrounds are CC DIS multijet and single top production, while CC Z, W and  
3685 NC Z contributions are small. The background due to multijets from photoproduction, where  
3686  $Q^2 \sim 0$ , can be reduced considerably due to the tagging of the small angle scattered electron  
3687 with an electron tagger. The result of a cut-based analysis is shown in Fig. 5.5 where clear Z  
3688 and  $H \rightarrow b\bar{b}$  peaks are seen. Assuming that the photoproduction background is vetoed with a  
3689 90 % efficiency, the resulting signal is shown in Fig. 5.5 corresponding to a SM  $H \rightarrow b\bar{b}$  signal  
3690 strength  $\delta\mu/\mu$  of 2 % for an integrated luminosity of 1000 fb<sup>-1</sup> and  $P_e = -0.8$ . This result  
3691 is consistent with earlier analysis and robust w.r.t. the update of the Higgs mass from 120 to  
3692 125 GeV confirming the high  $S/B > 1$  (see also [493] which used a different approach to estimate  
3693 the multijet photoproduction background). The result illustrates that even with harsh kinematic  
3694 requirements and already a small luminosity of 100 fb<sup>-1</sup>, this important decay channel could be  
3695 measured to an uncertainty of about 6 %.

3696 The stability of the cut-based results has been further shown for different hadronic calorimeter  
3697 resolution setups

$$\frac{\sigma}{E} = \frac{a}{\sqrt{E}} \oplus b \quad \text{for } |\eta| < |\eta_{\text{min}}|, \quad (5.2)$$

$$\frac{\sigma}{E} = \frac{c}{\sqrt{E}} \oplus d \quad \text{for } |\eta_{\text{min}}| < |\eta| < 5, \quad (5.3)$$

---

<sup>2</sup>The hadronic showering is not expected to change the kinematics of the DIS scattered lepton. This has been shown, see page 11 of Ref. [500], with the very good level of agreement of NC DIS electron kinematics with and without the ep-customized Pythia showering, i.e. for 99.8 % of events the kinematics in the momentum vector components and for 98 % the energy of the scattered electron are unchanged.

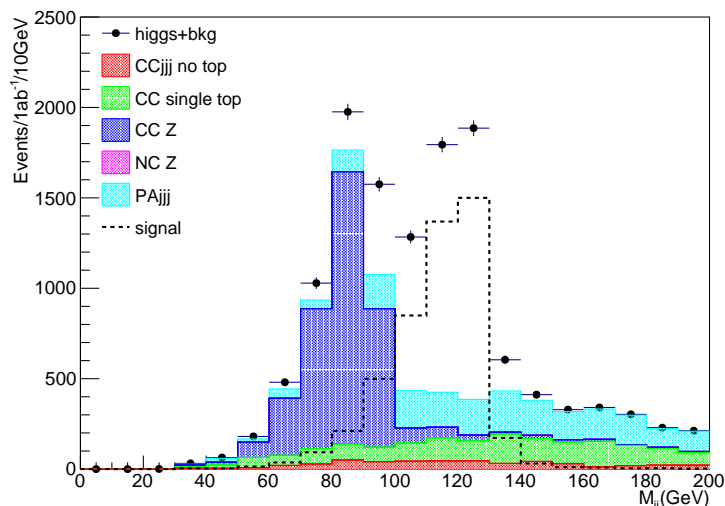


**Figure 5.5:** Invariant dijet mass distribution at DELPHES detector-level expected for  $1 \text{ ab}^{-1}$  and  $-80\%$  electron polarisation at LHeC. The  $S/B$  is about 2.9 for the events in the Higgs mass range of 100 to 130 GeV. Events are generated with MadGraph using  $M_H = 125 \text{ GeV}$  and showered with PYTHIA 6.4, and subject to cut-based event selection criteria, see text for further details. Note that samples are generated with a minimum dijet mass cut of 60 GeV.

3698 where for  $\eta_{\min} = 3$  the parameter  $b$  ( $d$ ) is varied within 1 (3) and 7 (9) % for two resolution  
 3699 parameters  $a$  ( $c$ ) of either 30 (60) and 35 (45) %. Alternatively, the central range was restricted  
 3700 to  $\eta_{\min} = 2$  with parameter  $b$  ( $d$ ) of 3 (5) % for resolution parameters  $a$  ( $c$ ) of 35 (45) %. While  
 3701 using the same analysis cuts, the signal yields varied within 34 %, it could be shown that with  
 3702 adjusted set of cuts (notably the choices of cuts for Higgs mass range,  $\Delta\phi_{b, MET}$ , and forward  
 3703  $\eta$ ) the SM  $H \rightarrow b\bar{b}$  signal strength  $\delta\mu/\mu$  varied with a fractional uncertainty of at most 7 %.

3704 The cut-based  $H \rightarrow b\bar{b}$  signal strength analyses are suffering from rather low acceptance times  
 3705 selection efficiencies in the range of 3 to 4 % only. Similarly a recent cut-based  $H \rightarrow c\bar{c}$  study [502]  
 3706 showed the potential of those measurements at LHeC and CEPC, however, due to the very harsh  
 3707 cuts and too simple analysis strategies with very limited outcome only. Modern state-of-the-  
 3708 art analysis techniques, e.g. as performed for finding  $H \rightarrow b\bar{b}$  at the LHC regardless of the  
 3709 overwhelming QCD jet background, are based on neural networks.

3710 Boosted Decision Tree (BDT)  $H \rightarrow b\bar{b}$  and  $H \rightarrow c\bar{c}$  analyses using the Toolkit for Multivariate  
 3711 Data Analysis with ROOT (TMVA) [503] are performed using independently produced signal  
 3712 and background samples based on the same setup as for the cut-based analyses, see Fig. 5.5.  
 3713 Those analyses start with loose preselections of at least three anti-kt jets with  $p_T > 15 \text{ GeV}$   
 3714 without any further heavy flavour tagging in addition to the CC DIS kinematic cuts of  $Q_h^2 > 400$   
 3715  $\text{GeV}^2$ ,  $y_h < 0.9$ , and missing energy  $E_T^{\text{miss}} > 20 \text{ GeV}$ . The invariant mass distributions using  
 3716 anti-kt  $R = 0.5$  jets are illustrated in Fig. 5.6, where the mass distributions in the upper plots  
 3717 illustrate in particular the single top contributions and the subsequent significant Higgs signal  
 3718 loss if simple anti-top cuts would be applied. In the lower plot of Fig. 5.6 the invariant dijet  
 3719 mass distribution of untagged Higgs signal candidates is seen clearly above the background  
 3720 contributions in the expected mass range of 100 to 130 GeV. It is observed that the remaining  
 3721 background is dominated by CC multi-jets. The quantities represented in the three distributions  
 3722 of Fig. 5.6 are important inputs for the BDT neural network in addition to further variables  
 3723 describing e.g. the pseudorapidities of the Higgs and forward jet candidates including jet and

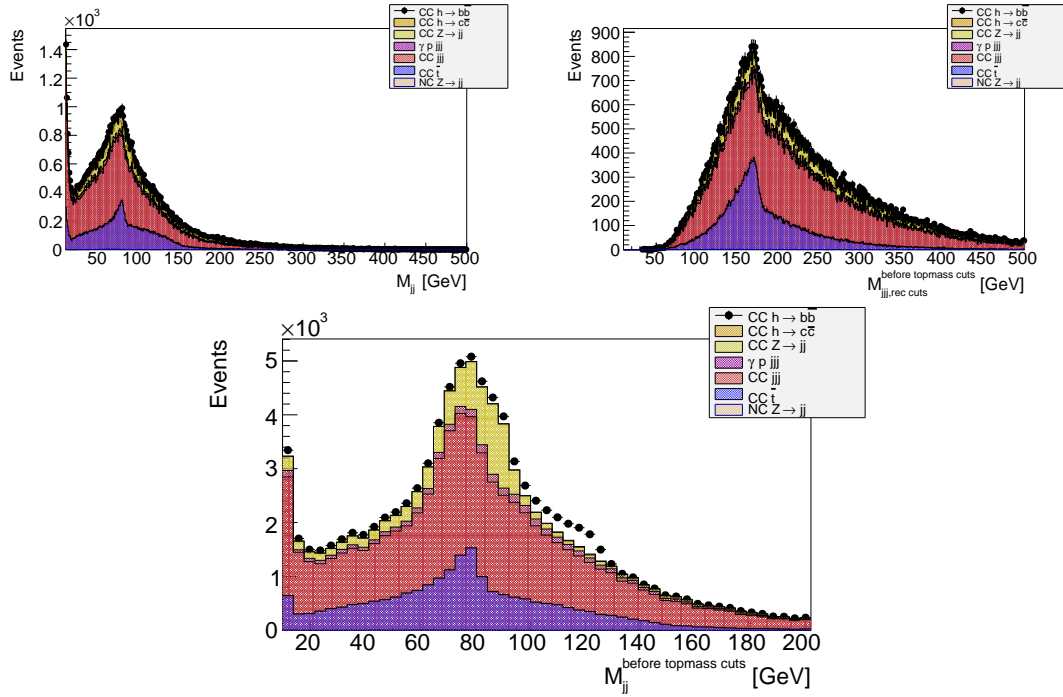


**Figure 5.6:** Invariant mass distributions at DELPHES detector level for an integrated luminosity of  $100 \text{ fb}^{-1}$  and  $-80\%$  electron polarisation. Events passed preselection cuts of  $Q_h^2 > 400 \text{ GeV}^2$ ,  $y_h < 0.9$ ,  $E_T^{\text{miss}} > 20 \text{ GeV}$  and at least three, flavour-untagged anti-kt  $R = 0.5$  jets with  $p_T > 15 \text{ GeV}$ . The different colours show the contributions per process, the photoproduction background ( $\gamma p \text{ jjj}$ ) is assumed to be vetoed with  $90\%$ . Note that samples are generated with a minimum dijet mass cut of  $60 \text{ GeV}$ . Upper left: Invariant dijet mass, showing  $W$  candidates from single top production (blue), based on combining jets with second and third lowest  $|\eta|$  values per event. Upper right: Invariant mass distribution combining the three highest  $p_T$  jets per event showing single top mass candidates (blue). Lower middle: Invariant dijet mass, showing Higgs candidates (black dots, including background), combining jets with the two lowest  $|\eta|$  values per event.

3724 track heavy flavour probabilities, see details below and further in Ref. [495].

3725 As a novel element in these analyses, heavy flavour tagging based on track and jet probabilities  
 3726 has been implemented into the DELPHES detector analysis following the Tevatron D0 experi-  
 3727 mental ansatz described e.g. in Ref. [504]. The resulting  $b$  and  $c$ -jet efficiency versus the light jet  
 3728 misidentification efficiencies are illustrated in Fig. 5.7 for assumed nominal impact parameter  
 3729 resolution of  $10$  ( $5$ )  $\mu\text{m}$  for tracks with  $0.5 < p_T < 5$  ( $> 5$ )  $\text{GeV}$  and three choices of distance  
 3730 parameter  $R = 0.5, 0.7, 0.9$  for the anti-kt jets. In particular for the charm tagging, impact  
 3731 parameters are studied with resolutions of  $5$  ( $2.5$ )  $\mu\text{m}$  (Half Vertex Resolution),  $20$  ( $10$ )  $\mu\text{m}$   
 3732 (Double Vertex Resolution) for tracks with  $0.5 < p_T < 5$  ( $> 5$ )  $\text{GeV}$  within  $|\eta| < 3.5$ . For a  
 3733 conservative light jet efficiency of  $5\%$ , the  $b$ -jet tagging efficiency is rather robust around  $60\%$   
 3734 for the considered nominal impact parameter performance and the three considered anti-kt dis-  
 3735 tance parameters, in slight favour of the anti-kt  $R = 0.5$  choice. For the expected charm tagging,  
 3736 however, an excellent impact parameter resolution and  $R = 0.5$  jets give the best tagging effi-  
 3737 ciency of around  $30\%$ . This means a significant improvement e.g. w.r.t. a  $23\%$  charm tagging  
 3738 efficiency for  $R = 0.9$  jets at a nominal impact parameter resolution. These tagging efficiencies  
 3739 can be considered as realistic but rather conservative in particular for the remaining light jet  
 3740 efficiency which is expected to be about  $0.1\%$  at a  $b$ -jet efficiency of  $60\%$  using LHC-style neural  
 3741 network based taggers.

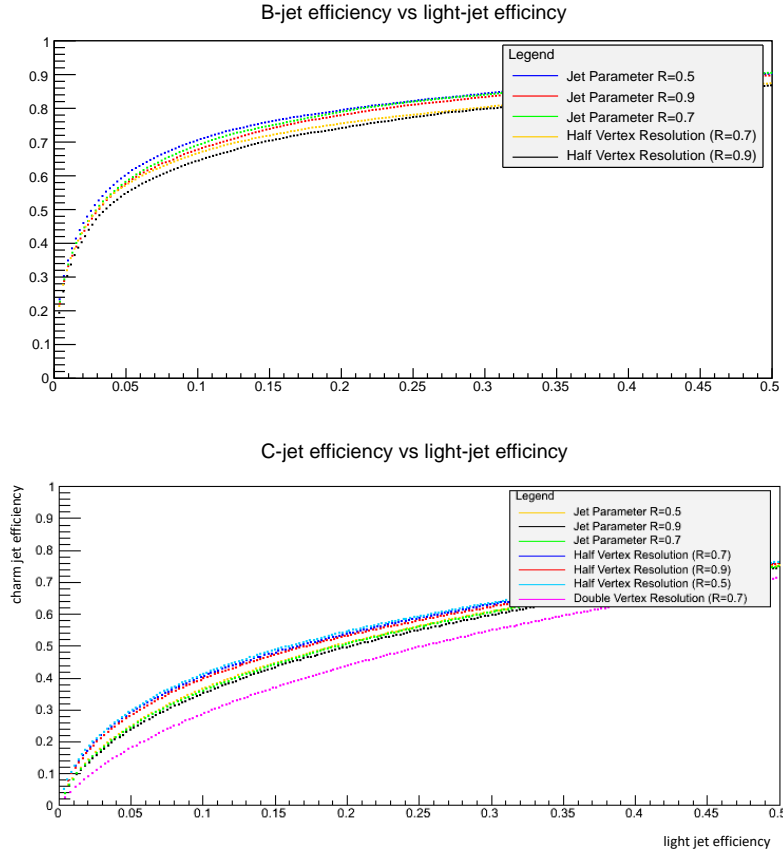


**Figure 5.7:** Expected average efficiency to tag a  $b$ -jet (upper plot) and charm-jet (lower plot) versus the light-jet efficiency (x-axis) based on Tevatron-style jet tagging [504]. Events are selected at DELPHES detector level using a CC multi-jet sample and for an integrated luminosity of  $100 \text{ fb}^{-1}$ . The coloured lines correspond to the choice of the anti-kt distance parameter  $R$  and different assumptions in the impact parameter resolution of 10 (5)  $\mu\text{m}$  (nominal, no text added in legend), 5 (2.5)  $\mu\text{m}$  (Half Vertex Resolution), 20 (10)  $\mu\text{m}$  (Double Vertex Resolution) for tracks with  $0.5 < p_T < 5 (> 5)$  GeV within  $|\eta| < 3.5$ .

3742 A series of BDT score tests has been performed using the preselected signal samples and CC  
3743 multi-jet as the main background sample to determine the optimal combination of  $R$  and impact  
3744 resolution parameters. The resulting number of  $H \rightarrow b\bar{b}(c\bar{c})$  signal events versus the BDT score  
3745 is illustrated in Fig. 5.8, which shows the evident interplay between detector performance and  
3746 choice of jet parameters  $R$ , where the  $R = 0.9$  anti-kt jets show the worst performance. At  
3747 a score of BDT=0, the highest number of signal events are achieved for  $R = 0.5$  anti-kt jets  
3748 for both charm and beauty decays, where the effect of the impact resolution is much more  
3749 stringent for the charm than for the beauty tagging. Following Fig. 5.8, the complete BDT-based  
3750  $H \rightarrow b\bar{b}(c\bar{c})$  analyses are performed for anti-kt  $R = 0.5$  jets and impact parameter resolution of  
3751 5 (2.5)  $\mu\text{m}$  (Half Vertex Resolution) for tracks with  $0.5 < p_T < 5 (> 5)$  GeV within  $|\eta| < 3.5$ .  
3752 The acceptance times efficiency values are about 28 % for the  $H \rightarrow b\bar{b}$  and about 11 % for the  
3753  $H \rightarrow c\bar{c}$  channel at BDT=0.

3754 The results of the BDT  $H \rightarrow b\bar{b}$  and  $H \rightarrow c\bar{c}$  analyses, assuming that each background contri-  
3755 bution is understood at the 2 % level via control regions and negligible statistical Monte Carlo  
3756 uncertainties for the background predictions for the signal region, are illustrated in Fig. 5.9 .  
3757 Using these assumptions, the resulting signal strengths are 0.8 % for the  $H \rightarrow b\bar{b}$  and 7.4 % for

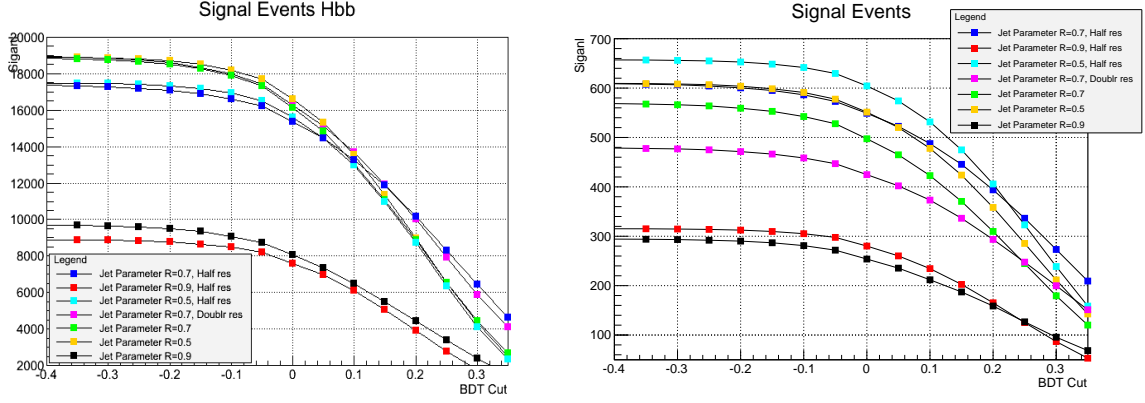


**Figure 5.8:** Expected  $H \rightarrow b\bar{b}$  (left) and  $H \rightarrow c\bar{c}$  (right) signal events as a function of the BDT score. Events are selected at DELPHES detector level for an integrated luminosity of  $1 \text{ ab}^{-1}$  and  $-80\%$  electron polarisation. The symbols correspond to the choice of the anti-kt distance parameter  $R$  and different assumptions in the impact parameter resolution of  $10$  ( $5$ )  $\mu\text{m}$  (nominal, no further text in legend added),  $20$  ( $10$ )  $\mu\text{m}$  (Doubl res),  $5$  ( $2.5$ )  $\mu\text{m}$  (Half res) for tracks with  $0.5 < p_T < 5$  ( $> 5$ )  $\text{GeV}$  within  $|\eta| < 3.5$ .

3758 the  $H \rightarrow c\bar{c}$  channel. For the latter, the SM Higgs decays, in particular  $H \rightarrow b\bar{b}$ , represent  
3759 also a part of the  $cc$  background contribution but can be controlled by the high precision of  
3760 the genuine  $bb$  result. Advanced analysis strategies to distinguish  $bb$  and  $cc$  SM Higgs decays  
3761 via several layers of neural networks are discussed e.g. in Ref. [505] for an  $250 \text{ GeV}$  ILC and  
3762  $M_H = 120 \text{ GeV}$ , where the expected  $H \rightarrow c\bar{c}$  cross section is  $6.9 \text{ fb}$  for  $M_H = 120 \text{ GeV}$  yields  
3763 a signal strength uncertainty of  $8.8\%$  in the  $ZH$  all hadronic channel ( $Z\phi q\bar{q}$ ) at an integrated  
3764 luminosity of  $250 \text{ fb}^{-1}$ . The ILC charm cross section is quite similar to the  $5.7 \text{ fb}$  cross section for  
3765  $M_H = 125 \text{ GeV}$  at LHeC. The number of preselected charm events and SM Higgs contributions  
3766 for the ILC analysis are at a similar level as in this analysis, while the non-Higgs background at  
3767 ILC is by a factor  $6.8$  larger than for the LHeC preselected events. Comparing the two results  
3768 gives confidence into the expected  $H \rightarrow c\bar{c}$  signal strength results at LHeC using the before  
3769 mentioned assumptions.

3770 In conclusion, Higgs to heavy flavour signal strength measurements require an excellent state-of-  
3771 the-art calorimetry with high acceptance and excellent resolution as well as an impact parameter  
3772 resolution as achieved e.g. with ATLAS inner b-layer. In addition, the details of the analysis  
3773 strategy utilising neural network and advanced statistical methods (e.g. via ROOSTat and  
3774 ROOFit, see e.g. complex analysis methods using constraints via well measured control regions  
3775 in signal fits [506]) will be important to control a high signal at low background yields where  
3776 the latter is expected to be constrained via control regions to better than a few %.

### 3777 5.1.7 Higgs Decay into WW

3778 Inclusive charged current scattering, the CC production of the Higgs boson with a  $WW$  decay  
3779 and the main backgrounds are illustrated in Fig. 5.10. The  $ep \rightarrow \nu H X \rightarrow \nu W^* W X$  process with  
3780 hadronic  $W$  decays causes a final state which to lowest order comprises the escaping neutrino  
3781 (missing energy MET) and  $4 + 1$  jets. The pure hadronic  $WW$  Higgs decay has a branching  
3782 ratio of about  $45\%$ . Using MadGraph (MG5) and a version of PYTHIA, customised for  $ep$   
3783 DIS, events were produced and analysed with a DELPHES description of the detector. For the  
3784 present study jets were reconstructed using the anti- $k_T$  algorithm with a  $\Delta R$  of  $0.7$ .

3785 The analysis of the fully generated events proceeds in the following steps:

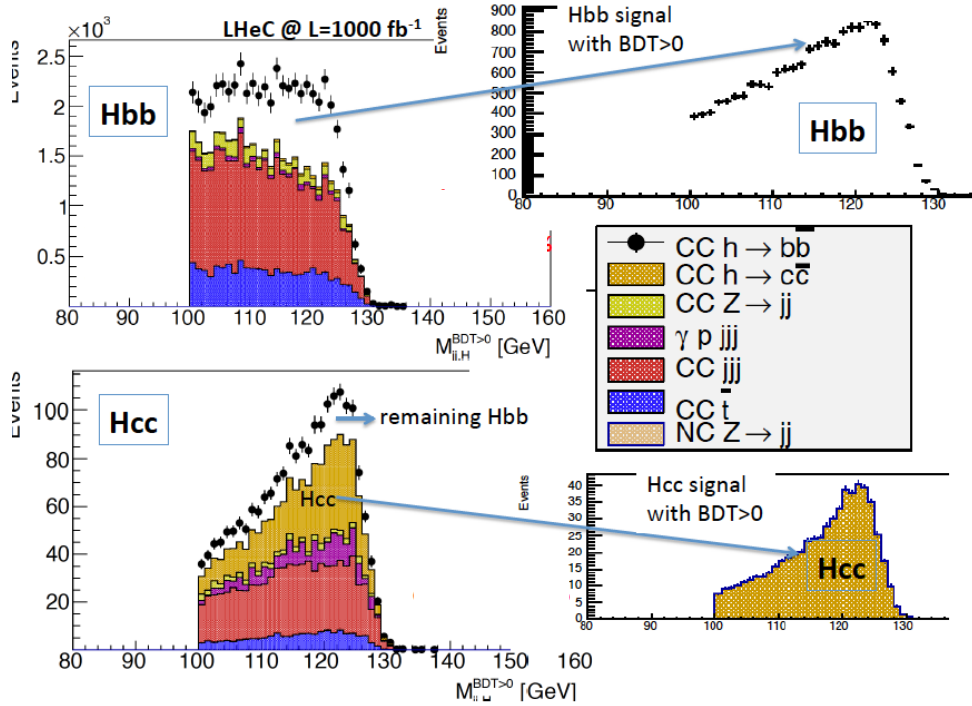


**Figure 5.9:** Result of the joint  $H \rightarrow b\bar{b}$  and  $H \rightarrow c\bar{c}$  analysis for an integrated luminosity of  $1 \text{ ab}^{-1}$  and  $-80\%$  electron polarisation at the LHeC. Left: Invariant mass distributions for the two channels with signal and background, see text. Right: Expected Higgs signal distributions after background subtraction. The background is assumed to be at the  $2\%$  level via control region measurements.

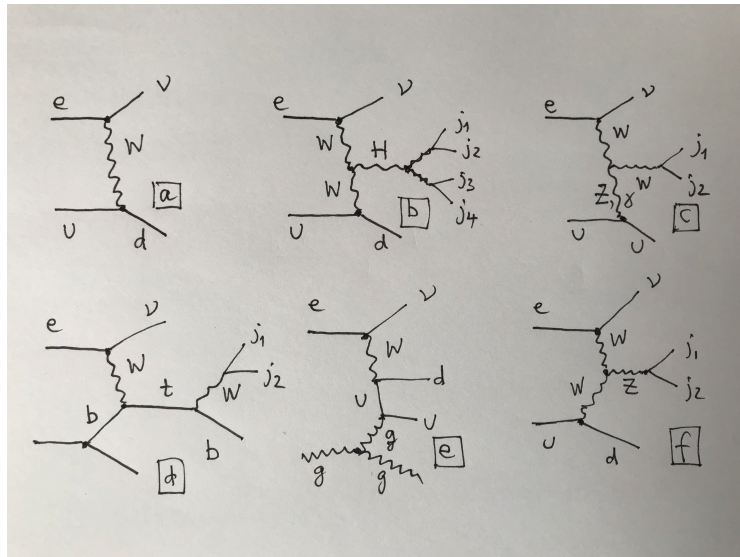


**Figure 5.10:** Typical lepton-parton diagrams relevant to the  $H \rightarrow WW$  analysis: a) inclusive charged current deep inelastic scattering into a neutrino (missing energy) and a scattered jet, here arising from the hadronisation of a d-quark; b) signal: CC DIS with a Higgs produced in the t-channel and its decay into a pair of W bosons which generates a four-jet final state, besides the forward jet. The other diagrams are examples to illustrate background channels which at higher orders, with extra emissions, may mimic the signal configuration: c) single W-boson production; d) single top-quark production; e) QCD multi-jet production and f) single Z-boson production.

- 3786 • Study of the reconstructed event configuration and recognition of its characteristics for  
3787 defining a set of loose cuts. These are: the  $p_T$  of any jet has to be larger than 6 GeV,  
3788 rapidity difference between the forward jet and the reconstructed 4-jet Higgs candidate  
3789 to be larger than 1.5, azimuthal difference between that Higgs candidate and either the  
3790 forward jet or the scattered lepton (MET) to be larger than 1, two-jet masses of the virtual  
3791 and the real  $W$  boson candidate to be larger than 12 GeV and below 90 GeV ( $Z$  mass).
- 3792 • Verification of truth matching to check that the combinatorial association of jets reproduces  
3793 the Higgs and its  $W$  decays (this is illustrated in Fig. 5.11).
- 3794 • Application of this algorithm to the simulated background samples. The MadGraph single  
3795  $W$ , top and  $Z$  production samples are turned to multi-jet background through PYTHIA.  
3796 The cross sections are reliably calculated as there is a hard scale available. The initial  
3797 cuts reduce this background to about 3% for single vector boson production and to 9%  
3798 for top.
- 3799 • Due to the size of the  $Hb\bar{b}$  decay and jet radiation, there occurs a residual background  
3800 from the Higgs itself which is also reduced to 3% of its MG5 value through the cuts.
- 3801 • The final background is due to multi-jets. The MadGraph cross section for a 4+1 jet  
3802 CC configuration is considered much too large in view of the cross section measurement  
3803 results as a function of the jet number, both at HERA and the LHC, see for example [507].  
3804 The sample was thus scaled using a conservative  $\alpha_s$  renormalisation to the inclusive cross  
3805 section. The initial cuts reduce the multi-jet background to about 13%.
- 3806 • Following a detailed training study, a BDT analysis was used. This determined a final  
3807 event number of about 12k for to a signal-to-background ratio of 0.23.

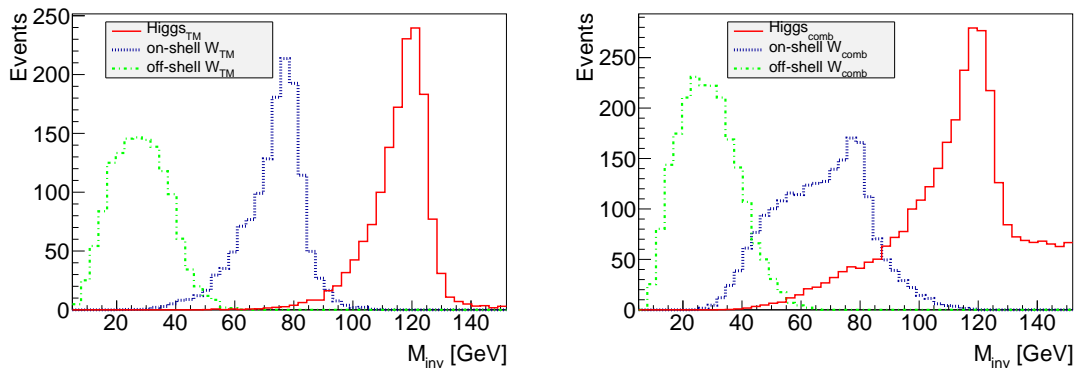


**Figure 5.11:** Reconstructed signal mass distributions (at DELPHES detector level) of truth matched events (left) and after the just combinatorial association of jets to the two  $W$  bosons forming Higgs candidates (right). Green: virtual  $W^*$  boson; blue:  $W$  boson; red: Higgs signal from  $W^*W$  reconstruction. It is observed that the combination causes some background while the respective signal peaks are clearly preserved with a purity of 68% that the correct forward jet is identified.

3808 The result of this analysis translates to an estimated uncertainty on  $\mu_{WW}$  of 1.9% at FCC-  
3809 eh. The 4-jet mass distribution after the BDT requirement exhibits a clear  $WW$  Higgs peak  
3810 (see Fig. 5.11) which illustrates the suitability to use the electron-proton environment for Higgs  
3811 measurements in indeed challenging final state configurations.

### 3812 5.1.8 Accessing Further Decay Channels

3813 Following the detailed studies of the  $b\bar{b}$  and  $c\bar{c}$  decay channels, presented above, a coarser anal-  
 3814 ysis was established for other frequent decay channels both in NC and CC. Here acceptances  
 3815 and backgrounds were estimated with MadGraph, and efficiencies, distinguishing leptonic and  
 3816 hadronic decay channels for  $W$ ,  $Z$ , and  $\tau$ , were taken from prospective studies on Higgs cou-  
 3817 pling measurements at the LHC [508]. This provided a systematic scale factor,  $f$ , on the pure  
 3818 statistical error  $\delta_s$ , which comprised the signal-to-background ratio,  $S/B$ , and the product of  
 3819 acceptance,  $A$ , and extra reconstruction efficiency  $\epsilon$ , according to

$$f = \sqrt{\frac{1 + \frac{B}{S}}{A \cdot \epsilon}} \quad (5.4)$$

3820 The error on the signal strength  $\mu_i$  for each of the Higgs decay channels  $i$  is determined as  
 3821  $\delta\mu_i/\mu_i = f_i \cdot \delta_s$ .

Parameter	$b\bar{b}$	WW	gg	$\tau\tau$	cc	ZZ	$\gamma\gamma$
Branching fraction	0.581	0.215	0.082	0.063	0.029	0.026	0.0023
Statistical error ( $\delta_s$ ) [%]	0.09	0.15	0.24	0.28	0.41	0.43	1.41
Acceptance ( $A$ )	0.14	0.10	0.40	0.40	0.11	0.10	0.40
Signal/background ( $S/B$ )	9	0.2	0.1	0.2	0.43	0.33	0.5
Extra efficiency ( $\epsilon$ )	1	0.3	0.5	0.43	1	0.5	0.7
Scale factor $f$	2.8	16	7.4	5.9	5.5	9.0	3.3

**Table 5.3:** Statistical uncertainty for the seven most abundant Higgs decay channels, for the charged current Higgs measurement prospects with the FCC-eh, together with their systematic scale factor  $f$ , Eq. 5.4, resulting from acceptance, background and efficiency effects as given. Note that the results for  $b\bar{b}$  and  $c\bar{c}$  are taken from the BDT analysis (Sect. 5.1.6) with efficiency 1. The  $WW$  result is replaced by the BDT analysis (Sect. 5.1.7) for quoting the expected signal strength uncertainty.

3822 To good approximation these factors apply to LHeC, HE-LHeC and FCC-eh because the de-  
 3823 tector dimensions and acceptances scale with the proton energy, conceptually using the same  
 3824 technology and very similar resolution assumptions. Therefore there is one main matrix used  
 3825 for the subsequent experimental deterioration of the pure statistics precision, both for CC and  
 3826 NC. Future detailed analyses will lead to refining this expectation which for the current purpose  
 3827 was beyond the scope of the study. The results of the analysis of uncertainties are summarised  
 in Tab. 5.3 for the CC channel at the FCC-eh. The resulting signal strength uncertainty values

Setup	$b\bar{b}$	$b\bar{b} \oplus \text{Thy}$	WW	gg	$\tau\tau$	cc	ZZ	$\gamma\gamma$
LHeC NC	2.3	2.4	17	16	15	20	35	42
LHeC CC	0.80	0.94	6.2	5.8	5.2	7.1	12	15
HE-LHeC NC	1.15	1.25	8.9	8.3	7.5	10	17	21
HE-LHeC CC	0.41	0.65	3.2	3.0	2.7	3.6	6.2	7.7
FCC-eh NC	0.65	0.82	5.0	4.7	4.2	5.8	10	12
FCC-eh CC	0.25	0.56	1.9	1.8	1.6	2.2	3.8	4.6

**Table 5.4:** Summary of estimates on the experimental uncertainty of the signal strength  $\mu$ , in per cent, for the seven most abundant Higgs decay channels, in charged and neutral currents for the LHeC, the HE-LHeC and the FCC-eh. The  $b\bar{b}$  channel is the one which is most sensitive to theoretical uncertainties and for illustration is given two corresponding columns, see Sect. 5.1.9.

3828

3829 are provided in Tab. 5.4. Note that for the beauty, charm and  $WW$  channels the table contains  
3830 the BDT analysis <sup>3</sup> results of Sect. 5.1.6 and Sect. 5.1.7, resp. The beauty and charm CC results  
3831 stem from the BDT analysis for LHeC and are applied to FCC-eh with a factor of about 1/3.  
3832 The CC  $WW$  results are due to the FCC-eh BDT analysis and are used for LHeC, enlarged by  
3833 a factor of 3.2, determined by the different cross sections and luminosities. For HE-LHC, the  
3834 values are about twice as precise as the LHeC values because the cross section is enlarged by  
3835 about a factor of two, see Tab. 5.1, and the integrated luminosity with  $2 \text{ ab}^{-1}$  twice that of the  
3836 LHeC. All signal strength uncertainties, in both CC and NC, for the three collider configurations  
are shown in Fig. 5.12.

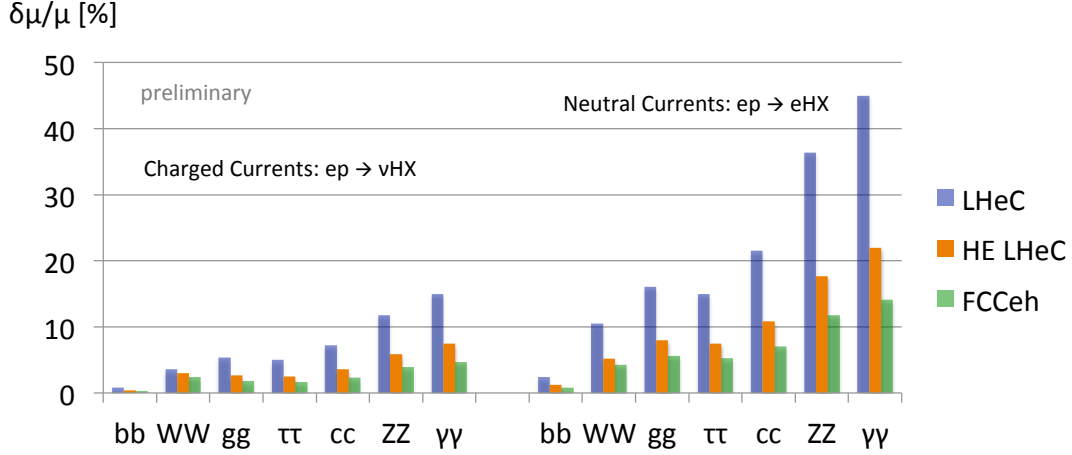


**Figure 5.12:** Uncertainties of signal strength determinations in the seven most abundant SM Higgs decay channels for the FCC-eh (green,  $2 \text{ ab}^{-1}$ ), the HE LHeC (brown,  $2 \text{ ab}^{-1}$ ) and LHeC (blue,  $1 \text{ ab}^{-1}$ ), in charged and neutral current DIS production.

3837

### 3838 5.1.9 Systematic and Theoretical Errors

3839 The signal strength is expressed relatively to a theoretical calculation of the charged current  
3840 Higgs cross section, including its decay into a chosen channel, according to

$$\mu = \frac{\sigma_{exp}}{\sigma_{thy}} = \frac{\sigma_{exp}}{\sigma_{Hty} \cdot br}. \quad (5.5)$$

3841 Consequently one can decompose the (relative) error of  $\mu$  into the genuine measurement error,  
3842 denoted as  $\delta\sigma_{exp}$ , including a possible systematic error contribution,  $E$ , and two further  
3843 components

$$\frac{\delta\mu}{\mu} = \left\{ \left( \frac{\delta\sigma_{exp}}{\sigma_{exp}} \right)^2 \cdot (1 \oplus E) + \left( \frac{\delta\sigma_{Hty}}{\sigma_{Hty}} \right)^2 + \left( \frac{\delta br}{br} \right)^2 \right\}^{1/2}, \quad (5.6)$$

3844 which are due to imperfections to theoretically model the Higgs production cross section,  $\sigma_{Hty}$ ,  
3845 and uncertainties on the branching ratio,  $br$ , in the channel under study. Note, that the experi-  
3846 mental uncertainty takes into account possible variations of the backgrounds which are estimated  
3847 conservatively and thus represent more than genuine statistics.

3848 The channel dependent signal strength uncertainties quoted in Tab. 5.4 are estimates of the  
3849 first, experimental term in Eq. 5.6 neglecting extra systematic error effects. They are derived as

<sup>3</sup>This is in very good agreement with the scale factor method: for example, the  $WW$  result in Tab. 5.3 leads to a value of 2.1% slightly worse than the BDT analysis.

3850 stated above from the purely statistical error ( $\delta_s = 1/\sqrt{N}$ ), its increase due to acceptance ( $A$ )  
 3851 and efficiency ( $\epsilon$ ) effects and, further, the modulation caused by the background-to-signal ratio  
 3852 ( $B/S$ ). These factors are all involved in the BDT analysis but the scale factor equation, Eq. 5.4,  
 3853 may be used to estimate further systematic effects for any channel. From the relation

$$\frac{\delta\sigma_{exp}}{\sigma_{exp}} = \delta_s \cdot \sqrt{\frac{1 + B/S}{A \cdot \epsilon}} \quad (5.7)$$

3854 the combined systematic error contribution,  $E$ , caused by variations  $\Delta$  of  $A$ ,  $\epsilon$  and the back-  
 3855 ground  $B$  can be estimated as

$$E = \frac{1}{2} \left\{ \left( \frac{\Delta A}{A} \right)^2 + \left( \frac{\Delta \epsilon}{\epsilon} \right)^2 + \left( \frac{\Delta B}{B} \cdot \frac{B/S}{1 + B/S} \right)^2 \right\}^{1/2}. \quad (5.8)$$

3856 The formula shows that if the background-to-signal ratio is very small, then the background  
 3857 effect is suppressed  $\propto B/S$ . If it is larger than 1, the relative uncertainty of the background  
 3858 enters as an additional component of the signal strength error.

3859 Given the fact that the experimental  $H \rightarrow b\bar{b}$  result in the CC reaction is especially precise,  
 3860 compare Tab. 5.4, an estimate was performed of the systematic error in this channel. The  
 3861 following effects were included: a variation of the light-quark misidentification by a factor 3, a  
 3862 variation of the reduction of the photo-production via tagging between 2 % and 10 %, a variation  
 3863 of the combined acceptance times efficiency effect by 10 % and a variation of the hadronic energy  
 3864 resolution, studied in Ref. [491], leading to a 7 % signal variation. The overall effect of these  
 3865 contributions determines a systematic error of about 10 % on  $\mu_{bb}$ , i.e.  $\delta\mu/\mu = 0.80 \pm 0.09$  for  
 3866  $H \rightarrow b\bar{b}$  at the LHeC in the CC channel. Similar levels of uncertainty are expected to occur for  
 3867 other channels but have not been estimated to such detail as those channels are measured less  
 3868 precisely.

3869 A separate effect arises from the measurement of the luminosity. While that will be measured  
 3870 about as accurate as 0.5 %, based on Bethe-Heitler scattering and its accurate description to  
 3871 higher-order QEDC [1], additionally it will be negligible to a good approximation: the LHeC,  
 3872 and its successors, will provide a very precise, determination of all parton distributions from  
 3873 the  $ep$  data alone. Any systematic mistake in the normalisation will therefore affect both the  
 3874 measured and the calculated cross section and drop out in their ratio  $\mu$ .

3875 A next uncertainty on the signal strength arises from the theoretical description of  $\sigma_{CCH}$  to which  
 3876 the measured cross section is normalised. From a simulation of the systematic uncertainties  
 3877 due to imperfect calibrations and extra efficiencies one may expect the cross section to be  
 3878 known to better than 1 %. The prediction will be available to N<sup>3</sup>LO,  $\alpha_s$  be determined to  
 3879 0.1 – 0.2 % precision, and it can be gauged with the inclusive cross section measurement. This  
 3880 uncertainty, following Eq. 5.8, enters directly as a contribution to the  $\mu$  measurement result. A  
 3881 0.5 % uncertainty, as can be seen in Tab. 5.4, becomes noticeable in most of the  $b\bar{b}$  results but  
 3882 is negligible for all other channels. In the present analysis values of 0.5 % and 1 % uncertainty  
 3883 have been considered and their effect on the  $\kappa$  result been evaluated, see Sect. 5.1.10.

3884 A final uncertainty is caused by the branching fractions and their uncertainty. A recent un-  
 3885 certainty estimate [485] quotes on the here most relevant  $H \rightarrow b\bar{b}$  branching ratio a theory  
 3886 contribution due to missing higher orders of 0.65 %, a parameterisation uncertainty depending  
 3887 on the quark masses of 0.73 %, and an  $\alpha_s$  induced part of 0.78 %. The LHeC, or similarly the  
 3888 higher energy  $ep$  colliders, will determine the  $b$  mass (in DIS) to about 10 MeV and  $\alpha_s$  to per  
 3889 mille precision [1] which would render corresponding uncertainty contributions to  $br_{bb}$  negligible.

3890 The genuine theoretical uncertainty would also be largely reduced with an extra order pQCD.  
 3891 In the subsequent study the contribution from the branching fraction uncertainty has been ne-  
 3892 glected. This may also be justified by the programme here sketched, and similarly for other  
 3893 future colliders: the  $ep$  colliders will measure the couplings, especially of the  $WW$ ,  $bb$  and  $ZZ$   
 3894 very precisely, which will enable an iterative treatment of the branching ratio uncertainties.

3895 It may be noticed [485] that the  $\alpha_s$  contribution to the  $H \rightarrow gg$  branching fraction uncertainty  
 3896 is about 3.7%, i.e. twice as large as the estimated signal strength measurement uncertainty of  
 3897 this channel at the FCC-eh. There arises another important benefit of the future  $ep$  colliders  
 3898 and their high precision DIS programme for precision Higgs physics at the combined  $ep$  &  $pp$   
 3899 facilities.

### 3900 5.1.10 Higgs Coupling Analyses

3901 In order to quantify possible deviations from the SM expectation one may use the  $\kappa$  parameter-  
 3902 isation framework, introduced in Ref. [509], which enables easy comparisons between different  
 3903 collider configurations independently of their ability to access the total Higgs decay width. The  $\kappa$   
 3904 formalism avoids extra complications occurring in EFT analyses that deal with extra constraints  
 3905 and complicate the genuine comparison of results. The EFT formalism tends to improve the  
 3906 perceived accuracy. In the EFT analysis of the ILC 250 GeV potential, for example, values are  
 3907 quoted for the  $Hbb$  coupling of 3.2% in the  $\kappa$  framework but 1.0% in a full EFT fit [510]<sup>4</sup>. It  
 3908 nevertheless would be very interesting to go beyond the  $\kappa$  framework also for the  $ep$  colliders  
 3909 here presented because out of the 2499 4-fermion parameters altogether  $13 \cdot n_g^4 = 1053$  involve  
 3910 leptons and quarks [511], for  $n_g = 3$  generations. This, however, has been beyond the scope  
 3911 of this study. In the following results are presented for the various  $ep$  collider configurations  
 3912 (Sect. 5.1.10).

3913 The  $\kappa$  parameters are factors to the various Higgs couplings, equal to one in the SM, which scale  
 3914  $\sigma_{NC/CC}$  with  $\kappa_{Z/W}^2$ , the width  $\Gamma^i$  for a channel  $i$  with  $\kappa_i^2$  and lead to replacing  $\Gamma_H$  by the sum  
 3915  $\sum_j \kappa_j \Gamma^j$ . This defines the following modifications of the cross sections (Eq. 5.1)

$$\sigma_{CC}^i = \sigma_{CC} br_i \cdot \kappa_W^2 \kappa_i^2 \frac{1}{\sum_j \kappa_j^2 br_j} \quad \text{and} \quad \sigma_{NC}^i = \sigma_{NC} br_i \cdot \kappa_Z^2 \kappa_i^2 \frac{1}{\sum_j \kappa_j^2 br_j}. \quad (5.9)$$

3916 Dividing these expressions by the SM cross section predictions one obtains the variations of the  
 3917 relative signal strengths,  $\mu^i$ , for charged and neutral currents and their  $\kappa$  dependence

$$\mu_{CC}^i = \kappa_W^2 \kappa_i^2 \frac{1}{\sum_j \kappa_j^2 br_j} \quad \text{and} \quad \mu_{NC}^i = \kappa_Z^2 \kappa_i^2 \frac{1}{\sum_j \kappa_j^2 br_j}. \quad (5.10)$$

3918 With seven decay channels considered in CC and NC, one finds that for each of the  $ep$  collider  
 3919 configurations there exist eight constraints on  $\kappa_W$  and  $\kappa_Z$  and two on the other five  $\kappa$  parameters.

---

<sup>4</sup> A spectacular difference is observed in [510] between the ratios of the  $HWW$  to  $HZZ$  couplings within the  $\kappa$  framework and in EFT. This ratio is quoted to be determined to 3.29% and to 0.07% precision, respectively. This likely is due to the custodial symmetry constraint in EFT which binds the  $WW$  and  $ZZ$  channels. Relying only on the EFT formalism would thus screen genuine differences between various colliders. In the particular case of interest here, an important complementarity between  $ep$  and  $e^+e^-$  would disappear. For the ILC 250 GeV case,  $\kappa_{WW}$  is quoted with an uncertainty of 3.31% while  $\kappa_{ZZ}$  is expected to be determined within 0.31%, a difference reflecting the dominance of  $Z$  Higgsstrahlung in  $e^+e^-$  and the small  $\sqrt{s}$  of the 250 GeV machine leading to a small  $WW$  contribution only. At the LHeC, the result is opposite, albeit to a less drastic extent. The analysis presented below leads to  $\delta\kappa_{WW} = 0.7\%$  and  $\delta\kappa_{ZZ} = 1.2\%$ . The NC  $e^+e^-$  reaction provides a better  $ZZ$  coupling while the CC  $ep$  process determines the  $WW$  coupling to higher accuracy, for comparable luminosities.

3920 Using the signal strength uncertainties as listed in Tab. 5.4 fits to all seven channels, in NC and  
3921 CC, are performed in a minimisation procedure to determine the resulting uncertainties for  
3922 the  $\kappa$  parameters. These are done separately for each of the  $ep$  collider configurations with  
3923 results listed in Tab. 5.5. A naive expectation would have been that  $\delta\kappa \simeq \delta\mu/2$ . Comparing  
3924 the results, for example for LHeC (top rows), of the signal strengths (Tab. 5.4) with the  $\kappa$  fit  
3925 results (Tab. 5.5) one observes that this relation holds approximately for the  $gg$ ,  $\tau\tau$ ,  $c\bar{c}$ ,  $\gamma\gamma$   
3926 channels. However, due to the dominance and high precision of  $\mu_{bb}$  and owing to the presence  
3927 of the  $WWH$  and  $ZZH$  couplings in the initial state, there occurs a reshuffling of the precisions  
3928 in the joint fit:  $\kappa_{bb}$  is relatively less precise than  $\mu_{bb}$  while both  $\kappa_{WW}$  and  $\kappa_{ZZ}$  become more  
3929 precise than naively estimated, even when one takes into account that the  $H \rightarrow WW$  decay in  
CC measures  $\kappa_{WW}^4$ . The seven channel results are displayed in Fig. 5.13.

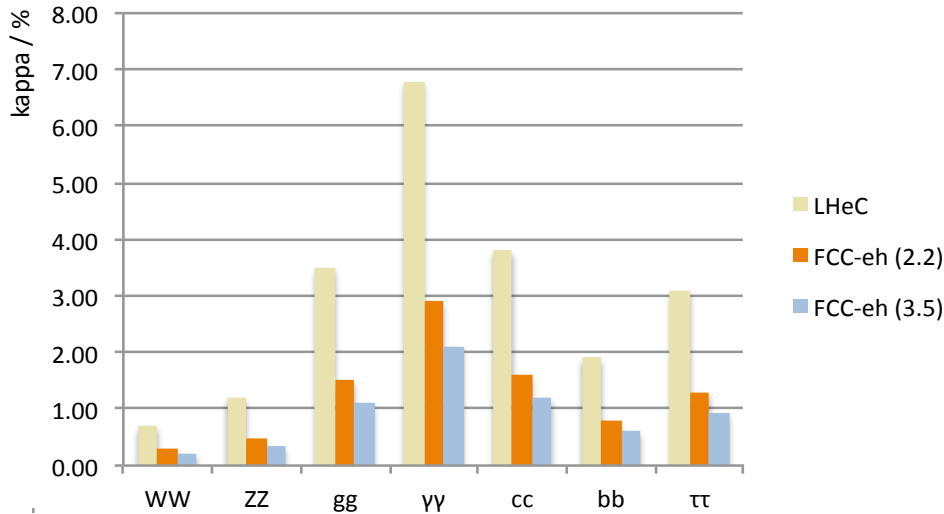


**Figure 5.13:** Summary of uncertainties of Higgs couplings from  $ep$  for the seven most abundant decay channels, for LHeC (gold), FCC-eh at 20 TeV proton energy (brown) and for  $E_p = 50$  TeV (blue).

3930

Setup	$b\bar{b}$	WW	gg	$\tau\tau$	cc	ZZ	$\gamma\gamma$
LHeC	1.9	0.70	3.5	3.1	3.8	1.2	6.8
HE-LHeC	1.0	0.38	1.8	1.6	1.9	0.6	3.5
FCC-eh	0.60	0.22	1.1	0.93	1.2	0.35	2.1

**Table 5.5:** Summary of  $\kappa$  uncertainty values as obtained from separate fits to the signal strength uncertainty estimates for the seven most abundant Higgs decay channels, in charged and neutral currents for the LHeC, the HE-LHeC and the FCC-eh, see text.

3931 In the electroweak theory there is an interesting relation between the ratio of the  $W$  and  $Z$   
3932 couplings and the mixing angle,

$$\frac{\sigma(WW \rightarrow H \rightarrow AA)}{\sigma(ZZ \rightarrow H \rightarrow AA)} = \frac{\kappa_W^2}{\kappa_Z^2} = (1 - \sin^2 \theta_W)^2 \quad (5.11)$$

3933 This relation can be particularly well tested with the  $ep$  colliders as they measure both  $WWH$   
3934 and  $ZZH$  in one experiment and common theoretical environment. If one assumes the  $WW$   
3935 and  $ZZ$  measurements to be independent, the resulting error on  $\sin^2 \theta_W \simeq 0.23$  is 0.003 for the

3936 LHeC and 0.001 for FCC-eh. However, this probably is smaller because there exist correlations  
 3937 in the measurements which a genuine data based analysis would have to evaluate and take into  
 3938 account.

3939 The effect of the theory uncertainties has been studied for the FCC-eh where the experimental  
 3940 precision is highest. Tab. 5.6 presents the results of a  $\kappa$  analysis using the CC and NC FCC-  
 3941 eh signal strength input (Tab. 5.4) neglecting the theoretical uncertainty and adding 0.5% or  
 3942 1% in quadrature, to only  $\mu_{bb}$  where it matters. This results in an about linear increase of  
 3943 the uncertainty for  $bb$  (by a factor of 1.5),  $WW$  (by 1.7) and  $ZZ$  (by 1.5), while all other  $\kappa$   
 3944 uncertainties only slightly deteriorate. The effect of such uncertainties for LHeC is much smaller  
 3945 as the  $\mu$  uncertainties are three times those of FCC-eh, see Tab. 5.4. Therefore, in the LHeC  
 case, the theory uncertainties are neglected.

Setup	$b\bar{b}$	WW	gg	$\tau\tau$	cc	ZZ	$\gamma\gamma$
FCC-eh (no thy)	0.60	0.22	1.1	0.93	1.2	0.35	2.1
FCC-eh (0.5% thy)	0.72	0.28	1.1	1.0	1.2	0.41	2.2
FCC-eh (1.0% thy)	0.91	0.37	1.1	1.0	1.3	0.53	2.3

**Table 5.6:** Summary of  $\kappa$  uncertainty values as obtained from separate fits to the signal strength uncertainty estimates for the seven most abundant Higgs decay channels, in charged and neutral currents for the FCC-eh, with no theoretical uncertainty, half a per cent and one per cent uncertainty added.

3946

3947 An interesting question regards the role of the electron beam polarisation. Assuming a maxi-  
 3948 mum polarisation of  $P = -0.8$ , the CC (NC) Higgs cross section is calculated to be 1.8 (1.09)  
 3949 times larger than that in unpolarised scattering. Therefore the signal CC and NC strength  
 3950 uncertainties scale like 1.34 and 1.09, respectively. This is studied for the LHeC. If the default  
 3951 fit is made, then the  $\kappa$  uncertainties quoted in Tab. 5.5 for  $bb$ ,  $WW$ ,  $gg$ ,  $\tau\tau$  and  $cc$  are enhanced  
 3952 by a factor of 1.28. This is due to the combined effect of CC and NC which diminishes the  
 3953 deterioration a bit, from 1.34 to 1.28. Thus, for example, the  $\kappa_{WW}$  uncertainty moves from  
 3954 0.7 to 0.9% in the unpolarised case. The uncertainty on  $\kappa_{ZZ}$  is enhanced only by a factor of  
 3955 1.14, becoming 1.38 instead of 1.21 because the NC channel has a particularly strong effect on  
 3956 the  $ZZH$  coupling. Since the prospect to detect the  $\gamma\gamma$  channel in NC is very poor, the  $\kappa_{\gamma\gamma}$   
 3957 uncertainty is enlarged by the full CC factor of 1.34. It is for maximum precision very desirable  
 3958 to have the beam polarised. This, together with electroweak physics, represents an important  
 3959 reason to continue to develop high current polarised electron sources.

### 3960 5.1.11 Parton Distributions

3961 The momentum distributions of partons inside the proton are best determined in deep inelas-  
 3962 tic electron-proton scattering because the pointlike electron (or lepton), being free of strong  
 3963 interactions, is able to probe proton substructure in a fundamentally clean way. The parton's  
 3964 momentum  $x$  can be computed with the scattered electron kinematics, there is no colour recon-  
 3965 nection in the final state, DIS theory is free of non-perturbative or hadronisation corrections.  
 3966 The experimental reconstruction is clean, even at FCC-eh where the pile-up is one, and the ra-  
 3967 diative corrections are suppressed through momentum conservation constraints. The kinematic  
 3968 reconstruction is redundant in the NC channel, enabling cross calibrations, and it uniquely dis-  
 3969 tinguishes NC and CC events. Furthermore, the four-momentum transfer squared,  $Q^2$ , can be  
 3970 freely prescribed, from the DIS minimum,  $Q^2 > M_p^2$ , up to the kinematic limit  $Q^2 \leq s$ , which  
 3971 at the LHeC (FCC-eh) is as large as  $1.68 (12) \cdot 10^6 \text{ GeV}^2$ . Due to the large collision energies

3972 of the new  $ep$  colliders here considered, neutral electromagnetic and neutral and charged weak  
3973 interactions simultaneously probe proton's structure over a huge kinematic range. When com-  
3974 plemented with charm and beauty tagging to determine the  $s$ ,  $c$ ,  $b$  distributions [1], this enables  
3975 the six quark contributions, including a separation of valence and sea quarks, to be completely  
3976 and precisely reconstructed free of symmetry assumptions or nuclear corrections for the first  
3977 time. This also enables determinations of the gluon distribution and the strong coupling con-  
3978 stant to unprecedented precision such as  $0.1 - 0.2\%$  on  $\alpha_s$ . This outstanding potential has been  
3979 discussed in Ref. [1, 213]. It is theoretically and practically superior to any attempt to deduce  
3980 PDFs from hadron-hadron collisions at the LHC or fixed target DIS scattering data. The LHeC,  
3981 when operating concurrently with the LHC, will therefore have a strong impact on LHC Higgs  
3982 physics, beyond the  $ep$  H measurements, because it will remove the PDF and  $\alpha_s$  uncertainties  
3983 which compromise the precision obtainable in  $pp$  Higgs physics.

3984 The uncertainties derived from PDFs and  $\alpha_s$  on Higgs coupling and cross section measurements  
3985 at the LHC will be rendered negligible with the LHeC. The recent evaluation of prospects for  
3986 Higgs measurements at the LHC by the CMS Collaboration presents theoretical errors, on signal  
3987 and background, and their contribution to the full uncertainty [512]. For the signal strength of  
3988 the  $H \rightarrow b\bar{b}$  decay, for example, CMS estimated a full uncertainty at HL-LHC of  $\mu_{bb}$  of  $7.2\%$   
3989 which is dominated by  $5.4\%$  (SigTh). The LHeC would essentially remove that uncertainty  
3990 and lead to a  $4.8\%$  total error if the BgdTh and Exp error were untouched. It so provided a  
3991 safer base for improvements than have been assumed to occur by CMS with their S2 scenario,  
3992 in which the theoretical uncertainty is just assumed to be halved.

3993 The role LHeC may play for LHC physics, not least on exploring the Higgs, depends on the  
3994 timeline of its installation. The earliest shutdown, when LHeC may come in, is LS4, in the early  
3995 thirties. It has been estimated [33] that LHeC would collect  $5 \text{ fb}^{-1}$  of integrated luminosity in  
3996 its first year of operation increasing to  $50 \text{ fb}^{-1}$  in three years. This means, that in its first year,  
3997 the LHeC experiment collected ten times the total luminosity which H1 registered in its lifetime  
3998 of 15 years, while after three years the luminosity was hundred times that of H1, taken at much  
3999 higher beam energies leading to higher cross sections at fixed  $x$  and  $Q^2$ . For  $pp$  Higgs physics  
4000 at the LHC, the precise determination of the gluon density,  $xg$ , at medium  $x \sim M_H/\sqrt{s} = 0.01$   
4001 is of crucial importance.

4002 Fig. 5.14 shows the precision one can expect to obtain for  $xg$  with the LHeC. One notices a very  
4003 large improvement with respect to HERA, using the combined H1 and ZEUS data in the LHeC  
4004 fit framework, but also the near saturation with respect to increasing the integrated luminosity,  
4005 comparing the result for  $50 \text{ fb}^{-1}$  with the ultimate set of  $1 \text{ ab}^{-1}$ . In other words, the precise  
4006 LHeC QCD information will be available from the first period of data taking and thus be in time  
4007 for the HL-LHC, many results of which require the full statistics (as for  $\mu_{bb}$  for which CMS [512]  
4008 quotes a statistical uncertainty of  $2.1\%$  within the projected HL-LC lifetime of  $3 \text{ ab}^{-1}$ ).

## 4009 5.2 Measuring the Top-quark–Higgs Yukawa Coupling

4010 Electron-proton collisions at high energy are known to provide a unique window of opportunity  
4011 to perform precision measurements in the top sector [378]. This is due to the large cross-sections  
4012 of the production of single top, which amounts to about  $2 \text{ pb}$  for  $E_e = 60 \text{ GeV}$  and  $E_p = 7 \text{ TeV}$ ,  
4013 where clean signatures are provided without the challenges posed by pile-up. As a result, the  
4014 cross-section of the SM in association with a single top in  $e^-p$  collisions is large enough to  
4015 perform competitive measurements. This includes the measurement of the absolute value of the  
4016 Top Yukawa coupling and, most prominently, its CP-phase [391].

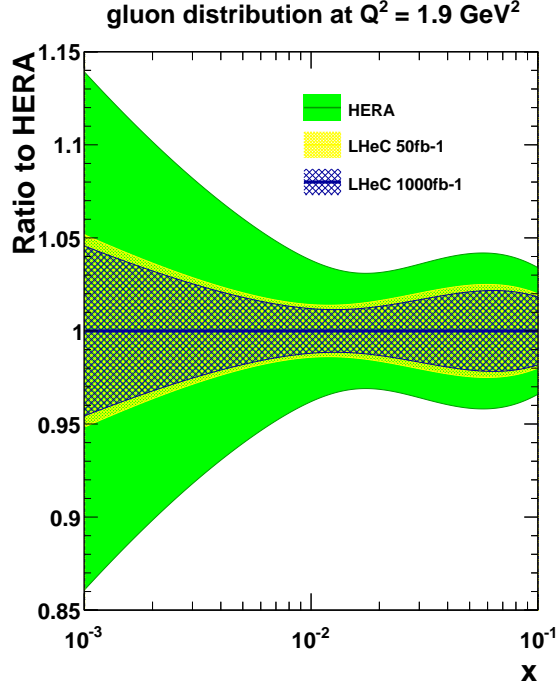


**Figure 5.14:** Uncertainty on the determination of the gluon distribution in the  $x$  range relevant for Higgs measurements at the LHC, based on the combined HERA data (outer band, green) and for the LHeC with the full data set (inner band, blue) and from the first running period (yellow, around the inner band). The LHeC uncertainties comprise full correlated systematic error estimates besides the statistics.

4017 In the SM, the Yukawa coupling of the third generation of quarks can be written down as:

$$\mathcal{L}_Y = -\frac{m_t}{v} \bar{t} t h - \frac{m_b}{v} \bar{b} b h, \quad (5.12)$$

where  $v \equiv (\sqrt{2}G_F)^{-1/2} = 2m_W/g \simeq 246$  GeV, and  $m_t$  ( $m_b$ ) is the mass of the top (bottom) quark. Due to the pure scalar nature of the Higgs boson in the SM, the top- and bottom-Higgs couplings are completely CP-even. To investigate any BSM contributions in terms of mixtures of CP-even and CP-odd states, we write a CP-phase dependent generalised Lagrangian as follows [513]:

$$\begin{aligned} \mathcal{L} = & -\frac{m_t}{v} \bar{t} [\kappa \cos \zeta_t + i\gamma_5 \sin \zeta_t] t h \\ & -\frac{m_b}{v} \bar{b} [\cos \zeta_b + i\gamma_5 \sin \zeta_b] b h. \end{aligned} \quad (5.13)$$

4018 Here,  $\zeta_t$  and  $\zeta_b$  are the phases of the top-Higgs and bottom-Higgs couplings, respectively. It is  
 4019 clear from the Lagrangian in Eq. (5.13) that  $\zeta_{t,b} = 0$  or  $\zeta_{t,b} = \pi$  correspond to a pure scalar state  
 4020 while  $\zeta_{t,b} = \frac{\pi}{2}$  to a pure pseudo scalar state. Thus, the ranges  $0 < \zeta_{t,b} < \pi/2$  or  $\pi/2 < \zeta_{t,b} < \pi$   
 4021 represent a mixture of the different CP-states. The case  $\kappa = 1$ ,  $\zeta_t = 0$  corresponds to the SM.

4022 In  $e^-p$  collisions, the top-Higgs couplings can be probed via associated production of the Higgs  
 4023 boson with an anti-top quark  $e^-p \rightarrow \bar{t} h \nu_e$ . It is necessary to consider a 5-flavour proton including  
 4024 the  $b$ -quark parton distribution. The Feynman diagrams for the process under investigation are  
 4025 shown in Fig. 5.15. It is important to note that three important couplings are involved, namely  
 4026  $hWW$ ,  $Wtb$  and the top-Higgs ( $tth$ ). A detailed study of  $hWW$  and  $Wtb$  couplings at the  $e^-p$   
 4027 collider have been performed in Refs. [378,514], respectively. For our studies we do not consider

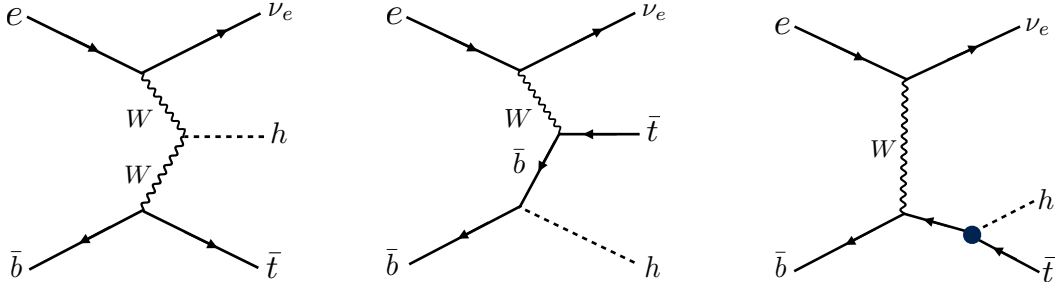


**Figure 5.15:** Leading order Feynman diagrams contributing to the process  $p e^- \rightarrow \bar{t} h \nu_e$  in high energy  $e^-p$  collisions. The black dot in the Feynman diagram on the right denotes the top-quark-Higgs coupling of interest in this section.

4028 the BSM bottom-Higgs coupling since the effect of the phase  $\zeta_b$  on the total production cross  
 4029 section or kinematics of top-Higgs production at the LHeC are negligible. Thus in what follows,  
 4030 we simply set  $\zeta_b = 0$ .

4031 In the context of the LHC, quantitatively an interesting feature can be observed: in the pure SM  
 4032 case there is constructive interference between the diagrams shown in Fig. 5.15, left and middle,  
 4033 for  $\zeta_t > \pi/2$  resulting in an enhancement in the total production cross section of associated  
 4034 top-Higgs significantly. This is also true for  $\zeta_t < \pi/2$  - however the degree of enhancement is  
 much smaller owing to the flipped sign of the CP-even part of the coupling.

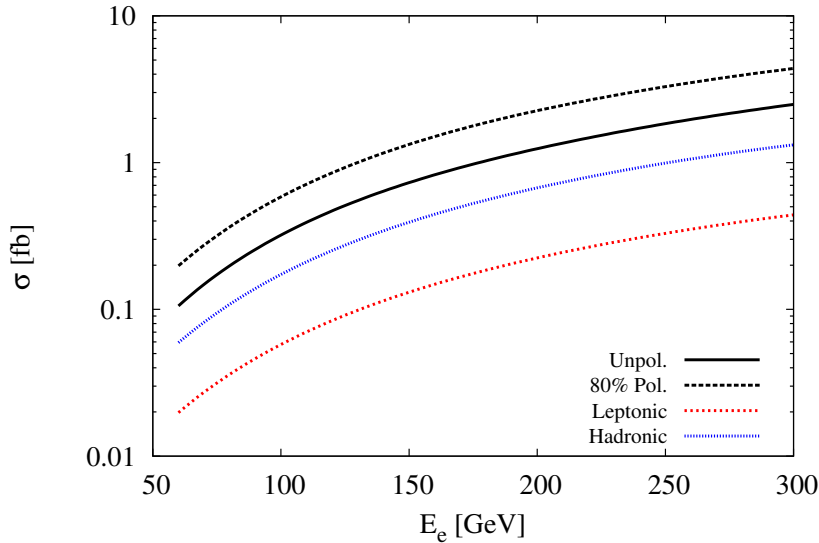


**Figure 5.16:** Cross-sections of the Higgs boson produced in association with a top quark in  $e^-p$  collisions with  $E_p = 7$  TeV. for different electron beam energies The dotted and solid *black* lines correspond to  $p e^- \rightarrow \bar{t} h \nu_e$  with and without longitudinal polarisation of the electron beam, respectively. The dotted *red* and *blue* lines correspond to  $\sigma \times \text{BR}$  for the leptonic and hadronic decay modes of  $\bar{t}$  where for this estimation we use basic cuts (see text).

4035

4036 We probe the sensitivity of the top-Higgs couplings in terms of  $\zeta_t$  by building a model file for  
 4037 the Lagrangian in Eq. (5.13) using `FeynRules` [515], and then simulating the charged current  
 4038 associated top-Higgs production channel  $p e^- \rightarrow \bar{t} h \nu_e$  (see Fig. 5.15), with  $h$  further decaying  
 4039 into a  $b\bar{b}$  pair and the  $\bar{t}$  decaying leptonically in the LHeC set-up with centre of mass energy  
 4040 of  $\sqrt{s} \approx 1.3$  TeV. Here we perform the analysis at parton level only where for signal and back-

4041 ground event generation we use the Monte Carlo event generator package `MadGraph5` [361].  
4042 We use `NNPDF23_lo_as_0130_qed` [516, 517] parton distribution functions for all event gener-  
4043 ations. The factorisation and renormalisation scales for the signal simulation are fixed at  
4044  $\mu_F = \mu_R = (m_t + m_h)/4$  while background simulations are done with the default `MadGraph5` [361]  
4045 dynamic scales. The  $e^-$  polarisation is assumed to be  $-80\%$ . We now list and explain various  
4046 kinematic observables that can serve as possible discriminants of a CP-odd  $t\bar{t}h$  coupling.

4047 In Fig. 5.16 we present the variation of the total cross section against the electron beam energy  
4048 for the signal process  $pe^- \rightarrow \bar{t}h\nu_e$ , by considering un-polarised and polarised  $e^-$  beam. Also,  
4049 the effect of branchings of  $h \rightarrow b\bar{b}$  and the  $\bar{t}$  decay for both leptonic and hadronic modes are  
4050 shown. Possible background events typically arise from  $W+$  multi-jet events,  $Wb\bar{b}\bar{b}$  with missing  
4051 energy which comes by considering only top-line, only Higgs-line, and without top- nor Higgs-  
4052 line, in charged and neutral current deep-inelastic scattering and in photo-production by further  
4053 decaying  $W$  into leptonic mode. We have estimated the cross sections for signal and all possible  
4054 backgrounds imposing only basic cuts on rapidity  $|\eta| \leq 10$  for light-jets, leptons and  $b$ -jets, the  
4055 transverse momentum cut  $p_T \geq 10$  GeV and  $\Delta R_{\min}=0.4$  for all particles.

4056 We now estimate the sensitivity of the associated top-Higgs production cross-section,  $\sigma(\zeta_t)$ , as  
4057 a function of the CP phase of the  $t\bar{t}h$ -coupling as shown in Fig. 5.17 by considering  $E_e = 60$   
4058 and with fixed  $E_p = 7$  TeV. The scale uncertainties are taken as  $(m_t + m_h)/8 \leq \mu_F = \mu_R \leq$   
4059  $(m_t + m_h)/2$ . Here  $\sigma(\zeta_t = 0)$  corresponds to the SM cross section. We notice that the cross section  
4060 is very sensitive to  $\zeta_t$  in the region  $\zeta_t > \frac{\pi}{2}$  where the interference between the diagrams becomes  
4061 constructive. Below  $\zeta_t = \frac{\pi}{2}$  the interference is still constructive though its degree decreases  
4062 with  $\zeta_t$ , thus increasing the cross section by around 5 times at  $\zeta_t = \frac{\pi}{2}$  which corresponds to  
4063 the pure CP-odd case. On the other hand, for pure CP-even case  $\zeta_t = \pi$  with opposite-sign of  
4064  $t\bar{t}h$ -coupling the cross section can be enhanced by up to 24 times for  $E_e = 60$  GeV. The scale  
uncertainty on an average is approximately 7% for  $E_e = 60$  GeV in the whole range of  $\zeta_t$ .

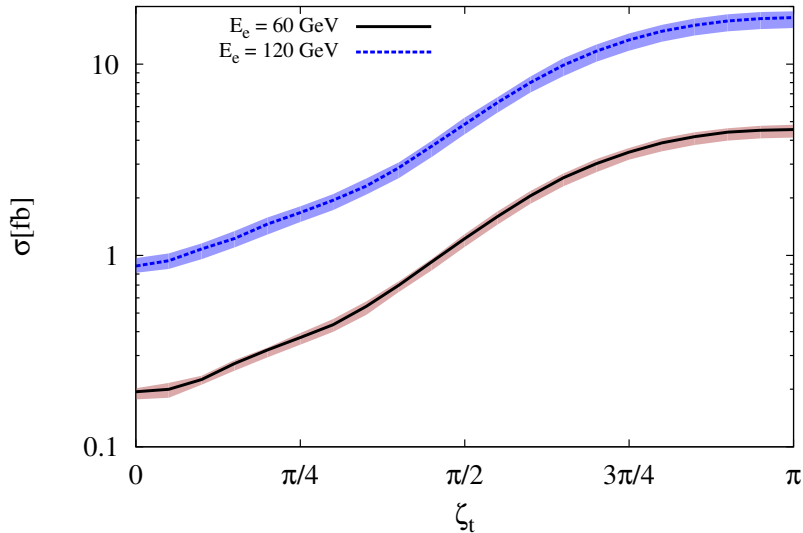


**Figure 5.17:** Total cross section of the Higgs boson produced in association with a single top as a function of  $\zeta_t$ , including scale uncertainties. The *black* solid and *blue* dotted lines correspond to  $E_e = 60$  and 120 GeV, respectively. These are obtained for fixed  $E_p = 7$  TeV and scales  $\mu_F = \mu_R = (m_t + m_h)/4$ .

4065

4066 In order to evaluate sensitivity to the measurement of the top Yukawa coupling and its P-phase,  
4067 we implement the following criteria to select events, referred to as the fiducial selection:

- 4068 •  $p_T \geq 20$  GeV for  $b$ -tagged jets and light-jets, and  $p_T \geq 10$  GeV for leptons.
  - 4069 • Since the LHeC collider is asymmetric, event statistics of final state particles are mostly  
4070 accumulated on the left or right sides of the transverse plane  $\eta = 0$  (depending on the  
4071 initial direction of  $p$  and  $e^-$ ) - we select events within  $-2 \leq \eta \leq 5$  for  $b$ -tagged jets while  
4072  $2 \leq \eta \leq 5$  for leptons and light-jets,
  - 4073 • The separation distance of all final state particles are taken to be  $\Delta R > 0.4$ .
  - 4074 • Missing transverse energy  $\cancel{E}_T > 10$  GeV to select the top events.
  - 4075 • Invariant mass windows for the Higgs through  $b$ -tagged jets and the top are required to  
4076 be  $115 < m_{bb} < 130$  GeV and  $160 < m_t < 177$  GeV, respectively, which are important to  
4077 reduce the background events substantially.
- 4078 In these selections the  $b$ -tagging efficiency is assumed to be 70%, with fake rates from  $c$ -initiated  
4079 jets and light jets to the  $b$ -jets to be 10% and 1%, respectively.

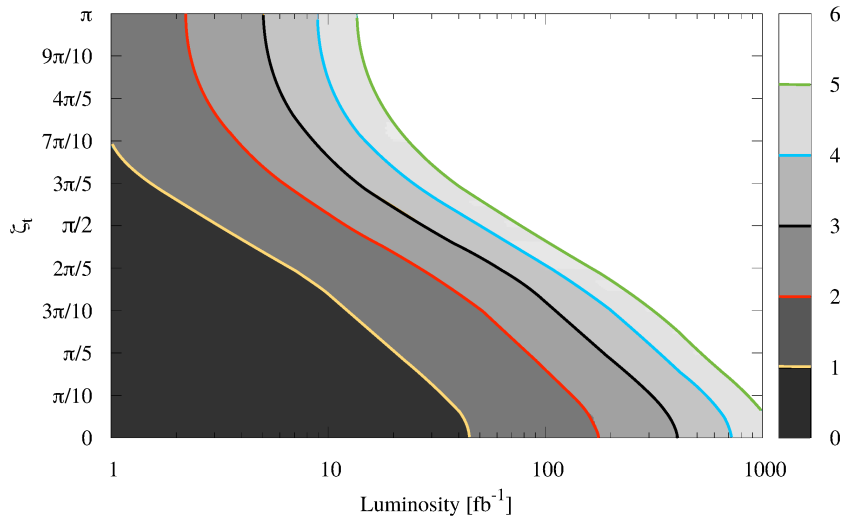


**Figure 5.18:** Exclusion contours for  $\zeta_t$  as a function of integrated luminosity for  $E_e = 60$  GeV and  $E_p = 7$  TeV. The regions beyond each contours are excluded for the particular luminosity, *black* and *red* solid lines correspond to  $3\sigma$  and  $2\sigma$  regions. Results are obtained based on fiducial cross-sections (see text).

4080 We estimated the exclusion regions of  $\zeta_t$  as a function of  $L$  in  $\text{fb}^{-1}$ . The exclusion is based  
4081 on significance using the Poisson formula, where  $S$  and  $B$  are the number of expected signal  
4082 and background events at a particular luminosity, respectively. Here we used 10% systematic  
4083 uncertainty for background yields only. In Fig. 5.18, we present exclusion contours at various  
4084 confidence levels for  $E_e = 60$  GeV – understandably, higher  $\sigma$ -contours demand larger luminosities.  
4085 It is also seen that there is a kink around  $\zeta_t = \pi/2$  such that for the region  $0 < \zeta_t < \pi/2$ , we  
4086 need larger luminosities for exclusion. This is in keeping with the feature exhibited in Fig. 5.17  
4087 where the constructive interference between the signal diagrams enhances the cross-section over  
4088 the SM value much more for  $\zeta_t > \pi/2$  thus requiring less luminosity to probe that region. For  
4089  $L = 100 \text{ fb}^{-1}$ , regions above  $\pi/5 < \zeta_t \leq \pi$  and  $3\pi/10 < \zeta_t \leq \pi$  are excluded at  $2\sigma$  and  $3\sigma$  C.L.  
4090 While around  $L = 400 \text{ fb}^{-1}$ , regions above  $\pi/6 < \zeta_t \leq \pi$  and  $\pi/4 < \zeta_t \leq \pi$  are excluded at  $4\sigma$   
4091 and  $5\sigma$  C.L., respectively.

4092 As a measure of comparison, that asymmetry studies at the HL-LHC [513] help probe up to  
4093  $\zeta_t = \pi/6$  for a total integrated luminosity of  $3 \text{ ab}^{-1}$ . Thus, it is clear that the LHeC provides a

4094 better environment to test the CP nature of Higgs boson couplings.

4095 For the integrated luminosity  $L = 1 \text{ ab}^{-1}$ , almost all values of  $\zeta_t$  can be excluded up to  $4\sigma$   
4096 C.L. While investigating the overall sensitivity of  $\zeta_t$  by applying these two observables, it is also  
4097 important to measure the accuracy of SM  $tth$  coupling  $\kappa$  at the LHeC energies. To measure the  
4098 accuracy of  $\kappa$  by using signal and background yields we use the formula  $\sqrt{(S+B)}/(2S)$  at a  
4099 particular luminosity. And for  $E_e = 60 \text{ GeV}$ , the measured accuracy at the design luminosity  
4100  $L = 1 \text{ ab}^{-1}$  is given to be  $\kappa = 1.00 \pm 0.17$  of its expected SM value, where a 10% systematic  
4101 uncertainty is been taken in background yields only.

4102 These results are obtained based on the evaluation of the fiducial cross-sections alone. As  
4103 pointed out in Ref. [391], a number of other observables carry sensitivity to the structure of the  
4104 top-Higgs Yukawa coupling, such as the rapidity difference between the top quark and the Higgs  
4105 boson and a number of angular variables. While the fiducial rate studied here is the single most  
4106 sensitive observable, it is evident that a multi-variate approach will significantly enhance the  
4107 sensitivity reported here.

### 4108 5.3 Higgs Decay into Invisible Particles

4109 The Higgs decay into invisible particles could be a key to BSM physics. The SM branching  
4110 ratio of  $H \rightarrow ZZ \rightarrow 4\nu$  is only 0.1%. Any sizable decay rate into invisible particles would  
4111 thus indicate an exotic decay, for example to dark matter particles. Its non-observation would  
4112 give the SM cross section measurement, reconstructing more than 99% of the ordinary decays  
4113 a higher meaning for constraining the total Higgs decay width.

4114 For the LHeC at a luminosity of  $1 \text{ ab}^{-1}$ , initial parton-level studies of this decay were presented  
4115 in Ref. [518], with the estimate of a two  $\sigma$  sensitivity to a branching fraction of 6%. For this  
4116 study, NC production via  $ZZ$  fusion  $eq \rightarrow eqZZ \rightarrow eqH$  was used, which has a cross section  
4117 of about 25 fb at the LHeC. The CC production via  $WW$  fusion has a larger cross section,  
4118 but entails a missing energy signal by itself which requires further study of potentially quite  
4119 some gain in precision. This channel, when employed for the invisible decay study, results in a  
4120 mono-jet signature which is hard to separate from the SM DIS CC background.

4121 The neutral current study has been repeated using the LHeC Higgs WG analysis tools, intro-  
4122 duced above: MadGraph, Pythia and Delphes. Similar to [518], an electron beam of 60 GeV  
4123 with a polarization of -80% is assumed. The basic event topology contains the scattered electron,  
4124 jet and missing transverse energy. Its main background results from SM  $W$  and  $Z$  productions  
4125 (followed by  $W \rightarrow \ell\nu$  and  $Z \rightarrow \nu\bar{\nu}$ ). In the study NC and CC  $W$  production and NC  $Z$  produc-  
4126 tion are considered, while single-top, NC multijets and  $W$  photoproduction were all found to be  
4127 negligible. Requiring missing transverse energy of 60 GeV, exactly one electron and one jet, and  
4128 no other leptons (including  $\tau$ ), as well as imposing several selection criteria on the kinematics of  
4129 electron, jet and missing transverse momentum, we get a two  $\sigma$  sensitivity to a branching ratio  
4130 of 7.2%, which is similar to the earlier result [518]. Fig. 5.19 shows the electron-jet invariant  
4131 mass distribution after the selection for the signal (normalized to a 100% branching ratio) and  
4132 the background.

4133 The analysis has been further refined with a usage of multivariate analysis (Boosted Decision  
4134 Tree in TVMA package). Basically the set of selection variables used in the cut-based analysis  
4135 above was used as inputs to the multivariate analysis, tuned to yield the best output score to  
4136 discriminate the signal from backgrounds. Fig. 5.20 shows the distribution of the discriminant

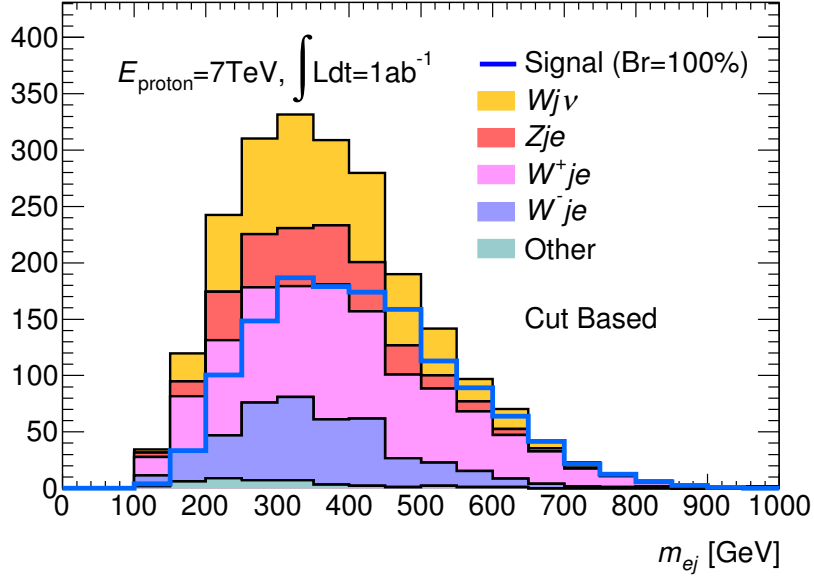


**Figure 5.19:** Electron-jet invariant mass distribution for the Higgs to invisible decay signal (normalized to 100% branching ratio) and the stacked backgrounds for an integrated luminosity of  $1 \text{ ab}^{-1}$  at the LHeC after all selection cuts.

4137 variable for the signal and background (both area normalised). An optimization on the statistical  
 4138 significance is found at the BDT score  $> 0.25$ , and the resulting mass distribution is shown  
 4139 in Fig. 5.21. With  $1 \text{ ab}^{-1}$  of integrated luminosity, a two  $\sigma$  sensitivity of 5.5% is obtained  
 4140 consistent with the previous results. For a comparison, an estimate of 3.5% is given for a HL-  
 4141 LHC sensitivity study on this channel [519]. The result on the LHeC may be further improved  
 4142 in the future with a refined BDT analysis when one introduces extra parameters, beyond those  
 4143 initially introduced with the cut based analysis.

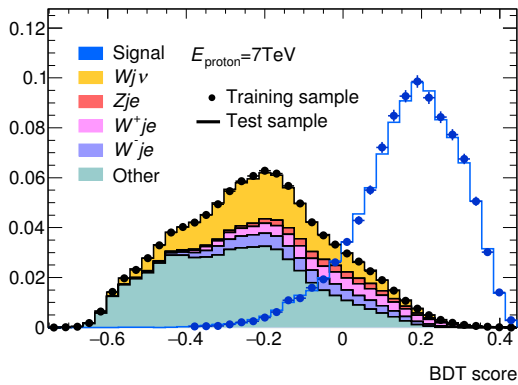


**Figure 5.20:** BDT output score distribution for the Higgs to invisible decay signal and the stacked backgrounds (both area normalized) at the LHeC.

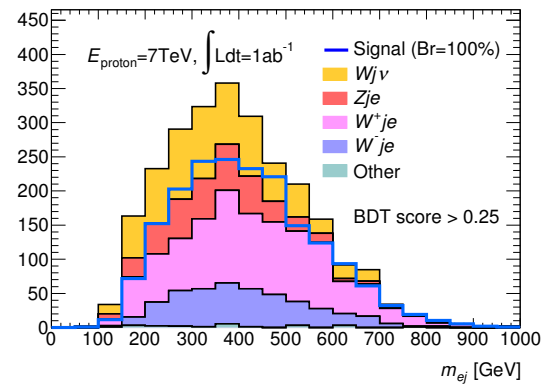


**Figure 5.21:** Electron-jet invariant mass distribution for the Higgs to invisible decay signal (normalized to 100% branching ratio) and the stacked backgrounds for an integrated luminosity of  $1 \text{ ab}^{-1}$  at the LHeC after the BDT score cut of 0.25.

4144 In these initial studies no systematic uncertainties were considered. This may be justified with  
 4145 the very a clean environment of electron-hadron collider, in which precise measurements of  $W$   
 4146 and  $Z$  production will be made, for example in their decays to muons, for accurately controlling

4147 the systematics in the background prediction to a negligible level.

4148 The BDT analysis was repeated for higher proton energies. At the HE-LHeC ( $E_p=13.5$  TeV)  
4149 the NC production cross section increases to 45 fb and the branching ratio sensitivity improves  
4150 to 3.4% because the luminosity is doubled in the configurations here assumed. At the FCC-eh,  
4151 the cross section rises to 120 fb and the sensitivity of the branching ratio reaches about 1.7%.

## Chapter 6

# Searches for Physics Beyond the Standard Model

### 6.1 Introduction

The LHC was originally envisioned as the ultimate machine to search for physics beyond the Standard Model at the TeV scale. Since electrons and quarks share only electroweak interactions, an electron-proton collider could allow to measure the same phenomena in a different environment with generally higher precision. It could add complementary search channels or lead to the discovery of a weak signal. The possibility for undiscovered NP below the TeV scale could thus be also addressed by the LHeC, which is projected to operate when the LHC will be in its high luminosity phase, in spite of the lower centre-of-mass energy. Exotic phenomena that can be studied at  $ep$  colliders have been reviewed, for example, in [520]. More recently, but when the LHC was only beginning to yield data in Run I, an overview of the potential of the LHeC for probing physics beyond the Standard Model has been given in the Conceptual Design Report [1]. Since then, stringent constraints on NP phenomena have been obtained from the LHC and the absence of hints from New Physics (NP) to date is presently changing this paradigm to two alternative scenarios: NP may actually reside at an even larger energy scale; NP may be at or below the TeV scale, but more weakly coupled, and thus hidden in the SM backgrounds [521].

A similar  $pp$ - $ep$  synergy could be envisaged with higher proton beam energies at the FCC 100 km tunnel. With an electron beam of 60 GeV, the expected centre-of-mass energies for  $ep$  could be 2.9 TeV for  $E_p = 19$  TeV (Low-Energy FCC) and 3.5 TeV for  $E_p = 50$  TeV (FCC). Below we list recent developments which discuss new physics opportunities at the LHeC and its potential future high-energy upgrades.

### 6.2 Extensions of the SM Higgs Sector

Presently, given the precision of measurements in the Higgs sector, it appears that the discovered 125 GeV scalar is indeed the SM Higgs boson. It is not absolutely clear, however, if the scalar potential is truly that of the SM or if it is extended, possibly with additional degrees of freedom. Several extensions of the Higgs sector have been proposed and can be studied at the  $ep$  colliders with results often complementary to those of  $pp$  colliders and other future facilities.

## 4181 6.2.1 Modifications of the Top-Higgs interaction

4182 In electron-proton collisions the heavy top-quarks can be produced in association with a Higgs  
 4183 boson, which allows us to study the sensitivity of the LHeC or the FCC-he to the top-Higgs  
 4184 ( $tH$ ) interaction. In Ref. [391] the sensitivity of the process  $pe^- \rightarrow \bar{t}H\nu_e$  to the CP nature of  
 4185 the  $tH$  coupling is investigated, by considering a CP phase  $\zeta_t$  at the  $ttH$  and  $bbH$  vertices. The  
 4186 authors conclude, based on several observables and with appropriate error fitting methodology,  
 4187 that better limits on  $\zeta_t$  are obtained at the LHeC than at the HL-LHC. At the design luminosity  
 4188 of  $1 \text{ ab}^{-1}$ , almost all values of  $\zeta_t$  are excluded up to  $4\sigma$  C.L. and the SM top-Higgs coupling  
 4189 could be measured relative to its SM value with a precision of  $\kappa = 1.00 \pm 0.17$ .

4190 Flavour changing neutral currents (FCNC) are completely absent at tree-level in the SM and  
 4191 strongly constrained especially by low energy experiments. Anomalous flavour changing neutral  
 4192 current Yukawa interactions between the top quark, the Higgs boson, and either an up or  
 4193 charm quark are documented in this paper (Chapter 3, Sec. 3.4.2). Among other studies, in  
 4194 Ref. [522] the authors consider the Higgs decay modes  $H \rightarrow \gamma\gamma, bb$  and  $\tau\tau$  and considering  
 4195  $E_e = 150 \text{ GeV}$ . The results are updated in Ref. [388] for  $E_e = 60 \text{ GeV}$ , including estimates for  
 4196 smaller electron beam energies, and the  $2\sigma$  sensitivity on the branching ratio  $\text{Br}(t \rightarrow uh)$  is  
 4197 found to be  $0.15 \times 10^{-2}$ . Making use of the polarisation of the electron beam and multivariate  
 4198 techniques, Ref. [523] shows that limits on the branching ratio  $\text{Br}(t \rightarrow uh)$  of  $\mathcal{O}(0.1)\%$  can be  
 4199 obtained, an improvement over present LHC limits of  $0.19\%$  [524, 525]. These results vary with  
 4200  $E_e$  and  $E_p$ .

## 4201 6.2.2 Charged scalars

4202 The prospects to observe a light charged Higgs boson through the decay  $H^+ \rightarrow c\bar{b}$  are inves-  
 4203 tigated within the framework of the Two Higgs Doublet Model (2HDM) Type III, assuming a  
 4204 four-zero texture in the Yukawa matrices and a general Higgs potential [526]. The charged cur-  
 4205 rent production processes  $e^-p \rightarrow \nu H^+q$  are considered. The analysed signature stems from the  
 4206 subsequent decay  $H^+ \rightarrow c\bar{b}$ . The parton level analysis accounts for irreducible SM backgrounds  
 4207 and considers scenarios up to a mass of  $200 \text{ GeV}$  which are consistent with present limits from  
 4208 Higgs and flavour physics. The authors show that for  $L = 100 \text{ fb}^{-1}$  a charged Higgs boson  
 4209 could be observed with about  $3 - 4\sigma$  significance. This is to be compared with results from  
 4210 present LHC searches in which strong limits are set on the branching fraction  $B(t \rightarrow H^+b)$ ,  
 4211 assuming  $B(H^+ \rightarrow c\bar{b}) = 1.0$  or  $B(H^+ \rightarrow c\bar{s}) = 1.0$  for the charged Higgs boson mass range  
 4212  $\sim 90 - 160 \text{ GeV}$  [527, 528].

4213 A similar study for the FCC-he (with  $\sqrt{s} \approx 3.5 \text{ TeV}$ ) is presented in Ref. [529], where a next-to-  
 4214 minimal supersymmetric model (NMSSM) was considered where  $H^\pm \rightarrow sc + su$ . Using dedicated  
 4215 optimisation techniques, the authors show that a light charged boson  $H^\pm$  can be observed with  
 4216 maximal significance of  $4.4 (2.2)\sigma$  provided its mass is at most  $m_{H^\pm} = 114(121) \text{ GeV}$ , for the  
 4217 total luminosity of  $1 \text{ ab}^{-1}$ .

4218 The Georgi-Machacek (GM) model extends the Higgs sector by including higher multiplet states  
 4219 while preserving custodial symmetry. The physical states include, besides the SM Higgs, a  
 4220 heavier singlet  $H$ , a triplet  $(H_3^+, H_3^0, H_3^-)$  and a quintuplet  $(H_5^{++}, H_5^+, H_5^0, H_5^-, H_5^{--})$ . The  
 4221  $H_5$  scalars do not couple to fermions and can therefore only be produced by vector boson  
 4222 fusion. An analysis for the prospects to discover the doubly charged Higgs bosons in the GM  
 4223 model at the LHeC and the FCC-he is presented in Ref. [530]. Therein the production of a  
 4224 doubly-charged member of five-plet Higgs-bosons ( $H_5^{\pm\pm}$ ), produced from vector boson fusion is

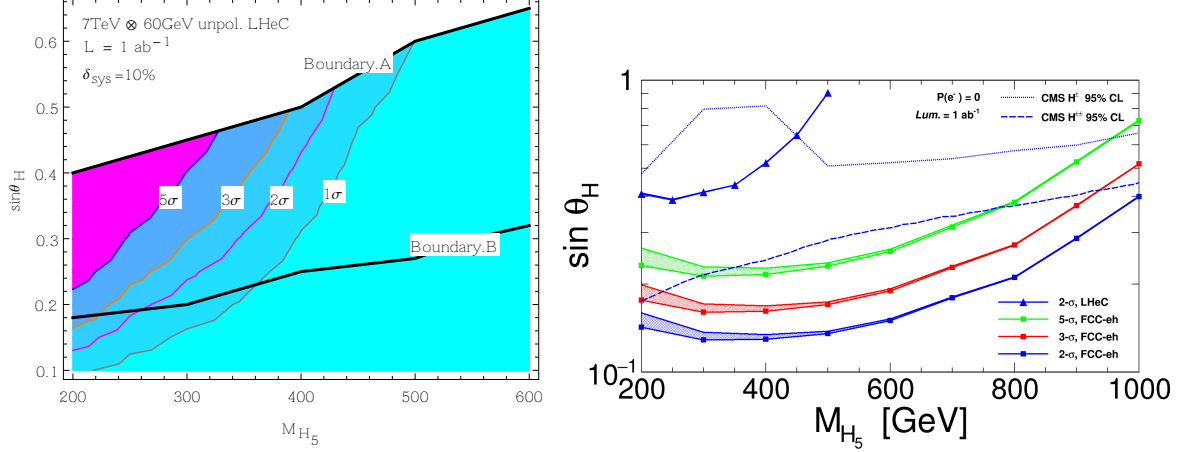


**Figure 6.1:** *Left:* Discovery contour with respect to  $\sin\theta_H$  and  $M(H_5^{++/--})$  at LHeC with unpolarized beam; *Right:* Limit Contours for the case of singly charged Higgs for FCC-eh and LHeC. The blue dotted curve and the blue dashed curves give the 95% CL limit from CMS for  $H_5^{+/-}$  and for  $H^{++/--}$  respectively [532, 533]. An unpolarized beam of integrated luminosity of  $1 \text{ ab}^{-1}$  and a 10% systematic uncertainty for background yields is assumed in both plots.

4225 studied. The authors find that 2 to 3 $\sigma$  limits can be obtained for mixings  $\sin(\theta_H)$  as low as 0.2,  
 4226 for  $M(H_5) < 300$  GeV. The prospects can be improved at the FCC-he collider, where doubly  
 4227 charged Higgs bosons can be tested for masses  $M_{H_5} < 400$  GeV, also for small scalar mixing  
 4228 angles (Fig. 6.1 (left)).

4229 The discovery prospects for the singly charged Higgs,  $H_5^\pm$ , in the Georgi-Machacek model are  
 4230 evaluated in Ref. [531]. The authors perform a multivariate analysis, including a fast detector  
 4231 simulation, and they consider the LHeC and the FCC-he for a mass range from 200–1000 GeV.  
 4232 They find that the LHeC can improve over current LHC limits on  $H_5^\pm$  for masses up to about  
 4233 400 GeV and scalar mixing angles  $\sin\theta_H \sim 0.5$  (Fig. 6.1 (right)).

### 4234 6.2.3 Neutral scalars

4235 Neutral scalar bosons generally appear in many extensions of the scalar potential. They can be  
 4236 added directly, as  $SU(1)$  singlets, or be part of higher representation  $SU(2)$  multiplets. They  
 4237 generally mix with the Higgs boson, from which they inherit a Higgs-like phenomenology.

4238 The potential of testing the heavier CP-even scalar that is contained in the 2HDM Type-I is  
 4239 presented in Ref. [534]. Therein, the lighter scalar particle is considered to be a SM-like Higgs  
 4240 boson and the properties of a heavy scalar, assumed to have the specific mass 270 GeV, is  
 4241 discussed. The authors state that the final state  $H \rightarrow hh$  is of particular interest, as it connects  
 4242 to the findings in Ref. [521].

4243 The prospects to search for a generic heavy neutral scalar particle are presented in detail  
 4244 Ref. [535]. The model is a minimal extension of the SM with one additional complex scalar  
 4245 singlet that mixes with the SM Higgs doublet, which governs its production and decay mode.  
 4246 The heavy scalar is produced via vector-boson fusion and decays into two vector bosons. A mul-  
 4247 tivariate analysis is performed and detector simulation is taken into account. Masses between  
 4248 200 and 800 GeV and scalar mixings as small as  $\sin^2\alpha \sim 10^{-3}$  are considered. The resulting  
 4249 sensitivity for a total luminosity of  $1 \text{ ab}^{-1}$  is shown in Fig. 6.2, including existing bounds from  
 4250 the LHC and future HL-LHC projections. A significant improvement over existing LHC limits

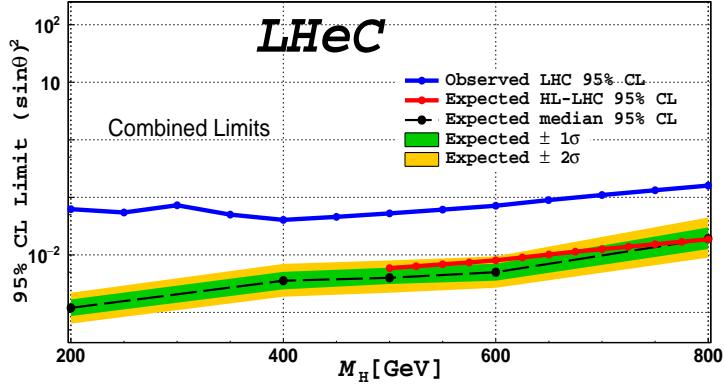


**Figure 6.2:** Expected exclusion limits (green and yellow bnds) for a heavy scalar search at the LHeC, assuming a systematic uncertainty on the SM background of 2% (from Ref. [535]). The blue line represents the current LHC limit at 95% CL as extracted from [536], the red line the forecast of the HL-LHC sensitivity via  $h_2 \rightarrow ZZ$  searches from Ref. [537]. The LHeC results correspond to an integrated luminosity of  $1 \text{ ab}^{-1}$ .

4251 is found, with the LHeC probing scalar boson masses below  $\sim 500 \text{ GeV}$ , a region which remains  
 4252 difficult at the HL-LHC.

4253 The scalar bosons from the 2HDM Type-III framework may give rise to flavour violating signa-  
 4254 tures, which is discussed in Ref. [538]. The prospects to observe the light and heavy CP-even  
 4255 neutral Higgs bosons via their decays into flavour violating  $b\bar{s}$  channels were studied with spe-  
 4256 cific Yukawa textures and a general Higgs potential. The considered signature consists in one jet  
 4257 originating from b-hadron fragmentation (b-tagged jets) and one light-flavour jet in the central  
 4258 rapidity region, with a remaining jet in the forward region. Relevant SM backgrounds were  
 4259 considered and it is found that flavour violating decays of the SM-like Higgs boson would be  
 4260 accessible with  $L = 100 \text{ fb}^{-1}$  at  $ep$  colliders, while for the heaviest scalar boson, with a mass of  
 4261 about  $170 \text{ GeV}$ , a total luminosity of about  $1 \text{ ab}^{-1}$  will give rise to  $\mathcal{O}(1)$  events.

4262 The prospects of observing the light CP-even neutral Higgs bosons via their decays into b-quarks,  
 4263 in the neutral and charged current production processes, considering the NMSSM framework, the  
 4264 MSSM with an additional singlet superfield, are studied in Ref. [539]. In this work the following  
 4265 constraints are incorporated into the spectrum: neutralino relic density corresponding to the  
 4266 observed dark matter relic density; direct and indirect mass bounds from searches for specific  
 4267 sparticles; the SM-like Higgs boson has a mass around  $126 \text{ GeV}$  and an invisible branching ratio  
 4268 below  $0.25$ . The signal is given by three jets plus an electron or missing transverse momentum  
 4269 ( $E_T^{\text{miss}}$ ) arising from the neutral (charged) current interaction, where two jets are required to be  
 4270 originating from a b-quark and the remaining jet is required to be in the forward region. For the  
 4271 cut-based analysis a number of reducible and irreducible SM backgrounds are considered and it  
 4272 includes a fast detector simulation with an adaption of the LHeC detector. It is found that the  
 4273 boson  $h_1$  could be observable for some of the NMSSM benchmark points, at up to  $2.5\sigma$  level in  
 4274 the  $e + 3j$  channel up to masses of  $75 \text{ GeV}$ ; in the  $3j + E_T^{\text{miss}}$  channel  $h_1$  could be discovered  
 4275 at  $2.4\sigma$  level up to masses of  $88 \text{ GeV}$  with  $L = 100 \text{ fb}^{-1}$ , and a  $5\sigma$  observation is possible with  
 4276  $\mathcal{L} = 1 \text{ ab}^{-1}$  for masses up to  $90 \text{ GeV}$ .

## 4277 6.2.4 Modifications of Higgs self-couplings

4278 As in the chapter on Higgs physics above, the  $e^-p$  collisions are a very convenient environment  
4279 to study the property of the SM Higgs boson itself. The latter is produced through vector-boson  
4280 fusion processes and the precise measurement of its properties provides a unique opportunity  
4281 to probe the interaction  $HVV$ , ( $V = W^\pm, Z$ ). These interactions are in general sensitive to  
4282 certain classes of beyond the SM physics, which can be parametrised, for instance, via higher  
4283 dimensional operators and their coefficients, cf. Refs. [484, 514, 540, 541].

4284 The prospects to infer the strengths of the two couplings  $HWW$  and  $HZZ$  were studied in  
4285 Refs. [514, 540] in the context of electron-proton collisions. The authors find that the higher-  
4286 dimensional operator coefficients can be tested for values around  $\mathcal{O}(10^{-1})$  at the LHeC. This  
4287 sensitivity is improved at the FCC-he due to larger centre-of-mass energies, which in general  
4288 enhances the vector-boson fusion cross sections.

4289 The Higgs self-coupling itself  $HHH$  can be tested through the measurement of the di-Higgs  
4290 production cross section as was shown in Ref. [484]. With appropriate error fitting methodology  
4291 this study illustrates that the Higgs boson self-coupling could be measured with an accuracy of  
4292  $g_{HHH}^{(1)} = 1.00_{-0.17(0.12)}^{+0.24(0.14)}$  of its expected SM value at  $\sqrt{s} = 3.5(5.0)$  TeV, considering an ultimate  
4293  $10 \text{ ab}^{-1}$  of integrated luminosity.

4294 An analysis presented in Ref. [541] studies the LHeC sensitivity to dimension-six operators. The  
4295 authors employ jet substructure techniques to reconstruct the boosted Higgs boson in the final  
4296 state. A shape analysis on the differential cross sections shows in some cases improvements with  
4297 respect to the high-luminosity LHC forecasts.

## 4298 6.2.5 Exotic Higgs boson decays

4299 The LHeC sensitivity to an invisibly decaying Higgs boson was investigated in Ref. [518]. Therein  
4300 the focus is on the neutral current production channel due to the enhanced number of observ-  
4301 ables compared to the charged current counterpart. The signal contains one electron, one jet  
4302 and large missing energy. A cut-based parton level analysis yields the estimated sensitivity of  
4303  $\text{Br}(h \rightarrow \text{invisible}) = 6\%$  at  $2\sigma$  level. Exotic decays of the Higgs boson into a pair of light spin-0  
4304 particles referred to as  $\Phi$  was discussed in Ref. [542]. The studied signature is a final state with  
4305 4 b-quarks, which is well motivated in models where the scalars can mix with the Higgs doublet,  
4306 and suffers from multiple backgrounds at the LHC. The analysis is carried out at the parton  
4307 level, where simple selection requirements render the signature nearly free of SM background  
4308 and makes  $\Phi$  with masses in the range [20, 60] GeV testable for a  $hVV$  ( $V = W, Z$ ) coupling  
4309 strength relative to the SM at a few per-mille level and at 95% confidence level.

4310 The prospects of testing exotic Higgs decays into pairs of light long-lived particles at the LHeC  
4311 were studied in Ref. [543] where it was shown that proper lifetimes as small as  $\mu\text{m}$  could be  
4312 tested, which is significantly better compared to the LHC. This is shown in Fig. 6.3 (left). This  
4313 information can be interpreted in a model where the long-lived particles are light scalars that mix  
4314 with the Higgs doublet, where both, production and decay, are governed by this scalar mixing  
4315 angle. The area in the mass-mixing parameter space that give rise to at least 3 observable  
4316 events with a displaced vertex are shown in Fig. 6.2. It is apparent that mixings as small as  
4317  $\sin^2 \alpha \sim 10^{-7}$  can be tested at the LHeC for scalar masses between 5 and 15 GeV (Ref. [Fischer  
4318 et al., input for ESPP]).

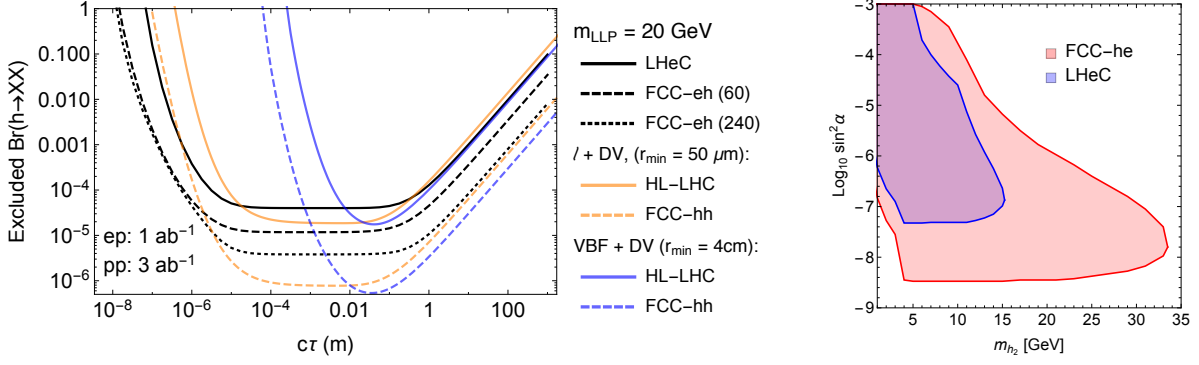


**Figure 6.3:** Sensitivity contours for displaced vertex searches for Higgs decays into long-lived scalar particles (LLP), which are pair produced from decays of the Higgs boson and decay themselves via scalar mixing into fully visible final states. Left: As a function of the LLP lifetime for a fixed mass from Ref. [543]. Right: For a specific model, where lifetime and production rate of the LLP are governed by the scalar mixing angle. The contours are for 3 events and consider displacements larger than  $50 \mu\text{m}$  to be free of background.

### 6.3 Searches for supersymmetry

Several SUSY scenarios might remain still elusive in searches performed at  $pp$  colliders. While the null results from current searches by the LHC experiments have produced impressive constraints on the SUSY coloured sector (squarks and gluinos) because of their large production cross sections in strong interactions, less stringent constraints have been placed on weakly-produced SUSY particles, namely neutralinos  $\tilde{\chi}^0$ , charginos  $\tilde{\chi}^\pm$ , and sleptons  $\tilde{\ell}^\pm$ . Some of these scenarios where  $ep$  colliders might have discovery potential complementary to that of the HL-LHC are discussed below. These include R-parity conserving SUSY models, e.g. motivated by dark matter, or R-parity violating SUSY models, e.g. including single production of bottom and top squarks and low mass gluinos.

#### 6.3.1 Search for the SUSY Electroweak Sector: prompt signatures

Electroweakino scenarios where charginos, neutralinos, and sleptons are close in mass can be characterised with the neutralino mass  $m$  and the mass splitting between charginos and neutralinos  $\Delta m$ . Scenarios with  $\Delta m < 50 \text{ GeV}$  are referred to as *compressed*. A subtlety arises for  $\Delta m \leq 1 \text{ GeV}$ , when the  $\tilde{\chi}_1^\pm/\tilde{\chi}_2^0$  becomes long lived and its decays are displaced. For  $\Delta m > 1 \text{ GeV}$  the decays are prompt, the visible decay products from  $\tilde{\ell}$  and  $\tilde{\chi}_1^\pm/\tilde{\chi}_2^0$  have very soft transverse momenta ( $p_T$ ) and the SM backgrounds are kinematically similar to the signal. The analyses therefore become challenging and sensitivities decrease substantially. Two SUSY scenarios are considered in Ref. [544] and depicted in Figure 6.4 where the LSP  $\tilde{\chi}_1^0$  is Bino-like,  $\tilde{\chi}_1^\pm$  and  $\tilde{\chi}_2^0$  are Wino-like with almost degenerate masses, and the mass difference between  $\tilde{\chi}_1^0$  and  $\tilde{\chi}_1^\pm$  is small. The signal is produced via the process “ $pe^- \rightarrow je^- \tilde{\chi}\tilde{\chi}$ ”, where  $\tilde{\chi} = \tilde{\chi}_1^0, \tilde{\chi}_1^\pm$  or  $\tilde{\chi}_2^0$ . Conservative leading order cross sections are considered for the SUSY signal models. The kinematic observables are input to the TMVA package to perform a multivariate analysis at the detector level.

In the compressed-slepton scenario, the case where the left-handed slepton  $\tilde{\ell}_L$  and sneutrino  $\tilde{\nu}$  are slightly heavier than  $\tilde{\chi}_1^\pm$  or  $\tilde{\chi}_2^0$  is considered. When fixing the mass difference  $\Delta m = m_{\tilde{\ell}} - m_{\tilde{\chi}_1^\pm, \tilde{\chi}_2^0} = 35 \text{ GeV}$  and ignoring the systematic uncertainty on the background, the analysis

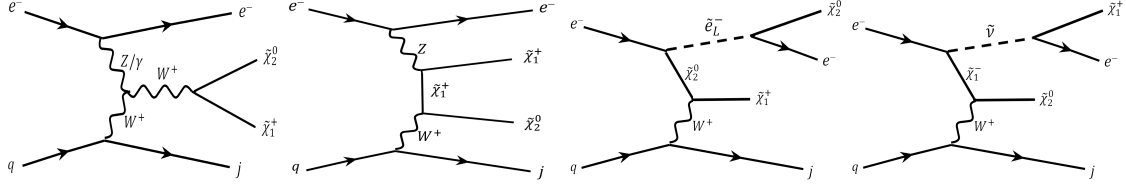


**Figure 6.4:** Representative production diagrams for the signal processes considered Ref. [544]. The *decoupled-slepton* scenario includes only the first two diagrams, while the *compressed-slepton* scenario includes all four diagrams.

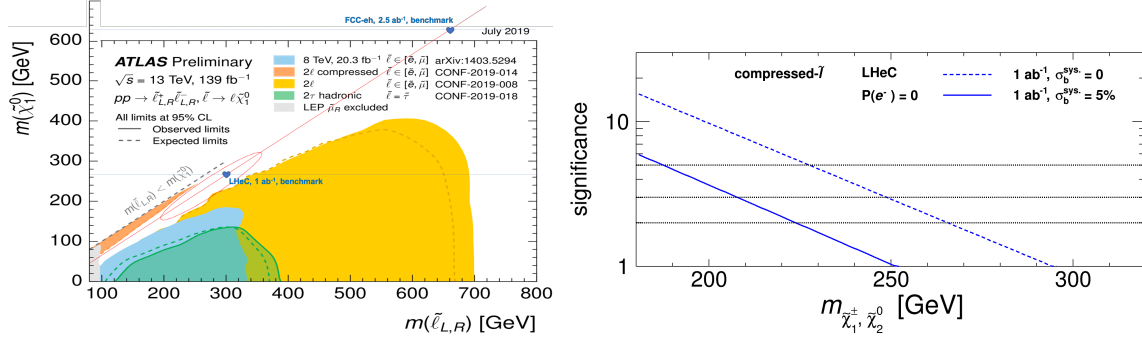


**Figure 6.5:** *Left:* Benchmark assumption on slepton masses and 2019 reach of current ATLAS searches for sleptons (Ref. ATLAS public twiki). *Right:* Significances as varying the masses of  $\tilde{\chi}_1^\pm$  and  $\tilde{\chi}_2^0$  for the compressed-slepton scenario at the LHeC with unpolarised beams and  $1 \text{ ab}^{-1}$  luminosity. For dashed (solid) curve, a systematic uncertainty of 0% (5%) on the background is considered. The figure is from Ref. [544].

4346 indicates that the  $2$  ( $5$ ) $\sigma$  limits on the  $\tilde{\chi}_1^\pm$ ,  $\tilde{\chi}_2^0$  mass are 616 (517) GeV for  $2.5 \text{ ab}^{-1}$  luminosity at  
 4347 the FCC-eh, and 266 (227) GeV for  $1 \text{ ab}^{-1}$  luminosity at the LHeC, respectively. An illustration  
 4348 of the model assumptions in terms of sleptons and neutralino masses and the current constraints  
 4349 at the LHC is presented in Fig. 6.5 (left). Results are illustrated in Fig. 6.5 (right). The effects  
 4350 of varying  $\Delta m$  are investigated: fixing  $m_{\tilde{\chi}_1^\pm, \tilde{\chi}_2^0}$  to be 400 GeV, it is found that at the FCC-eh  
 4351 the significance is maximal when  $\Delta m$  is around 20 GeV.

4352 In the decoupled-slepton scenarios where only  $\tilde{\chi}_1^0$ ,  $\tilde{\chi}_1^\pm$  and  $\tilde{\chi}_2^0$  are light and other SUSY particles  
 4353 are heavy and decoupled, the  $2\sigma$  limits obtained on the  $\tilde{\chi}_1^\pm$ ,  $\tilde{\chi}_2^0$  mass are 230 GeV for  $2.5 \text{ ab}^{-1}$   
 4354 luminosity at the FCC-eh when neglecting the systematic uncertainty on the background. Large  
 4355 systematic uncertainties on the SM background processes can substantially affect the sensitivity,  
 4356 hence good control of experimental and theoretical sources of uncertainties is very important.

4357 Finally, it is also found that the possibility of having a negatively polarised electron beam  
 4358 ( $P_{e^-} = 80\%$ ) could potentially extend the sensitivity to electroweakinos by up to 40%.

4359 Overall, since the sensitivity to the electroweak SUSY sector depends on the mass hierarchy  
 4360 of  $\tilde{\chi}_1^\pm$ ,  $\tilde{\chi}_1^0$ ,  $\tilde{\chi}_2^0$  and sleptons, and given the difficulty to probe efficiently small  $\Delta m$  regions at  
 4361 the current LHC and possibly at the HL-LHC, measurements at  $ep$  colliders may prove to offer  
 4362 complementary or additional reaches, in particular for the compressed scenarios.

### 4363 6.3.2 Search for the SUSY Electroweak Sector: long-lived particles

4364 Studies on Higgsinos ( $\chi$ ) with masses  $\mathcal{O}(100)$  GeV are motivated by natural SUSY theories and  
 4365 help to avoid large fine-tuning on the Higgs boson mass. In these scenarios the low energy

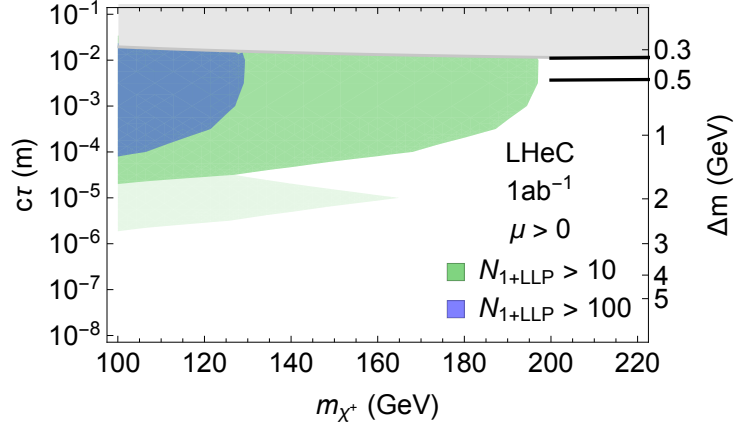


**Figure 6.6:** Exclusion limits on Higgsino masses as a function of their lifetime from Ref. [543]. Coloured regions denote where 10 or 100 events with at least one LLP decay are observed. Light shading indicates the uncertainty in the predicted number of events due to different hadronisation and LLP reconstruction assumptions. The black curves are the optimistic and pessimistic projected bounds from HL-LHC disappearing track searches.

4366 charginos ( $\chi^+$ )/neutralinos( $\chi^0$ ) are all Higgsino-like and their masses are nearly degenerate,  
 4367 only slightly above the neutralino.

4368 As mentioned above, a compressed spectrum with nearly degenerate masses results in a kinematic  
 4369 suppression of the heavier  $\chi^+$  decays into  $W^\pm\chi^0$ , which has twofold consequences: it yields final  
 4370 states without hard leptons; it enhances the  $\chi^+$  lifetime up to  $\mathcal{O}(1)$  mm. At the LHC the absence  
 4371 of hard leptons with sizable transverse momentum makes this signature difficult to investigate.  
 4372 One possibility is to search for the tracks from  $\chi^+$ , which effectively disappear once it decays  
 4373 and are thus called *disappearing tracks*.

4374 The discovery prospects for prompt signatures of electroweakino decays in electron-proton col-  
 4375 lisions are presented in Ref. [545]. The light  $\chi^+$  (and  $\chi^0$ ) can be produced in pairs via in vector  
 4376 boson fusion of the charged or neutral currents. A cut-based analysis of these processes at the  
 4377 LHeC, assuming prompt  $\chi^+$  decays, yields  $2\sigma$  discovery prospects for masses up to 120 GeV.

4378 Taking into account the finite lifetime of the charginos, two comments are in order: first, the  
 4379 lifetimes and boosts of the  $\chi^+$  are in general too small to resolve a disappearing track; second,  
 4380 the soft final state is not a problem per se and can in principle be observed.

4381 Instead of searching for a disappearing track, the long lifetimes of the  $\chi^+$  can be exploited  
 4382 via the measurement of the impact parameter of the soft hadronic final, as is discussed in  
 4383 Ref. [543]. The crucial machine performance parameters are the tracking resolution, which is  
 4384 as good as  $\mathcal{O}(10)\mu\text{m}$ , and the absence of pile up, which allows to identify and measure a single  
 4385 soft pion's impact parameter. In this way the LHeC can test  $\chi$  with masses up to 200 GeV, the  
 4386 corresponding sensitivity is shown in Fig. 6.6, and the bounds on disappearing track searches at  
 4387 the HL-LHC are shown as black lines in the figure. Considering non-prompt decays of Higgsinos  
 4388 thus significantly improves the discovery prospects compared to the prompt analysis. Further  
 4389 means of improving the prospects is an increased centre-of-mass energy, which enhances the  
 4390 production rate of the Higgsinos.

### 4391 **6.3.3 R-parity violating signatures**

4392 Supersymmetry typically evokes the so-called R-parity, which implies that each fundamental  
4393 vertex contains an even number of sparticles and helps preventing rapid proton decays. In  
4394 general, R-parity need not be an exact symmetry of the theory, such that interactions can be  
4395 present that allow for sparticles to decay into SM particles and include the possibility to violate  
4396 lepton and/or baryon number.

4397 R-parity violating interactions are particularly interesting in electron-proton collisions, where  
4398 single superpartners might be produced resonantly, and detected via the corresponding  $2 \rightarrow 2$   
4399 process. This is discussed in Refs. [546, 547] for the case of the *sbottom*, showing that a good  
4400 level of precision could be achieved at LHeC compared with all the knowledge derived from  
4401 indirect measurements.

4402 Single (anti-)top quark production associated with a lightest neutralino in the MSSM with  
4403 R-parity breaking coupling is investigated in Ref. [548] for the LHeC. The study includes calcu-  
4404 lations of the NLO QCD contributions and concluded that the available constraints would allow  
4405 a notable production rate.

4406 Certain SUSY scenarios might produce prompt signals of multiple soft jets, which generally  
4407 resemble QCD backgrounds at the LHC and are thus notoriously difficult to test. The largely  
4408 QCD-free environment of electron-proton collisions allows to test this class of signatures. One  
4409 example of this signal can come from gluinos, which are tested at the LHC via signatures that  
4410 involve large amounts of missing energy. If the gluino has an all-hadronic decay – as in R-parity  
4411 violating scenarios or Stealth SUSY models – the current experimental searches have a gap in  
4412 sensitivity for masses between about 50 to 70 GeV [549]. Gluinos within this gap can be tested at  
4413 the LHeC [550], where a three sigma exclusion sensitivity was demonstrated with simple signal  
4414 selection cuts.

## 4415 **6.4 Feebly Interacting Particles**

4416 New physics may interact with the SM via the so-called portal operators, including the vector,  
4417 scalar, pseudoscalar, or neutrino portal. In these scenarios, the SM is often extended by an  
4418 entire sector of new physics, comprising new forces and several particle species, which may be  
4419 connected to the big open questions of Dark Matter or the origin of neutrino mass.

4420 These hypothetical new sectors derive their typically very feeble interaction strength with the  
4421 known particles from mass mixing with a SM particle that shares their quantum numbers. Some  
4422 examples are being discussed below.

### 4423 **6.4.1 Searches for heavy neutrinos**

4424 The observation of neutrino oscillations requires physics beyond the SM that gives rise to the light  
4425 neutrino masses. One well-motivated class of models for this purpose is the so-called symmetry  
4426 protected type I seesaw scenario, which features heavy neutrinos with signatures that are in  
4427 principle observable at colliders, cf. Ref. [551] and references therein. A comprehensive overview  
4428 over collider searches for the heavy and mostly sterile neutrinos can be found in Ref. [552], where  
4429 the promising signatures for such searches at electron-proton colliders have been identified.

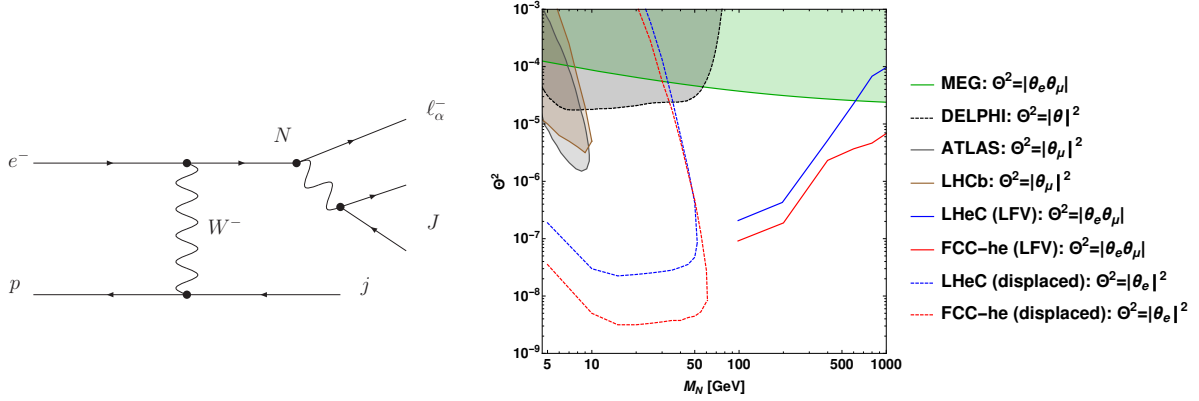


**Figure 6.7:** Left: Dominant tree-level production mechanism for sterile neutrinos at the LHeC. The sterile neutrino decay via the charged current gives rise to the so-called lepton flavor violating lepton-trijet signature. Right: Sensitivity of the LFV lepton-trijet searches (at 95 % C.L.) and the displaced vertex searches (at 95 % C.L.) from Ref. [553] compared to the current exclusion limits from ATLAS [555], LHCb [556], LEP [557], and MEG [558].

4430 In electron-proton collisions heavy neutrinos can be produced via the charged current, see the  
 4431 left panel of Fig. 6.7. The heavy neutrino production cross section is dependent on the active-  
 4432 sterile neutrino mixing with the electron flavour called  $|\theta_e|^2$ . The most promising searches at  
 4433 the LHeC are given by processes with lepton flavour violating final states and displaced  
 4434 vertices, the prospects of which are evaluated in Ref. [553] and are shown in the right panel of Fig. 6.7. It  
 4435 is remarkable, that the prospects to detect heavy neutrinos with masses above about 100 GeV  
 4436 are much better in electron-proton collisions compared to proton-proton or electron-positron,  
 4437 due to the much smaller reducible backgrounds.

4438 The prospects of heavy neutrino detection can be further enhanced with jet substructure tech-  
 4439 niques when the  $W$  boson in the decay  $N \rightarrow eW$ ,  $W \rightarrow jj$  is highly boosted. Ref. [554] shows  
 4440 that these techniques can help to distinguish the heavy neutrino signal from the few SM back-  
 4441 grounds. A considerable improvement in the bounds of  $|V_{eN}|^2$  over present limits from LHC,  
 4442  $0\nu 2\beta$  experiments and from electroweak precision data is obtained with  $1 \text{ ab}^{-1}$  of integrated  
 4443 luminosity at the LHeC.

4444 An alternative approach is employed in Ref. [559] where the dominant sterile neutrino inter-  
 4445 actions with the SM are taken to be higher dimension effective operators (parameterizing a  
 4446 wide variety of UV-complete new physics models) while contributions from neutrino mixing is  
 4447 neglected. The study shows prospects of Majorana neutrino detection for masses lower than  
 4448 700 and 1300 GeV can be discovered at the LHeC with  $E_e = 50$  and 150 GeV, respectively, for  
 4449  $E_p = 7 \text{ TeV}$ . Recently the influence of vector and scalar operators on the angular distribution of  
 4450 the final anti-lepton was investigated. The forward-backward asymmetry is studied in Ref. [560],  
 4451 wherein, in particular, the feasibility of initial electron polarisation as a discriminator between  
 4452 different effective operators is studied.

4453 Prospects of testing left-right symmetric models, featuring additional charged and neutral gauge  
 4454 bosons and heavy neutrinos, were studied in the context of electron-proton collisions in Refs. [561,  
 4455 562]. The authors show that the production of heavy right-handed neutrinos of mass  $\mathcal{O}(10^2-$   
 4456  $10^3) \text{ GeV}$  at the LHeC, with a lepton number violating final state, can yield information on  
 4457 the parity breaking scale in left-right symmetric theories. Heavy neutrinos of sub-TeV mass in  
 4458 inverse see-saw model with Yukawa coupling of  $\mathcal{O}(0.1)$  are investigated for the LHeC in Ref. [563].

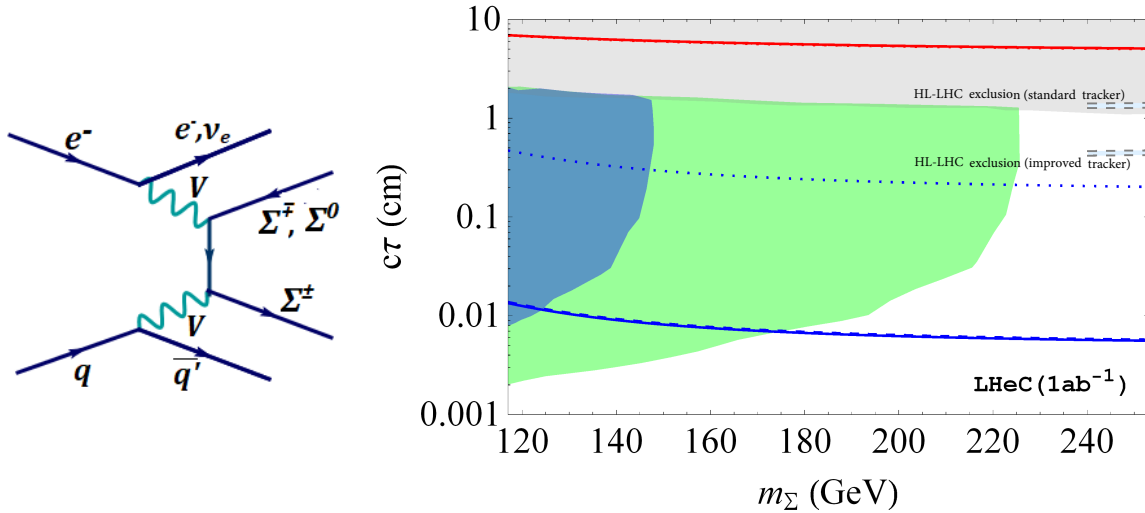


**Figure 6.8:** Left: Dominant production of triplet fermion pairs via their gauge interactions. Right: Prospects of displaced vertex searches from charged fermion triplet  $\Sigma^\pm$ . The blue and green shaded regions denote the expected observability of 10 (100) events, dashed lines denote HL-LHC exclusion sensitivity, and the red line is connected to the light neutrino properties. For details, see text and Ref. [564].

#### 4459 6.4.2 Fermion triplets in type III seesaw

4460 Another technically natural way of generating the light neutrino masses is the so-called Type  
 4461 III seesaw mechanism, which extends the SM with a fermion  $SU(2)$  triplet. In minimal versions  
 4462 of these models the neutral and charged triplet fermions have almost degenerate masses around  
 4463 the TeV scale.

4464 The prospects of studying this mechanism via searches for the new fermions are evaluated in  
 4465 Ref. [564], wherein signatures from long-lived particles at various experiments were considered.  
 4466 The triplet fermions are primarily produced through their gauge interactions, as shown in the  
 4467 left panel of Fig. 6.8, and can be observed via displaced vertices and disappearing track searches  
 4468 for masses of a few hundred GeV.

4469 The authors find that the LHeC can observe displaced vertices from the decays of the charged  
 4470 fermion triplet components via the soft pion impact parameters for triplet masses up to about  
 4471 220 GeV and has a complementary sensitivity to the light neutrino mass scale, which governs  
 4472 the lifetime of the neutral fermion, compared the LHC and MATHUSLA. The final results from  
 4473 Ref. [564] for the LHeC are shown in the right panel of Fig. 6.8.

#### 4474 6.4.3 Dark photons

4475 Minimal extensions of the SM often involve additional gauge factors. In particular the  $U(1)_X$  ex-  
 4476 tensions are interesting, because they are often connected to a dark charge that can be associated  
 4477 with the dark matter.

4478 An SM-extending  $U(1)_X$  predicts an additional gauge boson that naturally mixes with the  $U(1)_Y$   
 4479 factor of the SM kinetically [565]. This kinetic mixing lets the SM photon couple to fermions that  
 4480 carry the dark charge  $X$ , and the other gauge boson to the electric charge. Both interactions  
 4481 are suppressed by the mixing parameter  $\epsilon$ . In most models the additional gauge boson also

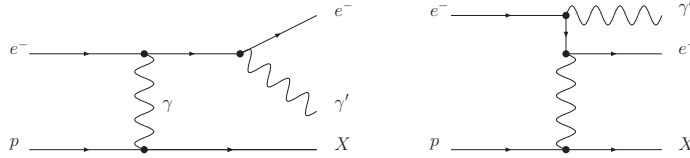


**Figure 6.9:** Feynman diagrams for the dark photon production processes in electron-proton collisions. Here  $p$  and  $X$  denotes a parton from the beam proton before and after the scattering process, respectively.

4482 receives a mass, possibly from spontaneous breaking of the  $U(1)_X$ , and the corresponding mass  
 4483 eigenstate is called a dark photon. Dark photons typically have masses around the GeV scale  
 4484 and their interactions are QED-like, scaled with the small mixing parameter  $\epsilon$ . It can decay to  
 4485 pairs of leptons, hadrons, or quarks, which can give rise to a displaced vertex signal due to its  
 4486 long lifetime.

4487 The prospects for the dark photon searches via their displaced decays in  $ep$  collisions are pre-  
 4488 sented in Ref. [566]. The dark photon production process targeted in this search is depicted  
 4489 in Fig. 6.9. The signal is given by the process  $e^-p \rightarrow e^-X\gamma'$ , where  $X$  denotes the final state  
 4490 hadrons, and the dark photon  $\gamma'$  decays into two charged fermions or mesons.

4491 The most relevant performance characteristics of the LHeC are the very good tracking resolution  
 4492 and the very low level of background, which allow the detection of a secondary vertex with a  
 4493 displacement of  $\mathcal{O}(0.1)$  mm.

4494 The resulting sensitivity contours in the mass-mixing parameter space are shown in Fig. 6.10,  
 4495 where the different colours correspond to different assumptions on the irreducible background  
 4496 and the solid and dashed lines consider different signal reconstruction efficiencies. Also shown  
 4497 for comparison are existing exclusion limits from different experiments, and the region that is  
 4498 currently investigated by the LHCb collaboration [567].

4499 The domain in parameter space tested in electron-proton collisions is complementary to other  
 4500 present and planned experiments. In particular for masses below the di-muon threshold, searches  
 4501 at the LHC are practically impossible. It is remarkable that dark photons in this mass range can  
 4502 be part of a dark sector that explains the observed Dark Matter in the Universe via a freeze-in  
 4503 mechanism, cf. e.g. Ref. [568].

#### 4504 6.4.4 Axion-like particles

4505 The axion is the Goldstone boson related to a global  $U(1)$  symmetry, which is spontaneously  
 4506 broken at the so-called Peccei-Quinn scale, assumed to be around the GUT scale. Its mass,  
 4507 being inversely proportional to the Peccei-Quinn scale, is therefore usually in the sub-eV regime  
 4508 and the axion provides a dynamical solution to the strong CP problem of the standard model.  
 4509 Axions are a very attractive candidate for *cold* dark matter, despite their tiny mass.

4510 Axion-like particles (ALP) are motivated by the original idea of the QCD axion and similarly,  
 4511 they are good dark matter candidates. ALPs are pseudoscalar particles that are usually assumed  
 4512 to be relatively light (i.e. with masses around and below one GeV) and couple to the QCD field  
 4513 strength. In addition, they may have a number of further interactions, for instance they can  
 4514 interact with the other fields of the SM and also mix with the pion. Particularly interesting is  
 4515 the possibility to produce ALPs via vector boson fusion processes.

4516 A recent study [569] has evaluated the prospects of detecting ALPs at the LHeC via the process

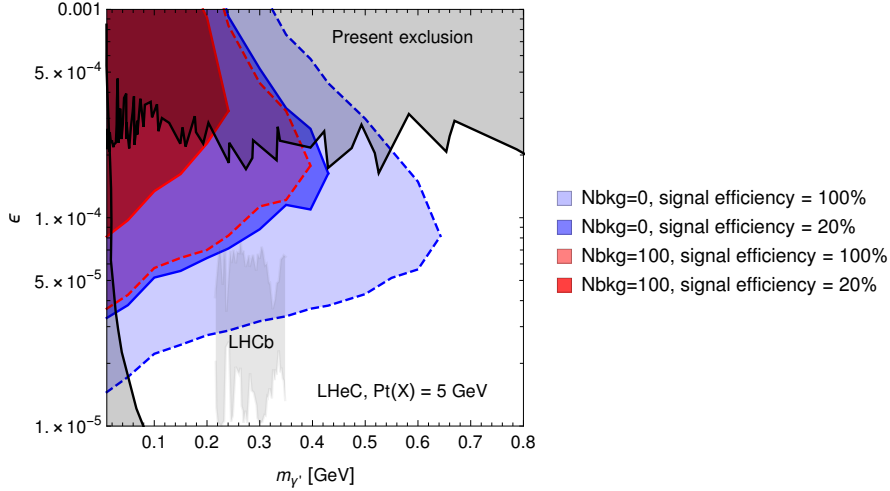


**Figure 6.10:** Projected sensitivity of dark photon searches at the LHeC via displaced dark photon decays from Ref. [566]. The sensitivity contour lines are at the 90 % confidence level and consider a transverse momentum cut on the final state hadrons of 5 GeV. The blue and red areas denote the assumption of zero and 100 background events, respectively, the solid and dashed lines correspond to a reconstruction efficiency of 100 % and 20 %, respectively. See Ref. [566] for details.

4517  $e^- \gamma \rightarrow e^- a$ , as shown in the left panel of Fig. 6.11, in a model independent fashion. The  
 4518 investigated signature is the decay  $a \rightarrow \gamma \gamma$ , which allows to test the effective ALP-photon  
 4519 coupling for ALPs with masses in the range of  $10 \text{ GeV} < m_a < 3 \text{ TeV}$ . It was found that  
 4520 sensitivities can improve current LHC bounds considerably, especially for ALP masses below  
 4521 100 GeV, as shown in the right panel of Fig. 6.11. The authors state that ALP searches at  $ep$   
 4522 colliders might become an important handle on this class of new physics scenarios [569].

## 4523 6.5 Anomalous Gauge Couplings

4524 New physics beyond the SM can modify SM interactions, for instance at the loop level. Such  
 4525 contributions could either modify the interaction strength of SM particles or introduce additional  
 4526 interactions that are not present in the SM, like flavour changing neutral couplings.

4527 Searches for anomalous couplings of top quarks are summarised in Section 3.4. They are  
 4528 parametrised via an effective Lagrangian and are studied by analysing specific processes. For  
 4529 example, anomalous  $Wtb$  couplings are studied in  $e^- p \rightarrow \nu_e \bar{t}$ , and anomalous  $t\bar{t}\gamma$  and  $t\bar{t}Z$  couplings  
 4530 are studied in top quark pair production. In addition FCNC  $tu\gamma$  and  $tuZ$  couplings are  
 4531 analysed in NC DIS single top quark production, and FCNC  $tHu$  couplings are investigated in  
 4532 CC DIS single top quark production. Limits on the corresponding FCNC branching ratios are  
 4533 discussed in Section 3.4.2 and summarised and compared to different colliders in Fig. 3.61.

4534 Triple gauge boson couplings (TGC)  $W^+W^-V$ ,  $V = \gamma, Z$  are precisely defined in the SM and any  
 4535 significant deviation from the predicted values could indicate new physics. Present constraints  
 4536 on anomalous triple vector boson couplings are dominated by LEP (but they are not free of  
 4537 assumptions) and the  $WWZ$  and  $WW\gamma$  vertices can be tested at LHeC in great detail.

4538 The search for anomalous  $WW\gamma$  and  $WWZ$  couplings with polarised electron beam were studied  
 4539 in Ref. [367] via the processes  $ep \rightarrow \nu q \gamma X$  and  $ep \rightarrow \nu q Z X$ . It was found that the LHeC  
 4540 sensitivity with  $E_e = 60 \text{ GeV}$  and  $L = 100/\text{fb}$  is comparable with existing experimental limits

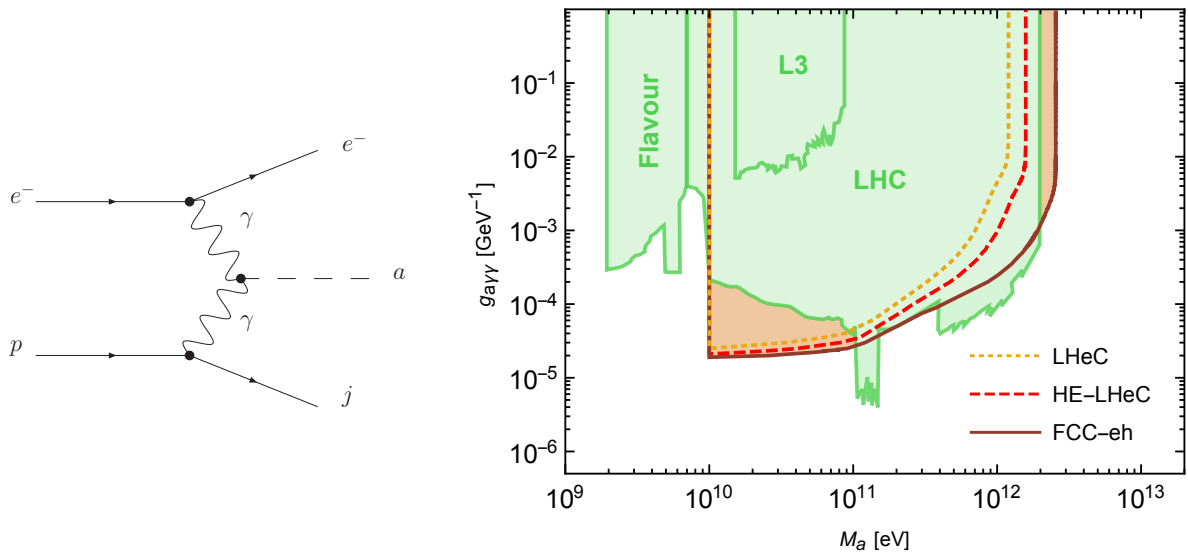


**Figure 6.11:** Left: Production of axion-like particles (ALPs) via photon fusion. Right: Projected sensitivity of the LHeC to ALPs coupling with photons at 95% CL. The existing exclusion limits are shown with the green regions. See Ref. [569] for details.

4541 from lepton and hadron colliders, and that anomalous  $Z$  couplings might be better, reaching  
 4542  $(\Delta\kappa_{\gamma,Z}, \lambda_{\gamma,Z})$  as small as  $\mathcal{O}(10^{-1}, 10^{-2})$ . In general, beam polarisation and larger electron beam  
 4543 energies improve the sensitivity, and the LHeC was found to give complementary information  
 4544 on the anomalous couplings compared to the LHC.

4545 The prospects of testing anomalous triple gauge couplings are also investigated in Ref. [366].  
 4546 Therein the authors study the kinematics of an isolated hard photon and a single jet with a  
 4547 substantial amount of missing transverse momentum. They show that the LHeC is sensitive  
 4548 to anomalous triple gauge couplings via the azimuthal angle differences in the considered final  
 4549 state. It is pointed out that in such an analysis it is possible to probe the  $WW\gamma$  vertex sep-  
 4550 arately, with no contamination from possible BSM contributions to the  $WWZ$  coupling. The  
 4551 estimations consider  $E_e = 100, 140, 200$  GeV and it is claimed that while higher energies yield  
 4552 better sensitivities, the differences are not very large. For  $L = 200/\text{fb}$  and  $E_e = 140$  GeV the  
 4553 exclusion power of the LHeC is superior to all existing bounds, including those from LEP.

4554 The process  $e^- p \rightarrow e^- \mu^+ \nu j$  is investigated in Ref. [368]. The analysis is carried out at the parton  
 4555 level and includes the cross section measurement and a shape analysis of angular variables, in  
 4556 particular of the distribution of the azimuthal angle between the final state forward electron and  
 4557 jet. It is shown that the full reconstruction of leptonic  $W$  decay can be used for  $W$  polarization  
 4558 which is another probe of anomalous triple gauge couplings. The results show that the LHeC  
 4559 could reach a sensitivity to  $\lambda_\gamma$  and  $\Delta\kappa_\gamma$  as small as  $\mathcal{O}(10^{-3})$  for  $L = 2 - 3/\text{ab}$ .

## 4560 6.6 Theories with heavy resonances and contact interaction

4561 In many other BSM scenarios, new physics will manifest itself by the presence of new resonances.  
 4562 Although the high centre-of-mass energy of  $pp$  colliders allow for a better in reach in most  
 4563 of these scenarios, the LHeC and FCC-eh, thanks to the clean collision environment and the  
 4564 virtual absence of pileup, can complement the LHC in the search for these new phenomena.

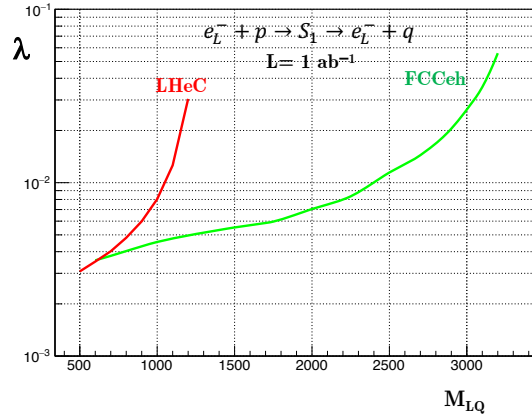


**Figure 6.12:** Estimated  $2\sigma$  significance for the coupling  $\lambda$  at LHeC and FCC-eh for the scalar lepto-quark  $S_1$  as a function of its mass, assuming  $1 \text{ ab}^{-1}$  luminosity.

4565 Deviations from Standard Model predictions could signal new physics even if it is at an energy  
 4566 scale beyond the centre-of-mass energy of the collider. In this case, the effective four-fermion  
 4567 contact interaction could be explained by the exchange of a virtual heavy particle, such as a  
 4568 leptoquark, a heavy boson or elementary constituents of quarks and leptons in composite models.  
 4569 The effective contact interaction scale then represents the typical mass scale of the new particles.  
 4570 Relevant studies on various topics including scalar and vector leptoquarks and excited leptons,  
 4571 are collected in this section.

### 4572 6.6.1 Leptoquarks

4573 In recent years the experiments that study heavy flavoured mesons have revealed intriguing hints  
 4574 for new physics in semileptonic decays of  $B$  mesons. A violation of lepton flavour universality  
 4575 at the level of 3 to  $5\sigma$  is apparent in both the charged current and neutral current mediated  
 4576 processes [570]. In this context BSM theories involving leptoquarks (LQs) have gained renewed  
 4577 interest as they can give rise to lepton universality violating decays of heavy mesons at tree  
 4578 level. Leptoquarks first appeared in Ref. [571] in Pati and Salam's  $SU(4)$  model, where lepton  
 4579 number was considered to be the fourth colour. They also appear in Grand Unified theories,  
 4580 extended technicolor models and compositeness models. The nomenclature and classification  
 4581 are based on their transformation properties under the SM gauge groups [572, 573].

4582 In  $ep$  collisions LQs can be produced in an s-channel resonance, the signature being a peak  
 4583 in the invariant mass of the outgoing  $\ell q$  system. Contrary to what is achievable in the LHC  
 4584 environment, it has been shown that at the LHeC many properties of the LQs can be measured  
 4585 with high precision [1].

4586 The search for LQs at the LHC is essentially insensitive to the coupling LQ-e-q, characterized  
 4587 by the parameter  $\lambda$ , since the dominant process is pair production via the strong interaction.  
 4588 Recent searches have therefore been able to exclude LQs of the first generation up to 1.4 TeV,  
 4589 assuming a branching ratio to charged leptons = 1.0. For other generations, the bounds are  
 4590  $\sim 1$  TeV. (for the latest results, see, for example Ref. [574, 575]). Nevertheless, there remains  
 4591 some parameter space where the LHeC can make a significant contribution in the search for  
 4592 LQs: cross-generational mixing:  $eq \rightarrow \mu q$ , or  $eq \rightarrow eb$ , for example, or if the branching ratio in  
 4593 the decay of the LQ to a charged lepton is very low.

4594 For LQs with masses below the centre-of-mass energy of the collider, suitable searches promise  
 4595 a sensitivity to  $\lambda$  as small as  $\mathcal{O}(10^{-3})$ . As shown in [576], production of the first generation  
 4596 scalar leptoquarks at LHeC can have much larger cross section than at the LHC. The authors  
 4597 also show that a sensitivity to the Yukawa coupling for the LQs called  $R_2^{5/3} \sim (\mathbf{3}, \mathbf{2}, 7/6)$  and  
 4598  $\tilde{R}_2^{2/3} \sim (\mathbf{3}, \mathbf{2}, 1/6)$  better than the electromagnetic strength ( $\sim 0.3$ ) of  $5\sigma$  can be reached up to a  
 4599 mass of 1.2 TeV.

4600 For the  $S_1$  scalar leptoquark  $(\bar{\mathbf{3}}, \mathbf{1}, 1/3)$ , an estimate of the sensitivity of the LHeC and the FCC-  
 4601 eh as a function of the LQ mass and LL Yukawa coupling is shown in Fig. 6.12, assuming  $1 \text{ ab}^{-1}$   
 4602 of integrated luminosity. Here, the signal was generated at leading order using MadGraph with  
 4603 the model files from Ref. [577], with hadronisation performed by Herwig7 [578, 579] and detector  
 4604 simulation with Delphes [380]. The SM background  $e^-p \rightarrow e^-j$  was also generated at leading  
 4605 order. A simple set of cuts on the  $p_T$  of the leading electron and jet and a window on the  
 4606 invariant mass of the  $e$ -jet system was applied.

4607 The  $\tilde{R}_2^{2/3}$  scalar LQ allows for coupling to right-handed neutrinos, providing interesting search  
 4608 channels. Its signatures at  $ep$  colliders have been investigated recently [580, 581]. In the lepton +  
 4609 jet final state, it is found that LHeC can probe up to 1.2 TeV at  $3\sigma$  significance with an  $e^-$  beam,  
 4610 and at  $5\sigma$  discovery with an  $e^+$  beam and  $1 \text{ ab}^{-1}$  of integrated luminosity. At FCC-eh, a  $5\sigma$   
 4611 discovery can be reached with an  $e^-$  beam up to  $\sim 2.3 \text{ TeV}$  and  $1 \text{ ab}^{-1}$  of integrated luminosity.

## 4612 6.6.2 Vector-like quarks

4613 In composite Higgs models, new vector-like quarks are introduced, in particular the top-partner  
 4614 ( $T$ ) with charge  $2/3$ . The prospects of detecting  $T$  at the LHeC are discussed in Ref. [582]. For  
 4615 this search a simplified model is considered where  $T$  is produced from positron proton scattering  
 4616 via intergenerational mixing and decays as  $T \rightarrow tZ$ , with the final state  $\nu_e \ell^+ \ell^- b j j'$ , considering  
 4617  $E_e = 140 \text{ GeV}$ . The authors find that for  $L = 1/\text{ab}$  masses for the top partner  $T$  around 800 GeV  
 4618 can be tested when the model-related coupling constants are  $\mathcal{O}(0.1)$  and that mixing between  
 4619  $T$  and the first generation quarks can significantly enhance the LHeC sensitivity.

4620 Another search strategy for singly produced top partners is given by their decays  $T \rightarrow Wb$  and  
 4621  $T \rightarrow th$ , which is presented in Ref. [583]. The analysis is based on a simplified model where  
 4622 the top partner is an  $SU_L(2)$  singlet and interacts only with the third generation of quarks. It  
 4623 considers collisions of positrons and protons with  $E_e = 140 \text{ GeV}$ , the analysis is carried out at  
 4624 the parton level and investigates the kinematic distributions of the final states. Useful kinematic  
 4625 variables for the  $bW$  final state were found to be the transverse momentum of the lepton,  $b$ -jet  
 4626 missing energy, while for the  $th$  final state the most useful observable is the transverse hadronic  
 4627 energy. For masses of  $\mathcal{O}(1) \text{ TeV}$  the LHeC is found to be sensitive to the new interactions when  
 4628 they are  $\mathcal{O}(0.1)$  for  $L = 1/\text{ab}$ , in agreement with [582]. A very similar analysis was performed  
 4629 for the  $T \rightarrow Wb$  signal channel with comparable results [584].

## 4630 6.6.3 Excited fermions ( $\nu^*$ , $e^*$ , $u^*$ )

4631 The potential of searches for excited spin-1/2 and spin-3/2 neutrinos are discussed in Ref. [585].  
 4632 For the analysis the authors consider effective currents that describe the interactions between  
 4633 excited fermions, gauge bosons, and SM leptons. For the signature, the production of the  
 4634 excited electron neutrino  $\nu^*$  and its subsequent decay  $\nu^* \rightarrow We$  with  $W \rightarrow jj$  was chosen. The  
 4635 analysis is carried out at the parton level, considers  $E_e = 60 \text{ GeV}$ , and consists in a study of

4636 the kinematic distributions of the final states. It is concluded that the signature can be well  
 4637 distinguished from backgrounds, and that other lepton-hadron colliders would be required to  
 4638 test the excited neutrinos of different flavours.

4639 Analyses in similar models, considering electron-proton collisions at energies of the FCC-he and  
 4640 beyond, were carried out for excited electron neutrinos and are presented in Ref. [586]. An  
 4641 analysis for the prospects of testing excited electrons is discussed in Ref. [587], and testing  
 4642 excited quarks in a composite model framework is investigated in Ref. [588].

#### 4643 6.6.4 Colour octet leptons

4644 Unresolved issues of the SM, like family replication and quark-lepton symmetry, can be addressed  
 4645 by composite models, where quarks, leptons, and gauge bosons are composite particles made up  
 4646 of more basic constituents. One general class of particles, predicted in most composite models,  
 4647 are colour octet leptons, which are bound states of a heavy fermion and a heavy scalar particle  
 4648 that is assumed to be colour-charged. In this scenario each SM lepton is accompanied by a colour  
 4649 octet lepton, which may have spin 1/2 or 3/2. Since they are unobserved, the compositeness  
 4650 scale is expected to be at least  $\mathcal{O}(1)$  TeV.

4651 At the LHeC, the colour octet partner of the electron  $e_8$  can be produced through the process  
 4652  $e^- p \rightarrow e_8 g + X$  and studied via its decays products. An analysis including the study of kinematic  
 4653 distributions that were obtained at the parton level is presented in Ref. [589]. It was shown that  
 4654 discovery prospects exist for masses of  $\mathcal{O}(\text{TeV})$ . A similar analysis is performed for the FCC-he  
 4655 at much higher energies in Ref. [590].

#### 4656 6.6.5 Quark substructure and Contact interactions

4657 Several long-standing questions arise in the SM, such as those enumerated in Section 1. Perhaps  
 4658 most seriously, the SM does not appear to provide a clear, dynamical *raison d'être* for the  
 4659 existence of quarks. Leptons and quarks appear in the Standard Model in a symmetric way,  
 4660 sharing electromagnetic interaction with the same charge quantization and with cancellation of  
 4661 anomaly in the family structure. This strongly suggests that they may be composed of the same  
 4662 fundamental constituents, or that they form a representation of an extended gauge symmetry  
 4663 group of a Grand Unified Theory.

4664 Assuming that the electron is a point-like particle, the quark substructure can be investigated  
 4665 by introducing a form factor  $f_q(Q^2)$  to describe deviations of the  $ep$  scattering cross section:

$$4666 \frac{d\sigma}{dQ^2} = \frac{d\sigma^{SM}}{dQ^2} f_q^2(Q^2) \quad (6.1)$$

$$4667 f_q^2(Q^2) \simeq 1 - \frac{R^2}{6} Q^2 \quad (6.2)$$

4668 Here,  $R$  is the rms electric charge quark radius. The present limit from HERA is  $4.3 \times 10^{-19}$   
 4669 m [591] while it is estimated that LHeC will be sensitive up to  $\sim 10^{-19}$  m [592].

4668 An electric precursor to QCD was formulated in 1969 that assumed that hadron constituents are  
 4669 highly electrically charged and where the strong attraction between positive and negative con-  
 4670 stituents was assumed to bind them together [593]. Neither the electric model nor a Schwinger's  
 4671 comparable model of monopoles [594] reproduce the observed particle spectrum of hadrons, or  
 4672 the observed pattern of weak interactions. The ATLAS Collaboration has recently reported

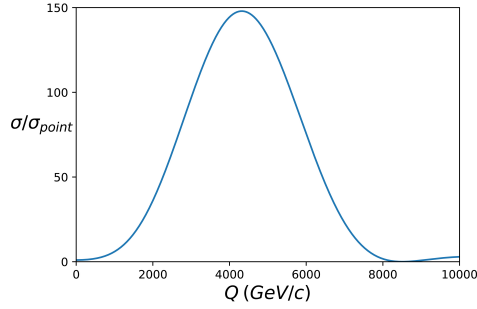


**Figure 6.13:** Form factor effect in the e-p interaction produced by substructure according to Model II of Hofstadter [596] with the model parameters given in the text.

4673 searches for free magnetic monopoles and free highly electrically charged particles produced in  
 4674  $pp$  collisions at 13 TeV [595]. No candidates were detected with one or two Dirac magnetic  
 4675 charges or with electric charges  $20e < |z| < 100e$ . This extends the results of previous searches  
 4676 made at lower energies and in cosmic rays or bulk matter. A simple picture of what might emerge  
 4677 with highly electrically charged constituents is obtained by modeling the proton's substructure  
 4678 by a charge of (say)  $21|e|$  smeared uniformly over a region of radius  $10^{-19}$  m, and two charges  
 4679 of  $-10|e|$  smeared over a larger region of radius  $2 \times 10^{-19}$  m. The model II by Hofstadter [596]  
 4680 predicts the form factor results shown in Fig. 6.13, consistent the HERA upper limit.

4681 More generally [597], contact interactions can be parametrized in the Lagrangian by coupling  
 4682 coefficients  $\eta_{ij}^q$  where the indices  $i, j$  indicate the left-handed or right-handed fermion helicities  
 4683 and  $q$  the quark flavor. The interaction can be of a scalar, vector or tensor nature and the  
 4684 interference with SM currents can be constructive or destructive. It has been estimated that  
 4685 the LHeC can be sensitive to a scale of contact interaction of  $\sim 40 - 60$  TeV with  $100 \text{ fb}^{-1}$  of  
 4686 integrated luminosity [592] while the present LHC limits are between 20 and 40 TeV, depending  
 4687 on the sign of the interference [598, 599].

## 4688 6.7 Summary and conclusion

4689 The lack of new physics at the LHC to date forces the community to develop new theoretical  
 4690 ideas as well as to explore the complementarities of  $pp$  machines with other possible future  
 4691 facilities. In the context of  $ep$  colliders, several studies are being carried out to understand the  
 4692 potential to search for new physics, i.e. considering that many interactions can be tested at high  
 4693 precision that are otherwise not easily accessible.

4694 At  $ep$  colliders, most BSM physics is accessed via vector-boson fusion, which suppresses the  
 4695 production cross section quickly with increasing mass. Nonetheless, scalar extensions of the SM  
 4696 as well as neutrino-mass related BSM physics can be well tested at  $ep$  due to the smallness and  
 4697 reducibility of the SM backgrounds. The absence of pile up and complicated triggering makes  
 4698 searches for soft-momenta final state particles feasible, so that results for BSM theories for  
 4699 example characterised by the presence of non-prompt, long-lived particles are complementary to  
 4700 those at the LHC. Additionally, the excellent angular acceptance and resolution of the detector  
 4701 also renders the LHeC a very suitable environment for displaced vertex searches. An increase  
 4702 in the centre-of-mass energy as high as the one foreseen at the FCC would naturally boost the  
 4703 reach in most scenarios considerably.

4704 Finally, it is worth noting that the LHeC can offer different or indirect ways to search for

4705 new physics. It was shown recently that Lorentz invariance violation in the weak vector-boson  
4706 sector can be studied in electron-proton scattering [600] via a Fourier-analysis of the parity  
4707 violating asymmetry in deep inelastic scattering. Moreover, New Physics could be related to  
4708 nucleon, nuclear, and top structure functions as discussed in Refs. [393, 601, 602]. Investigating  
4709 of the  $B_c^{(*)}$  meson and doubly heavy baryon also was shown to have discovery potential for New  
4710 Physics [603–605].

## Chapter 7

# Influence of the LHeC on Physics at the HL-LHC

After almost 10 years of scientific exploitation of the LHC and about  $175 \text{ fb}^{-1}$  of proton-proton collision data delivered to each of the ATLAS and CMS experiments, the sensitivity of a significant fraction of leading measurements and searches becomes limited by systematic uncertainties. Uncertainties induced by the strong interaction, in particular related to the proton structure, play a prominent role, and tend to saturate the physics reach of the experiments. This context will only become more evident when the LHC enters its high-luminosity era.

With high precision PDFs measured independently from the other LHC experiments, the LHeC project can resolve this situation. It allows a clean study of the pure QCD effects it aims at measuring, resolving the ambiguity between new physics effects at high mass and PDF uncertainties that intrinsically affects the interpretation of proton-proton data alone. At the weak scale, improved PDFs provide a significant boost to the achievable precision of measurements of the Higgs boson properties and of fundamental electroweak parameters. The LHeC is thus a perfect companion machine for the HL-LHC, allowing a full exploitation of the data and significantly extending its reach.

The present chapter illustrates this with a few selected examples in the domain of precision measurements of the  $W$ -,  $Z$ - and Higgs boson properties. The impact of precise PDFs on searches for TeV-scale new physics is also illustrated, as well as the impact of electron-nucleus scattering data on heavy-ion physics at the LHC.

## 7.1 Precision Electroweak Measurements at the HL-LHC

### 7.1.1 The effective weak mixing angle

Prospective studies for the measurement of the effective weak mixing angle using the forward-backward asymmetry,  $A_{\text{FB}}$ , in Drell-Yan di-lepton events at the HL-LHC were performed at ATLAS [606], CMS [607] and LHCb [608] and reported in the CERN report on Standard Model physics at the HL-LHC [147]. A brief summary is given here, focusing on the impact of the LHeC on this measurement.

At leading order, lepton pairs are produced through the annihilation of a quark and antiquark via the exchange of a  $Z$  boson or a virtual photon. The definition of  $A_{\text{FB}}$  is based on the angle

4741  $\theta^*$  between the initial- and final-state fermions:

$$A_{\text{FB}} = \frac{\sigma_{\text{F}} - \sigma_{\text{B}}}{\sigma_{\text{F}} + \sigma_{\text{B}}} \quad (7.1)$$

4742 where  $\sigma_{\text{F}}$  and  $\sigma_{\text{B}}$  are the cross sections in the forward ( $\cos \theta^* > 0$ ) and backward ( $\cos \theta^* < 0$ )  
4743 hemispheres, respectively.

4744 A non-zero  $A_{\text{FB}}$  in dilepton events arises from the vector and axial-vector couplings of elec-  
4745 troweak bosons to fermions. At tree level, the vector and axial-vector couplings of the  $Z$  boson  
4746 to a fermion  $f$  are

$$g_V^f = T_3^f - 2Q_f \sin^2 \theta_W, \quad g_A^f = T_3^f. \quad (7.2)$$

4747 The coupling ratio,  $g_V^f/g_A^f = 1 - 4|Q_f| \sin^2 \theta_W$ , generates the asymmetry: defining

$$\mathcal{A}_f = 2 \frac{g_V^f/g_A^f}{1 + (g_V^f/g_A^f)^2} \quad (7.3)$$

4748 one finds, for a given sub-process  $q\bar{q} \rightarrow \ell^+\ell^-$ ,

$$A_{\text{FB}} = \frac{3}{4} \mathcal{A}_q \mathcal{A}_\ell. \quad (7.4)$$

4749 As discussed in Chapt. 3 and Sect. 7.1.3 below, Eq. (7.2) is subject to radiative corrections  
4750 introducing the effective weak mixing angle  $\sin^2 \theta_{\text{eff}}^\ell$  in replacement of the leading order observable  
4751  $\sin^2 \theta_W$ . The asymmetry definitions downstream are however unchanged.

4752 The angle  $\theta^*$  is uniquely defined in  $e^+e^-$  collisions, where the directions of the  $e^+$  and  $e^-$   
4753 beams is known. In proton-antiproton collisions, at the Tevatron, the incoming quarks and  
4754 anti-quarks also have preferred directions, and a non-zero asymmetry exists for all lepton-pair  
4755 rapidities. At the LHC the beams are symmetric, and a non-zero asymmetry only appears for  
4756 high-rapidity events, as the direction of the longitudinal boost reflects, on average, the direction  
4757 of the incoming valence quark. While the expected  $Z$ -boson statistics are very large, with  
4758  $\mathcal{O}(3 \times 10^9)$  events expected in ATLAS and CMS, the measurement is thus highly affected by  
4759 PDF uncertainties, and in particular by the  $u$  and  $d$  valence and sea distributions.

4760 Prospective studies were performed by ATLAS, CMS and LHCb, including a discussion of  
4761 expected PDF uncertainties. The impact of LHeC PDFs was evaluated by ATLAS and is  
4762 discussed further. Tab. 7.1 compares the published ATLAS result [351] with the prospects for  
4763  $3 \text{ ab}^{-1}$ , for a variety of PDF sets. The statistical uncertainty is at the level of  $3 \times 10^{-5}$  with this  
4764 sample, and the experimental systematic uncertainties are improved by 10 – 25% depending on  
4765 the PDF scenario considered. While MMHT2014 [609] and CT14 [53] claim comparable PDF  
4766 uncertainties, the size of the PDF uncertainty is reduced at the HL-LHC thanks to the increased  
4767 sample size, which helps constraining this component *in situ*. The HL-LHC PDF set [89], which  
4768 incorporates the expected constraints from present and future LHC data, further decreases the  
4769 associated uncertainty by about 20%. The LHeC projection [610] results from a QCD fit to  
4770  $1 \text{ ab}^{-1}$  of  $ep$  scattering pseudodata, with  $E_e = 60 \text{ GeV}$  and  $E_p = 7 \text{ TeV}$ ; in this case, the PDF  
4771 uncertainty is subleading compared to the experimental systematics.

4772 Fig. 7.1 compares the ATLAS sensitivity studies of  $\sin^2 \theta_{\text{eff}}^\ell$  to previous measurements from the  
4773 LHC experiments [350–352, 611], and to the legacy measurements by the experiments at LEP  
4774 and SLC [347] and the Tevatron [349]. The precision of the measurement of the weak mixing  
4775 angle in  $Z$ -boson events, using  $3000 \text{ fb}^{-1}$  of  $pp$  collision data at  $\sqrt{s} = 14 \text{ TeV}$ , exceeds the  
4776 precision achieved in all previous single-experiments to date. The LHeC is thus essential in  
4777 exploiting the full potential of the HL-LHC data for this measurement.

Parameter	Unit	ATLAS (Ref. [351])	HL-LHC projection		
		MMHT2014	CT14	HL-LHC PDF	LHeC PDF
Centre-of-mass energy, $\sqrt{s}$	TeV	8	14	14	14
Int. luminosity, $\mathcal{L}$	$\text{fb}^{-1}$	20	3000	3000	3000
Experimental uncert.	$10^{-5}$	$\pm 23$	$\pm 9$	$\pm 7$	$\pm 7$
PDF uncert.	$10^{-5}$	$\pm 24$	$\pm 16$	$\pm 13$	$\pm 3$
Other syst. uncert.	$10^{-5}$	$\pm 13$	–	–	–
Total uncert., $\Delta \sin^2\theta_W$	$10^{-5}$	$\pm 36$	$\pm 18$	$\pm 15$	$\pm 8$

**Table 7.1:** The breakdown of uncertainties of  $\sin^2\theta_W$  from the ATLAS preliminary results at  $\sqrt{s} = 8$  TeV with  $20 \text{ fb}^{-1}$  [351] is compared to the projected measurements with  $3000 \text{ fb}^{-1}$  of data at  $\sqrt{s} = 14$  TeV for two PDF sets considered in this note. All uncertainties are given in units of  $10^{-5}$ . Other sources of systematic uncertainties, such as the impact of the MC statistical uncertainty, evaluated in Ref. [351] are not considered in the HL-LHC prospect analysis.

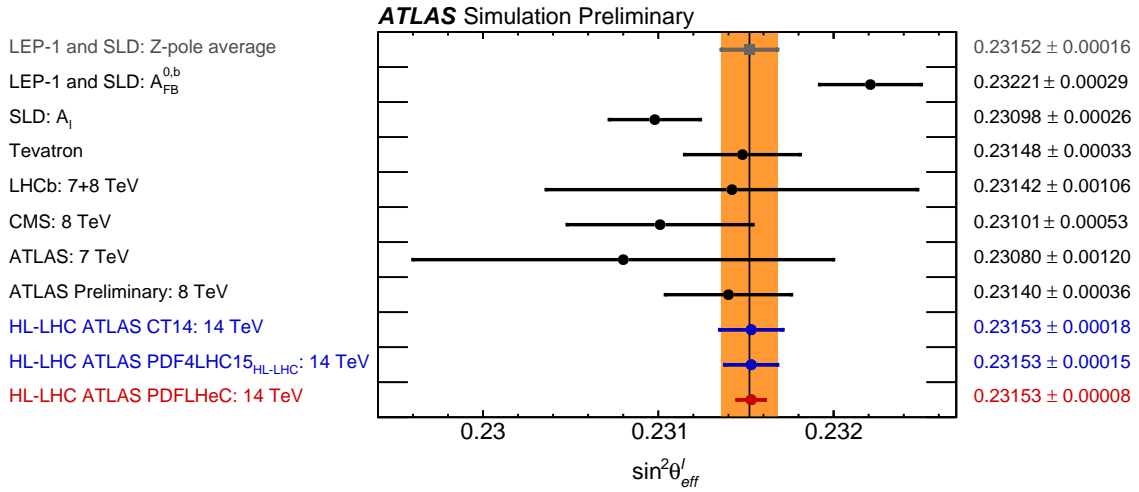


**Figure 7.1:** Comparison of measurements or combinations of  $\sin^2\theta_{\text{eff}}^l$  with the world average value (orange band) and the projected uncertainties of measurements at the HL-LHC. For the HL-LHC the central values are set to the world average value and uncertainties are displayed for different assumptions of the available PDF sets, similar to Tab. 7.1.

## 4778 7.1.2 The $W$ -boson mass

4779 This section summarises a prospective study describing prospects for the measurement of  $m_W$   
4780 with the upgraded ATLAS detector, using low pile-up data collected during the HL-LHC pe-  
4781 riod [612]. Similar features and performance are expected for CMS.

4782 Proton-proton collision data at low pile-up are of large interest for  $W$  boson physics, as the low  
4783 detector occupancy allows an optimal reconstruction of missing transverse momentum, and the  
4784  $W$  production cross section is large enough to achieve small statistical uncertainties in a moderate  
4785 running time. At  $\sqrt{s} = 14$  TeV and for an instantaneous luminosity of  $\mathcal{L} \sim 5 \times 10^{32} \text{ cm}^{-2}\text{s}^{-1}$ ,  
4786 corresponding to two collisions per bunch crossing on average at the LHC, about  $\times 10^7$   $W$  boson  
4787 events can be collected in one month. Such a sample provides a statistical sensitivity at the  
4788 permille level for cross section measurements, at the percent level for measurements of the  $W$   
4789 boson transverse momentum distribution, and below 4 MeV for a measurement of  $m_W$ .

4790 Additional potential is provided by the upgraded tracking detector, the ITk, which extends the

4791 coverage in pseudorapidity beyond  $|\eta| < 2.5$  to  $|\eta| < 4$ . The increased acceptance allows  $W$ -  
 4792 boson measurements to probe a new region in Bjorken  $x$  at  $Q^2 \sim m_W^2$ . This will in turn allow  
 4793 further constraints on the parton density functions (PDFs) from cross section measurements,  
 4794 and reduce PDF uncertainties in the measurement of  $m_W$ . A possible increase of the LHC  
 4795 centre-of-mass energy, such as the HE-LHC program with  $\sqrt{s} = 27$  TeV [613], could play a  
 4796 similar role on a longer timescale.

4797 Leptonic  $W$  boson decays are characterised by an energetic, isolated electron or muon, and sig-  
 4798 nificant missing transverse momentum reflecting the decay neutrino. The hadronic recoil,  $u_T$ , is  
 4799 defined from the vector sum of the transverse momenta of all reconstructed particles in the event  
 4800 excluding the charged lepton, and provides a measure of the  $W$  boson transverse momentum.  
 4801 Lepton transverse momentum,  $p_T^\ell$ , missing transverse momentum,  $E_T^{\text{miss}}$ , and the hadronic recoil  
 4802 are related through  $\vec{E}_T^{\text{miss}} = -(\vec{p}_T^\ell + \vec{u}_T)$ . The  $p_T^\ell$  and  $E_T^{\text{miss}}$  distributions have sharp peaks at  
 4803  $p_T^\ell \sim E_T^{\text{miss}} \sim m_W/2$ . The transverse mass  $m_T$ , defined as  $m_T = \sqrt{2p_T^\ell E_T^{\text{miss}} \cos(\phi_\ell - \phi_{\text{miss}})}$ ,  
 4804 peaks at  $m_T \sim m_W$ .

4805 Events are selected applying the following cuts to the object kinematics, after resolution correc-  
 4806 tions:

- 4807 •  $p_T^\ell > 25$  GeV,  $E_T^{\text{miss}} > 25$  GeV,  $m_T > 50$  GeV and  $u_T < 15$  GeV;
- 4808 •  $|\eta_\ell| < 2.4$  or  $2.4 < |\eta_\ell| < 4$ .

4809 The first set of cuts select the range of the kinematic peaks of the  $W$  boson decay products,  
 4810 restricting to the region of small  $p_T^W$  to maximise the sensitivity of the distributions to  $m_W$ .  
 4811 Two pseudorapidity ranges are considered, corresponding to the central region accessible with  
 4812 the current ATLAS detector, and to the forward region accessible in the electron channel with  
 4813 the ITk.

4814 The  $W$ -boson mass is determined comparing the final state kinematic peaks in the simulation  
 4815 to those observed in the data, and adjusting the value of  $m_W$  assumed in the former to optimise  
 4816 the agreement. The shift in the measured value of  $m_W$  resulting from a change in the assumed  
 4817 PDF set is estimated using a set of template distributions obtained for different values of  $m_W$   
 4818 and a given reference PDF set, and “pseudo-data” distributions obtained for an alternate set  
 4819 representing, for example, uncertainty variations with respect to the reference set. The PDF  
 4820 uncertainty for a given set is calculated by summing the shifts obtained for all uncertainty  
 4821 variations in quadrature.

4822 The PDF uncertainty is calculated for the CT14 [53], MMHT2014 [609], HL-LHC [89] and  
 4823 LHeC [610] PDF sets and their associated uncertainties. Compared to current sets such as  
 4824 CT14 and MMHT2014, the HL-LHC set incorporates the expected constraints from present and  
 4825 future LHC data; it starts from the PDF4LHC convention [90] and comes in three scenarios  
 4826 corresponding to more or less optimistic projections of the experimental uncertainties.

4827 The expected statistical and PDF uncertainties are illustrated in Tab. 7.2 and Fig. 7.2. The  
 4828 CT10 and CT14 sets yield comparable uncertainties. The MMHT2014 uncertainties are about  
 4829 30 % lower. The three projected HL-LHC PDF sets give very similar uncertainties; scenario 2  
 4830 is the most conservative and shown here. Compared to CT10 and CT14, a reduction in PDF  
 4831 uncertainty of about a factor of two is obtained in this case.

4832 The LHeC sample can be collected in about five years, synchronously with the HL-LHC op-  
 4833 eration. In this configuration, the neutral- and charged-current DIS samples are sufficient to  
 4834 disentangle the first and second generation parton densities without ambiguity, and reduce the

4835 PDF uncertainty below 2 MeV, a factor 5–6 compared to present knowledge. Also in this case  
 4836 the  $m_W$  measurement will benefit from the large  $W$  boson samples collected at the LHC, and  
 4837 from the combination of the central and forward categories. In this context, PDF uncertainties  
 4838 would be sub-leading even with  $1 \text{ fb}^{-1}$  of low pile-up LHC data.

Parameter	Unit	ATLAS (Ref. [342])		HL-LHC projection		
		CT10	CT14	HL-LHC	LHeC	LHeC
Centre-of-mass energy, $\sqrt{s}$	TeV	7	14	14	14	14
Int. luminosity, $\mathcal{L}$	$\text{fb}^{-1}$	5	1	1	1	1
Acceptance		$ \eta  < 2.4$	$ \eta  < 2.4$	$ \eta  < 2.4$	$ \eta  < 2.4$	$ \eta  < 4$
Statistical uncert.	MeV	$\pm 7$	$\pm 5$	$\pm 4.5$	$\pm 4.5$	$\pm 3.7$
PDF uncert.	MeV	$\pm 9$	$\pm 12$	$\pm 5.8$	$\pm 2.2$	$\pm 1.6$
Other syst. uncert.	MeV	$\pm 13$	-	-	-	-
Total uncert. $\Delta m_W$	MeV	$\pm 19$	13	7.3	5.0	4.1

**Table 7.2:** Measurement uncertainty of the  $W$ -boson mass at the HL-LHC for different PDF sets (CT14, HL-LHC PDF and LHeC PDF) and lepton acceptance regions in comparison with a measurement by ATLAS [342]. The HL-LHC projections are obtained from a combined fit to the simulated  $p_T^\ell$  and  $m_T$  distributions.

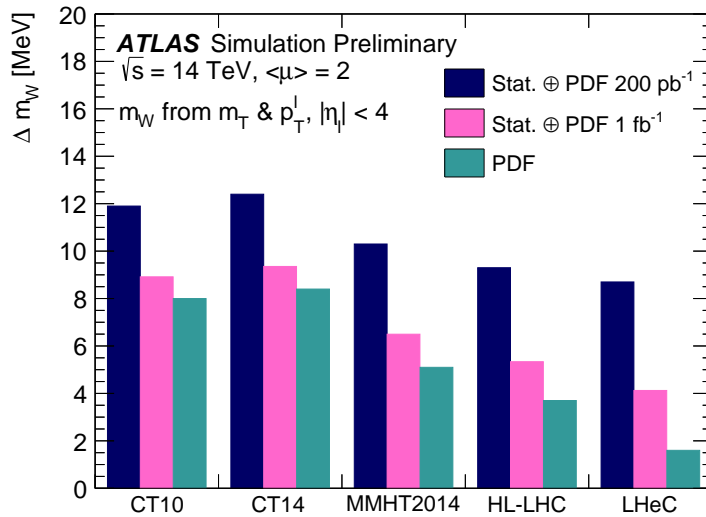


**Figure 7.2:** Measurement uncertainty of  $m_W$  at the HL-LHC with  $200 \text{ pb}^{-1}$  (dark blue) and  $1 \text{ fb}^{-1}$  (pink) of collected low pile-up data for different present and future PDF sets. The green area indicates the PDF uncertainty from those sets alone. The projections are obtained from a combined fit to the simulated  $p_T^\ell$  and  $m_T$  distributions in the acceptance  $|\eta| < 4$ .

### 4839 7.1.3 Impact on electroweak precision tests

4840 The theoretical expressions for the electroweak parameters discussed above are functions of the  
 4841 other fundamental constants of the theory. In the Standard Model, an approximate expression  
 4842 for  $m_W$ , valid at one loop for  $m_H > m_W$ , is [347]

$$m_W^2 = \frac{m_Z^2}{2} \cdot \left( 1 + \sqrt{1 - \frac{\sqrt{8} \cdot \pi \cdot \alpha_{em}}{G_F \cdot m_Z^2} \frac{1}{1 - \Delta r}} \right), \text{ where} \quad (7.5)$$

$$\Delta r = \Delta\alpha_{em} - \frac{\cos^2\theta_W}{\sin^2\theta_W} \Delta\rho, \text{ and} \quad (7.6)$$

$$\Delta\rho = \frac{3G_F m_W^2}{8\sqrt{2}\pi^2} \left[ \frac{m_{\text{top}}^2}{m_W^2} - \frac{\sin^2\theta_W}{\cos^2\theta_W} \left( \ln \frac{m_H^2}{m_W^2} - \frac{5}{6} \right) + \dots \right]. \quad (7.7)$$

4843 where  $\Delta r$  includes all radiative corrections to  $m_W$ ,  $\Delta\alpha_{em}$  is the difference between the electro-  
4844 magnetic coupling constant evaluated at  $q^2 = 0$  and  $q^2 = m_Z^2$ , and  $\Delta\rho$  is the quantum correction  
4845 to the tree-level relation  $\rho \equiv m_W/(m_Z \cos^2\theta_W) = 1$ , and defined as  $\rho = 1 + \Delta\rho$ .

4846 Similarly, approximate one-loop expressions for the vector and axial-vector couplings between  
4847 the  $Z$  boson and the fermions,  $g_V$  and  $g_A$ , are

$$g_V = \sqrt{1 + \Delta\rho} (T_3 - 2 \cdot Q \cdot (1 + \Delta\kappa) \sin^2\theta_W), \quad (7.8)$$

$$g_A = \sqrt{1 + \Delta\rho} T_3 \quad (7.9)$$

4848 where

$$\Delta\kappa = \frac{3G_F m_W^2}{8\sqrt{2}\pi^2} \left[ \frac{\cos^2\theta_W}{\sin^2\theta_W} \frac{m_{\text{top}}^2}{m_W^2} - \frac{10}{9} \left( \ln \frac{m_H^2}{m_W^2} - \frac{5}{6} \right) + \dots \right]. \quad (7.10)$$

4849 At two loops, also the strong coupling constant enters.

4850 A large class of theories beyond the SM predict particles that contribute to the  $W$ - and  $Z$ -  
4851 boson self-energies, modifying the above expressions. These modifications can generically be  
4852 parameterised using so-called *oblique* parameters, called  $S$ ,  $T$  and  $U$  [614]. Their values are by  
4853 definition 0 in the SM and, for example, a significant violation of the relation between  $m_W$ ,  $m_H$   
4854 and  $m_{\text{top}}$  would translate into non-zero values for  $S$  and  $T$ .

4855 A typical application of this formalism consists in using the measured properties of the  $W$   
4856 and  $Z$  bosons, the top quark mass, and the values of coupling constants, to derive an indirect  
4857 determination of the Higgs boson mass in the SM and compare the latter to the measured value.  
4858 Beyond the SM, the measured values can be used to derive allowed contours in the  $(S, T)$  plane.

4859 Present and future measurement uncertainties for the most relevant electroweak parameters are  
4860 summarised in Tab.7.3, and are used to evaluate the impact of the improved measurements  
4861 on electroweak precision tests. Specifically, we consider the effect of improved measurements  
4862 of  $m_W$  and  $\sin^2\theta_{\text{eff}}^\ell$  discussed in this chapter, and of the improved precision of  $\alpha_s$  discussed in  
4863 Chapter 3. In addition, we consider an ultimate precision of 300 MeV for the top quark mass,  
4864 measured at the LHC.

4865 The results are illustrated in Figs.7.3 and 7.4. The former results from a fit performed using  
4866 the GFitter framework [344], and compares the indirect determinations of the Higgs boson mass  
4867 for the present and expected measurement precisions. The indirect uncertainty in  $m_H$  reduces  
4868 from about 20 % to 10 %.

4869 Fig.7.4 was performed using HEPFIT [615], and compares allowed contours for the  $S$  and  $T$   
4870 parameters. Here also, the allowed region is reduced by a factor of about two from the improved  
4871 measurements of  $m_W$ ,  $\sin^2\theta_{\text{eff}}^\ell$ ,  $m_{\text{top}}$  and  $\alpha_s$ . Improved theoretical calculations in the SM will  
4872 provide an additional reduction of 10-15 %.

Parameter	Unit	Value	Uncertainty	
			Present	Expected
$m_Z$	MeV	91187.6	2.1	2.1
$m_W$	MeV	80385	15	5
$\sin^2\theta_{\text{eff}}^\ell$		0.23152	0.00016	0.00008
$m_{\text{top}}$	GeV	173.1	0.7	0.3
$\alpha_s(M_Z)$		0.1179	0.0010	0.0001

**Table 7.3:** Present uncertainties for the relevant EW precision observables [100, 143, 347], and their expected precision in the LHeC and HL-LHC era.

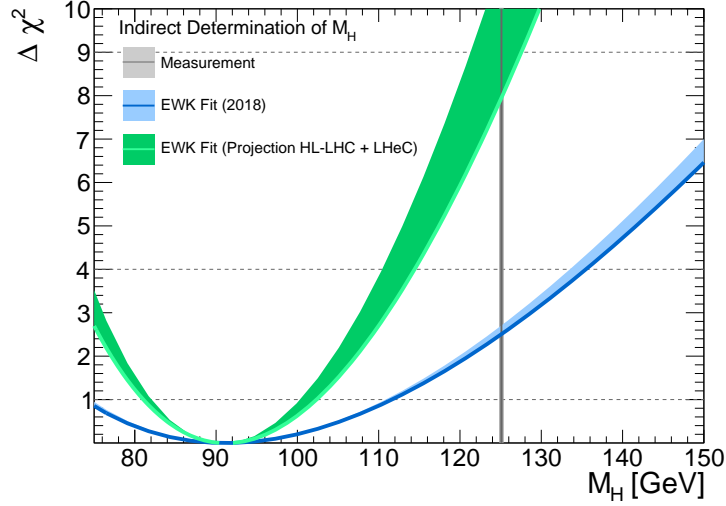


**Figure 7.3:** Comparisons of  $\chi^2$  distributions for different Higgs boson mass values, using present and future experimental uncertainties. The theoretical uncertainties are indicated by the filled areas. The Gfitter program [344] was used for this analysis.

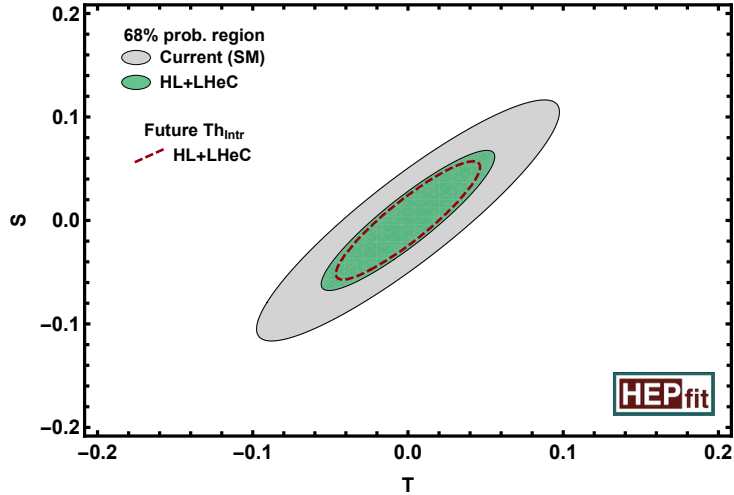


**Figure 7.4:** Allowed regions in the  $(S, T)$  plane. The grey and green areas indicate the currently allowed region and the LHeC projection, respectively. The dashed line indicates the effect of expected theoretical improvements. The HEPFIT program [615] was used for this analysis.

4873 In summary, the LHeC data promises significant improvements in the measurement precision  
 4874 of fundamental electroweak parameters such as  $m_W$  and  $\sin^2\theta_{\text{eff}}^\ell$ . The improved measurements  
 4875 enhance the sensitivity of electroweak tests by a factor of two or more.

## 4876 7.2 Higgs Physics

### 4877 7.2.1 Impact of LHeC data on Higgs cross section predictions at the LHC

4878 A detailed analysis of Higgs boson production cross sections was given in the report on Higgs  
 4879 Physics at the HL-LHC and HE-LHC [616]. Central values at  $\sqrt{s} = 14$  TeV and the corre-  
 4880 sponding uncertainties are reported in Tab. 7.4. Perturbative uncertainties (labelled  $\Delta\sigma_{\text{scales}}$  in  
 4881 Tab. 7.4) generally dominate compared to the contributions of  $\alpha_s$  and the PDFs. This is espe-  
 4882 cially true for gluon fusion, where the residual theoretical uncertainties correspond to missing  
 4883 corrections beyond N<sup>3</sup>LO in QCD, and for  $t\bar{t}H$  production which is known to NLO QCD+EW  
 4884 accuracy. The weak boson fusion,  $WH$  and  $ZH$  cross sections are known to NNLO QCD + NLO  
 4885 EW accuracy; residual theoretical uncertainties are smaller for these weak interaction processes.

4886 In Ref. [616],  $\alpha_s$ -related uncertainties are propagated assuming  $\alpha_s = 0.118 \pm 0.0015$ , and the  
 4887 assumed PDF uncertainties reflect the HL-LHC prospects [89]. They are in excess of 3% for  
 4888 gluon fusion and  $t\bar{t}H$ , below 2% for  $WH$  and  $ZH$ , and 0.4% for weak boson fusion. The LHeC  
 4889 uncertainties in Tab. 7.4 are calculated using MCFM [617], interfaced to PDFs determined from  
 4890 LHeC pseudodata as described in Chapter 3. Assuming the prospects for  $\alpha_s$  and PDFs described  
 4891 in Chapter 3, and with the exception of weak-boson fusion production, the corresponding un-  
 4892 certainties decrease by a factor 5 to 10.

Process	$\sigma_H$ [pb]	$\Delta\sigma_{\text{scales}}$	$\Delta\sigma_{\text{PDF}+\alpha_s}$	
			HL-LHC PDF	LHeC PDF
Gluon-fusion	54.7	5.4 %	3.1 %	0.4 %
Vector-boson-fusion	4.3	2.1 %	0.4 %	0.3 %
$pp \rightarrow WH$	1.5	0.5 %	1.4 %	0.2 %
$pp \rightarrow ZH$	1.0	3.5 %	1.9 %	0.3 %
$pp \rightarrow t\bar{t}H$	0.6	7.5 %	3.5 %	0.4 %

**Table 7.4:** Predictions for Higgs boson production cross sections at the HL-LHC at  $\sqrt{s} = 14$  TeV and its associated relative uncertainties from scale variations and two PDF projections, HL-LHC and LHeC PDFs,  $\Delta\sigma$ . The PDF uncertainties include uncertainties of  $\alpha_s$ .

4893 The important, beneficial role of  $ep$  PDF information for LHC Higgs physics can also be illus-  
 4894 trated using the predictions for the total cross section,  $pp \rightarrow HX$  at the LHC. This has recently  
 4895 been calculated [618] to N<sup>3</sup>LO pQCD. In Fig. 7.5 calculations of this cross section are shown  
 4896 for several recent sets of parton distributions, calculated with the iHix code [619], including the  
 4897 LHeC set.

4898 The effect of these improvements on Higgs boson coupling determination at the HL-LHC is at  
 4899 present modest, due to the combined effect of still significant perturbative uncertainties and  
 4900 of the expected experimental systematic uncertainties. The influence of the LHeC on these  
 4901 measurements is further discussed in the next section.

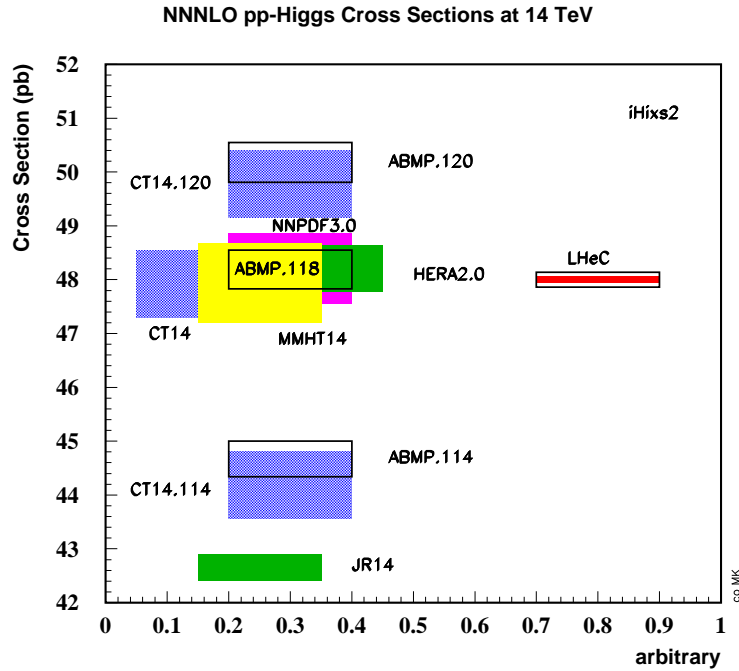


**Figure 7.5:** Cross sections of Higgs production calculated to  $N^3$ LO using the iHix program [619] for existing PDF parameterisation sets (left side) and for the LHeC PDFs (right side). The widths of the areas correspond to the uncertainties as quoted by the various sets, having rescaled the CT14 uncertainties from 90 to 68 % C.L. Results (left) are included also for different values of the strong coupling constant  $\alpha_s(M_Z^2)$ , from 0.114 to 0.120. The inner LHeC uncertainty band (red) includes the expected systematic uncertainty due to the PDFs while the outer box illustrates the expected uncertainty resulting from the determination of  $\alpha_s$  with the LHeC.

## 4902 7.2.2 Higgs Couplings from a simultaneous analysis of $pp$ and $ep$ collision 4903 data

4904 The LHC data collected during the Runs I and II have provided a first exploration of the prop-  
4905 erties of the Higgs boson. The so-called  $\kappa$  framework [620] – which allows modifications of the  
4906 SM-like couplings of the Higgs boson to each SM particle  $i$ , parameterised by coupling modifiers  
4907  $\kappa_i$  – has been widely used for the interpretation of these measurements. With current data, the  
4908  $\kappa$  parameters associated to the main couplings of the Higgs can be determined to a precision of  
4909 roughly 10-20 %, see e.g. [621].<sup>1</sup> This knowledge will be further improved at the high-luminosity  
4910 phase of the LHC, reaching a precision in many cases well below the 10 % level [616]. Even at the  
4911 HL-LHC it will be, however, difficult to obtain sensible measurements of certain Higgs interac-  
4912 tions, e.g. the coupling to charm quarks. Such gap could be covered by the precise measurements  
4913 of that channel at the LHeC, as described in Section 5.1, which brings a nice complementar-  
4914 ity between the measurements that would be possible at both machines. Furthermore, as also  
4915 explained in that section, the LHeC environment allows very precise determinations of certain  
4916 interactions, well beyond of what will be possible at the high-luminosity  $pp$  collider. In this  
4917 subsection we briefly describe the complementarity between the Higgs measurements at the  $pp$

<sup>1</sup>Note that at the LHC one can only determine coupling ratios.

4918 and  $ep$  colliders, illustrated via a combined fit to the HL-LHC and LHeC projections in the  $\kappa$   
 4919 framework.

4920 For a detail descriptions of the Higgs physics program at the LHeC we refer to Chapter 5. The  
 4921 only information not included in the fit presented in this section is that of the determination of  
 4922 the Top Yukawa coupling, since projections from that study are performed assuming any coupling  
 4923 other than  $\kappa_t$  to be SM like. Comments in this regard will be made, when necessary, below.  
 4924 For the HL-LHC inputs of the combined fit we rely on the projections presented in Ref. [616],  
 4925 as used in the comparison study in Ref. [622]. These HL-LHC inputs include projections for  
 4926 the total rates in the main production (ggF, VBF,  $VH$  and  $ttH$ ) and decay channels ( $H \rightarrow$   
 4927  $bb$ ,  $\tau\tau$ ,  $\mu\mu$ ,  $ZZ^*$ ,  $WW^*$ ,  $\gamma\gamma$ ,  $Z\gamma$ ). They are available both for ATLAS and CMS. Regarding  
 4928 the theory systematics in these projections, we assume the scenario S2 described in [616], where  
 4929 the SM theory uncertainties are reduced by roughly a factor of two with respect to their current  
 4930 values. Theory systematics are assumed to be fully correlated between ATLAS and CMS. These  
 4931 projections are combined with LHeC ones, where, as in Ref. [622], we use the future projections  
 4932 for the SM theory uncertainties in the different production cross sections and decay widths. In  
 4933 the  $\kappa$  fit performed here we assume: (1) no Higgs decays into particles other than the SM ones;  
 4934 (2) heavy particles are allowed to modify the SM loops, so we use effective  $\kappa$  parameters to  
 4935 describe the SM loop-induced processes, i.e. we use  $\kappa_g$ ,  $\kappa_\gamma$ ,  $\kappa_{Z\gamma}$  as free parameters. The total  
 4936 list of free parameters considered for this combined HLLHC+LHeC  $\kappa$  fit is, therefore,

$$\{\kappa_b, \kappa_t, \kappa_\tau, \kappa_c, \kappa_\mu, \kappa_Z, \kappa_W, \kappa_g, \kappa_\gamma, \kappa_{Z\gamma}\}, \quad (7.11)$$

4937 for a total of 10 degrees of freedom. Coupling modifiers associated to any other SM particles  
 4938 are assumed to be SM-like,  $\kappa_i = 1$ .

Parameter	Uncertainty		
	HL-LHC	LHeC	HL-LHC+LHeC
$\kappa_W$	1.7	0.75	0.50
$\kappa_Z$	1.5	1.2	0.82
$\kappa_g$	2.3	3.6	1.6
$\kappa_\gamma$	1.9	7.6	1.4
$\kappa_{Z\gamma}$	10	–	10
$\kappa_c$	–	4.1	3.6
$\kappa_t$	3.3	–	3.1
$\kappa_b$	3.6	2.1	1.1
$\kappa_\mu$	4.6	–	4.4
$\kappa_\tau$	1.9	3.3	1.3

**Table 7.5:** Results of the combined HL-LHC + LHeC  $\kappa$  fit. The output of the fit is compared with the results of the HL-LHC and LHeC stand-alone fits. The uncertainties of the  $\kappa$  values are given in per cent.

4939 The results of the HL-LHC+LHeC fit, which has been performed using the `HEPfit` code [615],  
 4940 are shown in Tab. 7.5 and Fig. 7.6 <sup>2</sup>. The increment in constraining power after adding the LHeC  
 4941 measurements is apparent for the couplings to  $W$  bosons and  $b$  quarks, bringing an improvement  
 4942 with respect to the HL-LHC result of a factor  $\sim 3$ . As explained at the beginning of this section,  
 4943 the LHeC measurements also bring the possibility of setting sensible constraints on the Higgs  
 4944 interactions with charm quarks, with a precision of roughly 4%. The HL-LHC measurements,  
 4945 in turn, fill some of the *gaps* in the fit at the LHeC, where there is little sensitivity to the

<sup>2</sup> The plot leaves out the results on  $\kappa_\gamma$ ,  $\kappa_{Z\gamma}$ ,  $\kappa_t$  and  $\kappa_\mu$  which are rarer channels all measured much better in  $pp$  than  $ep$ . It yet is interesting to observe that the global analysis also improves the  $\kappa_\gamma$  result from 1.9 to 1.4%.

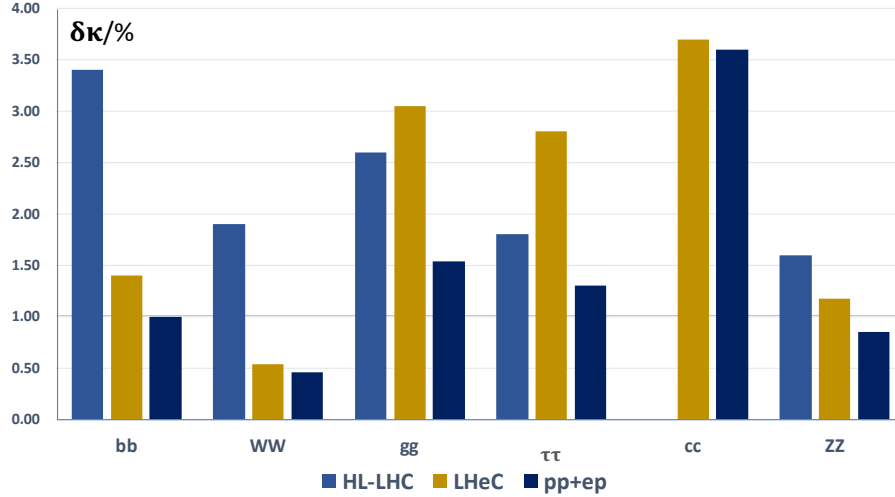


**Figure 7.6:** Results of the combined HL-LHC + LHeC  $\kappa$  fit. The output of the fit is compared with the results of the HL-LHC and LHeC stand-alone fits.

4946 couplings involved in rare Higgs decays, e.g.  $H \rightarrow \mu\mu$  and  $H \rightarrow Z\gamma$ . This makes apparent the  
4947 complementarity between the measurements at  $ep$  and  $pp$  machines, with the former leading  
4948 in terms of precision in the largest Higgs couplings, while the high-luminosity of the latter  
4949 brings sensitivity to the smaller interactions. Finally, as mentioned at the beginning, we did not  
4950 include in this combined  $ep+pp$  fit the projections for Top Yukawa interactions at the LHeC from  
4951 Section 5.2, as these were not derived in a global setup, but rather setting all other interactions  
4952 involved in  $\bar{t}H\nu_e$  product to their SM values. However, the main uncertainty from the other  $\kappa$   
4953 parameters is expected to come from the  $W$  and  $b$  couplings,  $\kappa_W$  and  $\kappa_b$ , which are determined  
4954 with an overall precision of  $\sim 0.8\%$  and  $2\%$ . Therefore one expects the LHeC result,  $\delta\kappa_t \sim 17\%$   
4955 for  $L = 1 \text{ ab}^{-1}$ , to be minimally affected. This number is, however, significantly less precise  
4956 than the HL-LHC projection of  $\sim 4\%$ , which is expected to dominate in a combined result.

## 7.3 Further precision Standard Model measurements at the HL-LHC

DB. New Section. Stil in progress.

The LHeC measurements and the results from their phenomenological interpretations will have an important impact on many areas of the HL-LHC physics programme. This goes far beyond the precision electroweak and the Higgs physics, as discussed at hand of dedicated analyses in the previous sections, and BSM or  $eA$  physics as discussed in the subsequent sections. In this section a few further selected topics of the Standard Model (SM) physics programme at the LHC and HL-LHC are discussed, where substantial improvements due to the LHeC can be expected.

In general, two distinct aspects can be considered for any SM measurement in that respect<sup>3</sup>:

- improvements of the analysis of the recorded event data, and
- improvements of the phenomenological interpretation of the measurements.

In order to assess the impact of the LHeC for the first bullet, one must recollect that an essential key ingredient of the analysis of any hadron collider data is the utilisation of phenomenological models, and commonly QCD inspired Monte Carlo (MC) event generators are employed. These are used for calibration, corrections of limited acceptance and resolution effects (*unfolding*), training of machine learning algorithms for event or object classification, extrapolations from the *fiducial* to the *full* phase space, estimates of different background sources and also signal extraction. Although the implemented models are derived from more fundamental equations like the QCD Lagrangian, a number of model parameters remain poorly known and have to be *tuned* with data. Also, since most models involve approximations and may be numerically limited, any model needs to be validated, or invalidated, with independent measurements prior to its usage, of course. With more and more data being recorded at the (HL-)LHC, statistical uncertainties become very small and systematic uncertainties are reduced due to improved calibration and analysis algorithms, so that uncertainties associated to the MC event models become important and are limiting the accuracy of the HL-LHC measurements. It must be noted, that the MC parameters should be tuned with data from another experiment in order to avoid a potential bias of the actual measurement due to experimental correlations.

For the second bullet, the phenomenological interpretation of hadron collider measurements, like for instance tests of pQCD or the determination of SM parameters (e.g.  $\alpha_s(M_Z)$ ,  $\sin^2\theta_{\text{eff}}^\ell$ ,  $m_W$ , the  $\kappa$  parameters, ...), the proton PDFs and SM parameter which are input to the prediction must be known with high accuracy, most noteworthy the value of  $\alpha_s(M_Z)$ .

The most important inputs of the LHeC to the HL-LHC measurements are of course the precise determination of the PDFs and  $\alpha_s(M_Z)$ , see Chapter 3. These will improve both, the data analysis and its interpretation. Beyond that, the measurements of charged particle spectra, jet shape and jet substructure observables, jet cross sections and event shape observables or heavy flavor cross sections will help to improve MC models further, for instance with the determination of charm and bottom-quark masses, heavy quark ( $c$ ,  $b$ ) fragmentation functions and fragmentation fractions, finding optimal choices for all scales involved in a MC model, or determining the optimal parameters for the parton shower,  $\Lambda_{\text{QCD}}$ . Such measurements can be performed with high precision at the LHeC, since DIS represents a superior QCD laboratory. This is because in the

---

<sup>3</sup>In some cases, a model- or physics parameter is directly extracted from the experiment data and the two applications are merged into a single analysis workflow, for instance in many LHC top-quark mass analyses. Additionally to these two aspects, of course, the complementarity of the physics case of  $ep$  collisions enhances our understanding of the fundamental laws of physics.

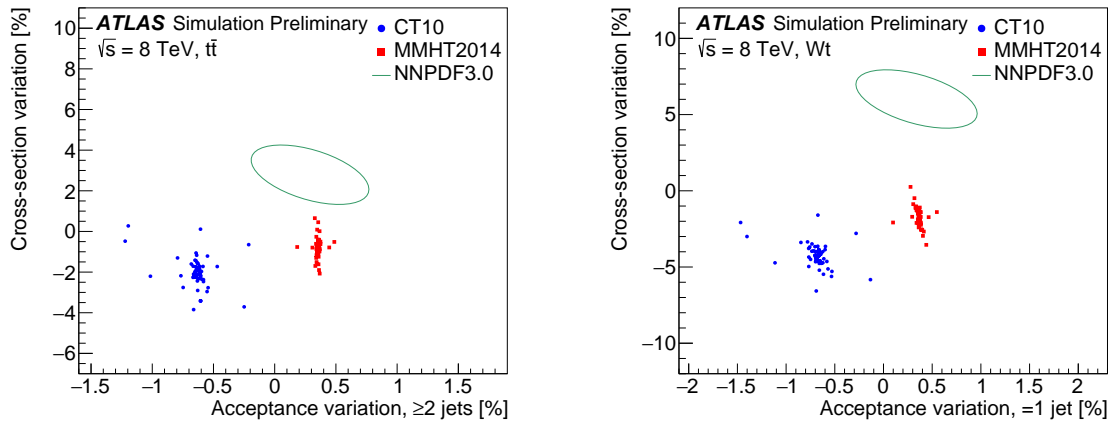


**Figure 7.7:** Left: Impact of PDF uncertainty from CT10 and MMHT2014 eigenvectors or NNPDF3.0 replicas, on the cross section and the acceptance correction for top pair production  $t\bar{t}$  (left) and single top production  $Wt$  (right) (taken from Ref. [623]). Events are selected with at least two jets or with exactly one jet, respectively. Depending on the PDF set and eigenvector employed, the cross sections varies by up to 5–7% for top-pair and more than 10% for single-top production. Also the acceptance correction varies by about 0.5–1% for different PDF sets, and can become as large as 2.5% for different PDF sets and eigenvectors. Since the acceptance correction has to be imposed for the measurement, the limited knowledge of the PDFs introduces a sizeable modelling uncertainty on the measurement.

4998 final state there is always a lepton, which is used for trigger and vertexing, and simultaneously  
 4999 a hadronic system which is then subject of interest. In addition the overconstraint kinematic  
 5000 system allows for the precise calibration of hadronic final state objects, and furthermore limiting  
 5001 effects like minimum bias or pile-up are absent.

5002 In the following, a few selected subjects are discussed at hand of LHC analyses performed with  
 5003 Run-I data at  $\sqrt{s} = 8$  or 13 TeV, and thus giving a tangible indication about challenges at future  
 5004 HL-LHC measurements:

- 5005 • The measurement of the integrated top-quark pair cross section represents an outstand-  
 5006 ing benchmark quantity for the entire field of top-quark physics. Its measurement for  
 5007 top-transverse momenta  $p_T^t > 400$  GeV in the *lepton+jets* decay channel yields a high  
 5008 experimental precision with both, small statistical and systematic uncertainties. However,  
 5009 its measurement precision is limited by theoretical uncertainties (also called *modelling*  
 5010 uncertainties), and the largest individual source stems from the PDFs [143, 624]. A related  
 5011 study of PDF effects on the acceptance correction for the integrated top-pair production  
 5012 cross section and single-top production  $Wt$  is displayed in Fig. 7.7. The acceptance correc-  
 5013 tion changes by up to 0.5–1% for different PDF sets, and can become as large as 2.5% for  
 5014 different PDF sets and eigenvectors. Another very important uncertainty for top-quark  
 5015 measurements is from the modelling of the parton shower. Both, uncertainties from the  
 5016 PDFs and from parton shower modelling, are expected to be significantly reduced with  
 5017 LHeC data.
- 5018 • The determination of the top-quark mass  $m_t$  from LHC data requires the precise modelling  
 5019 of the physics and all background processes with suitable MC models. Today, the value  
 5020 of  $m_t$  is determined most precisely from a combination of such individual analyses, and  
 5021 uncertainties of 0.4–0.8 GeV are reported [143, 625–629]. Any of these individual precision  
 5022 determinations are limited by model uncertainties, and therefore improvements at the  
 5023 HL-LHC cannot be obtained with more data, but only with improved models. Some of

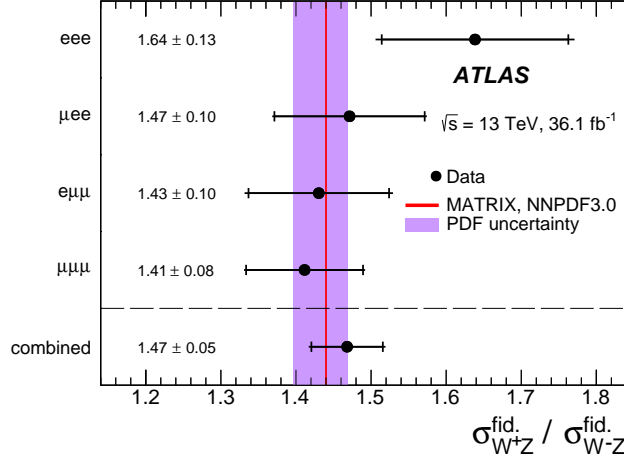


**Figure 7.8:** Measurement of the ratio of di-boson  $\sigma(W^+Z)/\sigma(W^-Z)$  integrated cross sections in a fiducial phase space for four different decay channels and their combination at  $\sqrt{s} = 13$  TeV in comparison with NNLO predictions [640, 641] (taken from Ref. [642]). The total uncertainties of the data points are dominated by statistical uncertainties and will be reduced in the future. The shaded violet band indicates the size of the PDF uncertainties and limit the overall interpretation of the measurement.

5024

the model uncertainties, e.g. PDF, parton shower, hadronisation or fragmentation related uncertainties can be expected to be reduced with LHeC data.

5025

5026

- At the HL-LHC also rare decay channels can be exploited for precision measurements. For example, the top-quark mass can be determined from top-quark pair production with a subsequent decay, where one  $b$ -quark hadronises into  $B$ -hadron which then decays through a  $J/\psi$ -meson into a pair of muons,  $t\bar{t} \rightarrow W^+bW^-b \rightarrow \ell\nu_\ell J/\psi (\rightarrow \mu^+\mu^-) Xqq'b$  [630]. Such a measurement requires the precise knowledge of  $b$ -quark fragmentation, which can be well measured at the LHeC, and such improving the HL-LHC measurement. (to be discussed.)

5027

5028

5029

5030

5031

5032

- The value of the strong coupling constant  $\alpha_s(M_Z)$  is one of the least known fundamental parameters in physics and an improved determination with new measurement constitutes a real challenge for LHC and HL-LHC experiments. A large number of observables at the LHC are *per-se* sensitive to  $\alpha_s(M_Z)$ , and its value was determined in the past from various definitions of jet cross section observables (see e.g. [122, 123, 631, 632]) or transverse energy-energy correlations [633],  $Z$ +jet cross sections [634], integrated [635] or differential top-quark cross sections [636], inclusive  $W$  or  $Z$  production [637, 638], prompt photon data [639], and many other observables (see Ref. [143] for a review). Although the harsh environment in high-luminosity hadron-hadron collisions requires sophisticated analysis techniques and dedicated measurements, small experimental uncertainties for  $\alpha_s(M_Z)$  could be achieved. Hence,  $\alpha_s$  determinations are nowadays limited due to theoretical uncertainties and the dominant uncertainties are most commonly PDF related [634, 635, 637, 638] (only for observables, where NNLO predictions are not yet applicable, the scale uncertainties may overshoot the PDF uncertainties). Therefore, already today the knowledge of the PDFs represent the limiting factor, and a significant reduction of the total uncertainty for  $\alpha_s(M_Z)$  can (only) be achieved with PDFs determined at the LHeC.

5033

5034

5035

5036

5037

5038

5039

5040

5041

5042

5043

5044

5045

5046

5047

5048

- The production of  $W^\pm Z$  pairs in  $pp$  collisions provides a crucial test of the electroweak sector of the SM, since di-boson production is sensitive to the gauge-boson self-interactions. Already small deviations in the observed distributions could provide indications for new physics. The process can be well measured in a high-pile up environment and can be

5049

5050

5051

5052 well separated from huge QCD background. However, due to the relatively small  $W^\pm Z$   
5053 cross sections high statistical precision can only be achieved with high luminosity. Recent  
5054 measurement of  $W^\pm Z$  pairs at  $\sqrt{s} = 13 \text{ TeV}$  based on  $36 \text{ fb}^{-1}$  of integrated luminosity  
5055 have been performed by ATLAS and CMS [642, 643]. In Fig. 7.8 the ratio of fiducial cross  
5056 sections  $\sigma_{W^+Z}/\sigma_{W^-Z}$  is displayed. The largest individual uncertainty is the statistical  
5057 uncertainty and therefore future measurements at the LHC and HL-LHC are of great  
5058 importance in order to reach higher precision. Nonetheless, already today, the overall  
5059 phenomenological interpretation is limited by PDF uncertainties, as visible from Fig. 7.8,  
5060 and these can be improved best with PDFs from LHeC.

5061 In the situation of the absence of indications for new physics, an important goal of the future  
5062 LHC and HL-LHC physics programme has to be devoted to precision measurements. From  
5063 the examples discussed above ( $W$ -boson mass and Higgs measurements are discussed in above's  
5064 sections), it becomes obvious that limiting factors of such measurements arise from the signal  
5065 and MC modelling, where PDF uncertainties constitute a limiting factor and also improved  
5066 understandings of parton shower, hadronisation and fragmentation processes are of importance.  
5067 These aspects can all be improved with independent precision measurements at the LHeC.

5068 Similarly, the phenomenological interpretation of many processes is already today limited by  
5069 PDF uncertainties, and as outlined,  $\alpha_s$  determinations, di-boson processes, top-mass or top-  
5070 cross section measurements, and many other topics, require a higher precision for PDFs already  
5071 today. In the HL-LHC era, where data and predictions are more precise, the detailed knowledge  
5072 of the PDFs will become of even greater importance.

## 5073 7.4 High Mass Searches at the LHC

### 5074 7.4.1 Strongly-produced supersymmetric particles

5075 The potential of the HL- and HE-LHC to discover supersymmetry was extensively discussed  
5076 in Ref. [644]. Here we focus on searches for gluinos within MSSM scenarios. Gluino pairs are  
5077 produced through the strong interaction, and their production cross section is relatively large;  
5078 naturalness considerations indicate that gluino masses should not exceed a few TeV and lie not  
5079 too far above the EW scale. Hence they are certainly among the first particles that could be  
5080 discovered at HL-LHC.

5081 In the following we assume that a simplified topology dominates the gluino decay chain, culmi-  
5082 nating in jets plus missing energy originating from a massless LSP,  $\tilde{\chi}_0$ . Ref. [644] evaluated the  
5083 sensitivity of the HL- and HE-LHC to gluino pair production with gluinos decaying exclusively  
5084 to  $q\bar{q}\tilde{\chi}_0$ , through off-shell first and second generation squarks, using a standard search for events  
5085 with jets and missing transverse energy. Currently, the reach for this simplified model with  
5086  $36\text{ fb}^{-1}$  of 13 TeV data is roughly 2 TeV gluinos, for a massless LSP [645, 646]. Extrapolating  
5087 to  $3\text{ ab}^{-1}$  at 14 TeV, the limit grows to 3.2 TeV. For  $15\text{ ab}^{-1}$  at 27 TeV, a limit of 5.7 TeV was  
5088 found.

5089 When deriving limits, an overall systematic uncertainty of 20% was assumed on the SM back-  
5090 ground contributions, and a generic 10% uncertainty was assumed on the signal normalisation,  
5091 not taking into account PDF-related uncertainties which are as large as 50% for gluinos around  
5092 3 TeV. The effect of this additional source of uncertainty was found to induce a variation in the  
5093 mass limit by  $\pm 200\text{ GeV}$  at the HL-LHC, and as much as  $\pm 500\text{ GeV}$  at the HE-LHC.

5094 We can revert this argument, and claim that with present PDF knowledge, mass limits could  
5095 be as low as 3.0 TeV and 5.3 TeV at the HL- and HE-LHC, respectively. Data from the LHeC  
5096 would make this contribution negligible compared to other sources of uncertainty. Compared  
5097 to the most conservative scenario, the increase in sensitivity would correspond to an increase in  
5098 centre-of-mass energy by approximately 5 to 10%.

### 5099 7.4.2 Contact interactions

5100 New, high-mass gauge bosons are most often searched for in resonant final states. Peaks in the  
5101 invariant-mass distributions of electron, muon or jet pairs directly reflect the presence of such  
5102 new particles; the accessible mass range is limited by the available centre-of-mass energy.

5103 Particles with a mass beyond the kinematic limit generally interfere with the  $Z$  boson and the  
5104 photon, generating non-resonant deviations in the invariant mass distributions. Such models  
5105 can be parameterised as contact interactions (CI) between two initial-state quarks and two  
5106 final-state leptons of given chirality:

$$\mathcal{L}_{\text{CI}} = \frac{g^2}{\Lambda^2} \eta_{ij} (\bar{q}_i \gamma_\mu q_i) (\bar{\ell}_i \gamma^\mu \ell_i), \quad (7.12)$$

5107 where  $i, j = \text{L or R}$  (for left- or right-handed chirality),  $g$  is a coupling constant set to be  $4\pi$  by  
5108 convention, and  $\Lambda$  is the CI scale. The sign of  $\eta_{ij}$  determines whether the interference between  
5109 the SM Drell–Yan (DY) process,  $q\bar{q} \rightarrow Z/\gamma^* \rightarrow \ell^+\ell^-$ , is constructive or destructive.

5110 The size and sign of the observed deviation with respect to the SM probes the scale and in-  
5111 terference pattern of the interaction. The sensitivity of the search is limited by experimental

5112 uncertainties (finite statistics and experimental systematic uncertainties) and by uncertainties  
 5113 in the theoretical modelling of the DY background.

5114 The most recent results of the ATLAS and CMS Collaborations [598, 599] are based on  $e^+e^-$   
 5115 and  $\mu^+\mu^-$  final states in  $36\text{ fb}^{-1}$  of data, and probe CI's up to a typical scale of 25 TeV, de-  
 5116 pending on the chirality and sign of the interaction coupling parameter. The limits derived by  
 5117 ATLAS, summarised in Tab. 7.6, accounted for theoretical uncertainties induced by the PDFs  
 5118 and by  $\alpha_s$ . The dominant PDF uncertainty was estimated from the 90% CL uncertainty in  
 5119 the CT14nnlo PDF set, adding an envelope from the comparison of the CT14nnlo, MMHT2014  
 5120 and NNPDF3.0 [647] central sets. The strong coupling constant uncertainty was propagated  
 5121 assuming  $\alpha_s = 0.118 \pm 0.003$ , with a subleading effect.

5122 The present study evaluates the sensitivity of this search at the HL-LHC. The increase in  
 5123 sensitivity is estimated using samples of Standard-Model like pseudo data, corresponding to the  
 5124 integrated luminosity of  $3\text{ ab}^{-1}$ . In a first step, both the experimental and theoretical systematic  
 5125 uncertainties are kept in the publication. In this regime, the extrapolated statistical uncertainty  
 5126 is typically a factor 5 to 10 smaller than the theoretical uncertainty. Improvements from the  
 5127 LHeC in  $\alpha_s$  and in the proton PDFs are incorporated in a second step. Assuming the prospects  
 5128 described in Chapter 3,  $\alpha_s$  and PDF uncertainties are smaller than the statistical fluctuations  
 5129 and can be neglected in first approximation.

5130 The results are summarised in Tab. 7.6. Everything else equal, increasing the sample size from  
 5131  $36\text{ fb}^{-1}$  to  $3\text{ ab}^{-1}$  enhances the CI reach by a typical factor of two. Accounting for the improve-  
 5132 ment in the theoretical modelling of the DY process brought by the LHeC brings another factor  
 5133 of 1.5–1.8 in the limits. In the last case, the limits reach well into range directly accessible with  
 5134 proton-proton collisions at  $\sqrt{s} = 100\text{ TeV}$ , as envisioned at the FCC-hh.

Model	ATLAS (Ref. [598])		HL-LHC	
	$\mathcal{L} = 36\text{ fb}^{-1}$ (CT14nnlo)	$\mathcal{L} = 3\text{ ab}^{-1}$ (CT14nnlo)	$\mathcal{L} = 3\text{ ab}^{-1}$ (LHeC)	
LL (constr.)	28 TeV	58 TeV	96 TeV	
LL (destr.)	21 TeV	49 TeV	77 TeV	
RR (constr.)	26 TeV	58 TeV	84 TeV	
RR (destr.)	22 TeV	61 TeV	75 TeV	
LR (constr.)	26 TeV	49 TeV	81 TeV	
LR (destr.)	22 TeV	45 TeV	62 TeV	

**Table 7.6:** Contact interaction limits from ATLAS based on  $36\text{ fb}^{-1}$  of data [598], and extrapolated to the full HL-LHC dataset ( $3\text{ ab}^{-1}$ ). The extrapolation is performed assuming the same PDF and  $\alpha_s$  uncertainties as in Ref. [598], and assuming the improved uncertainties as obtained from the LHeC.

## 5135 7.5 Heavy Ion Physics with $eA$ Input

5136 The study of hadronic collisions at RHIC and the LHC, proton-proton, proton-nucleus and  
 5137 nucleus-nucleus, has produced several observations of crucial importance for our understanding  
 5138 of QCD in complex systems where a large number of partons is involved [648, 649]. The different  
 5139 stages of a heavy ion collision, as we presently picture it, are schematically drawn in Fig 7.9.

5140 First, the hot and dense partonic medium created in heavy ion collisions, the quark-gluon plasma  
 5141 (QGP), experiences a collective behaviour of which azimuthal asymmetries and transverse spec-  
 5142 tra with a specific ordering in particle masses are the most prominent observables. This collec-

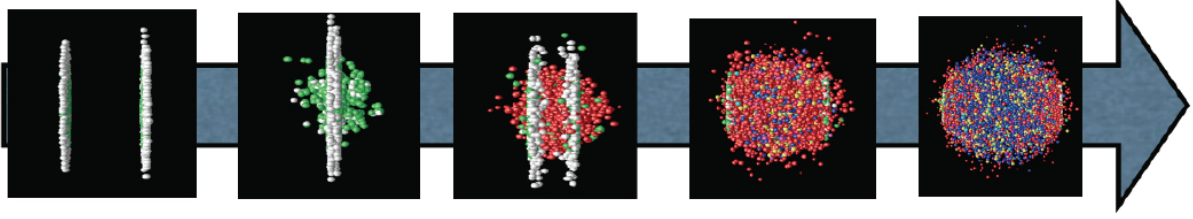


**Figure 7.9:** Sketch of a heavy ion collision with time running left to right, going from the approach of two ultrarelativistic Lorentz-contracted nuclei, the collision and parton creation in the central rapidity region, the beginning of expansion and formation of the QGP, the expansion of the QGP until hadronisation, and finally the expansion of the hadronic gas.

5143 tivity can be very well described by relativistic hydrodynamics [650]. For this description, the  
 5144 system has to undergo some dynamics leading to rough isotropisation in a short time,  $\lesssim 1$  fm/c,  
 5145 for which both strong and weak coupling explanations have been proposed [457].

5146 Second, collisions between smaller systems,  $pp$  and  $pA$ , show many of the features [454–456] that  
 5147 in heavy ion collisions are taken as indicative of the production of a dense hot partonic medium.  
 5148 The most celebrated of such features, the long rapidity range particle correlations collimated in  
 5149 azimuth, named the ridge (see Sec. 4.5), has been found in all collisions systems. The dynamics  
 5150 underlying this phenomena, either the formation of QGP and the existence of strong final state  
 5151 interactions, or some initial state dynamics that leaves imprint on the final observables, is under  
 5152 discussion [457].

5153 Finally, the QGP is extremely opaque to both highly energetic partons [651] and quarkonia [652]  
 5154 traversing it. These observables, whose production in  $pp$  can be addressed through perturba-  
 5155 tive methods, are called hard probes [653]. The quantification of the properties of the QGP  
 5156 extracted through hard probes is done by a comparison with predictions based on assuming a  
 5157 nuclear collision to be a superposition of collisions among free nucleons. Such predictions contain  
 5158 uncertainties coming both from nuclear effects other than those in QGP (named cold nuclear  
 5159 matter effects), and from uncertainties in the dynamics determining the interaction between the  
 5160 energetic parton or bound state and the medium. In the case of partons, this has motivated the  
 5161 development of sophisticated jet studies in heavy ion collisions [654].

5162  $eA$  collisions studied in the energy range relevant for the corresponding hadronic accelerator – the  
 5163 LHeC for the LHC – would substantially improve our knowledge on all these aspects and, indeed,  
 5164 on all stages of a heavy ion collisions depicted in Fig. 7.9. Besides, they can reduce sizeably the  
 5165 uncertainties in the extracted QGP parameters, the central goal of the heavy program for the  
 5166 understanding of the different phases of QCD. Here we provide three examples of such synergies:

- 5167 • Nuclear parton densities: The large lack of precision presently existing in the determina-  
 5168 tion of parton densities induce large uncertainties in the understanding of several signatures  
 5169 of the QGP. For example, for  $J/\psi$  suppression, its magnitude at midrapidity at the LHC is  
 5170 compatible with the sole effect of nuclear shadowing on nPDFs [652], see Fig. 7.10. While  
 5171 from data at lower energies and at forward and backward rapidities it is clear that this is  
 5172 not the only effect at work, only a reduction on the nPDF uncertainty as feasible at the  
 5173 LHeC, see Sec. 4.2, will make possible a precise quantification of the different mechanisms  
 5174 producing either suppression (screening, gluon dissociation, energy loss) or enhancement  
 5175 (recombination or coalescence), that play a role in this observable.
- 5176 • Initial conditions for the collective expansion and the small system problem: At present,  
 5177 the largest uncertainty in the determination of the transport coefficients of the partonic

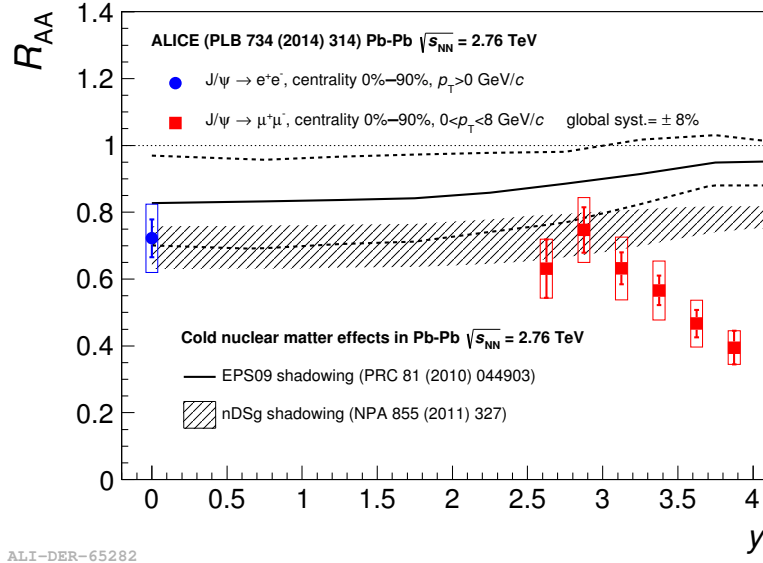


**Figure 7.10:** ALICE inclusive  $J/\psi$  nuclear modification factor versus rapidity [655], compared to nPDF calculations. Taken from [652].

5178 matter created in heavy ion collisions [656, 657] (see Fig. 7.11), required in hydrodynamic  
5179 calculations, and in our understanding of the speed of the approach to isotropisation and  
5180 of the dynamics prior to it [658], comes from our lack of knowledge of the nuclear wave  
5181 function and of the mechanism of particle production at small to moderate scales – i.e. the  
5182 soft and semihard regimes. Both aspects determine the initial conditions for the application  
5183 of relativistic hydrodynamics. This is even more crucial in the discussion of small systems,  
5184 where details of the transverse structure of protons are key [659] not only to provide  
5185 such initial conditions but also to establish the relative role of initial versus final state  
5186 dynamics. For example, the description of azimuthal asymmetries in  $pp$  and  $pPb$  collisions  
5187 at the LHC demands that the proton is modelled as a collection of constituent quarks or  
5188 hot spots [650, 659].  $ep$  and  $eA$  collisions at the LHeC can constrain both aspects in the  
5189 pertinent kinematic region, Secs. 3.2.5 and 4.3. Besides, they can clarify the mechanisms  
5190 of particle production and the possible relevance of initial state correlations on the final  
5191 state observables as suggested e.g. by CGC calculations, see Secs. 3.2.2 and 4.4, whose  
5192 importance for LHC energies can be established at the LHeC.

- 5193 • Impact on hard probes: Besides the improvement in the determination of nPDFs that  
5194 affects the quantification of hard probes, commented above,  $eA$  collisions can help to un-  
5195 derstand the dynamics of the probes by analysing the effects of the nuclear medium on  
5196 them. As two examples, the abundant yields of jets and large transverse momentum parti-  
5197 cles at the LHeC [1] will allow precise studies of the nuclear effects on jet observables and of  
5198 hadronisation inside the nuclear medium. These two aspects are of capital importance not  
5199 only in heavy ion collisions but also in small systems where the lack of jet modification is  
5200 the only QGP-like characteristics not observed in  $pPb$ . On the other hand, measurements  
5201 of exclusive quarkonium production at the LHeC [1] will provide a better understanding  
5202 of the cold nuclear matter effects on this probe, on top of which the effects of the QGP  
5203 will provide a quantitative characterisation of this new form of QCD matter.

5204 As discussed in Sec. 4.2,  $pPb$  and  $PbPb$  collisions at the LHC offer possibilities for constraining  
5205 nPDFs, through the measurement of EW vector boson production [663], dijets [423], D mesons at  
5206 forward rapidities [435] and exclusive charmonium and dijet photoproduction in ultraperipheral

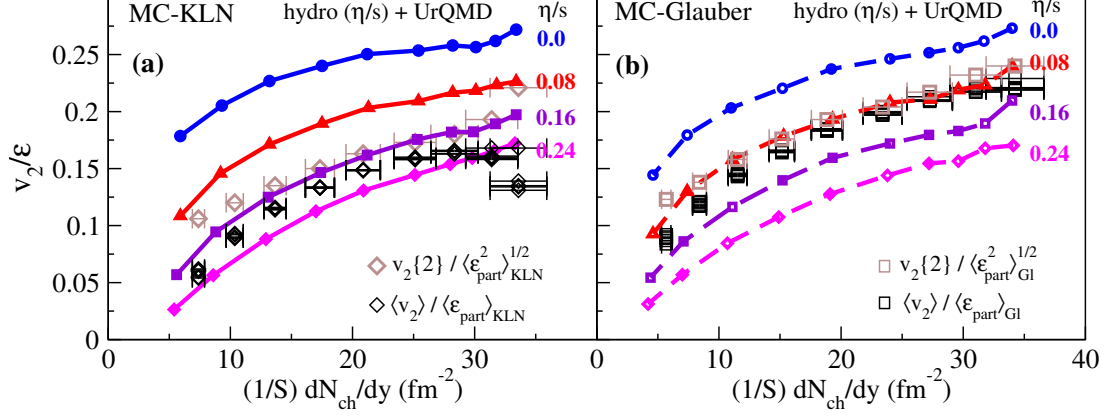


**Figure 7.11:** Comparison of the universal  $v_2(\eta/s)/\epsilon$  vs.  $(1/S)(dN_{\text{ch}}/dy)$  curves with experimental data for  $\langle v_2 \rangle$  [660],  $v_2\{2\}$  [661], and  $dN_{\text{ch}}/dy$  [662] from the STAR Collaboration. The experimental data used in (a) and (b) are identical, but the normalisation factors  $\langle \epsilon_{\text{part}} \rangle$  and  $S$  used on the vertical and horizontal axes, as well as the factor  $\langle \epsilon_{\text{part}}^2 \rangle^{1/2}$  used to normalize the  $v_2\{2\}$  data, are taken from the MC-KLN model in (a) and from the MC-Glauber model in (b). Theoretical curves are from simulations with MC-KLN initial conditions in (a) and with MC-Glauber initial conditions in (b). Taken from [656].

5207 collisions [664–666]. Specifically, dijets in UPCs could constrain nPDFs in the region  $10^{-3} \lesssim$   
5208  $x \lesssim 0.7$  and  $200 \lesssim Q^2 \lesssim 10^4 \text{ GeV}^2$ .  $eA$  collisions would provide more precise nPDFs, whose  
5209 compatibility with these mentioned observables would clearly establish the validity of collinear  
5210 factorisation and the mechanisms of particle production in collisions involving nuclei.

5211 Furthermore,  $eA$  offers another system where photon-photon collisions, recently measured in  
5212 UPCs at the LHC [667], can be studied. For example, the observed acoplanarity of the produced  
5213 muon pairs can be analysed in  $eA$  in order to clarify its possible origin and constrain the parton  
5214 densities in the photon.

5215 Finally, the possible existence of a new non-linear regime of QCD - saturation - at small  $x$  is  
5216 also under study at the LHC, for example using dijets in the forward rapidity region in  $p\text{Pb}$   
5217 collisions [668]. As discussed in Sec. 4.5, the ridge phenomenon (two particle correlations peaked  
5218 at zero and  $\pi$  azimuthal angles and stretched along the full rapidity of the detector) observed in  
5219 all collision systems,  $pp$ ,  $p\text{Pb}$  and  $\text{PbPb}$  at the LHC, has been measured in photoproduction on  
5220 Pb in UPCs at the LHC [458]. For the time being, its existence in smaller systems like  $e^+e^-$  [459]  
5221 at LEP and  $ep$  at HERA [460] has been scrutinised but the results are not conclusive. These  
5222 studies are fully complementary to those in  $ep$  and  $eA$ , where its search at the smallest possible  
5223 values of  $x$  at the LHeC would be most interesting. For example, the collision of the virtual  
5224 photon with the proton at the LHeC can be considered as a high energy collision of two jets or  
5225 “flux tubes”.

5226 In conclusion,  $ep$  and  $eA$  collisions as studied at the LHeC will have a large impact on the  
5227 heavy ion programme, as the comparison of the kinematic reach of DIS and hadronic machines  
5228 shown in Fig. 7.12 makes evident. It should be noted that there exist proposals for extending  
5229 such programme into Run 5 and 6 of the LHC [429], by running lighter ions and with detector  
5230 upgrades in ATLAS and CMS (starting in Run 4) and LHCb (Upgrade II [669]).

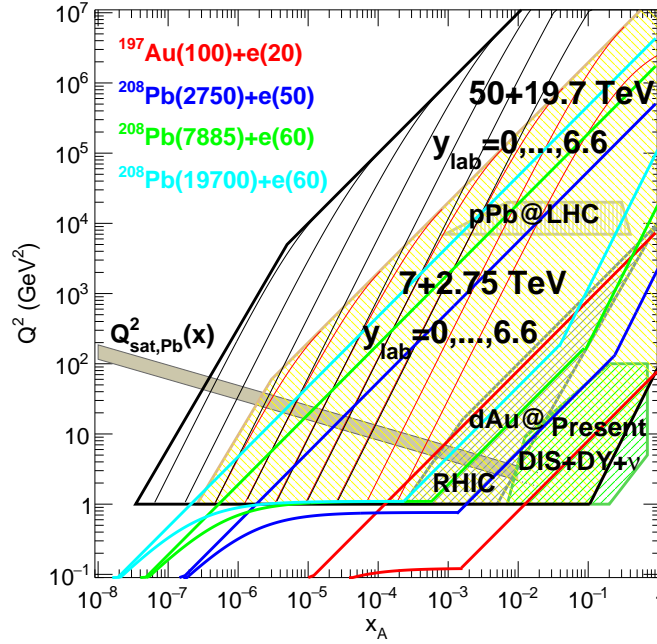


**Figure 7.12:** Kinematic regions in the  $x - Q^2$  plane explored by data sets (charged lepton and neutrino DIS, DY,  $dAu$  at RHIC and  $pPb$  at the LHC) used in present nPDF analyses [404], compared to the ones achievable at the EIC (red), the LHeC (ERL against the HL-LHC beams, dark blue) and two FCC-eh versions (with Pb beams corresponding to proton energies of 20 TeV - green and 50 TeV - light blue). Acceptance is taken to be  $1^\circ < \theta < 179^\circ$ , and  $0.01(0.001) < y < 1$  for the EIC (all other colliders). The areas delimited by thick brown and black lines show the regions accessible in  $pPb$  collisions at the LHC and the FCC-hh (50 TeV) respectively, while the thin lines represent constant rapidities from 0 (right) to 6.6 (left) for each case. The saturation scale  $Q_{sat}$  shown here for indicative purposes only, see also [405], has been drawn for a Pb nucleus considering an uncertainty  $\sim 2$  and a behaviour with energy following the model in [406]. Note that it only indicates a region where saturation effects are expected to be important but there is no sharp transition between the linear and non-linear regimes.

## Chapter 8

# The Electron Energy Recovery Linac

We studied different options for the electron accelerator for LHeC in Ref. [1], of which the Energy Recovery Linac (ERL) option is retained in this update of the CDR. This is due to the higher achievable luminosity of the Linac-Ring option, as compared to the Ring-Ring option, as well as the interference of the installation of an electron ring in the LHC tunnel with its operation [670]. The clear advantage of the ERL compared to its contenders in 2012 is the possibility to keep the overall energy consumption at bay, albeit, in its baseline configuration and size of the return arcs, operation is still limited to lepton energies below 70 GeV to avoid excessive synchrotron radiation losses. Since there is no fundamental beam loading in an ERL by its principle, higher average currents and thus higher luminosities would not lead to larger power consumption.

### 8.1 Introduction – Design Goals

The main guidelines for the design of the Electron ERL and the Interaction Region (IR) with the LHC are:

- electron-hadron operation in parallel with high luminosity hadron-hadron collisions in LHC/HL-LHC;
- centre-of-mass collision energy in the TeV scale;
- power consumption of the electron accelerator smaller than 100 MW;
- peak luminosity approaching  $10^{34} \text{ cm}^{-2}\text{s}^{-1}$ ;
- integrated luminosity exceeding by at least two orders of magnitude that achieved by HERA at DESY.

The electron energy  $E_e$  chosen in the previous version of the CDR [1] was 60 GeV. This could be achieved with an ERL circumference of 1/3 of that of the LHC. Cost considerations and machine–detector performance aspects, in particular the amount of synchrotron radiation losses in the IR, have led to define a new reference configuration with  $E_e = 49.2 \text{ GeV}$  and a circumference of  $\approx 5.4 \text{ km}$ , 1/5 of that of the LHC.

The ERL consists of two superconducting (SC) linacs operated in CW connected by at least three pairs of arcs to allow three accelerating and three decelerating passes (see Fig. 8.1). The length of the high energy return arc following the interaction point should be such as to provide a half RF period wavelength shift to allow the deceleration of the beam in the linac structures

5261 in three passes down to the injection energy and its safe disposal. SC Cavities with an unloaded  
 5262 quality factor  $Q_0$  exceeding  $10^{10}$  are required to minimise the requirements on the cryogenic  
 5263 cooling power and to allow an efficient ERL operation. The choice of having three accelerating  
 5264 and three decelerating passes implies that the circulating current in the linacs is six times the  
 5265 current colliding at the Interaction Point (IP) with the hadron beam.

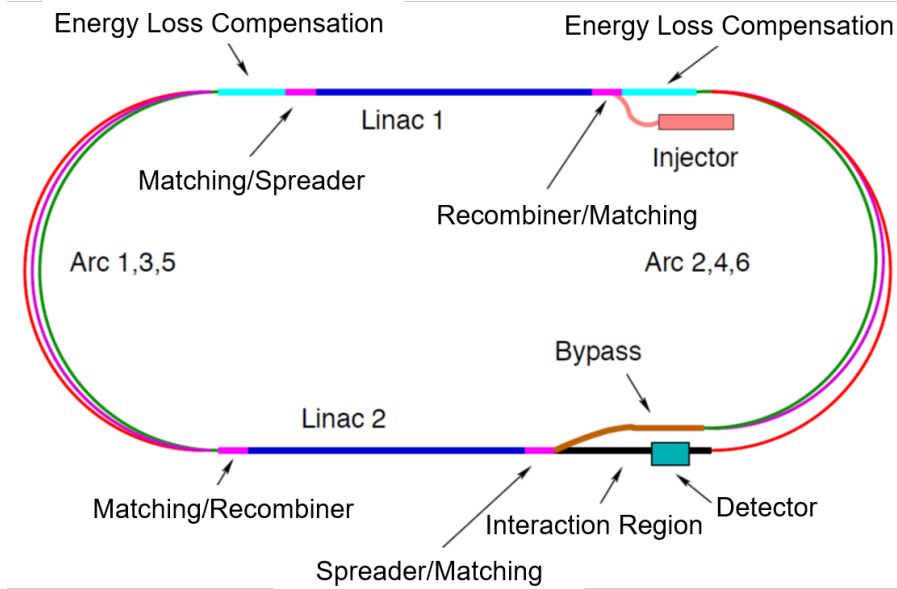


**Figure 8.1:** Schematic layout of the LHeC design based on an Energy Recovery Linac.

5266 The choice of an Energy Recovery Linac offers the advantage of a high brightness beam and it  
 5267 avoids performance limitations due to the beam-beam effect seen by the electron beam [671],  
 5268 which was a major performance limitation in many circular lepton colliders (e.g. LEP) and for  
 5269 the LHeC Ring-Ring option. The current of the ERL is limited by its source and an operational  
 5270 goal of  $I_e = 20$  mA has been set, corresponding to a bunch charge of 500 pC at a bunch frequency  
 5271 of 40 MHz. This implies operating the SRF cavities with the very high current of 120 mA for a  
 5272 virtual beam power (product of the beam current at the IP times the maximum beam energy) of  
 5273 1 GW. The validation of such performance in terms of source brightness and ERL 3-turn stable  
 5274 and efficient operation in the PERLE facility [8] is a key milestone for the LHeC design.

5275 A small beam size at the IP is required to maximize luminosity and approach peak luminosities  
 5276 of  $10^{34} \text{ cm}^{-2} \text{ s}^{-1}$  and integrated luminosities of  $1 \text{ ab}^{-1}$  in the LHeC lifetime. In particular  $\beta^* <$   
 5277  $10$  cm needs to be achieved for the colliding proton beam compatibly with the optics constraints  
 5278 imposed by the operation in parallel to proton-proton physics in the other IPs during the HL-  
 5279 LHC era [2]. The peak luminosity values quoted above exceed those at HERA by 2-3 orders of  
 5280 magnitude. The operation of HERA in its first, extended running period 1992–2000, provided  
 5281 and integrated luminosity of about  $0.1 \text{ fb}^{-1}$  for the H1 and ZEUS experiments, corresponding  
 5282 to the expected integrated luminosity collected over 1 day of LHeC operation.

## 5283 8.2 The ERL Configuration of the LHeC

5284 The main parameters of the LHeC ERL are listed in Tab. 8.1; their choices and optimisation  
 5285 criteria will be discussed in the following sections.

Parameter	Unit	Value
Injector energy	GeV	0.5
Total number of linacs		2
Number of acceleration passes		3
Maximum electron energy	GeV	49.19
Bunch charge	pC	499
Bunch spacing	ns	24.95
Electron current	mA	20
Transverse normalized emittance	$\mu\text{m}$	30
Total energy gain per linac	GeV	8.114
Frequency	MHz	801.58
Acceleration gradient	MV/m	19.73
Cavity iris diameter	mm	130
Number of cells per cavity		5
Cavity length (active/real estate)	m	0.918/1.5
Cavities per cryomodule		4
Cryomodule length	m	7
Length of 4-CM unit	m	29.6
Acceleration per cryomodule (4-CM unit)	MeV	289.8
Total number of cryomodules (4-CM units) per linac		112 (28)
Total linac length (with with spr/rec matching)	m	828.8 (980.8)
Return arc radius (length)	m	536.4 (1685.1)
Total ERL length	km	5.332

**Table 8.1:** Parameters of LHeC Energy Recovery Linac (ERL).

### 5286 8.2.1 Baseline Design – Lattice Architecture

5287 The ERL, as sketched in Fig. 8.1, is arranged in a racetrack configuration; hosting two super-  
5288 conducting linacs in the parallel straights and three recirculating arcs on each side. The linacs  
5289 are 828.8 m long and the arcs have 536.4 m radius, additional space of 76 m is taken up by  
5290 utilities like Spreader/Recombiner (Spr/Rec), matching and energy loss compensating sections  
5291 adjacent to both ends of each linac (total of 4 sections) [672]. The total length of the racetrack  
5292 is 5.332 km:  $1/5$  of the LHC circumference  $2 \cdot (828.8 + 2 \cdot 76 + 536.4\pi)$  m. Each of the two linacs  
5293 provides 8.114 GV accelerating voltage, therefore a 49.19 GeV energy is achieved in three turns.  
5294 After the collision with the protons in the LHC, the beam is decelerated in the three subsequent  
5295 turns. The injection and dump energy has been chosen at 0.5 GeV.

5296 Injection into the first linac is done through a fixed field injection chicane, with its last magnet  
5297 (closing the chicane) being placed at the beginning of the linac. It closes the orbit *bump* at the  
5298 lowest energy, injection pass, but the magnet (physically located in the linac) will deflect the  
5299 beam on all subsequent linac passes. In order to close the resulting higher pass *bumps*, the so-  
5300 called re-injection chicane is instrumented, by placing two additional opposing bends in front of  
5301 the last chicane magnet. The chosen arrangement is such that, the re-injection chicane magnets  
5302 are only *visible* by the higher pass beams. The second linac in the racetrack is configured exactly  
5303 as a mirror image of the first one, with a replica of the re-injection chicane at its end, which  
5304 facilitates a fixed-field extraction of energy recovered beam to the dump.

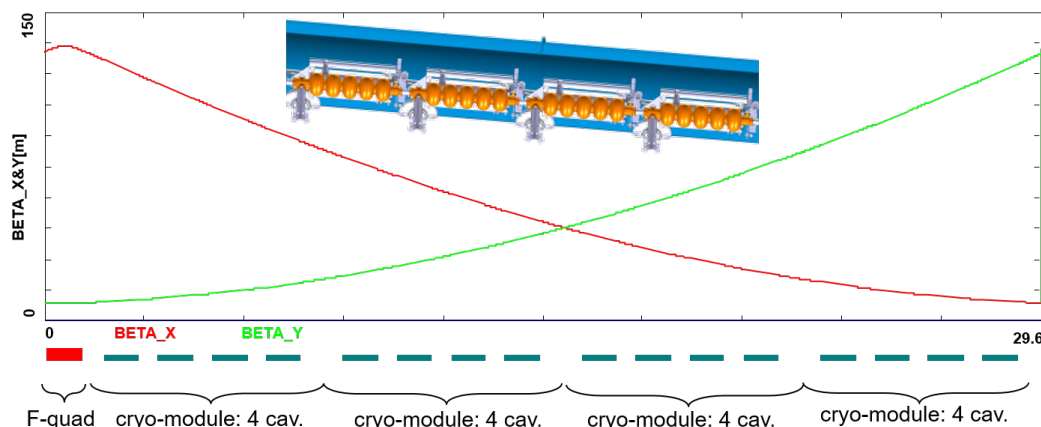


**Figure 8.2:** Layout of a half-cell composed out of four cryomodules (each hosting four, 5-cell cavities: top insert) and a focusing quad. Beta functions reflect 130° FODO optics.

### 5305 Linac Configuration and Multi-pass Optics

5306 Appropriate choice of the linac optics is of paramount importance for the transverse beam  
 5307 dynamics in a multi-pass ERL. The focusing profile along the linac (quadrupole gradients) need  
 5308 to be set (and they stay constant), so that multiple pass beams within a vast energy range may  
 5309 be transported efficiently. The chosen arrangement is such that adequate transverse focusing is  
 5310 provided for a given linac aperture. The linac optics is configured as a strongly focusing, 130°  
 5311 FODO. In a basic FODO cell a quadrupole is placed every four cryomodules, so that the full cell  
 5312 contains two groups of 16 RF cavities and a pair of quads (F, D) as illustrated in Fig. 8.2. The  
 5313 entire linac is built out of 14 such cells. Energy recovery in a racetrack topology explicitly requires  
 5314 that both the accelerating and decelerating beams share the individual return arcs [673]. This  
 5315 in turn, imposes specific requirements for TWISS function at the linacs ends: TWISS functions  
 5316 have to be identical for both the accelerating and decelerating linac passes converging to the  
 5317 same energy and therefore entering the same arc. There is an alternative scheme, proposed by  
 5318 Peter Williams [674], who has argued that it would be beneficial to separate the accelerating and  
 5319 decelerating arcs. This would simplify energy compensation systems and linac-to-arc matching,  
 5320 but at an higher cost of the magnetic system of the arcs. However, doubling number of arcs is  
 5321 a very costly proposition. On the other hand, C-BETA experiment is pioneering a multi-pass  
 5322 arcs to transport a vast energy range through the same beam-line and it still intends to use  
 5323 them for energy recovery. Our approach, based on proven, CEBAF-like, RLA technology [675]  
 5324 is somewhere in the 'middle'.

5325 To visualize beta functions for multiple accelerating and decelerating passes through a given  
 5326 linac, it is convenient to reverse the linac direction for all decelerating passes and string them  
 5327 together with the interleaved accelerating passes, as illustrated in Fig. 8.3. This way, the cor-  
 5328 responding accelerating and decelerating passes are joined together at the arc's entrance/exit.  
 5329 Therefore, the matching conditions are automatically built into the resulting multi-pass linac  
 5330 beamline. One can see that both linacs uniquely define the TWISS functions for the arcs: Linac  
 5331 1 fixes input to all odd arcs and output to all even arcs, while Linac 2 fixes input to all even  
 5332 arcs and output to all odd arcs. The optics of the two linacs are mirror-symmetric; They were  
 5333 optimised so that, Linac 1 is periodic for the first accelerating pass and Linac 2 has this feature  
 5334 for last decelerating one. In order to maximize the BBU threshold current [676], the optics is  
 5335 tuned so that the integral of  $\beta/E$  along the linac is minimised. The resulting phase advance per

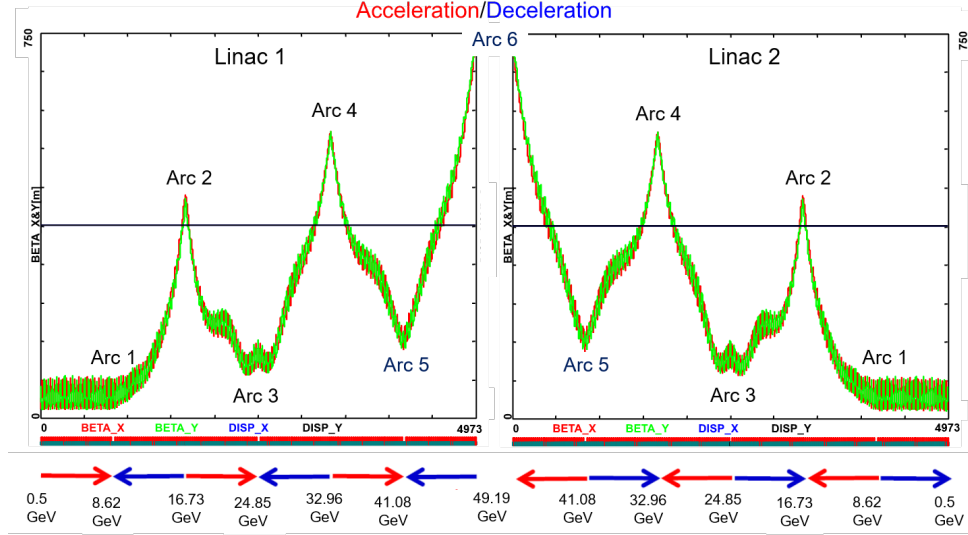


**Figure 8.3:** Beta function in the optimised multi-pass linacs (3 accelerating passes and 3 decelerating passes in each of two linacs). The matching conditions are automatically built into the resulting multi-pass linac beamline.

5336 cell is close to  $130^\circ$ . Non-linear strength profiles and more refined merit functions were tested,  
 5337 but they only brought negligible improvements.

### 5338 Recirculating Arcs – Emittance Preserving Optics

5339 Synchrotron radiation effects on beam dynamics, such as the transverse emittance dilution  
 5340 induced by quantum excitations have a paramount impact on the collider luminosity. All six  
 5341 horizontal arcs are accommodated in a tunnel of 536.4m radius. The transverse emittance  
 5342 dilution accrued through a given arc is proportional to the emittance dispersion function,  $H$ ,  
 5343 averaged over all arc's bends [677]:

$$\Delta\epsilon = \frac{2\pi}{3} C_q r_0 \langle H \rangle \frac{\gamma^5}{\rho^2}, \quad (8.1)$$

5344 where

$$C_q = \frac{55}{32\sqrt{3}} \frac{\hbar}{mc} \quad (8.2)$$

5345 and  $r_0$  is the classical electron radius and  $\gamma$  is the Lorentz boost. Here,  $H = (1 + \alpha^2)/\beta \cdot$   
 5346  $D^2 + 2\alpha DD' + \beta \cdot D'^2$  where  $D, D'$  are the bending plane dispersion and its derivative, with  
 5347  $\langle \dots \rangle = \frac{1}{\pi} \int_{\text{bends}} \dots d\theta$ .

5348 Therefore, emittance dilution can be mitigated through appropriate choice of arc optics (values  
 5349 of  $\alpha, \beta, D, D'$  at the bends). In the presented design, the arcs are configured with a FMC  
 5350 (Flexible Momentum Compaction) optics to ease individual adjustment of,  $\langle H \rangle$ , in various  
 5351 energy arcs.

5352 Optics design of each arc takes into account the impact of synchrotron radiation at different  
 5353 energies. At the highest energy, it is crucial to minimise the emittance dilution due to quantum  
 5354 excitations; therefore, the cells are tuned to minimise the emittance dispersion,  $H$ , in the bending  
 5355 sections, as in the TME (Theoretical Minimum Emittance) lattice. On the other hand, at the

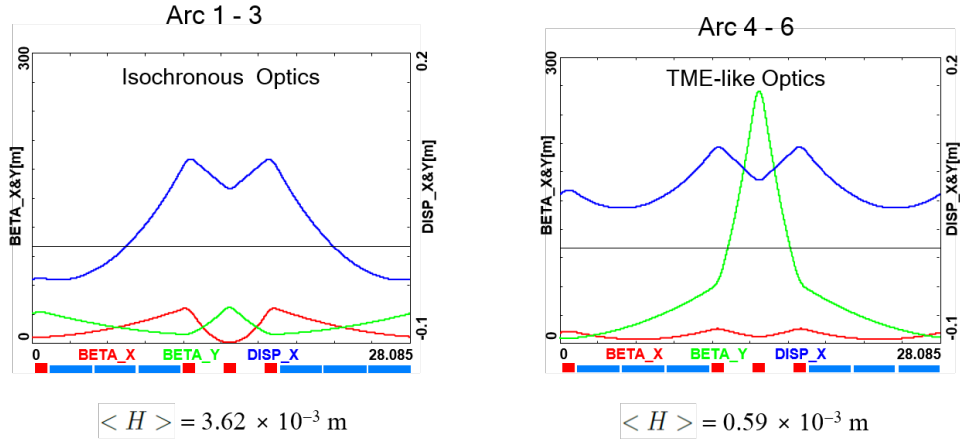


**Figure 8.4:** Two styles of FMC cells appropriate for different energy ranges. Left: lower energy arcs (Arc 1–3) configured with *Isochronous* cells, Right: higher energy arcs configured with *TME-like* cells. Corresponding values of the emittance dispersion averages,  $\langle H \rangle$ , are listed for both style cells.

5356 lowest energy, it is beneficial to compensate for the bunch elongation with isochronous optics.  
 5357 The higher energy arcs (4,5 and 6) configured with the TME cells are still quasi-isochronous. To  
 5358 fully compensate remnant bunch elongation one could set higher pass linacs slightly off-crest to  
 5359 compress the bunches, since one has full control of gang-phases for individual linac passes. All  
 5360 styles of FMC lattice cells, as illustrated in Fig. 8.4, share the same footprint for each arc. This  
 5361 allows us to stack magnets on top of each other or to combine them in a single design. Here,  
 5362 we use substantially shorter than in the 60 GeV design, 28.1 m, FMC cell configured with six  
 5363 3 m bends, in groups of flanked by a quadrupole singlet and a triplet, as illustrated in Fig. 8.4.  
 5364 The dipole filling factor of each cell is 63%; therefore, the effective bending radius  $\rho$  is 336.1 m.  
 5365 Each arc is followed by a matching section and a recombiner (mirror symmetric to spreader and  
 5366 matching section). Since the linacs are mirror-symmetric, the matching conditions described  
 5367 in the previous section, impose mirror-symmetric arc optics (identical betas and sign reversed  
 5368 alphas at the arc ends).

5369 Path-length adjusting chicanes were also foreseen to tune the beam time of flight in order to hit  
 5370 the proper phase at each linac injection. Later investigations proved them to be effective only  
 5371 with lower energy beams, as these chicanes trigger unbearable energy losses, if applied to the  
 5372 highest energy beams. A possible solution may consist in distributing the perturbation along  
 5373 the whole arc with small orbit excitations. This issue will be fully addressed in a subsequent  
 5374 section on 'Synchrotron Radiation Effects - Emittance Dilution'.

### 5375 **Spreaders and Recombiners**

5376 The spreaders are placed directly after each linac to separate beams of different energies and  
 5377 to route them to the corresponding arcs. The recombiners facilitate just the opposite: merging  
 5378 the beams of different energies into the same trajectory before entering the next linac. As  
 5379 illustrated in Fig. 8.5, each spreader starts with a vertical bending magnet, common for all  
 5380 three beams, that initiates the separation. The highest energy, at the bottom, is brought back  
 5381 to the horizontal plane with a chicane. The lower energies are captured with a two-step vertical  
 5382 bending adapted from the CEBAF design [675].

5383 Functional modularity of the lattice requires spreaders and recombiners to be achromats (both

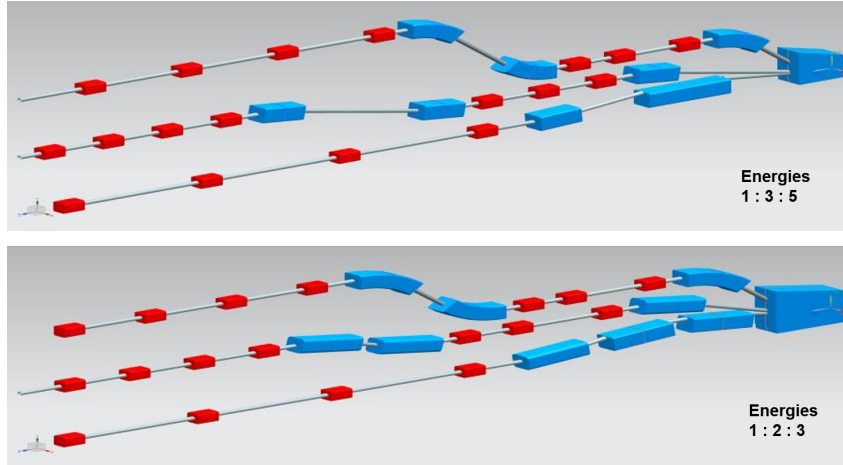


**Figure 8.5:** Layout of a three-beam switch-yard for different energy ratios: 1:3:5 and 1:2:3 corresponding to specific switch-yard geometries implemented on both sides of the racetrack

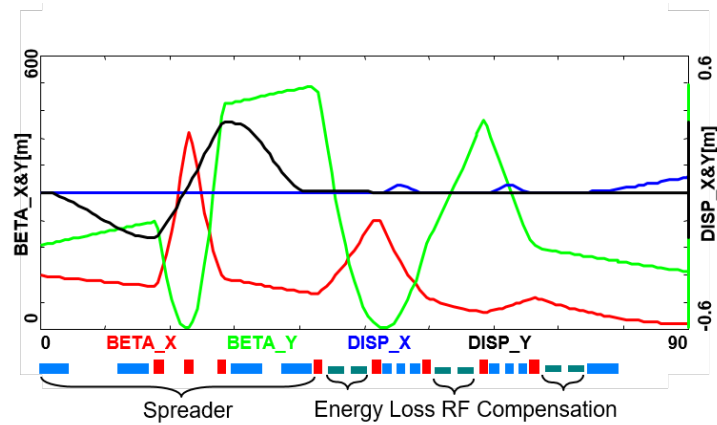


**Figure 8.6:** Spreader 3 (24.8 GeV) optics; featuring a vertical achromat with three dispersion suppressing quads in-between the two steps, a pair of path-length adjusting dogleg chicanes and four betatron matching quads, interleaved with three energy loss compensating sections (2-nd harmonic RF cavities marked in green).

5384 in the horizontal and vertical plane). To facilitate that, the vertical dispersion is suppressed by  
 5385 a pair of quadrupoles located in-between vertical steps; they naturally introduce strong vertical  
 5386 focusing, which needs to be compensated by the middle horizontally focusing quad. The overall  
 5387 spreader optics is illustrated in Fig. 8.6. Complete layout of two styles of switch-yard with  
 5388 different energy ratios is depicted in Fig. 8.5. Following the spreader, there are four matching  
 5389 quads to *bridge* the Twiss function between the spreader and the following 180° arc (two betas  
 5390 and two alphas). Combined spreader-arc-recombiner optics, features a high degree of modular  
 5391 functionality to facilitate momentum compaction management, as well as orthogonal tunability  
 5392 for both the beta functions and dispersion, as illustrated in Fig. 8.7.

### 5393 IR Bypasses

5394 After the last spreader the 49.19 GeV beam goes straight to the interaction region. However the  
 5395 lower energy beams; at 16.7 and 33.0 GeV, need to be further separated horizontally in order  
 5396 to avoid interference with the detector. Different design options for the bypass section were

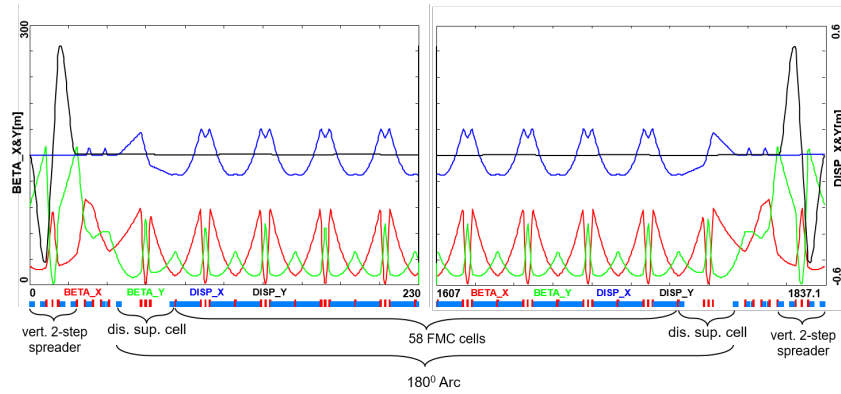


**Figure 8.7:** Complete Optics for Arc 3 (including switch-yard); featuring: low emittance 180° arc based on isochronous cells (30 cells flanked by dispersion suppression cell with missing dipoles on each side), spreaders and recombiners with matching sections and doglegs symmetrically placed on each side of the arc proper.

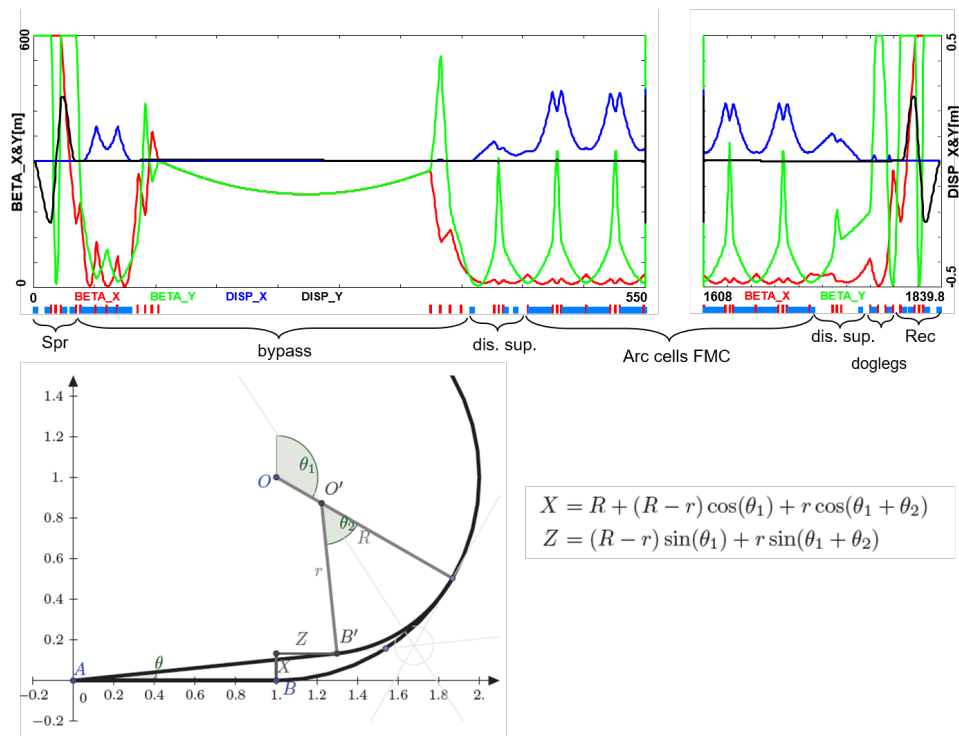


**Figure 8.8:** Optics and layout of Arc 4 including the detector bypass. The lattice (top insert) features a vertical spreader, an initial horizontal bending, a straight section, a modified dispersion suppressor, seven junction cells, and four regular cells. The bypass geometry (bottom insert), features a long IP line, AB, which for visual reasons has been purposely stretched, being actually about 1/5 of the arc radius. All geometric dependencies of the bypass parameters are summarized in the inserted formulae.

5397 explored [678] and the one that minimises the extra bending has been chosen and implemented  
 5398 in the lattice.

5399 Ten arc-like dipoles are placed very close to the spreader, to provide an initial bending,  $\theta$ , which  
 5400 results in  $X = 10$  m separation from the detector located 120 m downstream. The straight  
 5401 section of the bypass is approximately 240 m long. After the bypass, in order to reconnect to  
 5402 the footprint of Arc 6, 7 of 30 standard cells in Arc 2 and Arc 4 are replaced with 7 higher field,  
 5403 junction cells. The number of junction cells is a compromise between the field strength increase  
 5404 and the length of additional bypass tunnel, as can be inferred from the scheme summarised in  
 5405 Fig. 8.8. The stronger bending in the junction cells creates a small mismatch, which is corrected  
 5406 by adjusting the strengths of the quadrupoles in the last junction cell and in the first regular  
 5407 cell.

## 5408 Synchrotron Radiation Effects – Emittance Dilution

5409 ERL efficiency as a source of multi-GeV electrons for a high luminosity collider is limited by the  
 5410 incoherent synchrotron radiation effects on beam dynamics; namely the transverse emittance  
 5411 dilution and the longitudinal momentum spread (induced by quantum excitations). The first  
 5412 effect, the transverse emittance increase, will have a paramount impact on the collider luminosity,  
 5413 due to stringent limits on the allowed emittance increase. The second one, accrued momentum  
 5414 spread, governs asymmetries of accelerated and decelerated beam profiles. These asymmetries  
 5415 substantially complicate multi-pass energy recovery and matching, and ultimately they limit the  
 5416 energy reach of the ERLs due to recirculating arc momentum acceptance.

5417 Arc optics was designed to ease individual adjustment of momentum compaction (needed for the  
 5418 longitudinal phase-space control, essential for operation with energy recovery) and the horizontal  
 5419 emittance dispersion,  $H$ , in each arc. Tab. 8.2 lists arc-by-arc dilution of the transverse,  $\Delta\epsilon$ , and  
 5420 longitudinal,  $\Delta\sigma_{\frac{\Delta E}{E}}$ , emittance due to quantum excitations calculated using analytic formulas,  
 5421 Eqs. (8.3), (8.4) and (8.5), introduced by M. Sands [677]:

$$\Delta E = \frac{2\pi}{3} r_0 m c^2 \frac{\gamma^4}{\rho} \quad (8.3)$$

5422

$$\Delta\epsilon_N = \frac{2\pi}{3} C_q r_0 \langle H \rangle \frac{\gamma^6}{\rho^2}, \quad (8.4)$$

5423

$$\frac{\Delta\epsilon_E^2}{E^2} = \frac{2\pi}{3} C_q r_0 \frac{\gamma^5}{\rho^2}, \quad (8.5)$$

5424 where  $C_q$  is given by Eq. (8.2). Here,  $\Delta\epsilon_E^2$  is an increment of energy square variance,  $r_0$  is  
 5425 the classical electron radius,  $\gamma$  is the Lorentz boost and  $C_q \approx 3.832 \cdot 10^{-13}$  m for electrons (or  
 5426 positrons).

5427 Apart from the horizontal  $180^\circ$  arcs, there are other sources of emittance dilution due to syn-  
 5428 chrotron radiation, namely vertical Spreaders and Recoiners, as well as horizontal 'Doglegs'  
 5429 used to compensate seasonal variation of path-length. To minimise their contribution to the ver-  
 5430 tical emittance dilution, special optics with small vertical  $\langle H \rangle$  has been introduced in Spr/Rec  
 5431 sections. The effects on vertical emittance dilution coming from these beamlines (Spr/Rec) are  
 5432 summarized in Tab. 8.3.

5433 Similarly, the horizontal emittance dilution induced by the Doglegs (four dogleg chicanes per  
 5434 arc) in various arcs is summarized in Tab. 8.4. Each dogleg chicane is configured with four 1

Beamline	Beam energy [GeV]	$\Delta E$ [MeV]	$\Delta\epsilon_N^x$ [mm mrad]	$\Delta\sigma_{\frac{\Delta E}{E}}$ [%]
arc 1	8.62	0.7	0.0016	0.0005
arc 2	16.73	10	0.085	0.0027
arc 3	24.85	49	0.91	0.0072
arc 4	32.96	152	0.81	0.015
arc 5	41.08	368	3.03	0.026
arc 6	49.19	758	8.93	0.040

**Table 8.2:** Energy loss and emittance dilution (horizontal and longitudinal) due to synchrotron radiation generated by all six 180° arcs (not including Spreaders, Recombiners and Doglegs). Here,  $\Delta\sigma_{\frac{\Delta E}{E}} = \sqrt{\frac{\Delta\epsilon_E^2}{E^2}}$

Beamline	Beam energy [GeV]	$\Delta E$ [MeV]	$\Delta\epsilon_N^y$ [mm mrad]	$\Delta\sigma_{\frac{\Delta E}{E}}$ [%]
Spr/Rec 1	8.62	0.2	0.035	0.0008
Spr/Rec 2	16.73	3.0	0.540	0.0044
Spr/Rec 3	24.85	6.0	0.871	0.0066
Spr/Rec 4	32.96	21.6	5.549	0.0143
Spr/Rec 5	41.08	7.1	0.402	0.0062
Spr/Rec 6	49.19	39.2	3.92	0.0205

**Table 8.3:** Energy loss and emittance dilution (vertical and longitudinal) due to synchrotron radiation generated by a Spreader, or Recombiner of a given arc. Here,  $\Delta\sigma_{\frac{\Delta E}{E}} = \sqrt{\frac{\Delta\epsilon_E^2}{E^2}}$

5435 meter bends (1 Tesla each), so that they bend the lowest energy beam at 8.6 GeV by 2 degrees.  
5436 The corresponding path-lengths gained in the Doglegs of different arcs are also indicated.

Beamline	Beam energy [GeV]	$\Delta E$ [MeV]	$\Delta\epsilon_N^x$ [mm mrad]	$\Delta\sigma_{\frac{\Delta E}{E}}$ [%]	path-length [mm]
Doglegs 1	8.62	2	0.201	0.007	7.32
Doglegs 2	16.73	9	0.667	0.009	1.96
Doglegs 3	24.85	19	5.476	0.014	0.84
Doglegs 4	32.96	33	5.067	0.014	0.52
Doglegs 5	41.08	52	12.067	0.028	0.36
Doglegs 6	49.19	74	2.836	0.011	0.28

**Table 8.4:** Energy loss and emittance dilution (horizontal and longitudinal) due to synchrotron radiation generated by the Doglegs (four dogleg chicanes) of a given arc. Here,  $\Delta\sigma_{\frac{\Delta E}{E}} = \sqrt{\frac{\Delta\epsilon_E^2}{E^2}}$

5437 As indicated in Tab. 8.4, the Doglegs in the highest energy arcs, Arc 5 and Arc 6, provide only  
5438 sub mm path-length gain with large synchrotron radiation effects. They are not very effective  
5439 and generate strong, undesired emittance dilution. Therefore, it is reasonable to eliminate them  
5440 from both Arc 5 and 6. Instead, one could resort to an alternative path-length control via  
5441 appropriate orbit steering with both horizontal and vertical correctors present at every girder  
5442 and distributed evenly throughout the arc.

5443 Combining all three contributions: (180° arc, Spreader, Recombiner and Doglegs (no Doglegs in  
5444 Arcs 5 and 6), the net cumulative emittance dilution is summarized in Tab. 8.5.

Beamline	Beam energy [GeV]	$\Delta E$ [MeV]	$\Delta^{\text{cum}}\epsilon_N^x$ [mm mrad]	$\Delta^{\text{cum}}\epsilon_N^y$ [mm mrad]	$\Delta^{\text{cum}}\sigma_{\frac{\Delta E}{E}}$ [%]
Arc 1	8.62	3	0.2	0.1	0.01
Arc 2	16.73	25	1.0	1.2	0.03
Arc 3	24.85	80	7.3	2.9	0.06
Arc 4	32.96	229	13.2	14.0	0.12
Arc 5	41.08	383	16.2	14.8	0.16
<b>IR</b>	49.19	39	<b>16.2</b>	<b>18.7</b>	<b>0.18</b>
Arc 6	49.19	797	25.2	22.6	0.24
Arc 5	41.08	383	28.2	23.4	0.28
Arc 4	32.96	229	34.1	34.5	0.33
Arc 3	24.85	80	40.5	36.3	0.37
Arc 2	16.73	25	41.2	37.4	0.39
Arc 1	8.62	3	41.4	37.4	0.40
Dump	0.5		41.4	37.4	0.40

**Table 8.5:** Energy loss and cumulative emittance dilution (transverse and longitudinal) due to synchrotron radiation at the end of a given beam-line (complete Arc including: 180° arc, Spreader, Recombiner and Doglegs in arcs 1-4). The table covers the entire ER cycle: 3 passes 'up' + 3 passes 'down'. Cumulative emittance dilution values just before the IP (past Arc 5 and Spr 6), which are critical for the luminosity consideration are highlighted in 'bold'. That row accounts for contributions from Spr 6 (the last bending section before the IR) to energy loss, as well as the vertical and longitudinal emittance dilutions. Here,  $\Delta\sigma_{\frac{\Delta E}{E}} = \sqrt{\frac{\Delta\epsilon_E^2}{E^2}}$

5445 Tab. 8.5 shows, the LHeC luminosity requirement of total transverse emittance dilution in either  
5446 plane (normalized) at the IP (at the end of Arc 5), not to exceed 20 mm mrad (hor: 16.2 mm mrad  
5447 and ver: 18.7 mm mrad) is met by-design, employing presented low emittance lattices in both  
5448 the arcs and switch-yards.

5449 Finally, one can see from Eqs. (8.4) and (8.5) an underlying universal scaling of the transverse  
5450 (unnormalized) and longitudinal emittance dilution with energy and arc radius; they are both  
5451 proportional to  $\gamma^5/\rho^2$ . This in turn, has a profound impact on arc size scalability with energy;  
5452 namely the arc radius should scale as  $\gamma^{5/2}$  in order to preserve both the transverse and longi-  
5453 tudinal emittance dilutions, which is a figure of merit for a synchrotron radiation dominated  
5454 ERL.

### 5455 8.2.2 30 GeV ERL Options

5456 One may think of an upgrade path from 30 to 50 GeV ERL, using the same 1/5 of the LHC  
5457 circumference (5.4 km), footprint. In this scenario, each linac straight (front end) would initially  
5458 be *loaded* with 18 cryomodules, forming two 5.21 GV linacs. One would also need to decrease  
5459 the injector energy by factor of 5.21/8.11. The top ERL energy, after three passes, would reach  
5460 31.3 GeV. Then for the upgrade to 50 GeV, one would fill the remaining space in the linacs  
5461 with additional 10 cryomodules each; 2.9 GV worth of RF in each linac. This way the energy  
5462 ratios would be preserved for both 30 and 50 GeV ERL options, so that the same switch-yard  
5463 geometry could be used. Finally, one would scale up the entire lattice; all magnets (dipoles and  
5464 quads) by 8.11/5.21 ratio. If one wanted to stop at the 30 GeV option with no upgrade path,  
5465 then the 1/12 of the LHC circumference (2.2 km) would be a viable footprint for the racetrack,  
5466 featuring: two linacs, 533 m each, (18 cryomodules) and arcs of 136 m radius. Again, assuming  
5467 0.32 GeV injection energy, the top ERL energy would reach 31.3 GeV.

5468 **8.2.3 Component Summary**

5469 This closing section will summarise active accelerator components: magnets (bends and quads)  
 5470 and RF cavities for the 50 GeV baseline ERL. The bends (both horizontal and vertical) are  
 5471 captured in Tab. 8.6, while the quadrupole magnets and RF cavities are collected in Tab. 8.7.

5472 One would like to use a combined aperture (3-in-one) arc magnet design with 50 cm vertical  
 5473 separation between the three apertures, proposed by Attilio Milanese [679]. That would reduce  
 5474 net arc bend count from 2112 to 704. As far as the Spr/Rec vertical bends are concerned, the  
 5475 design was optimised to include an additional common bend separating the two highest passes.  
 5476 So, there are a total of 8 trapezoid B-com magnets, with second face tilted by 3° and large 10 cm  
 5477 vertical aperture, the rest are simple rectangular bends with specs from the summary Tab. 8.6.

Section	Arc dipoles (horiz.)				Spr/Rec dipoles (vert.)				<i>Dogleg</i> dipoles (horiz.)			
	<i>N</i>	<i>B</i> [T]	<i>g</i> /2[cm]	<i>L</i> [m]	<i>N</i>	<i>B</i> [T]	<i>g</i> /2[cm]	<i>L</i> [m]	<i>N</i>	<i>B</i> [T]	<i>g</i> /2[cm]	<i>L</i> [m]
Arc 1	352	0.087	1.5	3	8	0.678	2	3	16	1	1.5	1
Arc 2	352	0.174	1.5	3	8	0.989	2	3	16	1	1.5	1
Arc 3	352	0.261	1.5	3	6	1.222	2	3	16	1	1.5	1
Arc 4	352	0.348	1.5	3	6	1.633	2	3	16	1	1.5	1
Arc 5	352	0.435	1.5	3	4	1.022	2	3				
Arc 6	352	0.522	1.5	3	4	1.389	2	3				
Total	2112				36				64			

**Table 8.6:** 50 GeV ERL – Dipole magnet count along with basic magnet parameters: Magnetic field (*B*), Half-Gap (*g*/2), and Magnetic length (*L*).

Section	Quadrupoles				RF cavities			
	<i>N</i>	<i>G</i> [T/m]	<i>a</i> [cm]	<i>L</i> [m]	<i>N</i>	<i>f</i> [MHz]	cell	<i>G</i> <sub>RF</sub> [T/m]
Linac 1	29	1.93	3	1	448	802	5	20
Linac 2	29	1.93	3	1	448	802	5	20
Arc 1	255	9.25	2.5	1				
Arc 2	255	17.67	2.5	1				
Arc 3	255	24.25	2.5	1	6	1604	9	30
Arc 4	255	27.17	2.5	1	12	1604	9	30
Arc 5	249	33.92	2.5	1	18	1604	9	30
Arc 6	249	40.75	2.5	1	36	1604	9	30
Total	1576				968			

**Table 8.7:** 50 GeV ERL – Quadrupole magnet and RF cavities count along with basic magnet/RF parameters: Magnetic field gradient (*G*), Aperture radius (*a*), Magnetic length (*L*), Frequency (*f*), Number of cells in RF cavity (cell), and RF Gradient (*G*<sub>RF</sub>).

5478 **8.3 Electron-Ion Collisions**

5479 Besides colliding proton beams, the LHC also provides collisions of nuclear (fully-stripped ion)  
 5480 beams with each other (AA collisions) or with protons (*pA*). Either of these operating modes  
 5481 offers the possibility of electron-ion (*eA*) collisions in the LHeC configuration<sup>1</sup>

<sup>1</sup> In *pA* operation of the LHC the beams may be reversed (*Ap*) for some part of the operating time. Only one direction (ions in Beam 2) would provide *eA* collisions while the other would provide *ep* collisions at significantly

5482 Here we summarise the considerations leading to the luminosity estimates given in Tab. 2.4 for  
5483 collisions of electrons with  $^{208}\text{Pb}^{82+}$  nuclei, the nominal heavy ion species collided in the LHC.  
5484 Other, lighter, nuclei are under consideration for future LHC operation [429] and could also be  
5485 considered for electron-ion collisions.

5486 The heavy ion beams that the CERN injector complex can provide to the LHC, the HE-LHC  
5487 and the FCC provide a unique basis for high energy, high luminosity deep inelastic electron-ion  
5488 scattering physics. Since HERA was restricted to protons only, the LHeC or FCC-eh would  
5489 extend the kinematic range in  $Q^2$  and  $1/x$  by 4 or 5 orders of magnitude. This is a huge increase  
5490 in coverage and would be set to radically change the understanding of parton dynamics in nuclei  
5491 and of the formation of the quark gluon plasma.

5492 An initial set of parameters in the maximum energy configurations was given in [32]. The  
5493 Pb beam parameters are essentially those foreseen for operation of the LHC (or HL-LHC)  
5494 in Run 3 and Run 4 (planned for the 2020s). These parameters have already been largely  
5495 demonstrated [680] except for the major remaining step of implementing slip-stacking injection  
5496 in the SPS which would reduce the basic bunch spacing from 100 to 50 ns [681]. With respect  
5497 to the proton spacing of 25 ns, this allows the electron bunch intensity to be doubled while still  
5498 respecting the limit on total electron current. In fact, without the slip-stacking in the SPS,  
5499 the initial luminosity would be the same with a 100 ns Pb spacing (and quadrupled electron  
5500 bunch intensity). However one must remember that the evolution of the Pb beam intensity will  
5501 be dominated by luminosity burn-off by the concurrent PbPb collisions at the other interaction  
5502 points and integrated luminosity for both PbPb and ePb collisions will be higher with the higher  
5503 total Pb intensity. The details of this will depend on the operating scenarios, number of active  
5504 experiments, etc, and are not considered further here. The time-evolution of eA luminosity will  
5505 be determined by that of PbPb and pPb collisions, as discussed, for example, in Ref. [14,429,682].

5506 Combining these assumptions with the default 50 GeV electron ERL for LHeC and 60 GeV for  
5507 FCC-eh, yields the updated parameter sets and initial luminosities given in Tab. 2.4, earlier in  
5508 the present report.

5509 Radiation damping of Pb beams in the hadron rings is about twice as fast as for protons and can  
5510 be fully exploited since it takes longer to approach the beam-beam limit at the PbPb collisions  
5511 points. For the case of the FCC-hh [14], one can expect the emittance values in Tab. 2.4 to be  
5512 reduced during fills [14, 429, 682].

5513 The Pb beam will be affected by ultraperipheral collision effects, mainly bound-free pair pro-  
5514 duction and Coulomb dissociation of the nuclei, induced by the electromagnetic fields of the  
5515 electrons, seen as pulses of virtual photons. The relevant cross-sections will be similar to those  
5516 in pPb collisions which are down by a factor of  $Z^2$  compared to those in PbPb collisions and  
5517 can be neglected in practice.

## 5518 8.4 Beam-Beam Interactions

5519 In the framework of the Large Hadron electron Collider, the concept of an Energy Recirculating  
5520 Linac (ERL) allows to overcome the beam-beam limit that one would face in a storage ring. The  
5521 electron beam can be heavily disturbed by the beam collision process, while the large acceptance  
5522 of the ERL will still allow for a successful energy recovery during the deceleration of the beam  
5523 so that the power consumption is minimised. In order to compare the relevant beam-beam

---

reduced luminosity compared to the  $pp$  mode, since there would be fewer proton bunches of lower intensity.

5524 parameters and put them into the context of other colliders, two tables are shown highlighting,  
 5525 on the one hand, the parameters from LEP and LHC runs in Tab. 8.8, and on the other hand,  
 5526 the parameters planned for LHeC at HL-LHC in Tab. 8.9.

Parameter	Unit	LEP	LHC
Beam sizes $\sigma_x / \sigma_y$	$\mu\text{m}$	180 / 7	16.6 / 16.6
Intensity	$10^{11}$ particles/bunch	4.00	1.15
Energy	GeV	100	7000
$\beta_x^*/\beta_y^*$	cm	125/5	55/55
Crossing angle	$\mu\text{rad}$	0	0/285
Beam-beam tune shift $\Delta Q_x/\Delta Q_y$		0.0400/0.0400	0.0037/0.0034
Beam-beam parameter $\xi$		0.0700	0.0037

**Table 8.8:** Comparison of parameters for the LEP collider and LHC. Taken from CDR 2012, p.286.

Beam parameter	Unit	LHeC at HL-LHC	
		Proton beam	Electron beam
Energy	GeV	7000	49.19
Normalized emittance	mm·mrad	2.5	50
Beam sizes $\sigma_{x,y}$	$\mu\text{m}$	5.8	5.8
Intensity	$10^9$ particles/bunch	220.00	3.12
Bunch length $\sigma_s$	mm	75.5	0.6
$\beta_{x,y}^*$	cm	10.00	6.45
Disruption factor		$1.2 \times 10^{-5}$	14.5
Beam-beam parameter $\xi$		$1.52 \times 10^{-4}$	0.99

**Table 8.9:** Comparison of parameters for the LHeC at HL-LHC. The parameters presented correspond to the default design.

5527 In the case of LHeC, the  $\beta$ -functions at the interaction point are chosen such that the transverse  
 5528 beam sizes of the  $e^-$  and  $p^-$  beams are equal in both transverse planes. Although the proton and  
 5529 electron emittances are different, the beta functions at the interaction point are set accordingly  
 5530 so that the two beams conserve  $\sigma_x^e = \sigma_x^p$  and  $\sigma_y^e = \sigma_y^p$ .

#### 5531 8.4.1 Effect on the electron beam

5532 The disruption parameter for the electron beam is of the order of 14.5 which corresponds, in  
 5533 linear approximation, to almost 2 oscillations of the beam envelope within the proton bunch.  
 5534 The non linearity of the interaction creates a distortion of the phase space and a mismatch from  
 5535 the design optics (see Fig. 8.9). The mismatch and distortion can be minimized by tuning the  
 5536 Twiss parameters ( $\alpha^*, \beta^*$ ) at the interaction point.

5537 In a series of studies the optics parameters of the electron beam were tracked back to the  
 5538 interaction point in presence of the beam-beam forces in order to show the impact of the beam-  
 5539 beam effect for different values of the electron Twiss parameters at the IP. In addition, the  
 5540 influence of a waist shift from the IP (proportional to  $\alpha^*$ ), similar to changing the foci of the  
 5541 interacting beams, has been studied and allows to keep the electron beam for a longer time  
 5542 within the proton bunch, thus optimizing the luminosity. The modification of the electron  
 5543 beta function ( $\beta^*$ ) leads to more freedom and gives access, among all the possibilities, to two  
 5544 different optima regarding the luminosity and the mismatch from the design optics. The results  
 5545 are summarized in the contour plots of Fig. 8.10.

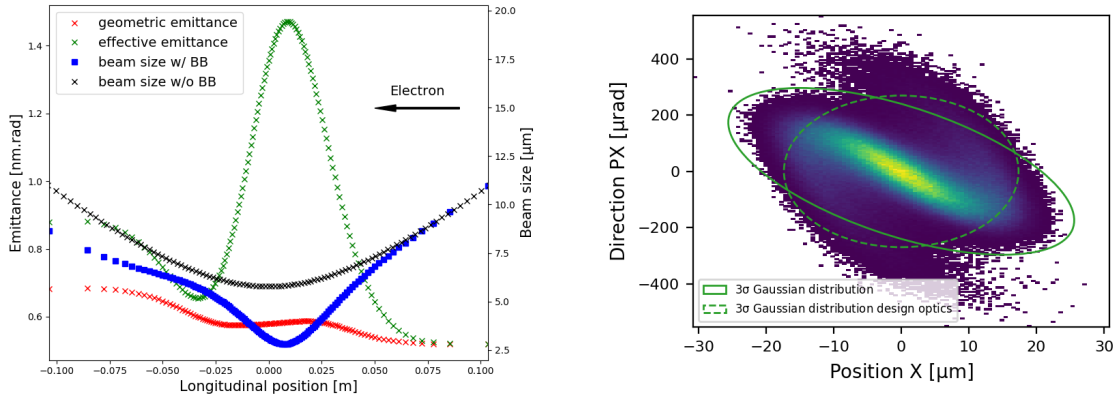


**Figure 8.9:** Left: Electron beam sizes with (blue) and without (black) the beam-beam forces exerted on the electron beam. The geometric emittance is represented in red and the effective emittance that takes into account the mismatch from the original optics is illustrated in green. Right: The horizontal phase space of the spent electron distribution backtracked to the interaction point.  $3\sigma$  Gaussian distributions are highlighted for the post-collided distribution (solid line) and the design optics (dashed line).

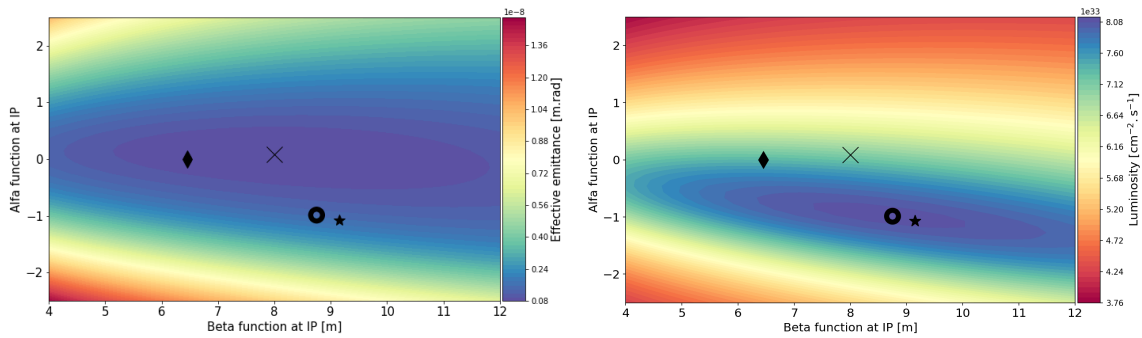


**Figure 8.10:** Left : Contour plot describing the effective emittance post collision as a function of the alfa and beta functions at IP. Right : Contour plot describing the luminosity as a function of the alfa and beta functions at the IP. The diamond marker represents the initial Twiss parameters, the circle shows the luminosity optimum, the cross symbolizes the smallest mismatch from the original optics and the star illustrates the minimal geometric emittance growth.

5546 As a consequence, the Twiss parameters at the interaction point can be set in a way, to minimize  
 5547 the mismatch of the optics (i.e. the effective emittance) or to maximize the luminosity. In case  
 5548 the optimization of the luminosity is chosen (see the circle marker in Fig. 8.10), a modified  
 5549 capture optics in the beam transfer to the arc structure will be needed to re-match the modified  
 5550 Twiss functions perturbed by the non-linear beam-beam effects.

5551 The effect of possible offsets between the two colliding beams has been characterized in previous  
 5552 beam-beam studies [683], and – if uncorrected – might lead to an electron beam emittance  
 5553 growth. The parameters for these studies have been updated and the results are presented in  
 5554 Fig. 8.11. As any offset between the two beams is amplified, it results in a larger increase of the  
 5555 beam envelope. As a solution, a fast feed-forward system is proposed, across the Arc 6, which  
 5556 would aim at damping the transverse motion so that the beam emittance can be recovered.  
 5557 Using two sets of kickers placed at the center and at the end of the arc, an offset of  $0.16\sigma$  can be  
 5558 damped. A single set cutting across the whole arc can correct a  $1\sigma$  offset with approximately  
 5559 4.4 kV.

5560 Additionally, the coupling of the beam-beam effect with long range wakefields has been ad-

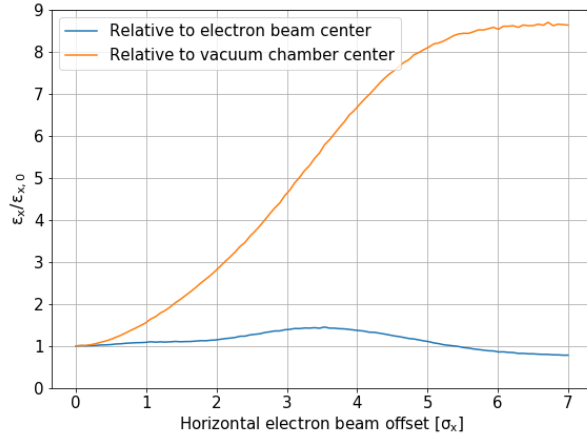


**Figure 8.11:** Electron beam emittance relative change with respect to its centroid (blue) and with respect to the vacuum chamber center (orange).

5561 dressed [683]. Assuming a misaligned bunch injected among a train of nominal bunches, the  
 5562 coupling of the beam-beam effect with the wakefields leads to a reduction of the damping of  
 5563 the excitation created by the misaligned bunch. Nevertheless it can be shown that the beam  
 5564 stability is conserved and the total amplification remains acceptable with respect to the study  
 5565 that was not considering the coupling.

#### 5566 8.4.2 Effect on the proton beam

5567 The beam-beam interaction between the electron and proton beams is asymmetric in terms of  
 5568 beam rigidities. Although the less energetic 49.19 GeV electron beam is heavily distorted by the  
 5569 strong 7 TeV proton beam, the proton beam will suffer from an emittance growth adding up  
 5570 turn by turn [683] due to the build up of the tiny disruption created by the offset between the  
 5571 beams. In fact, the previous studies gave a growth rate of around 0.01 %/s for a jitter of  $0.2 \sigma_x$ .  
 5572 As long as an adequate control of the bunches is preserved, this effect should lie in the shadow  
 5573 of other effects leading to emittance blow-up in the LHC (e.g. IBS). Since the electron beam  
 5574 energy decreased from 60 GeV to 49.19 GeV this study needs to be updated and the results  
 5575 should remain in agreement with the previous statement.

### 5576 8.5 Arc Magnets

5577 In this section, a conceptual design of the main magnets needed for the Linac-Ring (LR) accel-  
 5578 erator at 50 GeV is described. The number and types of magnets is listed in Tabs. 8.6 and 8.7.

#### 5579 8.5.1 Dipole magnets

5580 The bending magnets are used in the arcs of the recirculator. Each of the six arcs needs 352  
 5581 horizontal bending dipoles. Additional dipoles are needed in the straight sections: 36 vertical  
 5582 bending dipoles in the spreader/recombiner and 64 horizontal bending dipoles for the “dogleg”.  
 5583 These magnets are not considered at the moment.

5584 In the CDR issued in 2012 for a 60 GeV lepton ring (LR) , a design based on three independent  
 5585 dipoles stacked on top of each other was proposed. A post-CDR design with three apertures  
 5586 dipoles was introduced in 2014 [679]. This solution allows reducing the Ampere-turns and the  
 5587 production cost of the dipoles. For a 50 GeV LR, the three apertures dipole design is adapted  
 5588 to fulfil new magnetic field requirements.

5589 The 352 horizontal bending dipoles needed for each arc, combined in three apertures dipoles re-  
 5590 sult in a total of 704 units. These magnets are 3 m long and provide a field in the 30 mm aperture  
 5591 ranging from 0.087 T to 0.522 T depending on the arc energy, from 8.62 GeV to 49.19 GeV.

Parameter	Unit	Value
Beam energy	GeV	8.62 to 49.19
Magnetic field	T	0.087 to 0.522
Magnetic length	m	3
Vertical aperture	mm	30
Pole width	mm	90
Number of apertures		3
Distance between apertures	mm	500
Mass	8000	kg
Number of magnets		704
Current	A	4250
Number of turns per magnet		4
Current density	A/mm <sup>2</sup>	1
Conductor material		aluminum
Magnet resistance	mΩ	0.17
Power	kW	3
Total power consumption six arcs	MW	2.1
Cooling		air

**Table 8.10:** 50 GeV ERL – Main parameters of the three apertures bending magnets.

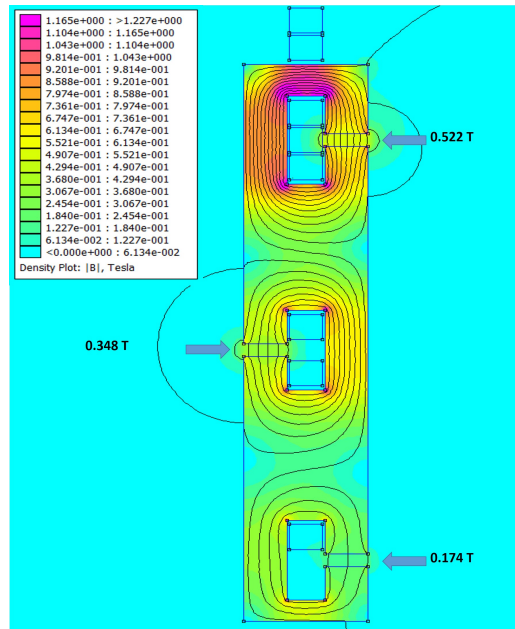


**Figure 8.12:** 50 GeV ERL - Cross section of the three apertures bending magnet, arc 2, 4 and 6 with 500 mm between consecutive arcs - Finite Element Method (FEM).

5592 In the proposed design, the three apertures are stacked vertically but offset transversely. This  
5593 allows recycling the Ampere-turns from one aperture to the other. The coils are centrally located  
5594 on the yoke and are made of simple aluminium bus-bars all powered in series. A current density  
5595 of  $1 \text{ A/mm}^2$  in the coils is sufficiently low to not have water-cooling but in order to limit the  
5596 temperature in the tunnel it may be required. Trim coils can be added on two of the apertures  
5597 to provide some tuning. Alternatively, each stage could be powered separately. The dipole yokes  
5598 are made of low carbon steel plates. The relevant parameters are summarised in Tab. 8.10 and  
5599 the cross section is illustrated in Fig. 8.12 for 500 mm between consecutive arcs.

## 5600 8.5.2 Quadrupole magnets

### 5601 Quadrupoles for recirculator arcs

5602 In total 1518 quadrupoles are needed for the recirculator arcs: 255 for each of the arcs one to four  
5603 and 249 for each of the arcs five and six. The required integrated gradients, comprised between  
5604 9.25 T and 40.75 T, can be achieved using one type of quadrupole one meter long. However,  
5605 instead of operating the magnets at low current for lower arcs energy, it can be considered to  
5606 have a shorter model 0.6 meter long for arcs one to three. These quadrupoles require water-  
5607 cooling for the coils. The relevant parameters are summarised in Tab. 8.11 and the cross section  
5608 is illustrated in Fig. 8.13 (left).

5609 In order to reduce the power consumption, it could be envisaged to use a hybrid configuration  
5610 for the quadrupoles, with most of the excitation given by permanent magnets. The gradient  
5611 strength could be varied by trim coils or by mechanical methods.

Parameter	Unit	Value
Beam energy	GeV	8.62 to 49.19
Field gradient	T/m	9.25 to 40.75
Magnetic length	m	1
Aperture radius	mm	25
Mass	kg	550
Number of magnets		1518
Current at 40.75 T/m	A	560
Number of turns per pole		17
Current density at 40.75 T/m	A/mm <sup>2</sup>	6.7
Conductor material		copper
Magnet resistance	mΩ	33
Power at 8.62 GeV	kW	0.5
Power at 16.73 GeV	kW	1.9
Power at 24.85 GeV	kW	3.7
Power at 32.96 GeV	kW	4.6
Power at 41.08 GeV	kW	7.2
Power at 49.19 GeV	kW	10.3
Total power consumption six arcs	MW	7.1
Cooling		water

**Table 8.11:** 50 GeV ERL – Main parameters of the arc quadrupoles.

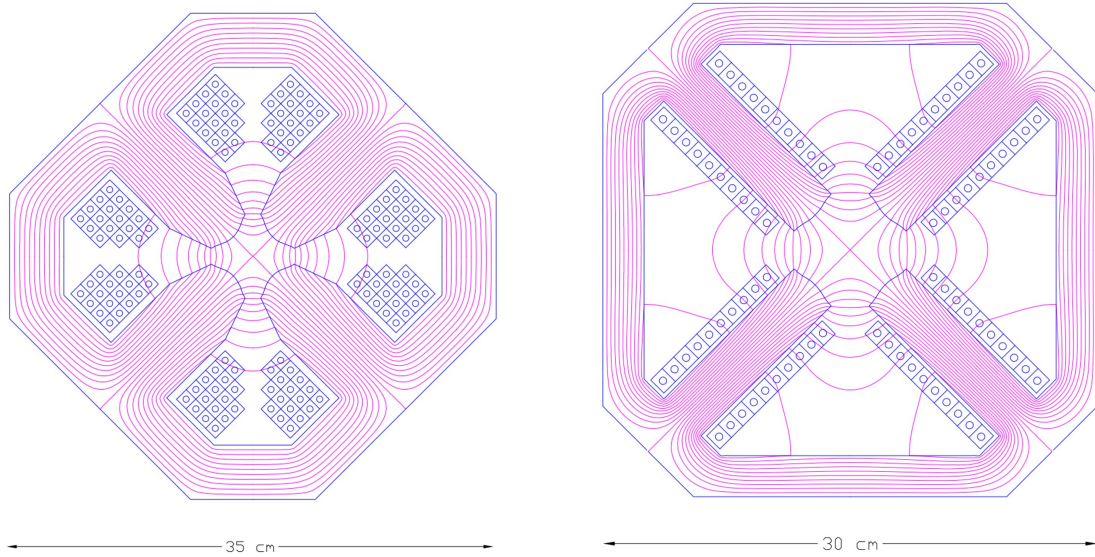


**Figure 8.13:** 50 GeV ERL. Left: Cross section of the arc quadrupole magnets. Right: Cross section of the linac quadrupole magnets.

## 5612 Quadrupoles for the two 8.1 GeV linacs

5613 In the two 8.1 GeV linacs, 29 + 29 quadrupoles, each providing 1.93 T integrated strength are  
 5614 required. The present design solution considers 30 mm aperture radius magnets. The relevant  
 5615 parameters are summarised in Tab. 8.12 and the cross section is illustrated in Fig. 8.13 (right).

Parameter	Unit	Value
Beam energy	GeV	8.62 to 49.19
Field gradient	T/m	7.7
Magnetic length	m	0.25
Aperture radius	mm	30
Mass	kg	110
Number of magnets		56
Current at 7.7 T/m	A	285
Number of turns per pole		10
Current density at 7.7 T/m	A/mm <sup>2</sup>	3
Conductor material		copper
Magnet resistance	mΩ	6
Power at 8.1 GeV	kW	0.5
Total power consumption 2 linacs	MW	0.03
Cooling		water

**Table 8.12:** 50 GeV ERL – Main parameters of the linac quadrupoles.

## 5616 8.6 LINAC and SRF

5617 Each of the two main linacs has an overall length of 828.8 m and provides an acceleration of  
 5618 8.114 GV. Each linac consists of 112 cryomodules, arranged in 28 units of 4 cryomodules with  
 5619 their focussing elements – each cryomodule contains four 5-cell cavities, optimised to operate with

5620 large beam current (up to 120 mA at the High Order Mode – HOM – frequencies). The operating  
 5621 temperature is 2 K; the cavities are based on modern SRF technology and are fabricated from  
 5622 bulk Nb sheets; they are described in detail in section 8.6.2 below. The nominal acceleration  
 5623 gradient is 19.73 MV/m.

5624 In addition to the main linacs, the synchrotron losses in the arcs will make additional linacs  
 5625 necessary, referred to here as the *loss compensation linacs*. These will have to provide different  
 5626 accelerations in the different arcs, depending on the energy of the beams as shown in Tab. 8.13.  
 5627 The quoted beam energies are at entry into the arc. Their natural placement would be at the  
 5628 end of the arcs just before the combiner, where the different energy beams are still separate. The  
 5629 largest of these linacs would have to compensate the SR losses at the highest energy, requiring a  
 5630 total acceleration of about 700 MV. The loss compensation linacs will be detailed in section 8.6.5  
 below.

Section	Beam energy [GeV]	$\Delta E$ [MeV]
Arc 1	8.62	3
Arc 2	16.73	25
Arc 3	24.85	80
Arc 4	32.96	229
Arc 5	41.08	383
Arc 6	49.19	836

**Table 8.13:** Synchrotron radiation losses for the different arc energies

5631

5632 Through all arcs but Arc 6, the beam passes twice, once while accelerated and once while decel-  
 5633 erated. It is planned to operate these additional *loss compensation linacs* at 1603.2 MHz, which  
 5634 allows energy compensation of both the accelerated and the decelerated beam simultaneously.  
 5635 This subject will be discussed in detail in a subsequent section 8.6.5.

### 5636 8.6.1 Choice of Frequency

5637 The RF frequency choice primarily takes into account the constraints of the LHC bunch repeti-  
 5638 tion frequency,  $f_0$ , of 40.079 MHz, while allowing for a sufficiently high harmonic,  $h$ , for a flexible  
 5639 system. For an ERL with  $n_{pass} = 3$  recirculating passes and in order to enable equal bunch  
 5640 spacing for the 3 bunches – though not mandatory – it was originally considered to suppress all  
 5641 harmonics that are not a multiple of  $n_{pass} \cdot f_0 = 120.237$  MHz. Initial choices for instance were  
 5642 721.42 MHz ( $h = 18$ ) and 1322.61 MHz ( $h = 33$ ) in consideration of the proximity to the frequen-  
 5643 cies used for state-of-the-art SRF system developments worldwide [684]. In synergy with other  
 5644 RF system developments at CERN though, the final choice was 801.58 MHz ( $h = 20$ ), where  
 5645 the bunching between the 3 recirculating bunches can be made similar but not exactly equal.  
 5646 Note that this frequency is also very close to the 805 MHz SRF proton cavities operating at the  
 5647 Spallation Neutron Source (SNS) at ORNL, so that one could leverage from the experience in  
 5648 regard to cryomodule and component design at this frequency.

5649 Furthermore, in the frame of an independent study for a 1 GeV CW proton linac, a capital  
 5650 plus operational cost optimisation was conducted [685]. This optimisation took into account  
 5651 the expenditures for cavities, cryomodules, the linac tunnel as well as the helium refrigerator  
 5652 expenses as a function of frequency and thus component sizes. Labor costs were included based  
 5653 on the existing SNS linac facility work breakdown structure. It was shown that capital plus  
 5654 operating costs could be minimised with a cavity frequency between 800 MHz and 850 MHz,

5655 depending also on the choice of the operating He bath temperature (1.8 K to 2.1 K). Clear benefit  
 5656 of operating in this frequency regime are the comparably small dynamic RF losses per installation  
 5657 length due to a relatively small BCS surface resistance as well as low residual resistance of  
 5658 the niobium at the operating temperature. This could be principally verified as part of the  
 5659 prototyping effort detailed in the next sub-section. Note that the cost optimum also favors  
 5660 cavities operating at rather moderate field levels ( $< 20$  MV/m). This comes as a benefit in  
 5661 concern of field emission and associated potential performance degradations.

## 5662 8.6.2 Cavity Prototype

5663 Given the RF frequency of 801.58 MHz, JLab has collaborated with CERN, and consequently  
 5664 proposed a five-cell cavity design that was accepted for prototyping, see Fig. 8.14. The cavity  
 shape has also been adopted for PERLE. Tab. 8.14 summarises the relevant cavity parameters.



**Figure 8.14:** Bare 802 MHz five-cell cavity design (RF vacuum) with a 130 mm iris and beam tube aperture.

5665

Parameter	Unit	Value
Frequency	MHz	801.58
Number of cells		5
active length $l_{act}$	mm	917.9
loss factor	V pC <sup>-1</sup>	2.742
$R/Q$ (linac convention)	$\Omega$	523.9
$R/Q \cdot G$ per cell	$\Omega^2$	28788
Cavity equator diameter	mm	327.95
Cavity iris diameter	mm	130
Beam tube inner diameter	mm	130
diameter ratio equator/iris		2.52
$E_{peak}/E_{acc}$		2.26
$B_{peak}/E_{acc}$	mT/(MV/m)	4.2
cell-to-cell coupling factor $k_{cc}$	%	3.21
TE <sub>11</sub> cutoff frequency	GHz	1.35
TM <sub>01</sub> cutoff frequency	GHz	1.77

**Table 8.14:** Parameter table of the 802 MHz prototype five-cell cavity.

5666 The cavity exhibits a rather large iris and beam tube aperture (130 mm) to consider beam-  
 5667 dynamical aspects such as HOM-driven multi-bunch instabilities. Despite the comparably large  
 5668 aperture, the ratio of the peak surface electric field,  $E_{pk}$ , respectively the peak surface magnetic  
 5669 field,  $B_{pk}$ , and the accelerating field,  $E_{acc}$ , are reasonably low, while the factor  $R/Q \cdot G$  is  
 5670 kept reasonably high, concurrently to limit cryogenic losses. This is considered as a generically  
 5671 well *balanced* cavity design [686]. The cavity cell shape also avoids that crucial HOMs will

5672 coincide with the main spectral lines (multiples of 801.58 MHz), while the specific HOM coupler  
 5673 development is pending.

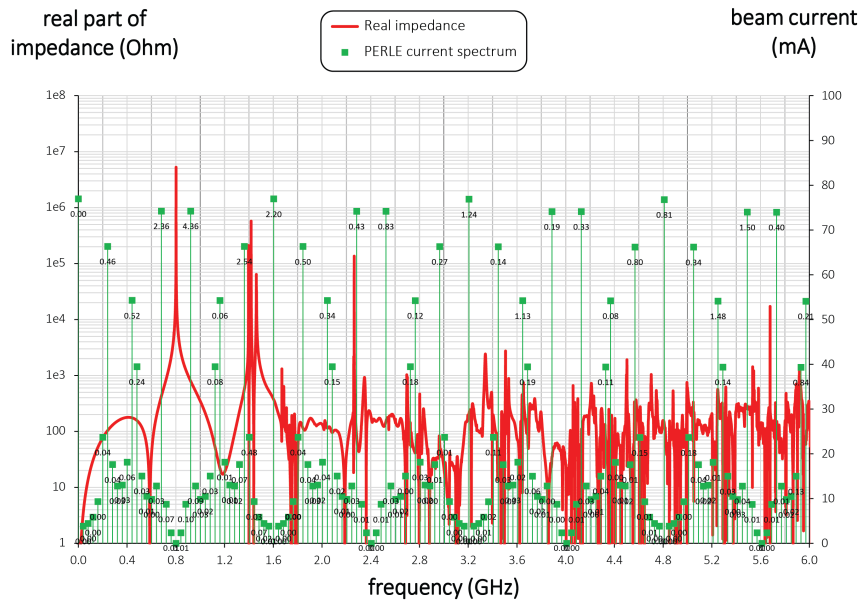


**Figure 8.15:** Real monopole impedance spectrum of the five-cell 802 MHz cavity prototype (red) together with the considered beam current lines (green) for the 3-pass PERLE machine (25 mA injected current). The numbers associated with the spectral lines denote the power dissipation (in Watt).

5674 Furthermore, as shown in Fig. 8.15 for the case of the bunch recombination pattern considered for  
 5675 PERLE originally, the much denser intermediate beam current lines (green) are not coinciding  
 5676 with cavity HOMs. Here the figure plots the real part of the beam-excited cavity monopole  
 5677 impedance spectrum up to 6 GHz, and denotes the power deposited at each spectral line (in  
 5678 Watt) for an injected beam current of 25 mA. For instance, the summation of the power in  
 5679 this spectral range results in a moderate 30 W. This covers the monopole modes with the  
 5680 highest impedances residing below the beam tube cutoff frequency. The HOM-induced heat has  
 5681 to be extracted from the cavity and shared among the HOM couplers attached to the cavity  
 5682 beam tubes. The fraction of the power escaping through the beam tubes above cutoff can be  
 5683 intercepted by beam line absorbers.

5684 Note that for Fig. 8.15 a single HOM-coupler end-group consisting of three scaled TESLA-  
 5685 type coaxial couplers was assumed to provide damping. Instead of coaxial couplers, waveguide  
 5686 couplers could be utilized, which for instance have been developed at JLab in the past for high  
 5687 current machines. These are naturally broadband and designed for high power capability, though  
 5688 some penalty is introduced as this will increase the complexity of the cryomodule. Ultimately,  
 5689 the aim is to efficiently damp the most parasitic longitudinal and transverse modes (each polar-  
 5690 ization). The evaluation of the total power deposition is important for LHeC to decide which  
 5691 HOM coupler technology is most appropriate to cope with the dissipated heat and whether  
 5692 active cooling of the couplers is a requirement.

5693 Though the prototype efforts focused on the five-cell cavity development, JLab also produced  
 5694 single-cell cavities, i.e. one further Nb cavity and two OFE copper cavities. The former has been  
 5695 shipped to FNAL for N-doping/infusion studies, whereas the latter were delivered to CERN for  
 5696 Nb thin-film coating as a possible alternative to bulk Nb cavities. In addition, a copper cavity  
 5697 was built for low power bench measurements, for which multiple half-cells can be mechanically  
 5698 clamped together. Presently, a mock-up can be created with up to two full cells. This cavity

5699 has been produced in support of the pending HOM coupler development. The ensemble of  
5700 manufactured cavities resonating at 802 MHz is shown in Fig. 8.16.

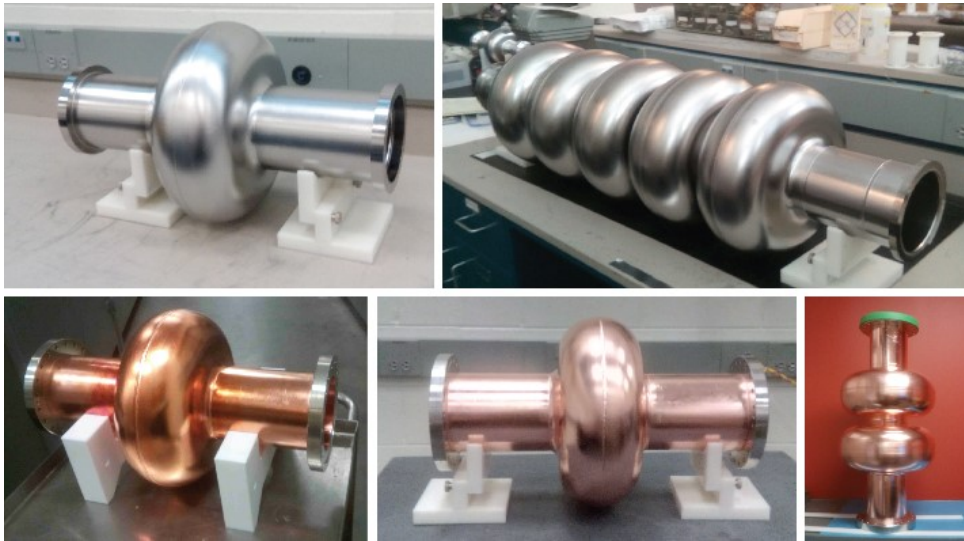


**Figure 8.16:** Ensemble of 802 MHz cavities designed and built at JLab for CERN. The Nb cavities have been tested vertically at 2 Kelvin in JLab's vertical test area.

5701 Results for the Nb cavities - made from fine grain high-RRR Nb - were encouraging since both  
5702 cavities reached accelerating fields,  $E_{acc}$ , slightly above 30 MV/m ultimately limited by thermal  
5703 breakdown (quench). Moreover, the RF losses were rather small as a benefit of the relatively  
5704 low RF frequency as anticipated. The residual resistance extracted from the measurement data  
5705 upon cooldown of the cavity was  $3.2 \Omega \pm 0.8 \Omega$ . This resulted in unloaded quality factors,  
5706  $Q_0$ , well above  $4 \times 10^{10}$  at 2 K at low field levels, while  $Q_0$ -values beyond  $3 \times 10^{10}$  could be  
5707 maintained for the five-cell cavity up to  $\sim 27$  MV/m (see Fig. 8.17). Only standard interior  
5708 surface post-processing methods were applied including bulk buffered chemical polishing, high  
5709 temperature vacuum annealing, light electropolishing, ultrapure high-pressure water rinsing,  
5710 and a low temperature bake-out. While the vertical test results indicate generous headroom for  
5711 a potential performance reduction once a cavity is equipped with all the ancillary components  
5712 and installed in a cryomodule, clean cavity assembly procedure protocols must be established  
5713 for the cryomodules to minimise the chance of introducing field-emitting particulates.

### 5714 8.6.3 Cavity-Cryomodule

5715 The ERL cryomodules hosting the superconducting RF cavities are a key component of the  
5716 accelerator. They should provide the proper mechanical, vacuum and cryogenic environment to  
5717 the SRF cavities equipped with their ancillaries systems: helium tank, power coupler and HOM  
5718 couplers. Each cryomodule is containing 4 superconducting 801.58 MHz 5-cells elliptical cavities  
5719 described in the previous chapters.

5720 Recently, several projects worldwide have designed cryomodules for elliptical cavities with a  
5721 cavity configuration (number, length and diameter) quite close to the one required by LHeC  
5722 ERL:

- 5723 • SNS [687]: two different sized cryomodules host either 4 elliptical 6-cells 805 MHz cavities  
5724 of  $\beta = 0.81$  or 4 elliptical 6-cells 805 MHz of  $\beta = 0.61$ ;

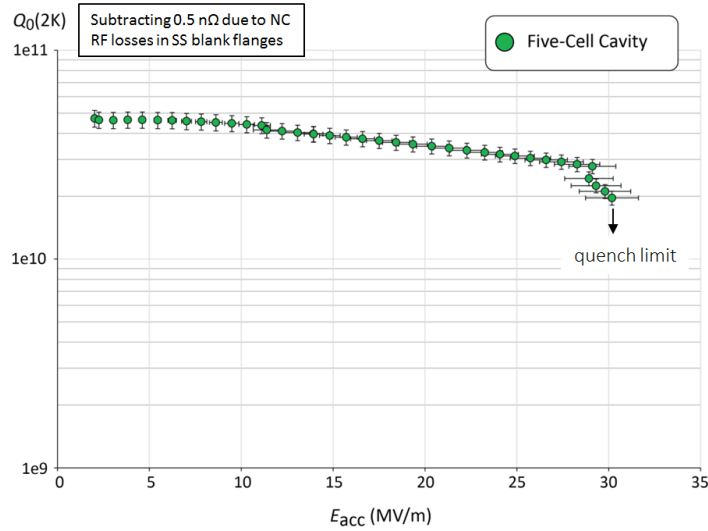


**Figure 8.17:** Vertical test result of the five-cell 802 MHz niobium cavity prototype.

- 5725 • SPL [688]: the cryomodule is designed to integrate 4 elliptical 5-cells 704 MHz cavities of  
5726  $\beta = 1$ ;
- 5727 • ESS [689]: two cryomodules of the same length can host either 4 elliptical 6-cells 704 MHz  
5728 cavities of  $\beta = 0.67$  or 4 elliptical 5-cells 704 MHz cavities of  $\beta = 0.85$ .

5729 These three cryomodule designs are based on two completely different concepts for the cavity  
5730 string support structure. SNS and ESS cryomodules are based on an intermediate support  
5731 system, called the spaceframe, which is horizontally translated inside the cryomodule vacuum  
5732 vessel. The low pressure cryogenic line is located above the cavities string and connected to the  
5733 cryogenic transfer line by a double angled connection, the jumper. RF waveguides are connected  
5734 underneath the cryomodule, using door-knob transition to the couplers. All the hanging and  
5735 alignment operations of the cavities string and shielding are implemented outside the vacuum  
5736 tank, using the spaceframe. In the ESS case, each cavity is hung by 2 sets of 4 cross rods. The  
5737 thermal shield is also hung to these rods by the mean of an aluminium “elastic boxes” that  
5738 allow the thermal shrinkage while maintaining the transverse stability. The thermal shield is  
5739 made of 2.5 mm thick aluminium and wrapped with multi-layer insulation. It is fastened directly  
5740 to the support rods of the cavities string.

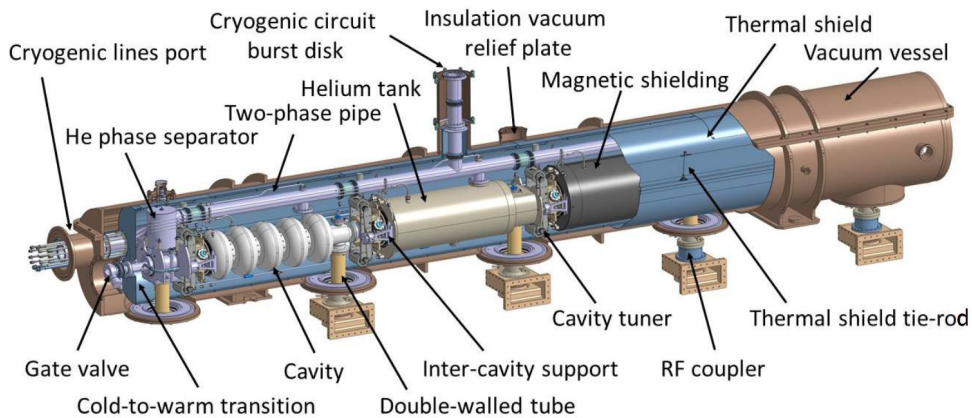


**Figure 8.18:** SPL cryomodule general assembly view

5741 In the SPL cryomodule, the cavity string is directly supported by the power coupler and with  
 5742 dedicated inter-cavity support features. Moreover, the SPL cryomodule integrates a full length  
 5743 demountable top lid, enabling the cavity string assembly from the cryomodule top (Fig. 8.18).  
 5744 The thermal shield is made of rolled aluminium sheets, and is composed of four main parts  
 5745 assembled before the vertical insertion of the string of cavities. The shield, wrapped with multi-  
 5746 layer insulation, is suspended to the vacuum vessel via adjustable tie rods in titanium alloy which  
 5747 also cope, by angular movements, with its thermal contractions. The cavity stainless steel helium  
 5748 tanks are connected by a 100-mm-diameter two-phase pipe placed above the cavities. This pipe  
 5749 ensures liquid feeding to the cavities by gravity, and is also used as a pumping line for gaseous  
 5750 helium.

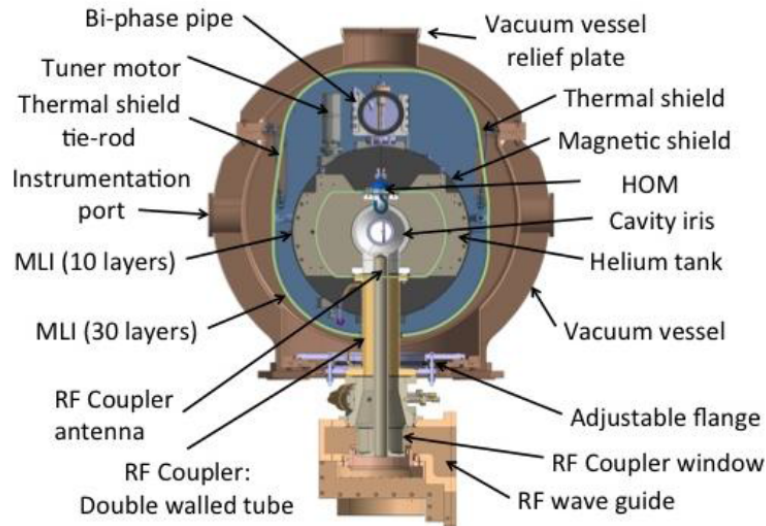


Figure 8.19: Cross-view of the SPL cryomodule

5751 With the aim of minimizing static heat loads from room temperature to 2 K by solid thermal  
 5752 conduction, the number of mechanical elements between the two extreme temperatures is re-  
 5753 duced to the strict minimum: the cavities are supported directly via the external conductor of  
 5754 the RF coupler (Fig. 8.19), the double-walled tube (DWT). The latter is made out of a stainless  
 5755 steel tube with an internal diameter of 100 mm, which is actively cooled by gaseous helium  
 5756 circulating inside a double-walled envelope in order to improve its thermal efficiency.

5757 An additional supporting point to keep cavity straightness and alignment stability within re-  
 5758 quirements is obtained by supporting each cavity on the adjacent one via the inter-cavity support,  
 5759 which is composed of a stem sliding inside a spherical bearing. As a result, a pure vertical sup-  
 5760 porting force is exchanged by adjacent cavities whereas all other degrees of freedom remain unre-  
 5761 strained allowing thermal contraction movements to occur unhindered. The thermo-mechanical  
 5762 behaviour of this supporting system has been extensively studied on a dedicated test bench at  
 5763 CERN, proving its efficiency and reliability.

5764 There are some specific additional constraints or requirements for a cryomodule to be used in  
 5765 an ERL, and some of them are quite challenging. The first set of constraints is linked to the CW  
 5766 operation of the cryomodules (contrary to SNS, SPL and ESS which are pulsed accelerators),  
 5767 where dynamic heat loads are much larger than the static ones. Thus, reaching high  $Q_0$  (low  
 5768 cryogenic losses) is a main objective in these machines and beside specific optimization on cavity  
 5769 design and preparation (such as N-doping), magnetic shielding should be carefully studied:  
 5770 material, operating temperature, numbers of layers, active and/or passive shielding. Another

5771 important constraint is linked to relative high power to be extracted by the HOM couplers:  
5772 thermal analysis should be carefully performed to have an optimized evacuation of the HOM  
5773 thermal load not to degrade the cryogenic performances of the cryomodule.

5774 We recently decided to push further away the analysis to use the SPL cryomodule for the LHeC  
5775 ERL, thanks to its geometrical compatibility with the LHeC ERL superconducting cavities,  
5776 but also because it fits quite well the overall ERL requirements. One of the clear advantages  
5777 of the SPL configuration is a much simplified assembly procedure (Fig. 8.20), with its top-lid  
configuration which also allows an easier maintenance.

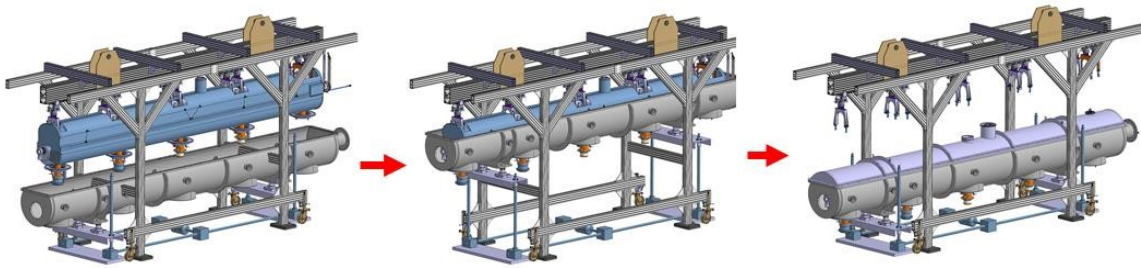


**Figure 8.20:** Cryomodule assembly procedure main steps

5778

5779 The first study performed was to analyse the possibility to integrate the ERL cavities instead  
5780 of the SPL ones. The 802 MHz cavities are a little bit shorter than the SPL ones and the cells  
5781 are also smaller in diameter. The beam port internal diameter is about the same, as well as  
5782 the power coupler port. As a result, the SPL cryomodule is well fitted to the ERL 802 MHz  
5783 superconducting cavities from the geometrical point of view, and they could be easily integrated  
5784 providing minor mechanical features adaptations.

5785 The second analysed point is the beam vacuum. As the SPL cryomodule existing design was  
5786 done for a prototype, intended for RF and cryogenic test only, without beam, the vacuum valve  
5787 is a VAT CF63 “vatterfly” valve with viton seal and manual actuator, which is not adapted for  
5788 a real operating cryomodule. Integration of an all-metal gate valve instead is not an issue and  
5789 we also designed a specific solution based on a two stages valves (Fig. 8.21) to adapt the already  
5790 fabricated SPL prototype cryomodule in order to be able to integrate the 802 MHz cavities.

5791 The third study performed is the compatibility of the SPL cryogenic features with the ERL  
5792 requirements. SPL was designed to operate 702 MHz cavities at 25 MV/m with a  $Q_0$  of  $5 \times 10^9$   
5793 with a 8.2 % duty cycle. The LHeC ERL will operate SRF cavities in CW regime, but at a lower  
5794 field (20 MV/m) and with a higher expected  $Q_0$  at the nominal gradient (about  $1.5 \times 10^{10}$ ).  
5795 As a result, and despite the different duty cycle, the dynamic cryogenic losses are estimated to  
5796 be only about 30 % more in the ERL case. The overall cryogenic dimensioning is then fully  
5797 compatible, providing some unavoidable adaptation of a few internal cryogenic piping. The  
5798 main issue still to address is the need and consequences of the HOM coupler cooling. Even if  
5799 the present engineering analysis showed that this point will not be a showstopper, it might have  
5800 an impact on some cryogenic piping and cooling circuit.

5801 Detailed engineering studies are being pursued to transform the SPL cryomodule prototype into  
5802 an ERL LHeC cryomodule prototype. We are taking benefit of all the design and fabrication  
5803 work previously performed on the SPL, and also on the fact some parts, such as the thermal and  
5804 magnetic shielding, are not yet fabricated and could be exactly adapted to the ERL requirements.  
5805 This will give the possibility to have an earlier full prototype cryomodule RF and cryogenic test as  
5806 compared to a standard experimental plan where the complete study and fabrication is starting

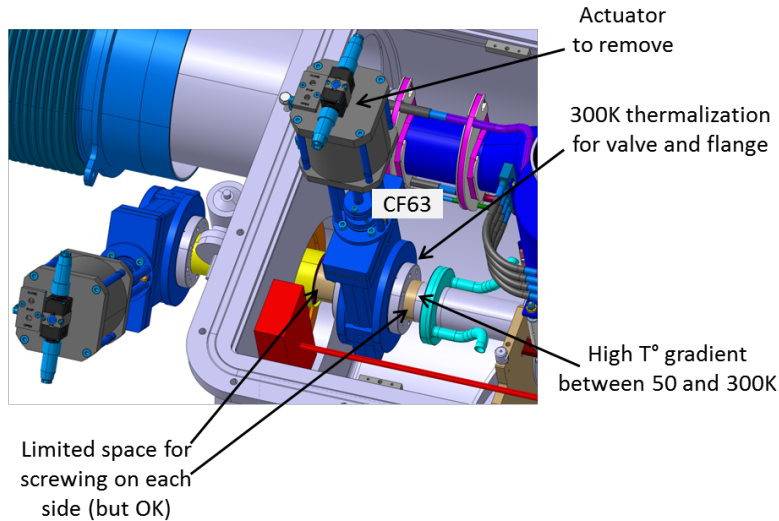


**Figure 8.21:** The two stages vacuum valve solution for adapting the SPL cryomodule prototype to the 802 MHz cavities of the LHeC ERL.

5807 from scratch.

## 5808 8.6.4 Electron sources and injectors

### 5809 Specification of electron sources

5810 Operation of the LHeC with an electron beam, delivered by a full energy ERL imposes specific  
 5811 requirements on the electron source. It should deliver a beam with the charge and temporal  
 5812 structure required at the Interaction Point. Additionally as during acceleration in a high energy  
 5813 ERL both longitudinal and transverse emittances of the beam are increased due to Synchrotron  
 5814 Radiation (SR), the 6D emittance of the beam delivered by electron source should be small  
 5815 enough to mitigate this effect. The general specification of the electron source are shown in  
 5816 Tab. 8.15. Some parameters in this table such as RMS bunch length, uncorrelated energy  
 5817 spread and normalised transverse emittance are given on the basis of the requirements for the  
 5818 acceleration in ERL and to pre-compensate the effects of SR. The most difficult of the parameters  
 5819 to specify is injector energy. It should be as low as possible to reduce the unrecoverable power  
 5820 used to accelerate the beam before injection into the ERL while still being high enough to deliver  
 5821 short electron bunches with high peak current. Another constraint on the injection energy is  
 5822 the average energy and energy spread of the returned beam. The average energy cannot be  
 5823 less than the energy of electron source, but the maximum energy in the spectrum should not  
 5824 exceed 10 MeV the neutron activation threshold. An injection energy of 7 MeV is a reasonable  
 5825 compromise to meet this constraint.

5826 The required temporal structure of the beam and the stringent requirements for beam emittance  
 5827 do not allow the use of conventional thermionic electron sources for the LHeC ERL without using  
 5828 a bunching process involving beam losses. While this option cannot completely be excluded as a  
 5829 source of unpolarised electrons. The additional requirement to deliver polarised beam can only  
 5830 be met with photoemission based electron sources.

5831 There are now four possible designs of electron sources for delivering unpolarised beams and  
 5832 (potentially) three for delivering polarised beams:

Parameter	Unit	Value
Booster energy	MeV	7*
Bunch repetition rate	MHz	40.1
Average beam current	mA	20
Bunch charge	pC	500
RMS bunch length	mm	3
Normalised transverse emittance	$\pi \cdot \text{mm} \cdot \text{mrad}$	<6
Uncorrelated energy spread	keV	10
Beam polarisation		Unpolarised/Polarised

**Table 8.15:** General specification of the LHeC ERL electron source.

- 5833 1. A thermionic electron source with RF modulated grid or gate electrode with following  
5834 (multi)stage compression and acceleration. The electron source could be either a DC  
5835 electron gun or an RF electron source in this case. Although these sources are widely used  
5836 in the injectors of Infra-Red FELs [690] their emittance is not good enough to meet the  
5837 specification of the LHeC injector. Moreover, thermionic sources cannot deliver polarised  
5838 electrons.
- 5839 2. A VHF photoemission source. This is a type of normal conducting RF source which  
5840 operates in the frequency range 160 MHz – 200 MHz. The relatively low frequency of these  
5841 sources means that they are large enough that sufficient cooling should be provided to  
5842 permit CW operation. This type of source has been developed for the new generation  
5843 of CW FELs such as LCLS-II [691], SHINE [692] and a back-up option of the European  
5844 XFEL upgrade [693], but they have not yet demonstrated the average current required  
5845 for the LHeC injector. The possibility of generating polarised electrons with this type of  
5846 source has not investigated yet.
- 5847 3. A superconducting RF photoemission source. This type of sources are under development  
5848 for different applications such as CW FEL's (ELBE FEL [694], SRF option of LCLS-II  
5849 injector [695], European XFEL upgrade [696]), as a basis of injectors for ERL's (bERLin-  
5850 Pro [697]) and for electron cooling (BNL [698]). Though this type of sources has already  
5851 demonstrated the possibility of delivering the average current, required for the LHeC with  
5852 unpolarised beams (BNL), and has the potential for operation with GaAs type photocath-  
5853 odes (HZDR) which are required for delivery of polarised beams, the current technology  
5854 of SRF photoelectron source cannot be considered as mature enough for use in the LHeC.
- 5855 4. A DC photoemission source. In this type of source the electrons are accelerated imme-  
5856 diately after emission by a potential difference between the source cathode and anode.  
5857 This type of source is the most common for use in ERL injectors. It has been used in the  
5858 projects which are already completed (JLAB [699], DL [700]), is being used for ongoing  
5859 projects (KEK [701], Cornell/CBeta [702]) and is planned to be used in new projects such  
5860 as the LHeC prototype PERLE [703]. The technology of DC photoemission sources is  
5861 well-developed and has demonstrated the average current and beam emittance required  
5862 for the LHeC ERL (Cornell). Another advantage of the photoelectron source with DC  
5863 acceleration is the possibility of operation with GaAs based photocathodes for deliver-  
5864 ing of polarised beam. Currently it's the only source, which can deliver highly polarised  
5865 electron beams with the current of several mA's which is already in the range of LHeC  
5866 specifications (JLab [704]).

5867 Based on this analysis at CDR stage we consider the use of DC photoemission source as a basic

5868 option, keeping in mind that in the course of the injector development other types of electron  
5869 sources may be considered, especially for providing of unpolarised beam.

## 5870 The LHeC unpolarised injector

The injector layout follows the scheme depicted in Fig. 8.22. Its design will be similar to the

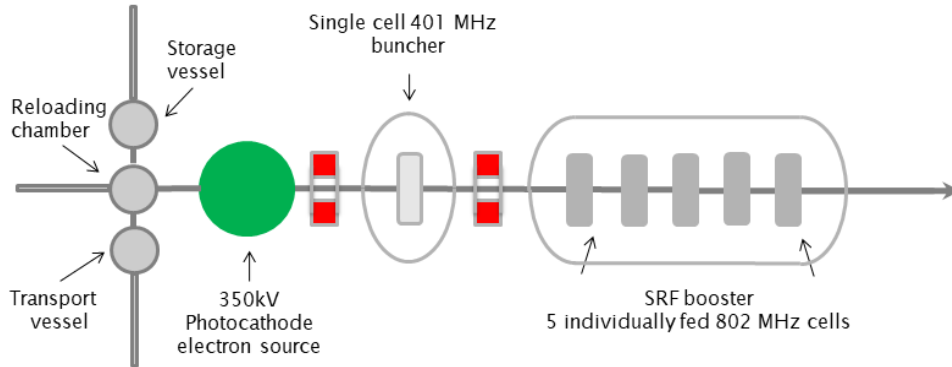


**Figure 8.22:** The layout of the unpolarised injector.

5871

5872 unpolarised variant of the PERLE injector [703]. The electron source with DC acceleration  
5873 delivers a CW beam with the required bunch charge and temporal structure. Immediately  
5874 after the source is a focusing and bunching section consisting of two solenoids with a normal  
5875 conducting buncher placed between them. The solenoids have two purposes. Firstly to control  
5876 the transverse size of the space charge dominated beam which will otherwise rapidly expand  
5877 transversely. This ensures that the beam will fit through all of the apertures in the injector  
5878 beamline. Secondly the solenoids are used for emittance compensation to counter the space  
5879 charge induced growth in the projected emittance. This is then followed by a superconducting  
5880 booster linac. This accelerates the beam up to its injection energy, provides further longitudinal  
5881 bunch compression and continues the emittance compensation process.

5882 The DC electron source will have an accelerating voltage of 350 kV using a high quantum ef-  
5883 ficiency antimonide based photocathode such as Cs<sub>2</sub>K<sub>2</sub>Sb. The photoinjector laser required for  
5884 this cathode type will be a 532 nm green laser. There will be a load lock system to allow pho-  
5885 tocathodes to be replaced without breaking the source vacuum. This significantly reduces the  
5886 down time required for each replacement which is a major advantage in a user facility such as  
5887 the LHeC where maximising uptime is very important. The cathode electrode will be mounted  
5888 from above similar to the Cornell [705] and KEK [706] sources. This electrode geometry makes  
5889 the addition of a photocathode exchange mechanism much easier as the photocathode can be  
5890 exchanged through the back of the cathode electrode. In addition the cathode electrode will be  
5891 shaped to provide beam focusing. The operational voltage of 350 kV for the source was chosen  
5892 as practical estimate of what is achievable. A higher voltage would produce better performance  
5893 but would be challenging to achieve in practice. The highest operational voltage successfully  
5894 achieved is 500 kV by the DC electron source that is used for the cERL injector [707]. However  
5895 350 kV is sufficient to achieve the required beam quality [703].

5896 **Polarised electron source for ERL**

5897 Providing polarised electrons has always been a challenging process, especially at relatively high  
 5898 average current as required for the LHeC. The only practically usable production mechanism  
 5899 of polarised electrons is the illumination of activated to Negative Electron Affinity (NEA) state  
 5900 GaAs based photocathodes with circularly polarised laser light. The vacuum requirements for  
 5901 these cathodes mean that this must be done in a DC electron source only. In the course of the  
 5902 last 30 years significant progress has been achieved in improving the performance of polarised  
 5903 electron sources. The maximum achievable polarisation has reached 90% and the maximum  
 5904 Quantum Efficiency (QE) of the photocathode at the laser wavelength of maximum polarisation  
 5905 has reached 6%. Meanwhile the implementation of a polarised electron source into the LHeC  
 5906 remains a challenge as the practical operational charge lifetime of the GaAs based photocathode  
 5907 does not exceed hundreds Coulombs (JLAB [708]) at an operational current in mA range.

In Fig. 8.23 a preliminary design of the LHeC polarised injector is shown. In general, the design

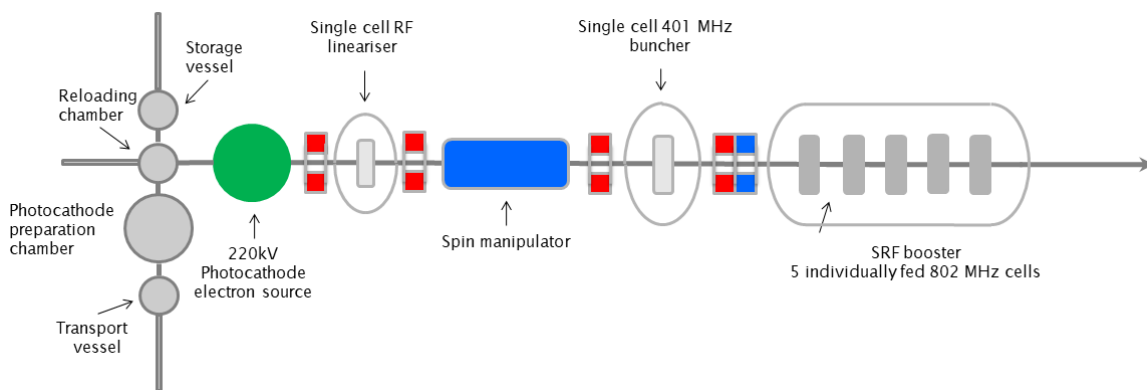


**Figure 8.23:** The layout of the polarised injector.

5908 of the polarised electrons injector is close to that of the unpolarised injector and is based on a  
 5909 DC electron source where a photocathode is illuminated by a pulsed laser beam. The choice of a  
 5910 DC source is dictated by the necessity of achieving extra high vacuum, with a pressure at a level  
 5911 of  $10^{-12}$  mbar, in the photocathode area. This level of vacuum is necessary for providing long  
 5912 lifetime of the photocathode. In order to reduce photocathode degradation caused by electron  
 5913 stimulated gas desorption, the accelerating voltage in the source is reduced to 220 kV. The main  
 5914 differences with unpolarised injector are the presence of a photocathode preparation system,  
 5915 permanently attached to the source, and a Wien filter based spin manipulator between the source  
 5916 and the buncher. In order to reduce depolarisation of the beam in the spin manipulator, caused  
 5917 by the space charge induced energy spread of the beam, an RF dechirper is installed between  
 5918 the source and the spin manipulator. The injector is also equipped with a Mott polarimeter to  
 5919 characterise the polarisation of the beam delivered by the source.  
 5920

5921 An important consideration of the operation with interchangeable photocathodes is minimisation  
 5922 of the down time required for the photocathode exchange. It typically takes few hours to replace  
 5923 the photocathode and to characterise polarisation of the beam. For large facility like LHeC this  
 5924 is unacceptable. A practical solution could be operation with 2 or more electron sources which  
 5925 operate in rotation similar to the way which was proposed at BNL [709]. Another motivation  
 5926 for using multi-source injector is the nonlinear dependence of photocathode charge lifetime on  
 5927 average beam current (JLAB [704]), which reduces with increasing of the average current. For  
 5928 example in case of 3 electron sources 2 of them can be operated with half operation frequency

5929 20.05 MHz in opposite phase delivering average current of 10 mA each, while the third is in stand  
 5930 by regime with freshly activated photocathode. The only time which is necessary to switch it  
 5931 on is the time required for rising the high voltage. Another advantage of using a multi-source  
 5932 scheme is the reduction of the average laser power deposited on the photocathode and as result  
 5933 relaxing requirements for the photocathode cooling. In order to implement the multi-source  
 5934 polarised electron injector, development of a deflection system which is able to merge the beams  
 5935 from different sources before the spin rotator is required.

### 5936 Lasers for electron sources

5937 In the proposed design of the LHeC injection system at least 2 lasers must be used. In the  
 5938 unpolarised electron injector, which is going to operate with antimionide-based photocathode,  
 5939 a laser with a wavelength of 532 nm is required. Typical initial QE of these photocathodes is  
 5940 10% and for practical application reduction of QE up to 1 % may be expected. For polarised  
 5941 electron source typical QE varies from 1 % down to 0.1 % and laser with a wavelength of 780 nm  
 5942 is required. The optimised parameters of the required lasers are summarised in Tab. 8.16. Laser  
 5943 temporal profile and spot size on the photocathode are given on the basis of source optimisation  
 for operation at 350 kV for unpolarised regime and 220 kV for polarised.

Laser beam parameter	Unit	Unpolarised mode	Polarised mode
Laser wavelength	nm	532	780
Laser pulse repetition rate	MHz	40.1	40.1
Energy in the single pulse at photocathode QE=1 %	$\mu\text{J}$	0.12	
Average laser power at photocathode QE=1 %	W	4.7*	
Energy in the single pulse at photocathode QE=0.1 %	$\mu\text{J}$		0.79
Average laser power at photocathode Qe=0.1 %	W		32*
Laser pulse duration	ps FWHM	118	80
Laser pulse rise time	ps	3.2	3.2
Laser pulse fall time	ps	3.2	3.2
Spot diameter on the photocathode surface	mm	6.4	8
Laser spot shape on the photocathode surface		Flat top	

**Table 8.16:** Parameters of the electron source drive laser.

5944

### 5945 8.6.5 Compensation of Synchrotron Radiation Losses

5946 Depending on energy, each arc exhibits fractional energy loss due to the synchrotron radiation,  
 5947 which scales as  $\gamma^4/\rho^2$  (see Eq. (8.3)). Arc-by-arc energy loss was previously summarised in  
 5948 Tab. 8.13. That energy loss has to be replenished back to the beam, so that at the entrance  
 5949 of each arc the accelerating and decelerating beams have the same energy, unless separate arcs  
 5950 are used for the accelerating and decelerating beams. Before or after each arc, a matching  
 5951 section adjusts the optics from and to the linac. Adjacent to these, additional cells are placed,  
 5952 hosting the RF compensating sections. The compensation makes use of a second harmonic  
 5953 RF at 1603.2 MHz to replenish the energy loss for both the accelerating and the decelerating  
 5954 beams, therefore allowing them to have the same energy at the entrance of each arc, as shown  
 5955 in Fig. 8.24.

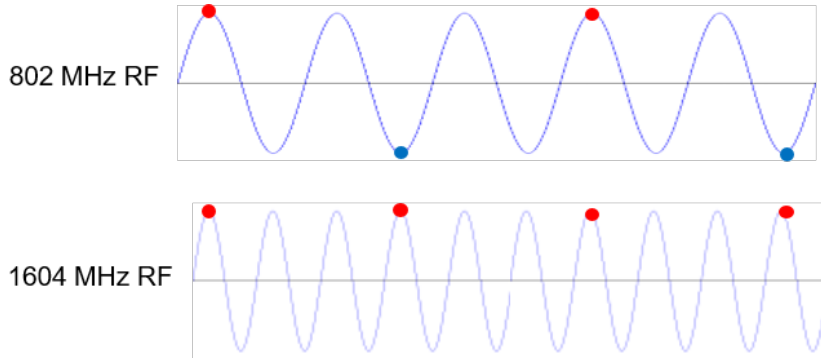


**Figure 8.24:** The second-harmonic RF restores the energy loss in both the accelerating and decelerating passes.

5956 Parameters of the RF compensation cryomodules, shown in Tab. 8.17, have been extrapolated  
 5957 from the ILC cavity design, expecting that the higher frequency and lower gradient would  
 support continuous operation.

Parameter	Unit	Value
Frequency	MHz	1603.2
Gradient	MV/m	30
Design		Nine cells
Cells length	mm	841
Structure length	m	1
Cavity per cryomodule		6
Cryomodule length	m	6
Cryomodule voltage	MV	150

**Table 8.17:** A tentative list of parameter for the compensating RF cryomodules extrapolated from the ILC design.

Section	$\Delta E$ [MeV]	$P$ [MW]	Cryomodules
Arc 1	3	0.2	0
Arc 2	25	1.2	0
Arc 3	80	4.0	1
Arc 4	229	11.5	2
Arc 5	383	19.1	3
Arc 6	836	41.8	6

**Table 8.18:** Arc-by-arc synchrotron radiated power and number of 2-nd harmonic RF cryomodules required to compensate energy loss.

5958

5959 The compensating cryomodules are placed into Linac 1 side of the racetrack, before the bending  
 5960 section of Arc 1, Arc 3, and Arc 5 and after the bending section of Arc 2, Arc 4, and Arc 6.  
 5961 This saves space on Linac 2 side to better fit the IP line and the bypasses. Note that with the  
 5962 current vertical separation of 0.5 m it will not be possible to stack the cryomodules on top of  
 5963 each other; therefore, they will occupy 36 m on the Arc 4 and Arc 6 side and 18 m on the Arc 3  
 5964 and Arc 5 side of the racetrack. Each of the compensating cavities in Arc 5 needs to transfer  
 5965 up to 1 MW to the beam. Although a 1 MW continuous wave klystron are available [710], the  
 5966 cryomodule integration and protection system will require a careful design. Tab. 8.18 shows the

5967 energy loss for each arc and the corresponding synchrotron radiated power, along with number  
5968 of cryomodules at 1603.2 MHz RF frequency required to replenish the energy loss.

## 5969 8.6.6 LINAC Configuration and Infrastructure

5970 Since the power supplied to the beam in the main linacs will be recovered, the average RF power  
5971 requirements at 802 MHz are relatively small and determined by the needs to handle transients  
5972 and microphonics.

5973 The RF power required for the second-harmonic RF system however is substantial – it can be  
5974 estimated from Tab. 8.13 with the nominal current of 20 mA.

5975 *some text is missing here.*

## 5976 8.7 Interaction Region

5977 The design of the LHeC Interaction region has been revised with respect to the LHeC CDR to  
5978 take into account the reduction of the electron energy from 60 GeV to 50 GeV and the latest  
5979 design of the HL-LHC optics and it has been optimized to minimize synchrotron radiation power  
5980 and critical energy at the IP.

### 5981 8.7.1 Layout

5982 The basic principle of the Linac-Ring IR design remains unchanged and it is shown in Fig. 8.25:  
5983 the two proton beams are brought onto intersecting orbits by strong separation and recombina-  
5984 tion dipoles. A collision of the proton beams at the IP is avoided by selecting appropriately its  
5985 location, i.e. by displacing it longitudinally with respect to the point where the two counter-  
5986 rotating proton beams would collide. The large crossing angle keeps the long range beam-beam  
5987 effect small and separates the beams enough to allow septum quadrupoles to focus only the  
5988 colliding beam (the anti-clockwise rotating LHC beam – Beam 2). The non-colliding beam (the  
5989 clockwise rotating LHC beam – Beam 1) is unfocused and passes the septum quadrupoles in a  
5990 field free aperture. The electron beam is brought in with an even larger angle, partly sharing  
5991 the field free aperture of the septum quadrupoles with the non-colliding beam. A weak dipole  
5992 in the detector region bends the electron beam into head-on collisions with the colliding proton  
5993 beam. The two proton beams are also exposed to the dipole field but, due to the large beam  
5994 rigidity, they are barely affected. After the interaction point a dipole with opposite polarity  
5995 separates the orbits of the electron and proton beam.

5996 The high electron current (cf. Tab. 8.1) required to approach the goal peak luminosity of  
5997  $10^{34} \text{ cm}^{-2} \text{ s}^{-1}$  poses a potential problem for the interaction region (IR) as it increases the al-  
5998 ready high synchrotron radiation.

5999 The ERL parameters are not the only major change the new IR design has to account for.  
6000 The first design of the quadrupole septa featured a separation of 68 mm for the two proton  
6001 beams. However, this design focused strongly on providing a field free region for the non-  
6002 colliding beam. Unfortunately, this led to a poor field quality for the strongly focused colliding  
6003 beam. The first quadrupole Q1 was a half quadrupole design effectively acting as a combined  
6004 function magnet with a dipole component of 4.45 T [711]. The sextupole field component was  
6005 also prohibitively high. Consequently, a new design approach focusing on the field quality in the

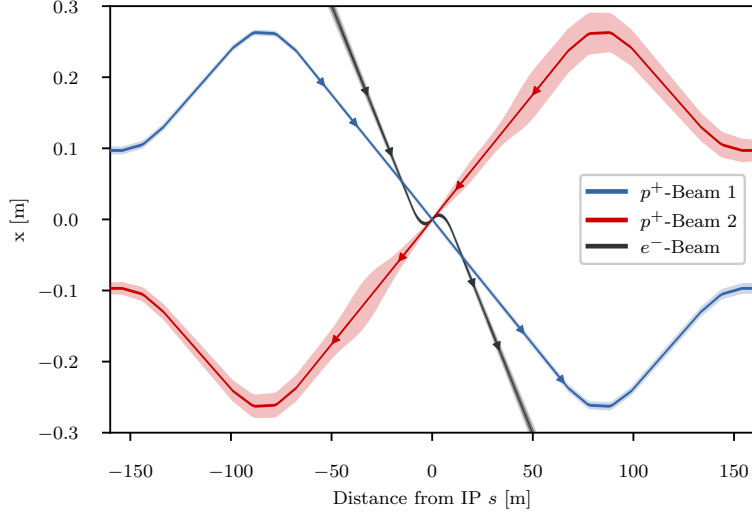


**Figure 8.25:** Geometry of the interaction region with  $10\sigma$  envelopes. The electron beam is colliding with the focussed anti-clockwise rotating LHC beam (Beam 2) while the clockwise rotating LHC beam is unfocussed and passes the Interaction Region without interacting with the other two beams

Magnet	Gradient [T/m]	Length [m]	Free aperture radius [mm]
Q1A	252	3.5	20
Q1B	164	3.0	32
Q2 type	186	3.7	40
Q3 type	175	3.5	45

**Table 8.19:** Parameters of the final focus quadrupole septa. The parameters of Q1A/B and Q2 are compatible with the Nb<sub>3</sub>Sn based designs from [712] assuming the inner protective layer of Q2 can be reduced to 5 mm thickness.

6006 quadrupole aperture was necessary. The parameters relevant for the interaction region design  
6007 are summarised in Tab. 8.19.

6008 It is noteworthy that the minimum separation of the two beams at the entrance of the first  
6009 quadrupole Q1A increased from 68 mm to 106 mm requiring a stronger bending of the electron  
6010 beam. This would increase the already high synchrotron radiation in the detector region even  
6011 more. In order to compensate this increase, it was decided to increase  $L^*$  (i.e. the distance from  
6012 the IP to the first superconducting septum quadrupole focussing Beam 2) to 15 m, an approach  
6013 that was shown to have a strong leverage on the emitted power [713].

6014 The increased separation of the two proton beams, the longer  $L^*$  and the overall longer final  
6015 focus triplet make longer and stronger separation and recombination dipoles necessary. The  
6016 dipoles differ from the arc dipoles in that the magnetic field in both apertures has the same  
6017 direction. Consequently the cross talk between both apertures is significant and the maximum  
6018 reachable field is lower. The new geometry keeps the required field below 5.6 T. The required  
6019 lengths and strength of these dipoles are listed in Tab. 8.20. It should be noted that the inter-  
6020 beam distance is different for each of the five magnets per side, so each magnet will likely require  
6021 an individual design. The design of the D1 dipoles is further complicated by the fact that an  
6022 escape line for neutral collision debris traveling down the beam pipe will be necessary [1], as well  
6023 as a small angle electron tagger. These issues have not been addressed so far, further studies  
6024 will require detailed dipole designs.

Magnet	Field strength [T]	Interbeam distance [mm]	Length [m]	Number
D1	5.6	$\geq 496$ mm	9.45	6
D2	4.0	$\geq 194$ mm	9.45	4
IP Dipole	0.21	-	10	-

**Table 8.20:** Parameters of the separation and recombination dipoles. The respective interbeam distances are given for the magnet with the lowest value.

6025 The first design of the LHeC interaction region featured detector dipoles occupying almost the  
6026 entire drift space between the interaction point and first quadrupole. The approach was to have  
6027 the softest synchrotron radiation possible to minimise the power. However, since the purpose  
6028 of the dipoles is to create a spacial separation at the entrance of the first quadrupole, it is  
6029 possible to make use of a short drift between dipole and quadrupole to increase the separation  
6030 without increasing the synchrotron radiation power. A dipole length of  $\frac{2}{3}L^*$  is the optimum in  
6031 terms of synchrotron radiation power [714]. Compared to the full length dipole it reduces the  
6032 power by 15.6% at the cost of a 12.5% higher critical energy. With an  $L^*$  of 15 m the optimum  
6033 length of the detector dipoles is 10 m. A magnetic field of 0.21 T is sufficient to separate the  
6034 electron and proton beams by 106 mm at the entrance of the first quadrupole. With these  
6035 dipoles and an electron beam current of 20 mA at 49.19 GeV the total synchrotron radiation  
6036 power is 38 kW with a critical energy of 283 keV to be compared with a power of 83 kW and a  
6037 critical energy of 513 keV for the electron beam energy of 60 GeV. More detailed studies on the  
6038 synchrotron radiation for different options and including a beam envelope for the electron beam  
6039 are summarised in Tab. 8.23 below.

6040 A schematic layout of the LHeC interaction region with the dipoles discussed above is shown in  
Fig. 8.26. The corresponding beam optics will be discussed in the following sections.

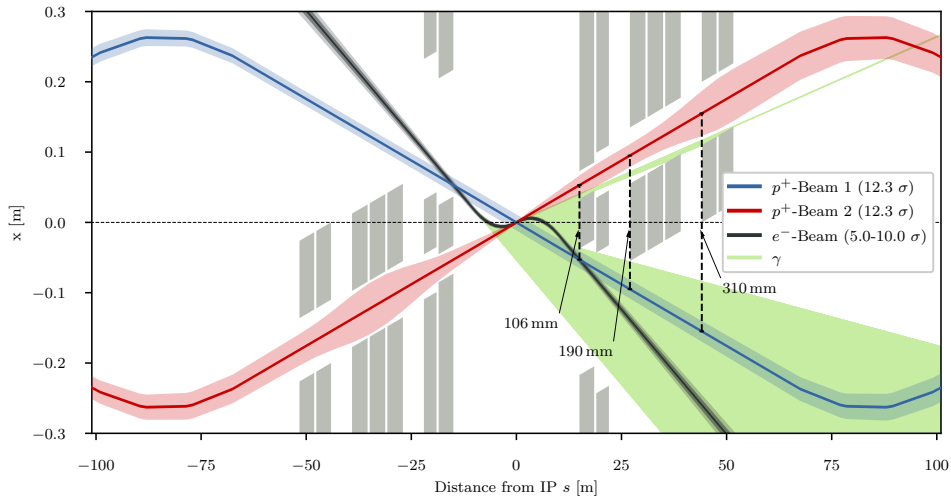


**Figure 8.26:** Schematic layout of the LHeC interaction region. The colliding proton beam and the electron beam are shown at collision energy while the non-colliding beam is shown at injection energy when its emittance is the largest.

6041

6042 **8.7.2 Proton Optics**

6043 As discussed above, the  $L^*$  was increased to 15 m in order to compensate the increased syn-  
 6044 chrotron radiation due to the larger separation. The final focus system is a triplet consisting  
 6045 of the quadrupoles Q1A and Q1B (see Tab. 8.19), three elements of the Q2 type and two of  
 6046 the Q3 type. Between the elements a drift space of 0.5 m was left to account for the magnet  
 6047 interconnects in a single cryostat. Between Q1 and Q2 as well as Q2 and Q3 a longer drift of  
 6048 5 m is left for cold-warm transitions, Beam Position Monitors (BPMs) and vacuum equipment.  
 6049 Behind Q3, but before the first element of the recombination dipole D1, another 16 m of drift  
 6050 space are left to allow for the installation of non-linear correctors in case the need arises, as well  
 6051 as a local protection of the triplet magnets from asynchronous beam dumps caused by failures  
 6052 of the beam dump kickers (MKD) as discussed below.

6053 As the recombination dipoles D1 and D2 for the LHeC interaction region require more space  
 6054 than the current ALICE interaction region, the quadrupoles Q4 and Q5 had to be moved further  
 6055 away from the IP. The position of Q6 is mostly unchanged but due to a need for more focusing  
 6056 the length was increased by replacing it with two elements of the MQM magnet class of LHC.

6057 With the triplet quadrupole parameters provided in Tab. 8.19 we were able to match optics with  
 6058 a minimum  $\beta^*$  of 10 cm. The corresponding optics are shown in Fig. 8.27 and feature maximum  
 $\beta$  functions in the triplet in the order of 20 km. With these large  $\beta$  functions, the free apertures

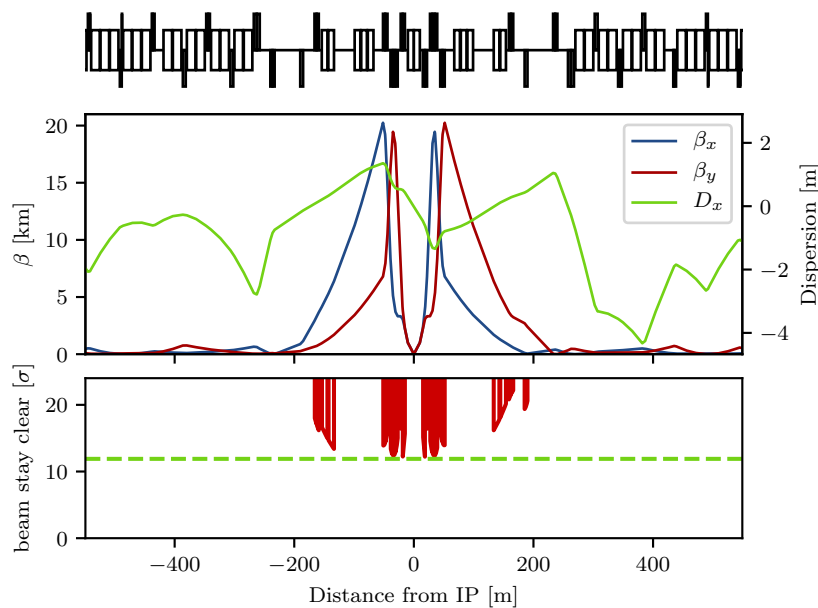


**Figure 8.27:** Optics (top) and beam stay clear (bottom) of the colliding beam with  $\beta^* = 10$  cm.

6059 of the quadrupoles leave just enough space for a beam stay clear of  $12.3\sigma$ , the specification of the  
 6060 LHC. This is illustrated in Fig 8.27. However, since the LHeC is supposed to be incorporated  
 6061 in the HL-LHC lattice, this minimum beam stay clear requires specific phase advances from  
 6062 the MKD kicker to the protected aperture as detailed later. The large  $\beta$  functions not only  
 6063 drive the aperture need in the final focus system, but also the required chromaticity correction  
 6064 in the adjacent arcs. To increase the leverage of the arc sextupoles, the Achromatic Telescopic  
 6065 Squeezing scheme (ATS) developed for HL-LHC [715] was extended to the arc upstream of IP2 for  
 6066 the colliding beam (Beam 2) (see Fig. 8.28). This limited the optical flexibility in the matching  
 6067

6068 sections of IR2, specifically of the phase advances between arc and IP2. As a consequence, the  
 6069 optical solution that has been found (Fig. 8.27) still has a residual dispersion of 15 cm at the IP  
 6070 and the polarities of the quadrupoles Q4 and Q5 on the left side of the IP break up the usual  
 6071 sequence of focusing and defocusing magnets. It needs to be studied whether this is compatible  
 with the injection optics. The latest optics designs can be found at the webpage [716].

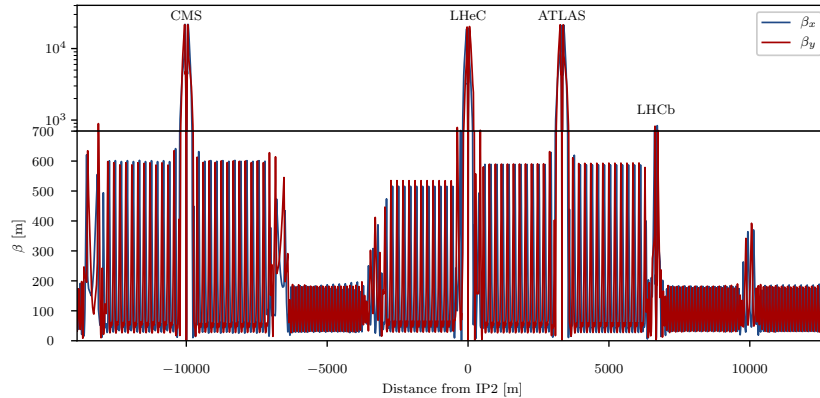


**Figure 8.28:** Optics of full ring of the colliding LHC proton beam (Beam 2).

6072

6073 The free apertures given in Tab. 8.19 include a 10 mm thick shielding layer in Q1 and 5 mm in  
 6074 Q2 and Q3. This is necessary to protect the superconducting coils from synchrotron radiation  
 6075 entering the magnets as can be seen in Fig. 8.26. The absorber must also protect the magnets  
 6076 from collision debris. Simulations of both synchrotron radiation and collision debris are yet to  
 6077 be conducted in order to confirm the feasibility of this design.

6078 A separation between the two proton beams in time is currently foreseen, i.e. while the orbits  
 6079 of the two proton beams do cross, the bunches do not pass through the IP at the same time.  
 6080 This approach is complicated by the fact that the timing of the bunches in the other three  
 6081 interaction points should not be affected. The easiest way to accomplish this is by shifting the  
 6082 interaction point of LHeC by a quarter of a bunch separation, i.e.  $6.25 \text{ ns} \times c \approx 1.87 \text{ m}$  upstream  
 6083 or downstream of the current ALICE IP, similar to what has been done for the LHCb detector  
 6084 in Point 8 of the LHC. This will of course have an impact in the integration of the detector in  
 6085 the underground cavern [717], however it seems feasible [718].

6086 The LHC protected aperture in the event of an asynchronous beam dump significantly depends  
 6087 on the phase advance between the MKD kicker and the local aperture protection [719]. This  
 6088 is due to the oscillation trajectory of bunches deflected during the kicker rise time. With a  
 6089 phase advance of  $0^\circ$  or  $180^\circ$  from the kicker to the protected aperture, a direct hit should be  
 6090 unlikely, so aperture bottlenecks should be close to that. For a beam stay clear of  $12.3\sigma$  a phase  
 6091 advance of less than  $30^\circ$  from either  $0^\circ$  or  $180^\circ$  was calculated to be acceptable [719]. The major  
 6092 complication comes from the fact that not only the final focus system of LHeC, but also of the  
 6093 two main experiments ATLAS and CMS need to have to correct phase advances and since the  
 6094 phase advances between IP2 (LHeC) and IP1 (ATLAS) are locked in the achromatic telescopic  
 6095 squeezing scheme there are few degrees of freedom to make adaptations.

6096 The Achromatic Telescopic Squeezing (ATS) scheme [715] is a novel optical solution proposed  
 6097 for the HL-LHC to strongly reduce the  $\beta^*$  while controlling the chromatic aberrations induced,  
 6098 among other benefits.

6099 The principles of the ATS as implemented for the HL-LHC are as follows: first, in the presqueeze

6100 stage, a standard matching procedure is performed in the interaction regions to obtain a value of  
6101  $\beta^*$  which is achievable in terms of quadrupole strengths and chromaticity correction efficiency,  
6102 in the case of HL-LHC this corresponds to IR1 and IR5. A further constraint at this point is  
6103 to match the arc cell phase advance on the regions adjacent to the low  $\beta^*$  interaction regions to  
6104 exactly  $\pi/2$ . Later, at the collision stage, the low  $\beta^*$  insertions remain unchanged and instead  
6105 the adjacent interaction regions contribute to the reduction of  $\beta^*$ , that is IR8 and IR2 for IR1,  
6106 and IR4 and IR6 for IR5. The  $\pi/2$  phase advance allows the propagation of  $\beta$ -waves in the  
6107 arc. If phased correctly with the IP, these  $\beta$ -waves will reach their maximum at every other  
6108 sextupoles, increasing the  $\beta$  function at their location at the same rate that the decrease in  $\beta^*$ .  
6109 The increase of the  $\beta$  function at the location of the sextupoles will result in an increase of their  
6110 efficiency, allowing the system to correct the high chromaticity produced by the high- $\beta$  function  
6111 in the inner triplet. This way, the ATS allows a further reduction of the  $\beta^*$  at the same time  
6112 that correcting the chromaticity aberrations produced in the low  $\beta$  insertions.

6113 Following the experience for HL-LHC, the ATS scheme was proposed for the LHeC project to  
6114 overcome some of the challenges of this design in terms of limits in the quadrupole strengths of  
6115 the interaction region and in the chromaticity correction.

6116 A first integration of the LHeC IR into the HL-LHC lattice using the ATS scheme for the  
6117 previous nominal case with  $\beta^* = 10$  cm and  $L^* = 10$  m was presented by extending the  $\beta$  wave  
6118 into the arc 23 [713]. The flexibility of this design was later explored to study the feasibility  
6119 of minimising  $\beta^*$ , to increase the luminosity, and increasing  $L^*$ , to minimise the synchrotron  
6120 radiation. It was found that increasing  $L^*$  to 15 m provided a good compromise but keeping the  
6121  $\beta^*$  to 10 cm.

6122 The changes made to the HLLHCV1.3 lattice [720] to obtain the LHeC lattice and the detailed  
6123 matching procedure are described in Ref. [721]. At the end of this process a lattice for the  
6124 required collision optics in all IRs ( $\beta^*=15$  cm for IR1 and IR5 and  $\beta^*=10$  cm for IR2) has  
6125 been obtained, with the appropriate corrections (crossing, dispersion, tune and chromaticity).  
6126 The phases between the MKD kicker in IR6 and the different low  $\beta^*$  triplets were also checked,  
6127 resulting in  $15^\circ$  from the horizontal for IR1,  $22^\circ$  for IR2 and  $26^\circ$  for IR5, therefore fulfilling the  
6128  $< 30^\circ$  requirement for all three IRs.

6129 Similarly the chromaticity correction for the LHeC lattice further develops from the HL-LHC  
6130 chromaticity correction scheme [721] allowing to correct the chromaticity for the case with  
6131  $\beta^* = 10$  cm in IP2 within the available main sextupole strength. Lattices with  $\beta^* = 7, 8$  and  
6132  $9$  cm and  $L^* = 15$  m were also successfully matched in terms of both the  $\beta^*$  and the chromaticity  
6133 correction. It must be noted however that these cases require a larger aperture in the inner  
6134 triplet.

6135 Dynamic aperture (DA) studies were performed to analyze the stability of the lattice designs  
6136 using SixTrack [722] on a thin-lens version of the LHeC lattice at collision ( $\beta^* = 0.15$  m in  
6137 IP1 and IP5,  $\beta^* = 10$  cm in IP2) over  $10^5$  turns with crossing angles on, 30 particles pairs per  
6138 amplitude step of  $2\sigma$ , 5 angles in the transverse plane and a momentum offset of  $2.7 \times 10^{-4}$ .  
6139 The energy was set to 7 TeV and the normalised emittance of the proton beam to  $\epsilon = 2.5 \mu\text{m}$ .  
6140 No beam-beam effects were included in this study.

6141 Previous DA studies had been performed for an earlier version of the LHeC lattice [713]. These  
6142 studies did not include triplet errors of either of the low- $\beta$  interaction regions, as these errors  
6143 were not available at that stage. These studies were updated for the newer version of the LHeC  
6144 lattice described in the previous sections and included errors on the triplets of IR1 and IR5. For  
6145 the case of IR2 errors tables for the new triplet are not yet available but it was estimated that

6146 the same field quality than the triplets for the HL-LHC IR can be achieved for these magnets,  
 6147 and therefore the same field errors were applied but adjusted to the LHeC triplet apertures.

6148 The initial DA resulted in  $7\sigma$  but following the example of HL-LHC and FCC studies [723] two  
 6149 further corrections were implemented: the use of non-linear correctors to compensate for the non  
 6150 linear errors in the LHeC IR, and the optimisation of the phase advance between IP1 and IP5.  
 6151 With these corrections the DA was increased to  $10.2\sigma$ , above the target of  $10\sigma$ . The case for  
 6152 lower  $\beta^*$ , particularly for the case of interest with  $\beta^* = 7\text{ cm}$  proved to be more challenging, as  
 6153 expected, when adding errors on the LHeC IR; however with the use of the latest corrections a  
 6154 DA of  $9.6\sigma$  was achieved, that is not far off from the target. The DA versus angle for both these  
 6155 cases are shown in Fig. 8.29. It is important to point out that the challenge for the  $\beta^*=7\text{ cm}$   
 6156 case comes instead from the quadrupole aperture and gradient requirements, particularly in the  
 first magnet.

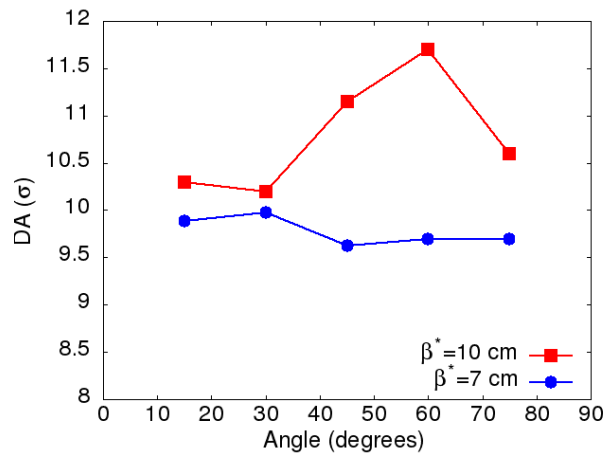


**Figure 8.29:** Dynamic aperture vs angle for 60 seeds for the LHeC lattice at collision for the cases  $\beta^* = 10\text{ cm}$  (red) and  $\beta^* = 5\text{ cm}$  in IP2.

6157

6158  $\beta^*$  values lower than 10 cm require a completely different final focus system as the lower  $\beta^*$  means  
 6159 the beam size in the triplet will become larger. Larger apertures are required and consequently  
 6160 the gradients in the quadrupoles will decrease. However similar integrated focusing strengths  
 6161 will be required so the overall length of the triplet will increase. As this will in turn increase the  
 6162  $\beta$  functions in the triplet further it is imperative to optimise the use of the available space. An  
 6163 example of available space is the drift between the detector region dipoles and the triplet magnets  
 6164 as shown in Fig. 8.30. The optimum dipole lengths in terms of synchrotron radiation power was  
 6165 determined to be  $2/3 \cdot L^*$  so a drift of 5 m is left. Now it is immediately clear that this region  
 6166 cannot be occupied by a superconducting quadrupole septum as that would effectively decrease  
 6167  $L^*$  and thus increase the synchrotron radiation power as a stronger separation is necessary.  
 6168 Instead it is thinkable that a normal conducting quadrupole septum can be built that either  
 6169 does not require a yoke or similar structure between the beams or has a very thin yoke, or a  
 6170 septum that has a very limited and controlled field in the region of the electron beam trajectory.  
 6171 In the later case it might even be used as part of the final focus system of the electron beam.  
 6172 Either way, it is clear that such a normal conducting septum must have a pole tip field way below  
 6173 the saturation limit of iron. The section on electron optics shows that a normal quadrupole of  
 6174 this kind can also have benefits in terms of synchrotron radiation, but studies remained to be  
 6175 done to make sure the parameters work for both cases. For our calculation a pole tip field of  
 6176 1 T was assumed. For  $\beta^* = 5\text{ cm}$  an aperture radius of 20 mm is required at a distance of 14 m  
 6177 from the IP, resulting in a pole tip field of 50 T/m for the normal conducting septum called Q0.

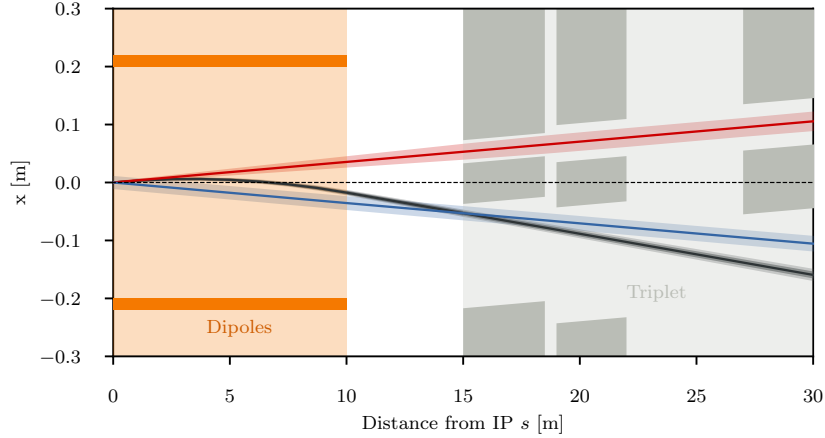


**Figure 8.30:** Empty space between the detector dipole and the superconducting quadrupoles of the final focus triplet.

6178 Possible ratios of apertures and gradients for the remaining triplet magnets were approximately  
 6179 based on the quadrupole parameters shown in Tab. 8.19, however these parameters would require  
 6180 a magnet design for confirmation. With the quadrupole parameters shown in Tab. 8.21 we were  
 able to obtain triplet optics that can accommodate a beam with a minimum  $\beta^*$  of 5 cm.

Magnet	Gradient [T/m]	Length [m]	Aperture radius [mm]
Q0 (nc)	50	3.0	20
Q1A	110	3.5	27
Q1B	162	5.0	37
Q2	123	5.0	62
Q3	123	4.5	62

**Table 8.21:** Parameters of the final focus quadrupole septa required to accommodate a  $\beta^*$  of 5 cm. The normal conducting quadrupole is called Q0 although it has the same polarity as Q1A/B.

6181

6182 The corresponding optics are shown in Fig. 8.31. So from the triplet point of view it appears  
 6183 possible to reach lower  $\beta^*$ , however many assumptions need verification: First the magnetic  
 6184 design for the normal conducting quadrupole septum must be shown to be possible. If there  
 6185 is a residual field in the space of the electron beam trajectory, the impact on the electron  
 6186 beam and the synchrotron radiation power must be evaluated. The parameters of the modified  
 6187 superconducting triplet quadrupole septa, although scaled conservatively, must be confirmed.  
 6188 Furthermore the larger aperture radius of Q1 might require a larger separation at the entrance of  
 6189 Q1, increasing the synchrotron power that is already critical. Thus a full design of such magnets  
 6190 is required. Lastly, the interaction region must be integrated into the full ring to verify that  
 6191 chromaticity correction is possible. Studies in Ref. [721] that were conducted on the normal  
 6192 triplet without regard for aperture constraints suggest that a chromaticity correction is only  
 6193 possible for a  $\beta^*$  down to around 7 cm.

6194 So far, the optics of the final focus system featured asymmetrically powered triplets on the two  
 6195 sides of the IP. This is inherited from the ALICE final focus system where the aperture is shared  
 6196 and the antisymmetry guarantees the same optics for both beams and similar chromaticities in  
 6197 both horizontal and vertical planes. In the LHeC final focus system however, the apertures of the  
 6198 quadrupoles are not shared between both beams, so the antisymmetry is not strictly necessary,

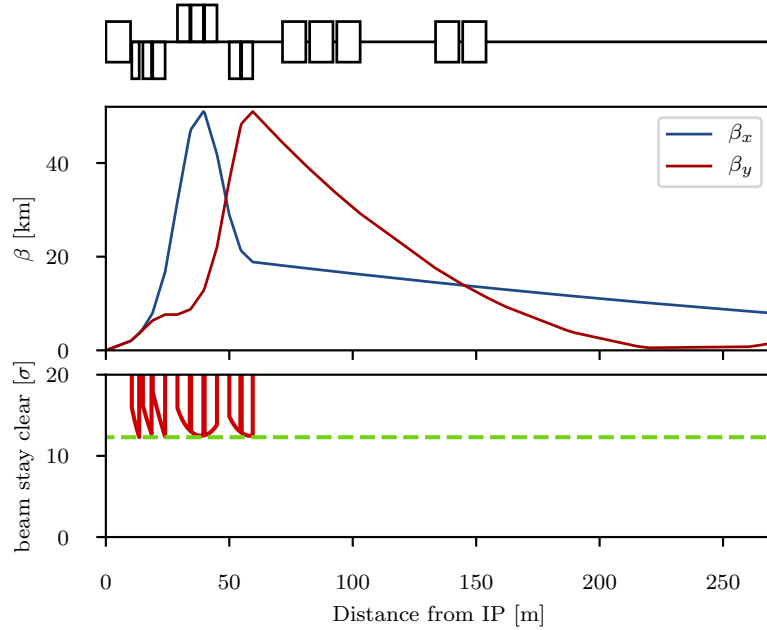


**Figure 8.31:** Optics (top) and beam stay clear (bottom) in the triplet region of colliding beam with  $B^* = 5$  cm.

6199 although it eases the integration in the full ring. An alternative approach that is worth studying  
6200 is a symmetric doublet. Doublets feature a large  $\beta$  function in one plane and a relatively low one  
6201 in the other plane for equal  $\beta$  functions at the IP. Since the non-colliding proton beam is of no  
6202 concern for LHeC it makes sense to create doublets on each side of the IP that have the peak  $\beta$   
6203 function in the horizontal plane as the chromaticity correction was limited in the vertical plane.  
6204 Furthermore, in a doublet the integrated focusing strength needed is lower as fewer quadrupoles  
6205 act against each other. This further reduces the chromaticity and should also reduce the overall  
6206 length of the final focus system. With the space saved by the doublet it is possible to either shift  
6207 the recombination dipoles D1 and D2 closer to the IP, reducing the needed integrated strengths,  
6208 or even to increase  $L^*$  to further reduce the synchrotron radiation power and critical energy.  
6209 In order to make best use of the available doublet quadrupole aperture, it is also thinkable to  
6210 collide with flat beams. The main disadvantage of symmetric doublets is the breaking of the  
6211 sequence of focusing and defocusing quadrupoles. As no changes should be made to the arcs,  
6212 the left-right symmetry needs to be broken up again in one of the matching sections, either by  
6213 introducing another quadrupole on one side of the IP, or by overfocusing the beam.

6214 At collision energy the non-colliding beam has no optics specification within the straight section.  
6215 Consequently the optics should transfer the beam from the left arc to the right arc without hitting  
6216 the aperture and at a specific phase advance. The same is true at injection energy, but with a  
6217 larger emittance, making the satisfaction of the aperture constraint more difficult. Thus it is  
6218 sufficient to find working injection optics, as no squeeze will be required for this beam. This  
6219 approach of course will require some tuning as at least one arc will apply the ATS scheme at  
6220 collision, but as the aperture constraint is less tight at higher energy there should be enough  
6221 degrees of freedom available.

6222 Finding injection optics appears trivial at first but is complicated by the fact that the distance  
6223 between the IP and the first quadrupole magnet Q4 is larger than 159 m. A total distance  
6224 of 318 m needs to be bridged without any focusing available. A solution has been found with

6225  $\beta^* = 92\text{ m}$  and  $\alpha^* = \pm 0.57$  with the required beam size in the quadrupole septa and Q4 [721].  
 6226 The corresponding optics are shown in Fig. 8.32. For the magnets Q4 and Q5 LHC quadrupoles

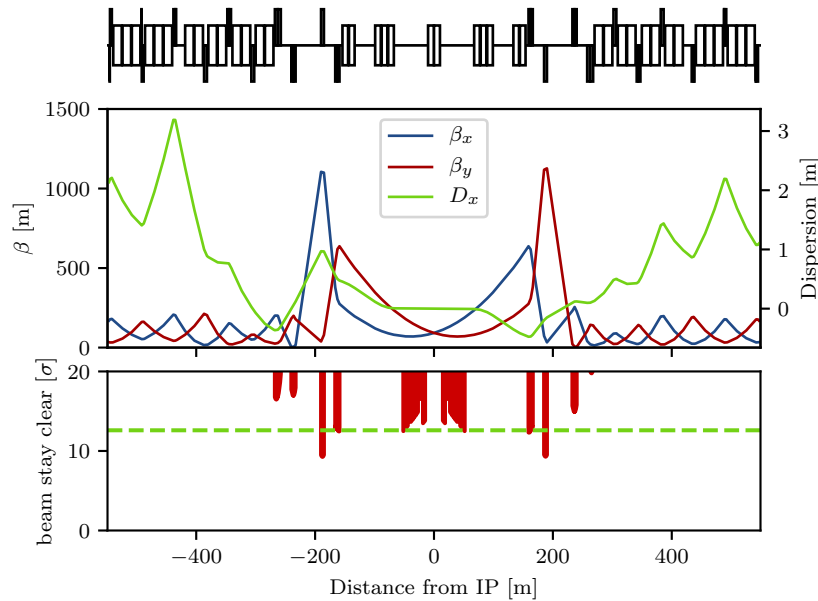


**Figure 8.32:** Optics (top) and beam stay clear of the non-colliding beam at injection energy. The Q5 quadrupole magnets on either side of the IP currently are aperture bottlenecks. It should be possible to mitigate this problem by replacing the magnets with longer, larger aperture magnets.

6226  
 6227 of the large aperture MQY type with 70 mm aperture diameter and a 160 T/m gradient were  
 6228 assumed. As can be seen in the aperture plot, the triplet quadrupole septa and Q4 are just below  
 6229 the minimum beam stay clear at injection of  $12.6\sigma$  but it is expected that nominal aperture can  
 6230 be achieved With some minor optimisation. However the Q5 magnets only have a beam stay  
 6231 clear of about  $9.2\sigma$  with little chance of decreasing the beam size without increasing it both  
 6232 in Q4 and in the quadrupole septa. Consequently it will be necessary to use quadrupoles with  
 6233 apertures larger than 106 mm and make up for the lower gradient by increasing the length or by  
 6234 using  $\text{Nb}_3\text{Sn}$  technology. At injection energy the remaining magnets in the IR have strengths  
 6235 according to the HL-LHC specification and thus do not pose any problems. However the injection  
 6236 optics shown in Fig. 8.32 will require some changes during the ramp as Q4, Q5 and Q6 would  
 6237 become too strong at collision energy. This is not considered a problem though, as the emittance  
 6238 shrinking will ease the aperture requirements.

6239 The non-colliding proton beam does not need to be focused and consequently passes the quadrupole  
 6240 septa of the colliding beam in the field free region.

6241 The large angle of  $7200\text{ }\mu\text{rad}$  between the two beams (compared to  $590\text{ }\mu\text{rad}$  in the high lumi-  
 6242 nosity IPs) should suffice to mitigate long range beam-beam effects, considering that the shared  
 6243 aperture is only 30 m long as opposed to the main experiments where the shared aperture exceeds  
 6244 a length of 70 m.

### 6245 8.7.3 Electron Optics

6246 First ideas of a possible layout and design of the LHeC IR have already been presented in Ref. [1].  
 6247 Based on the principles explained there, a further optimisation of the beam separation scheme

6248 has been established, with the ultimate goal of lowest synchrotron radiation power and critical  
 6249 energy in the direct environment of the particle detector. Depending on the requests from the  
 6250 actual detector geometry and shielding, the flexibility of the new IR layout allows to optimise  
 6251 for either side.

6252 The basic principle is – as before – based on the large ratio (approximately 140) of the proton  
 6253 to electron beam momentum (or beam rigidity,  $B\rho = p/e$ ) that makes a magnetic field based  
 6254 separation scheme the straightforward solution to the problem, using effective dipole fields.

6255 Boundary conditions are set however due to the limited longitudinal space, resulting from the  
 6256 distance of the first focusing elements of the proton lattice, located at  $L^* = 15$  m, and the need for  
 6257 sufficient transverse separation, defined by the technical design of this first proton quadrupole.  
 6258 The size of the two beams and – clear enough – the power of the emitted synchrotron radiation  
 6259  $P_{\text{syn}}$  and the critical energy  $E_{\text{crit}}$  have to be taken into account in addition. The well known  
 6260 dependencies of these two parameters on the beam energy  $E_e = m_e c^2 \gamma$  and bending radius  $\rho$   
 6261 are given by

$$P_{\text{syn}} = \frac{e^2 c}{6\pi\epsilon_0} \frac{\gamma^4}{\rho^2} \quad \text{and} \quad E_{\text{crit}} = \frac{3 \hbar c \gamma^3}{2 \rho}. \quad (8.6)$$

6262 The schematic layout of the original design of the electron interaction region shown in Fig. 8.26  
 is reproduced in Fig. 8.33 (a). The long dipole magnet B, used to deflect the electron beam, is

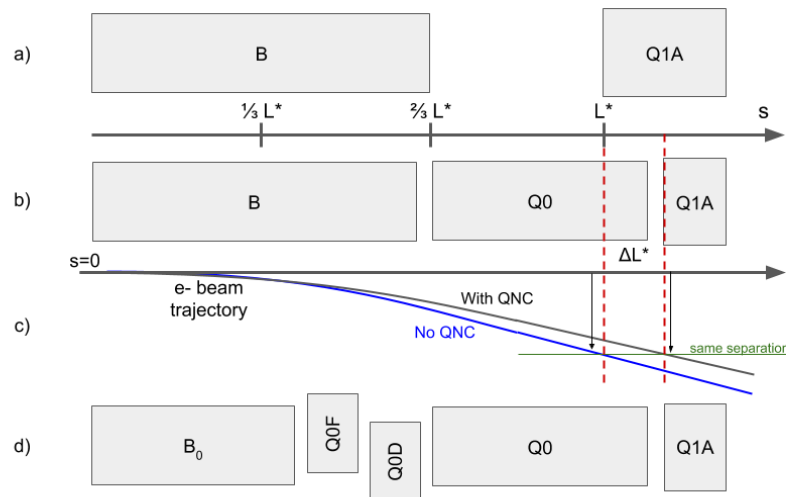


**Figure 8.33:** Separation scheme based on a long dipole magnet B (a) and improved layout using Q0, a normal conducting half-quadrupole as first focusing element of the proton beam (b). The last design features a doublet of off-centered quadrupoles to minimise the electron beam size at the entrance of Q1A (d).

6263  
 6264 embedded inside the detector structure which is ranging from  $-6$  m to  $4$  m around the interaction  
 6265 point, extended by  $\pm 1.65$  m of muon chamber. Basic interaction region designs with and without  
 6266 chromaticity correction were presented [724, 725] but were not fully integrated in the ERL. The  
 6267 electron final quadrupoles were placed at  $30$  m from the IP [726], compatible with the proton  
 6268 layout described above. While this approach is straightforward, the only parameter that can be  
 6269 used to minimise the power of the emitted synchrotron radiation is the length of the separator-  
 6270 dipole field [714]. In addition, the installation of the first focusing elements of the electron beam  
 6271 downstream of the triplet focussing the colliding proton beam leads to a considerable increase  
 6272 of the electron beam size in the separation plane.

6273 Lattices including chromaticity correction had a significant length of 150 m. However, the whole  
6274 straight section between Linac and arc is only 290 m long [1] and the IR design did not include a  
6275 matching and splitting section or a focus system for the spent, outgoing electron beam. Without  
6276 chromaticity correction in the electron final focus, aberrations at the IP decrease luminosity by  
6277 about 20% [727].

6278 Investigations have been launched to minimise critical energy and emitted synchrotron radiation  
6279 power by reducing the separation in two main steps:

- 6280 • introduce a compact mirror-plate half quadrupole (QNC) in front of Q1A (on the IP side)  
6281 to focus the colliding proton beam and provide a field free region for the electron and non-  
6282 interacting proton beam. This reduces the required bending field of the separation dipole  
6283 B for the same separation at Q1A. In addition, the normal conducting magnet QNC will  
6284 act as shielding of the superconducting triplet magnets that would otherwise be subject to  
6285 direct synchrotron radiation. Additional shielding is foreseen, to protect the SC magnets  
6286 and avoid as much as possible backshining to the detector. In addition, sufficient space  
6287 will be provided to correct the vertical orbit and coupling of the electrons coming from  
6288 the solenoid.
- 6289 • reduce the beam size of the electron beam by a very early focusing of the beam. As positive  
6290 side effect this leads to a considerable reduction of the chromaticity of the electron lattice.

6291 The first step is sketched in Fig. 8.33 (b) and the corresponding electron beam trajectory is  
6292 shown in Fig. 8.33 (c).

6293 The introduction of the mirror plate half quadrupole QNC allows to reduce the length of the  
6294 Q1A quadrupole while conserving the total integrated gradient, therefore leaving the overall  
6295 focusing properties of the proton lattice quasi untouched. The entry of Q1A is therefore moved  
6296 away from the IP to relax the separation fields.

6297 Scanning the Q1A entry position leads to either an optimum of the critical energy or to a  
6298 minimum of the emitted synchrotron power. Both cases are shown in Fig. 8.34 and for each of  
6299 them the new Q1A entry position has been determined. The power of the emitted radiation  
6300 is reduced by up to 28%. The colliding proton beam, passing through this half quadrupole  
6301 with a certain offset to guarantee sufficient beam stay clear, will receive a deflecting kick in the  
6302 horizontal plane of about 90  $\mu$ rad. It supports the dipole based beam separation, provided by  
6303 the so-called D1 / D2 magnets in LHC, and will be integral part of the LHC design orbit.

6304 The resulting beam optics of the protons differs only marginally from the original version and  
6305 only a slight re-match is needed. However by carefully choosing the gradient of the new magnet  
6306 the parameters of the superconducting proton quadrupoles are untouched and the phase advance  
6307 at the end of the interaction region lattice is conserved in both planes.

### 6308 **Improved Electron lattice**

6309 A further improvement of the emitted synchrotron power and critical energy is obtained by  
6310 introducing an early focusing scheme of the electrons, which leads to a reduced electron beam  
6311 size and thus to softer separation requirements.

6312 The reduction of the electron beam size is obtained by installing a quadrupole doublet in the  
6313 electron lattice between the separation dipole and the QNC (half-) quadrupole. A carefully  
6314 matched focusing strength of this doublet will minimise the  $\beta$  function of the electrons at the  
6315 location of Q1A. At the same time an effective dipole field, that is needed to maintain the

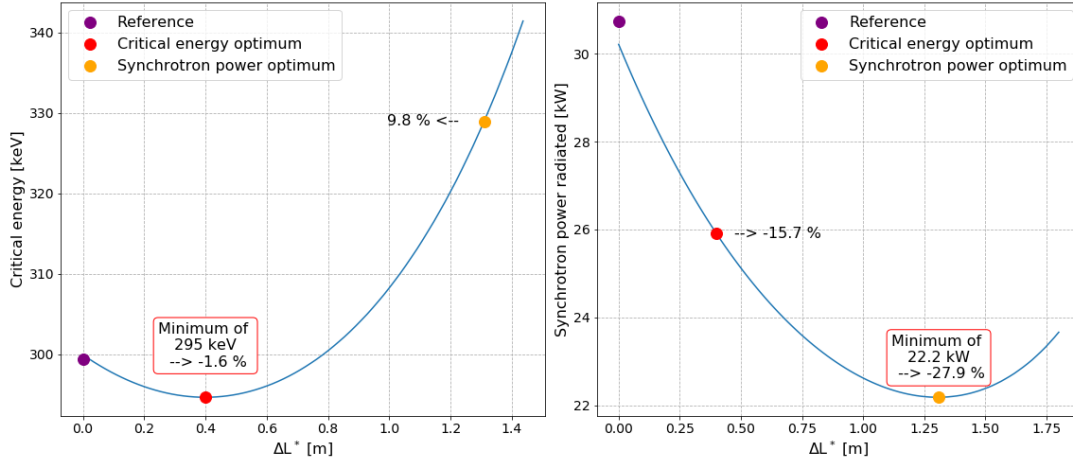


**Figure 8.34:** Improved critical energy and power of the synchrotron radiation for the half quadrupole based proton lattice. Left side: critical energy, right side: synchrotron radiation power. The horizontal axis refers to the shift  $\Delta L^*$  of the position of the first proton superconducting magnet Q1A.

6316 separation of proton and electron beams, is provided by shifting the magnet centres of the  
 6317 doublet lenses off axis. The horizontal offset of these quadrupoles has been chosen to provide  
 6318 the same bending radius as the separation dipole, thus leading in first order to the same critical  
 6319 energy of the emitted light in all separation fields. A detailed calculation of the divergence of the  
 6320 photons, the geometry of the radiation fan and the position of the absorbers and collimators will  
 6321 be one of the essential next steps within the so-called machine-detector-interface considerations.

6322 Fig. 8.33 (d) shows the new layout – compared to the previous version. The doublet providing  
 6323 the early focusing of the electron beam is embedded in the separator dipole, i.e. it is positioned  
 6324 at  $s = 6.3$  m and acts in combination with the separation dipole. The quadrupole gradients have  
 6325 been chosen for optimum matching conditions of the electron beam and the transverse shift of  
 6326 the field centres provide the same separation dipole effect as used in the long dipole.

6327 The early focusing of the electron beam allows for a softer separation of the beams, and leads  
 6328 therefore directly to a reduced critical energy  $E_{\text{crit}}$  and power  $P_{\text{syn}}$  of the emitted radiation.  
 6329 Fig. 8.35 shows the dependence of  $E_{\text{crit}}$  and  $P_{\text{syn}}$  on the  $\beta$ -function at  $s = L^*$  for the electron  
 6330 optics for different values of the required electron beam stay-clear expressed in units of the  
 6331 electron beam size  $\sigma$ . The beam separation has been re-calculated and the critical energy  
 6332 and radiation power are plotted. The graphs include different assumptions for the beam size  
 6333 considered. Including orbit tolerances, a beam stay-clear of  $20 \sigma$  is considered as the most  
 6334 relevant case, which refers to the red curve in the graph.

6335 In order to provide a complete study with the lattice featuring the off-centered quadrupoles, the  
 6336 new interaction region has been embedded in between the high energy end of the acceleration  
 6337 part of the linac and the *Arc 6* of the ERL, which marks the start of the energy recovery lattice.  
 6338 An optimum has been found for a beam optics with a beta function in the plane of the beam  
 6339 separation (i.e. horizontal) of  $\beta_x = 90$  m at  $L^* \approx 15$  m

6340 An improvement of about 9% for the critical energy and close to 25% of the radiated power is  
 6341 obtained, if an electron beam optics with  $\beta_x = 90$  m at the entrance of Q1A is used. For this  
 6342 most promising case the matched beam optics is shown in Fig. 8.36.

6343 The lower  $\beta$ -function of the electron beam at the focusing elements has the additional positive  
 6344 feature of reducing considerably the chromaticity of the new lattice, which is a crucial parameter

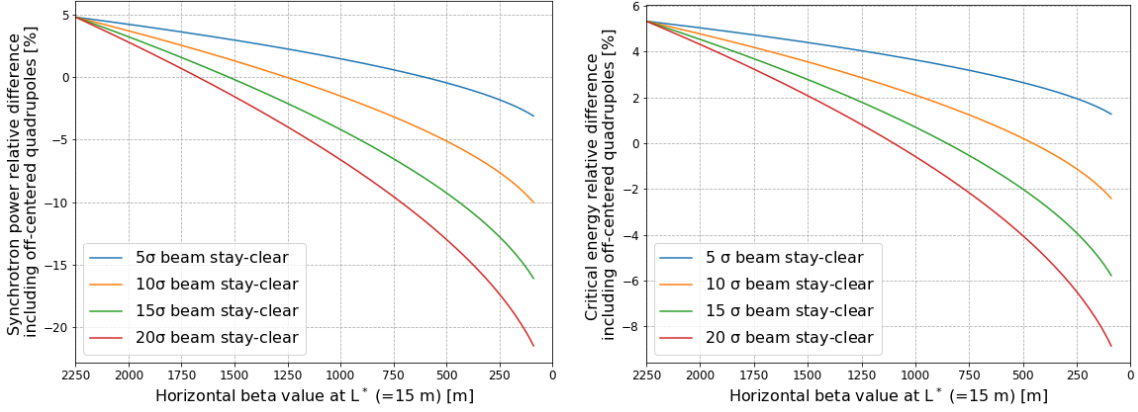


**Figure 8.35:** Relative difference with respect to the single dipole separation scheme for different values of the required beam stay-clear expressed in  $\sigma$ . Left : for the power of the emitted radiation, as function of the  $\beta$ -function of the electron beam at position  $s=15\text{m}$ . Left: for the critical energy of the emitted radiation, as function of the  $\beta$ -function of the electron beam at position  $s=15\text{m}$ . The early focusing of the electron beam allows for a much reduced separation field and thus to a reduced critical energy and power of the emitted radiation. The initial beta value is 2250 m.

6345 for the performance of the energy recovery process (details are described below in the chapter  
 6346 on tracking calculations). Compared to the dipole based separation and a late focusing,  $Q'$  is  
 6347 reduced to a level of 13 % horizontally and to a level of 11 % in the vertical plane. The details  
 6348 are listed in Tab. 8.22. Further studies will investigate the orbit correction scheme of the new  
 IR, and an eventual interplay of the solenoid fringe field and the quadrupoles.

	Dipole based separation	Early focusing scheme
$\xi_x$	-116	-15
$\xi_y$	-294	-32

**Table 8.22:** Chromaticity of the dipole based separation scheme and the new lattice based on early focusing, off-axis quadrupole lenses.

6349

6350 The influence of the electron doublet magnets on the proton optics is marginal – as can be  
 6351 expected due to the large difference in beam rigidity: If uncorrected, the electron doublet creates  
 6352 a distortion (a so-called *beta-beat*) of the proton optics of roughly 1 %. Still it has been calculated  
 6353 and taken into account in the context of a re-match of the proton beam optics.

6354 Combining the two improvement factors, namely the effective lengthening of  $L^*$  due to the  
 6355 use of a half quadrupole in front of the superconducting triplet, and the early focusing scheme  
 6356 in the lattice of the electrons, leads to an overall improvement of the interaction region with  
 6357 respect to synchrotron radiation power and critical energy that is shown in Fig. 8.37. The  
 6358 overall improvement factor is plotted with reference to the baseline dipole separation design  
 6359 with originally  $\beta = 2250\text{m}$  at the separation point  $s = L^*$ . Using a normal conducting half  
 6360 quadrupole in combination with the early focusing scheme, the power of the emitted synchrotron  
 6361 radiation is reduced by 48 % for an electron beam stay-clear of  $20\sigma$ .

6362 The estimated synchrotron radiation power and critical energy for the different optimisations  
 6363 are plotted in Fig. 8.37 and the results are summarised in Tab. 8.23. Referring to a beam energy  
 6364 of 49.19 GeV and the design current of 20 mA an overall power of 16.2 kW is emitted within one  
 6365 half of the interaction region.

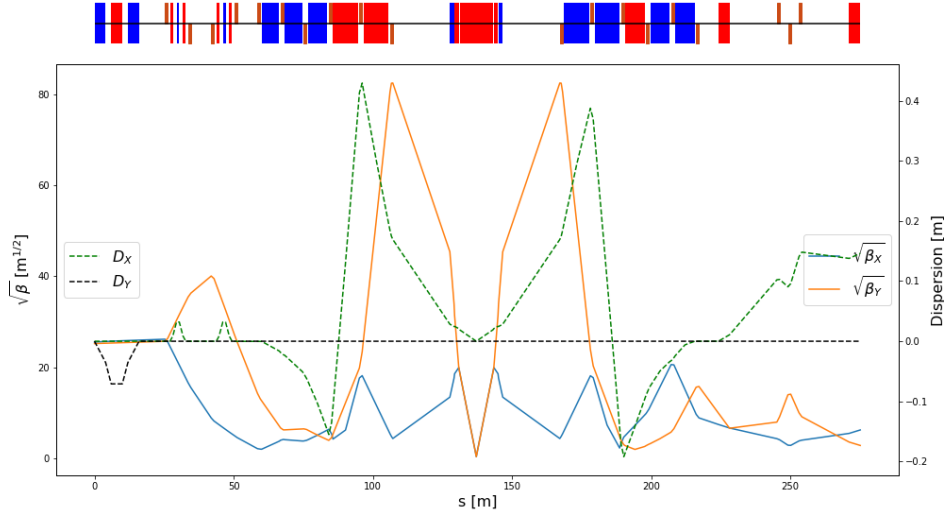


**Figure 8.36:** Electron beam optics for the new lattice including the early focusing scheme. The offset of the new doublet quadrupoles are chosen to provide the same separation field as in the dipole. The new optics is matched on the left side of the plot to the end of the acceleration linac. The right hand side is connected to Arc 6, the beginning of the decelerating ERL part. At the position of the first superconducting proton magnet the  $\beta$ -function in the (horizontal) separation plane of the electron beam is reduced to 90 m for lowest possible synchrotron radiation load.

Optimised scheme	Synchrotron radiation		Critical energy	
	Radiation power [kW]	Critical energy [keV]	Radiation power [kW]	Critical energy [keV]
Reference design	30.8	300	30.8	300
Dipole length optimum	26.8	336	30.8	300
Half quadrupole optimum	22.2	331	26.1	295
Off-centered quadrupoles opti.	19.3	290	22.1	259
Half quad. + Off-centered quad. opti.	16.2	265	17.4	255

**Table 8.23:** Synchrotron radiation power and critical energy for the different optimised separation schemes.

6366 Depending on the boundary conditions imposed by the integration of the particle detector, one  
 6367 of the two optimum layouts can be chosen – or a combination of both, i.e. an overall minimum  
 6368 defined by critical energy and radiated power.

6369 The basic main parameters of the proton mirror plate half quadrupole are summarised in  
 6370 Tab. 8.24 for the two optimum scenarios explained above: the optimum found for smallest  
 6371 synchrotron radiation power and the optimum for smallest critical energy of the emitted radi-  
 6372 ation. The values result from the optics studies of the previous sections. The presented gradients  
 6373 lead to a pole tip field of  $B_p \approx 1.3$  T.

6374 In both cases, the proton aperture radius has been chosen to include an orbit tolerance of 2 mm,  
 6375 a 10% tolerance on the beam size due to optics imperfections (beta-beating) and a beam size  
 6376 that corresponds to  $n = 15\sigma$  for a proton beam normalised emittance  $\varepsilon_p = 2.50\mu m$ . A value  
 6377 that is comfortably larger than the requirements of the HL-LHC standard lattice. The injection  
 6378 proton optics has been taken into account and although it features a larger emittance it clearly  
 6379 fit in the aperture, see the red dashed line in Fig. 8.38. The electron beam and the non-colliding  
 6380 proton beam will pass through the field free region delimited by the mirror plate.

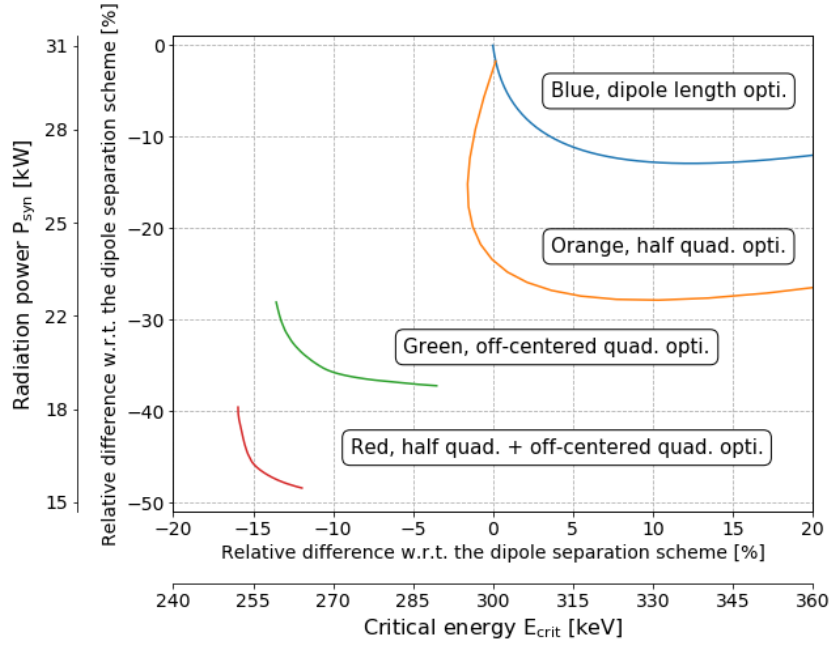


**Figure 8.37:** Relative differences with respect to the original single dipole separation scheme. The synchrotron radiated power is plotted as a function of the critical energy for different optimisation results: only optimising the dipole length (blue), only using a mirror quadrupole (orange), only using off-centered quadrupoles (green) and combining the mirror quadrupole with an earlier focusing (red).

Half quadrupole parameter	Unit	Minimum synchrotron radiation power	Minimum critical energy
$\gamma\epsilon_p$	mm-mrad	2.50	2.50
Gradient	T/m	48.2	50.7
Aperture radius	mm	27.0	25.6
Length	m	6.84	2.08

**Table 8.24:** Magnet gradient of the proposed half quadrupole for lowest synchrotron radiation power and lowest critical energy. An aperture of  $15\sigma + 20\%$  beta-beating + 2 mm orbit tolerances has been assumed.

6381 The aperture requirements inside the half quadrupole are determined on one side by the colliding  
6382 proton beam optics in the main aperture of the magnet. The beam separation scheme and optics  
6383 of electron and non-colliding proton beam on the other side have to fit into the field free region  
6384 beyond the mid plane of the mirror plate. As described below, a crossing angle of 7 mrad is  
6385 assumed for the non-colliding protons. These requirements are illustrated in Fig. 8.38. For  
6386 the case of smallest synchrotron radiation power, the three beams are plotted at the entrance  
6387 and exit of the quadrupole lens. For both proton beams the beam size shown in the graph  
6388 corresponds to 15 sigma plus 2 mm orbit tolerance and 10% beam size beating. Due to the  
6389 mini-beta optics the colliding proton beam fills nearly the given aperture of the magnet. The  
6390 non-colliding proton beam follows a relaxed optics with very limited aperture need. The envelope  
6391 of the electron beam is shown for 20  $\sigma$  beam size in both transverse planes.

6392 In contrast to the proton half quadrupole, the doublet magnets of the early focusing scheme  
6393 will house the three beams in one single aperture. In addition to the beam envelopes, the offset  
6394 that has been chosen to provide the beam separation effect has to be taken into account and

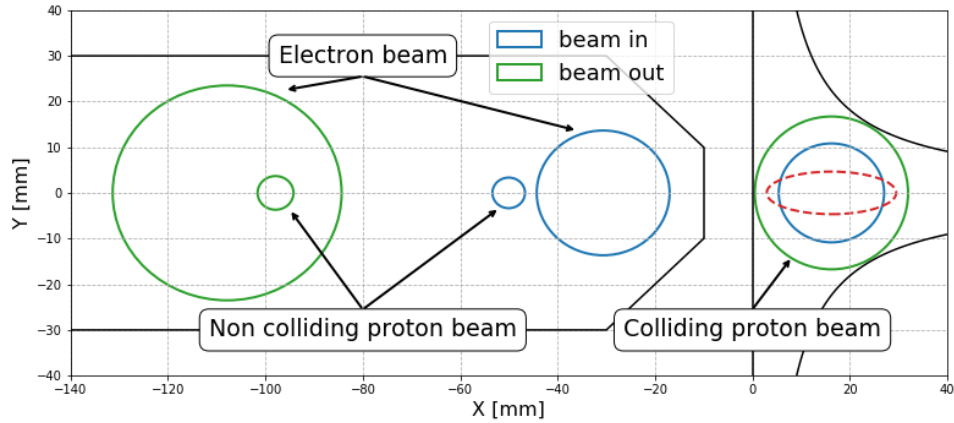


**Figure 8.38:** The position of the three beams at the entrance (blue) and exit (green) of the half quadrupole. The colliding proton beam is centered inside the main magnet aperture, while the second proton beam and the electrons are located in the field free region. The dashed red line represents the injection proton beam at the output of the half quadrupole.

6395 included in the aperture considerations.

In Fig. 8.39 the situation is visualised. On the left side the first off-center quadrupole (powered

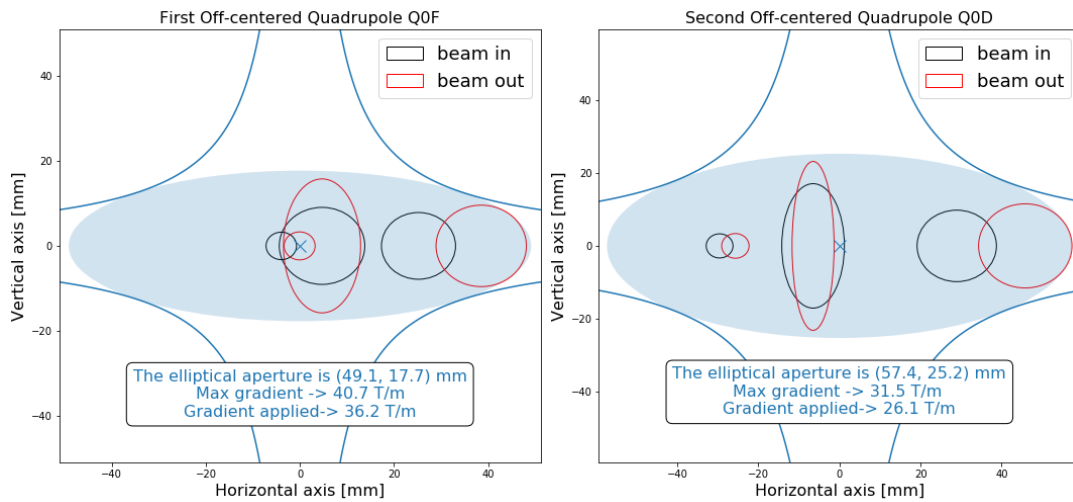


**Figure 8.39:** The position of the three beams at the entrance (black) and exit (red) of the electron doublet magnets. Following the internal convention,  $15\sigma$  plus 20% beta beating plus 2 mm orbit tolerances beam envelopes are chosen for the proton beams. The beam size of the electrons refer to  $20\sigma$ . From left to right the three beams are respectively the non colliding proton beam (tiny circles), electron beam (squeezed ellipses) and the colliding proton beam.

6396

6397 as focusing lens) is presented. Following the field direction, the electron beam is offset towards

6398 the outer side of the ring (right side of the plot) as defined by the proton beam closed orbit.

6399 The right part of the figure shows the second quadrupole (powered as defocusing lens) with

6400 the electron beam offset shifted to the other direction. In order to provide sufficient aperture

6401 for the three beams, an elliptical shape has been chosen for the vacuum chamber. It defines

6402 enough space for the beam envelopes and the off-centre design trajectories. The black ellipses

6403 correspond to the beams at the entrance of the magnet while the red shapes represent the beams

6404 at the exit. From left to right the three beams are respectively the non colliding proton beam

6405 (tiny circles), electron beam (squeezed ellipses) and the colliding proton beam. As defined before  
 6406 we refer to a beam size of  $20\sigma$  in case of the electrons and 15 sigma plus beta-beating plus 2  
 6407 mm orbit tolerance for the colliding and non-colliding proton beam.

6408 In this context it should be pointed out that the non-colliding proton beam, travelling in the  
 6409 same direction as the electrons, is shifted in time by half the bunch spacing. While the projected  
 6410 beam envelopes in Figs. 8.39 and 8.38 seem to overlap in the transverse plane, they are well  
 6411 separated by 12.5 ns, corresponding to 3.75 m, in the longitudinal direction.

6412 The minimum required gradients and pole tip radius of the quadrupoles of the doublet are listed  
 in Tab. 8.25. Following the increasing beam size after the IP, the two quadrupoles are optimised

Parameter	Unit	Q0F	Q0D
$\gamma\varepsilon_e$	mm·mrad	50	50
$\gamma\varepsilon_p$	mm·mrad	2.50	2.50
Gradient	T/m	36.2	26.1
Min. pole-tip radius	mm	28.9	38.1
Length	m	1.86	1.86

**Table 8.25:** Magnet gradient and pole tip aperture of the quadrupoles of the doublet for the synchrotron power optimum.

6413  
 6414 for sufficient free aperture for the collidng beams and their design orbits. Accordingly a different  
 6415 layout has been chosen for the magnets, to provide the best conditions for the radiation power  
 6416 and critical energy. An alternative approach has been studied, based on a single quadrupole  
 6417 design for both lenses of the doublet. While an optics solution still is possible, it does however  
 6418 not allow for minimum radiation power and sets more stringent requirements on the shielding  
 6419 and absorption of the synchrotron light fan.

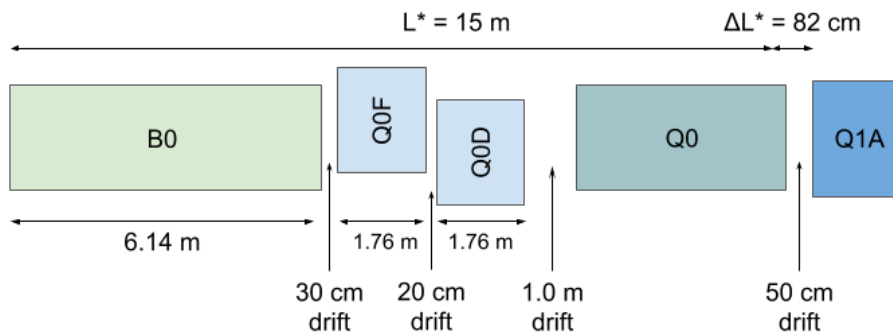


**Figure 8.40:** Possible optimised design featuring a 1.0 m drift between the off-centered quadrupoles and the half quadrupole in order to leave space for shielding material.

6420 The chromatic effect of the two lattice versions as a function of the momentum spread is shown  
 6421 in Fig. 8.41. The lattice based on a single dipole magnet and late focusing of the electron  
 6422 beam shows an increase of the  $\beta$  function of up to 40% in the vertical plane for particles with a  
 6423 momentum deviation up to the design value of  $\frac{\Delta p}{p} = 2.6 \cdot 10^{-4}$  (vertical cursor line in the graph)  
 6424 and a corresponding luminosity loss of 20% for those particles (see Fig. 8.42). The optimised  
 6425 design, based on the early focusing scheme, shows a much reduced chromatic effect and the  
 6426 resulting off-momentum beta-beating at the IP is limited to a few percent. As direct consequence  
 6427 the luminosity loss is well below the 1.5% level. A special local chromaticity correction scheme,  
 6428 therefore, dealing with the aberrations at IP, is thus not considered as necessary. Further studies

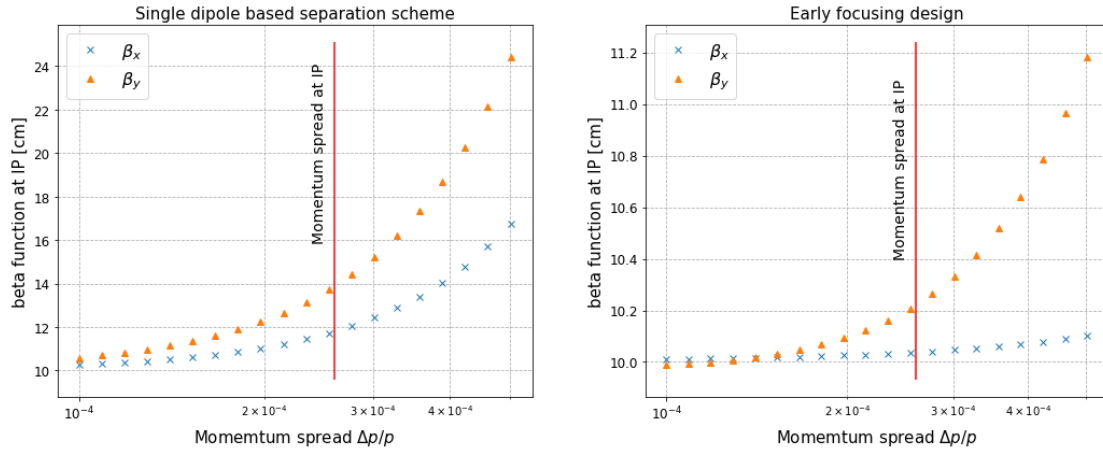


**Figure 8.41:** Beta function at the IP as a function of the momentum spread. Left : Situation for the single dipole based separation scheme. Right : With the design featuring an earlier focusing. The graphs show the increase of  $\beta^*$  due to the chromaticity of the lattice.

6429 will include the recirculation of the beam post-collision and the energy recovery performance and  
 6430 might nevertheless highlight the need of explicit sextupoles to mitigate the growing momentum  
 6431 spread through the deceleration process and to avoid beam losses.

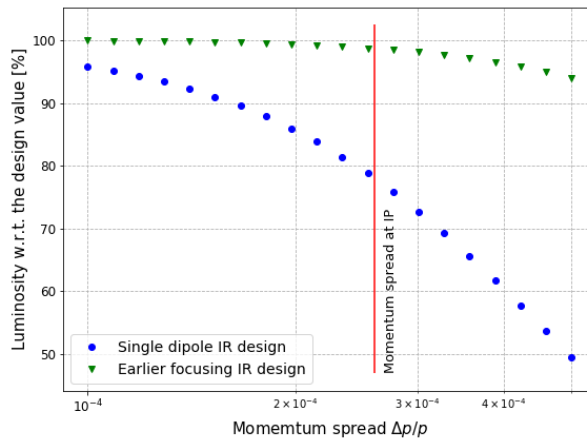


**Figure 8.42:** Luminosity as a function of the momentum spread for the single dipole based separation scheme (blue circles) and the design featuring an earlier focusing (green triangles).

## 6432 8.7.4 Interaction Region Magnet Design

### 6433 Triplet Magnet Design

6434 While the Q1 magnets remain in the range achievable with the well proven Nb-Ti superconduc-  
 6435 tors, operated at 1.8 K, the Q2 magnets require Nb<sub>3</sub>Sn technology at an operation temperature  
 6436 of 4.2 K. The working points on the load-line are given for both superconducting technologies in  
 6437 Fig. 8.43.

6438 The thickness of a coil layer is limited by the flexural rigidity of the cable, which will make the  
 6439 coil-end design difficult. Therefore multi-layer coils must be considered. However, a thicker,

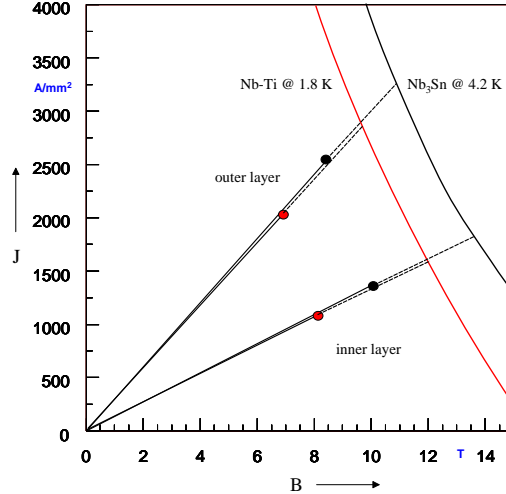


**Figure 8.43:** Working points on the load-line for both Nb-Ti and Nb<sub>3</sub>Sn variants of Q1A.

6440 multi-layer coil will increase the beam separation between the proton and the electron beams.  
 6441 The results of the field computation are given in Tab. 8.26.

Magnet parameter	Unit	Magnet type			
		Q1A	Q1B	Q2 type	Q3 type
Superconductor type		Nb-Ti	Nb-Ti	Nb <sub>3</sub> Sn	Nb <sub>3</sub> Sn
Coil aperture radius $R$	mm	20	32	40	45
Nominal current $I_{\text{nom}}$	A	7080	6260	7890	9260
Nominal gradient $g$	T/m	252	164	186	175
Percentage on the load line	%	78	64	71	75
Beam separation distance $S_{\text{beam}}$	mm	106-143	148-180	233-272	414-452

**Table 8.26:** Main triplet magnet parameters

6442 Unlike with the design proposed in the CDR of 2012 [1], the increased beam separation distance  
 6443 between the colliding proton beam and the electron beam makes it possible to neglect the fringe  
 6444 fields in the electron beam pipe. For the Q2 and Q3 magnets, the electron beam is outside  
 6445 of the quadrupole cold-mass and consequently, an HL-LHC inner-triplet magnet design can be  
 6446 adapted.

6447 For the Nb<sub>3</sub>Sn material we assume composite wire produced with the internal Sn process (Nb  
 6448 rod extrusions) [728]. The non-Cu critical current density is 2900 A/mm<sup>2</sup> at 12 T and 4.2 K.  
 6449 The filament size of 46 μm in Nb<sub>3</sub>Sn strands give rise to higher persistent current effects in  
 6450 the magnet. The choice of Nb<sub>3</sub>Sn would impose a considerable R&D and engineering design  
 6451 effort, which is however, not more challenging than other accelerator magnet projects, such as  
 6452 the HL-LHC.

6453 The conceptual design of the mechanical structure of the Q1 magnets is shown in Fig. 8.44  
 6454 (right). The necessary prestress in the coil-collar structure, which must be high enough to  
 6455 avoid unloading at full excitation, cannot be exerted with the stainless-steel collars alone. Two  
 6456 interleaved sets of yoke laminations (a large one comprising the area of the yoke keys and  
 6457 a smaller, floating lamination with no structural function) provide the necessary mechanical  
 6458 stability of the magnet during cooldown and excitation. Preassembled yoke packs are mounted

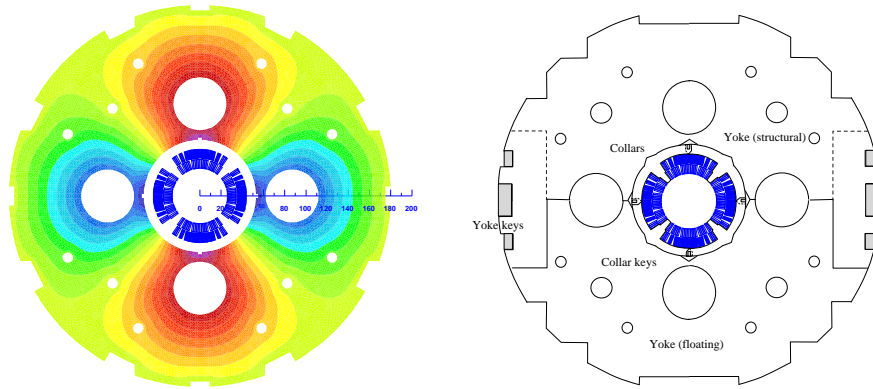


**Figure 8.44:** Conceptual design of the final focus septa Q1. Left: Magnetic vector potential (field lines). Right: Sketch of the mechanical structure.

6459 around the collars and put under a hydraulic press, so that the keys can be inserted. The sizing  
 6460 of these keys and the amount of prestress before the cooldown will have to be calculated using  
 6461 mechanical FEM programs. This also depends on the elastic modulus of the coil, which has to  
 6462 be measured with a short-model equipped with pressure gauges. Special care must be taken to  
 6463 avoid nonallowed multipole harmonics because the four-fold symmetry of the quadrupole will  
 6464 not entirely be maintained.

6465 For the Q2 and Q3 magnets, a HL-LHC inner triplet desing using a bladder and key mechanical  
 6466 structure can be adapted.

### 6467 Normal-Conducting Magnet Design

6468 The proposed mini-beta doublet of the electron lattice, providing an early focusing of the beam,  
 6469 and the normal conducting proton-half quadrupole are new magnet concepts. These have been  
 6470 studied conceptually to determine their technical feasibility. The geometry of the QNC magnet  
 6471 is shwon in Fig. 8.45 (left). Left of the mirror plate, the field free region will provide space for  
 6472 the electron beam and the non-colliding proton beam. The thickness of the mirror plate at the  
 6473 magnet mid-plane is 20 mm, allowing for sufficient mechanical stability at the minimal beam  
 6474 separation between the electron and proton beams.

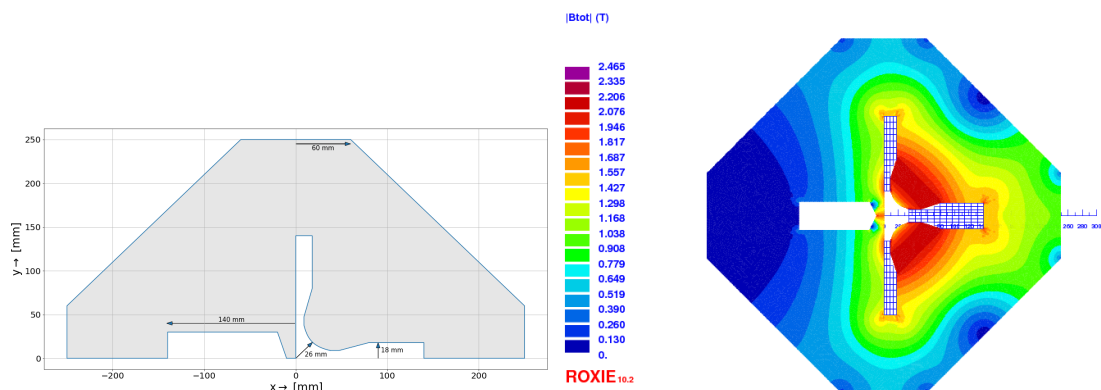


**Figure 8.45:** Left: Mechanical layout of the new half quadrupole for the proton beam. Right : Field distribution in the half quadrupole for the proton beam.

6475 Field calculations, using the magnet design code ROXIE [729] are presented in Fig. 8.45 (right).  
6476 The achieved field gradient is 50 T/m for a current of 400 A, assuming a current density of  
6477 21.14 A/mm<sup>2</sup>. This is in line with conductor geometries used for normal conducting magnets  
6478 installed in the CERN injector complex, for example, ID: PXMQNDD8WC, which is rated at  
6479 860 A corresponding to 45.45 A/mm<sup>2</sup>. A more comprehensive design study must also include a  
6480 further reduction of the multipole field components.

6481 The geometry of the Q0F and Q0D quadrupoles are given in Fig. 8.39 and the main specifications  
6482 are provided in Tab. 8.25. A maximum magnetic field of 1.2 T at the pole tip is well within  
6483 reach for a normal conducting quadrupole.

## 6484 8.8 Civil Engineering

6485 Since the beginning of the LHeC study which proposes a electron-hadron collider, various shapes  
6486 and sizes of the *eh* collider were studied around CERN region. Two main options were initially  
6487 considered, namely the Ring-Ring and the Linac-Ring. For civil engineering, these options  
6488 were studied taking into account geology, construction risks, land features as well as technical  
6489 constraints and operations of the LHC. The Linac-Ring configuration was selected, favouring  
6490 a higher achievable luminosity. This chapter describes the civil engineering infrastructure re-  
6491 quired for an Energy Recovery Linac (ERL) injecting into the ALICE cavern at Point 2 LHC.  
6492 Fig. 8.46 shows three options for the ERL of different sizes, represented as fractions of the LHC  
circumference, respectively 1/3, 1/4 and 1/5 of the LHC circumference.



**Figure 8.46:** Racetrack options proposed for LHeC at Point 2 of the LHC. The color coding illustrated different options with 1/3, 1/4 and 1/5 of the LHC circumference, resulting in different electron beam energies.

6493



Figure 8.47: Simplified map of Swiss geology.

6494 **8.8.1 Placement and Geology**

6495 The proposed siting for the LHeC is in the North-Western part of the Geneva region at the  
 6496 existing CERN laboratory. The proposed Interaction Region is fully located within existing  
 6497 CERN land at LHC Point 2, close to the village of St. Genis, in France. The CERN area is  
 6498 extremely well suited to housing such a large project, with well understood ground conditions  
 6499 having several particle accelerators in the region for over 50 years. Extensive geological records  
 6500 exist from previous projects such as LEP and LHC and more recently, further ground investi-  
 6501 gations have been undertaken for the High-Luminosity LHC project. Any new underground  
 6502 structures will be constructed in the stable molasse rock at a depth of 100–150 m in an area with  
 6503 low seismic activity.

6504 The LHeC is situated within the Geneva basin, a sub-basin of the large molassic plateau  
 6505 (Fig. 8.47). The molasse is a weak sedimentary rock which formed from the erosion of the  
 6506 Alps. It comprises of alternating layers of marls and sandstones (and formations of intermediate  
 6507 compositions), which show a high variety of strength parameters [730]. The molasse is overlaid  
 6508 by the Quaternary glacial moraines. A simplified geological profile of the LHC is shown in  
 6509 Fig. 8.48. Although placed mainly within the molasse plateau, one sector of the LHC is situated  
 6510 in the Jura limestone.

6511 The physical positioning of the LHeC has been developed based on the assumption that the  
 6512 maximum underground volume should be placed within the molasse rock and should avoid as  
 6513 much as possible any known geological faults or environmentally sensitive areas. Stable and dry,  
 6514 the molasse is considered a suitable rock type for Tunnel Boring Machines (TBM) excavation.  
 6515 In comparison, CERN has experienced significant issues with the underground construction of  
 6516 sector 3-4 in the Jura limestone. There were major issues with water ingress at and behind the  
 6517 tunnel face [731]. Another challenging factor for limestone is the presence of karsts. These are  
 6518 formed by chemical weathering of the rock and often they are filled with water and sediment,  
 6519 which can lead to water infiltration and instability of the excavation.

6520 The ERL will be positioned inside the LHC layout, in order to ensure that new surface facilities  
 6521 are located on existing CERN land. The proposed underground structures for the LHeC with

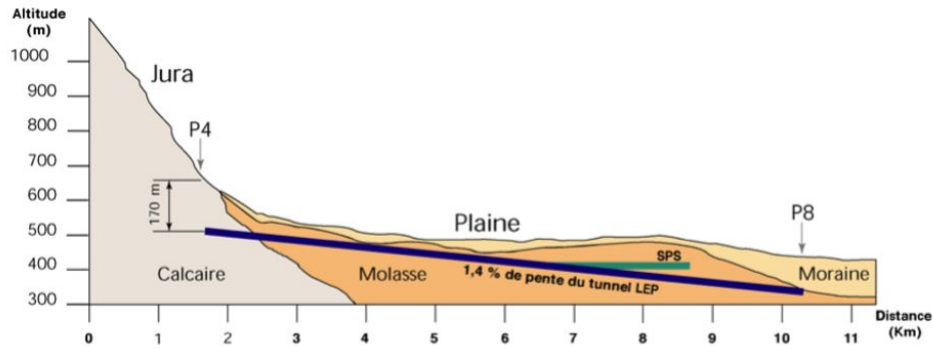


Figure 8.48: Geological profile of the LHC tunnel.

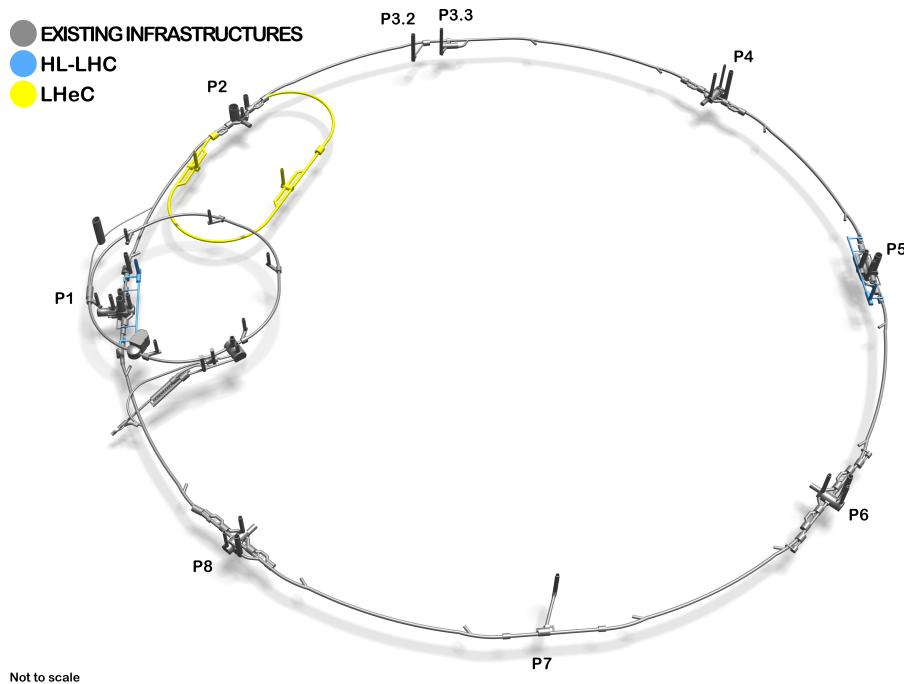


Figure 8.49: 3D Schematic showing proposed underground structures of LHeC (shwon in yellow). The HL-LHC structures are highlighted in blue.

6522 an electron beam energy of 60 GeV are shown in Fig. 8.49. The LHeC tunnel will be tilted  
 6523 similarly to the LHC at a slope of 1.4% to follow a suitable layer of molasse rock.

## 6524 8.8.2 Underground infrastructure

6525 The underground structures proposed for LHeC option 1/3 LHC require a 9 km long tunnel  
 6526 including two LINACs. The internal diameter of the tunnel is 5.5 m. Parallel to the LINACs, at  
 6527 10m distance apart, there are the RF galleries, each 1070 m long. Waveguides of 1 m diameter  
 6528 and four connection tunnels are connecting the RF galleries and LINACs. These structures are  
 6529 listed in Tab. 8.27. Two additional caverns, 25 m wide and 50 m long are required for cryogenics  
 6530 and technical services. These are connected to the surface via two 9 m diameter shafts, provided  
 6531 with lifts to allow access for equipment and personnel. Additional caverns are needed to house  
 6532 injection facilities and a beam dump. As shown in Tab. 8.27, the underground structures

Structure	Quantities	Span [m]	1/3 LHC	1/5 LHC
			Length [m]	Length [m]
Machine tunnels	-	5.5	9000	5400
Service caverns	2	25	50	50
Service shafts	2	9	80	80
Injection caverns	1	25	50	50
Dump cavern	1	16.8	90	90
Junction caverns	3	16.8	20	20
RF galleries	2	5.5	1070	830
Waveguide connections	50	1	10	10
Connection tunnels	4	3	10	10

**Table 8.27:** List of underground structures for LHeC for two different options with 1/3 or 1/5 of the LHC circumference.

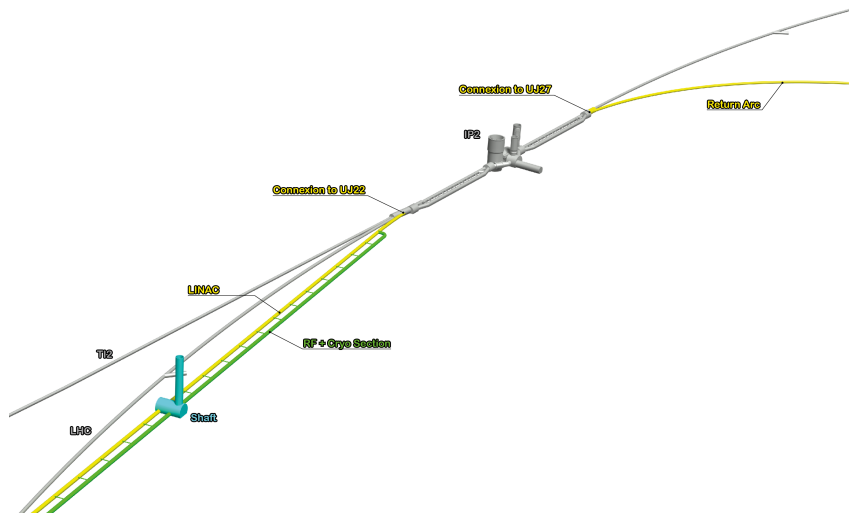


**Figure 8.50:** ERL injection area into IP2 and junction cavern

6533 proposed for LHeC options 1/5 LHC and 1/3 LHC are similar with the exception of the main  
6534 tunnel and the RF galleries which have different lengths.

6535 Shaft locations were chosen such that the surface facilities are located on CERN land. The scope  
6536 of work for surface sites is still to be defined. New facilities are envisaged for housing technical  
6537 services such as cooling and ventilation, cryogenics and electrical distribution.

6538 In addition to the new structures, the existing LHC infrastructure requires some modifications.  
6539 To ensure connection between LHC and LHeC tunnels, the junction caverns UJ22 and UJ27  
6540 need to be enlarged. Fig. 8.50 shows the location of these caverns. Localised parts of the cavern  
6541 and tunnel lining will be broken out to facilitate the excavation of the new spaces and the new  
6542 connections, requiring temporary support.

6543 Infrastructure works for LEP were completed in 1989, for which a design lifespan of 50 years  
6544 was specified. If the LHC infrastructure is to be re-used, refurbishment and maintenance works  
6545 are needed.



**Figure 8.51:** Left: Roadheader being used for shaft excavation at HL-LHC Point 1. Right: Rockbreaker used for new service tunnels excavation at HL-LHC Point 5 (Credit: Z. Arenas).

### 6546 8.8.3 Construction Methods

6547 A TBM would be utilised for the excavation of the main tunnel to achieve the fastest construc-  
 6548 tion. When ground conditions are good and the geology is consistent, TBMs can be two to four  
 6549 times faster than conventional methods. A double shield TBM could be employed, installing  
 6550 pre-cast segments as primary lining, and injecting grouting behind the lining.

6551 For the excavation of the shafts, caverns and connection tunnels, typical conventional techniques  
 6552 could be used. Similar construction methods used during HL-LHC construction can be adopted  
 6553 for LHeC, for example using roadheaders and rockbreakers. This machinery is illustrated in  
 6554 Fig. 8.51, showing the excavation works at Point 1. One main constraint that dictated what  
 6555 equipment to be used for the HL-LHC excavation, was the vibration limit. Considering the  
 6556 sensitivity of the beamline, diesel excavators have been modified and equipped with an electric  
 6557 motor in order to reduce vibrations that could disrupt LHC operation. Similar equipment could  
 6558 be required for LHeC, if construction works are carried out during operation of the LHC.

6559 Existing boreholes data around IP2 shows that the moraines layer is approximately 25–35 m deep  
 6560 before reaching the molasse. Temporary support of the excavation, for example using diaphragm  
 6561 walls is recommended. Once reaching a stable ground in dry conditions, common excavation  
 6562 methods can be adopted. The shaft lining will consist of a primary layer of shotcrete with  
 6563 rockbolts and an in-situ reinforced concrete secondary lining, with a waterproofing membrane  
 6564 in between the two linings.

### 6565 8.8.4 Civil Engineering for FCC-eh

6566 A facility allowing collisions between protons and electrons was considered in the study for the  
 6567 Future Circular Collider (FCC). Figure 8.52 shows the baseline position for FCC and the lepton  
 6568 ring located at Point L.

6569 During FCC feasibility stage, a bespoke GIS based tool (the Tunnel Optimisation Tool – TOT)  
 6570 was used to optimise the placement and layout of the FCC ring. The current baseline location  
 6571 was chosen such that the FCC tunnel is placed in preferable geology (90% of the tunnel is in  
 6572 molasse), the depth of the shafts and the overburden is minimised and tunnel under the Geneva  
 6573 Lake goes through the lake bed, passing though reasonably stable ground. More investigations  
 6574 are needed to determine the feasibility of tunnelling under the Geneva Lake. The baseline  
 6575 position also allows connections to the LHC. Figure 8.53 shows the geological profile of the

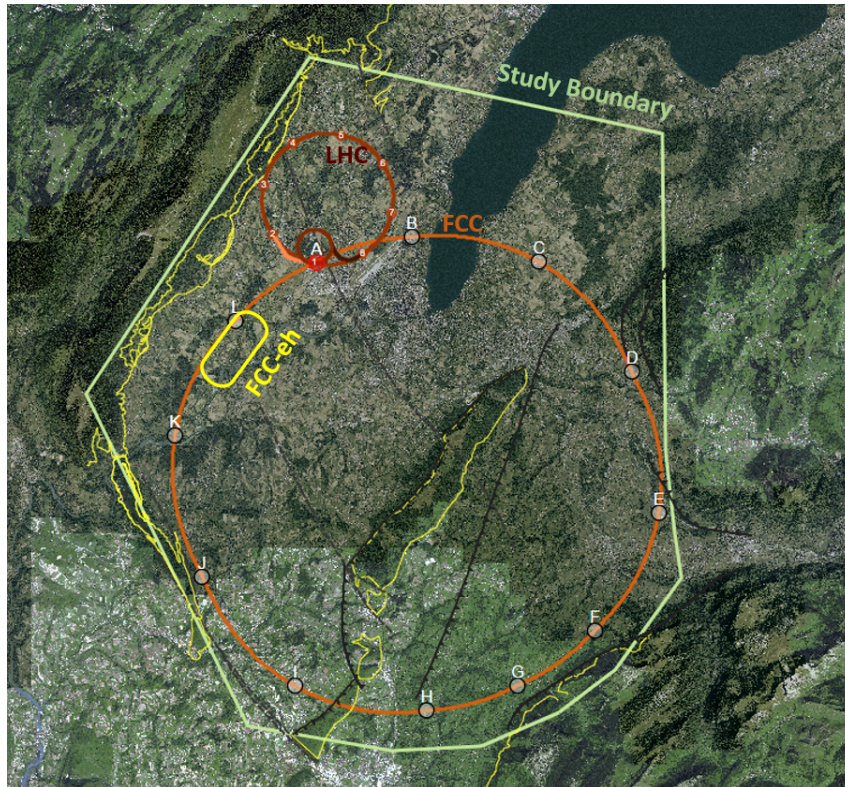


**Figure 8.52:** Baseline position and layout for FCC. The lepton ring location is shown at Point L.

6576 tunnel in baseline position. TOT was used to evaluate different layouts and positions for the  
 6577 FCC ring and assess the impact on the location of the lepton ring. The candidate locations for  
 6578 the *eh* IR were the experimental points A, B, G and L. Point L was selected because it provides  
 6579 good geological conditions, being fully housed in the molasse layer at a depth of around 180 m.  
 6580 In comparison, Point G is much deeper, Point A is challenging due to proximity of the LHC  
 6581 and Point B is located in a congested urban area. Similarly to LHeC, the lepton ring will be  
 6582 located inside the FCC ring, in this instance to avoid the Jura limestone. The entire FCC-eh  
 6583 infrastructure is located in the molasse.

6584 The geological data captured within the TOT tool was collected from various sources includ-  
 6585 ing previous underground projects at CERN, the French Bureau de Recherches Géologiques et  
 6586 Minières (BRGM), and existing geological maps and boreholes for geothermal and petroleum  
 6587 exploration. The data was processed to produce rock-head maps and to create the geological  
 6588 layers. No ground investigations have been conducted specifically for the FCC project [732]. In  
 6589 order to validate its baseline alignment and determine the geotechnical parameters required for  
 6590 the detailed design, site investigation campaigns will need to be carried out. Some boreholes  
 6591 exist in the region where the tunnel for the lepton ring will be built, reducing the uncertainty  
 6592 of the ground conditions. However, further ground investigations are needed in order to verify  
 6593 the boundary between geological layers. The geological features of interest in this region are the  
 6594 Allondon Fault and possible zones of poor rock and level of limestone, which should be avoided.

6595 The IP will be in the experimental cavern at point L, defined as an experimental point for FCC-  
 6596 hh. The layout of the ERL and the underground infrastructure for the FCC-eh is similar to  
 6597 LHeC (see Table 8.27), with the exception of the shafts which are 180 m deep. The schematic  
 6598 layout and proposed civil engineering structures are shown in Fig. 8.54.

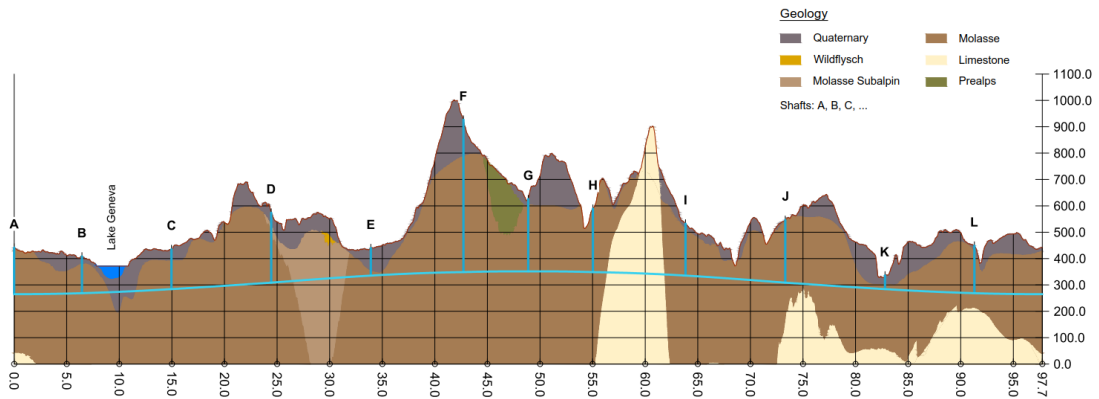


**Figure 8.53:** Geological profile along FCC tunnel circumference

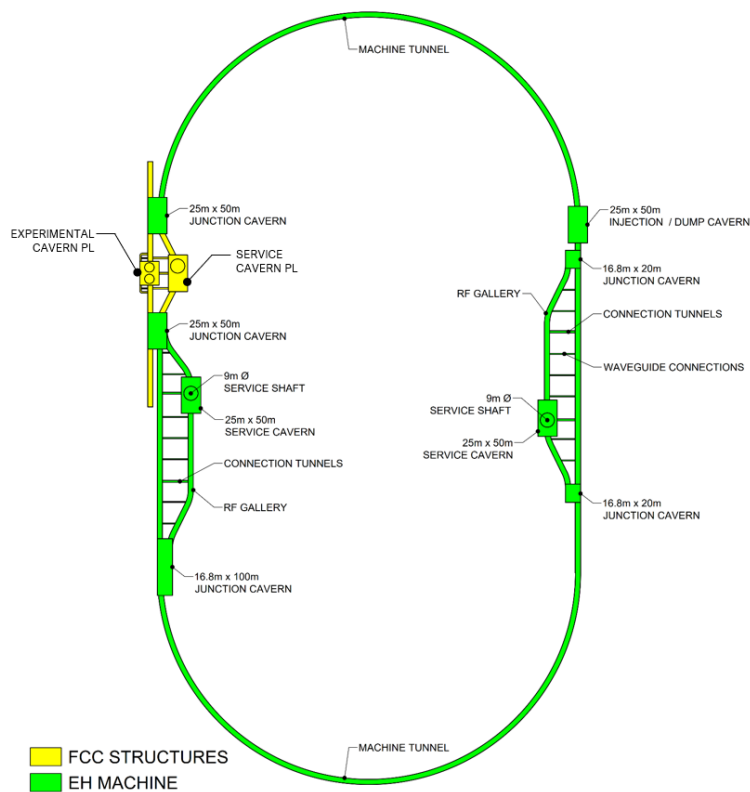


**Figure 8.54:** Schematic layout showing the proposed underground structures for FCC-eh

6599 The upper excavation for each shaft will be through the moraines. Based on available geological  
6600 data, the moraines layer should be approximately 30 m deep. Similar construction methods as  
6601 described in Section 8.8.3 could be used. For FCC, the alternative technology that has been  
6602 considered for deep shafts is using a Vertical Shaft Sinking Machine. The junction caverns  
6603 connecting the ERL tunnel with the FCC tunnel must be designed such that they fit the re-  
6604 quirements for the new collider and the lepton machine. The junction caverns near Point L  
6605 will connect three tunnels, the FCC main tunnel, the ERL tunnel and the RF galleries. These  
6606 caverns will have a 25 m span and 50 m length.

6607 For the FCC TBM excavations, different lining designs have been developed corresponding to  
6608 conditions of the rock [732]. Good ground conditions have been assumed based on available  
6609 geological information in the area where the ERL tunnels are positioned and a single-pass pre-  
6610 cast lining is proposed.

### 6611 **8.8.5 Cost estimates**

6612 The cost for underground civil engineering for FCC-eh facility was estimated to be approximately  
6613 430 MCHF. The construction programme for the lepton accelerator tunnels, caverns and shafts  
6614 is currently integrated into the overall FCC construction schedule.

6615 A detailed cost estimate was prepared for a 9 km ERL located at Point 2 of LHC, using the  
6616 same unit prices as for FCC. More recently for LHeC, the cost figures were adapted to fit the  
6617 smaller version, the 5.4 km racetrack at Point 2 (option 1/5 LHC). The civil engineering costs  
6618 amount to about 25 % of the total project costs. For the 9 km ERL (1/3 LHC option) the civil  
6619 engineering was estimated to 386 MCHF and for a 5.4 km configuration (1/5 LHC) the costs  
6620 would be 289 MCHF. These costs do not include surface structures. Where possible, existing  
6621 surface infrastructure will be re-used.

6622 The cost estimates include the fees for preliminary design, approvals and tender documents  
6623 (12 %), site investigations (2 %) and contractor's profit (3 %). The accuracy range of the cost  
6624 estimates at feasibility stage is  $\pm 30$  %.

### 6625 **8.8.6 Spoil management**

As with all construction projects, environmental aspects play an important role. A detailed study  
is being conducted at CERN to find a potential re-use for of the spoil that will be generated  
from the FCC underground excavations. The total amount of spoil calculated is approximately  
10 million cubic meters, of which 778,000 cubic metres of spoil would be generated from the  
lepton ring tunnel construction.

## Chapter 9

# Technology of ERL and PERLE

### 9.1 Energy Recovery Linac Technology - Status and Prospects

In instances where high beam power is required, the concept of energy recovery presents an attractive solution. Energy recovering linacs (ERLs) are a class of novel accelerators which are uniquely qualified to meet the demands for a wide variety of applications by borrowing features from traditional architectures to generate linac quality beams with near storage ring efficiency [733]. After acceleration through a linac section, the electrons in an ERL are returned 180° out of phase with respect to the radio frequency (RF) accelerating field for energy recovery. The beam deposits energy into cavity fields, which can then accelerate newly injected bunches, thereby effectively canceling the beam loading effects of the accelerated beam. Therefore ERLs can accelerate very high average currents with only modest amounts of RF power. Because the beam is constantly being renewed, it never reaches an equilibrium state. Consequently this provides flexibility to manipulate the phase space and tailor the beam properties for a specific application. Further, since the energy of the decelerated beam is approximately equal to the injection energy, the dump design becomes considerably easier.

#### 9.1.1 ERL Applications

Historically, nearly all ERLs built and operated were used to drive a free-electron laser (FEL). The requirement for high peak current bunches necessitated bunch compression and handling the attendant beam dynamical challenges. In recent years, ERLs have turned from being drivers of light sources toward applications for nuclear physics experiments, Compton backscattering sources and strong electron cooling. Unlike an FEL, these latter use cases require long, high charge bunches with small energy spread. Where once a short bunch length was the key performance metric, now there is a premium on maintaining a small correlated energy spread (with a commensurately long bunch).

#### 9.1.2 Challenges

Energy recovery linacs are not without their own set of challenges. In the following sections a brief survey of some of the most relevant are given. These include collective effects, such as space charge, the multipass beam breakup (BBU) instability, coherent synchrotron radiation (CSR) and the microbunching instability ( $\mu$ BI), beam dynamic issues such as halo, the interaction of

6656 the beam with the RF system and other environmental impedances as well as issues related to  
6657 common transport lines.

## 6658 **Space Charge**

6659 The role of space charge forces (both transverse and longitudinal) often dictate many operational  
6660 aspects of the machine. Maintaining beam brightness during the low energy injection stage is  
6661 vitally important. In addition to the low energy, ERL injectors must also preserve beam quality  
6662 through the merger system that directs the beam to the linac axis. Once injected into the  
6663 linac, the beam energy at the front end is often still low enough that space charge forces cannot  
6664 be neglected. Just as important is the longitudinal space charge (LSC) force which manifests  
6665 itself by an energy spread asymmetry about the linac on-crest phase [734]. The LSC wake acts  
6666 to accelerate the head of the bunch while decelerating the tail. Operating on the rising part  
6667 of the waveform leads to a decrease in the correlated energy spread, while accelerating on the  
6668 falling side leads to an increase. These observations inform where acceleration, and how the  
6669 longitudinal match, is performed.

## 6670 **Beam Breakup Instability**

6671 The beam breakup instability is initiated when a beam bunch passes through an RF cavity  
6672 off-axis, thereby exciting dipole higher-order modes (HOMs). The magnetic field of an excited  
6673 mode deflects following bunches traveling through the cavity. Depending on the details of the  
6674 machine optics, the deflection produced by the mode can translate into a transverse displacement  
6675 at the cavity after recirculation. The recirculated beam induces, in turn, an HOM voltage which  
6676 depends on the magnitude and direction of the beam displacement. Thus, the recirculated beam  
6677 completes a feedback loop which can become unstable if the average beam current exceeds the  
6678 threshold for stability [735]. Beam breakup is of particular concern in the design of high average  
6679 current ERLs utilizing superconducting RF (SRF) technology. If not sufficiently damped by the  
6680 HOM couplers, dipole modes with quality factors several orders of magnitude higher than in  
6681 normal conducting cavities can exist, providing a threat for BBU to develop. For single pass  
6682 ERLs, beam optical suppression techniques – namely, interchanging the horizontal and vertical  
6683 phase spaces to break the feedback loop between the beam and the offending HOM – are effective  
6684 at mitigating BBU [736].

## 6685 **Coherent Synchrotron Radiation**

6686 Coherent synchrotron radiation poses a significant challenge for accelerators utilizing high bright-  
6687 ness beams. When a bunch travels along a curved orbit, fields radiated from the tail of the bunch  
6688 can overtake and interact with the head. Rather than the more conventional class of head-tail  
6689 instabilities where the tail is affected by the actions of the head, CSR is a tail-head instability.  
6690 The net result is that the tail loses energy while the head gains energy leading to an undesirable  
6691 redistribution of particles in the bunch. Because the interaction takes place in a region of dis-  
6692 persion, the energy redistribution is correlated with the transverse positions in the bend plane  
6693 and can lead to projected emittance growth. While there has been much progress in recent years  
6694 to undo the effects of CSR in the bend plane with an appropriate choice of beam optics [737],  
6695 it is more difficult to undo the gross longitudinal distortion caused by the CSR wake. This is  
6696 particularly true in applications where the intrinsic energy spread is small and/or where the

6697 effect can accumulate over multiple recirculations. One possible mitigation is shielding the CSR  
6698 wake using an appropriately sized beam pipe [738].

### 6699 **Microbunching Instability**

6700 Microbunching develops when an initial density modulation, either from shot noise or from the  
6701 drive laser, is converted to energy modulations through short-range wakefields such as space  
6702 charge and CSR. The energy modulations are then transformed back to density modulations  
6703 through the momentum compaction of the lattice. Danger arises when a positive feedback is  
6704 formed and the initial modulations are enhanced. This phenomenon has been studied exten-  
6705 sively, both theoretically and experimentally, in bunch compressor chicanes [739, 740]. Only  
6706 recently has there been a concerted effort to study the microbunching instability in recirculating  
6707 arcs [741–743]. Because the beam is subject to space charge and/or CSR throughout an ERL,  
6708 density modulations can be converted to energy modulations. And because of the native mo-  
6709 mentum compaction of the lattice (in arcs, spreaders/recombiners, chicanes, etc.) those energy  
6710 modulations may be converted back to density modulations. Therefore, ERLs offer potentially  
6711 favorable conditions for seeding the microbunching instability, which requires careful attention  
6712 in the early design stages.

### 6713 **Halo**

6714 Halo is defined as the relatively diffuse and potentially irregularly distributed components of  
6715 beam phase space that can reach large amplitudes. It is of concern because ERL beams are  
6716 manifestly non-Gaussian and can have beam components of significant intensity beyond the  
6717 beam core [744]. Though sampling large amplitudes, halo responds to the external focusing of  
6718 the accelerator transport system in a predictable manner. It is therefore not always at large  
6719 spatial amplitude, but will at some locations instead be small in size but strongly divergent.  
6720 Halo can therefore present itself as *hot spots* in a beam distribution, and thus may be thought  
6721 of as a lower-intensity, co-propagating beam that is mismatched to the core beam focusing,  
6722 timing, and energy. Beam loss due to halo scraping is perhaps the major operational challenge  
6723 for higher-power ERLs. Megawatt-class systems must control losses at unshielded locations to  
6724 better than 100 parts-per-million to stay within facility radiation envelopes. Scaling to 100 MW  
6725 suggests that control must be at the part-per-million level. This has been demonstrated – but  
6726 only at specific locations within an ERL [745].

### 6727 **RF Transients**

6728 Dynamic loading due to incomplete energy recovery is an issue for all ERLs [746]. In some  
6729 machines it is due to unintentional errors imposed on the energy recovered beam; for instance,  
6730 path length errors in large-scale systems. In other machines, such as high power ERL-based FEL  
6731 drivers, it is done intentionally. In cases where there is the potential for rapid changes in the  
6732 relative phase of the energy recovered beam, dynamic loading would be difficult to completely  
6733 control using fast tuners. In such cases adequate headroom in the RF power will have to be  
6734 designed into the system. These transient beam-loading phenomena are widely unrecognized  
6735 and/or neglected. RF drive requirements for an ERL are often viewed as *minimal*, because in  
6736 steady-state operation the recovered beam notionally provides RF power for acceleration. It  
6737 has however been operationally established that RF drive requirements for ERLs are defined

6738 not by the steady-state, but rather by beam transients and environmental/design factors such  
6739 as microphonics [747]. As a result, the RF power required for stable ERL operation can differ  
6740 dramatically from naïve expectations.

## 6741 **Wakefields and Interaction of Beam with Environment**

6742 As with other system architectures intended to handle high-brightness beams, ERLs can be  
6743 performance-limited by wakefield effects. Not only can beam quality be compromised by in-  
6744 teraction of the beam with environmental impedances, there is also significant potential for  
6745 localized power deposition in beamline components. Resistive wall and RF heating have proven  
6746 problematic during ERL operation in the past [748]. Extrapolation of this experience to higher  
6747 bunch charges and beam powers leads to serious concern regarding heating effects. Careful  
6748 analysis and management of system component impedances is required.

## 6749 **Multi-turn, Common Transport**

6750 Future systems must evolve to utilize multiple turns; it is a natural cost optimization method [749]  
6751 and multi-turn systems can in principle provide performance equal to that of 1-pass up/down  
6752 ERLs at significantly lower cost. In addition to the use of multiple turns, cost control motivates  
6753 use of extended lengths of common transport, in which both accelerated and recovered passes  
6754 are handled simultaneously using the same beam lines. This presents unique challenges for high  
6755 energy ERLs, like LHeC in particular, where energy loss due to synchrotron radiation cannot  
6756 be ignored and causes an energy mismatch for common transport lines. But addressing these  
6757 challenges will open up exciting new opportunities for ERLs. In addition to PERLE and LHeC,  
6758 a multi-turn ERL design from Daresbury illustrates the manner in which the cost/complexity  
6759 optimum lies toward shorter linacs, more turns, and multiple beams in fewer beam lines [674].  
6760 This also drives the use of multiple turns in stacking rings for hadron cooling; the more turns  
6761 the cooling beam can be utilized, the lower the current required from the driver ERL, which  
6762 mitigates challenges associated with source lifetime [750].

### 6763 **9.1.3 ERL Landscape**

6764 One way to view the current state of ERLs globally is the so-called *ERL landscape* shown in  
6765 Fig. 9.1 [751]. Every data point represents a machine that demonstrated energy recovery and is  
6766 positioned in (maximum) energy and (average) current parameter space. For clarity, the plot is  
6767 restricted to continuous-wave (CW), SRF-based ERLs only and includes legacy machines, those  
6768 under construction and currently in operation as well as the LHeC and PERLE (proposed).  
6769 The size of the marker is indicative of the charge per bunch while a black line around the  
6770 marker indicates it was/is a *true ERL*. That is, where the beam power exceeds the installed  
6771 RF power (they are represented in the plot by the three FEL drivers that were designed, built,  
6772 commissioned and operated at Jefferson Laboratory).

6773 A cursory look at Fig. 9.1 illustrates several of the challenges facing the next generation of  
6774 ERLs. While getting from the current state-of-the-art to the LHeC requires only a modest  
6775 increase in average current, it requires a significant increase in bunch charge and addressing  
6776 the consequent collective effects [752]. Most significantly, however, is the leap in energy from  
6777 systems that have operated in the 100 MeV range to several tens of GeV. Note that PERLE is  
6778 strategically positioned to address incremental changes in both average current, bunch charge

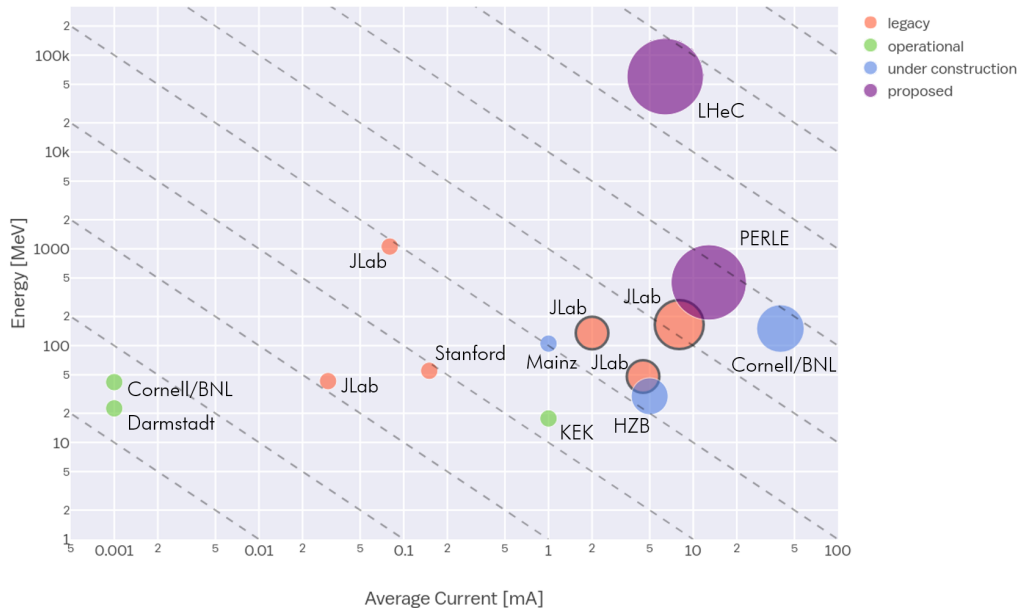


**Figure 9.1:** The *ERL landscape*, where data points are restricted to CW, SRF-based ERLs. The dashed lines represent lines of constant beam power – starting from 10 W in the lower left and going to 10 GW in the upper right. Note that both axes use a log scale.

6779 and energy. As such, it provides a convenient test bed facility to address the issues described  
 6780 previously [753]. Several ERLs are still in the nascent stages and as they ramp up beam power,  
 6781 will also be valuable in advancing the state-of-the-art. For instance, though it uses a Fixed Field  
 6782 Alternating Gradient (FFAG) arc, the Cornell/Brookhaven ERL Test Accelerator (CBETA) will  
 6783 address multi-turn energy recovery for the first time in an SRF system [754]. Note that with  
 6784 only minor modifications Jefferson Laboratory’s Continuous Electron Beam Accelerator Facility  
 6785 (CEBAF) could be operated with multi-pass energy recovery at several GeV using common  
 6786 transport with the same topology as LHeC (i.e. bisected linacs of equal energy gain with arcs  
 6787 vertically separated by energy using spreaders and recombiners) [755].

## 6788 9.2 The ERL Facility PERLE

6789 PERLE is a compact three-pass ERL based on SRF technology, a new generation machine  
 6790 uniquely covering the 10 MW power regime of beam current and energy. Its Conceptual Design  
 6791 Report appeared recently [4]. Apart from low energy experiments it could host, thanks to its  
 6792 beam characteristics, PERLE will serve as a hub for the validation of a broad range of accelerator  
 6793 phenomena and the development of ERL technology for future energy frontiers colliders which  
 6794 was introduced above. Particularly, the basic 3-turn configuration, design challenges and beam  
 6795 parameters (see Tab. 9.1) are chosen to enable PERLE as a testbed for the injection line and  
 6796 SRF technology development, as well as multi-turn and high current ERL operation techniques  
 6797 for the Large Hadron electron Collider. While the concept and promise of ERL’s has been  
 6798 kick-started by demonstration machines based on existing accelerator technology, PERLE will  
 6799 be the first machine designed from the ground up to use fully optimised ERL-specific designs  
 6800 and hardware.

6801 The PERLE collaboration involves today CERN, Jefferson Laboratory, STFC-Daresbury, Uni-  
 6802 versity of Liverpool, BINP-Novosibirsk and the newly formed Irene Curie Lab at Orsay. Four

6803 of these international partners have been pioneering the development of ERL technology, the  
6804 other are leading laboratories on SRF technology and accelerator physics. The Orsay Lab is  
6805 leading the effort to develop and later host PERLE at Orsay campus in close collaboration with  
6806 the LHeC coordination.

6807 The following PERLE summary focuses on the power challenge, the lattice, site and time sched-  
6808 ule. PERLE uses a cryo-module with four 5-cell cavities like the LHeC. The prototype cavity  
6809 production and test as well as the design status of the cryo-module are described in the LHeC  
6810 linac chapter. There one also finds a section on the source and injector and as well arc magnets,  
6811 dipoles of a 3-in-1 design and quadrupoles, which will similarly be used for PERLE.

### 6812 **9.2.1 Configuration**

6813 In its final configuration, a high average current electron beam (20 mA) is accelerated through  
6814 three passes to the maximum energy (500 MeV) in the superconducting RF CW linear acceler-  
6815 ators. The beam is then used for its intended purpose such as photon generation by Compton  
6816 back-scattering, a cooling source for ion beams or a beam for colliding against fixed targets. The  
6817 3-passes up in energy may significantly increase the energy spread or emittance of the electron  
6818 beam but the major part of the beam power remains. The beam is then sent back through the  
6819 accelerators again only this time roughly 180 degrees off the accelerating RF phase so the beam  
6820 is decelerated through the same number of passes and then sent to a beam dump at around the  
6821 injection energy. Several benefits arise from this configuration: the required RF power (and its  
6822 capital cost and required electricity) is significantly reduced to that required to establish the  
6823 cavity field; the beam power that must be dissipated in the dump is reduced by a large factor,  
6824 and often the electron beam dump energy can be reduced below the photo-neutron threshold so  
6825 that activation of the dump region can be reduced or eliminated.

### 6826 **9.2.2 Importance of PERLE towards the LHeC**

6827 PERLE is an important and necessary step accompanying the LHeC realisation. Together  
6828 with other ERL facilities, CBETA, bELRin-Pro and possibly others, it will bridge the gap of  
6829 power level between the currently reached maximum (CEBAF-ER at 1 MW) and the targeted  
6830 performances of LHeC (1 GW) by exploring a next higher operational power regime of around  
6831 10 MW. Moreover, sharing the same conceptual design with the LHeC, a racetrack configuration  
6832 with 3 acceleration and 3 deceleration passes, identical injection line and the same SRF system,  
6833 as well as the same beam current in the SRF cavities will allow to acquire with PERLE an  
6834 enormous insight on multiple pass operation and common transport from full energy, before and  
6835 possibly during LHeC operation too.

6836 Up to date, existing SRF systems have demonstrated stability at only a modest fraction ( $\leq 20\%$ )  
6837 of the current envisaged for the LHeC. Though threshold currents have been indirectly measured  
6838 at higher values, there is no direct evidence that multi-pass systems will be sufficiently resistant  
6839 to BBU at the higher current, nor has the sensitivity of the instability threshold to linac length,  
6840 dynamic range, and number of passes been directly or systematically measured as yet. PERLE  
6841 will provide a single datum on linac length, and can directly measure the dependence on the  
6842 number of passes and the turn-to-turn transfer matrix.

6843 The dynamic range (which is the ratio of injected/extracted energy to full energy) is a critical  
6844 design parameter, in as much as it defines the sensitivity of the overall system to magnetic

6845 field errors. Errors at full energy drive phase/energy errors that are magnified by adiabatic  
6846 anti-damping during recovery, and can exceed the dump acceptance should the errors be too  
6847 large. Thus, the field quality needed is inversely proportional to the ratio of full energy to dump  
6848 energy: that is, a very high energy machine (or one with very low dump energy) needs very  
6849 high-quality magnets. For PERLE, the dynamic range is 70 : 1 (7 MeV injected and 490 MeV  
6850 full energy). This implies a need of  $\Delta B/B_{dipole} \simeq 0.001\%$  field flatness (extrapolated from JLAB  
6851 ERL needs) to recover cleanly enough. This implies a tight constraint on magnet performances  
6852 and impact their cost, even when it is the SRF which drives the overall cost of the facility,  
6853 for LHeC. PERLE has a very large dynamic range and a transport system with considerable  
6854 symmetry and flexibility. It is therefore a suitable tool to explore this issue and evaluate the  
6855 cost implications for larger scale systems.

6856 Existing systems have operated at maximum 1 MW full beam power. This is too low for a precise  
6857 understanding and control of beam halo. Extrapolation to 10 MW will demand suppression of  
6858 localised losses to, or below, parts per million. Higher power requires a lower fractional loss.  
6859 It is not yet well understood how to do this - in particular, collimation systems require a more  
6860 optimised control of CW losses at rates observed in linacs. PERLE will provide a platform  
6861 on which the next step in understanding can be taken. Other halo effects may become visible  
6862 at only the higher CW powers under consideration in PERLE (including Touschek and intra-  
6863 beam scattering, beam-gas scattering, and ion trapping). These lead to scattering events that  
6864 adiabatically anti-damp and result in intolerable loss in the back end of the machine, limiting  
6865 dynamic range. There is no experience with these phenomena, although theoretical studies  
6866 suggest they are problematic. PERLE will be the first system capable of directly exploring  
6867 these issues.

6868 There are many collective effects that have proven challenging at lower beam powers - including  
6869 RF heating, resistive wall heating, THz emission heating... - that will have greater impact at  
6870 both higher power and higher energy. There are at present no operating ERL systems that can  
6871 study these. PERLE is the only system proposed or under construction that combines sufficient  
6872 beam power with sufficient operational flexibility to study and test mitigation algorithms and  
6873 methods. Without PERLE, higher energy/power machines will have very little insight regarding  
6874 these problems and lack the ability to test solutions.

6875 Beam quality preservation in the presence of collective effects is a significant challenge for modern  
6876 machines. In particular, Longitudinal Space Charge (LCS), Coherent Synchrotron Radiation  
6877 (CSR), and the micro-bunching instability have serious deleterious impact on performance, and  
6878 can prevent a machine from producing beam consistent with user requirements - or, worse, from  
6879 being able to operate at significant powers. PERLE probes the regions of parameter space  
6880 where these effects are observable, and offers an opportunity to benchmark models and explore  
6881 mitigation methods.

### 6882 9.2.3 PERLE Layout and Beam Parameters

6883 The PERLE accelerator complex is arranged in a racetrack configuration hosting two cryo-  
6884 modules (containing four, five-cell cavities operating at 801.6 MHz frequency), each located in  
6885 one of two parallel straights completed with a vertical stack of three recirculating arcs on each  
6886 side. The straights are 10 m long and the 180° arcs are 5.5 m across. Additional space is taken  
6887 by 4 m long spreaders/recombiners, including matching sections. As illustrated in Fig. 9.2, the  
6888 total footprint of PERLE is:  $24 \times 5.5 \times 0.8 \text{ m}^3$ , accounting for 40 cm vertical separation between  
6889 arcs. Each of the two cryo-modules provides up to 82 MeV energy boost per path. Therefore, in

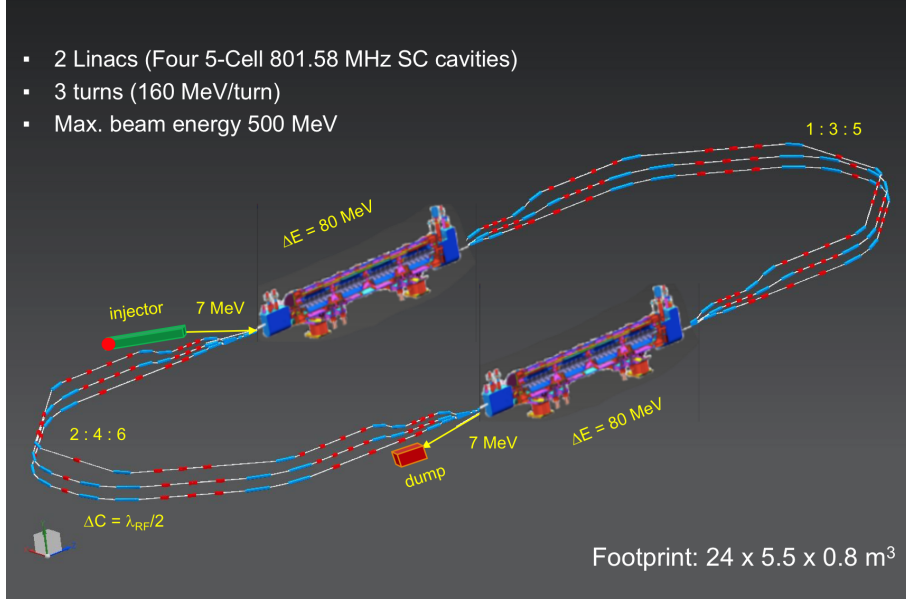


**Figure 9.2:** PERLE facility layout featuring two parallel linacs each hosting a cryomodule housing four 5-cell SC cavities, achieving 500 MeV in three passes, see text.

6890 three turns, a 492 MeV energy beam is generated. Adding the initial injection energy of 7 MeV  
 6891 yields the total energy of approximately 500 MeV. The main beam parameters of PERLE facility  
 are summarised in Tab. 9.1

Target parameter	Unit	Value
Injection energy	MeV	7
Electron beam energy	MeV	500
Norm. emittance $\gamma\epsilon_{x,y}$	mm-mrad	6
Average beam current	mA	20
Bunch charge	pC	500
Bunch length	mm	3
Bunch spacing	ns	25
RF frequency	MHz	801.6
Duty factor		CW

**Table 9.1:** Summary of main PERLE beam parameters.

6892

6893 As mentioned in the introduction, the essential PERLE parameters are the same as the LHeC.  
 6894 The frequency choice, emittance, beam current and the time structure are chosen regarding the  
 6895 requirements of the electron-proton collisions in the LHeC. Hereafter, we explain the choice of  
 6896 the frequency for the LHeC and thus for PERLE.

#### 6897 9.2.4 PERLE Lattice

6898 Multi-pass energy recovery in a racetrack topology explicitly requires that both the accelerat-  
 6899 ing and decelerating beams share the individual return arcs (Fig. 9.2). Therefore, the TWISS  
 6900 functions at the linac ends have to be identical, for both the accelerating and decelerating linac  
 6901 passes converging to the same energy and therefore entering the same arc.

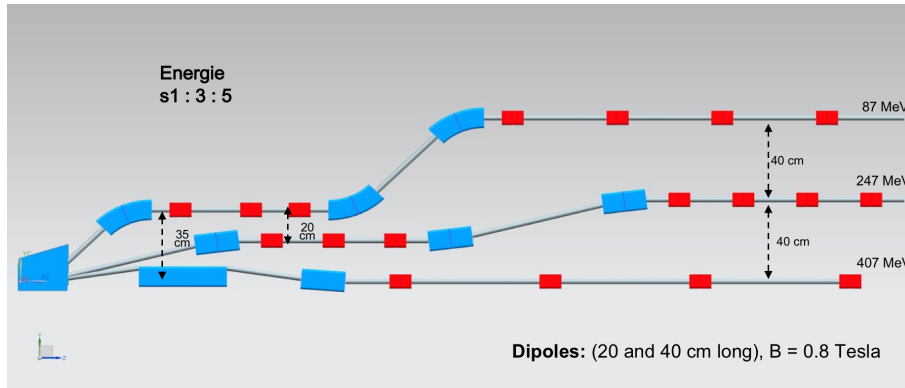


**Figure 9.3:** PERLE spreader design and matching to three circulating arcs.

6902 Injection at 7 MeV into the first linac is done through a fixed field injection chicane, with its  
 6903 last magnet (closing the chicane) being placed at the beginning of the linac. It closes the orbit  
 6904 bump at the lowest energy, injection pass, but the magnet (physically located in the linac) will  
 6905 deflect the beam on all subsequent linac passes. In order to close the resulting higher pass  
 6906 bumps, the so-called re-injection chicane is instrumented, by placing two additional bends in  
 6907 front of the last chicane magnet. This way, the re-injection chicane magnets are only visible by  
 6908 the higher pass beams. The spreaders are placed directly after each linac to separate beams of  
 6909 different energies and to route them to the corresponding arcs. The recombiners facilitate just  
 6910 the opposite: merging the beams of different energies into the same trajectory before entering  
 6911 the next linac. The spreader design (Fig. 9.3) consists of a vertical bending magnet, common  
 6912 for all three beams, that initiates the separation. The highest energy, at the bottom, is brought  
 6913 back to the horizontal plane with a chicane. The lower energies are captured with a two-step  
 6914 vertical bending. The vertical dispersion introduced by the first step bends is suppressed by the  
 6915 three quadrupoles located appropriately between the two steps. The lowest energy spreader is  
 6916 configured with three curved bends following the common magnet, because of a large bending  
 6917 angle ( $45^\circ$ ) the spreader is configured with. This minimises adverse effects of strong edge focusing  
 6918 on dispersion suppression in the spreader. Following the spreader there are four matching quads  
 6919 to bridge the TWISS function between the spreader and the following  $180^\circ$  arc (two betas and  
 6920 two alphas). All six,  $180^\circ$  horizontal arcs are configured with Flexible Momentum Compaction  
 6921 (FMC) optics to ease individual adjustment of M56 in each arc (needed for the longitudinal  
 6922 phase-space reshaping, essential for operation with energy recovery). The lower energy arcs (1,  
 6923 2, 3) are composed of four 45.6 cm long curved  $45^\circ$  bends and of a series of quadrupoles (two  
 6924 triplets and one singlet), while the higher arcs (4, 5, 6) use double length, 91.2 cm long, curved  
 6925 bends. The usage of curved bends is dictated by a large bending angle ( $45^\circ$ ). If rectangular  
 6926 bends were used, their edge focusing would have caused significant imbalance of focusing, which  
 6927 in turn, would have had adverse effect on the overall arc optics. Another reason for using curved  
 6928 bends is to eliminate the problem of magnet sagitta, which would be especially significant for  
 6929 longer, 91.2 cm, bends. Each arc is followed by a matching section and a recombiner (both  
 6930 mirror symmetric to previously described spreader and matching segments). As required in case  
 6931 of identical linacs, the resulting arc features a mirror symmetric optics (identical betas and sign  
 6932 reversed alphas at the arc ends).

6933 The presented arc optics with modular functionality facilitates momentum compaction manage-  
 6934 ment (isochronicity), as well as orthogonal tunability for both beta functions and dispersion.  
 6935 The path-length of each arc is chosen to be an integer number of RF wavelengths except for the  
 6936 highest energy pass, arc 6, whose length is longer by half of the RF wavelength to shift the RF

6937 phase from accelerating to decelerating, switching to the energy recovery mode.

### 6938 **9.2.5 The Site**

6939 The Irene Curie Lab Orsay intends to host PERLE. The footprint of this facility occupies a  
6940 rectangle of  $24 \times 5.5 \text{ m}^2$ . This area should be enclosed by shielding at a sufficient distance to  
6941 allow passage and maintenance operations. We estimate the required passage and half thickness  
6942 of the accelerator component to 2 m. A concrete shielding is assumed here to stop photons and  
6943 neutrons produced by halo electrons. A more detailed study of the radiation generated by the  
6944 impinging electron will be necessary at a following stage. An increase of the shielding required  
6945 could be alleviated by the use of denser materials.

6946 The PERLE operation at the design beam parameters (Tab. 9.1) required an in-depth study of  
6947 the machine failure scenario to estimate the power left in the machine during operation after  
6948 beam losses and how to handle and control it. The study aimed at looking if the PERLE facility  
6949 will be classified as INB (Infrastructure Nucleaire de Base) or not, with respect to the French  
6950 radioprotection and nuclear safety rules. This conclusion is crucial for the decision of hosting  
6951 PERLE at Orsay as such INB facilities require heavy regulation procedures and a very high  
6952 investment to fulfil the requirements and ensure the safety provisions to be implemented. The  
6953 outcome of the study had concluded that PERLE shall not be considered as INB, even if the  
6954 beam parameters are quite demanding, because for several failure scenarios the energy of the  
6955 beam is brought back to the injection energy and safely dumped, thanks to the recovery mode.  
6956 For other scenarios, hard interlocks and the machine safety system are fast enough to manage  
6957 the situation. The complete report of this study has been delivered by the IRSD team at Orsay.

6958 Besides the central area required for machine implementation, space needs to be allocated for the  
6959 auxiliary systems (power converters for magnets, septa and kickers, RF power, Water cooling,  
6960 Cryogenics, Electron source, Dump). One has also to consider sufficient space for experiments  
6961 that may use the PERLE beam. These have been sketched in the PERLE CDR [4]. As a rough  
6962 estimate one would need to triple the area of the accelerator itself to accommodate all services,  
6963 with shielding included. The building that is foreseen to host this version of PERLE is a former  
6964 experimental hall (Super ACO). It is equipped with cranes and electricity. The ground of the  
6965 building is made of concrete slabs with variable ground resistance. More than half of the hall  
6966 area has a sufficient resistance to allow the installation PERLE. Being next to the tunnel of the  
6967 old Orsay Linac and close to the *Igloo*, where new accelerators are being installed currently, the  
6968 building is partially shielded and some equipment (water-cooling circuits, electrical transformer)  
6969 can be shared with the other machines. The building gives the possibility to install the RF source  
6970 and the power supplies at a different level than the accelerator. An existing control room that  
6971 overlooks the experimental hall may be used for PERLE. Since all the accelerators installed  
6972 nearby are based on warm technology, a cryogenic plant will be built. All the needed support  
6973 for infrastructure could be assured by the CPER program. Altogether, this appears to be a well  
6974 suitable place which has the great advantage to be available.

### 6975 **9.2.6 Staging Strategy and Time Schedule**

6976 The PERLE configuration (Cf. Fig. 9.2) entails the possibility to construct PERLE in stages,  
6977 starting by installing a single linac in the first straight and initially replacing the second one  
6978 by beam lines. Such a consideration is determined by the existence of the SPL cryomodule  
6979 at CERN (see the discussion in Chapter 9), which will permit a rather rapid realisation of a

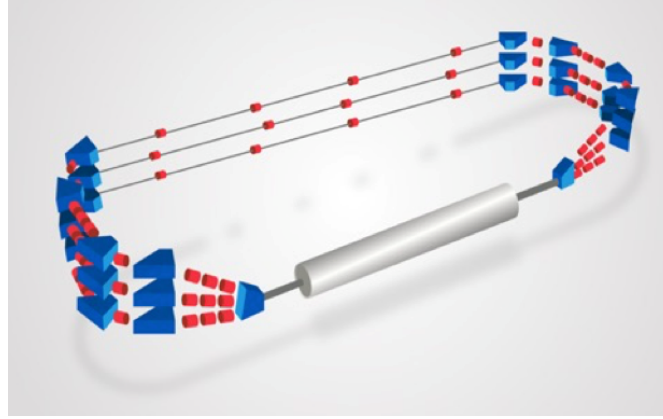


**Figure 9.4:** PERLE-Phase 1 layout featuring a single Linac in the first straight and beam line in the second straight, achieving 250 MeV in three passes.

6980 250 MeV machine, in what currently and tentatively is considered Phase 1 of PERLE. This will  
 6981 allow in relatively short time to test with beam the various SRF components, to prove the  
 6982 multi-turn ERL operation and to gain essential operation experience. Nevertheless, important  
 6983 achievements and steps are needed to realise these purposes. A tentative time schedule for the  
 realisation of Phase 1 of PERLE is presented in Tab.9.2.

Phase 1 milestone	Targeted date	Collaborator(s) involvement
<u>Studies &amp; prototyping</u>		
Dressed cavity design completion	Oct 2019	CERN-JLAB
SPL cryomodule design completion	May 2020	CERN
Injection line design completion	Mid 2020	STFC-Univ. Liverpool
Final design cavity fabrication and V. test	Mid 2020	JLAB-CERN
Arc and switchyard dipole prototypes	End 2020	BINP Novosibirsk
Booster cryomodule design completion	End 2021	–
Technical Design Report	End 2021	All
<u>Assembling, test &amp; installation</u>		
DC gun installation (1)	Early 2021	STFC
Booster assembly & RF test (2)	Mid 2023	STFC
Injector installation & commissioning (3)	End 2023	STFC
SPL cryomodule assembly and RF test (2)	Early 2024	CERN
Sequential installation at Orsay (4)	End 2024	–
Phase 1 operation	2025	Open to all

**Table 9.2:** Tentative time schedule to realise PERLE at Orsay in its first phase. (1) Most likely the Gun upgrade will be deferred to Phase 2 and Phase 1 will use the 5 mA ALICE DC gun which was received at Orsay on May 2019; (2) Booster test requires installation of cryogenics, RF power source, shielding, CC; (3) Injection line commissioning requires installation of cryogenics, RF power source, shielding, beam dump, diagnostics, CC, photocathode laser, vacuum, cabling, safety control systems, fluids, etc.; (4) only one spreader and one recombiner are needed for Phase 1. Final arc configuration will be installed.

6984

6985 It is foreseen from the beginning to size the infrastructure and equipment as for their final use  
 6986 (beam dump, cryogenics, cooling circuit, shielding, electrical power, etc.)

6987 The second phase is for the realisation of PERLE at its design parameters, as a 10 MW machine  
 6988 which requires the nominal electron current, i.e. the upgraded  $e^-$  gun and the completion of

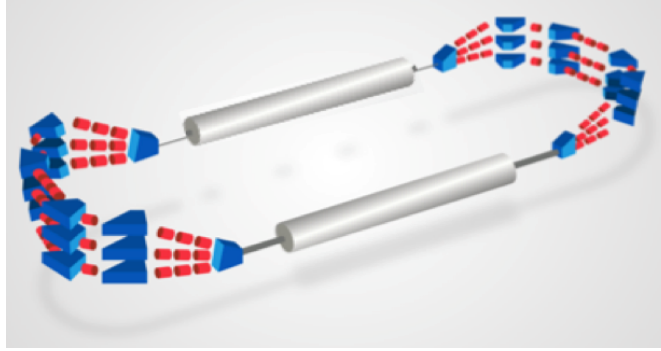


**Figure 9.5:** PERLE-Phase 2 layout featuring two Linac in each straight, achieving 500 MeV in three passes.

6989 the production of a further cryo-module, possibly newly designed. Also, a second spreader and  
 6990 recombiner need to be installed on both sides of the second cryo-module. The timeline of this  
 6991 second phase is given in Tab. 9.3. It is expected that the PERLE Collaboration will evolve which  
 will affect these plans.

Phase 2 milestone	Targeted date	Collaborator(s) involvement
DC gun upgrade	2026	STFC
Second cryomodule completion	2027	CERN
PERLE phase 2 operation	2028	Open to all

**Table 9.3:** Tentative plans for Phase 2 of PERLE.

6992

### 6993 9.2.7 Concluding Remark

6994 Currently the focus of the planning for PERLE is on the development of ERL as a means for high  
 6995 power, large energy accelerator design, technology and realisation. PERLE has a considerable  
 6996 potential for low energy particle and nuclear physics too. Its intensity is orders of magnitude  
 6997 higher than that of ELI. This opens a huge field of physics and industrial applications for a  
 6998 user facility once the machine has been understood and operates close to its design in a reliable  
 6999 manner. With recent increased interest in energy recovery technology applications at LHeC,  
 7000 but also FCC and EIC, PERLE may become an important cornerstone for future high energy  
 7001 and nuclear physics. The re-use of power is a *per se* green technology which is an example as  
 7002 to how science may react to the low power requirements of our time.

## Chapter 10

# Experimentation at the LHeC

### 10.1 Introduction

The LHeC Conceptual Design Report [1] contained a very detailed description of a core detector concept for the LHeC. At the time of writing, the target luminosity was of order  $10^{33} \text{ cm}^{-2} \text{ s}^{-1}$  and, whilst evidence was building, the Higgs boson had yet to be discovered. A detector design based on established technologies either in use by the LHC General Purpose Detectors or being developed for their upgrades was found to be adequate to realise the physics priorities of the project at the time and could comply with the *ep* machine constraints at an affordable cost, provided the angular acceptance was sufficient (nominally to within  $1^\circ$  of the beamline).

This chapter provides a short overview of a revised detector design, with more detail on those aspects which have been substantially updated since the 2012 version (notably the central tracking). To a large extent, the considerations in the CDR are still valid and are taken forward here. However, this update also profits from the evolution of the design in the subsequent years in light of changes in the experiment's interaction region and running conditions, the updated and longer term physics priorities with the higher achievable luminosities, and also introduces new technologies where they are becoming available. In more detail, the major considerations which motivate an update of the detector with respect to the 2012 baseline are:

- The design instantaneous luminosity has been extended considerably. The increased luminosity to the level of  $10^{34} \text{ cm}^{-2} \text{ s}^{-1}$  translates into a higher pile-up, reaching a maximum of around 1, compared with 0.1 previously. Whilst this is still far from the values of order 200 planned for the HL-LHC, it still has implications in terms of unfolding the hardest scattering processes from multiple overlaid minimum bias events, in particular pushing the design towards higher granularity. It also requires a reassessment of radiation hardness requirements, including the use of more radiation hard detectors in specific regions.
- The increased luminosity and the confirmation of a Higgs boson discovery at a mass of around 125 GeV open new opportunities for the LHeC to provide a set of precision measurements of Higgs properties, in particular, percent-level measurements of many of its couplings. The possibility of obtaining world-leading measurements of couplings to beauty and charm place a heavy emphasis on the inner tracking and vertexing. The tracking region has therefore been extended radially. The requirement to maximise the acceptance for Higgs decays places an even heavier requirement on angular coverage than was the case in 2012, with forward tracking and vertexing being of particular importance.

- 7036 • The fast development of detector technologies and related infrastructure in some areas ne-  
7037 cessitates a fresh look at the optimum choices. Most notably, silicon detector technologies  
7038 have advanced rapidly in response to both commercial and particle physics requirements.  
7039 The low material budget and potential high granularity and radiation hardness offered by  
7040 monolithic active pixel sensor (MAPS) solutions such as HV-CMOS are particularly at-  
7041 tractive and can reasonably be assumed to be in wide use in future particle physics collider  
7042 detector contexts.
- 7043 • There have been changes in the interaction region and the shape and nature of the magnetic  
7044 fields in which the LHeC detector is required to operate. In particular, the dipole field,  
7045 required to steer the electron beam and allow for head-on collisions, permeates the inner  
7046 parts of the detector throughout its longitudinal extent, bringing corresponding challenges.
- 7047 • The long term, high energy, high luminosity world collider physics program, including FCC  
7048 and possibilities in the Far East as well as the ultimate use of the LHC in  $pp$  mode for two  
7049 more decades, will require precise, independent, measurements to determine PDFs over an  
7050 even wider range of  $x$  and  $Q^2$  than has previously been possible. The implication for the  
7051 LHeC is a need to further improve and extend the detector acceptance and performance,  
7052 especially in the forward region.
- 7053 • Options in which the LHeC centre-of-mass energy is increased require a further rein-  
7054 forcement of the detector design in the forward (outgoing proton) direction, increasing the  
7055 overall size of the detector. In particular the calorimetry depth scales so as to fully contain  
7056 particles from very high energy forward-going hadronic showers and to allow for precise  
7057 measurements of actual and missing energy.

7058 The design described in the following addresses the points above, leading to a somewhat revised  
7059 and more ambitious baseline tracking detector design than was the case in 2012. Whilst they  
7060 are both realisable in terms of technology readiness, in some sense the 2012 and 2020 versions  
7061 can be considered as two example solutions to the LHeC detector needs, towards the lower and  
7062 higher ends of the spectrum of performance and cost, respectively. The design is performed  
7063 using the DD4hep [756] framework.

7064 The updated detector requirements point towards the need for higher spatial resolution, im-  
7065 proved precision in energy and momentum measurements and enhanced primary and secondary  
7066 vertexing capabilities. The design must be optimised for accurate measurements of hadronic jets  
7067 and missing transverse energy, as well as isolated charged and neutral particle production. Both  
7068 the overall event kinematics (much larger proton than electron beam energy) and the specific  
7069 acceptance requirements for the key Higgs production process imply an asymmetric design with  
7070 enhanced hadronic final state detection capabilities in the forward direction (i.e. at low azimuthal  
7071 angles  $\theta$ ). A dipole magnet bends the electron beam into head-on collision with the colliding  
7072 proton beam and after the interaction point a further dipole with opposite polarity separates  
7073 the orbits of the electron and proton beam. These weak bending dipoles are placed outside of  
7074 the tracker and electromagnetic calorimeter regions. The resulting synchrotron radiation fan  
7075 has to be given free space and the beam pipe geometry is designed specifically to accommodate  
7076 it. The residual synchrotron radiation background requires an advanced detector layout such  
7077 that all components can tolerate the load.

7078 **10.2 Overview of Main Detector Elements**

7079 A side projection overview of the revised detector design is shown in Fig. 10.1, illustrating the  
 7080 main detector components. The overall size remains compact by recent standards, with overall  
 7081 dimensions of approximately 13 m in length and 9 m in diameter, small compared with ATLAS  
 7082 ( $45 \times 25$  m) and even CMS ( $21 \times 15$  m). The inner silicon tracker contains a central barrel  
 7083 component ('Tracker'), with additional disks in the forward and backward directions ('Tracker  
 7084 Fwd' and 'Tracker Bwd', respectively). It is surrounded at larger radii by the Electromag-  
 7085 netic Barrel ('EMC-Barrel') and in the forward and backward directions by the electromagnetic  
 7086 forward and backward plug calorimeters ('FEC-Plug-Fwd' and 'BEC-Plug-Bwd', respectively).  
 7087 The solenoid magnet is placed at radii immediately outside the EMC-Barrel, and is housed in  
 7088 a cryostat, which it shares with the weak dipole, which is required by the machine to achieve  
 7089 head-on collisions of the electron beam with the colliding proton beam. The Hadronic-Barrel  
 7090 calorimeter (HCAL-Barrel) is located at radii beyond the solenoid and dipole, whilst the for-  
 7091 ward and backward hadronic plug detectors (FHC-Plug-Fwd and BHC-Plug-Bwd, respectively)  
 7092 lie beyond their electromagnetic counterparts in the longitudinal coordinate. The Muon Detec-  
 7093 tor forms a near-hermetic envelope around all other parts of the main detector. It has a mixture  
 7094 of triggering and measurement-focused layers using similar technologies to those employed by  
 7095 ATLAS, as described in the 2012 CDR.

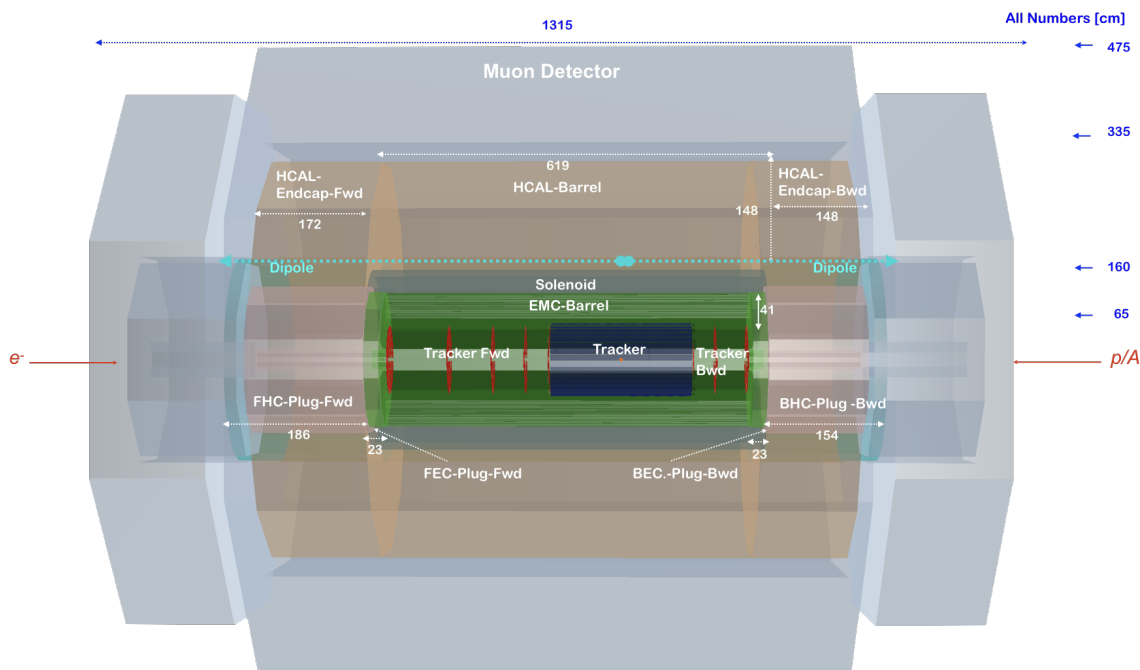


**Figure 10.1:** Side view of the new baseline LHeC detector concept, providing an overview of the main detector components and their locations. See text for details.

7096 A magnified view of the inner part of the detector, including the magnet elements, is shown in  
 7097 Fig. 10.2. The solenoid and steering dipoles enclose the electromagnetic calorimeters and the  
 7098 tracker setup completely, the steering dipoles extending over the full 10 m length of the inner  
 7099 detector and forward and backward plugs. If liquid argon is chosen for the sensitive material  
 7100 in the EMC as in the 2012 design, the EMC will be mounted inside the cryostat, alongside the  
 7101 solenoid and dipoles. The hadronic calorimeter components remain outside the cryostat and  
 7102 magnet elements under all circumstances.

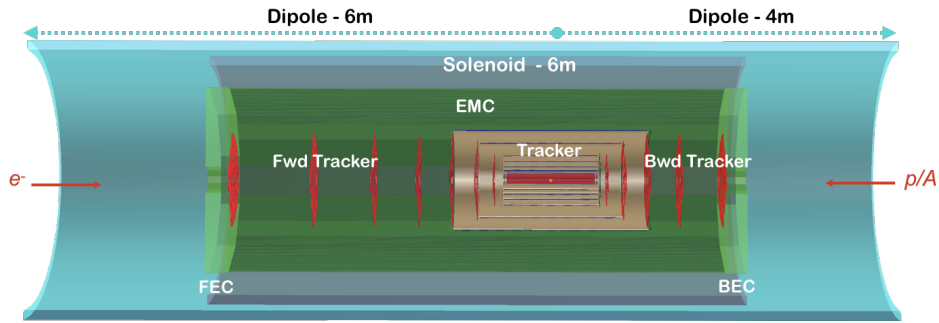


**Figure 10.2:** Zoomed side projection of the central part of the updated detector design, illustrating the solenoid and electron-beam-steering dipoles. See text for further details

7103 Exploiting the current state of the art, the beam pipe is constructed of beryllium of 2.5 – 3 mm  
 7104 thickness. As in the 2012 CDR, the beam pipe has an asymmetric shape in order to accommodate  
 7105 the synchrotron radiation fan from the dipole magnets. It is thus 2.2 cm distant from the  
 7106 interaction region, except in the outer rear direction of the synchrotron fan, where it is increased  
 7107 to 10.0 cm with a semi-elliptical profile. The beam pipe shape has implications for the design  
 7108 of the inner detector components, as illustrated in Fig. 10.3. The first layer of the barrel  
 7109 tracker follows the circular-elliptical beam pipe shape as closely as possible, with the profiles of  
 7110 subsequent layers reverting to a circular geometry.

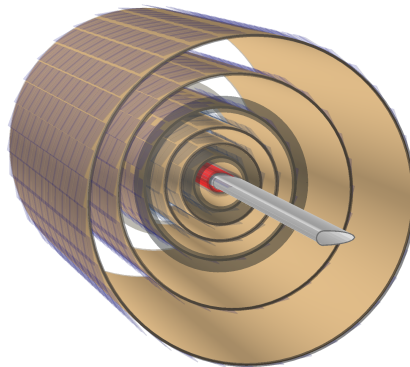


**Figure 10.3:** End-on view of the arrangement of the inner barrel tracker layers around the beam pipe.

### 7111 10.3 Inner Tracking

7112 A schematic view of the updated tracking region is shown in Fig. 10.4. The layouts in the  
 7113 central, forward and backward directions have been separately optimised using the tkLayout  
 7114 performance estimation tool for silicon trackers [757]. The result is seven concentric barrel  
 7115 layers with the innermost layer approximately 3 cm from the beam line and approximately equal  
 7116 radial spacing thereafter, supplemented by seven forward wheels and five backward wheels of  
 7117 which, respectively, four and two are mounted beyond the central tracker enclosure.

7118 HV-CMOS MAPS sensors are employed, restricting dead material associated with the sensors  
 7119 to 0.1 mm. The strip detector sensors have a larger thickness of 0.2 mm. The exact silicon

7120 solutions chosen change with radial distance from the interaction point, so as to provide the  
 7121 highest spatial resolution in the layers closest to the the interaction point. The barrel is formed  
 7122 from one layer of pixel-wafers, with three layers of macro-pixels between 10 cm and 30 cm and a  
 7123 further three layers of strip-sensors beyond 30 cm.

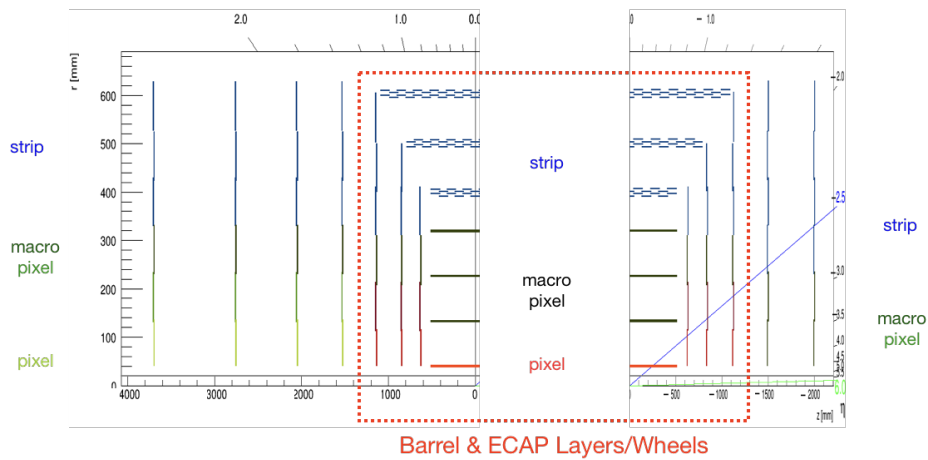


**Figure 10.4:** Schematic side-view of the tracker, subdivided into forward and backward parts and including disks as well as barrel components. The layers/wheels forming the barrel part are enclosed by the red-dotted box. The innermost pixel layers are coloured red, the macro-pixel layers are shown in black and the strip detectors in blue. For the forward and backward wheels (outside the dashed red box), the pixels, macro-pixels and strip detectors are shown in light green, dark green and blue, respectively.

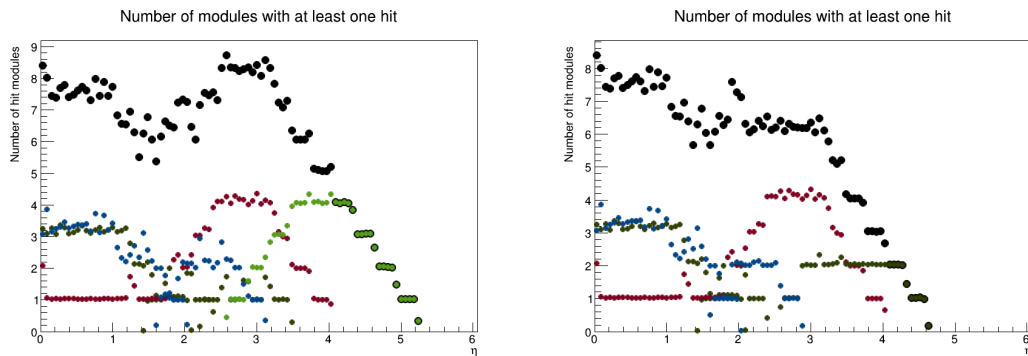


**Figure 10.5:** Numbers of silicon layers that provide acceptance for charged particles as a function of absolute value of pseudorapidity in the forward (left) and backward (right) directions, summed across the central, forward and backward trackers. The distributions are broken down according to sensor type, with colour coding of red for pixels, light or dark green for macro-pixels, blue for strips and black for the sum.

7124 Tabs. 10.1 and 10.2 summarise the overall basic properties of the tracker modules, including  
 7125 total numbers of channels and total area of silicon coverage, as well as spatial resolutions and  
 7126 material budgets. The inner barrel has a pseudorapidity coverage  $|\eta| < 3.3$  for hits in at least  
 7127 one layer, increasing to  $|\eta| < 4.1$  when the endcaps are also taken into account. The additional  
 7128 disks beyond the central tracker enclosure extend the coverage to  $\eta = 5.3$  and  $\eta = -4.0$  in the  
 7129 forward and backward directions, respectively. Fig. 10.5 shows these features in more detail,  
 7130 displaying the numbers of layers that provide acceptance as a function of pseudorapidity in both  
 7131 the forward and backward directions, also broken down into different sensor types. Charged  
 7132 particles are sampled in between 6 and 8 layers throughout the entire range  $-3 < \eta < 4$ , with

Tracker (LHeC) <sup>1)</sup>	Inner Barrel			ECAP		
	pix	pix <sub>macro</sub>	strip	pix	pix <sub>macro</sub>	strip
$\eta_{\max}, \eta_{\min}$	3.3, -3.3	2.1, -2.1	1.4, -1.4	$\pm[4.1, 1.8]$	$\pm[2.4, 1.5]$	$\pm[2.0, 0.9]$
Layers (Barrel)	1	3	3			
Wheels (ECAP)				2	1	1-3
Modules/Sensors	320	4420	3352	192	192	552
Total Si area [m <sup>2</sup> ]	0.3	4.6	17.6	0.8	5.6	3.3
Read-out-Channels [10 <sup>6</sup> ]	224.5	1738	20.6	322.4	73.3	17.0
pitch <sup><math>r-\phi</math></sup> [ $\mu\text{m}$ ]	$\sim 25$	$\sim 100$	$\sim 100$	$\sim 25$	$\sim 100$	$\sim 100$
pitch <sup><math>z</math></sup> [ $\mu\text{m}$ ]	$\sim 50$	$\sim 400$	50k <sup>2)</sup>	$\sim 50$	$\sim 400$	10k <sup>2)</sup>
Average $X_0/\Lambda_I$ [%]	7.2 / 2.2			2.2 / 0.7		

<sup>1)</sup> Based on tklayout calculations [757]

<sup>2)</sup> Reaching pitch <sup>$r-\phi$</sup>  when using two wafer layers rotated by 20 mrad is achievable.

**Table 10.1:** Summary of the main properties of the Barrel and Endcap tracker modules in the revised LHeC detector configuration based on calculations performed using tkLayout. For each module, the rows correspond to the pseudorapidity coverage, numbers of barrel and disk layers, numbers of sensors, total area covered by silicon sensors, numbers of readout channels, the hardware pitches affecting the ( $r - \phi$ ) and the  $z$  resolution, respectively and the average material budget in terms of radiation lengths and interaction lengths. Where appropriate, the numbers are broken down into separate contributions from pixels, macro-pixels and strips. See Tab. 10.2 for a sum of all tracker components.

7133 sampling in at least two layers provided for  $-4 < \eta < 5$ .

7134 As can be seen in Tabs. 10.1 and 10.2, spatial resolutions in the  $r - \phi$  plane are at the level of  
7135  $7.5 - 9.5 \mu\text{m}$  for all of the tracking modules. These resolutions are propagated using tkLayout  
7136 to produce simulated charged particle transverse momentum resolutions, as shown in Fig. 10.6.  
7137 Both active and passive material contributions are included, with a 2.5 mm beam pipe thickness.  
7138 An excellent resolution ( $\delta p_T/p_T$ ) at the level of 1 - 2% is achieved over a wide range of pseudo-  
7139 dorapidity and transverse momentum. The precision degrades slowly in the forward direction,  
7140 remaining at the sub 10 % level up to very forward pseudorapidities  $\eta \sim 4.5$ . Central tracks with  
7141 transverse momenta up to 1 TeV are measured with 10 - 20 % precision.

7142 A major requirement of the tracking detectors will be the precise determination of vertex coordi-  
7143 nates and of track impact parameters relative to the primary vertex in order to give the best  
7144 possible sensitivity to secondary vertices from heavy flavour decays, for example for the study of  
7145 the Higgs in its dominant  $b\bar{b}$  decay mode. The simulated results for longitudinal and transverse  
7146 track impact parameter resolutions using the full new tracking layout are shown in Fig. 10.7.  
7147 The resolutions are at the highly competitive level of 10 - 50  $\mu\text{m}$  over a wide range of transverse  
7148 momentum and pseudorapidity, extending well into the forward direction.

7149 The total material budget contribution from the sensors summed across all layers is given in  
7150 Tab. 10.2. This is largest for the inner barrel, where it amounts to 7.2 % of a radiation length.  
7151 The sensors in the central tracker endcap and the forward and backward tracking rings contribute  
7152 3.0 %, 2.5 % and 0.9 % of a radiation length, respectively. These material contributions are all  
7153 small on the scale of the average  $0.35X_0$  contributed by the beam pipe. The material budget  
7154 simulations, propagated for the full system and including passive contributions, are shown in  
7155 Fig. 10.8. The use of thin sensors keeps the total material to the level of 0.2 - 0.4 $X_0$  throughout  
7156 the entire tracking region up to  $\eta \sim 5$ .

Tracker (LHeC) <sup>1)</sup>	Fwd Tracker			Bwd Tracker		Total
	pix	pix <sub>macro</sub>	strip	pix <sub>macro</sub>	strip	(incl. Tab. 10.1)
$\eta_{\max}, \eta_{\min}$	5.3, 2.6	3.5, 2.2	3.1, 1.6	-4.6, -2.5	-2.9, -1.6	5.3, -4.6
Wheels	2	1	3	2	4	
Modules/Sensors	180	180	860	72	416	10736
Total Si area [m <sup>2</sup> ]	0.8	0.9	4.6	0.4	1.8	40.7
Read-out-Channels [10 <sup>6</sup> ]	404.9	68.9	26.4	27.6	10.6	2934.2
pitch <sup>r-<math>\phi</math></sup> [ $\mu$ m]	$\sim 25$	$\sim 100$	$\sim 100$	$\sim 100$	$\sim 100$	
pitch <sup>z</sup> [ $\mu$ m]	$\sim 50$	$\sim 400$	50k <sup>2)</sup>	$\sim 400$	10k <sup>2)</sup>	
Average $X_0/\Lambda_I$ [%]	6.7 / 2.1			6.1 / 1.9		
incl. beam pipe [%]						40 / 25

<sup>1)</sup> Based on tklayout calculations [757]

<sup>2)</sup> Reaching pitch<sup>r- $\phi$</sup>  when using two wafer layers rotated by 20 mrad is achievable.

**Table 10.2:** Summary of the main properties of the forward and backward tracker modules in the revised LHeC detector configuration based on calculations performed using tkLayout. For each module, the rows correspond to the pseudorapidity coverage, numbers of barrel and disk layers, numbers of sensors, total area covered by silicon sensors, numbers of readout channels, the hardware pitches affecting the ( $r - \phi$ ) and the  $z$  resolution, respectively and the average material budget in terms of radiation lengths and interaction lengths. Where appropriate, the numbers are broken down into separate contributions from pixels, macro-pixels and strips. The column *Total* contains the sum of corresponding values of table 10.1.

## 10.4 Calorimetry

7157

7158 The 2012 CDR detector design leaned heavily on current technologies employed by ATLAS  
7159 for calorimetry in the barrel region, adopting a lead / liquid argon sampling electromagnetic  
7160 calorimeter with an accordion geometry and a steel / scintillating tile sampling hadronic com-  
7161 ponent. For the updated detector described here, an alternative solution of a lead / scintillator  
7162 electromagnetic calorimeter has been investigated. This has the advantage of removing the need  
7163 for cryogenics, whilst maintaining an acceptable performance level. The liquid argon option is  
7164 not excluded yet and will be evaluated further-on. The hadronic calorimeter retains the steel  
7165 and scintillating tile design, similar to ATLAS. As in the 2012 CDR, plug sampling calorimeters  
7166 are also incorporated at large  $|\eta|$ , the forward and backward components using tungsten and  
7167 lead absorber material, respectively, with both using silicon based sensitive readout layers. The  
7168 steel structures in the central and plug calorimetry close the outer field of the central solenoid.  
7169 The main features of the new calorimeter layout are summarised in Tab. 10.3 and 10.4. The  
7170 pseudorapidity coverage of the electromagnetic barrel is  $-1.4 < \eta < 2.4$ , whilst the hadronic  
7171 barrel and its end cap cover  $-1.5 < \eta < 1.9$ . Also including the forward and backward plug  
7172 modules, the total coverage is very close to hermetic, spanning  $-5.0 < \eta < 5.5$ . The total  
7173 depth of the electromagnetic section is 30 radiation lengths in the barrel and backward regions,  
7174 increasing to almost  $50X_0$  in the forward direction where particle and energy densities are high-  
7175 est. The hadronic calorimeter has a depth of between 7.1 and 9.6 interaction lengths, with the  
7176 largest values in the forward plug region.

7177 The performance of the new calorimeter layout has been simulated by evaluating the mean sim-  
7178 ulated response to electromagnetic (electron) and hadronic (pion) objects with various specific  
7179 energies using GEANT4 [758] and interpreting the results as a function of energy in terms of  
7180 sampling ( $a$ ) and material / leakage ( $b$ ) terms in the usual form  $\sigma_E/E = a/\sqrt{E} \oplus b$ . Example  
7181 results from fits are shown for the barrel electromagnetic and hadronic calorimeters in Fig. 10.9  
7182 and for the forward plug electromagnetic and hadronic calorimeters in Fig. 10.10. The results

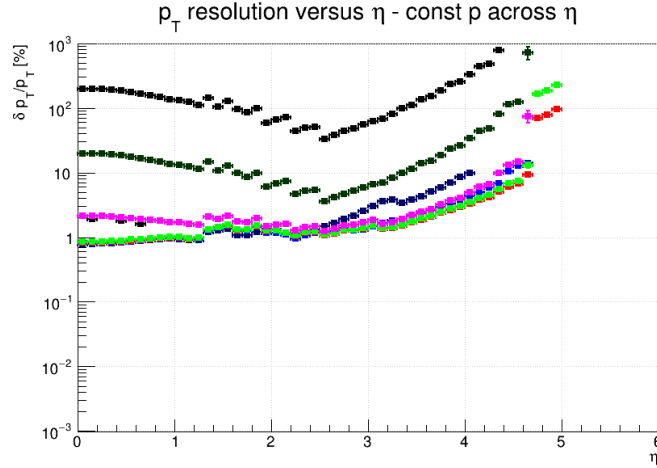


**Figure 10.6:** Simulated transverse momentum track resolution using all modules in the revised LHeC tracking system. Results are shown in terms of fractional  $p_T$  resolution as a function of pseudorapidity for several constant momenta,  $p = 100$  MeV (Black), 1 GeV (Dark Blue), 2 GeV (Light Blue), 5 GeV (Red), 10 GeV (Light Green), 100 GeV (Magenta), 1 TeV (Dark Green) and 10 TeV (Black, top).

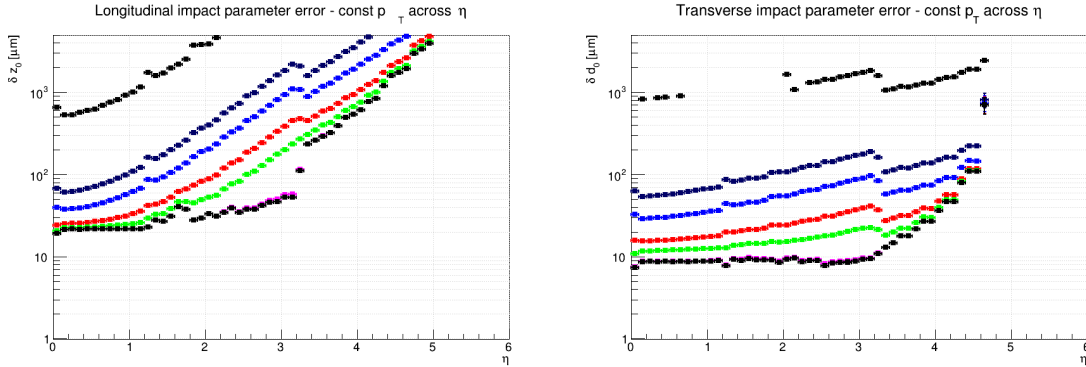


**Figure 10.7:** Simulated longitudinal (left) and transverse (right) impact parameter resolutions using all modules in the revised LHeC tracking system. Results are shown as a function of pseudorapidity for several constant momenta,  $p = 100$  MeV (Black), 1 GeV (Dark Blue), 2 GeV (Light Blue), 5 GeV (Red), 10 GeV (Light Green), 100 GeV (Magenta), 1 TeV (Dark Green) and 10 TeV (Black, top).

7183 for the  $a$  and  $b$  parameters are summarised in Tabs. 10.3 and 10.4. The response of the barrel  
7184 electromagnetic calorimeter to electrons in terms of both sampling ( $a = 12.4\%$ ) and material  
7185 ( $b = 1.9\%$ ) terms is only slightly worse than that achieved with liquid argon sampling in the  
7186 2012 CDR. The resolutions of the forward and backward electromagnetic plug calorimeters are  
7187 comparable to those achieved in the 2012 design. A similar pattern holds for the hadronic re-  
7188 sponse, with sampling terms at the sub-50% level and material terms of typically 5% throughout  
7189 the barrel end-caps and forward and backward plugs.

## 7190 10.5 Muon Detector

7191 Muon identification is an important aspect for any general purpose HEP experiment like the  
7192 LHeC. At the LHeC the muon detector can widen the scope and the spectrum of many mea-  
7193 surements, of which only a few are listed here:

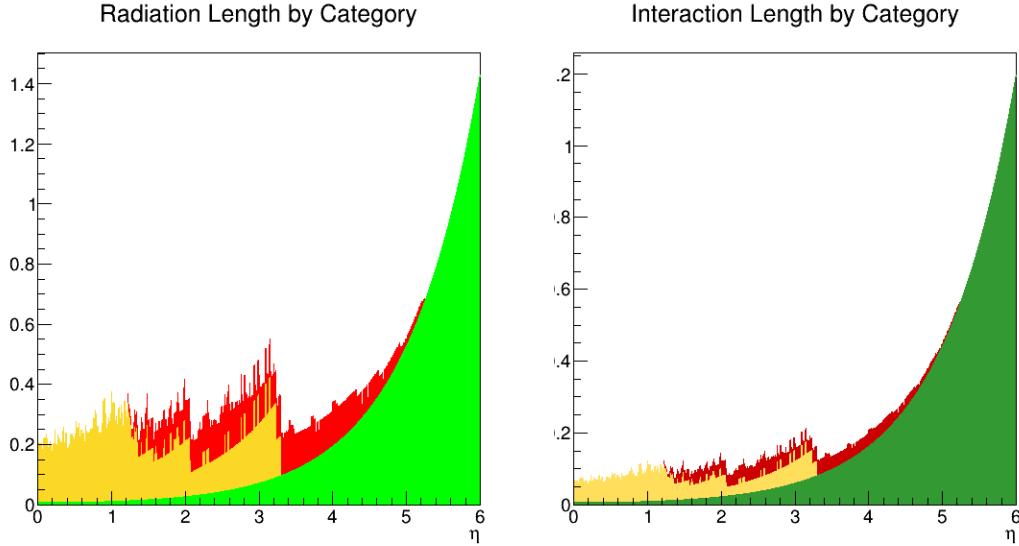


**Figure 10.8:** Material contributions from the tracking modules as a function of pseudorapidity. Results are given in terms of radiation lengths (left) and hadronic interaction lengths (right). The results are broken down into contributions from barrel modules (yellow) and endcap / additional disk modules (red) and are compared with the contribution from the 2.5 mm beam pipe (green).

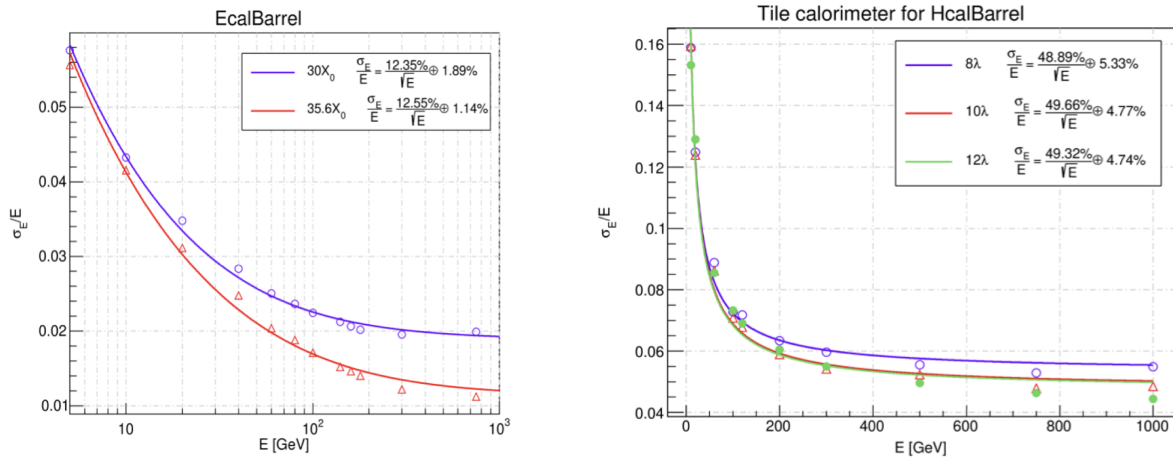


**Figure 10.9:** Crystal Ball fitted energy dependent resolution for the barrel electromagnetic (left) and barrel hadronic (right) calorimeters EMC and HCAL, respectively. The first (*a*) term includes shower fluctuations and transverse leakages and the second (*b*) term includes leakages from the calorimeter volume longitudinally.

- 7194 • Higgs decay,
- 7195 • Semi-leptonic decays of heavy flavoured hadrons,
- 7196 • Vector meson production,
- 7197 • Direct  $W$  and  $Z$  production,
- 7198 • Di-muon production,
- 7199 • Leptoquarks, lepton flavour violation, and other BSM phenomena.

7200 The primary target of the muon detector at the LHeC is to provide a reliable muon tag signature  
 7201 which can be uniquely used in conjunction with the central detector for muon identification,

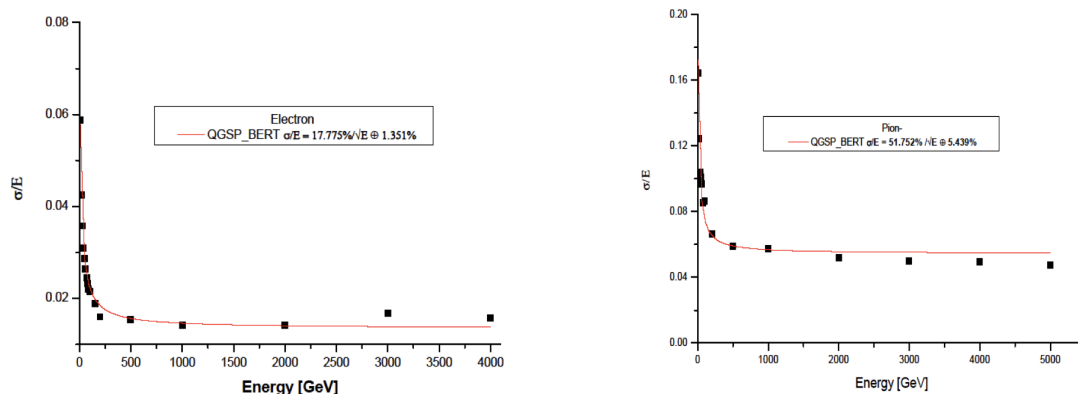


**Figure 10.10:** Crystal Ball fitted energy dependent resolution for the forward electromagnetic (left) and forward hadronic (right) plug calorimeters FEC and FHC, respectively. The first (*a*) term includes shower fluctuations and transverse leakages and the second (*b*) term includes leakages from the calorimeter volume longitudinally.

Calo (LHeC)	EMC		HCAL		
	Barrel	Ecap Fwd	Barrel	Ecap Bwd	
Readout, Absorber	Sci,Pb	Sci,Fe	Sci,Fe	Sci,Fe	
Layers	38	58	45	50	
Integral Absorber Thickness [cm]	16.7	134.0	119.0	115.5	
$\eta_{\max}, \eta_{\min}$	2.4, -1.4	1.9, 1.0	1.6, -0.7	-1.5, -1.0	
$\sigma_E/E = a\sqrt{E} \oplus b$	[%]	12.4/1.9	46.5/3.8	48.23/5.6	51.7/4.3
$\Lambda_I / X_0$	$X_0 = 30.2$	$\Lambda_I = 8.2$	$\Lambda_I = 8.3$	$\Lambda_I = 7.1$	
Total area Sci	[m <sup>2</sup> ]	1174	1403	3853	1209

**Table 10.3:** Basic properties and simulated resolutions of barrel calorimeter modules in the new LHeC detector configuration. For each of the modules, the rows indicate the absorber and sensitive materials, the pseudorapidity coverage, the contributions to the simulated resolution from the sampling (*a*) and material (*b*) terms in the form *a/b*, the depth in terms of radiation or interaction lengths and the total area covered by the sensitive material.

**GEANT4** [758] simulation based fits using crystal ball function [759] [760] [761].

7202 triggering and precision measurements. This option also well fits the constraints of limited  
7203 space<sup>1</sup> and the lack of a dedicated magnetic field as in the baseline design. The muon chambers  
7204 surround Muon chambers surround the central detector and covering as far as possible the solid  
7205 angle and provide, by means of a compact multilayer structure, a pointing trigger and a precise  
7206 timing measurement which is used to separate muons coming from the interaction point from  
7207 cosmics, beam halo or non prompt particles. This tagging feature does not include the muon  
7208 momentum measurement which is performed only in conjunction with the central detector. A  
7209 trigger candidate in the muon detector is characterised by the coincidence over a majority of  
7210 the layers in a range of  $\eta$ ,  $\phi$ , and  $t$  compatible with an *ep* interaction of interest in the main  
7211 detector. The muon candidates are combined with the trigger information coming from the  
7212 central detector (mainly the calorimetry at Level 1 trigger) to reduce the fake rate or more  
7213 complex event topologies.

<sup>1</sup>As in the 2012 CDR, the baseline LHeC detector including the muon system and all of the services and supports is expected to fit into the octagonal shape envelop of the L3 magnet (11.6 m minimum diameter).

Calo (LHeC)	FHC Plug Fwd	FEC Plug Fwd	BEC Plug Bwd	BHC Plug Bwd
Readout, Absorber	Si,W	Si,W	Si,Pb	Si,Cu
Layers	300	49	49	165
Integral Absorber Thickness [cm]	156.0	17.0	17.1	137.5
$\eta_{\max}, \eta_{\min}$	5.5, 1.9	5.1, 2.0	-4.4, -4.5	-4.5, -5.0
$\sigma_E/E = a/\sqrt{E} \oplus b$ [%]	51.8/5.4	17.8/1.4	14.4/2.8	49.5/7.9
$\Lambda_I / X_0$	$\Lambda_I = 9.6$	$X_0 = 48.8$	$X_0 = 30.9$	$\Lambda_I = 9.2$
Total area Si [m <sup>2</sup> ]	1354	187	187	745

**Table 10.4:** Basic properties and simulated resolutions of forward and backward plug calorimeter modules in the new LHeC detector configuration. For each of the modules, the rows indicate the absorber and sensitive materials, the pseudorapidity coverage, the contributions to the simulated resolution from the sampling ( $a$ ) and material ( $b$ ) terms in the form  $a/b$ , the depth in terms of radiation or interaction lengths and the total area covered by the sensitive material.

**GEANT4** [758] simulation based fits using crystal ball function [759] [760] [761].

7214 Concerning the choice of the technologies for the muon detector, at the the time of the 2012  
7215 CDR the LHC experiments and the ongoing R&D programs in HEP detector indicated the  
7216 options in use in ATLAS and CMS and their planned upgrades as adequate for LHeC. With the  
7217 exception of the very forward region, muon and background rates in LHeC are expected to be  
7218 lower than in  $pp$  and with less busy event topologies. The option of an LHeC muon detector  
7219 composed by layers of Resistive Plate Chambers (RPC), providing the Level 1 trigger and a 2 two  
7220 coordinate ( $\eta, \phi$ ) measurement possibly aided by Monitored Drift Tubes (MDT) for additional  
7221 precision measurement appears to be still valid. Recent developments as presented in LHC  
7222 Phase 2 Upgrade Technical Design Reports ( [762,763]) do further strengthen this choice. New  
7223 thin-RPC (1 mm gas gap) operated with lower HV, provide a sharper time response (few ns),  
7224 a higher rate capability (tens of kHz/cm<sup>2</sup>), and extend the already good aging perspective. A  
7225 crucial role is coming from the advances on low-noise high-bandwidth front-end electronics which  
7226 can also improve the performance of older detectors. Similar arguments also hold for smaller  
7227 tube MDTs (15 mm diameter) which provide lower occupancy and eight-fold rate capability.

7228 Fig. 10.11 shows an adaptation for LHeC of an RPC-MDT assembly as will be implemented for  
7229 the inner muon layer of ATLAS already during the Phase-1 upgrade as pilot for the Phase-2. A  
7230 triplet of thin gap RPCs each with 2 coordinate measurement, is combined with two superlayers  
7231 of small MDTs. It is also important to note the reduced volume of this structure, in particular  
7232 of the RPC part which would provide the muon tag. For the LHeC a baseline would be having  
7233 one or two of such stations forming a near-hermetic envelope around the central detector.

7234 Finally, as already presented in the 2012 CDR, detector extensions, with a dedicated magnetic  
7235 field in the muon detector, be this a second solenoid around the whole detector or extra dipole  
7236 or toroid in the forward region are, at this stage, left open as possible developments only for  
7237 upgrade scenarios for a late installation in the FCC.

## 7238 10.6 Forward and Backward Detectors

7239 In the 2012 CDR, initial plans for beamline instrumentation were provided for the LHeC. In the  
7240 backward direction, low angle electron and photon calorimeters were placed with the primary  
7241 intention of measuring luminosity via the Bethe-Heitler process  $ep \rightarrow eXp$  and the side-effect of  
7242 providing an electron tagger to identify photoproduction ( $\gamma p \rightarrow X$ ) processes at intermediate  $y$

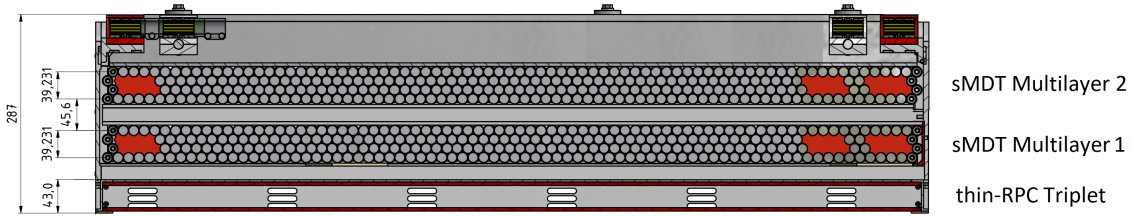


**Figure 10.11:** A transverse view of a RPC-MDT assembly as adapted from a drawing of the ATLAS Phase-1 muon upgrade [762]. In this case a station is composed of an RPC triplet for trigger and 2-coordinate readout and two MDT superlayers for precise track measurements.

7243 values. The current design carries forward the 2012 version of this backward instrumentation,  
 7244 though it will need to be revisited in the future in light of the synchrotron load in the updated  
 7245 magnet design.

7246 In the forward direction, Roman pot detectors were included in the region of  $z \sim 420$  m, capable  
 7247 of detecting scattered protons over a range of fractional energy loss  $10^{-3} < \xi < 3 \times 10^{-2}$  and wide  
 7248 transverse momentum acceptance, based on extensive previous work in the LHC context by the  
 7249 FP420 collaboration. This also forms the basis of forward proton tagging in the revised design.  
 7250 However, as is the case at ATLAS and CMS / TOTEM, further Roman pot detectors in the  
 7251 region of 200 m and (with HL-LHC optics) perhaps around 320 m would extend the acceptance  
 7252 towards higher  $\xi$  values up to around 0.2 allowing the study of diffractive processes  $ep \rightarrow eXp$   
 7253 where the dissociation system  $X$  has a mass extending into the TeV regime. It is worth noting  
 7254 that Roman pot technologies have come of age at the LHC, with the TOTEM collaboration  
 7255 operating 14 separate detectors at its high point. Silicon sensor designs borrowed from the  
 7256 innermost regions of the ATLAS and CMS vertexing detectors have been used, providing high  
 7257 spatial resolution and radiation hardness well beyond the needs of LHeC. Very precise timing  
 7258 detectors based on fast silicon or Cherenkov radiation signals from traversing protons in quartz  
 7259 or diamond have also been deployed. It is natural that these advances and the lessons from their  
 7260 deployment at the LHC will be used to inform the next iteration of the LHeC design.

7261 The forward beamline design also incorporates a zero angle calorimeter, designed primarily  
 7262 to detect high energy leading neutrons from semi-inclusive processes in  $ep$  scattering and to  
 7263 determine whether nuclei break up in  $eA$  events. This component of the detector was not  
 7264 considered in detail in 2012 and is therefore discussed here.

### 7265 10.6.1 Zero-Degree (Neutron) Calorimeter

7266 The Zero-Degree Calorimeter (ZDC) measures final state neutral particles produced at angles  
 7267 near the incoming hadron beam direction. They typically have large longitudinal momentum  
 7268 ( $x_F \gg 10^{-2}$ ), but with transverse momentum of order of  $\Lambda_{\text{QCD}}$ . Such a calorimeter has been  
 7269 instrumented in experiments for  $ep$  collisions (H1 and ZEUS) and for  $pp$ ,  $pA$  and  $AA$  collisions at  
 7270 RHIC (STAR and PHENIX) and at the LHC (ATLAS, CMS, ALICE and LHCf at the ATLAS  
 7271 IP). The detector's main focus is to study the soft-hard interplay in the QCD description of  $ep$   
 7272 and  $eA$  collisions by studying the dependence of forward-going particles with small transverse  
 7273 momentum on the hard variables e.g.  $Q^2$  and  $x$ . The detector also allows the tagging of spectator  
 7274 neutrons to detect nuclear breakup in  $eA$  collisions. It also enables the precise study of the EMC  
 7275 effect by using neutron-tagged DIS on small systems, such as  $e^3\text{He} \rightarrow ed + n \rightarrow eX + n$ . For  
 7276 heavier ions, several tens of neutrons may enter within the aperture of the ZDC. Inclusive  $\pi^0$   
 7277 production has been measured by the LHCf experiments for  $pp$  collisions. It is of great

7278 interest to compare with DIS measurements at the same proton energies. Precise understanding  
7279 of the inclusive spectrum of the forward-going particles is a key ingredient in simulating air  
7280 showers from ultra-high energy cosmic rays.

### 7281 **Physics requirement for forward neutron and $\pi^0$ production measurement**

7282 It is known from various HERA measurements that the slope parameter  $b$  is about  $8 \text{ GeV}^{-2}$  in the  
7283 exponential parameterisation  $e^{bt}$  of the  $t$  distribution of leading neutrons. In order to precisely  
7284 determine the slope parameter it is necessary to measure the transverse momentum of the  
7285 neutrons up to or beyond 1 GeV. The aperture for forward neutral particles does not have to be  
7286 very large, thanks to the large boost on the proton and heavy ion beam. For example, collisions  
7287 with  $E_p = 7 \text{ TeV}$  need 0.14 mrad for  $p_T = 1 \text{ GeV}$  neutrons at  $E_{\text{particle}}/E_{\text{beam}} \equiv x_F = 1.0$ , or  
7288 0.56 mrad for  $x_F = 0.25$ .

7289 The energy or  $x_F$  resolution for neutrons would not be a dominant factor thanks to the high  
7290 energy of the produced particles. The energy resolution of a neutron with  $x_F = 0.1$  is about  
7291 2% for cutting-edge hadron calorimeters with  $\sigma_E/E = 50\%/\sqrt{E}$ , where  $E$  is in GeV. Such a  
7292 resolution can be achieved if non-unity  $e/h$  can be compensated either by construction of the  
7293 calorimeter or by software weighting, and if the size of the calorimeter is large enough so that  
7294 shower leakage is small.

7295 On the other hand, the resolution requirement on the transverse momentum is rather stringent.  
7296 For example, 1 mm resolution on hadronic showers from the neutron measured at 100 m down-  
7297 stream from the interaction point corresponds to 0.01 mrad or 70 MeV, which is rather moderate  
7298 ( $\leq 10\%$  resolution for large  $p_T$  hadrons with  $p_T > 700 \text{ MeV}$ ). For smaller  $p_T$  it is more appro-  
7299 priate to evaluate the resolution in terms of  $t \simeq -(1 - x_F)p_T^2$  i.e.  $\Delta t \simeq 2(\Delta p_T)p_T$  at  $x_F = 1$ .  
7300 At  $t = 0.1 \text{ GeV}^2$  or  $p_T \simeq 300 \text{ MeV}$ ,  $\Delta t$  is about 50%. A shower measurement with significantly  
7301 better than 1 mm position resolution, therefore, would improve the  $t$ -distribution measurement  
7302 significantly.

7303 According to the current LHC operation conditions with  $\beta^* = 5 \text{ cm}$ , the beam spread is  $8 \times$   
7304  $10^{-5} \text{ rad}$  or 0.56 GeV. This is much larger than the required resolution in  $p_T$ . It is, therefore,  
7305 neither possible to measure the particle flow nor control the acceptance of the forward aperture.  
7306 For precision measurement of forward particles, it is necessary to have runs with  $\beta^* \geq 1 \text{ m}$ ,  
7307 corresponding to  $\sigma(p_T) < 70 \text{ MeV}$ .

7308 The calorimeter should be able to measure more than 30 neutrons of 5 TeV for tagging spectator  
7309 neutrons from heavy-ion collisions. The dynamic range of the calorimeter should exceed 100 TeV  
7310 with good linearity.

7311 As for  $\pi^0$  measurements, the LHCf experiment has demonstrated that a position resolution of  
7312  $200 \mu\text{m}$  on electromagnetic showers provides good performance for the inclusive photon spectrum  
7313 measurements [764]. This also calls for fine segmentation sampling layers.

### 7314 **ZDC location for the Linac-Ring IP design**

7315 According to the IP design, a possible location for the ZDC is after the first bending of the  
7316 outgoing colliding proton beam at around  $Z = 110 \text{ m}$ , where no beam magnet is placed (see  
7317 Fig. 10.12). It is anyhow planned to place a neutral particle dump around this location in order  
7318 to protect accelerator components. A ZDC could serve as the first absorbing layer at zero  
7319 degrees.

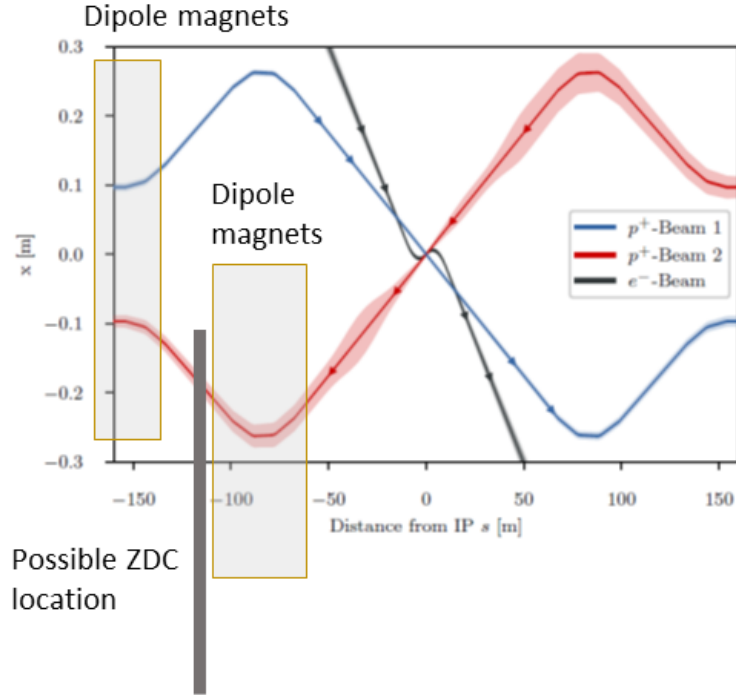


**Figure 10.12:** Possible location for a ZDC for the linac–ring design of LHeC. The solid rectangle represents the ZDC. The two boxes in front of and behind the ZDC indicate the locations for bending magnets.

7320 The aperture to the ZDC would be determined by the last quadrupole magnet at around  $z = 50$  m.  
 7321 Assuming a typical aperture for the LHC magnets of 35 mm, the aperture could be as large as  
 7322 0.7 mrad. The horizontal aperture of the dipole magnets between 75 and 100 m would be larger  
 7323 since otherwise the magnets receive significant radiation from neutral particles produced from  
 7324 the collisions at the IP. Even if the aperture is limited by the vertical aperture of the last dipole  
 7325 at  $z = 100$  m, the aperture is 0.35 mrad, corresponding to 2.4 GeV in  $p_T$  for 7 GeV particles.  
 7326 This fulfills the physics requirement.

7327 The space for the ZDC location in the transverse direction should be at least  $\pm 2\lambda_I$  to avoid  
 7328 large leakage of hadronic showers. This can be achieved if the proton beam traverses inside the  
 7329 calorimeter, about 20 cm from the centre of the calorimeter. The total size of the calorimeter  
 7330 could then be  $60 \times 60 \times 200$  cm or larger according to the current layout of the beam and  
 7331 accelerator components. This would provide about  $\pm 3\lambda_I$  in the transverse direction and about  
 7332  $10\lambda_I$  in depth.

### 7333 Radiation requirement for the ZDC

7334 It can safely be assumed that the energy spectrum of the neutral particles produced in  $ep$   
 7335 and  $pp$  events are very similar. According to the LHCf simulation, their tungsten–scintillator  
 7336 sandwich calorimeter receives about  $30 \text{ Gy/nb}^{-1}$  or  $10^8 \text{ events/nb}^{-1}$  assuming  $\sigma_{pp}^{\text{tot}} = 100 \text{ mb}$ ,  
 7337 i.e.  $3 \times 10^{-7} \text{ Joule/event}$ . This means that about 1/4 of the total proton beam energy ( $7 \text{ TeV} \simeq$   
 7338  $1.12 \times 10^{-6} \text{ Joule/event}$ ) is deposited in 1 kg material in  $pp$  collisions. The  $ep$  total cross section  
 7339 is  $68 \mu\text{b}$  or  $680 \text{ kHz}$  at  $10^{34} \text{ cm}^2\text{s}^{-1}$ . A 7 TeV beam or  $1.12 \times 10^{-6} \text{ Joule/event}$  corresponds  
 7340 to  $0.76 \text{ Joule/s}$  at this instantaneous luminosity. A quarter of the total dose is then about

7341 0.2 Gy/sec or 0.02 Gy/nb, which is in accordance with the expectation from  $\sigma_{pp}^{\text{tot}} \simeq 10^3 \sigma_{ep}^{\text{tot}}$ . The  
7342 contribution from beam-gas interactions is estimated to be much smaller ( $\mathcal{O}(100 \text{ kHz})$ ).

7343 Assuming that the ZDC is always operational during LHeC running, one year of  $ep$  operation  
7344 amounts to 2.5 MGy/year assuming  $10^7$  sec operation, or  $\mathcal{O}(10 \text{ MGy})$  throughout the lifetime of  
7345 the LHeC operation. This approximately corresponds to  $10^{14} - 10^{15}$  1 MeV neutron equivalent.

### 7346 Possible calorimeter design

7347 The high dose of  $\mathcal{O}(10 \text{ MGy})$  requires calorimeters based on modern crystals (e.g. LYSO) or  
7348 silicon as sampling layers, at least for the central part of the calorimeter where the dose is  
7349 concentrated. Since we also need very fine segmentation for photons, it is desirable to use finely  
7350 segmented silicon pads of order of 1 mm. As for the absorbers, tungsten should be used for good  
7351 position resolution of photons and the initial part of hadronic showers.

7352 In the area outside the core of the shower i.e. well outside the aperture, the dose may be much  
7353 smaller and small scintillator tiles could be used for absorbers, which allows measurements with  
7354 good  $e/h$  ratio. If we choose a uniform design using silicon across the detector, the segmentation  
7355 of the outer towers could be order of a few cm, which still makes it possible to use software  
7356 compensation technology developed for ILC calorimeters. It may also be possible to use lead  
7357 instead of tungsten for outer towers to reduce the cost.

## 7358 10.7 Detector Installation and Infrastructure

7359 The usual constraints that apply to HEP detector integration and assembly studies, are made  
7360 here also. They hold even tighter since the detector has to be installed in the shortest allowable  
7361 time, given by the duration of an LHC machine shutdown, which is typically two years. Since the  
7362 new LHeC detector would be installed at the place of IP2, see Fig. 10.13, time needed to remove  
7363 the old detector and its services has to be added to the overall schedule. Thus the only realistic  
7364 possibility to accomplish the timely dismantling of the old detector and the installation of the  
7365 new one is to complete as much as possible the assembling and testing of the LHeC detector  
7366 on surface, where the construction can proceed without impacting on the LHC physics runs.  
7367 Condition for doing this, is the availability of equipped free space at LHC-P2 surface, namely a  
7368 large assembly hall with one or two cranes. To save time, most of the detector components have  
7369 been designed to match the handling means available on site, i.e. bridge crane in surface hall  
7370 and experiment cavern. Nevertheless, a heavy lifting facility (about 300 tons capacity) will be  
7371 rented for the time needed to lower the heaviest detector components, such as HCal barrel and  
7372 plug modules. Large experience with this will be acquired during LHC Long Shutdown 3, when  
7373 a significant part of ATLAS and CMS detectors will be replaced by new elements. At CMS, for  
7374 instance, a new Endcap Calorimeter weighing about 220 tons will be lowered into the experiment  
7375 cavern, a scenario very close to what is here envisaged for the LHeC detector assembly.

7376 The detector has been split in the following main parts for assembly purposes:

- 7377 • Coil cryostat, including the superconducting coil, the two integrated dipoles and eventually  
7378 the EMCal.
- 7379 • Five HCal tile calorimeter barrel modules, fully instrumented and cabled (5).
- 7380 • Two HCal plugs modules, forward and backward (2).



**Figure 10.13:** View on the hall surface infrastructure at Point 2, near St.Genis.

- 7381      • Two EMCal plugs, forward and backward (2).
- 7382      • Inner Tracking detector (1).
- 7383      • Beam-pipe (1).
- 7384      • Central Muon detector (1 or 2).
- 7385      • Endcaps Muon detector (2).

7386 The full detector, including the Muon chambers, fits inside the former L3 detector Magnet Yoke,  
 7387 once the four large doors are taken away. The goal is to prevent losing time in dismantling the  
 7388 L3 Magnet barrel yoke and to make use of its sturdy structure to hold the detector central part  
 7389 on a platform supported by the magnet crown, whilst the Muon chambers will be inserted into  
 7390 lightweight structures (space-frames) attached to the inner surface of the octagonal L3 magnet.

7391 The assembly on surface of the main detector elements, as previously defined, can start at any  
 7392 time, providing that the surface facilities are available, without sensible impact on the LHC  
 7393 run. The Coil system commissioning on site ( $t = 0$ ) could require 3 months and preparation for  
 7394 lowering three months, including some contingency. In the same time window, the L3 Magnet  
 7395 will be freed up and prepared for the new detector <sup>2</sup>. Lowering of the main detector components  
 7396 into the cavern, illustrated in Fig. 10.14, is supposed to take one week per piece (15 pieces in  
 7397 total). Underground integration of the central detector elements inside the L3 Magnet would  
 7398 require about 6 months, cabling and connection to services some 8 to 10 months, in parallel  
 7399 with the installation of the Muon chambers, the Tracker and the Calorimeter Plugs. Fig. 10.15  
 7400 shows the installed complete detector housed in the L3 magnet support.

<sup>2</sup> The actual delay depends on the level of activation and the procedure adopted for dismantling the existing detector. Here again the experience acquired during the long shutdown (LS) 2 with the upgrades of ALICE and LHCb and later with ATLAS and CMS upgrades during LS3 will provide important insight for defining procedures and optimising the schedule.

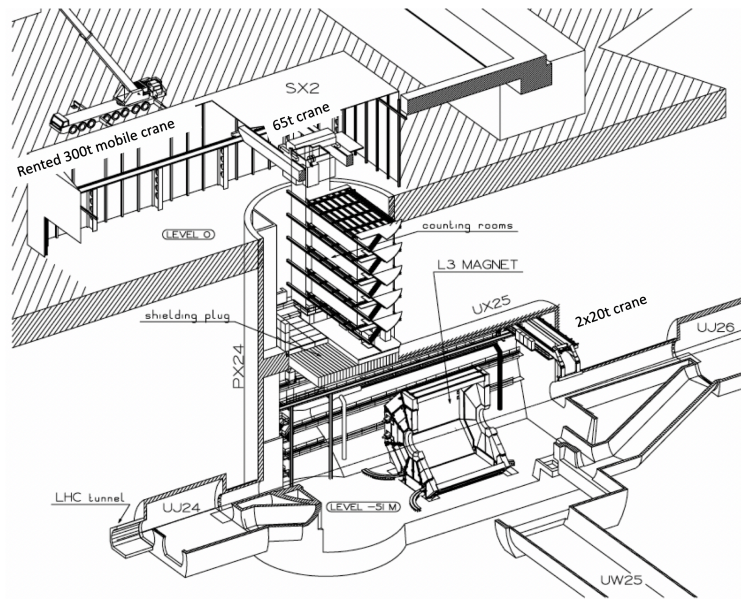


**Figure 10.14:** View on the cavern infrastructure at Point 2. In the centre one recognises the support structure of the magnet of the L3 experiment which is thought to house and support also the LHeC detector, not least for its removal would cost significant extra time.

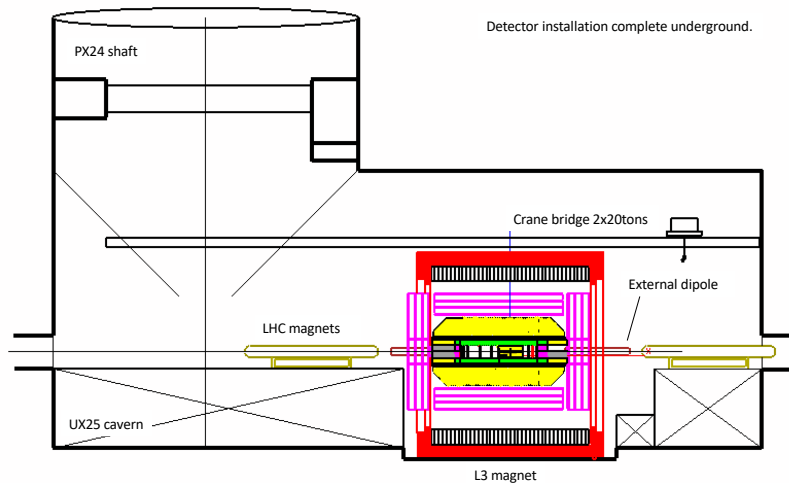


**Figure 10.15:** View on the LHeC detector, housed in the L3 magnet support structure, after installation at the interaction point.

7401 The total estimated time, from the starting of the testing of the Coil system on surface to the  
 7402 commissioning of the detector underground is thus 20 months. The beam-pipe bake out and  
 7403 vacuum pumping could take another 3 months and the final detector check-out one additional  
 7404 month. Some contingency (2–3 months in total) is foreseen at the beginning and the end of the  
 7405 installation period. A sketch of the installation schedule is provided in Fig. 10.16

7406 Concerning the detector infrastructures, not much can be said at this stage. The LHeC detector  
 7407 superconducting coil will need cryogenics services and a choice has to be made between pur-

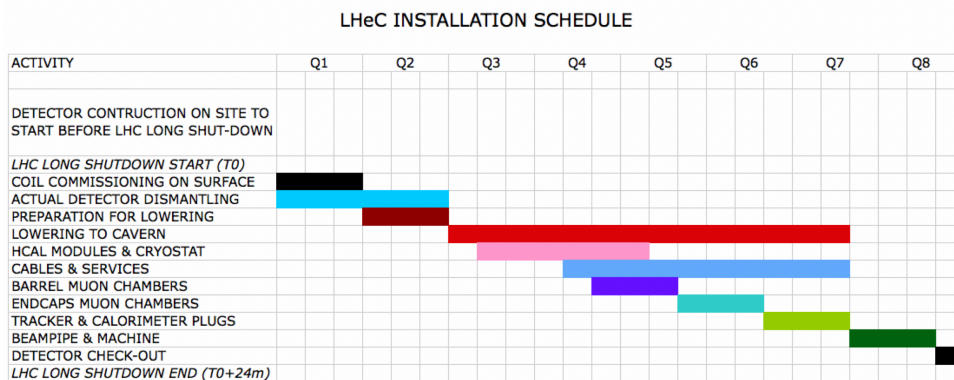


**Figure 10.16:** Time schedule of the sequential installation of the LHeC detector in point 2 as described in the text.

7408 chasing a dedicated liquid helium refrigeration plant or profit of the existing LHC cryogenics  
 7409 infrastructures to feed the detector magnet. Electrical and water cooling network present at  
 7410 LHC-P2 are already well sized for the new detector and only minor interventions are expected  
 7411 there.

## 7412 10.8 Detector Design for a Low Energy FCC-eh

7413 Although not the primary focus of this document, it is worth noting that a full detector design  
 7414 has also been carried out for an *ep* facility based on an FCC tunnel with proton-ring magnet  
 7415 strengths limited such that the proton energy is 20 TeV. The basic layout is similar to the LHeC  
 7416 detector. Similar or better performance is obtained compared with the LHeC detector, provided  
 7417 that additional disks are included in the forward and backward trackers and the calorimeter  
 7418 depths are scaled logarithmically with the beam energies. The basic layout is shown in Fig. 10.17.

Tracker (lowE-FCCeh) <sup>1)</sup>	Fwd Tracker			Bwd Tracker		Total (incl. Tab. 10.1)
	pix	pix <sub>macro</sub>	strip	pix <sub>macro</sub>	strip	
$\eta_{\max}, \eta_{\min}$	5.6, 2.6	3.8, 2.2	3.5, 1.6	-4.6, -2.6	-2.8, -1.6	5.3, -4.6
Wheels	2	1	3	3	3	
Modules/Sensors	288	288	1376	216	1248	12444
Total Si area [m <sup>2</sup> ]	1.35	1.45	7.35	1.0	6.5	49.85
Read-out-Channels [10 <sup>6</sup> ]	647.9	110.2	42.3	82.7	38.3	3317.2
pitch <sup>r-<math>\phi</math></sup> [ $\mu$ m]	$\sim 25$	$\sim 100$	$\sim 100$	$\sim 100$	$\sim 100$	
pitch <sup>z</sup> [ $\mu$ m]	$\sim 50$	$\sim 400$	50k <sup>2)</sup>	$\sim 400$	10k <sup>2)</sup>	
Average $X_0/\Lambda_I$ [%]	6.7 / 2.1			6.1 / 1.9		
incl. beam pipe [%]						40 / 25

<sup>1)</sup> Based on tklayout calculations [757]

<sup>2)</sup> Reaching pitch<sup>r- $\phi$</sup>  when using two wafer layers rotated by 20mrad is achievable.

**Table 10.5:** Summary of the main properties of the forward and backward tracker modules in the revised LHeC detector configuration based on calculations performed using tkLayout. For each module, the rows correspond to the pseudorapidity coverage, numbers of barrel and disk layers, numbers of sensors, total area covered by silicon sensors, numbers of readout channels, the hardware pitches affecting the ( $r - \phi$ ) and the  $z$  resolution, respectively and the average material budget in terms of radiation lengths and interaction lengths. Where appropriate, the numbers are broken down into separate contributions from pixels, macro-pixels and strips. The column *Total* contains the sum of corresponding values of barrel tracker modules which are identical to the LHeC barrel layout table 10.1.

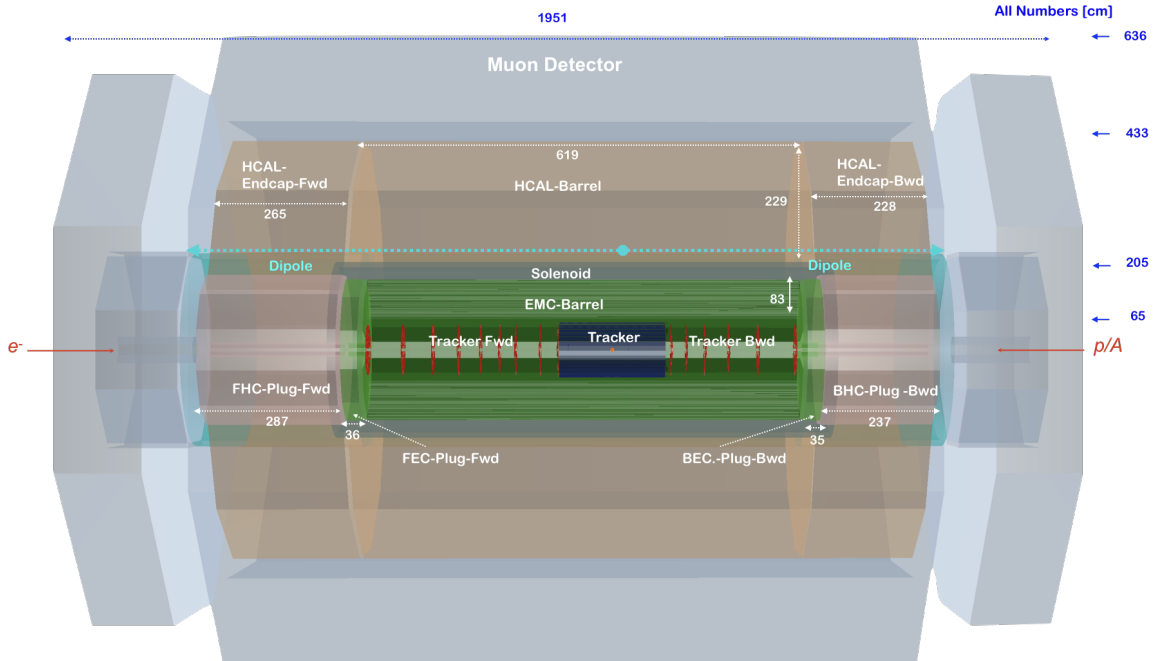


**Figure 10.17:** Side view of a low energy FCCeh ( $E_p = 20$  TeV) concept detector, designed using the DD4hep framework [756], showing the essential features. The solenoid is again placed between the ECAL-Barrel and Hadronic-Barrel calorimeters and is housed in a cryostat in common with the beam steering dipoles extending over the full length of the barrel and plug hadronic calorimeters. The sizes have been chosen such that the solenoid/dipoles and ECAL-Barrel systems as well as the whole tracker are also suitable to operate after an upgrade of the beam energy to  $E_p = 50$  TeV.

Calo (lowE-FCCeh)	EMC		HCAL	
	Barrel	Ecap Fwd	Barrel	Ecap Bwd
Readout, Absorber	Sci,Pb	Sci,Fe	Sci,Fe	Sci,Fe
Layers	49	91	68	78
Integral Absorber Thickness [cm]	36.6	206.0	184.0	178.0
$\eta_{\max}, \eta_{\min}$	2.8, -1.7	2.0, 0.8	1.6, -0.8	-1.4, -1.8
$\sigma_E/E = a\sqrt{E} \oplus b$	[%] 12.6/1.1	38.9/3.3	42.4/4.2	40.6/3.5
$\Lambda_I / X_0$	$X_0 = 66.2$	$\Lambda_I = 12.7$	$\Lambda_I = 11.3$	$\Lambda_I = 11.0$
Total area Sci	[m <sup>2</sup> ] 2915	4554	12298	3903

**Table 10.6:** Basic properties and simulated resolutions of barrel calorimeter modules in a scaled LHeC detector configuration, illustrating a low energy FCC detector setup. For each of the modules, the rows indicate the absorber and sensitive materials, the pseudorapidity coverage, the contributions to the simulated resolution from the sampling ( $a$ ) and material ( $b$ ) terms in the form  $a/b$ , the depth in terms of radiation or interaction lengths and the total area covered by the sensitive material.

**GEANT4** [758] simulation based fits using crystal ball function [759] [760] [761].

Calo (lowE-FCCeh)	FHC	FEC	BEC	BHC
	Plug Fwd	Plug Fwd	Plug Bwd	Plug Bwd
Readout, Absorber	Si,W	Si,W	Si,Pb	Si,Cu
Layers	296	49	59	238
Integral Absorber Thickness [cm]	256.9	29.6	27.9	220.8
$\eta_{\max}, \eta_{\min}$	5.8, 1.8	5.4, 1.8	-5.1, -5.2	-5.2, -5.6
$\sigma_E/E = a/\sqrt{E} \oplus b$	[%] 61.9/0.5	26.5/0.4	24.7/0.4	46.7/4.4
$\Lambda_I / X_0$	$\Lambda_I = 15.5$	$X_0 = 84.7$	$X_0 = 50.2$	$\Lambda_I = 14.7$
Total area Si	[m <sup>2</sup> ] 2479	364	438	1994

**Table 10.7:** Basic properties and simulated resolutions of forward and backward plug calorimeter modules in a scaled LHeC detector configuration, illustrating a low energy FCC detector setup. For each of the modules, the rows indicate the absorber and sensitive materials, the pseudorapidity coverage, the contributions to the simulated resolution from the sampling ( $a$ ) and material ( $b$ ) terms in the form  $a/b$ , the depth in terms of radiation or interaction lengths and the total area covered by the sensitive material.

**GEANT4** [758] simulation based fits using crystal ball function [759] [760] [761].

# Chapter 11

## Conclusion

The Large Hadron Collider determines the energy frontier of experimental collider physics for the next two decades. Following the current luminosity upgrade, the LHC can be further upgraded with a high energy, intense electron beam such that it becomes a twin-collider facility, in which  $ep$  collisions are registered concurrently with  $pp$ . A joint ECFA, CERN and NuPECC initiative led to a detailed conceptual design report (CDR) [1] for the Large Hadron Electron Collider published in 2012. The present paper represents an update of the original CDR in view of new physics and technology developments.

The LHeC uses a novel, energy recovery linear electron accelerator which enables TeV energy electron-proton collisions at high luminosity, of  $O(10^{34}) \text{ cm}^{-2}\text{s}^{-1}$ , exceeding that of HERA by nearly three orders of magnitude. The discovery of the Higgs boson and the surprising absence of BSM physics at LHC demand to extend the experimental base of particle physics suitable to explore the energy frontier, beyond  $pp$  collisions at the LHC. The LHC infrastructure is the largest single investment the European and global particle physics community ever achieved, and the addition of an electron accelerator a most appropriate way to build on it, and to sustain the HL-LHC programme by adding necessary elements which are provided by high energy deep inelastic scattering. As has been shown in this paper, the external DIS input transforms the LHC to a much more powerful facility, with a resolution of matter substructure, a more precise Higgs programme challenging and complementing that of a next  $e^+e^-$  collider and with a hugely extended potential to find new physics beyond the Standard Model.

The very high luminosity and the substantial extension of the kinematic range in deep inelastic scattering compared to HERA, make the LHeC on its own a uniquely powerful TeV energy collider. Realising the *Electrons for LHC* programme developed with the previous and the present white papers, will create the cleanest, high resolution microscope accessible to the world, one may term a “CERN Hubble Telescope for the Micro-Universe”. It is directed to unravel the substructure of matter encoded in the complex dynamics of the strong interaction, a necessary input for the HL-LHC and for future hadron colliders. This regards the complete resolution of the partonic densities in a unprecedented range of small dimensions, the foundations for new, generalised views on proton structure and the long awaited clarification of the QCD dynamics at high densities, as are observed at small Bjorken  $x$ . New high precision measurements on diffraction and vector mesons will shed new light on the puzzle of confinement. As a complement to the LHC and a possible future  $e^+e^-$  machine, the LHeC would scrutinise the Standard Model (SM) deeper than ever before, and possibly discover new physics in the electroweak and chromodynamic sectors. Through the extension of the kinematic range by about three orders of magnitude in lepton-nucleus (eA) scattering, the LHeC is the most powerful electron-ion

7455 research facility one can build in the next decades, for elucidating the chromodynamic origin of  
7456 the Quark-Gluon-Plasma and clarifying the partonic substructure and dynamics inside nuclei  
7457 for the first time. The Higgs programme is very rich as it relies on CC and NC precision  
7458 measurements for which an inverse ab is desirable to achieve. The BSM prospects as on right-  
7459 handed neutrinos, long lived particles and electroweak SUSY are indeed exciting due to the high  
7460 energy and absence of pile-up in  $ep$ .

7461 The LHeC physics programme reaches far beyond any specialised goal which underlines the  
7462 unique opportunity for particle physics to build a novel laboratory for accelerator based energy  
7463 frontier research at CERN. The project is fundable within the CERN budget, and not preventing  
7464 much more massive investments into the further future. It offers the possibility for the current  
7465 generation of accelerator physicists to build a new collider using and developing novel technology  
7466 while preparations proceed for the next grand step in particle physics for generations ahead.

7467 The main innovation through the LHeC is the first ever high energy application of energy recov-  
7468 ery technology, based on high quality superconducting RF developments, a major contribution  
7469 to the development of *green* collider technology which is an appropriate response to demands  
7470 of our time. The ERL technique is more and more seen to have major further applications, be-  
7471 yond  $ep$  at HE-LHC and FCC-eh, such as for FCC-ee, as a  $\gamma\gamma$  Higgs facility or, beyond particle  
7472 physics, as the highest energy XFEL of hugely increased brightness.

7473 The paper describes the plans and configuration of PERLE, the first 10 MW power ERL facility  
7474 which is being prepared in international collaboration for built at Irene Curie Laboratory at  
7475 Orsay. PERLE has adopted the 3-pass configuration, cavity and cryomodule technology, source  
7476 and injector layout, frequency and electron current parameters from the LHeC. This qualifies  
7477 it to be the ideal machine to accompany the development of the LHeC. With its challenging  
7478 parameters, such as an intensity exceeding that of ELI by orders of magnitude, PERLE has  
7479 an independent, far reaching low energy nuclear and particle physics programme with new and  
7480 particularly precise measurements. It also has a possible program on industrial applications,  
7481 which have not been discussed in the present paper.

7482 The LHeC provides an opportunity for building a novel collider detector which is sought for as  
7483 the design of the HL-LHC detector upgrades is approaching completion. A novel  $ep$  experiment  
7484 enables modern detection technology, such as HV CMOS Silicon tracking, to be further developed  
7485 and exploited in a new generation,  $4\pi$  acceptance, no pile-up, high precision collider detector in  
7486 the decade(s) hence. This paper presented an update of the 2012 detector design, in response  
7487 to demands from the development of physics, especially Higgs and BSM, and technology in  
7488 detectors and analysis.

7489 The next steps in this development are rather clear: it needs PERLE to proceed, limited funds for  
7490 prototypes, especially of the IR magnets, be made available and a proto-detector Collaboration  
7491 to emerge such that in a few years time a decision on building the LHeC at CERN may be taken,  
7492 in the context also of what these years may bring for physics, with higher LHC luminosity, for  
7493 Asia, with decisions about ILC and CEPC, and for the further future and support of CERN as  
7494 the world's leading laboratory for particle physics, including its way of cooperation globally and  
7495 with its surrounding major laboratories.

7496 The recent history teaches a lesson about the complementarity required for energy frontier  
7497 particle physics. In the seventies and eighties, CERN hosted the  $p\bar{p}$  energy frontier, with UA1  
7498 and UA2, and the most powerful DIS experiments with muons (EMC, BCDMS, NMC) and  
7499 neutrinos (CDHSW, CHARM), while  $e + e^-$  physics was pursued at PEP, PETRA and also  
7500 TRISTAN. Following this, the Fermi scale could be explored with the Tevatron, HERA and

7501 LEP. The here advertised next logical step is to complement the HL-LHC by a most powerful  
7502 DIS facility, the LHeC, while preparations will take shape for a new  $e^+e^-$  collider, currently at  
7503 CERN and in Asia. This scenario would give a realistic and yet exciting base for completing  
7504 the exploration of TeV scale physics which may not be achieved with solely the LHC.

7505 The ERL concept and technology here presented has the potential to accompany the FCC for  
7506 realising the FCC-eh machine when the time comes for the next, higher energy hadron collider,  
7507 and the search for new physics at the O(10) TeV scale.

## 7508 **Acknowledgement**

7509

7510 The analyses and developments here presented would not have been possible without the CERN  
7511 Directorate and other labs and Universities supporting this study. We thank the technicians  
7512 contributing to this work, such as with their competence in building the first 802 MHz SC  
7513 cavity. We thank many colleagues for their interest in this work and a supportive attitude when  
7514 time constraints could have caused lesser understanding. Special thanks are also due to the  
7515 members and chair of the International Advisory Committee for their attention and guidance  
7516 to the project. From the beginning of the LHeC study, it has been supported by ECFA and its  
7517 chairs which was a great help and stimulus for undertaking this work which has been performed  
7518 outside our usual duties. During the time, a number of students, in master and PhD courses,  
7519 have made very essential contributions to this project for which we are especially grateful. This  
7520 also extends to colleagues with whom we have been working closely but who meanwhile left this  
7521 development, perhaps temporarily, or work at non-particle physics institutions while wishing  
7522 LHeC success. The current situation of particle physics reminds us on the potential we have  
7523 when resources and prospects are unified, for which this study is considered to be a contribution.

## 7524 **Appendix A**

# 7525 **Statement of the International** 7526 **Advisory Committee**

7527 End of 2014, the CERN Directorate appointed an International Advisory Committee (IAC) for  
7528 advice on the direction of energy frontier electron-hadron scattering at CERN, for their mandate  
7529 see below. The committee and its chair, em. DG of CERN Herwig Schopper, was reconfirmed  
7530 when a new DG had been appointed. The IAC held regular sessions at the annual LHeC  
7531 workshops in which reports were heard by the co-coordinators of the project, Oliver Brüning  
7532 and Max Klein. Its work and opinion shaped the project development considerably and it was  
7533 pivotal for the foundation of the PERLE project. The committee was in close contact and  
7534 advised especially on the documents, on the LHeC [5,7] and PERLE [8], submitted end of 2018  
7535 to the update of the European strategy on particle physics. In line with the present updated  
7536 LHeC design report and the strategy process, which began in 2018 and is due to conclude in  
7537 spring 2020, the IAC formulated a brief report to the CERN DG, in which its observations  
7538 and recommendations have been summarised. This report was also sent to the members of the  
7539 European particle physics strategy group. It is reproduced here.

## 7540 **Report by the IAC on the LHeC to the DG of CERN**

7541 The development of the LHeC project was initiated by CERN and ECFA, in cooperation  
7542 with NuPECC. It culminated in the publication of the Conceptual Design Report (CDR),  
7543 arXiv:1206.2913 in 2012, which received by now about 500 citations. In 2014, the CERN Di-  
7544 rectorate invited our committee to advise the CERN Directorate, and the Coordination Group,  
7545 on the directions of future energy frontier electron-hadron scattering as are enabled with the  
7546 LHC and the future FCC (for the mandate see below). In 2016, Council endorsed the HL-LHC,  
7547 which offers a higher LHC performance and strengthened the interest in exploring the Higgs  
7548 phenomenon. In view of the imminent final discussions for the European Road Map for particle  
7549 physics, a short summary report is here presented.

## 7550 Main Developments 2014–2019

7551 A series of annual workshops on the LHeC and FCC-eh was held, and this report is given  
7552 following the latest workshop <https://indico.cern.ch/event/835947> , October 24/25, 2019.

7553 Based on recent developments concerning the development of the LHC accelerator and physics,  
7554 and the progress in technology, a new default configuration of the LHeC and FCC-eh has been  
7555 worked out with a tenfold increased peak luminosity goal, of  $10^{34} \text{ cm}^{-2} \text{ s}^{-1}$ , as compared to the  
7556 CDR. A comprehensive paper, “The LHeC at the HL-LHC”, is being finalised for publication  
7557 this year.

7558 Within this work, it has been shown that the LHeC represents the cleanest, high resolution  
7559 microscope the world can currently build, a seminal opportunity to develop and explore QCD,  
7560 to study high precision Higgs and electroweak physics and to substantially extend the range  
7561 and prospects for accessing BSM physics, on its own and in combination of pp with ep. The  
7562 LHeC, in eA scattering mode, has a unique discovery potential on nuclear structure, dynamics  
7563 and QGP physics.

7564 Intense eh collisions with LHeC and FCC-eh are enabled through a special electron-beam race-  
7565 track arrangement with energy recovery linac (ERL) technology. If LHeC were to be considered  
7566 either on its own merits, or as a bridge project to FCC-eh, it seemed important to find a config-  
7567 uration, which could be realised within the existing CERN budget. Several options were studied  
7568 and found.

7569 Before a decision on such a project can be taken, the ERL technology has to be further developed.  
7570 Considerable progress has been made in the USA, and a major effort is now necessary to develop  
7571 it further in Europe. An international collaboration (ASTeC, BINP, CERN, Jefferson Lab,  
7572 Liverpool, Orsay) has been formed to realise the first multi-turn 10 MW ERL facility, PERLE  
7573 at Orsay, with its main parameters set by the LHeC and producing the first encouraging results  
7574 on 802 MHz cavity technology, for the CDR see arXiv:1705.08783.

7575 This radically new accelerator technology, ERL, has an outstanding technical (SRF), physics  
7576 (nuclear physics) and industrial (lithography, transmutations, ..) impact, and offers possible  
7577 applications beyond ep (such as a racetrack injector or ERL layout for FCC-ee, a high energy  
7578 FEL or  $\gamma\gamma$  collider).

### 7579 In conclusion it may be stated

- 7580 • The installation and operation of the LHeC has been demonstrated to be commensurate  
7581 with the currently projected HL-LHC program, while the FCC-eh has been integrated into  
7582 the FCC vision;
- 7583 • The feasibility of the project as far as accelerator issues and detectors are concerned has  
7584 been shown. It can only be realised at CERN and would fully exploit the massive LHC  
7585 and HL-LHC investments;
- 7586 • The sensitivity for discoveries of new physics is comparable, and in some cases superior,  
7587 to the other projects envisaged;
- 7588 • The addition of an ep/A experiment to the LHC substantially reinforces the physics pro-  
7589 gram of the facility, especially in the areas of QCD, precision Higgs and electroweak as  
7590 well as heavy ion physics;
- 7591 • The operation of LHeC and FCC-eh is compatible with simultaneous pp operation; for  
7592 LHeC the interaction point 2 would be the appropriate choice, which is currently used by  
7593 ALICE;

- 7594       • The development of the ERL technology needs to be intensified in Europe, in national  
7595 laboratories but with the collaboration of CERN;  
7596       • A preparatory phase is still necessary to work out some time-sensitive key elements, es-  
7597 pecially the high power ERL technology (PERLE) and the prototyping of Intersection  
7598 Region magnets.

## 7599 **Recommendations**

7600 i) It is recommended to further develop the ERL based ep/A scattering plans, both at LHC  
7601 and FCC, as attractive options for the mid and long term programme of CERN, resp. Before  
7602 a decision on such a project can be taken, further development work is necessary, and should  
7603 be supported, possibly within existing CERN frameworks (e.g. development of SC cavities and  
7604 high field IR magnets).

7605

7606 ii) The development of the promising high-power beam-recovery technology ERL should be in-  
7607 tensified in Europe. This could be done mainly in national laboratories, in particular with the  
7608 PERLE project at Orsay. To facilitate such a collaboration, CERN should express its interest  
7609 and continue to take part.

7610

7611 iii) It is recommended to keep the LHeC option open until further decisions have been taken.  
7612 An investigation should be started on the compatibility between the LHeC and a new heavy ion  
7613 experiment in Interaction Point 2, which is currently under discussion.

7614

7615 After the final results of the European Strategy Process will be made known, the IAC considers  
7616 its task to be completed. A new decision will then have to be taken for how to continue these  
7617 activities.

7618

7619 Herwig Schopper, Chair of the Committee,

Geneva, November 4, 2019

## 7620 **Mandate of the International Advisory Committee**

7621 Advice to the LHeC Coordination Group and the CERN directorate by following the develop-  
7622 ment of options of an ep/eA collider at the LHC and at FCC, especially with: Provision of  
7623 scientific and technical direction for the physics potential of the ep/eA collider, both at LHC  
7624 and at FCC, as a function of the machine parameters and of a realistic detector design, as well  
7625 as for the design and possible approval of an ERL test facility at CERN. Assistance in building  
7626 the international case for the accelerator and detector developments as well as guidance to the  
7627 resource, infrastructure and science policy aspects of the ep/eA collider. (December 2014)

## Members of the Committee

Sergio Bertolucci (Bologna)  
Nichola Bianchi (INFN, now Singapore)  
Frederick Bordy (CERN)  
Stan Brodsky (SLAC)  
Oliver Brüning (CERN, coordinator)  
7629 Hesheng Chen (Beijing)  
Eckhard Elsen (CERN)  
Stefano Forte (Milano)  
Andrew Hutton (Jefferson Lab)  
Young-Kee Kim (Chicago)

Max Klein (Liverpool, coordinator)  
Shin-Ichi Kurokawa (KEK)  
Victor Matveev (JINR Dubna)  
Aleandro Nisati (Rome I)  
Leonid Rivkin (PSI Villigen)  
Herwig Schopper (CERN, em.DG, Chair)  
Jürgen Schukraft (CERN)  
Achille Stocchi (Orsay)  
John Womersley (ESS Lund)

# Bibliography

- [1] LHeC Study Group, J. L. Abelleira *et al.*, *J. Phys.* G39 (2012) 075001, [arXiv:1206.2913](#).
- [2] G. Apollinari, I. Béjar Alonso, O. Brüning, P. Fessia, M. Lamont, L. Rossi and L. Tavian (eds.), *High-Luminosity Large Hadron Collider (HL-LHC)*, vol. 4. CERN Yellow Rep. Monogr., CERN-2017-007-M, 2017.
- [3] L. Rossi and O. Brüning, “Progress with the High Luminosity LHC project at CERN,” in *Proceedings, 10th International Particle Accelerator Conference (IPAC2019): Melbourne, Australia, May 19-24, 2019*, Jun 2019.
- [4] D. Angal-Kalinin *et al.*, *J. Phys.* G45 (2018) 065003, [arXiv:1705.08783](#).
- [5] LHeC Study Group, O. Brüning, M. Klein *et al.*, “Exploring the Energy Frontier with Deep Inelastic Scattering at the LHC,” A Contribution to the Update of the European Strategy on Particle Physics, CERN-ACC-NOTE-2018-0084, Dec 2018.
- [6] LHeC and PERLE Collaborations, O. Brüning, M. Klein *et al.*, *J. Phys.* G46 (2019) 123001.
- [7] LHeC Study Group, O. Brüning, M. Klein *et al.*, “Addendum. Exploring the Energy Frontier with Deep Inelastic Scattering at the LHC,” A Contribution to the Update of the European Strategy on Particle Physics, CERN-ACC-NOTE-2018-0085, Dec 2018.
- [8] PERLE Collaboration, M. Klein, A. Stocchi *et al.*, “PERLE: A High Power Energy Recovery Facility for Europe,” A Contribution to the Update of the European Strategy on Particle Physics, CERN-ACC-NOTE-2018-0086, Dec 2018.
- [9] S. Hossenfelder, *Lost in math*. Basic Books, New York, 2018.
- [10] G. Altarelli, *Frascati Phys. Ser.* 58 (2014) 102, [arXiv:1407.2122](#).
- [11] J. De Hondt, “Talk on the Future of Particle Physics and on ECFA Matters,” Plenary Session, ECFA, CERN, November, 2019.
- [12] FCC Collaboration, A. Abada *et al.*, *Eur. Phys. J.* C79 (2019) 474.
- [13] FCC Collaboration, A. Abada *et al.*, *Eur. Phys. J.* ST 228 (2019) 261.
- [14] FCC Collaboration, A. Abada *et al.*, *Eur. Phys. J.* ST 228 (2019) 755.
- [15] CEPC-SPPC Study Group, M. Ahmad *et al.*, “CEPC-SPPC Preliminary Conceptual Design Report. 2. Accelerator,” IHEP-CEPC-DR-2015-01, IHEP-AC-2015-01, 2015.
- [16] CEPC Study Group, M. Dong *et al.*, “CEPC Conceptual Design Report: Volume 2 - Physics & Detector,” 2018. [arXiv:1811.10545](#).
- [17] R. P. Feynman, *Photon-hadron interactions*. Westview Press, Reading, MA, 1972.
- [18] E. D. Bloom *et al.*, *Phys. Rev. Lett.* 23 (1969) 930.
- [19] M. Breidenbach, J. I. Friedman, H. W. Kendall, E. D. Bloom, D. H. Coward, H. C. DeStaebler, J. Drees, L. W. Mo and R. E. Taylor, *Phys. Rev. Lett.* 23 (1969) 935.
- [20] R. P. Feynman, *Phys. Rev. Lett.* 23 (1969) 1415.
- [21] J. D. Bjorken and E. A. Paschos, *Phys. Rev.* 185 (1969) 1975.
- [22] C. Y. Prescott *et al.*, *Phys. Lett.* 77B (1978) 347.
- [23] S. Weinberg, *Phys. Rev. Lett.* 19 (1967) 1264.
- [24] B. H. Wiik, *Acta Phys. Polon.* B16 (1985) 127.
- [25] M. Klein and R. Yoshida, *Prog. Part. Nucl. Phys.* 61 (2008) 343, [arXiv:0805.3334](#).

- [26] A. De Rujula, S. L. Glashow, H. D. Politzer, S. B. Treiman, F. Wilczek and A. Zee, *Phys. Rev. D* **10** (1974) 1649.
- [27] FCC Collaboration, A. Abada *et al.*, *Eur. Phys. J. ST* **228** (2019) 1109.
- [28] F. Marhauser *et al.*, “802 MHz ERL Cavity Design and Development,” in *Proceedings, 9th International Particle Accelerator Conference (IPAC 2018): Vancouver, BC Canada, April 29-May 4, 2018*, 2018.
- [29] V. N. Litvinenko, T. Roser and M. Chamizo Llatas, [arXiv:1909.04437](https://arxiv.org/abs/1909.04437).
- [30] O. Brüning, “FCC-eh Cost Estimate,” CERN-Acc-Note-2018-0061, 2018.
- [31] A. Bogacz, “The LHeC ERL - Optics and Performance Optimisation,” Talk given at ERL Workshop, Berlin, 2019.
- [32] O. Brüning, J. Jowett, M. Klein, D. Pellegrini, D. Schulte and F. Zimmermann, “Future Circular Collider Study FCC-eh Baseline Parameters,” 2017. CERN FCC-ACC-RPT-012.
- [33] F. Bordry *et al.*, “Machine Parameters and Projected Luminosity Performance of Proposed Future Colliders at CERN,” 2018. [arXiv:1810.13022](https://arxiv.org/abs/1810.13022).
- [34] T. J. Hobbs, J. T. Londergan, D. P. Murdock and A. W. Thomas, *Phys. Lett. B* **698** (2011) 123, [arXiv:1101.3923](https://arxiv.org/abs/1101.3923).
- [35] J. C. Collins, D. E. Soper and G. F. Sterman, *Adv. Ser. Direct. High Energy Phys.* **5** (1989) 1, [arXiv:hep-ph/0409313](https://arxiv.org/abs/hep-ph/0409313).
- [36] LHeC Study Group, J. L. Abelleira *et al.*, “On the Relation of the LHeC and the LHC,” 2012. [arXiv:1211.5102](https://arxiv.org/abs/1211.5102).
- [37] H1 and ZEUS Collaborations, H. Abramowicz *et al.*, *Eur. Phys. J. C* **75** (2015) 580, [arXiv:1506.06042](https://arxiv.org/abs/1506.06042).
- [38] H1 and ZEUS Collaborations, F. Aaron *et al.*, *JHEP* **1001** (2010) 109, [arXiv:0911.0884](https://arxiv.org/abs/0911.0884).
- [39] HERAFitter Group, S. Alekhin *et al.*, *Eur. Phys. J. C* **75** (2015) 304, [arXiv:1410.4412](https://arxiv.org/abs/1410.4412).
- [40] H1 Collaboration, F. Aaron *et al.*, *Eur. Phys. J. C* **64** (2009) 561, [arXiv:0904.3513](https://arxiv.org/abs/0904.3513).
- [41] M. Botje, *Comput. Phys. Commun.* **182** (2011) 490, [arXiv:1005.1481](https://arxiv.org/abs/1005.1481).
- [42] M. Botje, “Erratum for the time-like evolution in QCDNUM,” 2016. [arXiv:1602.08383](https://arxiv.org/abs/1602.08383).
- [43] R. Thorne, *Phys.Rev. D* **73** (2006) 054019, [arXiv:0601245](https://arxiv.org/abs/0601245).
- [44] R. Thorne, *Phys.Rev. D* **86** (2012) 074017, [arXiv:1201.6180](https://arxiv.org/abs/1201.6180).
- [45] F. James and M. Roos, *Comp. Phys. Comm.* **10** (1975) 343.
- [46] U. Bassler and G. Bernardi, *Nucl. Instrum. Meth. A* **361** (1995) 197–208, [arXiv:hep-ex/9412004](https://arxiv.org/abs/hep-ex/9412004).
- [47] J. Blümlein and M. Klein, “Kinematics and resolution at future e p colliders,” in *1990 DPF Summer Study on High-energy Physics: Research Directions for the Decade (Snowmass 90) Snowmass, Colorado, June 25-July 13, 1990*, 1990.
- [48] R. Abdul Khalek, S. Bailey, J. Gao, L. Harland-Lang and J. Rojo, [arXiv:1906.10127](https://arxiv.org/abs/1906.10127).
- [49] S. J. Brodsky and G. R. Farrar, *Phys. Rev. Lett.* **31** (1973) 1153.
- [50] S. J. Brodsky and G. R. Farrar, *Phys. Rev. D* **11** (1975) 1309.
- [51] V. A. Matveev, R. M. Muradian and A. N. Tavkhelidze, *Lett. Nuovo Cim.* **7** (1973) 719.
- [52] HERAFitter Group, S. Alekhin *et al.*, *Eur. Phys. J. C* **75** (2015) 304, [arXiv:1410.4412](https://arxiv.org/abs/1410.4412).
- [53] S. Dulat *et al.*, *Phys. Rev. D* **93** (2016) 033006, [arXiv:1506.07443](https://arxiv.org/abs/1506.07443).
- [54] W. G. Seligman *et al.*, *Phys. Rev. Lett.* **79** (1997) 1213–1216, [arXiv:hep-ex/9701017](https://arxiv.org/abs/hep-ex/9701017).
- [55] NuTeV Collaboration, M. Tzanov *et al.*, *Phys. Rev. D* **74** (2006) 012008, [arXiv:hep-ex/0509010](https://arxiv.org/abs/hep-ex/0509010).
- [56] CHORUS Collaboration, G. Onengut *et al.*, *Phys. Lett. B* **632** (2006) 65–75.
- [57] J. P. Berge *et al.*, *Z. Phys. C* **49** (1991) 187–224.
- [58] NOMAD Collaboration, O. Samoylov *et al.*, *Nucl. Phys. B* **876** (2013) 339–375, [arXiv:1308.4750](https://arxiv.org/abs/1308.4750).
- [59] ATLAS Collaboration, G. Aad *et al.*, *Phys. Rev. Lett.* **109** (2012) 012001, [arXiv:1203.4051](https://arxiv.org/abs/1203.4051).
- [60] CMS Collaboration, S. Chatrchyan *et al.*, *JHEP* **02** (2014) 013, [arXiv:1310.1138](https://arxiv.org/abs/1310.1138).
- [61] ATLAS Collaboration, G. Aad *et al.*, *JHEP* **05** (2014) 068, [arXiv:1402.6263](https://arxiv.org/abs/1402.6263).
- [62] ATLAS Collaboration, M. Aaboud *et al.*, *Eur. Phys. J. C* **77** (2017) 367, [arXiv:1612.03016](https://arxiv.org/abs/1612.03016).
- [63] S. Alekhin, J. Blümlein and S. Moch, *Phys. Lett. B* **777** (2018) 134–140, [arXiv:1708.01067](https://arxiv.org/abs/1708.01067).

- [64] A. M. Cooper-Sarkar and K. Wichmann, *Phys. Rev. D* **98** (2018) 014027, [arXiv:1803.00968](#).
- [65] H. Abdolmaleki *et al.*, [arXiv:1907.01014](#).
- [66] O. Behnke, A. Geiser and M. Lisovskyi, *Prog. Part. Nucl. Phys.* **84** (2015) 1–72, [arXiv:1506.07519](#).
- [67] O. Zenaiev, *Eur. Phys. J. C* **77** (2017) 151, [arXiv:1612.02371](#).
- [68] M. A. G. Aivazis, F. I. Olness and W.-K. Tung, *Phys. Rev. Lett.* **65** (1990) 2339.
- [69] M. A. G. Aivazis, F. I. Olness and W.-K. Tung, *Phys. Rev. D* **50** (1994) 3085, [arXiv:hep-ph/9312318](#).
- [70] M. A. G. Aivazis, J. C. Collins, F. I. Olness and W.-K. Tung, *Phys. Rev. D* **50** (1994) 3102, [arXiv:hep-ph/9312319](#).
- [71] R. S. Thorne and R. G. Roberts, *Eur. Phys. J. C* **19** (2001) 339, [arXiv:hep-ph/0010344](#).
- [72] S. Alekhin, J. Blümlein and S. Moch, *Phys. Rev. D* **86** (2012) 054009, [arXiv:1202.2281](#).
- [73] S. Alekhin, J. Blümlein and S. Moch, *Phys. Rev. D* **89** (2014) 054028, [arXiv:1310.3059](#).
- [74] S. Alekhin, J. Blümlein, S. Klein and S. Moch, *Phys. Rev. D* **81** (2010) 014032, [arXiv:0908.2766](#).
- [75] S. Forte, E. Laenen, P. Nason and J. Rojo, *Nucl. Phys. B* **834** (2010) 116, [arXiv:1001.2312](#).
- [76] A. D. Martin, W. J. Stirling, R. S. Thorne and G. Watt, *Eur. Phys. J. C* **70** (2010) 51, [arXiv:1007.2624](#).
- [77] R. D. Ball, V. Bertone, F. Cerutti, L. Del Debbio, S. Forte, A. Guffanti, J. I. Latorre, J. Rojo and M. Ubiali, *Nucl. Phys. B* **849** (2011) 296, [arXiv:1101.1300](#).
- [78] R. D. Ball, M. Bonvini and L. Rottoli, *JHEP* **11** (2015) 122, [arXiv:1510.02491](#).
- [79] S. Moch, B. Ruijl, T. Ueda, J. A. M. Vermaseren and A. Vogt, *JHEP* **10** (2017) 041, [arXiv:1707.08315](#).
- [80] F. Herzog, S. Moch, B. Ruijl, T. Ueda, J. A. M. Vermaseren and A. Vogt, *Phys. Lett. B* **790** (2019) 436–443, [arXiv:1812.11818](#).
- [81] G. Das, S.-O. Moch and A. Vogt, [arXiv:1912.12920](#).
- [82] R. D. Ball, *AIP Conf. Proc.* **1819** (2017) 030002, [arXiv:1612.03790](#).
- [83] S. J. Brodsky, P. Hoyer, C. Peterson and N. Sakai, *Phys. Lett.* **93B** (1980) 451.
- [84] S. J. Brodsky, A. Kusina, F. Lyonnet, I. Schienbein, H. Spiesberger and R. Vogt, *Adv. High Energy Phys.* **2015** (2015) 231547, [arXiv:1504.06287](#).
- [85] S. J. Brodsky and S. Gardner, *Phys. Rev. Lett.* **116** (2016) 019101, [arXiv:1504.00969](#).
- [86] G. F. de Teramond and S. J. Brodsky, *Phys. Rev. Lett.* **102** (2009) 081601, [arXiv:0809.4899](#).
- [87] SELEX Collaboration, A. Ocherashvili *et al.*, *Phys. Lett. B* **628** (2005) 18, [arXiv:hep-ex/0406033](#).
- [88] ANDY Collaboration, L. C. Bland *et al.*, [arXiv:1909.03124](#).
- [89] R. Abdul Khalek, S. Bailey, J. Gao, L. Harland-Lang and J. Rojo, *Eur. Phys. J. C* **78** (2018) 962, [arXiv:1810.03639](#).
- [90] J. Butterworth *et al.*, *J. Phys. G* **43** (2016) 023001, [arXiv:1510.03865](#).
- [91] H. Paukkunen and P. Zurita, *JHEP* **12** (2014) 100, [arXiv:1402.6623](#).
- [92] C. Schmidt, J. Pumplin, C. P. Yuan and P. Yuan, *Phys. Rev. D* **98** (2018) 094005, [arXiv:1806.07950](#).
- [93] B.-T. Wang, T. J. Hobbs, S. Doyle, J. Gao, T.-J. Hou, P. M. Nadolsky and F. I. Olness, *Phys. Rev. D* **98** (2018) 094030, [arXiv:1803.02777](#).
- [94] T. J. Hobbs, B.-T. Wang, P. M. Nadolsky and F. I. Olness, *PoS DIS2019* (2019) 247, [arXiv:1907.00988](#).
- [95] G. Zweig, “An SU(3) model for strong interaction symmetry and its breaking. Version 1,” 1964.
- [96] H. Fritzsch, M. Gell-Mann and H. Leutwyler, *Phys. Lett.* **47B** (1973) 365–368.
- [97] D. J. Gross and F. Wilczek, *Phys. Rev. Lett.* **30** (1973) 1343–1346.
- [98] H. D. Politzer, *Phys. Rev. Lett.* **30** (1973) 1346–1349.
- [99] G. Dissertori, *Adv. Ser. Direct. High Energy Phys.* **26** (2016) 113–128, [arXiv:1506.05407](#).
- [100] Particle Data Group, M. Tanabashi *et al.*, *Phys. Rev. D* **98** (2018) 030001.
- [101] D. d’Enterria *et al.*, *PoS ALPHAS2019* (2019) 001, [arXiv:1907.01435](#).
- [102] K. H. Streng, T. F. Walsh and P. M. Zerwas, *Z. Phys. C* **2** (1979) 237.
- [103] H1 Collaboration, F. D. Aaron *et al.*, *Eur. Phys. J. C* **67** (2010) 1, [arXiv:0911.5678](#).
- [104] S. D. Ellis and D. E. Soper, *Phys. Rev. D* **48** (1993) 3160–3166, [arXiv:hep-ph/9305266](#).

- [105] H1 Collaboration, C. Adloff *et al.*, *Eur. Phys. J. C*13 (2000) 397, [arXiv:hep-ex/9812024](#).
- [106] H1 Collaboration, C. Adloff *et al.*, *Eur. Phys. J. C*19 (2001) 289, [arXiv:hep-ex/0010054](#).
- [107] H1 Collaboration, C. Adloff *et al.*, *Phys. Lett. B*542 (2002) 193, [arXiv:hep-ex/0206029](#).
- [108] H1 Collaboration, A. Aktas *et al.*, *Eur. Phys. J. C*33 (2004) 477, [arXiv:hep-ex/0310019](#).
- [109] H1 Collaboration, A. Aktas *et al.*, *Eur. Phys. J. C*37 (2004) 141, [arXiv:hep-ex/0401010](#).
- [110] H1 Collaboration, A. Aktas *et al.*, *Phys. Lett. B*653 (2007) 134, [arXiv:0706.3722](#).
- [111] H1 Collaboration, F. D. Aaron *et al.*, *Eur. Phys. J. C*65 (2010) 363, [arXiv:0904.3870](#).
- [112] H1 Collaboration, V. Andreev *et al.*, *Eur. Phys. J. C*75 (2015) 65, [arXiv:1406.4709](#).
- [113] H1 Collaboration, V. Andreev *et al.*, *Eur. Phys. J. C*77 (2017) 215, [arXiv:1611.03421](#).
- [114] ZEUS Collaboration, J. Breitweg *et al.*, *Phys. Lett. B*479 (2000) 37, [arXiv:hep-ex/0002010](#).
- [115] ZEUS Collaboration, S. Chekanov *et al.*, *Eur. Phys. J. C*23 (2002) 13, [arXiv:hep-ex/0109029](#).
- [116] ZEUS Collaboration, S. Chekanov *et al.*, *Phys. Lett. B*547 (2002) 164, [arXiv:hep-ex/0208037](#).
- [117] ZEUS Collaboration, S. Chekanov *et al.*, *Eur. Phys. J. C*35 (2004) 487, [arXiv:hep-ex/0404033](#).
- [118] ZEUS Collaboration, S. Chekanov *et al.*, *Nucl. Phys. B*765 (2007) 1, [arXiv:hep-ex/0608048](#).
- [119] ZEUS Collaboration, S. Chekanov *et al.*, *Phys. Lett. B*649 (2007) 12, [arXiv:hep-ex/0701039](#).
- [120] ZEUS Collaboration, H. Abramowicz *et al.*, *Eur. Phys. J. C*70 (2010) 965, [arXiv:1010.6167](#).
- [121] ZEUS Collaboration, H. Abramowicz *et al.*, *Phys. Lett. B*691 (2010) 127, [arXiv:1003.2923](#).
- [122] CMS Collaboration, V. Khachatryan *et al.*, *JHEP* 03 (2017) 156, [arXiv:1609.05331](#).
- [123] K. Rabbertz, *Springer Tracts Mod. Phys.* 268 (2017) 1.
- [124] ATLAS Collaboration, M. Aaboud *et al.*, *JHEP* 09 (2017) 020, [arXiv:1706.03192](#).
- [125] ATLAS Collaboration, M. Aaboud *et al.*, *JHEP* 05 (2018) 195, [arXiv:1711.02692](#).
- [126] J. Currie, T. Gehrmann and J. Niehues, *Phys. Rev. Lett.* 117 (2016) 042001, [arXiv:1606.03991](#).
- [127] J. Currie, T. Gehrmann, A. Huss and J. Niehues, *JHEP* 07 (2017) 018, [arXiv:1703.05977](#).
- [128] T. Gehrmann *et al.*, *PoS RADCOR2017* (2018) 074, [arXiv:1801.06415](#).
- [129] T. Kluge, K. Rabbertz and M. Wobisch, “FastNLO: Fast pQCD calculations for PDF fits,” in *Proceedings, 14th International Workshop of deep inelastic scattering (DIS 2006), Tsukuba, Japan, April 20-24, 2006*, 2006. [arXiv:hep-ph/0609285](#).
- [130] D. Britzger, K. Rabbertz, F. Stober and M. Wobisch, “New features in version 2 of the fastNLO project,” in *Proceedings, 20th International Workshop on Deep-Inelastic Scattering and Related Subjects (DIS 2012): Bonn, Germany, March 26-30, 2012*, 2012. [arXiv:1208.3641](#).
- [131] D. Britzger *et al.*, *Eur. Phys. J. C*79 (2019) 845, [arXiv:1906.05303](#).
- [132] H1 Collaboration, V. Andreev *et al.*, *Eur. Phys. J. C*77 (2017) 791, [arXiv:1709.07251](#).
- [133] R. Kogler, *Measurement of jet production in deep-inelastic e p scattering at HERA*. PhD thesis, Hamburg U., 2011.
- [134] CMS Collaboration, V. Khachatryan *et al.*, *JINST* 12 (2017) P02014, [arXiv:1607.03663](#).
- [135] ATLAS Collaboration, M. Aaboud *et al.*, “Determination of jet calibration and energy resolution in proton-proton collisions at  $\sqrt{s} = 8$  TeV using the ATLAS detector,” 2019. [arXiv:1910.04482](#).
- [136] J. R. Ellis, E. Gardi, M. Karliner and M. A. Samuel, *Phys. Lett. B*366 (1996) 268, [arXiv:hep-ph/9509312](#).
- [137] S. J. Brodsky and X.-G. Wu, *Phys. Rev. D*85 (2012) 034038, [arXiv:1111.6175](#). [Erratum: *Phys. Rev. D*86,079903(2012)].
- [138] S. J. Brodsky and X.-G. Wu, *Phys. Rev. Lett.* 109 (2012) 042002, [arXiv:1203.5312](#).
- [139] S. J. Brodsky and L. Di Giustino, *Phys. Rev. D*86 (2012) 085026, [arXiv:1107.0338](#).
- [140] M. Mojaza, S. J. Brodsky and X.-G. Wu, *Phys. Rev. Lett.* 110 (2013) 192001, [arXiv:1212.0049](#).
- [141] S. J. Brodsky, M. Mojaza and X.-G. Wu, *Phys. Rev. D*89 (2014) 014027, [arXiv:1304.4631](#).
- [142] S.-Q. Wang, S. J. Brodsky, X.-G. Wu, J.-M. Shen and L. Di Giustino, *Phys. Rev. D*100 (2019) 094010, [arXiv:1908.00060](#).
- [143] Particle Data Group, M. Tanabashi *et al.*, “2019 Update of the Review of Particle Physics,”. <http://pdg.lbl.gov/2019/>. unpublished.

- [144] Flavour Lattice Averaging Group, S. Aoki *et al.*, [arXiv:1902.08191](#).
- [145] D. Boito, M. Golterman, K. Maltman, J. Osborne and S. Peris, *Phys. Rev. D* **91** (2015) 034003, [arXiv:1410.3528](#).
- [146] Gfitter Group, M. Baak, J. Cúth, J. Haller, A. Hoecker, R. Kogler, K. Mönig, M. Schott and J. Stelzer, *Eur. Phys. J. C* **74** (2014) 3046, [arXiv:1407.3792](#).
- [147] P. Azzi *et al.*, *CERN Yellow Rep. Monogr.* **7** (2019) 1–220, [arXiv:1902.04070](#).
- [148] I. Abt, A. M. Cooper-Sarkar, B. Foster, V. Myronenko, K. Wichmann and M. Wing, *Phys. Rev. D* **96** (2017) 014001, [arXiv:1704.03187](#). [*Phys. Rev. D* **96**, 014001(2017)].
- [149] M. Dasgupta and G. P. Salam, *J. Phys. G* **30** (2004) R143, [arXiv:hep-ph/0312283](#).
- [150] H1 Collaboration, A. Aktas *et al.*, *Eur. Phys. J. C* **46** (2006) 343–356, [arXiv:hep-ex/0512014](#).
- [151] ZEUS Collaboration, S. Chekanov *et al.*, *Nucl. Phys. B* **767** (2007) 1–28, [arXiv:hep-ex/0604032](#).
- [152] D. Kang, C. Lee and I. W. Stewart, *Phys. Rev. D* **88** (2013) 054004, [arXiv:1303.6952](#).
- [153] Z.-B. Kang, X. Liu and S. Mantry, *Phys. Rev. D* **90** (2014) 014041, [arXiv:1312.0301](#).
- [154] D. Kang, C. Lee and I. W. Stewart, *PoS DIS2015* (2015) 142.
- [155] G. Abelof, R. Boughezal, X. Liu and F. Petriello, *Phys. Lett. B* **763** (2016) 52–59, [arXiv:1607.04921](#).
- [156] S. Höche, S. Kuttimalai and Y. Li, *Phys. Rev. D* **98** (2018) 114013, [arXiv:1809.04192](#).
- [157] J. Currie, T. Gehrmann, E. W. N. Glover, A. Huss, J. Niehues and A. Vogt, *JHEP* **05** (2018) 209, [arXiv:1803.09973](#).
- [158] T. Gehrmann, A. Huss, J. Mo and J. Niehues, [arXiv:1909.02760](#).
- [159] H1 Collaboration, C. Adloff *et al.*, *Eur. Phys. J. C* **29** (2003) 497–513, [arXiv:hep-ex/0302034](#).
- [160] H1 Collaboration, A. Aktas *et al.*, *Phys. Lett. B* **639** (2006) 21–31, [arXiv:hep-ex/0603014](#).
- [161] ZEUS Collaboration, S. Chekanov *et al.*, *Phys. Rev. D* **76** (2007) 072011, [arXiv:0706.3809](#).
- [162] ZEUS Collaboration, H. Abramowicz *et al.*, *Nucl. Phys. B* **864** (2012) 1–37, [arXiv:1205.6153](#).
- [163] M. Klasen, *Rev. Mod. Phys.* **74** (2002) 1221–1282, [arXiv:hep-ph/0206169](#).
- [164] M. Glück, E. Reya and A. Vogt, *Phys. Rev. D* **46** (1992) 1973–1979.
- [165] K. Sasaki, T. Ueda and T. Uematsu, *CERN Proc.* **1** (2018) 7.
- [166] H1 and ZEUS Collaborations, H. Abramowicz *et al.*, *JHEP* **09** (2015) 149, [arXiv:1503.06042](#).
- [167] H1 and ZEUS Collaborations, H. Abramowicz *et al.*, *Eur. Phys. J. C* **78** (2018) 473, [arXiv:1804.01019](#).
- [168] A. J. Larkoski, I. Moulton and B. Nachman, [arXiv:1709.04464](#).
- [169] J. R. Andersen *et al.*, “Les Houches 2017: Physics at TeV Colliders Standard Model Working Group Report,” 2018. [arXiv:1803.07977](#).
- [170] F. Ringer, *PoS ALPHAS2019* (2019) 010.
- [171] I. I. Balitsky and L. N. Lipatov, *Sov. J. Nucl. Phys.* **28** (1978) 822. [*Yad. Fiz.* **28**, 1597(1978)].
- [172] E. A. Kuraev, L. N. Lipatov and V. S. Fadin, *Sov. Phys. JETP* **45** (1977) 199. [*Zh. Eksp. Teor. Fiz.* **72**, 377(1977)].
- [173] L. N. Lipatov, *Sov. Phys. JETP* **63** (1986) 904. [*Zh. Eksp. Teor. Fiz.* **90**, 1536(1986)].
- [174] V. S. Fadin and L. N. Lipatov, *Phys. Lett. B* **429** (1998) 127, [arXiv:hep-ph/9802290](#).
- [175] M. Ciafaloni and G. Camici, *Phys. Lett. B* **430** (1998) 349, [arXiv:hep-ph/9803389](#).
- [176] J. Blümlein and A. Vogt, *Phys. Rev. D* **58** (1998) 014020, [arXiv:hep-ph/9712546](#).
- [177] D. A. Ross, *Phys. Lett. B* **431** (1998) 161, [arXiv:hep-ph/9804332](#).
- [178] Y. V. Kovchegov and A. H. Müller, *Phys. Lett. B* **439** (1998) 428, [arXiv:hep-ph/9805208](#).
- [179] E. Levin, *Nucl. Phys. B* **545** (1999) 481, [arXiv:hep-ph/9806228](#).
- [180] N. Armesto, J. Bartels and M. A. Braun, *Phys. Lett. B* **442** (1998) 459, [arXiv:hep-ph/9808340](#).
- [181] M. Ciafaloni, *Nucl. Phys. B* **296** (1988) 49.
- [182] B. Andersson, G. Gustafson and J. Samuelsson, *Nucl. Phys. B* **467** (1996) 443.
- [183] J. Kwiecinski, A. D. Martin and P. J. Sutton, *Z. Phys. C* **71** (1996) 585, [arXiv:hep-ph/9602320](#).
- [184] J. Kwiecinski, A. D. Martin and A. M. Stasto, *Phys. Rev. D* **56** (1997) 3991, [arXiv:hep-ph/9703445](#).

- [185] G. P. Salam, *JHEP* 07 (1998) 019, [arXiv:hep-ph/9806482](#).
- [186] M. Ciafaloni, D. Colferai and G. P. Salam, *JHEP* 10 (1999) 017, [arXiv:hep-ph/9907409](#).
- [187] M. Ciafaloni, D. Colferai and G. P. Salam, *Phys. Rev. D* 60 (1999) 114036, [arXiv:hep-ph/9905566](#).
- [188] M. Ciafaloni, D. Colferai, D. Colferai, G. P. Salam and A. M. Stasto, *Phys. Lett. B* 576 (2003) 143, [arXiv:hep-ph/0305254](#).
- [189] M. Ciafaloni, D. Colferai, G. P. Salam and A. M. Stasto, *Phys. Lett. B* 587 (2004) 87, [arXiv:hep-ph/0311325](#).
- [190] M. Ciafaloni, D. Colferai, G. P. Salam and A. M. Stasto, *Phys. Rev. D* 68 (2003) 114003, [arXiv:hep-ph/0307188](#).
- [191] M. Ciafaloni, D. Colferai, G. P. Salam and A. M. Stasto, *JHEP* 08 (2007) 046, [arXiv:0707.1453](#).
- [192] G. Altarelli, R. D. Ball and S. Forte, *Nucl. Phys. B* 575 (2000) 313, [arXiv:hep-ph/9911273](#).
- [193] G. Altarelli, R. D. Ball and S. Forte, *Nucl. Phys. B* 599 (2001) 383, [arXiv:hep-ph/0011270](#).
- [194] G. Altarelli, R. D. Ball and S. Forte, *Nucl. Phys. B* 621 (2002) 359, [arXiv:hep-ph/0109178](#).
- [195] G. Altarelli, R. D. Ball and S. Forte, *Nucl. Phys. B* 674 (2003) 459, [arXiv:hep-ph/0306156](#).
- [196] G. Altarelli, R. D. Ball and S. Forte, *Nucl. Phys. B* 799 (2008) 199, [arXiv:0802.0032](#).
- [197] R. S. Thorne, *Phys. Rev. D* 64 (2001) 074005, [arXiv:hep-ph/0103210](#).
- [198] A. Sabio Vera, *Nucl. Phys. B* 722 (2005) 65, [arXiv:hep-ph/0505128](#).
- [199] M. Bonvini, S. Marzani and T. Peraro, *Eur. Phys. J. C* 76 (2016) 597, [arXiv:1607.02153](#).
- [200] V. Bertone, S. Carrazza and J. Rojo, *Comput. Phys. Commun.* 185 (2014) 1647, [arXiv:1310.1394](#).
- [201] M. Bonvini, S. Marzani and C. Muselli, *JHEP* 12 (2017) 117, [arXiv:1708.07510](#).
- [202] R. Gandhi, C. Quigg, M. H. Reno and I. Sarcevic, *Phys. Rev. D* 58 (1998) 093009, [arXiv:hep-ph/9807264](#).
- [203] IceCube Collaboration, M. G. Aartsen *et al.*, *JINST* 12 (2017) P03012, [arXiv:1612.05093](#).
- [204] J. Kwiecinski, A. D. Martin and A. M. Stasto, *Phys. Rev. D* 59 (1999) 093002, [arXiv:astro-ph/9812262](#).
- [205] IceCube Collaboration, M. G. Aartsen *et al.*, *Nature* 551 (2017) 596, [arXiv:1711.08119](#).
- [206] T. K. Gaisser, *Cosmic rays and particle physics*. 1990. <http://www.cambridge.org/uk/catalogue/catalogue.asp?isbn=0521326672>.
- [207] IceCube Collaboration, M. G. Aartsen *et al.*, *Phys. Rev. Lett.* 113 (2014) 101101, [arXiv:1405.5303](#).
- [208] G. Gelmini, P. Gondolo and G. Varieschi, *Phys. Rev. D* 61 (2000) 056011, [arXiv:hep-ph/9905377](#).
- [209] A. Bhattacharya, R. Enberg, Y. S. Jeong, C. S. Kim, M. H. Reno, I. Sarcevic and A. Stasto, *JHEP* 11 (2016) 167, [arXiv:1607.00193](#).
- [210] L. N. Hand, D. G. Miller and R. Wilson, *Rev. Mod. Phys.* 35 (1963) 335.
- [211] G. Miller *et al.*, *Phys. Rev. D* 5 (1972) 528.
- [212] E. M. Riordan, A. Bodek, M. Breidenbach, D. L. Dubin, J. E. Elias, J. I. Friedman, H. W. Kendall, J. S. Poucher, M. R. Sogard and D. H. Coward, *Phys. Rev. Lett.* 33 (1974) 561.
- [213] M. Klein, “Future Deep Inelastic Scattering with the LHeC,” in *From My Vast Repertoire ...: Guido Altarelli’s Legacy*, A. Levy, S. Forte and G. Ridolfi (eds.), p. 303. 2019. [arXiv:1802.04317](#).
- [214] H1 Collaboration, F. D. Aaron *et al.*, *Eur. Phys. J. C* 71 (2011) 1579, [arXiv:1012.4355](#).
- [215] G. Altarelli and G. Martinelli, *Phys. Lett.* 76B (1978) 89.
- [216] M. Glück, E. Hoffmann and E. Reya, *Z. Phys.* C13 (1982) 119.
- [217] C. Ewerz and O. Nachtmann, *Annals Phys.* 322 (2007) 1670, [arXiv:hep-ph/0604087](#).
- [218] H. Abdolmaleki *et al.*, *Eur. Phys. J. C* 78 (2018) 621, [arXiv:1802.00064](#).
- [219] H1 Collaboration, V. Andreev *et al.*, *Eur. Phys. J. C* 74 (2014) 2814, [arXiv:1312.4821](#).
- [220] ATLAS Collaboration, G. Aad *et al.*, *Phys. Rev. D* 85 (2012) 072004, [arXiv:1109.5141](#).
- [221] G. Altarelli, *Nuovo Cim.* C035N1 (2012) 1, [arXiv:1106.3189](#).
- [222] J. Blümlein and M. Klein, *Nucl. Instrum. Meth.* A329 (1993) 112.
- [223] S. Bentvelsen, J. Engelen and P. Kooijman, “Reconstruction of  $(x, Q^{*2})$  and extraction of structure functions in neutral current scattering at HERA,” in *Workshop on Physics at HERA Hamburg, Germany, October 29-30, 1991*, 1992.

- [224] U. Bassler and G. Bernardi, *Nucl. Instrum. Meth.* A426 (1999) 583, [arXiv:hep-ex/9801017](#).
- [225] A. H. Müller, *Nucl. Phys.* B335 (1990) 115.
- [226] R. D. Ball, V. Bertone, M. Bonvini, S. Marzani, J. Rojo and L. Rottoli, *Eur. Phys. J.* C78 (2018) 321, [arXiv:1710.05935](#).
- [227] S. Carrazza, S. Forte, Z. Kassabov, J. I. Latorre and J. Rojo, *Eur. Phys. J.* C75 (2015) 369, [arXiv:1505.06736](#).
- [228] J. Rojo and F. Caola, “Parton distributions and small-x QCD at the Large Hadron Electron Collider,” in *17th International Workshop on Deep-Inelastic Scattering and Related Subjects (DIS 2009): Madrid, Spain, April 26-30, 2009*, Berlin, Germany, 2009. [arXiv:0906.2079](#).
- [229] J. Bartels, K. J. Golec-Biernat and H. Kowalski, *Phys. Rev.* D66 (2002) 014001, [arXiv:hep-ph/0203258](#).
- [230] K. J. Golec-Biernat and S. Sapeta, *Phys. Rev.* D74 (2006) 054032, [arXiv:hep-ph/0607276](#).
- [231] K. Golec-Biernat and S. Sapeta, *JHEP* 03 (2018) 102, [arXiv:1711.11360](#).
- [232] J. Gao, L. Harland-Lang and J. Rojo, *Phys. Rept.* 742 (2018) 1, [arXiv:1709.04922](#).
- [233] V. Bertone, R. Gauld and J. Rojo, *JHEP* 01 (2019) 217, [arXiv:1808.02034](#).
- [234] A. Accardi *et al.*, *Eur. Phys. J.* A52 (2016) 268, [arXiv:1212.1701](#).
- [235] A. V. Belitsky, X.-d. Ji and F. Yuan, *Phys. Rev.* D69 (2004) 074014, [arXiv:hep-ph/0307383](#).
- [236] N. N. Nikolaev and B. G. Zakharov, *Z. Phys.* C49 (1991) 607.
- [237] N. Nikolaev and B. G. Zakharov, *Z. Phys.* C53 (1992) 331.
- [238] N. N. Nikolaev and B. G. Zakharov, *J. Exp. Theor. Phys.* 78 (1994) 598. [Zh. Eksp. Teor. Fiz.105,1117(1994)].
- [239] N. N. Nikolaev, B. G. Zakharov and V. R. Zoller, *Z. Phys.* A351 (1995) 435.
- [240] A. H. Müller, *Nucl. Phys.* B415 (1994) 373.
- [241] A. H. Müller and B. Patel, *Nucl. Phys.* B425 (1994) 471, [arXiv:hep-ph/9403256](#).
- [242] U. Amaldi and K. R. Schubert, *Nucl. Phys.* B166 (1980) 301.
- [243] S. Munier, A. M. Stasto and A. H. Müller, *Nucl. Phys.* B603 (2001) 427, [arXiv:hep-ph/0102291](#).
- [244] N. Armesto and A. H. Rezaeian, *Phys. Rev.* D90 (2014) 054003, [arXiv:1402.4831](#).
- [245] H. Kowalski and D. Teaney, *Phys. Rev.* D68 (2003) 114005, [arXiv:hep-ph/0304189](#).
- [246] H. Kowalski, L. Motyka and G. Watt, *Phys. Rev.* D74 (2006) 074016, [arXiv:hep-ph/0606272](#).
- [247] G. Watt and H. Kowalski, *Phys. Rev.* D78 (2008) 014016, [arXiv:0712.2670](#).
- [248] Y. Hatta, B.-W. Xiao and F. Yuan, *Phys. Rev. Lett.* 116 (2016) 202301, [arXiv:1601.01585](#).
- [249] T. Altinoluk, N. Armesto, G. Beuf and A. H. Rezaeian, *Phys. Lett.* B758 (2016) 373, [arXiv:1511.07452](#).
- [250] H. Mantysaari, N. Muller and B. Schenke, *Phys. Rev.* D99 (2019) 074004, [arXiv:1902.05087](#).
- [251] F. Salazar and B. Schenke, *Phys. Rev.* D100 (2019) 034007, [arXiv:1905.03763](#).
- [252] H. Mäntysaari and B. Schenke, *Phys. Rev. Lett.* 117 (2016) 052301, [arXiv:1603.04349](#).
- [253] H. Mäntysaari and B. Schenke, *Phys. Rev.* D94 (2016) 034042, [arXiv:1607.01711](#).
- [254] H. Mäntysaari and B. Schenke, *Phys. Lett.* B772 (2017) 832, [arXiv:1703.09256](#).
- [255] H. Mäntysaari and B. Schenke, *Phys. Rev.* D98 (2018) 034013, [arXiv:1806.06783](#).
- [256] J. Cepila, J. G. Contreras and J. D. Tapia Takaki, *Phys. Lett.* B766 (2017) 186, [arXiv:1608.07559](#).
- [257] D. Bendova, J. Cepila and J. G. Contreras, *Phys. Rev.* D99 (2019) 034025, [arXiv:1811.06479](#).
- [258] M. Krelina, V. P. Goncalves and J. Cepila, *Nucl. Phys.* A989 (2019) 187, [arXiv:1905.06759](#).
- [259] H1 Collaboration, C. Adloff *et al.*, *Z. Phys.* C76 (1997) 613, [arXiv:hep-ex/9708016](#).
- [260] ZEUS Collaboration, J. Breitweg *et al.*, *Eur. Phys. J.* C1 (1998) 81, [arXiv:hep-ex/9709021](#).
- [261] P. Newman and M. Wing, *Rev. Mod. Phys.* 86 (2014) 1037, [arXiv:1308.3368](#).
- [262] V. N. Gribov, *Sov. Phys. JETP* 29 (1969) 483. [Zh. Eksp. Teor. Fiz.56,892(1969)].
- [263] J. C. Collins, *Phys. Rev.* D57 (1998) 3051, [arXiv:hep-ph/9709499](#). [Erratum: Phys. Rev.D61,019902(2000)].
- [264] A. Berera and D. E. Soper, *Phys. Rev.* D53 (1996) 6162, [arXiv:hep-ph/9509239](#).

- [265] L. Trentadue and G. Veneziano, *Phys. Lett.* B323 (1994) 201.
- [266] N. Armesto, P. R. Newman, W. Slominski and A. M. Stasto, *Phys. Rev.* D100 (2019) 074022, [arXiv:1901.09076](#).
- [267] H. Khanpour, *Phys. Rev.* D99 (2019) 054007, [arXiv:1902.10734](#).
- [268] H1 Collaboration Collaboration, A. Aktas *et al.*, *Eur.Phys.J.* C48 (2006) 715, [arXiv:hep-ex/0606004](#).
- [269] ZEUS Collaboration Collaboration, S. Chekanov *et al.*, *Nucl.Phys.* B816 (2009) 1, [arXiv:0812.2003](#).
- [270] H1 Collaboration Collaboration, F. Aaron *et al.*, *Eur.Phys.J.* C72 (2012) 2074, [arXiv:1203.4495](#).
- [271] H1 and ZEUS Collaborations, F. D. Aaron *et al.*, *Eur. Phys. J.* C72 (2012) 2175, [arXiv:1207.4864](#).
- [272] ZEUS Collaboration, S. Chekanov *et al.*, *Nucl. Phys.* B713 (2005) 3, [arXiv:hep-ex/0501060](#).
- [273] H1 Collaboration, A. Aktas *et al.*, *Eur. Phys. J.* C48 (2006) 749, [arXiv:hep-ex/0606003](#).
- [274] ZEUS Collaboration Collaboration, S. Chekanov *et al.*, *Nucl.Phys.* B831 (2010) 1, [arXiv:0911.4119](#).
- [275] H1 Collaboration, F. Aaron *et al.*, *Eur.Phys.J.* C71 (2011) 1578, [arXiv:1010.1476](#).
- [276] V. N. Gribov and L. N. Lipatov, *Sov. J. Nucl. Phys.* 15 (1972) 675. [*Yad. Fiz.*15,1218(1972)].
- [277] V. N. Gribov and L. N. Lipatov, *Sov. J. Nucl. Phys.* 15 (1972) 438. [*Yad. Fiz.*15,781(1972)].
- [278] G. Altarelli and G. Parisi, *Nucl. Phys.* B126 (1977) 298.
- [279] Y. L. Dokshitzer, *Sov. Phys. JETP* 46 (1977) 641. [*Zh. Eksp. Teor. Fiz.*73,1216(1977)].
- [280] J. C. Collins and W.-K. Tung, *Nucl. Phys.* B278 (1986) 934.
- [281] R. S. Thorne and W. K. Tung, [arXiv:0809.0714](#).
- [282] J. F. Owens, *Phys. Rev.* D30 (1984) 943.
- [283] M. Glück, E. Reya and A. Vogt, *Z. Phys.* C53 (1992) 651.
- [284] R. S. Thorne and R. G. Roberts, *Phys. Rev.* D57 (1998) 6871, [arXiv:hep-ph/9709442](#).
- [285] ATLAS Collaboration, G. Aad *et al.*, *Phys. Lett.* B754 (2016) 214–234, [arXiv:1511.00502](#).
- [286] D. Britzger, J. Currie, T. Gehrmann, A. Huss, J. Niehues and R. Žlebčík, *Eur. Phys. J.* C78 (2018) 538, [arXiv:1804.05663](#).
- [287] Z. Nagy, *Phys. Rev.* D68 (2003) 094002, [arXiv:hep-ph/0307268](#).
- [288] S. J. Brodsky, G. F. de Teramond, H. G. Dosch and J. Erlich, *Phys. Rept.* 584 (2015) 1, [arXiv:1407.8131](#).
- [289] G. F. de Teramond, H. G. Dosch and S. J. Brodsky, *Phys. Rev.* D87 (2013) 075005, [arXiv:1301.1651](#).
- [290] V. de Alfaro, S. Fubini and G. Furlan, *Nuovo Cim.* A34 (1976) 569.
- [291] G. Veneziano, *Nuovo Cim.* A57 (1968) 190.
- [292] A. Deur, S. J. Brodsky and G. F. de Teramond, *Prog. Part. Nucl. Phys.* 90 (2016) 1, [arXiv:1604.08082](#).
- [293] G. Grunberg, *Phys. Lett.* 95B (1980) 70. [Erratum: *Phys. Lett.*110B,501(1982)].
- [294] J. D. Bjorken, *Phys. Rev.* 148 (1966) 1467.
- [295] A. Deur *et al.*, *Phys. Rev. Lett.* 93 (2004) 212001, [arXiv:hep-ex/0407007](#).
- [296] A. Deur, Y. Prok, V. Burkert, D. Crabb, F. X. Girod, K. A. Griffioen, N. Guler, S. E. Kuhn and N. Kvaltine, *Phys. Rev.* D90 (2014) 012009, [arXiv:1405.7854](#).
- [297] A. Deur *et al.*, *Phys. Rev.* D78 (2008) 032001, [arXiv:0802.3198](#).
- [298] S. J. Brodsky and H. J. Lu, *Phys. Rev.* D51 (1995) 3652, [arXiv:hep-ph/9405218](#).
- [299] S. J. Brodsky, G. F. de Teramond and A. Deur, *Phys. Rev.* D81 (2010) 096010, [arXiv:1002.3948](#).
- [300] A. Deur, S. J. Brodsky and G. F. de Teramond, *Phys. Lett.* B750 (2015) 528, [arXiv:1409.5488](#).
- [301] S. J. Brodsky, G. F. de Teramond, A. Deur and H. G. Dosch, *Few Body Syst.* 56 (2015) 621, [arXiv:1410.0425](#).
- [302] A. Deur, V. Burkert, J.-P. Chen and W. Korsch, *Phys. Lett.* B650 (2007) 244, [arXiv:hep-ph/0509113](#).
- [303] A. Deur, V. Burkert, J. P. Chen and W. Korsch, *Phys. Lett.* B665 (2008) 349, [arXiv:0803.4119](#).
- [304] S. J. Brodsky, *J. Phys. Conf. Ser.* 1137 (2019) 012027.
- [305] G. P. Lepage and S. J. Brodsky, *Phys. Lett.* 87B (1979) 359.
- [306] A. V. Efremov and A. V. Radyushkin, *Phys. Lett.* 94B (1980) 245.
- [307] S. J. Brodsky, G. F. De Teramond and H. G. Dosch, *Phys. Lett.* B729 (2014) 3, [arXiv:1302.4105](#).

- [308] S. J. Brodsky, *Few Body Syst.* 57 (2016) 703, [arXiv:1601.06328](#).
- [309] R. S. Sufian, G. F. de Téramond, S. J. Brodsky, A. Deur and H. G. Dosch, *Phys. Rev. D* 95 (2017) 014011, [arXiv:1609.06688](#).
- [310] HLFHS Collaboration, G. F. de Téramond, T. Liu, R. S. Sufian, H. G. Dosch, S. J. Brodsky and A. Deur, *Phys. Rev. Lett.* 120 (2018) 182001, [arXiv:1801.09154](#).
- [311] T. Gutsche, V. E. Lyubovitskij, I. Schmidt and A. Vega, *Phys. Rev. D* 91 (2015) 114001, [arXiv:1501.02738](#).
- [312] T. Gutsche, V. E. Lyubovitskij and I. Schmidt, *Phys. Rev. D* 94 (2016) 116006, [arXiv:1607.04124](#).
- [313] H. G. Dosch, G. F. de Téramond and S. J. Brodsky, *Phys. Rev. D* 91 (2015) 085016, [arXiv:1501.00959](#).
- [314] S. J. Brodsky, G. F. de Téramond, H. G. Dosch and C. Lorcé, *Int. J. Mod. Phys. A* 31 (2016) 1630029, [arXiv:1606.04638](#).
- [315] M. Nielsen, S. J. Brodsky, G. F. de Téramond, H. G. Dosch, F. S. Navarra and L. Zou, *Phys. Rev. D* 98 (2018) 034002, [arXiv:1805.11567](#).
- [316] G. F. de Téramond, H. G. Dosch and S. J. Brodsky, *Phys. Rev. D* 91 (2015) 045040, [arXiv:1411.5243](#).
- [317] S. L. Glashow, *Nucl. Phys.* 22 (1961) 579.
- [318] S. Weinberg, *Phys. Rev. Lett.* 27 (1971) 1688.
- [319] S. Weinberg, *Phys. Rev. D* 5 (1972) 1412.
- [320] A. Salam and J. C. Ward, *Phys. Lett.* 13 (1964) 168.
- [321] P. W. Higgs, *Phys. Lett.* 12 (1964) 132.
- [322] P. W. Higgs, *Phys. Rev. Lett.* 13 (1964) 508.
- [323] F. Englert and R. Brout, *Phys. Rev. Lett.* 13 (1964) 321.
- [324] H1 Collaboration, A. Aktas *et al.*, *Phys. Lett.* B632 (2006) 35, [arXiv:hep-ex/0507080](#).
- [325] ZEUS Collaboration, H. Abramowicz *et al.*, *Phys. Rev. D* 93 (2016) 092002, [arXiv:1603.09628](#).
- [326] H1 Collaboration, V. Andreev *et al.*, *Eur. Phys. J. C* 78 (2018) 777, [arXiv:1806.01176](#).
- [327] M. Klein and T. Riemann, *Z. Phys.* C24 (1984) 151.
- [328] M. Böhm and H. Spiesberger, *Nucl. Phys.* B294 (1987) 1081.
- [329] D. Yu. Bardin, C. Burdik, P. C. Khristova and T. Riemann, *Z. Phys.* C42 (1989) 679.
- [330] W. Hollik, D. Yu. Bardin, J. Blümlein, B. A. Kniehl, T. Riemann and H. Spiesberger, “Electroweak parameters at HERA: Theoretical aspects,” in *Workshop on physics at HERA Hamburg, Germany, October 29-30, 1991*, 1992.
- [331] M. Böhm and H. Spiesberger, *Nucl. Phys.* B304 (1988) 749.
- [332] D. Yu. Bardin, K. C. Burdik, P. K. Khristova and T. Riemann, *Z. Phys.* C44 (1989) 149.
- [333] A. Sirlin, *Phys. Rev. D* 22 (1980) 971.
- [334] M. Böhm, H. Spiesberger and W. Hollik, *Fortsch. Phys.* 34 (1986) 687.
- [335] W. F. L. Hollik, *Fortsch. Phys.* 38 (1990) 165.
- [336] H1 Collaboration, F. D. Aaron *et al.*, *JHEP* 09 (2012) 061, [arXiv:1206.7007](#).
- [337] D. Britzger and M. Klein, *PoS DIS2017* (2018) 105.
- [338] H. Spiesberger, “EPRC: A program package for electroweak physics at HERA,” in *Future physics at HERA. Proceedings, Workshop, Hamburg, Germany, September 25, 1995-May 31, 1996. Vol. 1, 2*, 1995.
- [339] G. Cowan, K. Cranmer, E. Gross and O. Vitells, *Eur. Phys. J. C* 71 (2011) 1554, [arXiv:1007.1727](#).  
[Erratum: *Eur. Phys. J. C* 73 (2013) 2501].
- [340] CDF and D0 Collaborations, [arXiv:1204.0042](#).
- [341] ALEPH, DELPHI, L3, OPAL, LEP Electroweak Collaboration, S. Schael *et al.*, *Phys. Rept.* 532 (2013) 119, [arXiv:1302.3415](#).
- [342] ATLAS Collaboration, M. Aaboud *et al.*, *Eur. Phys. J. C* 78 (2018) 110, [arXiv:1701.07240](#). [Erratum: *Eur. Phys. J. C* 78, no.11, 898 (2018)].
- [343] J. de Blas, M. Ciuchini, E. Franco, S. Mishima, M. Pierini, L. Reina and L. Silvestrini, *JHEP* 12 (2016) 135, [arXiv:1608.01509](#).

- [344] J. Haller, A. Hoecker, R. Kogler, K. Mönig, T. Peiffer and J. Stelzer, *Eur. Phys. J. C* **78** (2018) 675, [arXiv:1803.01853](#).
- [345] MuLan Collaboration, V. Tishchenko *et al.*, *Phys. Rev. D* **87** (2013) 052003, [arXiv:1211.0960](#).
- [346] M. Schott, “Global EW fits: experimental and theoretical issues,” Talk presented at the Ultimate Precision at Hadron Colliders, Sarclay, France, 2019.
- [347] ALEPH, DELPHI, L3, OPAL, SLD Collaborations, LEP Electroweak Working Group, SLD Electroweak Heavy Flavour Groups, S. Schael *et al.*, *Phys. Rept.* **427** (2006) 257, [arXiv:hep-ex/0509008](#).
- [348] D0 Collaboration, V. M. Abazov *et al.*, *Phys. Rev. D* **84** (2011) 012007, [arXiv:1104.4590](#).
- [349] CDF and D0 Collaborations, T. A. Aaltonen *et al.*, *Phys. Rev. D* **97** (2018) 112007, [arXiv:1801.06283](#).
- [350] LHCb Collaboration, R. Aaij *et al.*, *JHEP* **11** (2015) 190, [arXiv:1509.07645](#).
- [351] ATLAS Collaboration, T. A. collaboration, .
- [352] CMS Collaboration, A. M. Sirunyan *et al.*, *Eur. Phys. J. C* **78** (2018) 701, [arXiv:1806.00863](#).
- [353] J. Erler, “Global fits of the SM parameters,” in *7th Large Hadron Collider Physics Conference (LHCP 2019) Puebla, Puebla, Mexico, May 20-25, 2019*, 2019. [arXiv:1908.07327](#).
- [354] J. Erler and M. Schott, *Prog. Part. Nucl. Phys.* **106** (2019) 68, [arXiv:1902.05142](#).
- [355] ZEUS Collaboration, S. Chekanov *et al.*, *Phys. Lett. B* **672** (2009) 106, [arXiv:0807.0589](#).
- [356] H1 Collaboration, F. D. Aaron *et al.*, *Eur. Phys. J. C* **64** (2009) 251, [arXiv:0901.0488](#).
- [357] H1 and ZEUS Collaborations, F. D. Aaron *et al.*, *JHEP* **03** (2010) 035, [arXiv:0911.0858](#).
- [358] U. Baur and D. Zeppenfeld, *Nucl. Phys. B* **325** (1989) 253.
- [359] U. Baur, B. A. Kniehl, J. A. M. Vermaseren and D. Zeppenfeld, “Single W and Z production at LEP / LHC,” in *ECFA Large Hadron Collider Workshop, Aachen, Germany, 4-9 Oct 1990: Proceedings.2.*, 1990.
- [360] U. Baur, J. A. M. Vermaseren and D. Zeppenfeld, *Nucl. Phys. B* **375** (1992) 3.
- [361] J. Alwall, R. Frederix, S. Frixione, V. Hirschi, F. Maltoni, O. Mattelaer, H. S. Shao, T. Stelzer, P. Torrielli and M. Zaro, *JHEP* **07** (2014) 079, [arXiv:1405.0301](#).
- [362] NNPDF Collaboration, R. D. Ball, V. Bertone, S. Carrazza, L. Del Debbio, S. Forte, A. Guffanti, N. P. Hartland and J. Rojo, *Nucl. Phys. B* **877** (2013) 290, [arXiv:1308.0598](#).
- [363] K. Hagiwara, S. Ishihara, R. Szalapski and D. Zeppenfeld, *Phys. Rev. D* **48** (1993) 2182.
- [364] K. Hagiwara, S. Ishihara, R. Szalapski and D. Zeppenfeld, *Phys. Lett. B* **283** (1992) 353.
- [365] A. De Rujula, M. B. Gavela, P. Hernandez and E. Masso, *Nucl. Phys. B* **384** (1992) 3.
- [366] S. S. Biswal, M. Patra and S. Raychaudhuri, [arXiv:1405.6056](#).
- [367] I. T. Cakir, O. Cakir, A. Senol and A. T. Tasci, *Acta Phys. Polon. B* **45** (2014) 1947, [arXiv:1406.7696](#).
- [368] R. Li, X.-M. Shen, K. Wang, T. Xu, L. Zhang and G. Zhu, *Phys. Rev. D* **97** (2018) 075043, [arXiv:1711.05607](#).
- [369] M. Köksal, A. A. Billur, A. Gutiérrez-Rodríguez and M. A. Hernández-Ruíz, [arXiv:1910.06747](#).
- [370] A. Gutiérrez-Rodríguez, M. Köksal, A. A. Billur and M. A. Hernández-Ruíz, [arXiv:1910.02307](#).
- [371] CMS Collaboration, A. M. Sirunyan *et al.*, *Phys. Lett. B* **772** (2017) 21, [arXiv:1703.06095](#).
- [372] CMS Collaboration, A. M. Sirunyan *et al.*, [arXiv:1907.08354](#).
- [373] S. Villa, *Nucl. Phys. Proc. Suppl.* **142** (2005) 391, [arXiv:hep-ph/0410208](#).
- [374] K. O. Mikaelian, M. A. Samuel and D. Sahdev, *Phys. Rev. Lett.* **43** (1979) 746.
- [375] S. J. Brodsky and R. W. Brown, *Phys. Rev. Lett.* **49** (1982) 966.
- [376] R. W. Brown, K. L. Kowalski and S. J. Brodsky, *Phys. Rev. D* **28** (1983) 624. [Addendum: *Phys. Rev. D* **29**, 2100(1984)].
- [377] M. A. Samuel and J. H. Reid, *Prog. Theor. Phys.* **76** (1986) 184.
- [378] S. Dutta, A. Goyal, M. Kumar and B. Mellado, *Eur. Phys. J. C* **75** (2015) 577, [arXiv:1307.1688](#).
- [379] A. O. Bouzas and F. Larios, *Phys. Rev. D* **88** (2013) 094007, [arXiv:1308.5634](#).
- [380] S. Ovin, X. Rouby and V. Lemaitre, “DELPHES, a framework for fast simulation of a generic collider experiment,” 2009. [arXiv:0903.2225](#).
- [381] CMS Collaboration, V. Khachatryan *et al.*, *JHEP* **06** (2014) 090, [arXiv:1403.7366](#).

- [382] H. Sun, *PoS DIS2018* (2018) 167.
- [383] CMS Collaboration, V. Khachatryan *et al.*, *Phys. Lett. B*736 (2014) 33–57, [arXiv:1404.2292](#).
- [384] J. A. Aguilar-Saavedra, *Acta Phys. Polon.* B35 (2004) 2695–2710, [arXiv:hep-ph/0409342](#).
- [385] J. Charles *et al.*, *Phys. Rev. D*91 (2015) 073007, [arXiv:1501.05013](#).
- [386] I. Turk Cakir, A. Yilmaz, H. Denizli, A. Senol, H. Karadeniz and O. Cakir, *Adv. High Energy Phys.* 2017 (2017) 1572053, [arXiv:1705.05419](#).
- [387] O. Cakir, A. Yilmaz, I. Turk Cakir, A. Senol and H. Denizli, *Nucl. Phys. B*944 (2019) 114640, [arXiv:1809.01923](#).
- [388] H. Sun and X. Wang, *Eur. Phys. J. C*78 (2018) 281, [arXiv:1602.04670](#).
- [389] J. A. Aguilar-Saavedra and T. Riemann, “Probing top flavor changing neutral couplings at TESLA,” in *5th Workshop of the 2nd ECFA, Obernai, France, October 16-19, 1999*, 2001. [arXiv:hep-ph/0102197](#).
- [390] Top Quark Working Group, K. Agashe *et al.*, “Working Group Report: Top Quark,” in *Community Summer Study on the Future of U.S. Particle Physics: Minneapolis, MN, USA, July 29-August 6, 2013*, 2013. [arXiv:1311.2028](#).
- [391] B. Coleppa, M. Kumar, S. Kumar and B. Mellado, *Phys. Lett. B*770 (2017) 335–341, [arXiv:1702.03426](#).
- [392] S. Atag and B. Sahin, *Phys. Rev. D*73 (2006) 074001.
- [393] G. R. Boroun, *Phys. Lett. B*744 (2015) 142–145, [arXiv:1503.01590](#).
- [394] European Muon Collaboration, J. J. Aubert *et al.*, *Phys. Lett.* 123B (1983) 275.
- [395] J. Gomez *et al.*, *Phys. Rev. D*49 (1994) 4348.
- [396] New Muon Collaboration, P. Amaudruz *et al.*, *Nucl. Phys. B*441 (1995) 3, [arXiv:hep-ph/9503291](#).
- [397] New Muon Collaboration, M. Arneodo *et al.*, *Nucl. Phys. B*441 (1995) 12, [arXiv:hep-ex/9504002](#).
- [398] New Muon Collaboration, M. Arneodo *et al.*, *Nucl. Phys. B*481 (1996) 3.
- [399] European Muon Collaboration, J. Ashman *et al.*, *Z. Phys. C*57 (1993) 211.
- [400] New Muon Collaboration, M. Arneodo *et al.*, *Nucl. Phys. B*481 (1996) 23.
- [401] New Muon Collaboration, P. Amaudruz *et al.*, *Nucl. Phys. B*371 (1992) 3.
- [402] M. Arneodo, *Phys. Rept.* 240 (1994) 301.
- [403] D. F. Geesaman, K. Saito and A. W. Thomas, *Ann. Rev. Nucl. Part. Sci.* 45 (1995) 337.
- [404] K. J. Eskola, P. Paakkinen, H. Paukkunen and C. A. Salgado, *Eur. Phys. J. C*77 (2017) 163, [arXiv:1612.05741](#).
- [405] C. A. Salgado *et al.*, *J. Phys. G*39 (2012) 015010, [arXiv:1105.3919](#).
- [406] K. J. Golec-Biernat and M. Wusthoff, *Phys. Rev. D*59 (1998) 014017, [arXiv:hep-ph/9807513](#).
- [407] L. Frankfurt, V. Guzey and M. Strikman, *Phys. Rept.* 512 (2012) 255, [arXiv:1106.2091](#).
- [408] F. Gelis, E. Iancu, J. Jalilian-Marian and R. Venugopalan, *Ann. Rev. Nucl. Part. Sci.* 60 (2010) 463, [arXiv:1002.0333](#).
- [409] Y. V. Kovchegov and E. Levin, *Camb. Monogr. Part. Phys. Nucl. Phys. Cosmol.* 33 (2012) 1.
- [410] B. L. Ioffe, V. S. Fadin and L. N. Lipatov, *Quantum chromodynamics: Perturbative and nonperturbative aspects*, vol. 30. Cambridge Univ. Press, 2010.
- [411] J. Collins, *Camb. Monogr. Part. Phys. Nucl. Phys. Cosmol.* 32 (2011) 1.
- [412] H. Paukkunen, *Nucl. Phys. A*967 (2017) 241, [arXiv:1704.04036](#).
- [413] H. Paukkunen, *PoS HardProbes2018* (2018) 014, [arXiv:1811.01976](#).
- [414] K. J. Eskola, H. Paukkunen and C. A. Salgado, *JHEP* 04 (2009) 065, [arXiv:0902.4154](#).
- [415] D. de Florian, R. Sassot, P. Zurita and M. Stratmann, *Phys. Rev. D*85 (2012) 074028, [arXiv:1112.6324](#).
- [416] K. Kovarik *et al.*, *Phys. Rev. D*93 (2016) 085037, [arXiv:1509.00792](#).
- [417] H. Khanpour and S. Atashbar Tehrani, *Phys. Rev. D*93 (2016) 014026, [arXiv:1601.00939](#).
- [418] NNPDF Collaboration, R. Abdul Khalek, J. J. Ethier and J. Rojo, *Eur. Phys. J. C*79 (2019) 471, [arXiv:1904.00018](#).
- [419] H. Paukkunen and C. A. Salgado, *JHEP* 07 (2010) 032, [arXiv:1004.3140](#).

- [420] K. Kovarik, I. Schienbein, F. I. Olness, Y. Yu, C. Keppel, J. G. Morfin, J. F. Owens and T. Stavreva, *Phys. Rev. Lett.* **106** (2011) 122301, [arXiv:1012.0286](#).
- [421] H. Paukkunen and C. A. Salgado, *Phys. Rev. Lett.* **110** (2013) 212301, [arXiv:1302.2001](#).
- [422] N. Armesto, *J. Phys.* **G32** (2006) R367, [arXiv:hep-ph/0604108](#).
- [423] K. J. Eskola, P. Paakkinen and H. Paukkunen, *Eur. Phys. J.* **C79** (2019) 511, [arXiv:1903.09832](#).
- [424] N. Armesto, H. Paukkunen, J. M. Penín, C. A. Salgado and P. Zurita, *Eur. Phys. J.* **C76** (2016) 218, [arXiv:1512.01528](#).
- [425] A. Kusina, F. Lyonnet, D. B. Clark, E. Godat, T. Jezo, K. Kovarik, F. I. Olness, I. Schienbein and J. Y. Yu, *Eur. Phys. J.* **C77** (2017) 488, [arXiv:1610.02925](#).
- [426] N. Armesto, A. Capella, A. B. Kaidalov, J. Lopez-Albacete and C. A. Salgado, *Eur. Phys. J.* **C29** (2003) 531, [arXiv:hep-ph/0304119](#).
- [427] N. Armesto, A. B. Kaidalov, C. A. Salgado and K. Tywoniuk, *Eur. Phys. J.* **C68** (2010) 447, [arXiv:1003.2947](#).
- [428] S. J. Brodsky, I. Schmidt and J.-J. Yang, *Phys. Rev.* **D70** (2004) 116003, [arXiv:hep-ph/0409279](#).
- [429] Z. Citron *et al.*, “Future physics opportunities for high-density QCD at the LHC with heavy-ion and proton beams,” in *HL/HE-LHC Workshop: Workshop on the Physics of HL-LHC, and Perspectives at HE-LHC Geneva, Switzerland, June 18-20, 2018*, 2018. [arXiv:1812.06772](#).
- [430] M. Klein, *EPJ Web Conf.* **112** (2016) 03002.
- [431] LHeC Study Group, H. Paukkunen, *PoS DIS2017* (2018) 109, [arXiv:1709.08342](#).
- [432] E. C. Aschenauer, S. Fazio, M. A. C. Lamont, H. Paukkunen and P. Zurita, *Phys. Rev.* **D96** (2017) 114005, [arXiv:1708.05654](#).
- [433] LHCb Collaboration, R. Aaij *et al.*, *JHEP* **10** (2017) 090, [arXiv:1707.02750](#).
- [434] LHCb Collaboration, R. Aaij *et al.*, *Phys. Rev.* **D99** (2019) 052011, [arXiv:1902.05599](#).
- [435] K. J. Eskola, I. Helenius, P. Paakkinen and H. Paukkunen, [arXiv:1906.02512](#).
- [436] I. Helenius, K. J. Eskola and H. Paukkunen, *JHEP* **09** (2014) 138, [arXiv:1406.1689](#).
- [437] J. Pumplin, D. Stump, R. Brock, D. Casey, J. Huston, J. Kalk, H. L. Lai and W. K. Tung, *Phys. Rev.* **D65** (2001) 014013, [arXiv:hep-ph/0101032](#).
- [438] N. Armesto, “Nuclear pdfs.” 2nd FCC Physics Workshop (CERN, January 15th-19th 2018), 2018.
- [439] N. Armesto, *PoS HardProbes2018* (2019) 123.
- [440] T. Lappi and H. Mäntysaari, *Phys. Rev.* **C87** (2013) 032201, [arXiv:1301.4095](#).
- [441] A. J. Baltz, *Phys. Rept.* **458** (2008) 1, [arXiv:0706.3356](#).
- [442] V. N. Gribov and A. A. Migdal, *Sov. J. Nucl. Phys.* **8** (1969) 583. [*Yad. Fiz.*8,1002(1968)].
- [443] L. L. Frankfurt, G. A. Miller and M. Strikman, *Ann. Rev. Nucl. Part. Sci.* **44** (1994) 501, [arXiv:hep-ph/9407274](#).
- [444] C. Marquet, M. R. Moldes and P. Zurita, *Phys. Lett.* **B772** (2017) 607, [arXiv:1702.00839](#).
- [445] L. L. Frankfurt and M. I. Strikman, *Phys. Lett.* **B382** (1996) 6.
- [446] H. Kowalski, T. Lappi, C. Marquet and R. Venugopalan, *Phys. Rev.* **C78** (2008) 045201, [arXiv:0805.4071](#).
- [447] A. H. Mueller and H. Navelet, *Nucl. Phys.* **B282** (1987) 727.
- [448] M. Deak, F. Hautmann, H. Jung and K. Kutak, *Eur. Phys. J.* **C72** (2012) 1982, [arXiv:1112.6354](#).
- [449] J. L. Albacete and C. Marquet, *Phys. Rev. Lett.* **105** (2010) 162301, [arXiv:1005.4065](#).
- [450] T. Lappi and H. Mäntysaari, *Nucl. Phys.* **A908** (2013) 51, [arXiv:1209.2853](#).
- [451] A. Stasto, S.-Y. Wei, B.-W. Xiao and F. Yuan, *Phys. Lett.* **B784** (2018) 301, [arXiv:1805.05712](#).
- [452] A. van Hameren, P. Kotko, K. Kutak, C. Marquet, E. Petreska and S. Sapeta, *JHEP* **12** (2016) 034, [arXiv:1607.03121](#). [Erratum: *JHEP*02,158(2019)].
- [453] CMS Collaboration, V. Khachatryan *et al.*, *JHEP* **09** (2010) 091, [arXiv:1009.4122](#).
- [454] S. Schlichting and P. Tribedy, *Adv. High Energy Phys.* **2016** (2016) 8460349, [arXiv:1611.00329](#).
- [455] C. Loizides, *Nucl. Phys.* **A956** (2016) 200, [arXiv:1602.09138](#).
- [456] B. Schenke, *Nucl. Phys.* **A967** (2017) 105, [arXiv:1704.03914](#).
- [457] P. Romatschke, *Eur. Phys. J.* **C77** (2017) 21, [arXiv:1609.02820](#).

- [458] ATLAS Collaboration, “Two-particle azimuthal correlations in photo-nuclear ultra-peripheral Pb+Pb collisions at 5.02 TeV with ATLAS,” ATLAS-CONF-2019-022, 2019.
- [459] A. Badea, A. Baty, P. Chang, G. M. Innocenti, M. Maggi, C. Mcginn, M. Peters, T.-A. Sheng, J. Thaler and Y.-J. Lee, *Phys. Rev. Lett.* **123** (2019) 212002, [arXiv:1906.00489](#).
- [460] ZEUS Collaboration, “Two-particle azimuthal correlations as a probe of collective behaviour in deep inelastic  $ep$  scattering at HERA,” 2019. [arXiv:1912.07431](#).
- [461] CMS Collaboration, S. Chatrchyan *et al.*, *Phys. Lett.* **B724** (2013) 213–240, [arXiv:1305.0609](#).
- [462] CMS Collaboration, V. Khachatryan *et al.*, *Phys. Lett.* **B765** (2017) 193–220, [arXiv:1606.06198](#).
- [463] S. D. Glazek, S. J. Brodsky, A. S. Goldhaber and R. W. Brown, *Phys. Rev.* **D97** (2018) 114021, [arXiv:1805.08847](#).
- [464] J. D. Bjorken, S. J. Brodsky and A. Scharff Goldhaber, *Phys. Lett.* **B726** (2013) 344, [arXiv:1308.1435](#).
- [465] S. J. Brodsky, H.-C. Pauli and S. S. Pinsky, *Phys. Rept.* **301** (1998) 299, [arXiv:hep-ph/9705477](#).
- [466] P. A. M. Dirac, *Rev. Mod. Phys.* **21** (1949) 392.
- [467] D. Ashery, *Nucl. Phys. Proc. Suppl.* **161** (2006) 8, [arXiv:hep-ex/0511052](#).
- [468] G. Bertsch, S. J. Brodsky, A. S. Goldhaber and J. F. Gunion, *Phys. Rev. Lett.* **47** (1981) 297.
- [469] L. Frankfurt, G. A. Miller and M. Strikman, *Phys. Rev.* **D65** (2002) 094015, [arXiv:hep-ph/0010297](#).
- [470] S. J. Brodsky, C.-R. Ji and G. P. Lepage, *Phys. Rev. Lett.* **51** (1983) 83.
- [471] S. J. Brodsky and A. H. Müller, *Phys. Lett.* **B206** (1988) 685.
- [472] S. J. Brodsky, I. A. Schmidt and G. F. de Teramond, *Phys. Rev. Lett.* **64** (1990) 1011.
- [473] S. J. Brodsky and H. J. Lu, *Phys. Rev. Lett.* **64** (1990) 1342.
- [474] S. J. Brodsky, I. Schmidt and S. Liuti, [arXiv:1908.06317](#).
- [475] ATLAS Collaboration, G. Aad *et al.*, *Phys. Lett.* **B716** (2012) 1, [arXiv:1207.7214](#).
- [476] CMS Collaboration, S. Chatrchyan *et al.*, *Phys. Lett.* **B716** (2012) 30, [arXiv:1207.7235](#).
- [477] G. S. Guralnik, C. R. Hagen and T. W. B. Kibble, *Phys. Rev. Lett.* **13** (1964) 585–587. [,162(1964)].
- [478] A. A. Migdal and A. M. Polyakov, *Sov. Phys. JETP* **24** (1967) 91–98. [*Zh. Eksp. Teor. Fiz.*51,135(1966)].
- [479] S. Gori, C. Grojean, A. Juste and A. Paul, *JHEP* **01** (2018) 108, [arXiv:1710.03752](#).
- [480] T. Cohen, N. Craig, G. F. Giudice and M. McCullough, *JHEP* **05** (2018) 091, [arXiv:1803.03647](#).
- [481] J. Blümlein, G.J.van Oldenborgh and R. Rückl, *Nucl. Phys.* **B395** (1993) 35–59, [arXiv:hep-ph/9209219](#).
- [482] J. Pumplin, D. R. Stump, J. Huston, H. L. Lai, P. M. Nadolsky and W. K. Tung, *JHEP* **07** (2002) 012, [arXiv:hep-ph/0201195](#).
- [483] J. Alwall, R. Frederix, S. Frixione, V. Hirschi, F. Maltoni, O. Mattelaer, H.-S. Shao, T. Stelzer, P. Torrielli and M. Zaro, *Journal of High Energy Physics* **2014** (2014) .
- [484] M. Kumar, X. Ruan, R. Islam, A. S. Cornell, M. Klein, U. Klein and B. Mellado, *Phys. Lett.* **B764** (2017) 247–253, [arXiv:1509.04016](#).
- [485] LHC Higgs Cross Section Working Group Collaboration, D. de Florian *et al.*, [arXiv:1610.07922](#).
- [486] D. M. Asner *et al.*, “ILC Higgs White Paper,” in *Proceedings, 2013 Community Summer Study on the Future of U.S. Particle Physics: Snowmass on the Mississippi (CSS2013): Minneapolis, MN, USA, July 29-August 6, 2013*, 2013. [arXiv:1310.0763](#).  
<http://www.slac.stanford.edu/econf/C1307292/docs/submittedArxivFiles/1310.0763.pdf>.
- [487] H. Abramowicz *et al.*, *Eur. Phys. J.* **C77** (2017) 475, [arXiv:1608.07538](#).
- [488] FCC Collaboration, A. Abada *et al.*, .
- [489] Higgs Cross Section Working Group, <https://twiki.cern.ch/twiki/bin/view/LHCPhysics/CERNYellowReportPageBR> .
- [490] T. Han and B. Mellado, *Phys. Rev.* **D82** (2010) 016009, [arXiv:0909.2460](#).
- [491] M. Tanaka, *Bachelor Thesis, Tokyo Institute of Technology (in Japanese)* (2014) .
- [492] E. Kay, *Master Thesis, Liverpool University* (2014) .
- [493] U. Klein, *Poster at 37th International Conference on High Energy Physics (ICHEP), Valencia* (2014) .
- [494] U. Klein, *Talk at Chavannes* (2015) .
- [495] D. Hampson and I. Harris, *Theses, Liverpool University* (2016 and 2017) .

- [496] ATLAS Collaboration, M. Aaboud *et al.*, *Phys. Lett. B*786 (2018) 59–86, [arXiv:1808.08238](#).
- [497] CMS Collaboration, A. M. Sirunyan *et al.*, *Phys. Rev. Lett.* 121 (2018) 121801, [arXiv:1808.08242](#).
- [498] ATLAS and CMS Collaborations, *CERN Yellow Rep. Monogr.* 7 (2019) Addendum, [arXiv:1902.10229](#).
- [499] T. Sj strand, S. Mrenna and P. Skands, *Journal of High Energy Physics* 2006 (2006) 026?026.
- [500] , *Talk at Chavannes* (2014) . [https://indico.cern.ch/event/278903/contributions/631181/attachments/510303/704309/Chavannes\\_UKLein\\_20.01.2014.pdf](https://indico.cern.ch/event/278903/contributions/631181/attachments/510303/704309/Chavannes_UKLein_20.01.2014.pdf).
- [501] J. de Favereau, C. Delaere, P. Demin, A. Giammanco, V. Lema tre, A. Mertens and M. Selvaggi, *Journal of High Energy Physics* 2014 (2014) .
- [502] R. Li, B.-W. Wang, K. Wang, X. Zhang and Z. Zhou, *Phys. Rev. D*100 (2019) 053008, [arXiv:1905.09457](#).
- [503] A. H cker *et al.*, “TMVA - Toolkit for Multivariate Data Analysis,” CERN-OPEN-2007-007, 2007. [arXiv:physics/0703039](#).
- [504] S. Greder, *b quark tagging and cross-section measurement in quark pair production at D0*. PhD thesis, Louis Pasteur U., Strasbourg I, 2004.
- [505] Y. Banda, T. Lastovicka and A. Nomerotski, “Measurement of the higgs boson decay branching ratio to charm quarks at the ilc,” 2009.
- [506] ATLAS Collaboration, G. Aad *et al.*, *Phys. Rev. D*100 (2019) 032007, [arXiv:1905.07714](#).
- [507] ATLAS Collaboration, M. Aaboud *et al.*, *Eur. Phys. J. C*77 (2017) 361, [arXiv:1702.05725](#).
- [508] C. Englert, R. Kogler, H. Schulz and M. Spannowsky, *Eur. Phys. J. C*76 (2016) 393, [arXiv:1511.05170](#).
- [509] LHC Higgs Cross Section Working Group Collaboration, S. Dittmaier *et al.*, [arXiv:1101.0593](#).
- [510] T. Barklow, K. Fujii, S. Jung, R. Karl, J. List, T. Ogawa, M. E. Peskin and J. Tian, *Phys. Rev. D*97 (2018) 053003, [arXiv:1708.08912](#).
- [511] M. Trott, *Invited Talk at the LHeC Workshop, Chavannes* (2014) .
- [512] C. Collaboration, *CMS PAS FTR-18-011* (2018) .
- [513] S. D. Rindani, P. Sharma and A. Shivaji, *Phys. Lett. B*761 (2016) 25, [arXiv:1605.03806](#).
- [514] S. S. Biswal, R. M. Godbole, B. Mellado and S. Raychaudhuri, *Phys. Rev. Lett.* 109 (2012) 261801, [arXiv:1203.6285](#).
- [515] A. Alloul, N. D. Christensen, C. Degrande, C. Duhr and B. Fuks, *Comput. Phys. Commun.* 185 (2014) 2250, [arXiv:1310.1921](#).
- [516] R. D. Ball *et al.*, *Nucl. Phys. B*867 (2013) 244, [arXiv:1207.1303](#).
- [517] NNPDF Collaboration, C. S. Deans, “Progress in the NNPDF global analysis,” in *Proceedings, 48th Rencontres de Moriond on QCD and High Energy Interactions: La Thuile, Italy, March 9-16, 2013*, 2013. [arXiv:1304.2781](#). <https://inspirehep.net/record/1227810/files/arXiv:1304.2781.pdf>.
- [518] Y.-L. Tang, C. Zhang and S.-h. Zhu, *Phys. Rev. D*94 (2016) 011702, [arXiv:1508.01095](#).
- [519] C. Bernaciak, T. Plehn, P. Schichtel and J. Tattersall, *Phys. Rev. D*91 (2015) 035024, [arXiv:1411.7699](#).
- [520] R. J. Cashmore *et al.*, *Phys. Rept.* 122 (1985) 275–386.
- [521] S. Buddenbrock, A. S. Cornell, Y. Fang, A. Fadol Mohammed, M. Kumar, B. Mellado and K. G. Tomiwa, *JHEP* 10 (2019) 157, [arXiv:1901.05300](#).
- [522] W. Liu, H. Sun, X. Wang and X. Luo, *Phys. Rev. D*92 (2015) 074015, [arXiv:1507.03264](#).
- [523] X. Wang, H. Sun and X. Luo, *Adv. High Energy Phys.* 2017 (2017) 4693213, [arXiv:1703.02691](#).
- [524] ATLAS Collaboration, M. Aaboud *et al.*, *Phys. Rev. D*98 (2018) 032002, [arXiv:1805.03483](#).
- [525] CMS Collaboration, V. Khachatryan *et al.*, *JHEP* 02 (2017) 079, [arXiv:1610.04857](#).
- [526] J. Hernandez-Sanchez, O. Flores-Sanchez, C. G. Honorato, S. Moretti and S. Rosado, *PoS CHARGED2016* (2017) 032, [arXiv:1612.06316](#).
- [527] CMS Collaboration, A. M. Sirunyan *et al.*, *JHEP* 11 (2018) 115, [arXiv:1808.06575](#).
- [528] CMS Collaboration, V. Khachatryan *et al.*, *JHEP* 12 (2015) 178, [arXiv:1510.04252](#).
- [529] S. P. Das, J. Hernandez-Sanchez, S. Moretti and A. Rosado, [arXiv:1806.08361](#).
- [530] H. Sun, X. Luo, W. Wei and T. Liu, *Phys. Rev. D*96 (2017) 095003, [arXiv:1710.06284](#).
- [531] G. Azuelos, H. Sun and K. Wang, *Phys. Rev. D*97 (2018) 116005, [arXiv:1712.07505](#).
- [532] CMS Collaboration, A. M. Sirunyan *et al.*, *Phys. Rev. Lett.* 119 (2017) 141802, [arXiv:1705.02942](#).

- [533] CMS Collaboration, A. M. Sirunyan *et al.*, *Phys. Rev. Lett.* **120** (2018) 081801, [arXiv:1709.05822](#).
- [534] C. Mosomane, M. Kumar, A. S. Cornell and B. Mellado, *J. Phys. Conf. Ser.* **889** (2017) 012004, [arXiv:1707.05997](#).
- [535] L. Delle Rose, O. Fischer and A. Hammad, *Int. J. Mod. Phys. A* **34** (2019) 1950127, [arXiv:1809.04321](#).
- [536] CMS Collaboration, A. M. Sirunyan *et al.*, *JHEP* **06** (2018) 127, [arXiv:1804.01939](#). [Erratum: *JHEP* **03**,128(2019)].
- [537] CMS Collaboration, “Search for a new scalar resonance decaying to a pair of Z bosons at the High-Luminosity LHC,” CMS-PAS-FTR-18-040, 2019.
- [538] S. P. Das, J. Hernández-Sánchez, S. Moretti, A. Rosado and R. Xoxocotzi, *Phys. Rev. D* **94** (2016) 055003, [arXiv:1503.01464](#).
- [539] S. P. Das and M. Nowakowski, *Phys. Rev. D* **96** (2017) 055014, [arXiv:1612.07241](#).
- [540] I. T. Cakir, O. Cakir, A. Senol and A. T. Tasci, *Mod. Phys. Lett. A* **28** (2013) 1350142, [arXiv:1304.3616](#).
- [541] H. Hesari, H. Khanpour and M. Mohammadi Najafabadi, *Phys. Rev. D* **97** (2018) 095041, [arXiv:1805.04697](#).
- [542] S. Liu, Y.-L. Tang, C. Zhang and S.-h. Zhu, *Eur. Phys. J. C* **77** (2017) 457, [arXiv:1608.08458](#).
- [543] D. Curtin, K. Deshpande, O. Fischer and J. Zurita, *JHEP* **07** (2018) 024, [arXiv:1712.07135](#).
- [544] G. Azuelos, M. D’Onofrio, S. Iwamoto and K. Wang, [arXiv:1912.03823](#).
- [545] C. Han, R. Li, R.-Q. Pan and K. Wang, *Phys. Rev. D* **98** (2018) 115003, [arXiv:1802.03679](#).
- [546] S. Kuday, *J. Korean Phys. Soc.* **64** (2014) 1783–1787, [arXiv:1304.2124](#).
- [547] R.-Y. Zhang, H. Wei, L. Han and W.-G. Ma, *Mod. Phys. Lett. A* **29** (2014) 1450029, [arXiv:1401.4266](#).
- [548] X.-P. Li, L. Guo, W.-G. Ma, R.-Y. Zhang, L. Han and M. Song, *Phys. Rev. D* **88** (2013) 014023, [arXiv:1307.2308](#).
- [549] J. A. Evans and D. Mckeen, “The Light Gluino Gap,” 2018. [arXiv:1803.01880](#).
- [550] D. Curtin, K. Deshpande, O. Fischer and J. Zurita, *Phys. Rev. D* **99** (2019) 055011, [arXiv:1812.01568](#).
- [551] S. Antusch and O. Fischer, *JHEP* **05** (2015) 053, [arXiv:1502.05915](#).
- [552] S. Antusch, E. Cazzato and O. Fischer, *Int. J. Mod. Phys. A* **32** (2017) 1750078, [arXiv:1612.02728](#).
- [553] S. Antusch, O. Fischer and A. Hammad, [arXiv:1908.02852](#).
- [554] A. Das, S. Jana, S. Mandal and S. Nandi, *Phys. Rev. D* **99** (2019) 055030, [arXiv:1811.04291](#).
- [555] ATLAS Collaboration, G. Aad *et al.*, [arXiv:1905.09787](#).
- [556] S. Antusch, E. Cazzato and O. Fischer, *Phys. Lett. B* **774** (2017) 114–118, [arXiv:1706.05990](#).
- [557] DELPHI Collaboration, P. Abreu *et al.*, *Z. Phys. C* **74** (1997) 57–71. [Erratum: *Z. Phys.* **C75**,580(1997)].
- [558] MEG Collaboration, J. Adam *et al.*, *Phys. Rev. Lett.* **110** (2013) 201801, [arXiv:1303.0754](#).
- [559] L. Duarte, G. A. González-Sprinberg and O. A. Sampayo, *Phys. Rev. D* **91** (2015) 053007, [arXiv:1412.1433](#).
- [560] L. Duarte, G. Zapata and O. A. Sampayo, *Eur. Phys. J. C* **78** (2018) 352, [arXiv:1802.07620](#).
- [561] S. Mondal and S. K. Rai, *Phys. Rev. D* **93** (2016) 011702, [arXiv:1510.08632](#).
- [562] M. Lindner, F. S. Queiroz, W. Rodejohann and C. E. Yaguna, *JHEP* **06** (2016) 140, [arXiv:1604.08596](#).
- [563] S. Mondal and S. K. Rai, *Phys. Rev. D* **94** (2016) 033008, [arXiv:1605.04508](#).
- [564] S. Jana, N. Okada and D. Raut, [arXiv:1911.09037](#).
- [565] B. Holdom, *Phys. Lett.* **166B** (1986) 196–198.
- [566] M. D’Onofrio, O. Fischer and Z. S. Wang, “Searching for Dark Photons at the LHeC and FCC-he,” 2019. [arXiv:1909.02312](#).
- [567] LHCb Collaboration, R. Aaij *et al.*, *Phys. Rev. Lett.* **120** (2018) 061801, [arXiv:1710.02867](#).
- [568] S. Heeba and F. Kahlhoefer, “Probing the freeze-in mechanism in dark matter models with  $U(1)'$  gauge extensions,” 2019. [arXiv:1908.09834](#).
- [569] C.-X. Yue, M.-Z. Liu and Y.-C. Guo, *Phys. Rev. D* **100** (2019) 015020, [arXiv:1904.10657](#).
- [570] HFLAV Collaboration, Y. S. Amhis *et al.*, [arXiv:1909.12524](#).
- [571] J. C. Pati and A. Salam, *Phys. Rev. D* **10** (1974) 275–289. [Erratum: *Phys. Rev.* **D11**,703(1975)].

- [572] W. Buchmuller, R. Ruckl and D. Wyler, *Phys. Lett. B*191 (1987) 442–448. [Erratum: *Phys. Lett. B*448,320(1999)].
- [573] I. Doršner, S. Fajfer, A. Greljo, J. F. Kamenik and N. Košnik, *Phys. Rept.* 641 (2016) 1–68, [arXiv:1603.04993](https://arxiv.org/abs/1603.04993).
- [574] ATLAS Collaboration, “ATLAS Exotics Searches,” [https://atlas.web.cern.ch/Atlas/GROUPS/PHYSICS/CombinedSummaryPlots/EXOTICS/ATLAS\\_Exotics\\_Summary/ATLAS\\_Exotics\\_Summary.pdf](https://atlas.web.cern.ch/Atlas/GROUPS/PHYSICS/CombinedSummaryPlots/EXOTICS/ATLAS_Exotics_Summary/ATLAS_Exotics_Summary.pdf).
- [575] CMS Collaboration, “Overview of CMS Exo Results,” [https://twiki.cern.ch/twiki/pub/CMSPublic/SummaryPlotsEX013TeV/EX0\\_barchart\\_Jan19.svg](https://twiki.cern.ch/twiki/pub/CMSPublic/SummaryPlotsEX013TeV/EX0_barchart_Jan19.svg).
- [576] J. Zhang, C.-X. Yue and Z.-C. Liu, *Mod. Phys. Lett. A*33 (2018) 1850039.
- [577] I. Doršner and A. Greljo, *JHEP* 05 (2018) 126, [arXiv:1801.07641](https://arxiv.org/abs/1801.07641).
- [578] M. Bahr *et al.*, *Eur. Phys. J. C*58 (2008) 639–707, [arXiv:0803.0883](https://arxiv.org/abs/0803.0883).
- [579] J. Bellm *et al.*, *Eur. Phys. J. C*76 (2016) 196, [arXiv:1512.01178](https://arxiv.org/abs/1512.01178).
- [580] S. Mandal, M. Mitra and N. Sinha, *Phys. Rev. D*98 (2018) 095004, [arXiv:1807.06455](https://arxiv.org/abs/1807.06455).
- [581] R. Padhan, S. Mandal, M. Mitra and N. Sinha, [arXiv:1912.07236](https://arxiv.org/abs/1912.07236).
- [582] Y.-J. Zhang, L. Han and Y.-B. Liu, *Phys. Lett. B*768 (2017) 241–247.
- [583] Y.-B. Liu, *Nucl. Phys. B*923 (2017) 312–323, [arXiv:1704.02059](https://arxiv.org/abs/1704.02059).
- [584] L. Han, Y.-J. Zhang and Y.-B. Liu, *Phys. Lett. B*771 (2017) 106–112.
- [585] A. Ozansoy, V. Ar? and V. Çetinkaya, *Adv. High Energy Phys.* 2016 (2016) 1739027, [arXiv:1607.04437](https://arxiv.org/abs/1607.04437).
- [586] A. Caliskan, *Adv. High Energy Phys.* 2017 (2017) 4726050, [arXiv:1706.09797](https://arxiv.org/abs/1706.09797).
- [587] A. Caliskan and S. O. Kara, *Int. J. Mod. Phys. A*33 (2018) 1850141, [arXiv:1806.02037](https://arxiv.org/abs/1806.02037).
- [588] Y. O. Günayd?n, M. Sahin and S. Sultansoy, *Acta Phys. Polon.* B49 (2018) 1763, [arXiv:1707.00056](https://arxiv.org/abs/1707.00056).
- [589] M. Sahin, *Acta Phys. Polon.* B45 (2014) 1811, [arXiv:1302.5747](https://arxiv.org/abs/1302.5747).
- [590] Y. C. Acar, U. Kaya, B. B. Oner and S. Sultansoy, *J. Phys. G*44 (2017) 045005, [arXiv:1605.08028](https://arxiv.org/abs/1605.08028).
- [591] ZEUS Collaboration, H. Abramowicz *et al.*, *Phys. Lett. B*757 (2016) 468–472, [arXiv:1604.01280](https://arxiv.org/abs/1604.01280).
- [592] A. F. Zarnecki, “Leptoquarks and Contact Interactions at LeHC,” in *Proceedings, 16th International Workshop on Deep Inelastic Scattering and Related Subjects (DIS 2008): London, UK, April 7-11, 2008*, 2008. [arXiv:0809.2917](https://arxiv.org/abs/0809.2917).
- [593] P. C. M. Yock, *Int. J. Theor. Phys.* 2 (1969) 247–254.
- [594] J. S. Schwinger, *Science* 165 (1969) 757–761.
- [595] ATLAS Collaboration, G. Aad *et al.*, *Phys. Rev. Lett.* 124 (2020) 031802, [arXiv:1905.10130](https://arxiv.org/abs/1905.10130).
- [596] R. Hofstadter, *Rev. Mod. Phys.* 28 (1956) 214–254.
- [597] A. F. Zarnecki, *Eur. Phys. J. C*11 (1999) 539–557, [arXiv:hep-ph/9904334](https://arxiv.org/abs/hep-ph/9904334).
- [598] ATLAS Collaboration, M. Aaboud *et al.*, *JHEP* 10 (2017) 182, [arXiv:1707.02424](https://arxiv.org/abs/1707.02424).
- [599] CMS Collaboration, A. M. Sirunyan *et al.*, *JHEP* 04 (2019) 114, [arXiv:1812.10443](https://arxiv.org/abs/1812.10443).
- [600] A. Michel and M. Sher, *Phys. Rev. D*100 (2019) 095011, [arXiv:1909.10627](https://arxiv.org/abs/1909.10627).
- [601] G. R. Boroun, *Chin. Phys. C*41 (2017) 013104, [arXiv:1510.02914](https://arxiv.org/abs/1510.02914).
- [602] G. R. Boroun, B. Rezaei and S. Heidari, *Int. J. Mod. Phys. A*32 (2017) 1750197, [arXiv:1606.02864](https://arxiv.org/abs/1606.02864).
- [603] H.-Y. Bi, R.-Y. Zhang, H.-Y. Han, Y. Jiang and X.-G. Wu, *Phys. Rev. D*95 (2017) 034019, [arXiv:1612.07990](https://arxiv.org/abs/1612.07990).
- [604] K. He, H.-Y. Bi, R.-Y. Zhang, X.-Z. Li and W.-G. Ma, *J. Phys. G*45 (2018) 055005, [arXiv:1710.11508](https://arxiv.org/abs/1710.11508).
- [605] H.-Y. Bi, R.-Y. Zhang, X.-G. Wu, W.-G. Ma, X.-Z. Li and S. Owusu, *Phys. Rev. D*95 (2017) 074020, [arXiv:1702.07181](https://arxiv.org/abs/1702.07181).
- [606] ATLAS Collaboration Collaboration, “Prospect for a measurement of the Weak Mixing Angle in  $pp \rightarrow Z/\gamma^* \rightarrow e^+e^-$  events with the ATLAS detector at the High Luminosity Large Hadron Collider,” ATL-PHYS-PUB-2018-037, CERN, Geneva, Nov 2018. <https://cds.cern.ch/record/2649330>.
- [607] CMS Collaboration Collaboration, “A proposal for the measurement of the weak mixing angle at the HL-LHC,” CMS-PAS-FTR-17-001, CERN, Geneva, 2017. <https://cds.cern.ch/record/2294888>.
- [608] W. J. Barter, “Prospects for measurement of the weak mixing angle at LHCb,” LHCb-PUB-2018-013, CERN-LHCb-PUB-2018-013, CERN, Geneva, Nov 2018. <https://cds.cern.ch/record/2647836>.

- [609] L. A. Harland-Lang, A. D. Martin, P. Motylinski and R. S. Thorne, *Eur. Phys. J. C* **75** (2015) 204, [arXiv:1412.3989](#).
- [610] M. Klein and V. Radescu, “Partons from the LHeC,” CERN-LHeC-Note-2013-002, Jul 2013.
- [611] ATLAS Collaboration, G. Aad *et al.*, *JHEP* **09** (2015) 049, [arXiv:1503.03709](#).
- [612] ATLAS Collaboration Collaboration, “Prospects for the measurement of the W-boson mass at the HL- and HE-LHC,” ATL-PHYS-PUB-2018-026, CERN, Geneva, Oct 2018. <http://cds.cern.ch/record/2645431>.
- [613] F. Zimmermann, *ICFA Beam Dynamics Newsletter* **72** (2017) 138.
- [614] M. E. Peskin and T. Takeuchi, *Phys. Rev. D* **46** (1992) 381–409.
- [615] J. De Blas *et al.*, [arXiv:1910.14012](#).
- [616] M. Cepeda *et al.*, *CERN Yellow Rep. Monogr.* **7** (2019) 221, [arXiv:1902.00134](#).
- [617] J. Campbell and T. Neumann, *JHEP* **12** (2019) 034, [arXiv:1909.09117](#).
- [618] B. Mistlberger, *JHEP* **05** (2018) 028, [arXiv:1802.00833](#).
- [619] F. Dulat, A. Lazopoulos and B. Mistlberger, *Comput. Phys. Commun.* **233** (2018) 243, [arXiv:1802.00827](#).
- [620] LHC Higgs Cross Section Working Group Collaboration, A. David *et al.*, “LHC HXSWG interim recommendations to explore the coupling structure of a Higgs-like particle,” 2012. [arXiv:1209.0040](#).
- [621] ATLAS Collaboration, G. Aad *et al.*, *Phys. Rev. D* **101** (2020) 012002, [arXiv:1909.02845](#).
- [622] J. de Blas *et al.*, “Higgs Boson Studies at Future Particle Colliders,” 2019. [arXiv:1905.03764](#).
- [623] ATLAS Collaboration, “Study of correlation of PDF uncertainty in single top and top pair production at the LHC,” ATL-PHYS-PUB-2015-010, Geneva, May 2015.
- [624] CMS Collaboration, V. Khachatryan *et al.*, *Phys. Rev. D* **94** (2016) 072002, [arXiv:1605.00116](#).
- [625] CDF and D0 Collaborations, T. E. W. Group and T. Aaltonen, [arXiv:1608.01881](#).
- [626] CMS Collaboration, V. Khachatryan *et al.*, *Phys. Rev. D* **93** (2016) 072004, [arXiv:1509.04044](#).
- [627] ATLAS Collaboration, M. Aaboud *et al.*, *Phys. Lett. B* **761** (2016) 350–371, [arXiv:1606.02179](#).
- [628] CMS Collaboration, A. M. Sirunyan *et al.*, *Eur. Phys. J. C* **77** (2017) 354, [arXiv:1703.02530](#).
- [629] CMS Collaboration, A. M. Sirunyan *et al.*, *Eur. Phys. J. C* **78** (2018) 891, [arXiv:1805.01428](#).
- [630] ATLAS Collaboration, “Prospects for measurement of the top quark mass using  $t\bar{t}$  events with  $J/\psi \rightarrow \mu^+\mu^-$  decays with the upgraded ATLAS detector at the High Luminosity LHC.” Dec 2018.
- [631] D. Britzger, K. Rabbertz, D. Savoie, G. Sieber and M. Wobisch, *Eur. Phys. J. C* **79** (2019) 68, [arXiv:1712.00480](#).
- [632] ATLAS Collaboration, M. Aaboud *et al.*, *Phys. Rev. D* **98** (2018) 092004, [arXiv:1805.04691](#).
- [633] ATLAS Collaboration, M. Aaboud *et al.*, *Eur. Phys. J. C* **77** (2017) 872, [arXiv:1707.02562](#).
- [634] M. Johnson and D. Maître, *Phys. Rev. D* **97** (2018) 054013, [arXiv:1711.01408](#).
- [635] T. Klijnsma, S. Bethke, G. Dissertori and G. P. Salam, *Eur. Phys. J. C* **77** (2017) 778, [arXiv:1708.07495](#).
- [636] CMS Collaboration, A. M. Sirunyan *et al.*, *Submitted to: Eur. Phys. J.* (2019) , [arXiv:1904.05237](#).
- [637] CMS Collaboration, A. M. Sirunyan *et al.*, “Determination of the strong coupling constant  $\alpha_s(m_Z)$  from measurements of inclusive  $W^\pm$  and Z boson production cross sections in proton-proton collisions at  $\sqrt{s} = 7$  and 8 TeV,” 2019. [arXiv:1912.04387](#).
- [638] D. d’Enterria and A. Poldaru, “Strong coupling  $\alpha_s(m_Z)$  extraction from a combined NNLO analysis of inclusive electroweak boson cross sections at hadron colliders,” 2019. [arXiv:1912.11733](#).
- [639] B. Bouzid, F. Iddir and L. Semlala, [arXiv:1703.03959](#).
- [640] M. Grazzini, S. Kallweit, D. Rathlev and M. Wiesemann, *Phys. Lett. B* **761** (2016) 179–183, [arXiv:1604.08576](#).
- [641] M. Grazzini, S. Kallweit and M. Wiesemann, *Eur. Phys. J. C* **78** (2018) 537, [arXiv:1711.06631](#).
- [642] ATLAS Collaboration, M. Aaboud *et al.*, *Eur. Phys. J. C* **79** (2019) 535, [arXiv:1902.05759](#). Auxiliary figure.
- [643] CMS Collaboration, A. M. Sirunyan *et al.*, *JHEP* **04** (2019) 122, [arXiv:1901.03428](#).
- [644] X. Cid Vidal *et al.*, *CERN Yellow Rep. Monogr.* **7** (2019) 585–865, [arXiv:1812.07831](#).
- [645] ATLAS Collaboration, M. Aaboud *et al.*, *Phys. Rev. D* **97** (2018) 112001, [arXiv:1712.02332](#).
- [646] CMS Collaboration, A. M. Sirunyan *et al.*, *JHEP* **05** (2018) 025, [arXiv:1802.02110](#).

- [647] NNPDF Collaboration, R. D. Ball *et al.*, *JHEP* 04 (2015) 040, [arXiv:1410.8849](#).
- [648] N. Armesto and E. Scapparini, *Eur. Phys. J. Plus* 131 (2016) 52, [arXiv:1511.02151](#).
- [649] W. Busza, K. Rajagopal and W. van der Schee, *Ann. Rev. Nucl. Part. Sci.* 68 (2018) 339, [arXiv:1802.04801](#).
- [650] P. Romatschke and U. Romatschke, *Relativistic Fluid Dynamics In and Out of Equilibrium*. Cambridge Monographs on Mathematical Physics. Cambridge University Press, 2019. [arXiv:1712.05815](#).
- [651] Y. Mehtar-Tani, J. G. Milhano and K. Tywoniuk, *Int. J. Mod. Phys. A* 28 (2013) 1340013, [arXiv:1302.2579](#).
- [652] A. Andronic *et al.*, *Eur. Phys. J. C* 76 (2016) 107, [arXiv:1506.03981](#).
- [653] “Proceedings, 9th International Conference on Hard and Electromagnetic Probes of High-Energy Nuclear Collisions: Hard Probes 2018 (HP2018),” SISSA, 2018. <https://pos.sissa.it/345>.
- [654] H. A. Andrews *et al.*, [arXiv:1808.03689](#).
- [655] ALICE Collaboration, B. B. Abelev *et al.*, *Phys. Lett. B* 734 (2014) 314, [arXiv:1311.0214](#).
- [656] H. Song, S. A. Bass, U. Heinz, T. Hirano and C. Shen, *Phys. Rev. Lett.* 106 (2011) 192301, [arXiv:1011.2783](#). [Erratum: *Phys. Rev. Lett.* 109, 139904 (2012)].
- [657] H. Niemi, K. J. Eskola and R. Paatelainen, *Phys. Rev. C* 93 (2016) 024907, [arXiv:1505.02677](#).
- [658] J. Liu, C. Shen and U. Heinz, *Phys. Rev. C* 91 (2015) 064906, [arXiv:1504.02160](#). [Erratum: *Phys. Rev. C* 92, no. 4, 049904 (2015)].
- [659] B. Schenke, P. Tribedy and R. Venugopalan, *Phys. Rev. Lett.* 108 (2012) 252301, [arXiv:1202.6646](#).
- [660] J.-Y. Ollitrault, A. M. Poskanzer and S. A. Voloshin, *Phys. Rev. C* 80 (2009) 014904, [arXiv:0904.2315](#).
- [661] STAR Collaboration, J. Adams *et al.*, *Phys. Rev. C* 72 (2005) 014904, [arXiv:nucl-ex/0409033](#).
- [662] STAR Collaboration, B. I. Abelev *et al.*, *Phys. Rev. C* 79 (2009) 034909, [arXiv:0808.2041](#).
- [663] CMS Collaboration, A. M. Sirunyan *et al.*, [arXiv:1905.01486](#).
- [664] V. Guzey and M. Zhalov, *JHEP* 10 (2013) 207, [arXiv:1307.4526](#).
- [665] J. G. Contreras, *Phys. Rev. C* 96 (2017) 015203, [arXiv:1610.03350](#).
- [666] V. Guzey and M. Klasen, *Eur. Phys. J. C* 79 (2019) 396, [arXiv:1902.05126](#).
- [667] ATLAS Collaboration, M. Aaboud *et al.*, *Phys. Rev. Lett.* 121 (2018) 212301, [arXiv:1806.08708](#).
- [668] ATLAS Collaboration, M. Aaboud *et al.*, *Phys. Rev. C* 100 (2019) 034903, [arXiv:1901.10440](#).
- [669] R. Aaij *et al.*, “Expression of Interest for a Phase-II LHCb Upgrade: Opportunities in flavour physics, and beyond, in the HL-LHC era,” CERN-LHCC-2017-003, CERN, Geneva, Feb 2017.
- [670] O. Brüning, “Accelerator design.” Presented at the lhec workshop, June 2015.
- [671] D. Brandt, H. Burkhardt, M. Lamont, S. Myers and J. Wenninger, *Rept. Prog. Phys.* 63 (2000) 939.
- [672] D. S. D. Pellegrini, A. Latina and S. Bogacz, *Phys. Rev. ST-AB* 121004 (2015) .
- [673] S. A. Bogacz *et al.*, *ICFA Beam Dynamics Newsletter* 71 (2017) 135.
- [674] P. Williams, “A Staged, Multi-User X-Ray Free Electron Laser and Nuclear Physics Facility based on a Multi-Pass Recirculating Superconducting CW Linac,” in *Proceedings, Future Light Sources 2018, Shanghai*, 2018.
- [675] 12 GeV CEBAF Upgrade, Reference Design: [www.jlab.org/physics/GeV/accelerator](http://www.jlab.org/physics/GeV/accelerator) (2012).
- [676] G. Hoffstaetter and I. Bazarov, *Phys. Rev. ST-AB* 7 (2004) .
- [677] J. S. Schwinger, *Phys. Rev.* 70 (1946) 798.
- [678] D. Pellegrini, *Ph.D. Thesis, EPFL, Switzerland* (2016) .
- [679] A. Milanese, *Talk presented at the LHeC workshop at CERN* (2014) .
- [680] J. Jowett *et al.*, “The 2018 heavy-ion run of the LHC,” in *Proceedings, 10th International Particle Accelerator Conference (IPAC2019): Melbourne, Australia, May 19-24, 2019*, 2019.
- [681] T. Argyropoulos, T. Bohl, A. Lasheen, G. Papotti, D. Quartullo and E. Shaposhnikova, “Momentum slip-stacking in CERN SPS for the ion beams,” in *Proceedings, 10th International Particle Accelerator Conference (IPAC2019): Melbourne, Australia, May 19-24, 2019*, 2019.
- [682] M. Schaumann, *Phys. Rev. ST Accel. Beams* 18 (2015) 091002, [arXiv:1503.09107](#).
- [683] O. Brüning *et al.*, *ICFA Beam Dynamics Newsletter* 68 (2015) 46.

- [684] R. Calaga and E. Jensen, “A Proposal for an ERL Test Facility at CERN,” in *Proceedings, 4th International Particle Accelerator Conference (IPAC 2013): Shanghai, China, May 12-17, 2013*, 2013. <http://JACoW.org/IPAC2013/papers/wepwo049.pdf>.
- [685] F. Marhauser, “Cost Rationales for an SRF Proton Linac,” in *Proceedings, 5th International Particle Accelerator Conference (IPAC 2014): Dresden, Germany, June 15-20, 2014*, 2014.
- [686] F. Marhauser, “Recent results on a multi-cell 802 mhz bulk nb cavity.” Presented at fcc week 2018, [https://indico.cern.ch/event/656491/contributions/2932251/attachments/1629681/2597650/5\\_cell\\_Cavity\\_Marhauser.pdf](https://indico.cern.ch/event/656491/contributions/2932251/attachments/1629681/2597650/5_cell_Cavity_Marhauser.pdf), 2018.
- [687] W. Schneider, I. Campisi, E. Daly, T. Hiatt, J. Hogan, P. Kneisel, D. Machie, J. Preble, C. Rode, T. Whitlatch *et al.*, “Design of the sns cryomodule,” in *Proceedings, the 2001 Particle Accelerator Conference (PACS2001)*, 2001.
- [688] V. Parma *et al.*, “Conceptual design of the superconducting proton linac short cryo-module,” in *Proceedings of the SRF2011, Chicago, July*, 2011.
- [689] G. Olivier, J. Thermeau and P. Bosland, “Ess cryomodules for elliptical cavities,” in *Proceedings of the 2013 Superconducting Radio Frequency Conference*, 2013.
- [690] H. Bluem, D. Dowell, A. Todd and L. Young, “High Brightness Thermionic Electron Gun Performance,” in *Procings, 50th Advanced ICFA Beam Dynamics Workshop on Energy Recovery Linacs (ERL’11), Tsukuba, Japan, Oct. 2011*, 2011.
- [691] F. Sannibale *et al.*, “The VHF-Gun, the LBNL High-Brightness Electron Photo-Injector for MHz-Class Repetition-Rate Applications,” in *High-Brightness Sources and Light-Driven Interactions*, Optical Society of America, 2016.
- [692] Z. Wang, Q. Gu, G. Wang and M. Zhao, “Injector Physics Design at SHINE,” in *Proceedings, 10th International Particle Accelerator Conference (IPAC’19), Melbourne, Australia, 19-24 May 2019*, JACoW Publishing, Geneva, Switzerland, Jun. 2019.
- [693] G. Shu, Y. Chen, S. Lal, H. Qian, H. Shaker and F. Stephan, “FIRST DESIGN STUDIES OF A NC CW RF GUN FOR EUROPEAN XFEL,” in *Proceedings, 10th International Particle Accelerator Conference (IPAC’19), Melbourne, Australia, 19-24 May 2019*, JACoW Publishing, Geneva, Switzerland, Jun. 2019.
- [694] J. Teichert *et al.*, *Nuclear Instruments and Methods in Physics Research Section A: Accelerators, Spectrometers, Detectors and Associated Equipment* 743 (2014) 114.
- [695] J. Bisognano *et al.*, “Wisconsin srf electron gun commissioning,” in *Proceedings, North American Particle Accelerator Conf. (NAPAC’13), Pasadena, CA, USA, Sep.-Oct. 2013*, 09 2013. <http://accelconf.web.cern.ch/AccelConf/PAC2013/papers/tupma19.pdf>.
- [696] E. Vogel *et al.*, “SRF Gun Development at DESY,” JACoW, Geneva, Sep 2018.
- [697] A. Neumann, and others, “Status of SRF Gun for bERLinPro,” in *Proceedings, ERL’19, Berlin, Germany, Sept. 2019*, 2019.
- [698] Belomestnykh, S.A. and others, “Commissioning of the 112 MHz SRF Gun,” in *Proceedings, 17th Int. Conf. RF Superconductivity, Whistler, Canada, Sep. 2015*, 2015.
- [699] Hernandez-Garcia, C. and others, “JLab FEL DC Gun,” in *Proceedings, 45th ICFA Advanced Beam Dynamics Workshop on Energy Recovery LINAC Workshop (ERL’09), Ithaca, NY, USA, June 2009*, 2009.
- [700] L. B. Jones, J. W. McKenzie, K. J. Middleman, B. L. Militsyn, Y. M. Saveliev and S. L. Smith, *Journal of Physics: Conference Series* 298 (2011) 012007.
- [701] R. Kato, Y. Honda, H. Kawata, T. Miyajima, N. Nakamura, H. Sakai, M. Shimada, Y. Tanimoto, K. Tsuchiya, “Ir-fel project at the cerl and future euv-fel lithography,” in *Presented at the 39th Int. Free Electron Laser Conf. (FEL’19), Hamburg, Germany, Aug. 2019*, 2019.
- [702] Hoffstaetter, G.H. and others, “CBETA: The Cornell/BNL 4-turn ERL with FFAG Return Arcs for eRHIC Prototyping,” in *Proceedings, 28th Linear Accelerator Conf. (LINAC’16)*, East Lansing, MI, USA, 2016.
- [703] B. Hounsell, W. Kaabi, M. Klein, B. Militsyn and C. Welsch, “Optimisation of the PERLE injector,” in *Proceedings, ERL’19, Berlin, Germany, Sept. 2019*, 2019.
- [704] R. Suleiman, P. Adderley, J. Grames, J. Hansknecht, M. Poelker and M. Stutzman, *AIP Conference Proceedings* 1970 (2018) 050007, <https://aip.scitation.org/doi/pdf/10.1063/1.504022>.
- [705] C. K. Sinclair *et al.*, “Performance of a very high voltage photoemission electron gun for a high brightness, high average current ERL injector,” in *Proceedings, 22nd Particle Accelerator Conf. (PAC’07), Albuquerque, NM, USA, 2007*.

- [706] N. Nishimori, R. Nagai, S. Matsuba, R. Hajima, M. Yamamoto, T. Miyajima, Y. Honda, H. Iijima, M. Kuriki and M. Kuwahara, *Applied Physics Letters* 102 (2013) 234103.
- [707] N. Nishimori, R. Nagai, R. Hajima, M. Yamamoto, Y. Honda, T. Miyajima and T. Uchiyama, *Phys. Rev. Accel. Beams* 22 (2019) 053402.
- [708] W. Liu, Y. Chen, W. Lu, A. Moy, M. Poelker, M. Stutzman and S. Zhang, *Applied Physics Letters* 109 (2016) 252104, <https://doi.org/10.1063/1.4972180>.
- [709] E. Wang, *AIP Conference Proceedings* 1970 (2018) 050008, <https://aip.scitation.org/doi/pdf/10.1063/1.5040227>.
- [710] A. Zaltsman and R. Lambiase, *Proceedings of the 24-th Particle Accelerator Conference, PAC-2011, TUP125* (2011) .
- [711] B. Parker, “Latest Developments and Progress on the IR magnet design.” presented at the LHeC and FCC-eh Workshop, Sept 2017.
- [712] B. Parker, “Superconducting Magnet Concepts for Electron Hadron Collider IRs.” Presented at the electrons for the lhc - lhec/fcch and perle workshop, Sept 2018.
- [713] E. Cruz-Alaniz, D. Newton, R. Tomás and M. Korostelev, *Phys. Rev. ST Accel. Beams* 18 (2015) 111001.
- [714] R. Martin and R. Tomás Garcia, “Length optimization of the detector region dipoles in LHeC and FCC-eh,” CERN-ACC-2018-0042, CERN, Geneva, Oct 2018. <http://cds.cern.ch/record/2644892>.
- [715] S. Fartoukh, *Phys. Rev. ST Accel. Beams* 16 (2013) 111002.
- [716] “Lattice repository.” <https://gitlab.cern.ch/lhec-optics/lhec-lattice>, 2019.
- [717] A. Gaddi, “Installation Issues of eh Detectors (LHC and FCC),” Talk presented at the LHeC and FCC-eh Workshop, CERN, Sept 2017.
- [718] A. Gaddi. Private communication, Jan 2019.
- [719] R. Bruce, C. Bracco, R. De Maria, M. Giovannozzi, S. Redaelli, R. Tomás Garcia, F. M. Velotti and J. Wenninger, “Updated parameters for HL-LHC aperture calculations for proton beams,” CERN-ACC-2017-0051, CERN, Geneva, Jul 2017. <https://cds.cern.ch/record/2274330>.
- [720] R. De Maria *et al.*, “HLLHCv1.3 Optics repository.” <http://lhc-optics.web.cern.ch/lhc-optics/HLLHCv1.3/>.
- [721] E. Cruz-Alaniz, R. Martin and R. Tomás, “LHeC optics with  $\beta^* = 10$  cm and  $L^* = 15$  m,” CERN-XXX-2019-XXX, CERN, Geneva, 2019.
- [722] Sixtrack web site: <http://sixtrack.web.cern.ch/SixTrack/>.
- [723] E. Cruz-Alaniz, J. L. Abelleira, L. van Riesen-Haupt, A. Seryi, R. Martin and R. Tomás, “Methods to increase the dynamic aperture of the fcc-hh lattice,” in *Proceedings. International Particle Accelerator Conference (IPAC'18), Vancouver, Canada, 2018*, JACoW, Geneva, Switzerland, May 2018.
- [724] F. Zimmermann *et al.*, “Interaction-Region Design Options for a Linac-Ring LHeC,” in *Proceedings, International Particle Accelerator Conference (IPAC'10), Kyoto, Japan, May 23-28, 2010*, JACoW, Geneva, Switzerland, May 2010.
- [725] J. L. Abelleira, H. Garcia, R. Tomás and F. Zimmermann, “Final-Focus Optics for the LHeC Electron Beam Line,” in *Proceedings, International Particle Accelerator Conference (IPAC'12), New Orleans, Louisiana, USA, May 20-25, 2012*, JACoW, Geneva, Switzerland, May 2012.
- [726] LHeC Study Group, FCC-eh Study Group, PERLE Collaboration, G. Arduini, O. Brüning and M. Klein, *PoS DIS2018* (2018) 183.
- [727] R. Tomás, “LHeC interaction region,” Talk presented at DIS 2012 Workshop, Bonn, 2012.
- [728] J. Parrell *et al.*, *IEEE Transactions on Applied Superconductivity* (2003) .
- [729] S. Russenschuck, *Field computation for accelerator magnets: analytical and numerical methods for electromagnetic design and optimization*. Wiley, Weinheim, 2010.
- [730] V. Fern, E.J. and Di Murro, K. Soga, Z. Li, L. Scibile and J. Osborne, (2018) . <https://doi.org/10.1016/j.tust.2018.04.003>.
- [731] C. Laughton, *International Journal of Mining and Geological Engineering* (1988) .
- [732] E. by M. Benedikt *et al.*, .
- [733] C. Tennant, “Energy Recovery Linacs,” in *Challenges and Goals for Accelerators in the XXI Century*, O. Brüning and S. Myers (eds.), World Scientific, 2016.

- [734] C. Tennant, “Progress at the Jefferson Laboratory FEL,” in *Particle accelerator. Proceedings, 23rd Conference, PAC’09, Vancouver, Canada, May 4-8, 2009*, 2010.  
[http://www1.jlab.org/UI/publications/view\\_pub.cfm?pub\\_id=8641](http://www1.jlab.org/UI/publications/view_pub.cfm?pub_id=8641).
- [735] G. H. Hoffstaetter and I. V. Bazarov, *Phys. Rev. ST Accel. Beams* 7 (2004) 054401.
- [736] D. R. Douglas *et al.*, *Phys. Rev. ST Accel. Beams* 9 (2006) 064403.
- [737] S. Di Mitri, M. Cornacchia and S. Spampinati, *Phys. Rev. Lett.* 110 (2013) 014801.
- [738] M. G. Fedurin, D. Kayran, V. Yakimenko, A. V. Fedotov, V. Litvinenko and P. Muggli, *Conf. Proc.* C110328 (2011) 1677.
- [739] S. Heifets, G. Stupakov and S. Krinsky, *Phys. Rev. ST Accel. Beams* 5 (2002) 064401.
- [740] Z. Huang and K.-J. Kim, *Phys. Rev. ST Accel. Beams* 5 (2002) 074401.
- [741] S. Di Mitri and M. Cornacchia, *EPL (Europhysics Letters)* 109 (2015) 62002.
- [742] C.-Y. Tsai, D. Douglas, R. Li and C. Tennant, *Phys. Rev. Accel. Beams* 19 (2016) 114401.
- [743] C.-Y. Tsai, S. Di Mitri, D. Douglas, R. Li and C. Tennant, *Phys. Rev. Accel. Beams* 20 (2017) 024401.
- [744] D. Douglas *et al.* Jefferson Laboratory Technical Note 12-017, 2012.
- [745] R. Alarcon *et al.*, *Phys. Rev. Lett.* 111 (2013) 164801.
- [746] T. Powers and C. Tennant, “Implications of incomplete energy recovery in srf-based energy recovery linacs,” in *Proceedings of the 2007 ICFR Workshop on Energy Recovery Linacs, Daresbury, UK*, 2007.
- [747] T. Powers, “Control of Microphonics for Narrow Control Bandwidth Cavities,” Talk presented at the 2017 International Conference on RF Superconductivity, Lanzhou, China, 2017.
- [748] S. Benson *et al.*, *Conf. Proc.* C070625 (2007) 79.
- [749] T. Powers, “Optimization of SRF Linacs,” in *Proceedings of the 2013 International Conference on RF Superconductivity, Paris, France*, 2013.
- [750] S. Benson *et al.*, “Development of a Bunched-Beam Electron Cooler for the Jefferson Lab Electron-Ion Collider,” in *Proceedings, 9th International Particle Accelerator Conference (IPAC 2018), Vancouver, BC Canada*, 2018.
- [751] C. Tennant. <https://userweb.jlab.org/~tennant/>.
- [752] C. Tennant, “Analysis of the Baseline PERLE Lattice,” Jefferson Laboratory Technical Note 18-031, 2018.
- [753] D. Douglas *et al.*, ““Why PERLE?” Historical Context and Technological Motivation,” Jefferson Laboratory Technical Note 18-014, 2018.
- [754] G. H. Hoffstaetter *et al.*, “CBETA Design Report, Cornell-BNL ERL Test Accelerator,” 2017.  
[arXiv:1706.04245](https://arxiv.org/abs/1706.04245).
- [755] T. Satogata *et al.*, “ER@CEBAF: A test of 5-pass energy recovery at CEBAF,” Program Advisory Committee Proposal, June 2016.
- [756] M. Frank, F. Gaede, M. Petric and A. Sailer, “Aidasoft/dd4hep,” Oct. 2018.
- [757] CMS Collaboration, G. Bianchi, *JINST* 9 (2014) C03054.
- [758] GEANT4 Collaboration, S. Agostinelli *et al.*, *Nucl. Instrum. Meth. A* 506 (2003) 250.
- [759] M. Oreglia, *A Study of the Reactions  $\psi' \rightarrow \gamma\gamma\psi$* . PhD thesis.  
<https://search.proquest.com/docview/303269954>.
- [760] J. E. Gaiser, *Charmonium Spectroscopy From Radiative Decays of the  $J/\psi$  and  $\psi'$* . PhD thesis.  
<https://search.proquest.com/docview/303269954>.
- [761] T. Skwarnicki, *A study of the radiative CASCADE transitions between the Upsilon-Prime and Upsilon resonances*. PhD thesis, Cracow, INP, 1986.  
<http://www-library.desy.de/cgi-bin/showprep.pl?DESY-F31-86-02>.
- [762] ATLAS Collaborartion Collaboration, “Technical Design Report for the Phase-II Upgrade of the ATLAS Muon Spectrometer,” 2017.
- [763] CMS Collaborartion Collaboration, “The Phase-2 Upgrade of the CMS Muon Detectors,” 2017.
- [764] LHCf Collaboration, O. Adriani *et al.*, *Phys. Lett. B* 780 (2018) 233, [arXiv:1703.07678](https://arxiv.org/abs/1703.07678).